

STRESSES AT WELD TOES
IN
TUBULAR JOINTS IN OFFSHORE STRUCTURES

by

Kim Stephen Elliott, B.Tech.

Thesis submitted to the University of Nottingham
for the degree of Doctor of Philosophy
October 1987.

**BEST COPY
AVAILABLE**

Poor quality text in
the original thesis.

This thesis is dedicated to
the 123 men who died on
board the offshore rig
Alexander L. Kielland which
capsized on 27 March 1980.

ABSTRACT

The accurate prediction of stress concentration factors (SCF) at weld toes is recognised as one of the most important factors in the design, against fatigue failure, of welded tubular joints in offshore structures. The objectives of this work are i) to study the influence of some important tubular joint and weld profile geometric parameters on the elastic SCFs at weld toes, ii) compare these values with strains which could be measured by strain gauges, and iii) to determine plastic-elastic strain distributions after local yielding has occurred in the weld.

Using 3-d frozen-stress, photoelastic techniques elastic SCFs were determined in non-overlapped corner K joints in balanced axial loading and in X joints in axial loading. For typical tube parameters, results have been obtained for different brace angles, brace spacings, weld size, weld angle and weld toe radii in the crown and saddle planes at the brace and chord wall ends of the weld. They have been presented as the product of a shell SCF K_S and a notch SCF K_n .

K_S , which was measured at the weld toe, depends on position in the brace intersection, brace angle, brace spacing and weld size. K_n depends on weld toe radius, weld angle and weld size.

Large scale 2-d photoelastic and finite element models were used to study the influence of weld profile "qualities" on K_S and K_n . Weld shapes conforming with minimum profiling requirements are called "uncontrolled". Improved weld shapes with concave profiles are called "controlled". The reductions in SCFs, due to the different profiles, depend on position (crown or saddle) when the results are presented for identical weld geometry.

Plastic-elastic and residual plastic strains were obtained in 2-d steel weldments using reflection photoelasticity and moire interferometry experimental techniques. A moire interferometer, using Helium-Neon laser light and high sensitivity diffraction gratings was designed and built for this purpose. Strains were measured in the range $20\mu\epsilon$ to 2%. Strain concentration factors of between 13 and 17 were determined in models in which the corresponding elastic values were 3.6 and 4.6 respectively.

TABLE OF CONTENTS

	Page No.
ABSTRACT	
NOTATION	vi
CHAPTER 1 INTRODUCTION	
1.1 General Assessment of the Use of Welded Tubular Joints in Offshore Structures	1
1.2 Definitions of Stresses in Tubular Joints	2
1.3 Design Against Fatigue Failure by Reductions in SCFs	4
1.4 The Relevance of Plastic-Elastic Strains	6
1.5 Objectives of This Work	7
1.6 Methods of Analysis	7
CHAPTER 2 LITERATURE REVIEW	
2.1 Introduction	12
2.2 Tubular Joint Stresses and Shell SCFs	13
2.3 Stresses at Weld Toes	26
2.4 Plastic-Elastic Investigations in Tubular and Welded Joints	31
CHAPTER 3 ANALYSIS OF PROBLEM AND MODEL DESIGN	
3.1 General Considerations	53
3.2 Design of 3-d Photoelastic Models	55
3.3 Design of 2-d Photoelastic and Finite Element Models	61
3.4 Design of 2-d Steel Models	66

CHAPTER 4	EXPERIMENTAL TECHNIQUES	
4.1	Introduction	87
4.2	Experimental and Numerical Methods	89
4.3	Model Manufacture	104
4.4	Dimensional Accuracy and Material Properties	110
4.5	Loading	114
4.6	Measurement	120
CHAPTER 5	ANALYSIS OF READINGS	
5.1	Determination of Stresses by Photoelasticity	161
5.2	Determination of Elastic and Plastic-Elastic Strains using Reflection Photoelasticity	168
5.3	Displacements and Strains using Moiré Interferometry	171
CHAPTER 6	RESULTS	
6.1	Presentation of Results	184
6.2	Elastic Stress and Strain Distributions	185
6.3	Elastic Stress Concentration Factors	194
6.4	Stress Zones	206
6.5	Plastic-Elastic Strain Distributions	207
6.6	Plastic-Elastic Strain Concentration Factors	213
6.7	Extent of Plastic Regions	214
6.8	Effect of Out-of-Plane Strains on In-Plane Strains	214
CHAPTER 7	ANALYSIS OF ERRORS	
7.1	3-d Photoelastic Methods	274
7.2	2-d Photoelastic Methods	283
7.3	Finite Element Methods	286

	Page No.
7.4 Reflection Photoelasticity	288
7.5 Moire Interferometry Methods	290
7.6 Summary of Errors	294
 CHAPTER 8 DISCUSSION	
8.1 Application of Stress Analysis Techniques to the Determination of Stresses in Tubular and Welded Joints	298
8.2 Evaluation of Results to Design Requirements	301
8.3 Discussion on Stress Concentration Factors	308
8.4 Relationship between Surface Stress Dis- tributions and Strain Gauge Positions and Types	313
8.5 Quantitative Analysis of Plastic-Elastic Strains using Moire Fringe Patterns	316
8.6 The Effect of Plastic-Elastic and Residual Strains on Design	316
 CHAPTER 9 CONCLUSIONS	
9.1 Synopsis of This Work	321
9.2 Elastic Stresses in 3-d Tubular Joints	321
9.3 Elastic Stresses in 2-d Joints in the Planes of Symmetry in Tubular Joints	322
9.4 Plastic-Elastic and Plastic Residual Strains	323
9.5 The Contribution of this Work to Offshore Structures Research Programmes	324
9.6 Recommendations for Future Work	325
 APPENDIX 1	327
APPENDIX 2	329
REFERENCES	334
ACKNOWLEDGMENTS	341

NOMENCLATURE

A. Definitions

Brace: The (usually) smaller diameter members which terminate at a tubular joint.

Chord: The larger diameter member which does not terminate at a tubular joint.

Controlled Weld Profile: An improved profile in which additional weld beads are deposited to add a definite size fillet at the chord weld toe of an uncontrolled profile.

Extrapolated Hot-Spot Stress: The value of the stress obtained by linear extrapolation to the weld toe of the stress distribution immediately beyond the notch zone.

Gap Separation: The meridional and/or circumferential distance at the chord surface between outside brace wall intersection points.

Hot-Spot Stress: The maximum extrapolated stress found in a welded joint.

Node: Tubular intersection comprising a chord and one or several brace(s).

Nominal Stress (or Strain): The mean axial stress (or strain) in a loaded brace measured remote from the tubular joint.

Non-Overlapped Joint: Tubular joints in which the only connections are between braces and the chord, i.e. each brace is separate from every other brace.

Notch Zone: The distance to the commencement of the linear stress distribution measured from the weld toe, both along the surfaces and through the thickness of a joint.

Offset: The distance along the chord axis between the intersection of co-planar brace axes with the chord axis.

Simple Joint: Any junction within a tubular joint or node comprising a brace wall, chord wall and weld fillet.

Stress (or Strain) Concentration Factor: The maximum elastic stress (or strain) in a simple joint divided by the nominal stress (or strain) in the brace in which the stress (or strain) concentration is found.

Stress (or Strain) Index: The measured stress (or strain) at any point divided by the nominal stress (or strain) in the brace in tension in a tubular joint.

Uncontrolled Weld Profile: A profile conforming to the minimum profiling requirements of an appropriate code of practice.

Weld Fillet: The material joining a brace stub to the chord tube.

Weld Toe: The intersection of the weld fillet with the outer tube walls.

B. Notation

$L, D, d, T, t, g, g', e, \theta, \omega, \phi, P$	tubular joint dimensions, and loading defined in Fig. 3.1
$w, h, H, r, r_1, G, \alpha, \varphi$	weld profile dimensions defined in Fig. 3.7
a	moire fringe spacing
e	error
e_{sd}	standard error
f	frequency of virtual reference grating (moire)
α	distance to point load in 2-d loading system defined in Fig. 3.6.
n	fringe order in reflection photoelasticity
u, v	components of displacements parallel to x and y axis respectively (moire)
z	stress zone
A	moire fringe gradient cross sectional area
C, C'	controlled weld profile, material constant and shear lag coefficient in reflection photoelasticity

E	Young's modulus
F	material fringe value ; frequency of model grating
I	stress indices = σ/σ_{nom}
J	strain indices = $\varepsilon/\varepsilon_{nom}$
K	stress concentration factors, defined in Fig. 1.3
N	fringe order (moire and transmission photo-elasticity)
N_{nom}	nominal fringe order in a loaded brace
P	load
S	distance from a weld toe
U	uncontrolled weld profile
α	angle of incident light in moire reference grating $2L/D$
β	angle of diffracted light in moire model grating d/D
γ	shear strain $D/2T$
γ_{nom}	mean maximum shear strain in a brace wall
δ	deflection
ε	direct strain
ζ	g/D
η	ratio of cartesian to principal stresses
η'	ratio of SCFs in controlled and uncontrolled weld toes
θ, ω, ψ	angles of rotation defined in Fig. 4.5.
λ	wavelength of light, direction of point load in 2-d loading system defined in Fig. 3.6
ν	Poisson's ratio

σ	stress
δ	maximum stress
$\sigma_{nom}, \epsilon_{nom}$	mean axial stress or strain in a brace loaded in tension
$\sigma'_{nom}, \epsilon'_{nom}$	mean axial stress or strain in each brace
τ	shear stress
	t/T
Δ	increment
ϕ	inclination of σ_1 to a plane of symmetry

C. Suffices

b	brace	c	chord
o	outside brace and chord	i	inside brace, chord or fillet
s	shell		
g	geometric	n	notch
m	meridional; model	t	weld toe
l	linear (a stress zone)	h	hoop
x, y, z	cartesian values	1, 2, 3	principal values
HS	hot-spot	L	photoelastic layer

D. Superscripts

r	residual (strain)
e	elastic (strain)
aux	auxiliary (in moire work)
m	using meridional strains only
p	plastic reversal (strain)

E. Abbreviations

API	American Petroleum Institute
AWS	American Welding Society
BSI	British Standards Institution
FE	Finite Elements
MFV	Material Fringe Value
SCF	Stress Concentration Factor
SNCF	Strain Concentration Factor

CHAPTER 1
INTRODUCTION

1.1 General Assessment of the Use of Welded Tubular Joints in Offshore Structures

The type of tubular members studied in this work are circular hollow sections. Although the tubes themselves have an efficient distribution of material, the joining of several tubes (of equal or different sizes) to form simple connections disrupts the uniform load paths enjoyed in the tubes and a potential failure site is created at every intersection.

The use of tubular joints in structures, including offshore oil and gas drilling rigs, is well documented. Over 1,000 tubular structures have been fabricated for use in offshore work since 1947; a year roughly coincidental with the rapid development of welding processes and of special machines to profile the ends of the tubes. In fixed offshore drilling platforms, welded tubular joints are used to form the connections in a tubular space frame, known as the jacket. Typically, a jacket may contain between 40 and 80 such joints. Each joint comprises one uninterrupted through tube, called the chord, and several smaller tubes, called braces, which terminate at, and are joined to the chord. See Fig. 1.1.

Following a number of failures of these joints in the 1950's and 1960's, extensive large scale testing and experimental model analysis was carried out because the behaviour of the joints is difficult to predict analytically. The tests showed that although the joints satisfied static and ultimate strength requirements, e.g. adequate shear thickness, premature failure occurred at the welded intersection

under fatigue loading. The Wöhler or S-N curve which relates cycles at failure and the maximum stress in a member was found to be applicable to the fatigue failure of complex tubular joints. Because of the sensitivity of this mode of failure, a 10% under-prediction in maximum stress could result in a 30% over-prediction in fatigue life. It is now well established that the most influential factors governing fatigue life are as follows:

- i) loading
- ii) tubular joint geometry
- iii) weld quality and profile
- iv) material
- v) environment

This work deals with the effects of items ii) and iii) on the magnitudes and locations of maximum stresses in certain types of tubular joints. The effects on fatigue of loading modes were studied by McDonald et al (e.g. 1); of material by Cotton (2); and of the environment, e.g. corrosion, by Wylde et al (e.g. 3).

1.2 Definitions of Stresses in Tubular Joints

The chord and braces forming a tubular joint can be considered as a number of members which act like beams. The loads in each of these 'beams' are calculated by conventional structural analysis, assuming rigid joints. The most important load is the axial force, but out-of-plane and in-plane bending are also significant; the shears and torsion of a member about its axis are usually unimportant. With particular joint dimensions (D , T , d , t , θ , defined in Fig. 1.1), lengths of members and their positions, nominal membrane stresses in each brace of the joint can be calculated assuming no distortion of the members and linear stress distribution across each member. These stresses are here referred

to as nominal stresses, σ_{nom} . With these assumptions

$$\sigma_{nom} = f(D, T, d, t, \theta, \text{loads for each brace})$$

However, because the chord is a thin-walled tube, the loads in the braces ovalise the chord and consequently distort the braces. These distortions cause bending of walls of the tubes. See Fig. 1.2. The gradients along the axes of the tubes of the associated wall bending moments vary so slowly in the vicinity of the junctions of the tube walls that they are considered to be linear. See Fig. 1.3. A shell stress concentration factor K_s to quantify this shell bending is defined as

$$K_s = \frac{\text{linearly extrapolated surface stress at weld toe}}{\text{'beam' stress, } \sigma_{nom}}$$

Linear extrapolation is implicit in finite element calculations using shell type finite elements (Kuang (4)) and explicit in the use of strain gauge measurements from acrylic (Wordsworth (5)) and steel (Irvine (6)) models.

With the definition of σ_{nom} incorporating the effects of tube size and inclination, it was assumed that, primarily,

$$K_s = f(\text{brace spacing } g, \text{ dihedral angle } \phi)$$

However, the above ignores the real shape of the joint. The presence of a brace (and the associated weld) causes additional stress concentrations in the chord due to the increases of wall thickness which change the stiffness of the chord wall AND due to the discontinuity of the outside surface of the chord. A notch stress concentration factor K_n to take account of these local effects is defined as

$$K_n = \frac{\hat{\sigma}}{K_s \sigma_{nom}} = \frac{\text{maximum stress in fillet}}{\text{surface stress linearly extrapolated to toe}}$$

These values occur at different positions because the maximum surface

stress does not occur at the weld toe but at a small distance in the weld toe fillet arc (see Fig. 1.3). Because it deals with the additional stress concentrating effects, it was assumed that, primarily,

$$K_{nc} = f(\text{weld toe shape } r_c/T, \alpha_c \text{ and weld size } H/T)$$

for the chord end of the weld and

$$K_{nb} = f(r_b/t, \alpha_b \text{ and } h/t)$$

for the brace end.

1.3 Design Against Fatigue Failure by Reductions in SCFs

Often, when a welded tubular joint fails under fatigue loading, the fatigue crack initiation site is at the toe of the weld. This is not only the location of surface discontinuities such as flaws, crack like defects and undercuttings, but is also the position of stress concentrations. The problem is thus two-fold and two avenues of investigation are required;

- i) a global analysis of tubular joints that ignores the shape and size of the weld, known as the "extrapolation or hot-spot method", and
- ii) the determination of local stresses (on a microscopic scale relative to i) in the weld toe fillets, known as "effect of weld profile".

1.3.1 Extrapolation, or Hot-Spot Methods

Surface strain measurements in steel tubular joints are usually obtained from electric resistance strain gauges attached to the outer surface of the tubes. The stresses computed from the strains are used to predict hot-spot SCFs. Because the latter occurs in the weld toe fillet, it is necessary to extrapolate the stresses from two (or more)

points as shown in Fig. 1.4. It is therefore evident from the definition of K_s given above, that, if gauges are located in the region where surface stresses decay linearly with distance, hot-spot and shell SCFs are synonymous terms.

The hot-spot method is widely adopted because it places the SCFs from many different tubular joint geometries on a common basis. The shell SCFs obtained from continuous stress distributions in this work assist in the interpretation of hot-spot SCF and examine the errors therein.

1.3.2 Effect of Weld Profile

Welded joints that conform to the requirement of a welding code are known as prequalified. Some of the prequalified details for complete joint penetration fillet welds in tubular joints are the subject of possible amendments to API (7) and AWS (8) welding codes. To support these proposals, fracture mechanics solutions are sought for a comprehensive range of tubular joint geometries and for fillet welds with various profile "qualities". See Fig. 1.5 . One of the guidelines previously implemented to eliminate local stress concentrations where crack-like defects occur at the weld toe is that a weld should blend smoothly with the parent chord wall. These are idealised requirements in which stress distributions are expected to be similar to those near butt welds, where for thick sections the AWS welding code controls weld angle and the radius to prevent drastic reductions in fatigue strength, known as the "size effect".

This is not possible with fillet welded tubular connections because of the large number of geometric configurations. Different degrees of profile control at different positions in the tubular joint are necessary to maintain fatigue strength. The 1980 edition of the API code introduced particular items of guidance with regard to profile control. A

finished weld was designated "profiled" (Fig. 1.5d) or "non-profiled" (Fig. 1.5a); the profiled weld merging smoothly with the parent plate and the non-profiled weld requiring no specific profile treatment. The significant difference between the S-N fatigue life curves appropriate to each type of weld obviously placed importance on the definition of profile control. To eliminate these ambiguities in this work, weld profiles were designated "controlled" and "uncontrolled" in which the features of each were quite distinct.

1.4 The Relevance of Plastic-Elastic Strains

It has been observed (9, 10) that during the first load cycle in fatigue tests on tubular joints, local yielding occurs at hot-spot positions near to weld toes. Strains exceeding yield values have been measured by small gauges placed as near to the weld toe as possible; typically 1.5 mm from the toe. However, it is unlikely that actual plastic-elastic strains have been measured at "real" weld toes. Attempts to model the plastic-elastic behaviour of 3-d joints using finite element methods must consider the mechanical properties of the different materials at the toe of a weld. These are weld metal, heat affected zones and parent plate.

Because plasticity precedes cracking, the behaviour of these joints during the crack initiation period is important. The relevance of plastic-elastic and residual plastic strains (in the important positions in a tubular joint) is of strain amplitude, i.e. the difference in these values for typical loadings. These have been measured in this work in real steel joints which represent the important positions in a tubular joint.

1.5 Objectives of This Work

The objectives of this work are:

- i) to study the influence of brace inclination, brace spacing, weld size, weld angle and fillet radius on the elastic shell and notch SCF at the brace and chord ends of the saddle and crown, at the heel and toe positions of usual shapes of joints used in offshore structures,
- ii) to determine elastic surface strain and stress distributions near the welds of multibrace tubular joints and to relate elastic hot-spot stresses to strains which could be measured by strain gauges.
- iii) to determine elastic, plastic-elastic and residual plastic strain distributions near to weld toes of real steel weldments manufactured to offshore specifications.

1.6 Methods of Analysis

Four experimental and one numerical methods of analysis were used to study elastic stresses and plastic-elastic strains in the vicinity of weld toes. Because of the large number of tubular joint and weld profile geometries used in an offshore structure, a sub-structuring approach was adopted. Small (approximately 1/6 to 1/8) scale three-dimensional (3-d) photoelastic models were first used to determine 3-d stress fields for different tube configurations. These results were used to design half- to full scale 2-d photoelastic, finite element and steel models.

The design of these models is described in Chapter 3. All models were designed in accordance with appropriate codes of practice with regard to shape and loading.

The experimental techniques given in Chapter 4 describe manufacture

of the models and testing apparatus, and measurement of stress and/or strain. In Chapter 5 the link between experimental output data and useful stress and/or strain information is made in the analysis of readings.

Chapter 6 gives the results of the work. Elastic stress results are separate from plastic-elastic strain results. For both, distributions of surface and through-thickness stresses and strains show the behaviour of particular models. Maximum values in fillets and linearly extrapolated values at weld toes are noted and the influence of the various geometric parameters on the stress or strain concentration factors follow.

All results are quoted for the intended geometric parameters and perfect loading conditions. The analysis of errors given in Chapter 7 describes the accumulation of error in the magnitudes of SCFs and SNCFs due to dimensional deviation, alignment and magnitude of loads, measurement of stress or strain and interpretation of results.

In the discussion in Chapter 8, the suitability of the methods of analysis is reviewed. The behaviour of welded tubular joints on global and local scales is discussed. The implications of the results of this work on the prediction of hot-spot peak fillet stresses are highlighted. Comparisons are made with the results from other work which was given in the literature survey in Chapter 2.

The important conclusions and relevance of this work in the context of an overall offshore structures research programme are summarised in Chapter 9.

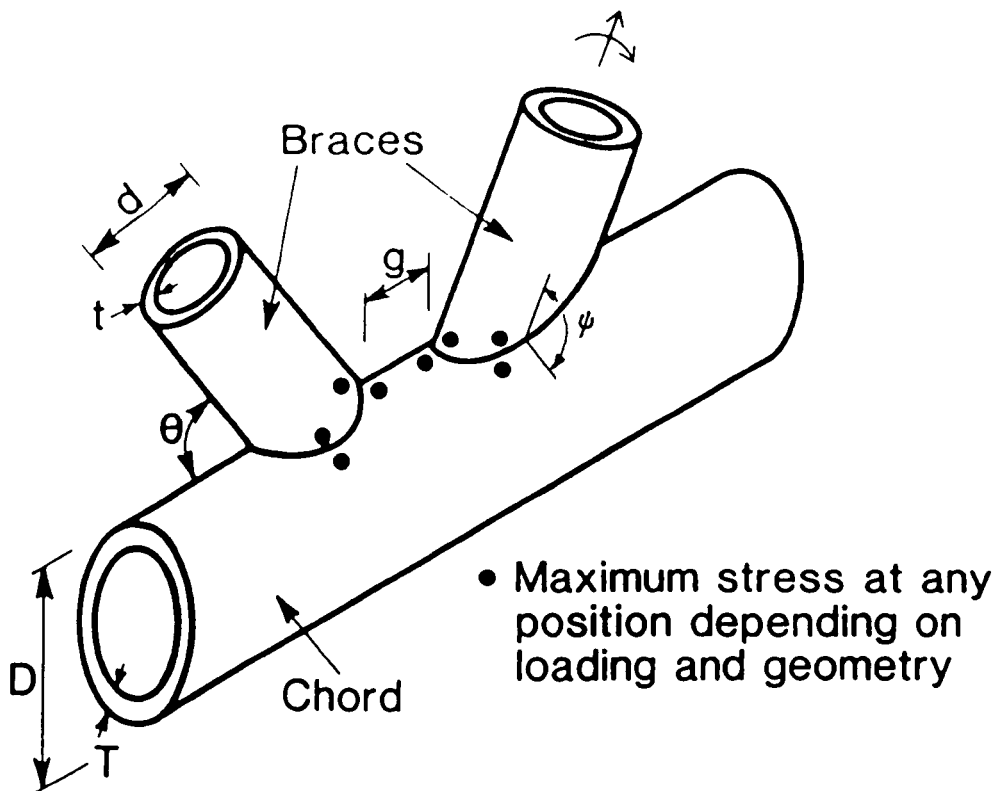


Fig. 1.1 Definition of a Tubular K Joint and Hot-Spot Positions

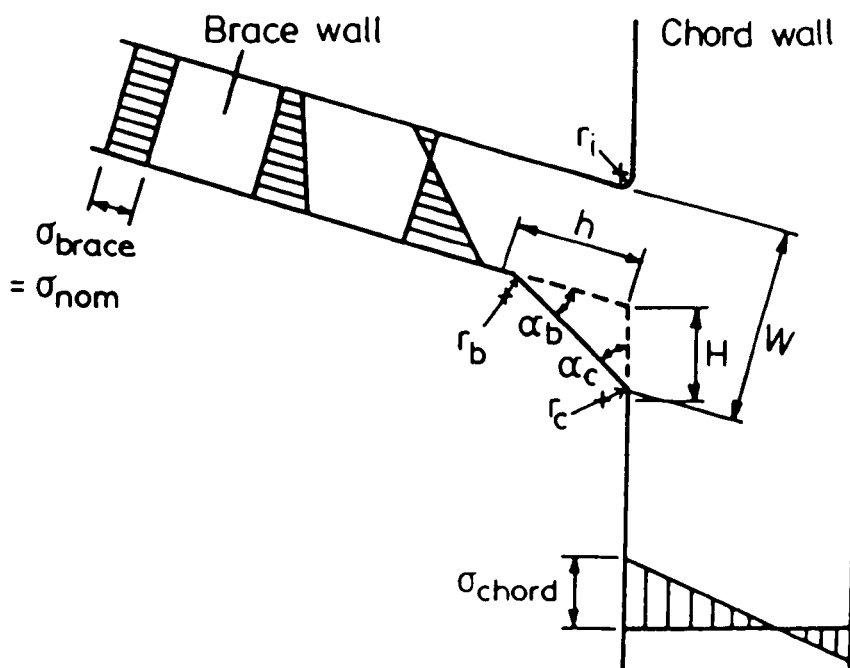


Fig. 1.2 Definition of Weld Profile and Stresses in a Simple Joint

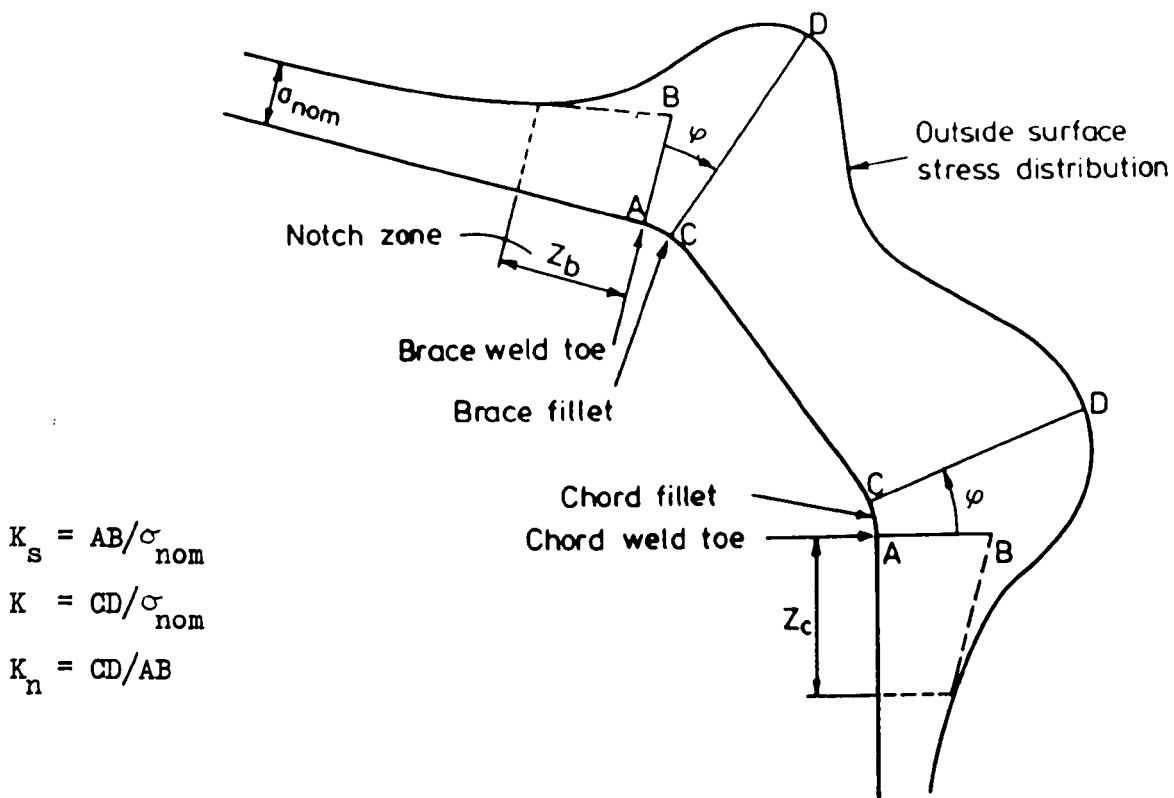


Fig. 1.3 Definitions of Stress, Shell and Notch Concentration Factors

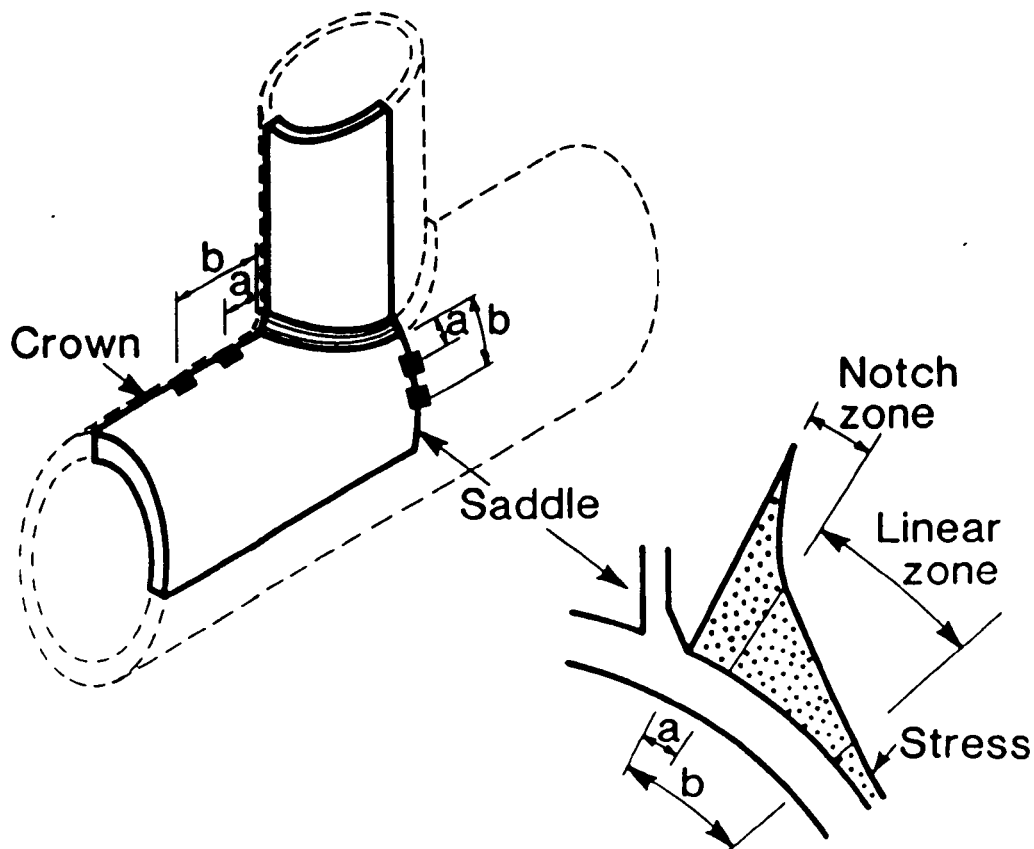


Fig. 1.4 Hot-Spot Extrapolation Methods from Strain Gauge Readings or Continuous Stress Distributions

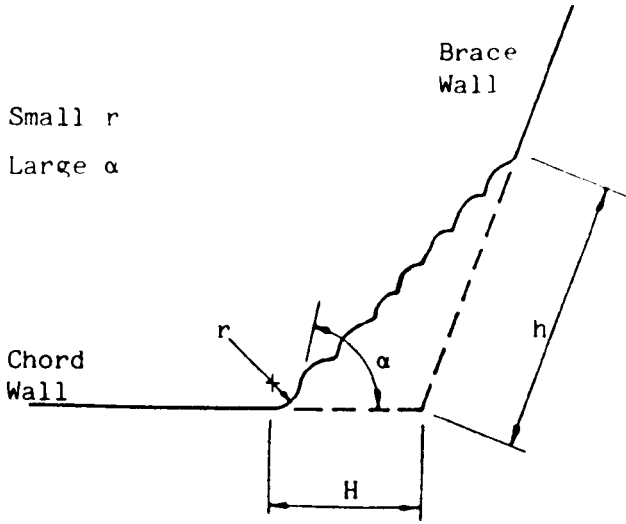


Fig. 1.5a Uncontrolled Weld Toe Profile

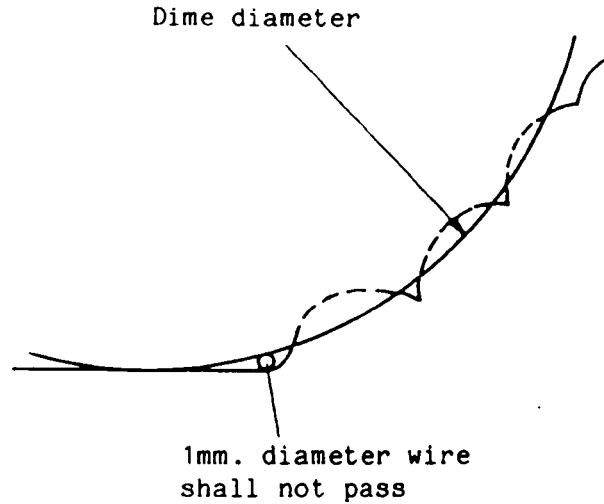


Fig. 1.5b Weld Beads Ground Off

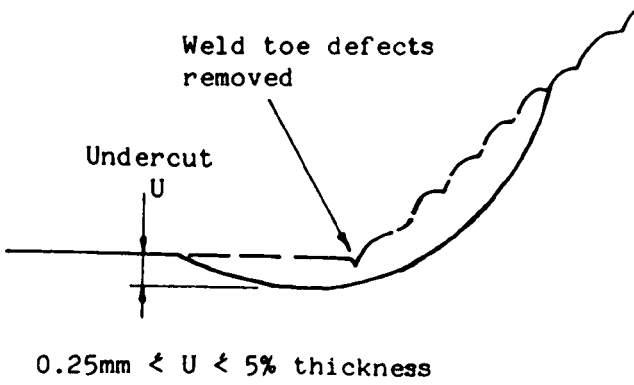


Fig. 1.5c Fully Ground Weld Toe

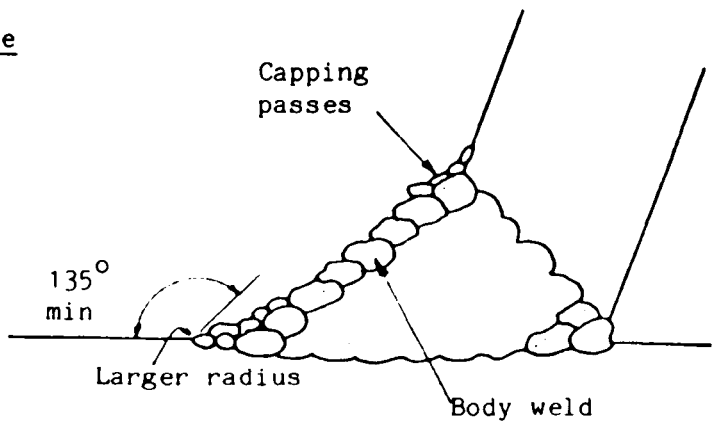


Fig. 1.5d Improved Weld Profiles

Fig. 1.5 Weld Profile Improvement Methods

CHAPTER 2
LITERATURE REVIEW

2.1 Introduction

During the last twenty years extensive research has been carried out on the fatigue performance of welded tubular joints. Individual investigations, in addition to the larger co-operative programmes, have recognised fatigue as one of the most important factors in the design of offshore structures. Some of the results of these investigations have since been transcribed into recommendations for the design, manufacture and inspection of welded tubular joints to prevent fatigue failure. In general this has relied on a family of S-N curves; plots of maximum stress range against the number of load cycles to failure, that have been developed for a wide range of typical weld features. Because S-N curves are extremely sensitive to variations in stress range, it is important to obtain accurate and reliable values for maximum stresses in tubular joints.

A large amount of data now exists on the subject of surface stresses near the intersections of tubular members. This is a complex three-dimensional problem. Mathematical solutions have, in general, failed to predict maximum values and generate stress distributions for the most simple of connections. Investigations have therefore used experimental and numerical methods of stress (or strain) analysis.

The experimental techniques used were i) static strain gauge tests on small scale acrylic models, ii) static and fatigue strain gauge tests on (real) welded, scaled or full-size steel joints, and iii) photoelastic techniques. All three methods are being used today.

The numerical techniques used were i) analytical and ii) finite element modelling. The development of computers, in the mid 1970's, which were sufficiently powerful to analyse three-dimensional tubular joints using finite elements eliminated further attempts to produce satisfactory analytical models.

Investigations have, in the main, obtained tube wall surface stresses on idealised tube-to-tube connections with no weld, or have measured strains at positions which do not record the effect of welds. However, recent work has dealt exclusively in determining the localised stresses, known as notch stresses, that occur near to the toes of welds. Attempts have also been made to study the spread of plasticity from weld toes using steel models and finite element representations of steel joints. The literature review deals with these subjects in the following sections:

- 2.2 Tubular joint stress distributions and geometric (or shell) SCFs,
- 2.3 Effect of weld profile on (elastic) stresses at weld toes, and
- 2.4 Plastic-elastic effects in tubular joints.

2.2 Tubular Joint Stresses and Shell SCFs

2.2.1 Review of Codes of Practice

BS 6235 : 1982 (11) states that fatigue lives of a tubular joint must be adequate both on the chord and brace sides of a weld. A long term distribution of peak stress range at every location on a joint is required to estimate probable fatigue life. The code requires that local peak stresses should be those which are as near as possible to the connection without being influenced by the weld profile. This stress which is referred to as 'hot-spot stress' should be determined by accepted practices; including finite element analysis, parametric equations or experimental evidence.

DoEn Guidance Notes (12) define the hot-spot stress used in experimental stress analysis of tubular joints as the greatest value around the brace/chord intersection of the extrapolation to the weld toe of the geometric stress distribution near the weld toe. This implies that the stresses used to describe fatigue behaviour should incorporate the effects of overall and local tube geometry, i.e. shell stresses, but omit the concentrating effects of weld geometry.

API RP2A (7) considers local stresses at tubular connections in terms of geometric SCFs because the microscale notch effects near weld toes are reflected in the appropriate choice of S-N curve. The curves should be nominated with regard to the severity of the notch effects in terms of weld profile qualities. The hot-spot strain should be measured by gauges adjacent and perpendicular to the run of the weld. The code also notes that where empirical equations, e.g. (4), derived by finite element methods are used, differences between mid-plane intersections and actual hot-spot locations must be taken into account, along with stiffening effects of the actual weld geometry.

AWS D1.1-84 (8) states that the adequacy of simple T, Y and K tubular connections in fatigue should be determined by testing an accurately scaled model or by theoretical analysis (e.g. finite element methods). In defining hot-spot stress or strain range the code states that this is on the outside surface of intersecting members at the toe of the weld joining them - measured after shakedown in model or prototype connection or calculated with best available theory.

2.2.2 Surface Stress and Strain Distributions Near Weld Toes

Bouwkamp, University of California

Bouwkamp published a series of papers (e.g. 13,14) on different approaches towards a solution for stress distributions and the behaviour of tubular connections. Much of the future work carried out by other

investigators takes its direction from his "state-of-the-art" synopsis published in 1966 (13). Brittle lacquer, photoelastic, strain gauge and full scale static loading techniques were used on tubular joints incorporating gusset plates, stiffening rings, grouted columns and local wall thickening. Fig. 2.1a shows the principal stresses in a thick walled unreinforced K joint ($\gamma = 11.5$, $\tau = 0.33$). The writer has reproduced this in Fig. 2.1b in terms of the mean axial stress in the diagonal brace. Bouwkamp expressed surprise at finding the maximum stress at the crown toe ($\psi = 145^\circ$) of the inclined brace, rather than at the saddle in the same brace. This was attributed to the interaction between the two braces which stiffened the crown and encourages load transfer to these positions. Perhaps Bouwkamp had unwittingly chosen the optimum gap at which brace interaction causes greater stresses at the crown than do chord wall deformations at the saddle. The gap parameter was $g/D = 0.11$.

In a later paper (14) Bouwkamp studied the influence of weld defects on surface stress using full size tubular K joints with, and without complete weld penetration. Because of the configuration of a typical jacket structure and the local stiffening effect of the chord by all braces, unloaded brace stubs were introduced in another plane to the one containing the loaded braces. The joints were instrumented using cross gauges in crown planes and rosettes in the saddle planes on all tube walls. Single gauges measured nominal brace strains remote from the intersections.

The results are important in the interpretation of results in welded tubular joints in which weld defects are not detected or ignored. The chord wall strains for the non-defective and defective joints were virtually identical; defective joint strains were only 2% to 7% greater. Hence load transfer through the chord was unaffected by the weld defect. The brace wall strains for the defective joints were 4% to 11% greater

at the saddle positions, and 15% to 30% greater at the crown positions than comparative strains in correctly constructed and repaired joints.

Gulati et al, Brown and Root, Inc.

Gulati et al (15) expanded the use of parametric equations developed for single plane K and KT joints to applications involving multibrace, multiplane joints subjected to combined loading. It was suggested that connection interactions consist of i) stiffening effects on the evaluation of the chord tube between adjacent braces, and ii) interaction of stress fields when two (or more) braces are loaded.

Additional stiffness caused by adding co-planar brace(s) was found to decrease SCFs at saddle positions and increase SCFs in the crown plane between the braces. This was attributed to the extra load carrying capacity of the chord wall in this region. Little emphasis was placed on the gap parameter, g/D which is shown by Wordsworth (5) to be significant in the crown plane. The interaction of elastic stress fields for combined loading was shown to be by direct superposition providing the geometry of the node, and the positions and number of braces were not varied.

Fessler, Little and Shellard, University of Nottingham, U.K.

Fessler, Little and Shellard (16, 17) and Little (18) used three-dimensional, frozen stress photoelastic techniques to determine principal surface stresses along tube walls and in large radii fillets. The details of this experimental technique are given in Section 4.2.1. Models were single plane K and KT type joints (see Fig. 2.2a) with and without overlap, in balanced axial loading. Stresses obtained in the crown and saddle planes are shown in Fig. 2.2b. Although the outside wall weld fillets were smooth circular arcs of radius $r = 0.5t$ and the internal fillets had a smaller radius $r_1 < 0.1t$, maximum stress concentrations were found in the outer surface fillets at an angular position of 10° to 25° from the chord weld toe.

Stress distributions appropriate to the saddle junction of a 90° brace show regions of linearity from $0.35T$ to $1.50T$ from chord weld toes, and from $0.36t$ to $2.35t$ from brace weld toes. Shell SCFs obtained by linear extrapolation to the crotch of the joint (called X_j in ref. 16) and maximum SCFs in the fillet (called I_f) are summarised in Table 2.1. The results are for different crown and saddle positions and give notch factors I_f/X_j for fillets of equal radius which occur at different positions on a single tubular joint.

The subject of local surface stress gradients has been investigated elsewhere.

Ohtake et al. Sumitomo Metal Industries Ltd., Japan

From static and fatigue tests on high-strength steel ($\sigma_y \gg 800 \text{ N/mm}^2$) K joints, Ohtake et al (17) showed chord wall surface (hoop and meridional) stress distributions in the saddle plane near to a $\theta = 90^\circ$ brace. Results for two joints, which differed only in chord wall thickness ($\gamma = 11.6$ and 16), showed that the distance to the first point of contraflexure in the chord wall, measured in the hoop direction from the chord weld toe, was virtually independent of γ ; the angular distances being 13° and 15° of an arc. Because the chord shell SCFs were approximately proportional to γ , outside wall surface stress gradients, expressed in terms of chord wall thickness T , were found to be independent of T . These are important findings in a plane of symmetry because weld toe SCFs are strongly influenced by stress gradients.

Wylde. Welding Institute, Cambridge U.K.

Tests carried out on welded tubular K and KT joints of chord dimensions $D = 457 \text{ mm}$ and $T = 16 \text{ mm}$ were reported by Wylde (10). The joints, with and without overlap, were tested under balanced axial load or out-of-plane bending. Some of the joints, e.g. a non-overlapped K, were comprehensively strain gauged to determine complete stress distributions

in the braces and chord as shown in Fig. 2.3. Principal stress vectors are shown for (a) the start of a fatigue test (b) after 5×10^6 cycles and (c) 9×10^6 cycles; the latter corresponding to a point just prior to through thickness cracking of the chord wall at the saddle near brace-A ($\theta = 90^\circ$). Although the stress at the original hot-spot reduced to a low level, the stresses in the remainder of the joint were found to be similar to those at the start of the test. This suggests that if improvements were made to the weld profile only in the region of the original hot-spot, fatigue life would be greatly increased.

Chord wall surface strain distributions in the crown plane between the braces showed the effects of brace proximity on weld toe strain (or stress) concentrations. Brace interaction resulted in the extrapolated strain at the weld toe of the (lesser loaded) 90° brace being virtually zero. The strain at the weld toe of the inclined brace was increased due to the large bending gradients in the gap region. Hence, for joint optimisation a critical value of g/D or g/T may exist in which the hot-spot for a K joint in balanced axial load transfers from the saddle to the crown toe position.

2.2.3 Through-thickness Stress Distributions near Weld Toes

Fessler and Marston. University of Nottingham, U.K.

Fessler and Marston (20, 21) developed and used an automatic micro-polariscope to study through-thickness chord wall stresses in 3-d photoelastic models of tubular K-joints. Slices cut from frozen stress models were examined in a modified optical microscope in which the minimum intensity of light was measured by a photomultiplier. The positioning of the point under observation and fringe readings were automated to enable stress separation using Frocht's shear different method (22).

Marston studied joints in the crown and saddle planes with three different weld shapes. These are shown, with the tubular joint

configuration, in Fig. 2.4. A total of six Araldite models were made using the precision-casting technique, developed by Fessler and Perla (23) and Little (18). The correct weld profiles were formed on identical pairs of models. Each brace was loaded separately in axial tension.

The results were presented in terms of direct cartesian (hoop, meridional and radial) and shear stress indices, i.e. multiples of σ_{nom} in the 90° brace, for a large number of chord sections in the crown and saddle (90° brace only) planes. An example is given in Fig. 2.5.

The plots show that hoop and meridional stress linearity exists in all directions to a point near to the outside wall surface in the vicinity of either a fillet, or the intersection of a brace wall. The distance from the outside wall or fillet surface to this point was called notch zone. Marston quantified the stresses within the notch zone as a through-thickness notch factor. This is the difference between the maximum surface stress and the stress extrapolated to the same surface from the linear distribution. These are given in Table 2.2 for the different weld shapes, positions and brace loading.

The results show that the extent of notch stress is greater at saddle positions where the chord walls are predominantly in bending.

2.2.4 Existing Parametric Formulae for SCFs

There are several alternative equations available for the prediction of hot spot SCFs at different positions in tubular joints. In these equations SCFs are given in terms of the geometric parameters relevant to the particular tubular configuration, e.g. T, Y, K, N or X, and loading, for which they were developed. The equations are of the usual form

$$SCF = C \cdot \gamma^a \cdot \tau^b \cdot \alpha^c \cdot \zeta^d \cdot f_1(\beta) \cdot \sin^e f_2(\theta) \quad \dots (2.1)$$

where C, a, b, c, d, e = constants

$f_1 f_2$ = algebraic functions

$\gamma, \tau, \alpha, \zeta, \beta$ = geometric parameters

θ = inclination of brace to chord tube

Wordsworth and Smedley. Lloyds Register of Shipping, London

The technique of using strain gauges to obtain stress distributions along the surfaces of small scale acrylic models of tubular joints was used by Wordsworth and Smedley (24) and Wordsworth (5). Parametric equations were developed to predict the SCFs at different positions in T, Y and X type joints (24) and in K and KT type joints (5) for all brace loading modes. Some of these formulae are summarised in Table 2.3. They are given for the chord side of the intersection at crown and saddle positions.

The basic concept of this work was that a K or KT joint may be likened to a T or Y joint on to which additional braces are added. If other co-planar braces were loaded, chord deformations resulting from these may extend to the original brace and superimpose, by adding or subtracting (depending on the sense of load), stresses at the intersections.

SCFs were effectively shell SCFs measured at the 'crotch'; the intersection of the outside brace and chord wall surfaces. Notch stresses near the crotch were ignored. Most of the tests on K and KT joints were done on models without fillets at the crotch. In ref. (5) Wordsworth refers to an earlier paper which shows that "the introduction of a fillet transposes the stress distribution, by a distance of about half the fillet leg length, away from the crotch". This recognises the effect stress gradients have on weld toe SCFs. A weld leg length correction factor $(1 + x/T)^{-\frac{1}{3}}$, where x is weld leg length, was proposed. This is multiplied by the SCFs obtained from the equations in Table 2.3. This factor was derived mainly from tests on T joints with model fillets. Tests carried out on K joints indicated that the correction factor was "of the right order for this type of joint" although it varied for

different loading modes because of different surface stress gradients.

Kuang et al. Exxon Production Research Co., Houston

Kuang et al presented several papers (e.g. 4 , 25) in which a large number of tubular T, Y, K and KT joints were analysed by finite element methods using flat facet-shell elements. The joints were divided into 'basic regions' and four levels of mesh refinement were used to reflect the regional variations in surface stress gradients. The analytical hot-spot, where SCFs were measured, was at the intersection line of the mid-surface of the brace and chord. This imposed the complication of qualifying all results for SCFs with the position where they were measured, as Kuang demonstrated in Fig. 2.6a. Fig. 2.6b shows that stresses measured on the outside chord and brace walls are sensitive to this position if the distance from the intersection is less than 0.5 inch.

The results of the analyses were used to produce some parametric SCF equations given in Table 2.3. The applicability and accuracy of these equations was verified by comparison with the empirical equations obtained by other investigators, namely Reber, Beale and Toprac, and Visser. These references are given in (4). Evaluation of these equations revealed disagreement as to the significance of the various geometric parameters. Kuang presented his data in a form which he considered to be appealing to most designers; algebraic or trigonometric functions of the dimensionless ratio of physical tube dimensions.

Gibstein. DnV, Norway

Gibstein (26) used 3-d thin shell finite elements to derive similar parametric equations as Kuang for tubular T joints. These are also given in Table 2.3. The results showed the influence of the individual parameters α , γ , τ and β on principal stress around brace/chord intersections.

Efthymiou and Durkin. Koninklijke/Shell Exploration, Netherlands

A comprehensive study leading to parametric equations for SCFs in T and Y, and gap/overlap K tubular joints was reported by Efthymiou and Durkin (27). They used a finite element programme 'PMB SHELL' that was developed specifically to model welded tubular joints using 3-d curved elements. The development and compliance to tubular joint stress analysis of these elements was reported by Liaw et al (28) in 1976. Efthymiou modelled flat fillet weld profiles around entire brace-to-chord (or brace-to-brace, for overlap) intersections. Although SCFs were obtained by the extrapolated "hot-spot" method, the results reflected the contribution made to joint stiffness by the weld fillet. Some of the parametric equations are listed in Table 2.3.

Efthymiou noted that differences in SCFs predicted by the equations of other investigations were due to different end conditions and effective span to chord diameter ($\alpha = 2L/D$) ratios. The stresses at weld toes were found to be smaller for short chord lengths because the natural decay of stress, associated with chord ovalisation, was interrupted. For chord slenderness ratios in the range $8 < \gamma < 16$, effective span did not influence SCFs when $\alpha >$ about 10. Crown values were not affected by this.

Gap and overlap K and N joints were extensively studied; about 100 combinations of loading and geometry. The effect of the brace gap in the crown plane was found to be significant at the chord weld toe for $g/D < 0.25$ and $\gamma = 16$. For other values of γ , the SCF v g/D curves were asymptotic elsewhere, suggesting that the parameter g/T characterises this effect. Brace SCFs were not significantly affected showing that stresses due to chord wall bending were dissipated through the large mass of the 'weld'.

Pan et al. Exxon Production Research Co.

Pan et al (29) suggested that the gap parameter was a measure of additional strengthening between co-planar braces and found that above g/D values of approximately 0.2, static failure load was independent of the gap. Here was further evidence of the correlation between static strength and stresses at intersections of tubular joints. This is also supported by Marshall and Graff (30).

Buitrago et al. Exxon Production Research Co.

The parametric equations developed by Buitrago et al (31) were for Y and non-overlapped K joints. The computer program used in the finite element program was TKJOINT; the same program used by Kuang. However an alternative approach was adopted for this work in which influence factors λ were given in terms of joint geometry and load case at potential hot-spot locations. The locations were crown toe and saddle positions at the brace and chord ends of welds. The combined hot-spot SCF is obtained by super-position of stresses induced by each brace load as follows:

$$SCF = \sum_{i=1}^m \sum_{j=1}^m \lambda_{ij} \sigma_{ij} \quad \dots (2.2)$$

σ_{ij} = nominal stress in brace "i" under load "j"

λ_{ij} = influence factor for each brace and load case

m = number of loaded braces

n = number of load cases considered

The influence factors for K joints in axial loading are given in Table 2.3.

2.2.4.1 Comparison of Empirical Equations for Each Geometric Parameter

The variation in SCF values predicted by the parametric equations developed by Wordsworth, Kuang, Efthymiou and Buitrago for γ , β , τ , ζ and θ are shown in Fig. 2.7. The values were obtained for a K joint in

balanced axial loading at the chord end of the weld at the saddle position near the brace of greatest inclination. The results were determined for the geometric parameters γ , β and τ used in this work for corner K joints, i.e. $\gamma = 12.5$ and $\beta = \tau = 0.5$. Other convenient values were $\zeta = 0.1$ and $\theta = 45^\circ$.

2.2.5 Unified Approach to Hot-Spot Stress Determination

Back, Wardenier and Kurobane¹. Delft University, Netherlands & Kumamoto University, Japan¹.

The large number of data and parametric equations derived made it apparent that there was a need for a common approach to stress related fatigue analysis. Back, Wardenier and Kurobane (32) reviewed the various (mainly European) techniques for fatigue analysis; in particular the "hot-spot" strain (or stress) range method. Several methods were being used to determine the strain-life behaviour of tubular joints. These were distinguished by either i) nominal or ii) hot-spot stress methods. In (i) the stress concentration is indirectly considered by classification of the joint using different S-N curves, or by taking into account geometrical parameters and multiplying the stress level in S-N curves by a certain factor. Kurobane noted that in Japan, direct relationships between static and fatigue strengths are assumed to depend on the same geometrical parameters. (Marshall and Graff (30) support this concept and show how the geometrical parameters which influence static strength joint efficiency may be utilised in finite element analyses to develop design equations for the fatigue life of complex tubular joints.)

In (ii) Back states that the hot-spot strain (or stress) must be clearly defined before results presented in S-N plots can be discussed. Because the influence of the weld toe is difficult to determine and its effect on maximum stress changes along the run of the weld, the extrapolated hot-spot stress method was developed. The method relies on

linear extrapolation to the weld toe of stresses measured at prescribed distances from it. See also Fig. 1.4.

Irvine. UKAEA, Risley, U.K.

These distances were given by Irvine (6) as shown in Fig. 2.8. They represent the extent of linear surface stress decay with distance from the intersection of two tubes, or, in the presence of a weld, from its toe. Brace wall bending stresses decay fairly linearly in an axial direction for distances of $0.8\sqrt{rt}$, and are negligible at about $5\sqrt{rt}$. The distance parameter \sqrt{rt} is a function of the characteristic length for a cylinder in bending. Notch stresses, which arise because of the abrupt change in geometry at a weld, were found to extend for a distance of $0.2\sqrt{rt}$ from the weld toe. Because weld dimensions on a tubular joint (to AWS standards) are related to brace wall thickness, the size of the notch zone should scale with increasing size of joint.

Gurney (33) found no correlation with brace radius and suggested a distance of about $0.4T$ instead of $0.2\sqrt{rt}$. The extent of the linear stress regions in Fig. 2.8 were agreed by the European Community of Steel and Coal (ECSC) Technical Working Party on Tubular Joint Testing. The expressions were empirical.

Irvine (34) reviewed the stress analysis methods used in the U.K. Offshore Steels Research Project (UKOSRP). These were strain gauge tests on full-size steel and small scale acrylic models, finite element analyses of these joints, and photoelastic studies of models with welds as featured on steel models. A tubular T-joint was used to study the differences in techniques. The outside surface stress distributions obtained from the four methods are shown in Fig. 2.9 for a saddle position. The closest agreement in results is between the steel and photoelastic tests because both were modelled with real weldments. The absence of welds in the acrylic models, and lack of physical thick-

ness (not stiffness) in the thin shell finite elements, were responsible for the differences in stress distributions and SCFs at the most critical positions.

Irvine also clarified a difficulty that occurs at certain locations, particularly at the saddle of inclined braces, where the stress perpendicular to the run of a weld is not a maximum principal stress. Rosette gauges should be used to detect this and the value quoted as hot-spot stress is the extrapolated maximum principal stress.

2.3 Stresses at Weld Toes

2.3.1 Weld Toe Notch Factors

Gibstein, DnV, Norway

The stress-fatigue behaviour of tubular joints with welds of irregular and undefined geometry was studied by Gibstein (35). Strain distributions were used to characterise different positions around the brace-to-chord intersection of T and Y joints as either 'notch free' or 'notch effective'.

At certain locations, i.e. most brace and some chord ends of welds, linearity extended to within 1.6 mm of the weld toe. Extrapolated weld toe values were obviously 'notch free'. In welds that did not blend smoothly with tube walls a rapid, non-linear increase in strain commencing at about 4 mm from the weld toe was measured. This distance was independent of wall thickness, position (i.e. chord or brace) and loading. The severity of the notch effect varied between different models and along the same weld front. Its numerical definition is shown in Fig. 2.10 as the ratio between the stress at a weld toe divided by the stress at the same position which corresponds to a 'notch free' condition. Notch numbers at chord weld toes were 1.24 to 1.36 for fillet welds of varied but unspecified geometry.

Dover and Connolly. University College London

Dover and Connolly (36) reported on a fracture mechanics approach to the fatigue behaviour of welded tubular T, Y and K joints. The results of strains measured in the near weld region on outside chord walls in full-size steel (grade 50D) joints were combined with crack growth data to provide experimental verification of theoretical and numerical fatigue models.

The results of stress analysis gave weld toe SCFs in excess of extrapolated geometric SCFs (K_G) by a value K_W called the weld SCF. It was anticipated K_W would show large variations, around the tubular intersection, due to changes in weld geometry. The results given in the paper did not confirm this. A possible explanation was that some gauges were positioned too far from the weld toe to measure the full notch effect. The authors concluded that if K_W could be determined, it may be possible to model early fatigue crack growth.

Atzori and Pappalettere. Bari University, Italy

Several papers have been published by Atzori and Pappalettere et al (37, 38, 39, 40) on the evaluation of peak and weld toe SCFs and surface stress gradients very close to weld toes using finite element methods and strain gauged X and T plate specimens.

The most recent work by Pappalettere (39) derived surface stress distributions in cruciform specimens in which the variable parameters were weld toe radii, in the range $0.08 < r/t < 0.316$, and lack of penetration (LOP) 0%, 50% and 100% of the specimen wall thickness. Shapes, dimensions and loading are shown in Fig. 2.11a. Strains were measured using gauge chains with ten measuring grids 0.51 mm or 0.79 mm long. In some instances, gauges were attached in the arc of the toe fillet. Finite element models were studied with identical geometries.

The stress distributions shown in Fig. 2.11b are for full penetration

joints with two different weld toe radii. The variation in the maximum stress indices $K = \sigma_{\text{local}}/\sigma_{\text{nom}}$ with r/t is shown in Fig. 2.11c. The results fit the empirical expression

$$K = A(r/T)^b \quad \dots (2.3)$$

Values for A and b are given in Table 2.4.

Atzori and Pappalettere (40) used finite elements with a very fine mesh in the weld toe region (Fig. 2.12a) to determine the magnitudes and positions of SCFs, and surface stress distributions in fillet welded T-plate joints. In the models, weld toe radii ($r = 1$ mm), weld angle (45°) and weld leg length ($h = 1.5t$) were constant. The range of wall thicknesses was $t = 2$ to 100 mm. Typical surface stress distributions are shown in Fig. 2.12b. The variation of peak (in the toe fillet) and weld toe SCF with r/T is summarised in Fig. 2.12c for different loading. The exponential increase in K with decreasing r/t may be (in part) due to the angular position φ of the maximum stress in the fillet. The value of φ increased from (approx.) 10° to 25° for $r/t = 0.5$ to 0.01.

Lawrence et al. University of Illinois

Similar, concurrent work to that of Pappalettere was carried out by Lawrence et al (41) on five different butt and fillet welded joints shown in Fig. 2.13a. Surface and through-thickness stress distributions were obtained using finite element methods. A very fine mesh was used to model circular arcs at weld toes.

Lawrence found that the position of maximum stress was confined to a very small region approximately $0.16r$ ($r =$ weld toe radius = 0.76 mm). The angular position of the stress concentrations, measured around the fillet from the toe, was 15° for a 45° weld angle. The variation in K with t/r shown in Fig. 2.13b is a power function

$$K = 1 + \alpha (t/r)^{0.5} \quad \dots (2.4)$$

in which the constant α represents the macrogeometry and loading condition of the weldment. Some of the values for α given for axial and bending tests are summarised in Table 2.5.

For the butt welded specimen loaded in tension, the coefficient α_A increases with weld angle θ according to the approximate expression

$$\alpha_A = 0.33 \sin^{0.5} \theta \quad \dots (2.5)$$

2.3.2 Local Stress Gradients at Weld Toes

Marston (21) showed that in tubular joints, chord wall through-thickness stresses were sufficiently linear to be resolved into axial and bending components.

Burdekin et al. UMIST, U.K.

Burdekin et al (42) explored this theme in a stress and fracture mechanics analysis of fatigue crack propagation in tubular T joints. Using finite element techniques, crown and saddle intersections were modelled with 'single' or 'double' size, wedge shaped weld profiles. The results, reproduced in Table 2.6, show considerable reductions in SCF at the saddle where surface stress gradients are known to be large. Reductions, in the order of 10%, were recorded at the crown where stress gradients are smaller. The severity of surface stress gradients are probably associated with the relative magnitudes of bending and axial stresses near to weld toes. Fig. 2.14 shows the effect of β and τ on the degree of bending. The proportion of bending was greater at the saddle than at the crown, and greater for small values of β at the crown. The influence of τ is contained within a $\pm 4\%$ scatterband.

SCFs were compared with those derived from the parametric equations of Efthymiou (27) and Wordsworth (5). The results compared favourably

with Efthymiou's equations at the crown, but over estimated at the saddle. However, results were equal when the weld leg length $h = 0.3t$. The implications of these results suggest that SCFs should be qualified with the actual weld profiles used, particularly weld size at saddle positions.

2.3.3 Weld Shape and Toe Profile Investigations

Marshall. Shell, Houston, Texas

Several investigators have studied the effects of weld profile on the fatigue performance of tubular joints. Recommendations for methods to improve U.S. field practice were given by Marshall (43). Although different S-N curves, e.g. API X-1 and X-2, were used in anticipation of different weld profiles, attempts to enforce profile control brought mixed results. The self-shielded FCAW process gave large beads in the vertical and overhead positions. This led to an unacceptable amount of weld toe grinding in order to satisfy the requirements of the so-called "dime-test" and to remove crack like defects, flaws and undercut at the positions of maximum stress. These criteria are summarised in Fig. 2.15.

Marshall (43) suggested an alternative approach to practical weld profile control called "profile design". These are shown in Fig. 2.16 for the different positions in the brace to chord connection. The intentions are clear; flat profiles are first laid down using a high deposition rate process followed by a definite size fillet at the chord weld toe. The new fillet has to i) be large enough to transfer the position of peak SCF to a lower stress field, ii) be made using electrodes with good wetting characteristics to provide generous toe radii, iii) limit the weld toe angle to (approx.) 45° , and iv) be hot enough to avoid the formation of hard heat affected zones.

Back and Vaessen. Delft University, Netherlands.

One of the parameters responsible for the control of stress concentrations at weld toes is the weld finishing. This was studied by Back and Vaessen (44) on full-size, steel tubular T joints. The weld finishing techniques used were toe grinding and improved profiles. The "ordinary" and "improved" profiles are shown in Fig. 2.17a. Chord wall surface strain index distributions are shown in Fig. 2.17 for the two profiles. Extrapolated weld toe SNCFs are greater in the ordinary profile because strain gradients are larger and the SNCF is measured nearer to the brace wall. The small reduction in surface strain gradients for the improved profile was attributed to the stiffening effect of the larger weld, a smoother toe profile and/or normal scatter in strain gauge results. The writers concluded that the main reduction in strain concentration factors for improved weld profiles were due to shifting of the weld toe into a lower stress field.

2.4 Plastic-Elastic Investigations in Tubular and Welded Joints

There appears to be a paucity of information on the plastic-elastic behaviour of welded tubular joints, particularly experimental work. The post yielded behaviour of these joints has been largely ignored by investigators and generally accepted as a localised problem in which the effects have been intrinsically absorbed in the design rules against fatigue failures.

Despite the apparent absence of an experimental method which can measure plastic strains at weld toes, a few investigators have attempted to quantify the effects of plasticity on tubular joint performance.

2.4.1 Effect of Tensile Overstrain at Weld Toes

Bouwkamp and Mukhopadhyay. University of California

The development of local strains, near weld toes, which exceed yield strain cause residual plastic strains. Bouwkamp (9) found tensile overstrain of welded tubular T-joints reduced fatigue life by an order of magnitude when maximum strain ϵ_{\max} was 4 times yield strain ϵ_y . Tests were carried out on ASTM grade A36 steel (\approx grade 50D) in which the ratio of the strain amplitude $\epsilon_{\max}/\epsilon_y$ was varied from 0.6 to 4.0. Strains were measured in regions assumed to contain residual welding stress and near to stress concentrations. The results for the first loading cycle showed a non-linear load-strain relationship and substantial residual plastic strain. SNCFs for different geometries were 4.1 and 6.0. Subsequent load responses were elastic with SNCFs = 1.7 and 2.3 respectively. The initial residual state of stress and subsequent development of large strains (during the first load cycle) prior to essentially an elastic behaviour was found to be common to welded tubular joints.

2.4.2 Plastic-Elastic Strain Distributions

Yoshida et al. University of Tokyo

The elastic and plastic-elastic behaviour of a tubular T-joint was studied by Yoshida et al (45) using shell and solid analysis finite element programs. The tubular joint was sub-divided into two regions. For detailed behaviour near the intersection of the tubes, a 3-d elasto-plastic deformation solid analysis was used. The elements were layered through the thickness to represent progressive plastification. An iterative, incremental method based on the changing stiffness of the joint was adopted to satisfy equilibrium during each load or displacement step. Elsewhere, flat plate elements were used. The composite

mesh is shown in Fig. 2.18a.

Tube material ($\sigma_y = 383 \text{ N/mm}^2$) and full penetration fillet welds ($\sigma_y = 501 \text{ N/mm}^2$) of convex, flat and concave profile were assumed to be perfectly plastic solids. The concave and convex weld profiles were circular arcs of 20 mm radius. Surface strain distributions in the saddle plane given in Fig. 2.18b show the effects of weld profile and weld leg length. At $P = 14t$, $\epsilon_{\text{nom}} = 175\mu\epsilon$. SNCFs in the order of 9.5 to 12.5 were measured. Decrease in weld toe strains in convex and concave profiles was 11%. The flat to concave profile reduction in strain was 5%. Yoshida found no effect on SNCF due to profile at the crown.

The extent of plasticity, based on $\sigma_{\text{nom}} = 56 \text{ N/mm}^2 = 0.145 \sigma_y$, is shown in Fig. 2.18c. The depth of the plastic region in the chord wall is about $0.35 T$ from the outside surface and $0.5t$ in the brace wall. The size of the plastic zone is fairly large for this loading considering that typical working values of $\sigma_{\text{nom}} = 140$ to 200 N/mm^2 . Plasticity appears to be spreading more rapidly in the (weaker) parent plate than in the weld. This suggests that material properties at weld toes are as important as geometry after the onset of yielding.

Tieyun and Shuiyun. Shanghai Jiao Tong University

Tieyun (46) formulated plastic-elastic finite element techniques to study the spread of plasticity in tubular T and Y joints. The accuracy of the program was checked against strain gauge measurements made on full size, low carbon steel, tubular Y joints of identical geometry, loaded in axial compression. Hot-spot stress-strain curves were in good agreement up to 0.8% strain. Load contours, representing the edges of plastic zones for the experimental and numerical methods, are shown in Fig. 2.19a. The results showed plasticity developing first in the chord wall at the saddle position and, progressed more rapidly around the intersection line of the tubes than in a circumferential direction.

Elastic and plastic strains were also computed by finite element methods along the intersection of brace and chord tubes. Chord wall strain distributions are shown in Fig. 2.19b.

Table 2.1

Summary of Extrapolated Shell (X_j) and Peak Fillet (I_f) SCFs for

K and KT Non-Overlapped Joints (16)

Junction No.	Type of joint	Location on model	Angles θ ψ		SCFs ¹					
					Chord values			Brace values		
					X_j	I_f	I_f/X_j	X_j	I_f	I_f/X_j
1	K	Crown	45°	45°	0.50	0.99	1.98	0.80	1.77	2.21
	KT	heel			0.49	0.93	1.90	0.50	1.99	3.98
6	KT				-1.51	-1.60	1.06	-0.28	-1.57	5.61
2	K	Crown	45°	135°	1.20	3.75	3.13	2.38	3.75	1.57
	KT	toe			2.20	4.00	1.82	2.60	4.00	1.53
5	KT				-3.75	-4.91	1.31	-3.58	-4.91	1.37
3	K	Crown	90°	90°	-2.90	-4.50	1.55	-3.50	-4.50	1.29
	KT				-1.10	-2.75	2.50	-2.20	-2.75	1.25
4	K				N/A	-1.68	-	N/A	-1.68	-
	KT				-1.60	-3.15	1.97	-2.70	-3.15	1.17
7	K	Saddle	90°	120°	-2.70	-4.75	1.76	-3.20	-4.75	1.48

1. All values expressed in terms of mean axial stress in brace in tension

N/A = values not available.

Table 2.2

Estimates of Through-Thickness Chord Wall Notch Factors and Extents (21)a) $\theta = 90^\circ$ Brace loaded

Position	Brace		Weld Profile ¹	Notch Factor I_n	Extent of Notch Effect ²
	θ	ψ			
Crown (remote from other brace)	90°	90°	S	2.1	0.13T
			R	1.1	0.15T
			C	0.9	0.07T
Crown (near to other brace)	90°	90°	S	1.2	0.15T
			R	1.5	0.13T
			C	0.6	0.07T
Crown	45°	45°	R	0.5	0.17T
			C	0.6	0.11T
Saddle	90°	120°	S	5.3	0.28T
			C	2.6	0.20T

b) $\theta = 45^\circ$ Brace loaded

Crown	45°	135°	C	2.8	0.19T
		45°	C	1.1	0.19T
Saddle	90°	120°	C	1.0	0.13T

Notes

1. S = Sharp; R = Radius; C = Chamfer welds defined in Fig. 2.4.
2. Distance from outside surfaces to commencement of maximum linear through-thickness stress.

Table 2.3

Some Parametric Equations for SCFs in Tubular T, Y, K and X Joints

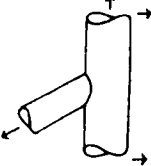
Joint Type & Loading	Author	Chord Saddle SCF	Chord Crown SCF
	Wordsworth	$\gamma\tau\beta(6.78 - 6.42\beta^{0.5}) \sin^m \theta$ where $m = 1.7 + 0.7\beta^3$	$K'_c + K_o K'_c$ where $K'_c = (0.7 + 1.37 \gamma^{0.5} \tau(1 - \beta))(2 \sin^{0.5} \theta - \sin^2 \theta)$ $K_o = \frac{\tau(2\gamma\beta - \tau)(0.5\alpha - \beta/\sin \theta) \sin \theta}{2\gamma - 3}$ $K'_c = 1.05 + \frac{30\tau^{1.5}(1.2 - \beta)(\cos^4 \theta + 0.15)}{\gamma}$
T & Y Joints	Kuang	$1.98\alpha^{0.06} e^{-1.28\beta} \tau^{0.81} \tau^{1.33} \sin^{1.69} \theta$	
	Gibstein $\theta = 90^\circ$	$(1.5 - 3.88\beta - 0.47\tau^2)(\alpha/2)^{0.06}$ $\tau^{0.87} \tau^{1.37}$	
	Wordsworth ($\theta_1 > \theta_2$)	$\gamma\tau\beta(6.78 - 6.42\beta^{0.5}) \times \left[\sin^m \theta_1 \left\{ \frac{\sin \theta_1}{\sin \theta_2} \right\}^{1.8} \right]$ $- \sin^m \theta_2 ((0.012\gamma) 2\tau/3 + 0.4) \left\{ \frac{\sin \theta_1}{\sin \theta_2} \right\}^{1.8}$	$1.1\tau^{0.65} \left\{ \frac{\sin \theta_1}{\sin^{0.5} \theta_2} \right\} 2\tau^{0.05/\beta} (1.5\beta^{0.25} - \beta^2)$
	Kuang ($\theta_1 = \theta_2$)	$1.505\tau^{0.666} \tau^{1.104} \beta^{-0.06} \rho^{0.067} \sin^{1.52} \theta$	
	Efthymiou ($\theta_1 > \theta_2$) Balanced to $\pm 15\%$	$\tau^{0.5} \tau^{0.9} (0.67 - \beta^2 + 1.16\beta) \sin \theta_1 \left\{ \frac{\sin \theta_1}{\sin \theta_2} \right\}^{0.3}$ $\times (1.64 + 0.29\beta^{-0.38} \arccos(\beta))$	
K Joints	Buitrago	$SCF = K_1 \sigma_1 + K_2 \sigma_2$ $K_1 = 1.017 \tau^{1.33} \tau^{1.51} \cos^{1.8} (1.57\beta^3)$ $\alpha^{-0.30} \sin^{2.47} \theta_1 \sin^{-0.12} \theta_2$ $K_2 = 213.7 \cos^6 (9.87/\tau) \tau^2$ $((3.513 \cos^{0.675} (1.57\beta) - 1.12) \tau^{-0.21})$ $\alpha^{-1.07} \sin^{2.36} (1.57 \sin^2 \theta_1) \sin^{1.15} \theta_2$	$SCF = K_1 \sigma_1 + K_2 \sigma_2$ $1.934 \tau^{0.19} \tau^{1.13} \tau^{0.15} \tau^{0.6} \tau^{0.62} \tau^{0.12}$ $\alpha \sin \theta_1 \sin \theta_2$ $K_2 = 0.938 \tau^{-0.12} \tau^{0.96} \tau^{0.26} \tau^{0.75} \tau^{0.61} \tau^{-0.22}$ $\alpha \sin \theta_1 \sin \theta_2 \tau$
	Wordsworth	$1.7 \tau \tau \beta (2.42 - 2.28\beta^{2.2})$ $\sin \beta^2 (15 - 14.4\beta) \theta$	

Table 2.4

Constants of the Empirical Expression for SCFs obtained
by Pappalettere (39)

Loading	L.O.P.	A	b
Axial	0%	1.23	-0.305
	50%	1.42	-0.318
	100%	1.91	-0.314
Bending	0%	1.03	-0.281
	50%	1.04	-0.282
	100%	1.04	-0.295

L.O.P. = lack of penetration

A and b defined in equation 2.3.

Table 2.5

Elastic Notch Stress Concentration Coefficients² for Different Weldments (41)

Joint ref. in Fig. 2.13a	Description ¹	Geometry (Fig. 2.13a)	Axial	Bending
			α_A	α_B
A	T-joint, FPFW, Fixed ends	$\theta = 45^\circ$	0.35	0.19
B	X-joint, PPFW	$\theta = 45^\circ$ $2c/t = 0$	0.35	0.19
		" $2c/t = 0.5$	0.38	"
		" $2c/t = 0.75$	0.41	"
		" $2c/t = 1$	0.45	"
D	Double V groove butt weld	$\theta = 10^\circ$	0.13	-
		$\theta = 15^\circ$	0.18	-
		$\theta = 30^\circ$	0.23	-
		$\theta = 45^\circ$	0.27	0.165
		$\theta = 60^\circ$	0.31	-

Notes

1. FPFW, full penetration fillet weld

PPFW, partial " " "

2. α defined in equation 2.4.

Table 2.6

Comparison of parametric equation values for radial SCF with those from F.E. studies with single and double welds (42)

β	τ	Parametric SCF		Single Weld SCF		Double Weld SCF	
		Crown	Saddle	Crown	Saddle	Crown	Saddle
0.56	1.0	9.18	8.35	4.3	9.06	4.1	3.8
0.56	0.64	6.35	3.42	2.92	3.25	2.42	1.35
0.35	0.8	4.81	7.93	3.23	8.55	3.14	6.48
0.35	0.64	3.84	5.08	2.51	5.75	2.31	4.07
0.63	0.8	5.15	8.06	2.69	7.84	2.69	3.37
0.63	0.64	4.24	5.16	2.24	4.61	2.12	1.94
0.63	1.0	6.60	8.07	3.61	8.45	3.43	3.90

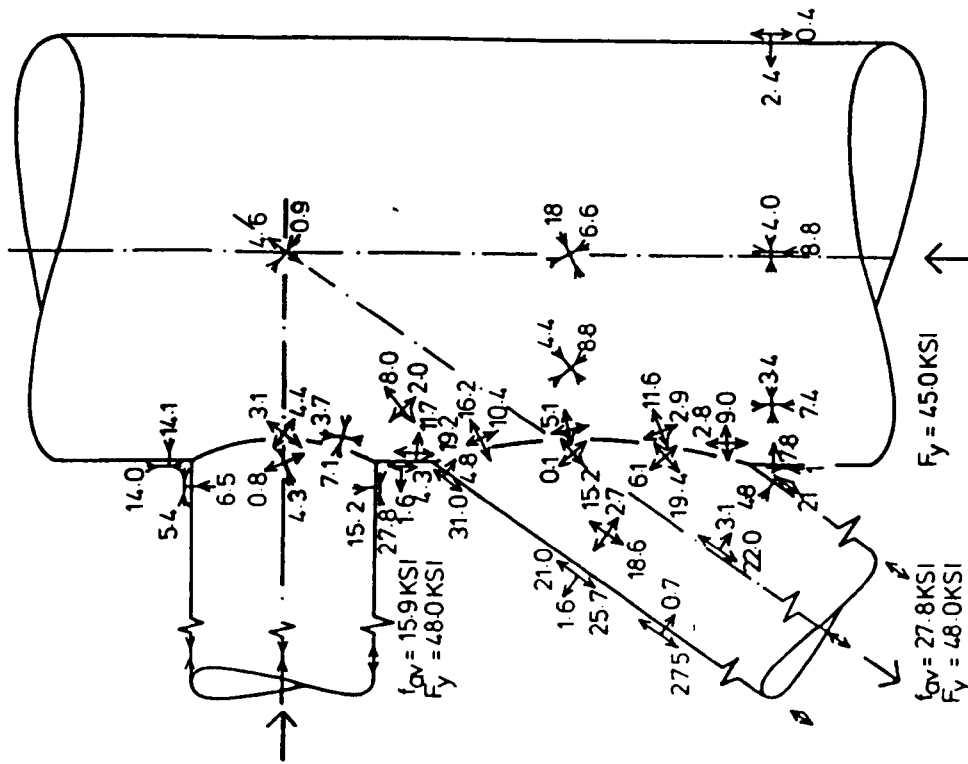


Fig. 2.1a Principal Stresses in K Joint under Balanced Axial Loading (after Bouwkamp (13))

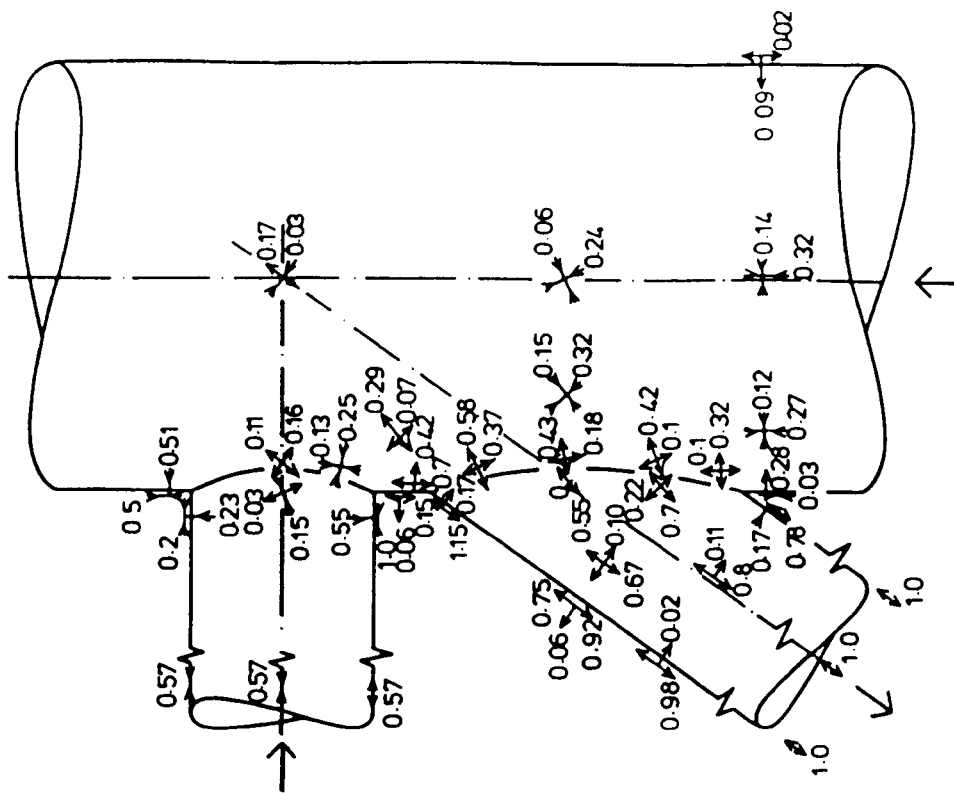


Fig. 2.1b Principal Stress Indices based on Mean Axial Stress in Diagonal Brace (after Bouwkamp (13))

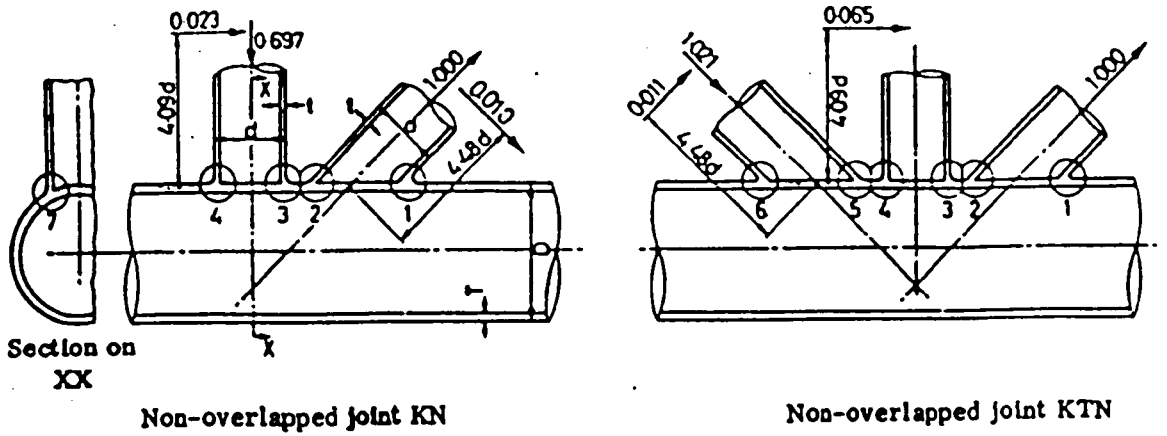
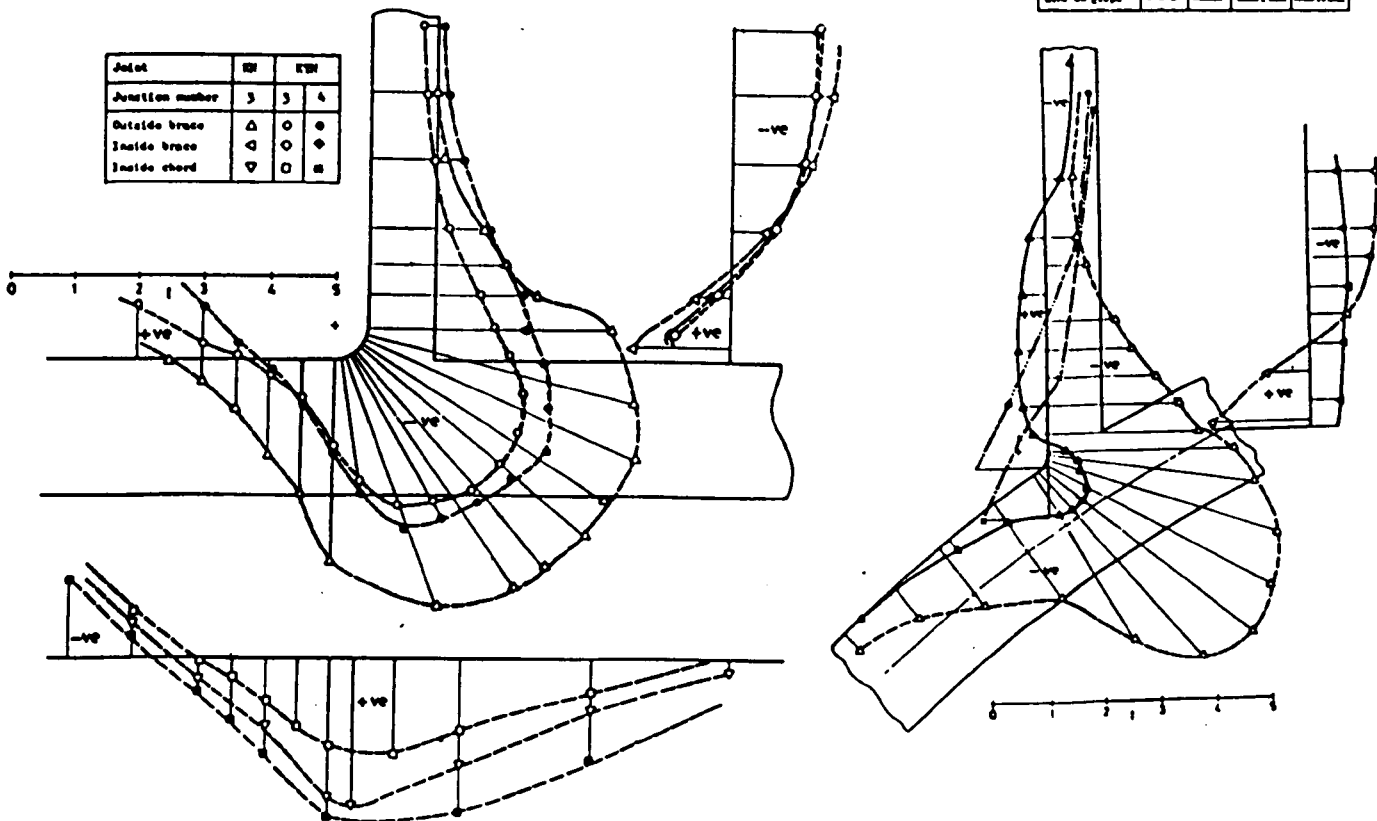


Fig. 2.2a Geometry and Loading in Photoelastic Models used by Fessler and Little (16)

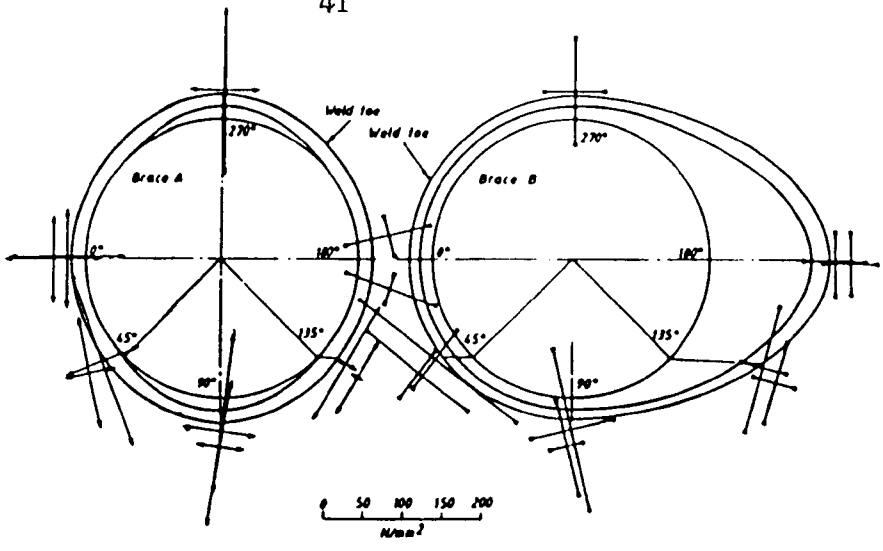
Joint	KN		KTN	
	Photoelastic	Flotte element	Photoelastic	Flotte element
Outside brace	△	▲	△	▲
Inside brace	◁	◀	◁	◀
Line on graph	- - -	—	- - -	—



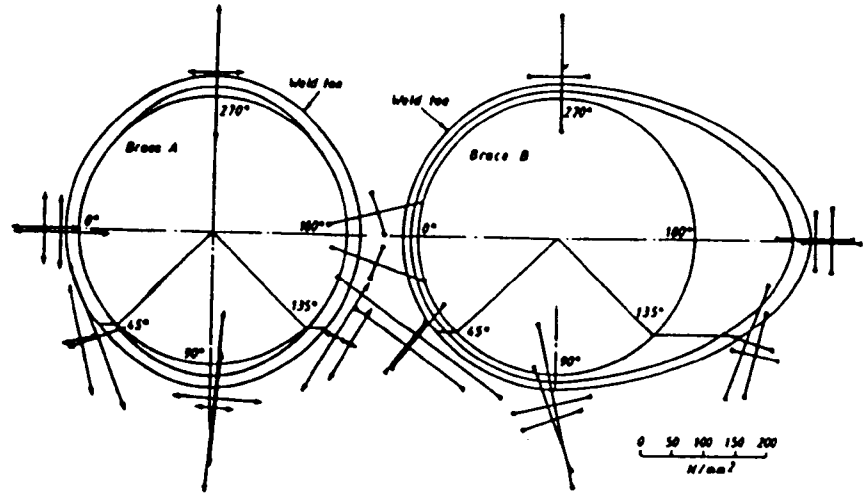
Meridional stress indices in junctions 3 and 4 of the non-overlapped models.

Meridional stress indices in junction 7 of the K models

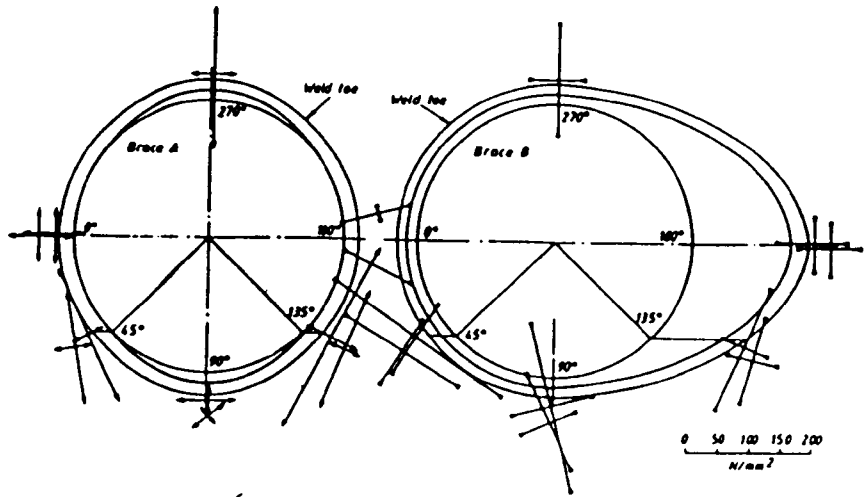
Fig. 2.2b Surface Stress Indices Distributions in K and KT Tubular Joints (after Little (16))



a) Elastic loads at $\sigma_{nom} = 50 \text{ N/mm}^2$



b) After 5×10^6 cycles



c) After 9×10^6 cycles

Fig. 2.3 Directions and Magnitudes of Principal Stresses in Chord Wall of $90^\circ/45^\circ$ K-type Tubular Joint (after Wylde (10))

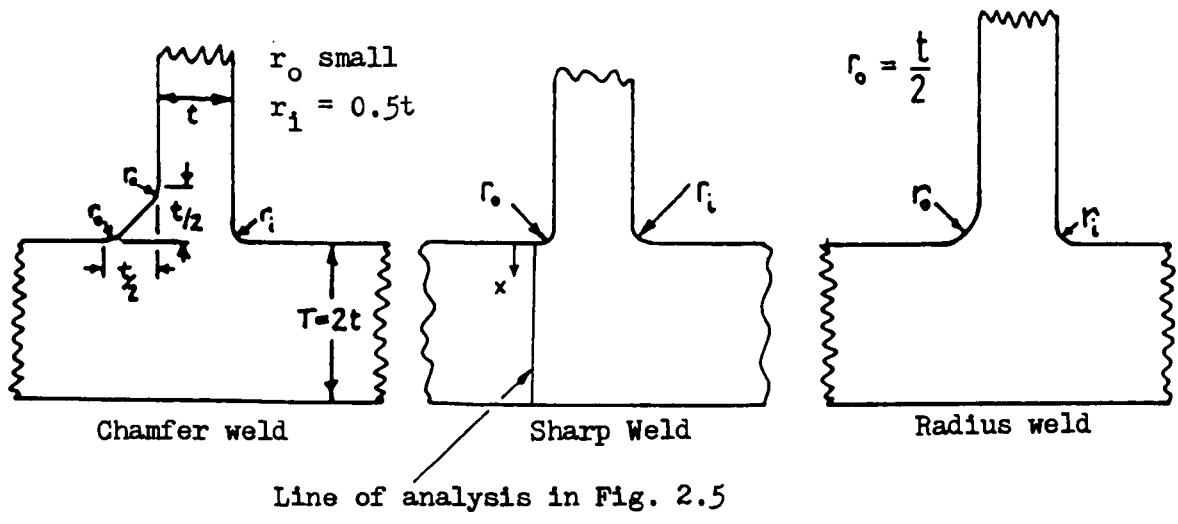
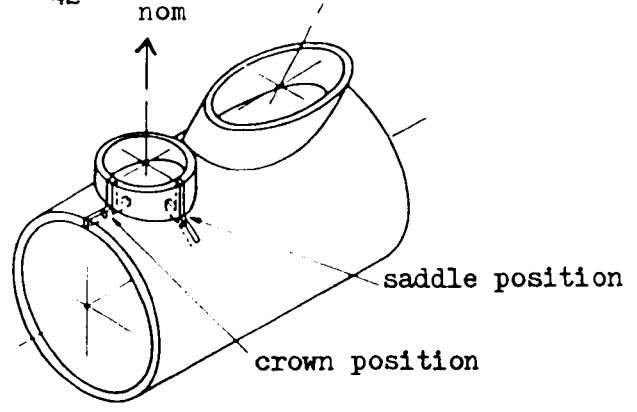


Fig. 2.4 Tubular Joint Configuration and Weld Profiles used by Fessler and Marston (20)

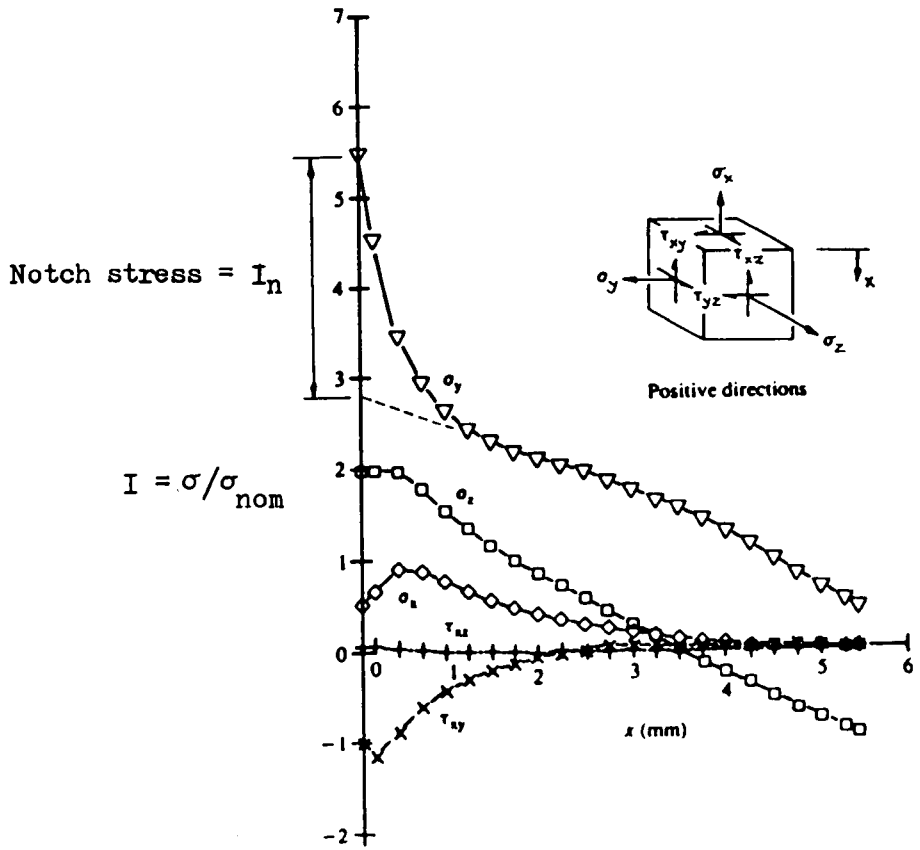


Fig. 2.5 Chord Wall Through-thickness Cartesian Stress Distributions for Sharp Weld Profile and $\theta = 90^\circ$ Brace. (After Fessler and Marston (20))

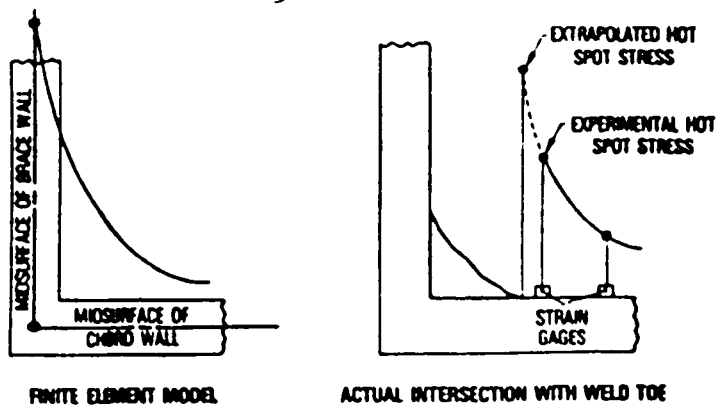


Fig. 2.6a Hot-Spot Positions used in Different Prediction Methods

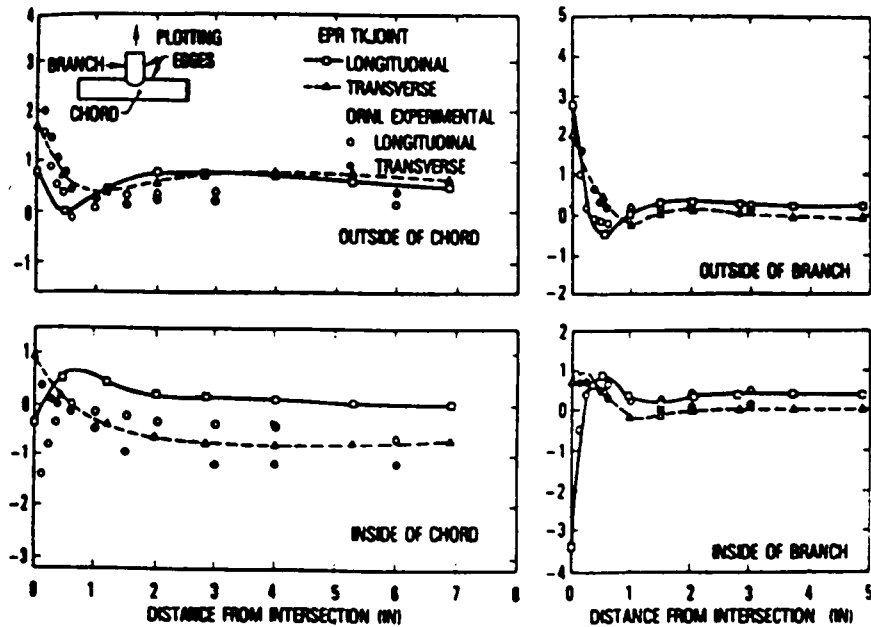


Fig. 2.6b Surface Stress Indices in Tubular K Joint Showing Importance of the Definition of the True Intersection (after Kuang et al (25))

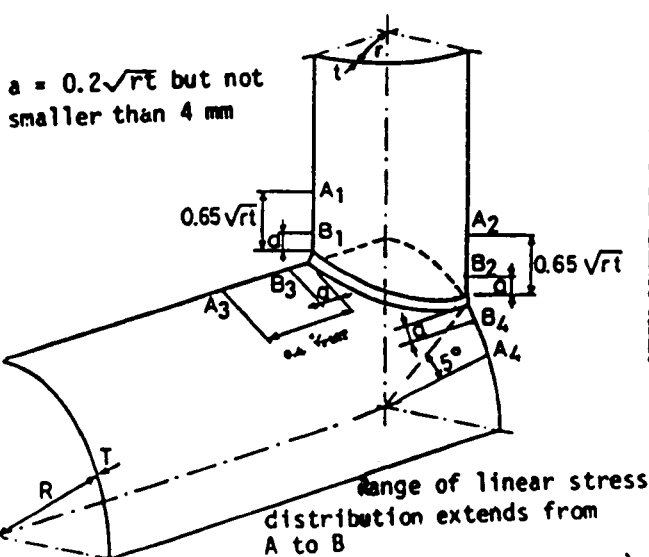


Fig. 2.8 Locations of Strain Gauges for Linear Extrapolation Methods (after Irvine (6))

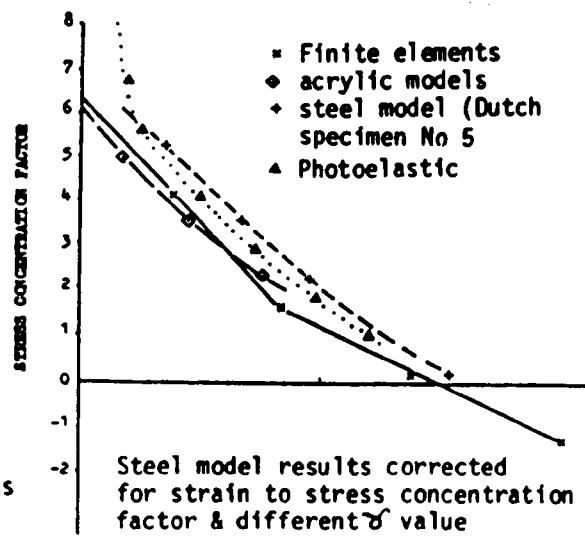
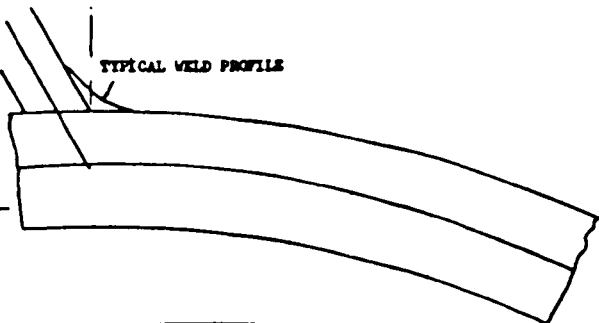


Fig. 2.9 Comparison of Surface Stresses obtained using Different Experimental Techniques (after Irvine (34))



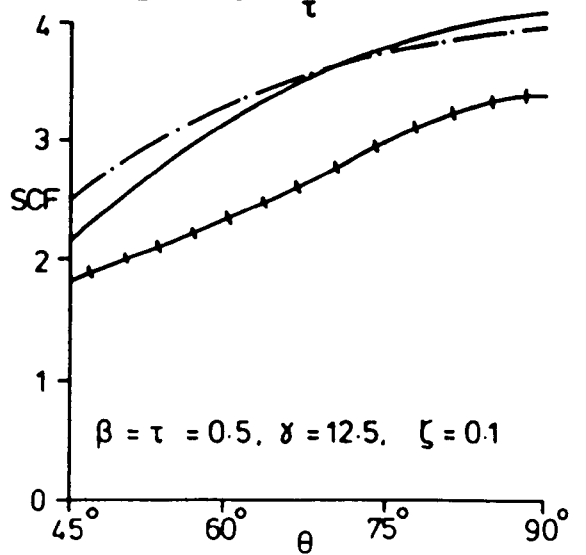
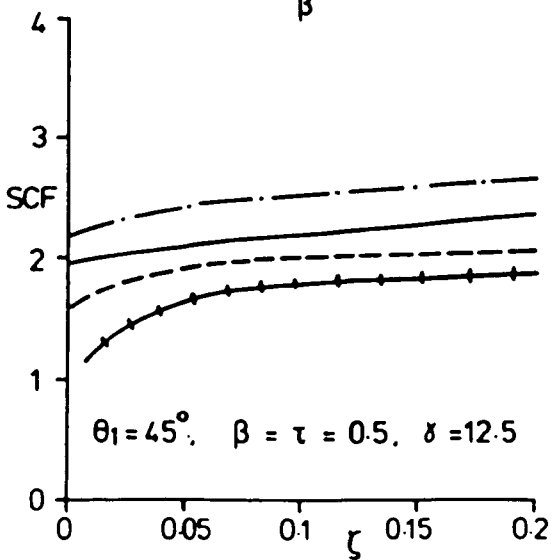
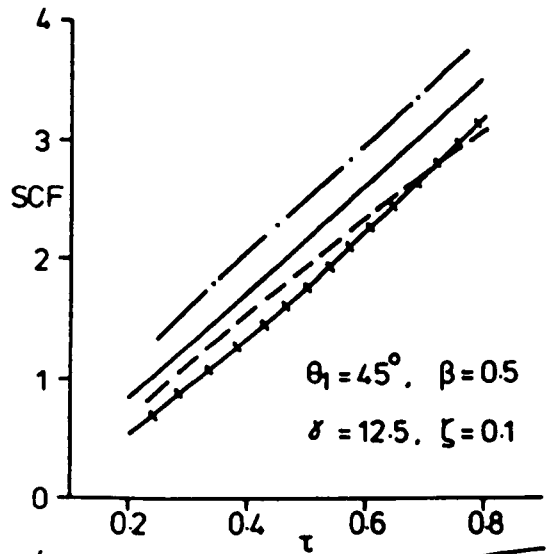
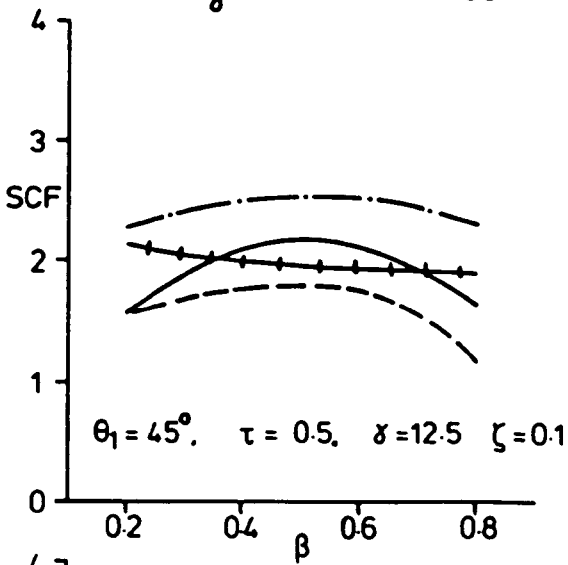
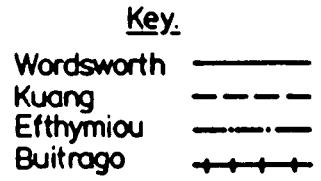
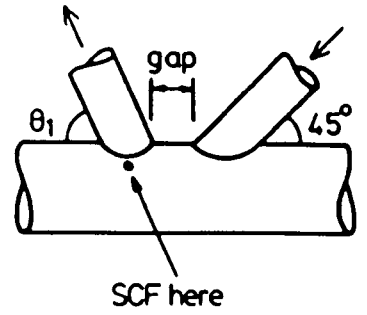
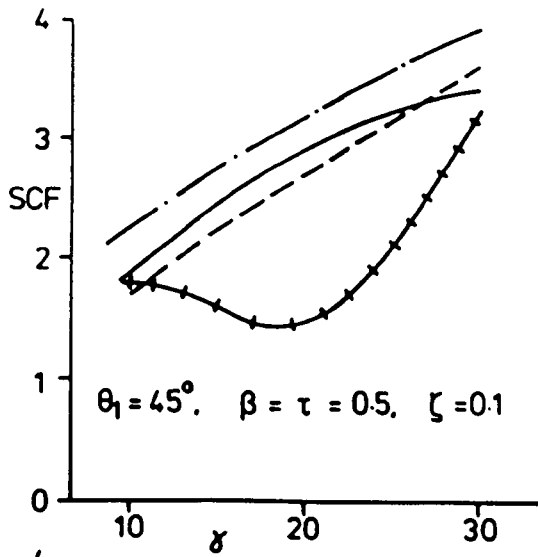
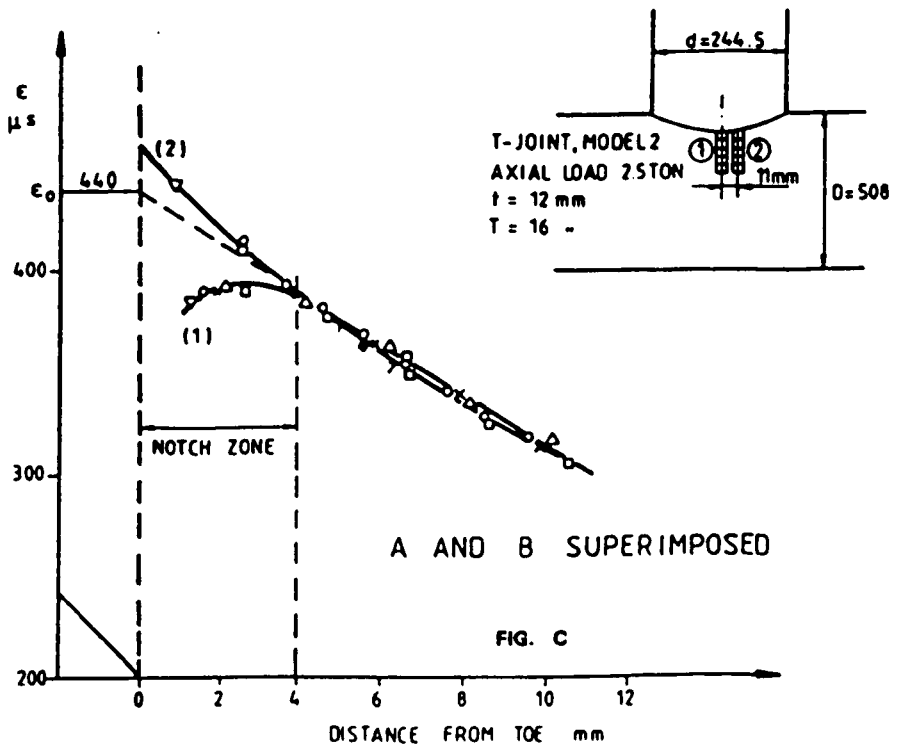
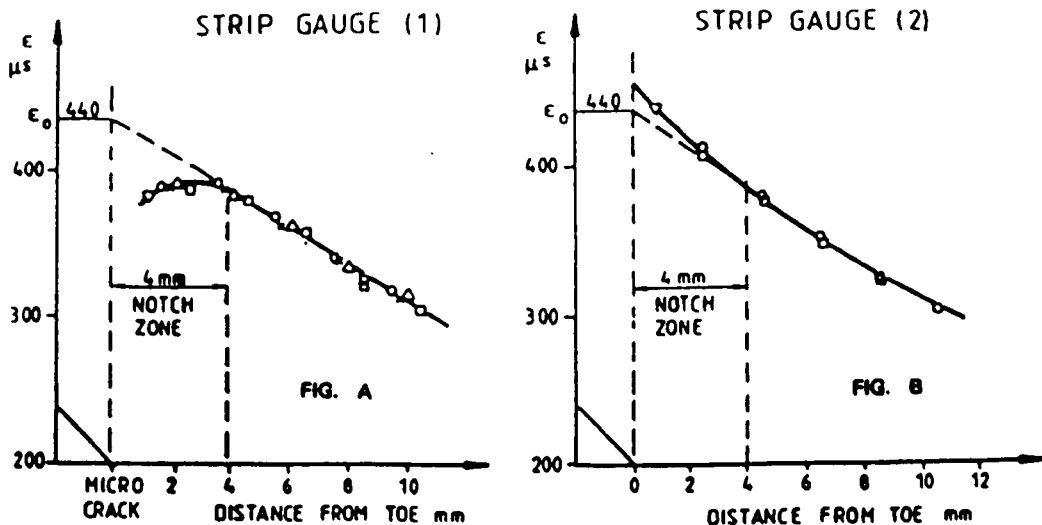
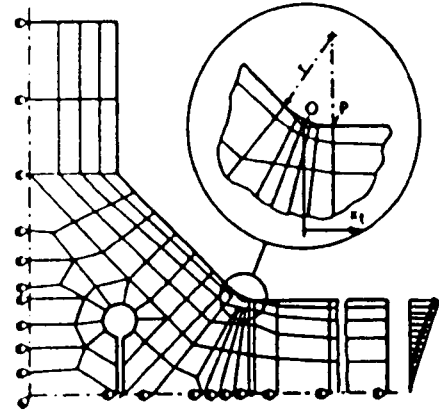
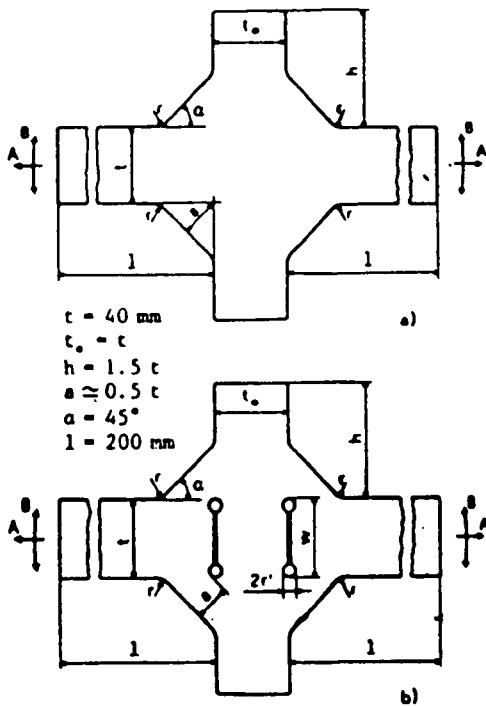


Fig. 2.7 Comparison of Empirical SCF Values obtained from Parametric Equations



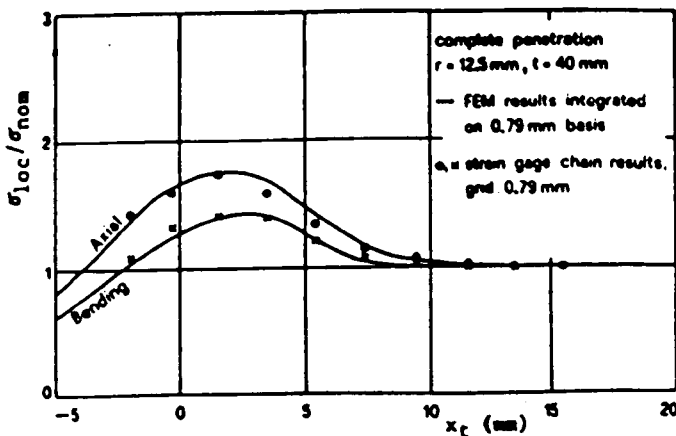
DETERMINATION OF THE NOTCH ZONE BY SUPERPOSITION OF STRAIN READINGS TAKEN 11 MM APART. NOTE THAT DnV'S DEFINITION PROVIDES THE SAME ϵ_0 VALUE INDEPENDENT OF NOTCH.

Fig. 2.10 Identification of Notch Zones using Surface Strain Distributions (after Gibstein (35))

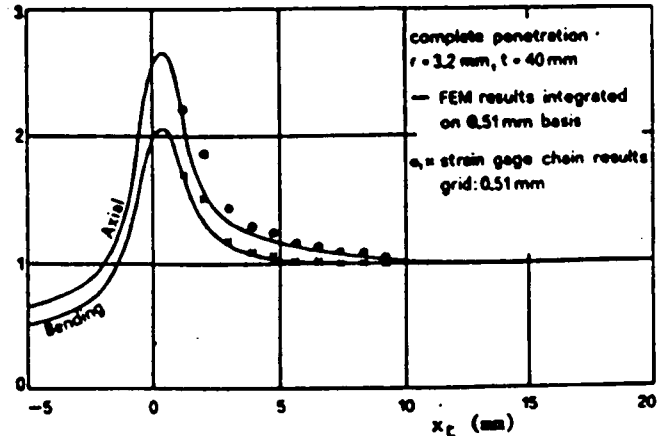


Example of structure analyzed for the case of a complete lack of penetration joint under bending.

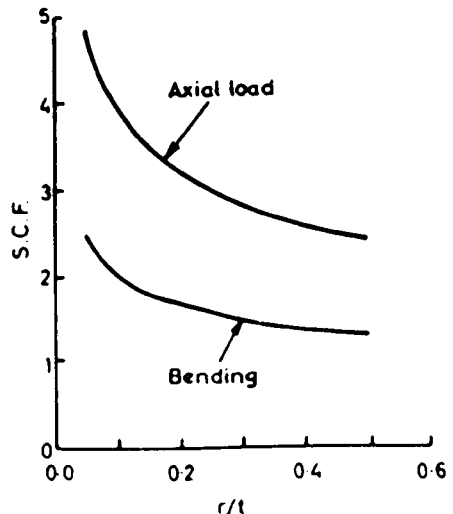
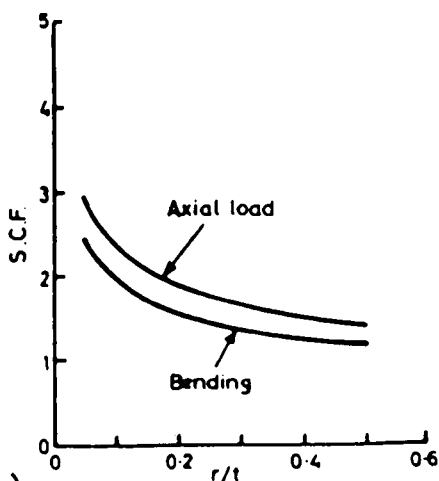
- a) Cruciform joint geometries analyzed:
 a) complete penetration joint;
 b) complete lack of penetration joint.



b) Results obtained for the complete penetration joint; strain gages with ten 0.79mm-grid



Results obtained for the complete penetration joint; strain gages with ten 0.51mm-grid.



c) Fig. 2.11 Specimen Geometry and Results of Finite Element Investigation into Stresses at Weld Toes (after Atzori and Pappalettere (39))

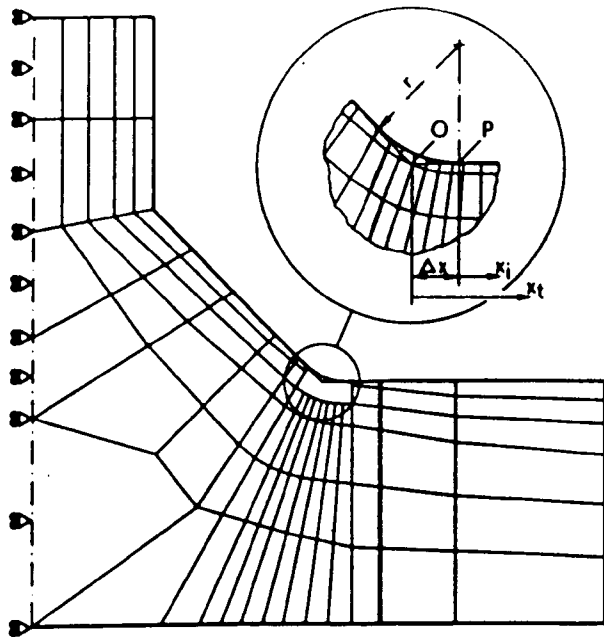


Fig. 2.12a Weld Toe Geometry and F.E. Mesh

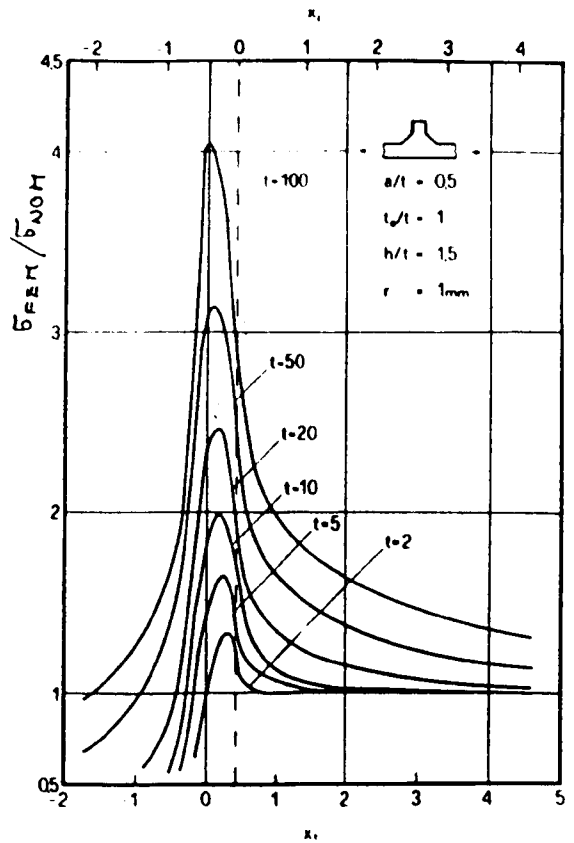


Fig. 2.12b Surface Stresses for Different r/T Values

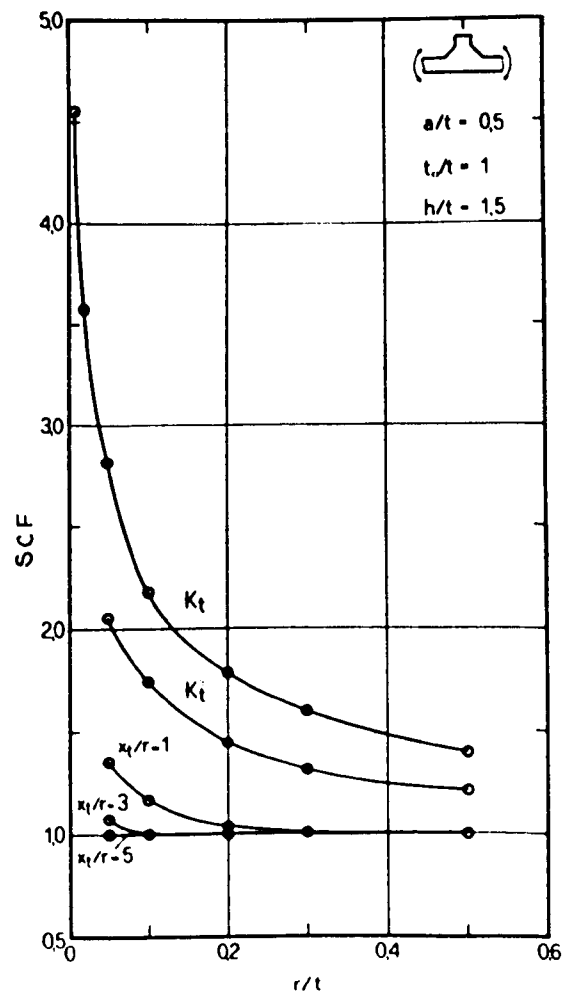
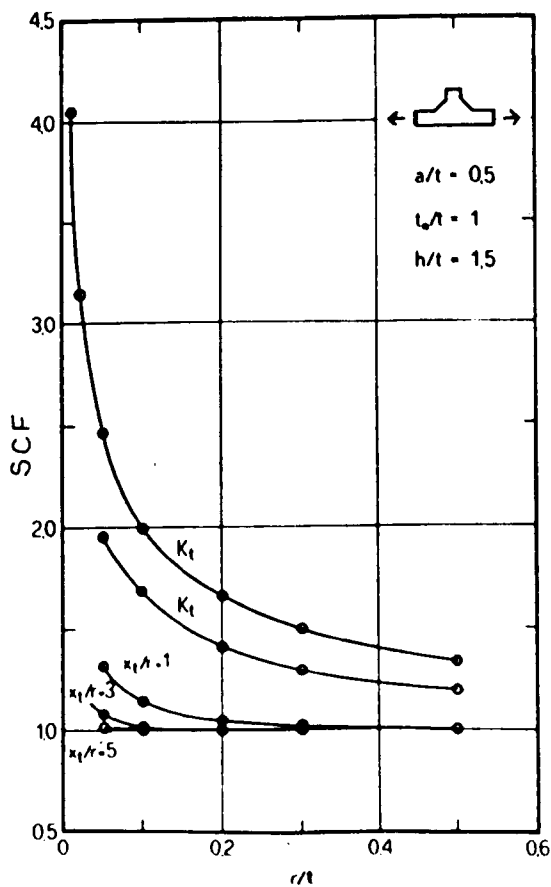


Fig. 2.12c Variation in SCFs with r/T Values (after Atzori and Pappalettere (40

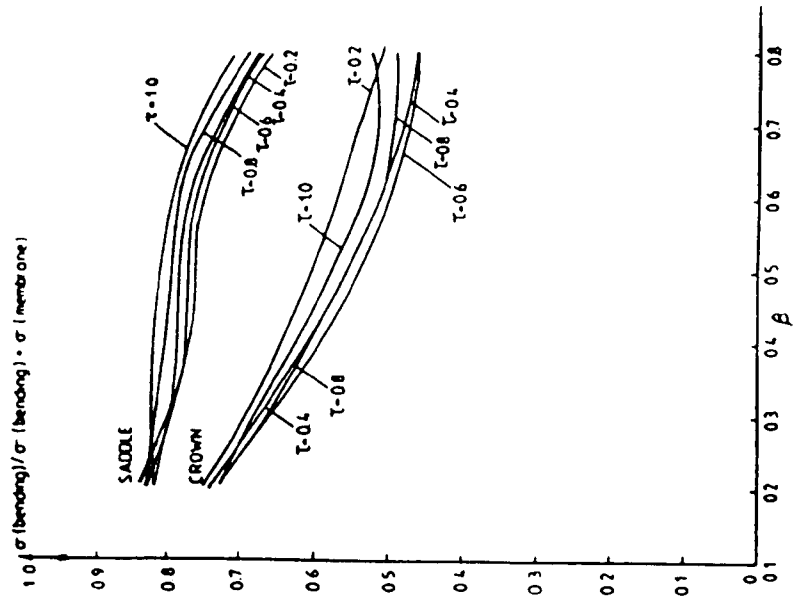


Fig. 2.14 Ratio of Bending to Total Stress in Chord Wall of Tubular T Joint (after Burdekin (42))

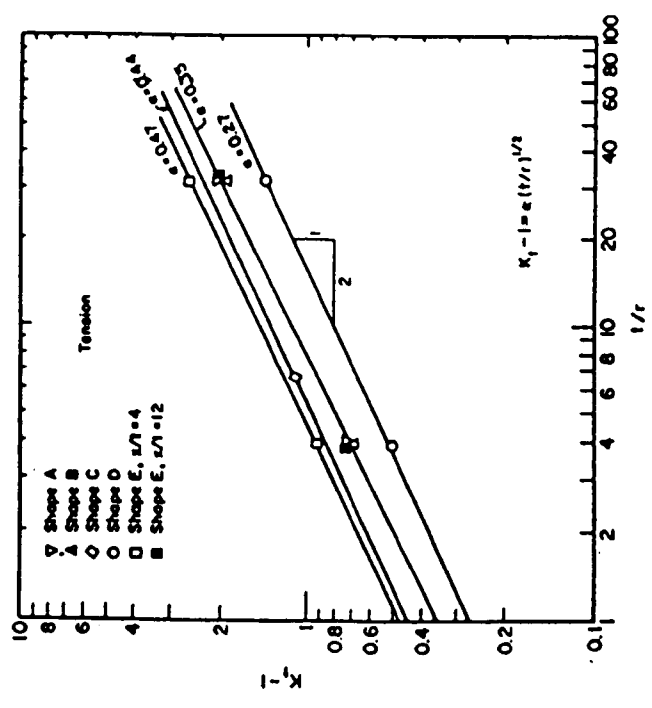


Fig. 2.13b Variation of SCF (K_t-1) with r/T values for Different Geometries (after Lawrence (41))

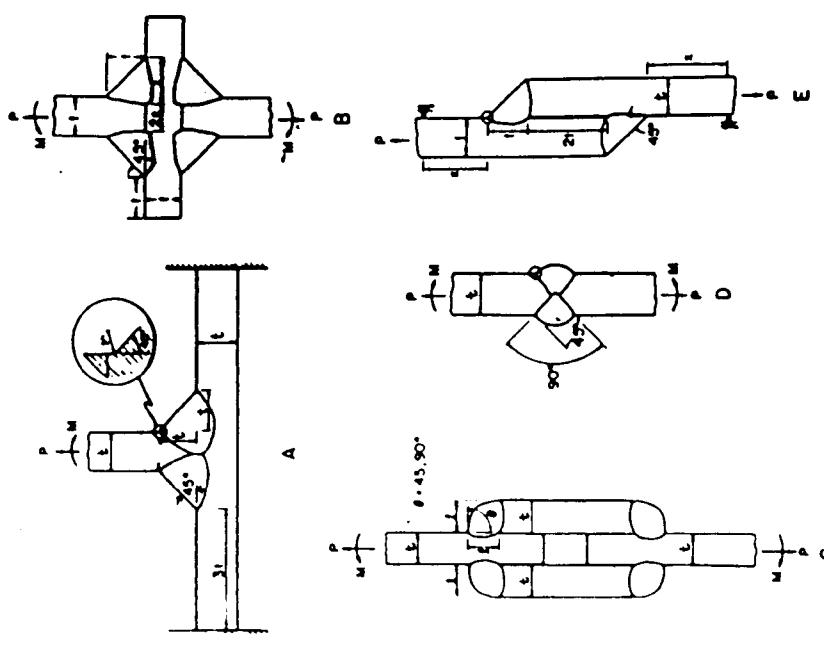


Fig. 2.13a Geometry of Models Studied by Lawrence (41))

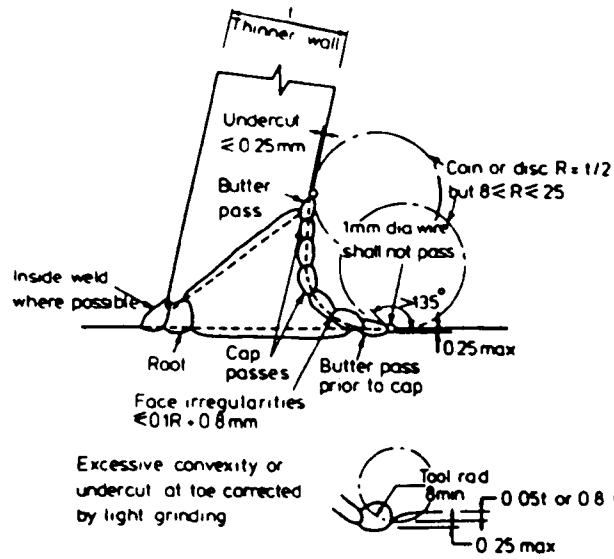
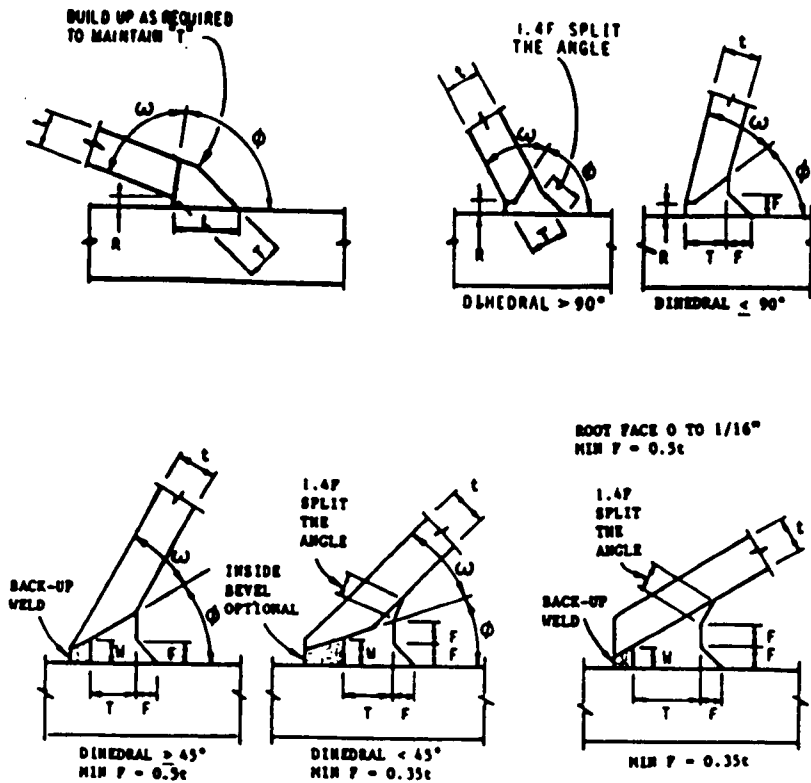


Fig. 2.15 Requirements for Weld Profile Control (after Marshall (43))



MINIMUM "F" AS SHOWN. "F" NOT REQUIRED TO BE GREATER THAN 5/8" (16mm). FELLETS SHALL ALSO SATISFY MINIMUM SIZES OF AWS TABLE 2.7

Fig. 2.16 Proposed AWS Standard Weld Shapes with Profile Control at Different Positions in Tubular Joints (after Marshall (43))

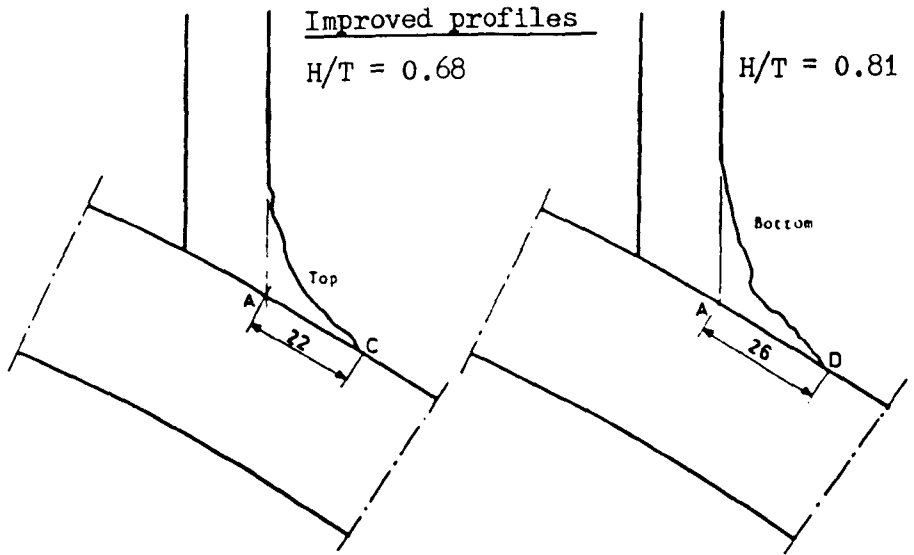


Fig. 2.17a Ordinary and Improved Weld Profiles used in Dutch tests by Back and Vaessen (44))

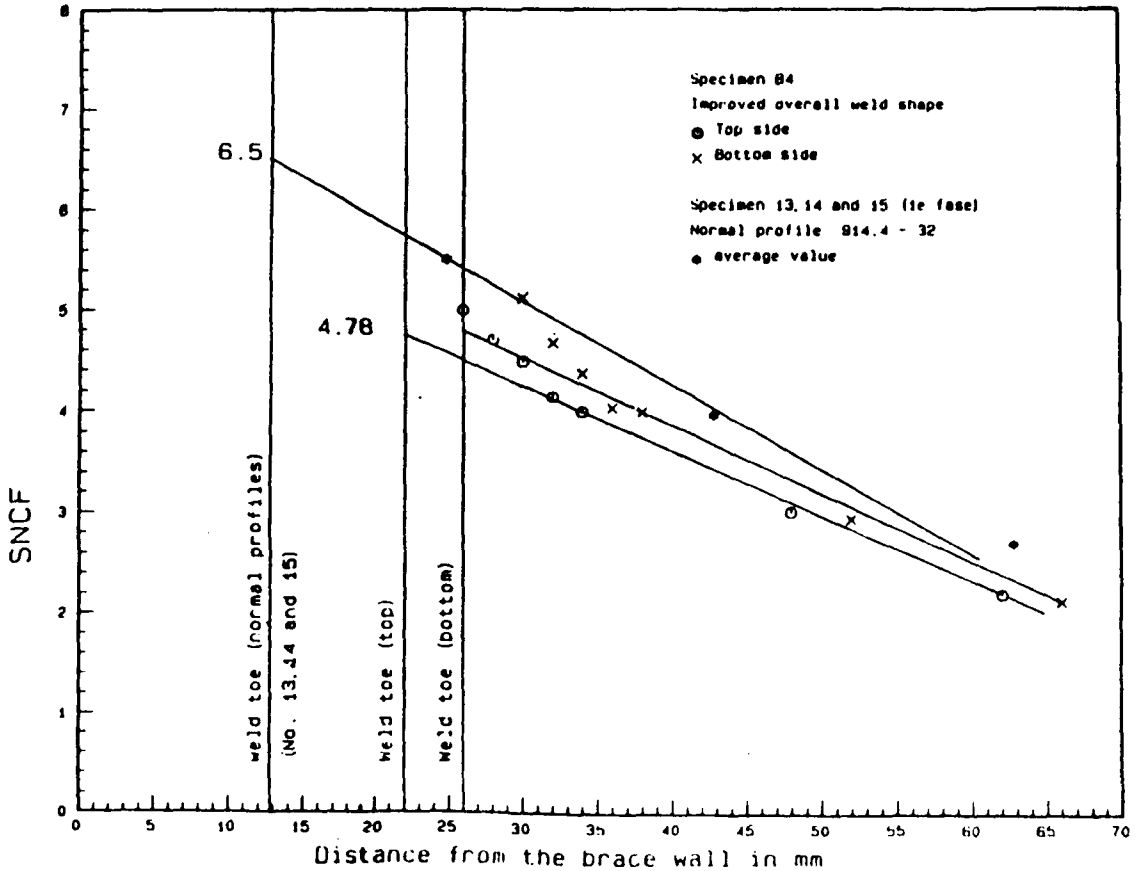
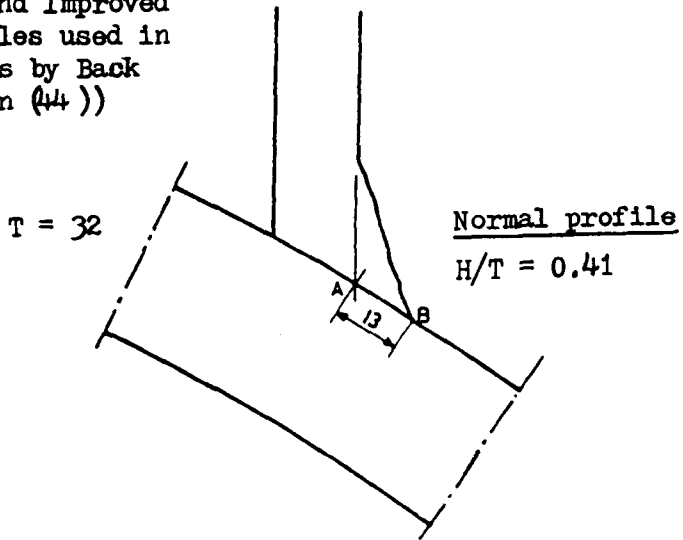


Fig. 2.17b Chord Wall Surface Strains for 2 Different Weld Profiles after Back (44))

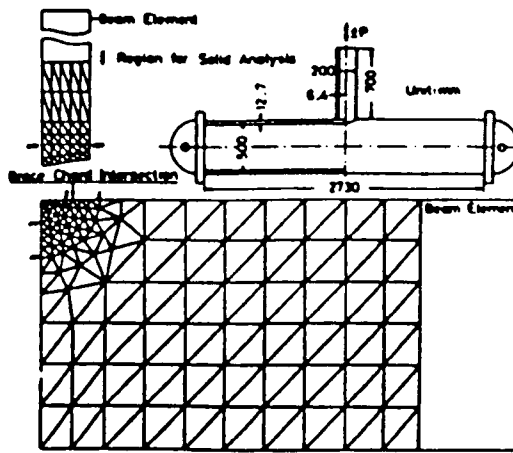


Fig. 2.18a Model Geometry and F.E. Mesh Used by Yoshida (45)

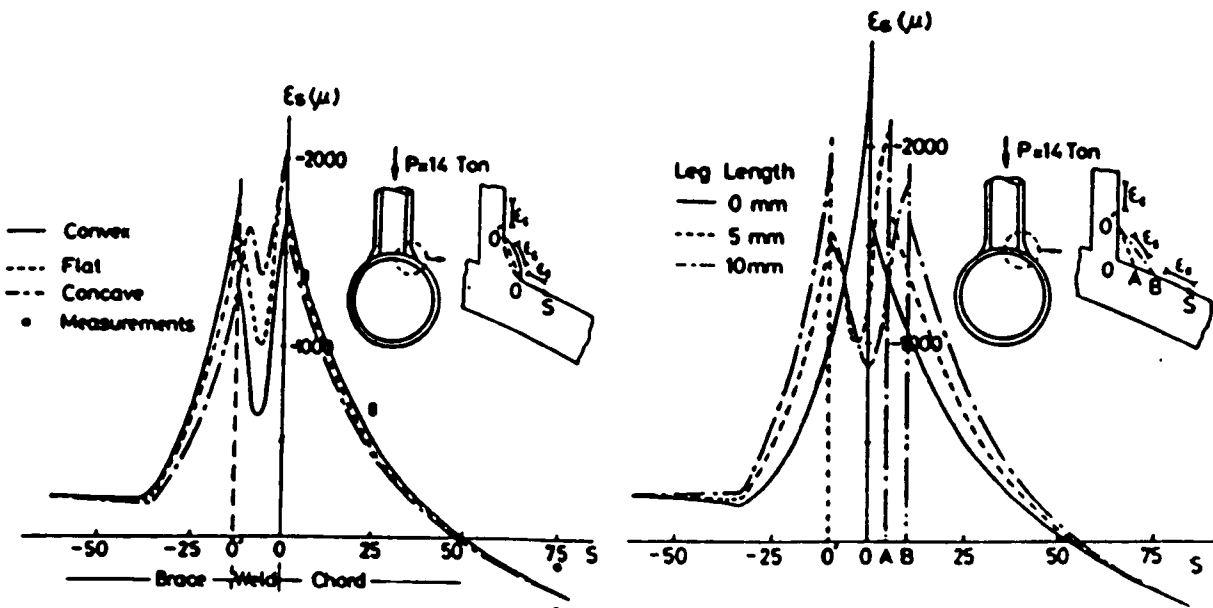


Fig. 2.18b Surface Strains for 1) 3 Different Weld Profiles, and 11) 3 Different Weld Leg Lengths (after Yoshida (45))

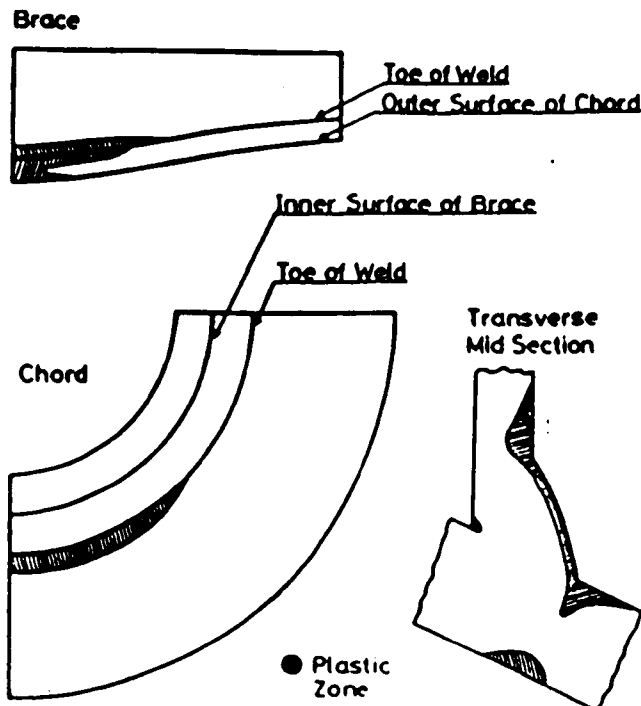


Fig. 2.18c Extent of Plasticity at Brace Stress = 56 N/mm^2 (after Yoshida (45))

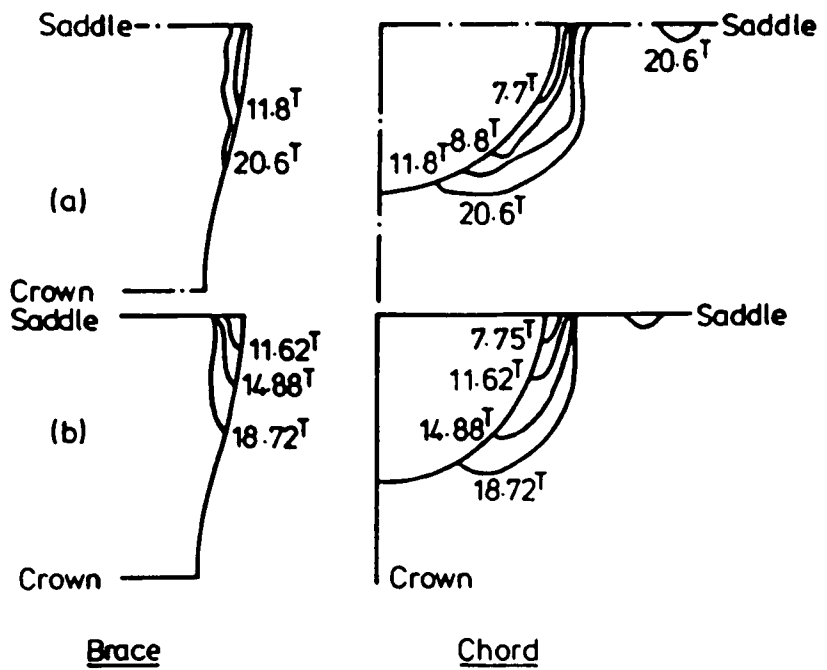
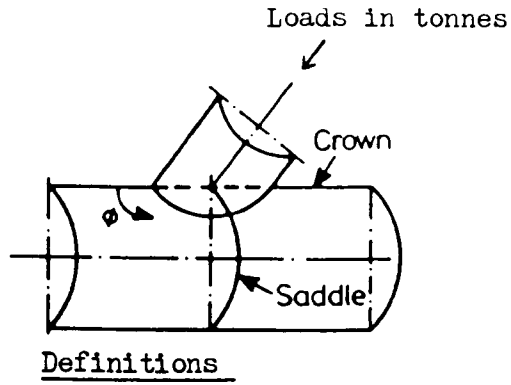


Fig. 2.19a **Extent** of Plasticity at Different Brace Loads (after Teyun (46))

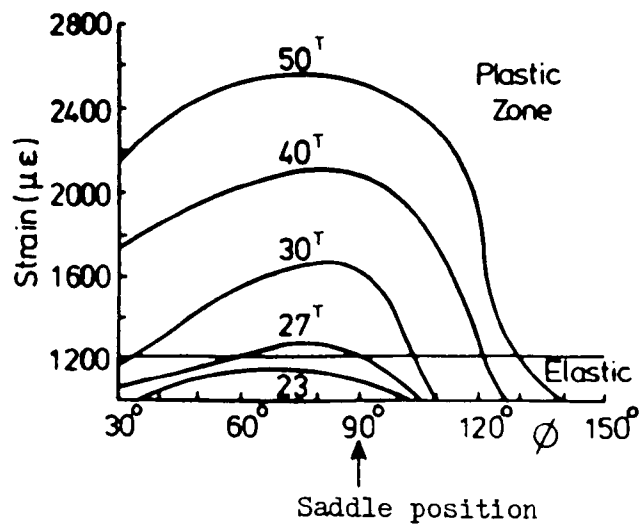


Fig. 2.19b Plastic Strains at Different Brace Loads around Brace-Chord Intersection Line (after Teyun (46))

CHAPTER 3

ANALYSIS OF PROBLEM AND MODEL DESIGN

3.1 General Considerations

The large number of geometric configurations and loading modes in the tubular steel jacket of an offshore structure is minimised by basing the investigation on the weld and assessing shapes and loading modes according to their effects on the stresses at, and near the weld toes. The curvature of any tube in an offshore structure is very much smaller than the curvature of the most generously dressed (radiused) weld. Therefore the curvature of the 'run' of the weld is unimportant and the diameter-to-thickness ratios D/T and d/t have little influence on the stress distribution near the weld toe. It therefore seems reasonable to assume that the effects of the shape parameters D/T and d/D , d/t and θ for every brace in the joint are included in the nominal brace stress σ_{nom} and that brace proximity g and dihedral angle ψ control the shell SCFs K_g . The length of plain chord surface g' (see Fig. 3.1) is a more realistic parameter than g , the distance between the (extended) tube surfaces, because the latter defines a distance between positions inside two welds. Stress concentration factors are usually measured at weld toes at the end of the plain chord surface.

Because the curvature of the weld toe predominates, the greatest stresses are fillet stresses usually in the plane perpendicular to the fillet surface. Cross sections of the tubular joint, perpendicular to the run of the weld, may be considered as "simple joints" consisting of two tube walls and a small weld fillet. The shape of the tube walls forming a simple joint is therefore defined by the chord plate thickness T , the brace plate thickness t and the local dihedral angle between them ψ .

Stress distributions are also known to be affected by the proximity of other fillets and the extent of the weld fillet from the intersection of the outer tube surfaces. These effects have to be established.

The effect of the weld on maximum stresses at hot-spot locations is to interrupt and modify the outside wall surface stress distribution near to weld toes. Stress gradients are usually large at hot-spots and because peak stresses are nearly always found at the weld toe, weld size is an important parameter. Weld shape is also known to influence the maximum stress because of the localised notch effects near to weld toes, (6).

The influential parameters involved in the stress distributions near to weld toes are therefore:

- i) brace proximity, i.e. the real gap between weld toes where maximum stresses are found,
- ii) brace inclination, i.e. the local dihedral angle between the outside chord and brace walls,
- iii) weld size, i.e. the distance to the weld toe from the intersection of outside chord and brace walls, and
- iv) weld toe profile, i.e. the shape of the weld fillet where it merges with the outer tube walls.

Three dimensional (3-d), frozen stress photoelastic models were used to determine surface stress distributions and obtain shell SCFs. The effects of brace proximity and brace inclination were investigated using non-overlapped corner K joints, shown in Fig. 3.1 and 3.2. The effects of weld size and (to a limited extent) brace inclination were investigated using X joints, shown in Fig. 3.3. The outer and inner surface stresses obtained from these models were used to establish equivalent two-dimensional (2-d) systems in the planes of symmetry of 3-d models. These simple joints were represented using large scale, flat models with accurate weld profiles.

2-d models were used to investigate the effects of weld toe profile and weld size on peak and notch SCFs. Photoelastic and finite element methods were used to study elastic stresses. Steel weldments were manufactured to study plastic-elastic effects.

3.2 Design of 3-d Photoelastic Models

3.2.1 Geometric Parameters and Dimensions

There are two types of 3-d models; multibrace corner-K (called CK) joints and X joints. In each, the geometric parameters that were selected for the investigation were varied over a realistic and experimentally convenient range of values. These are given later. In all 3-d models the chord diameter $D = 200$ mm.

The parameters which were shown in the previous section to be less important on the stresses near weld toes were constant. These were

γ , β , τ and α . The values assigned to these were as follows.

a) $\gamma_r = D/2T = 12.5$. Data given in (47) show that the most frequently used values of γ in offshore jacket installations are in the range $10 < \gamma < 20$. The lower practical limit of γ is 10 at which plate cannot be cold rolled to a greater curvature. A value of 12.5 was therefore chosen as being typical and similar to previous photoelastic work on welded tubular K joints (16, 20).

b) $\beta = d/D = 0.5$. This is shown (47) to be most frequent in the range $0.4 < \beta < 0.6$. Inspection of well known parametric formulae (e.g. 5) show SCFs for single plane K joints to be maximum when $\beta = 0.5$. This value was also used previously (16, 20).

c) $\tau = t/T = 0.5$. This is shown (47) to be most frequent in the range $0.5 < \tau < 0.9$. There is general agreement (4, 5, 27) that chord SCFs increase (almost) linearly with τ and that maximum SCFs are found at the chord end of welds (where fatigue cracks commonly occur) when

$\tau > 0.4$ (5). A value of 0.5 was also used previously (16, 20).

d) $\alpha = 2L/D$. In the corner K models the chord was made as long as possible but for the physical restrictions in the loading tank which limited α to 10. Analysis of a cylinder subjected to a radial line load (48) showed bending deformation to be small beyond $0.63D$ from the point of load application. The distance from the end of the model to the nearest brace wall was $1.58D$. (Efthymiou (27) has shown that for the geometry used in this work, chord wall SCFs at the saddle position in a T joint are not affected by chord length when $\alpha > (\text{about}) 11.$)

For the X node, the length of the chord was restricted to the width of the tank because the braces had to be located in line with the length of the tank. The maximum value of α was 6.6. This caused concern because it is known that the length of an open ended tube affects the diametrical deformation and shell bending stresses at mid-length. The length to radius ratio $\alpha = L/R$ of chords in offshore structures is much greater than can be modelled. It was therefore necessary to determine the length of chord that would exhibit, at the middle, deformation characteristics similar to an infinitely long tube of identical geometric parameters and brace configuration to the photoelastic model.

Roark and Young (49) suggest that a tube, when subjected to diametrical point loading at mid-length, is effectively infinite when L/R exceeds 18. Deformation decays in an exponential sinusoidal manner and there exists points of contraflexure along the tube. Experiments were carried out to find these points and to determine whether a shorter tube ($L/R < 18$) would exhibit similar deformation characteristics to the long tube when cut in the vicinity of these points. A model was assembled using centrifugally spun Araldite tubes manufactured for the tubular joint flexibility work by Mockford (50). The tube parameters and angles associated with

flexibility are θ , ω , γ , β and e/D . The nearest available parameters to the photoelastic model in this work were $\gamma = 12.35$ and $\beta = 0.53$. Two braces were glued onto the chord to give $\theta = 90^\circ$, $\omega = 180^\circ$ and $e/D = 0$. The maximum length of chord available was $6.7D$ or $14R$. Although this was less than the ratio quoted by Roark, the loading conditions (with respect to deformation in the plane of symmetry) were less onerous. The model was mounted in an Instron testing machine with the brace axes vertical. It was loaded in axial compression through ball bearings centred on brace caps. Dial gauges (with 0.001 mm graduations) measured horizontal diametrical deformation at selected points along the length of the tube. This was repeated for other lengths of chord.

Typical brace load v chord deformation curves are given in Fig. 3.4 for $\alpha = 14$ to show elastic linearity and hysteresis. In calculating the stiffness term δ/P (mm per N) the mean of at least three loading cycles was taken. Non-dimensional values δ_{ER}/P were calculated. The data is presented in Fig. 3.5 for different lengths of chord. A value for Young's Modulus of the chord of 3260 N/mm^2 was determined by Mockford. In this figure, horizontal dotted lines indicate the normalised value of δ_{ER}/P at selected positions along the chord for $\alpha = 14$. Their intersections with each stiffness curve represent a length of chord L_0 in which diametrical deformation is equal to that of a chord of length $14R$. These results show that deformations measured up to $2.67R$ from mid-span were the same as for a long chord in the range $5.90 < L/R < 6.05$. The length of the chord in the photoelastic models was therefore chosen as $6.0R$. It was assumed that the hoop and radial stiffnesses of the thin segmental air traps used in stress freezing the models were negligible.

3.2.2 Corner K Models

3.2.2.1 Variable Parameters and Loading

The models used to study brace inclination and proximity were non-overlapped corner K nodes having four different brace to chord inclinations in each model and three different brace gap separations in three different models. These are prefixed "CK".

Co-planar brace angles of $\theta_1 = 90^\circ$ and $\theta_2 = 135^\circ$ in Plane I, and $\theta_1 = 60^\circ$ and $\theta_2 = 150^\circ$ in Plane II (see Fig. 3.2) cover the range of θ . The braces were at least $2.3d$ long. It was also convenient and economical to make each model with four braces with four different inclinations θ on one chord in a corner K configuration with equal spacing g in the axial and circumferential directions. This determines ω , the angle between planes I and II. Separate models were used to vary the brace spacing. For models CK1, CK1R and 2 it is the minimum allowed by API recommendations (7) for a typical 48 inch diameter chord in a horizontal frame, which is $g = 2$ inches. In models CK3 and 4, g is the approximate distance at which the opposing forces in the balanced axial loading system were expected to optimise interactive chord wall bending. (This data was obtained from the 3-d analysis of Little (16)). In model CK5 the circumferential brace gap separation was given by the two co-planar brace axes being orthogonal, i.e. $\omega = 90^\circ$.

As shown in the development of the chord surface in Fig. 3.2, braces have been arranged to minimise the inevitable "saddle offset" to make it unimportant. Because the proximity effect is likely to be affected by the load in the brace wall which is near to the weld being studied, unloaded as well as loaded braces were included. The unloaded braces were introduced in another meridional plane making a corner K configuration as shown in Plate 3.1, and schematically in Fig. 3.1.

The selected loading mode was balanced axial loading of two co-planar

braces. The loads and reactions for each model are given in Fig. 3.6a. This figure shows that part of the chord, adjacent to the braces in compression, carries the reactions to the load components parallel to the chord axis. The (small) transverse chord end reactions resulting from brace axis offset e in the plane of loading are also given in Fig. 3.6a.

The reasons for using balanced axial loadings were that Fessler and Edwards (51) showed that in single plane K models of cast steel nodes (with tapered collars and fully blended radii) in balanced axial loading, stress concentrations exist at all locations in the brace-chord intersection. This permitted a full investigation of stresses in crown and saddle positions. For out-of-plane and/or in-plane bending, stresses were found to be negligible at crown and/or saddle positions respectively.

Dimensions and loading details of the 3-d corner K models are summarised in Table 3.1.

3.2.2.2 Weld Profile

The fillet weld shape is based on API recommendations for a stress-relieved, full-penetration, single-sided weld, as shown in Fig. 3.7a. The maximum recommended projection onto chord surfaces (from internal root) was $1.75t$, and a leg length h was controlled by a weld preparation angle of $\phi/2$. The weld toe radii represented by the external radii r depend mainly on the type and size of electrode used. The root gap G in Fig. 3.7a is represented by the internal radius r_1 in Fig. 3.7b to proportionate scale.

Consideration was also given to the intended materials; reasonable weld angles and weld leg lengths were chosen so that the effects of small changes in profile could be observed photoelastically. The outer and inner fillet toe radii were derived from structural steel weldments of 25 mm thick to 50 mm thick plates with $\phi = 90^\circ$ and 120° using approved

offshore weld procedures. Their outer toe radius varied accidentally in the range $0.015 < r/t < 0.140$, the mean being about $r/t = 0.06$. In the 3-d photoelastic model the intended range was $0.05 < r/t < 0.20$. The intended internal radius was $0.05 < r_1/t < 0.1$. The weld profile used in the 3-d CK models is shown in Fig. 3.7b.

Design dimensions and geometry for each of the joints in the planes defined in Fig. 3.2 are given in Table 3.2. The actual values for each model are given in Section 4, Tables 4.1 to 4.6.

3.2.3 X Models

3.2.3.1 Variable Parameters and Loading

The models used to study weld profile effects with brace inclination were X nodes having two diametrically opposite braces of equal inclination and diameter. X nodes were used because they are uncomplicated by the proximity of other braces and bending of the chord does not have to be considered.

For the first X node, a brace angle $\theta = 90^\circ$ was chosen because this angle gives the greatest stresses and this configuration has two planes of symmetry. Brace-to-chord wall thickness ratios $\tau = t/T = 0.5$ and 0.3 were selected for the braces, leading to realistic d/t ratios of 25.0 and 41.7 . A diameter ratio $\beta = 0.5$ gives a dihedral angle $\psi = 120^\circ$ at the saddle. A brace angle $\theta = 60^\circ$ allows direct comparison of crown toe and saddle positions for the same dihedral angle of $\psi = 120^\circ$. A value of $\theta = 60^\circ$ was therefore selected for the second 3-d configuration with $\beta = \tau = 0.5$. The 3-d X models are shown in Fig. 3.3.

All braces were made $3.8d$ long to ensure a uniform load distribution around the circumference of the brace. Irvine (6) suggests that bending stresses in the brace become negligible at $5d$ from the intersection. This length of brace was not possible to model. Using finite element methods Wong et al (52) have shown $3.8d$ to be sufficient to ensure a

uniform axial load distribution in a brace. X nodes were loaded in axial tension. The ends of the chord were free to ovalise as shown in Fig. 3.6b and Plate 3.2.

3.2.3.2 Weld Profile

Two sizes of weld were used:

- i) "Uncontrolled" (prefix U), flat fillet profiles, having steep weld angles and small toe radii, conforming to the minimum API requirement for weld projection onto the outer chord wall of $0.25t$. See Fig. 3.7c.
- ii) "Controlled" (prefix C), improved profile, with specific butter and capping bead control at the chord end of the weld. Figs. 3.7d and e show the controlled profiles for obtuse and acute joints, respectively.

The two weld profiles were formed in the models in the positions shown in Fig. 3.3. Different weld profiles were formed on the same braces in the X90 model because this model has two planes of symmetry, and on different braces on the X60⁰ node because this model has only one plane of symmetry which occurs at the crown.

The local dihedral angle changes continuously between the crown and saddle position. The weld profiles given in Fig. 3.7c, d and e were formed at these positions for the distance of 20 mm either side of a plane of symmetry, with gradual transitions between these regions of constant profile. The intended ranges for the outer and inner toe radii were the same as the corner K nodes specified in Section 3.2.2.2.

Design dimensions and geometry for the models are given in Table 3.3. The actual values are given in Section 4, Tables 4.7 and 4.8.

3.3 Design of 2-d Photoelastic and Finite Element Models

3.3.1 General Design Concepts

The effects of weld profile, weld size and the local dihedral angle between brace and chord walls were studied using full size and approximately

half size, two-dimensional photoelastic and finite element models. The cross-section of every part of any single-brace tubular joint can be represented by a T or Y junction of two straight walls. The lengths of these walls depend on the stress distribution which is to be copied in these simple models and must be sufficient to ensure that the strips represent the essential features of the tube joints. Useful data may be obtained if the 3-d surface stress distributions can be reproduced in 2-d arrangements. It was assumed that the fillet stresses are caused by tension and bending of the chord and brace walls.

The correct equivalent 2-d loading was obtained from 3-d results in a non-overlapped K joint (16) and X90 node (from this work). Three values of $\psi = 90^\circ$, 120° and 135° , the inclination of the brace wall to the chord wall, were chosen to determine equivalent tensions and bending moments acting on the brace and chord strips of a 2-d model. For each of these, the positions and values of stress indices at the inner and outer surfaces in 3-d models were recorded. The means and semi-differences of opposite values were plotted and the best values of mean tension and "cantilever" bending determined from them. The positions of zero bending moment defined the distance a_1 , a_2 and a_3 in Fig. 3.6c. P_1 , P_2 , P_3 are the resultants of the mean tensions and transverse forces causing bending. Angle λ defines the inclination of force P to the axis of each wall. The positions and directions of the loads are given in Table 3.4.

The stress field in a homogenous joint near weld toes may be described in terms of weld and joint geometry and loading conditions. The individual geometric parameters interact. For an isolated junction (large g/T) the stress distribution at the weld depends on the local dihedral angle ϕ , weld leg lengths H/T and h/t , local weld toe angles α_c and α_b and weld toe radius ratios r_c/T and r_b/t . The basis for the design of the two-dimensional models involved the separation of these geometric weld

parameters. The most important position is at, or near to the usual crack initiation site at the chord weld toe. To generate the maximum useful data at this position, changes in parameters were made primarily at the chord toe; the brace leg parameters being dependent on these. All 2-d models used in this work originate from the planes of symmetry of small scale ($D = 132$ mm and 200 mm) 3-d models analysed by Little (16) or the author. The 3-d models used were;

- i) K node; comprising $\theta = 45^\circ$ and $\theta = 90^\circ$ co-planar braces in balanced axial loading (16).
- ii) X90 node; comprising $\theta = 90^\circ$ braces loaded in axial tension and as shown in Fig. 3.3

In the design of weld shapes, API (7) and AWS (8) welding codes define the shape of the cross-section of a weld in terms of the brace wall thickness t . Fig. 3.7f shows the shape of a fully radiused weld used in previous 3-d stress analysis (16) in which $r = 0.5t$ and $r_1 = 0.1t$. This weld profile was used in this work to determine the equivalent 2-d loading system by close agreement of 3-d and 2-d surface stresses in the tube walls and fillet.

Weld profiles shown in Figs. 3.7b, c and d were also used in 2-d models. The schedule for the models was as follows;

Parent 3-d Model	3-d Model Details		Weld types and profile
	Position	θ ψ	
K	Crown	90° 90°	Fully blended Uncontrolled fillet Controlled fillet
K	Crown	45° 135°	Fully blended
K & X	Saddle	90° 120°	Fully blended Uncontrolled fillet, with and without toe grinding Controlled fillet

The reason for selecting the 2-d models listed above was to examine the effect of weld profile on some of the most extreme global conditions that exist in typical tubular joints, i.e. X node (axially loaded) and single plane K node (balanced axial loading). SCFs in X nodes may exceed 15 whereas in balanced K nodes SCFs are typically 3 to 4.

3.3.2 2-d Photoelastic Models

The models used to study the "uncontrolled" and "controlled" profiles were made as large as possible (to fit in the confines of a polariscope) and to allow considerable reductions in both brace and chord wall thicknesses. Initially the brace wall thickness was $t = 40$ mm and the chord wall thickness was $T = 80$ mm. To study the size effect of scaling down (or up) of individual member wall thicknesses, the models were modified in the following sequence

$$\frac{t}{T} = \frac{40}{80}, \quad \frac{32}{80}, \quad \frac{32}{71.1}, \quad \frac{32}{64}, \quad \frac{25}{64}, \quad \frac{25}{50}, \quad \frac{20}{50}$$

hence $\tau = 0.50, 0.40, 0.45, 0.50, 0.39, 0.50, 0.40$

The weld profiles were geometrically scaled up from the intended, not actual, welds used on the 3-d X nodes. (Differences are unavoidable in 3-d models because of their size). These were very accurate profiles. For each model given in the above schedule, identical pairs were manufactured differing only in the profile at the chord end of the weld; giving either the "uncontrolled" or "controlled" profile. Weld toe radii r were the same for all these models; initially $r = 0.8$ mm when $T = 80$ mm. Weld angles α_c and weld leg lengths H were constant for each profile type. Thus, a range of values for r/T and H/T were achieved by reducing the wall thickness T .

Some models were used to study only one of the weld toe parameters. Brace and chord wall thicknesses were constant; either $T = 80$ mm, 50 mm or 30 mm depending on the parameter being studied. In all these models,

$\tau = 0.5$. A range of values for the weld profile parameters r/T , α_c and H/T was achieved by modifying the weld fillet.

The dimensions and shape parameters of these models are given in Table 3.5 and shown in Fig. 3.8a to e.

3.3.3 2-d Photoelastic Models with Weld Toe Grinding

It is known that a significant improvement in fatigue strength is obtained if weld defects are completely removed by toe grinding (33). Considerable changes in weld toe profile are obviously made because grinding must penetrate into the plate surface. A series of 2-d photoelastic models with different depths of penetration were designed to study the effect on the SCF and, because of the inevitable reduction in chord wall thickness, the stresses near to the edge of the ground profile.

Models in the saddle planes of K and X nodes with uncontrolled weld profiles were chosen for analysis. The radius of grinding was obtained from profiles given by Back (44) measuring (approx.) 4 mm for a 32 mm chord wall. A convenient value of $r/T = 0.1$ was therefore used. The minimum and maximum depths of penetration were in accordance with the requirements of the DoEn Guidance Notes (12). The direction of grinding was such that the centre of the grinding tool moved on a line perpendicular to the chord wall at the intersection of the original weld toe. The dimensions and shape parameters of the models are given in Table 3.6 and shown in Fig. 3.8f.

3.3.4 2-d Finite Element Models

Finite element models were designed to study surface and through-thickness stresses for a range of uncontrolled weld shapes for the crown position of a $\theta = \psi = 90^\circ$ joint only. 3-d photoelastic work showed that large differences in weld size have virtually no effect on the stiffness of the joint. Hence, the same 2-d finite element arrangement

was used to model fillet and fully blended welds in the range $0.05 < H/T < 0.50$. Weld toe radii to chord wall thickness ratios were studied in the range $0.02 < r/T < 0.25$, and weld angle α_c was varied from 24° to 83° .

The design of the mesh is described in Experimental Techniques, Section 4.2.3. The geometric parameters for all F.E. models are given in Table 3.7 and shown in Fig. 3.8c to e.

3.3.5 2-d Model Loading

The models were loaded by the equivalent three-point loading system shown in Fig. 3.6c. The positions and directions of the equivalent loads are given in Table 3.4. The positions (expressed in terms of wall thickness) and directions of the loads were kept constant for the range of values for t , T and ϕ studied. This was justified by the small differences in the positions of the loads at the saddle of the X90 node for $\tau = 0.5$ and $\tau = 0.35$ obtained from 3-d analysis.

3.4. Design of 2-d Steel Models

3.4.1 General Considerations

The changes, from elastic to plastic-elastic conditions, that take place near to weld toes during yielding were studied. The onset of local yielding, which is known to take place near to weld toes at the positions of the maximum strain concentration factor (SNCF), or hot-spot, affects the magnitude of the SNCF. These are usually obtained by linear extrapolation of strains measured by remote gauges. Should the gauge nearest the weld toe measure plastic strains, results would be spurious and difficult to interpret.

Local yielding in the weld toe region also affects the position of the maximum strain. This has to be established to assess the importance of the mechanical properties of the different materials in this region. The degree of strain hardening and re-distribution of stress at very large plastic strain levels may also affect crack initiation life.

The strains (and stresses) in the region of plasticity depend on

- i) weld toe profile, including flaws, cracks, undercut etc.
- ii) local loading conditions, eg predominant wall bending
- iii) the extent of heat affected zones (HAZ)
- iv) mechanical properties of HAZ, parent plate and weld material

Items i) and ii) are the subject of the elastic stress analysis.

The investigation into the plastic-elastic behaviour of tubular joints was based on items i) to iv). The effects of these parameters on the strains near to weld toes which exceed the elastic limit were studied using real weldments. 2-d steel models were made from the weldments and tested in the as-welded and stress relieved conditions.

3.4.2 Geometric Parameters and Dimensions

The design of the steel models aimed to generate maximum data using only two joint shapes, the 'crown' and 'saddle' positions of a $\theta = 90^\circ$ brace-to-chord connection. To enable direct comparison with elastic values, the joints were geometrically similar to the 2-d Araldite models, i.e. $t/T = 0.5$: $d/D = 0.5$: $D/T = d/t = \infty$. Flat steel plates, welded at 90° and 120° to each other, were used as shown in Fig. 3.9. A typical chord wall thickness of $T = 50$ mm was chosen. The lengths of the weldments were 250 mm. Because of the practical difficulties in achieving intended weld sizes, only the actual dimensions and geometric parameters of the weldments are given. See Table 4.14. The models cut from the weldments were 10 mm thick for use with reflection photoelasticity methods, and 4 mm thick for use with moire interferometry methods. The experimental techniques appropriate to these methods are described in Chapter 4.

3.4.3 Design of Welds

The weldments were designed to API and AWS recommendations with

regard to weld preparation angle, root gap preparation and distance, and weld projection onto the chord wall. To determine the contribution to strength of the weld material, two grades of electrode were specified; grade E51 having a yield strength comparable to the parent (grade 50D) plate and grade E43, a common product. Different weld toe geometries could be produced by using 2.5 mm and 4 mm diameter electrodes on each of the two types of joints. However, because toe radii vary accidentally over a large range, it was decided to combine electrode grade and rod diameter; 4 mm E51 electrode for models 90/A and 120/A; and 2.5 mm E43 electrode for the final passes of models 90/B and 120/B. These weld profiles were designated "uncontrolled" because no special profiling or post weld dressing was carried out.

Models 120/C were modifications of models 120/A using the same grade and diameter electrode. These weld profiles were designated "controlled" because a definite size filler was added at the chord weld toe of an uncontrolled profile. The weld toe radii were specified intentionally large and weld angles small. These profiles are occasionally referred to by other investigators as "improved". The controlled profile was designed in accordance with the recommendations made by Marshall (43) for modifications to the AWS standard weld profile.

3.4.4 Steel Model Loading

The models were loaded using the same three point loading designed for the 2-d photoelastic models; the positions and directions of loads are previously given. The load capacity of the system was determined by the nominal maximum stress of 300 N/mm^2 , i.e. about 0.85 yield stress, in the brace wall. The load capacity was thus 30 kN for the 4 mm thick models used with the moire interferometry method of strain analysis. A 50 ton Denison tensile testing machine was used for the 10 mm thick models used in the reflection photoelasticity work.

Table 3.1
Design Shapes of 3-d Models

Model Ref.	Loaded Plane	Model Parameters and Angles						
		Compression Brace θ_1	Tension Brace θ_2	g/T All	g'/T Crown	Saddle	e/D	ω
CK1	I	90°	135°	1.250	0.45	0.44	+0.1535	66°
CK1R	"	"	"	"	0.71	0.64	"	"
CK3	"	"	"	3.875	3.00	3.44	+0.2585	78°
CK2	II	60°	150°	1.250	0.51	0.57	-0.3165	66°
CK4	"	"	"	3.875	3.00	3.00	-0.2105	78°
CK5	"	"	"	6.500	5.70	6.00	-0.1045	90°

For all models; L = 945mm (nominal)

D = 200mm

D/T = 25

t/T = d/D = 0.5

For all welds; h/t = 1/sin ϕ

H/T = 0.375/sin ϕ

r_b/t = 0.05 to 0.20 (intended range)

r_c/T = 0.025 to 0.10 (intended range)

Table 3.2
 CK-
 Three-Dimensional Model Design Geometry

Joint No.	Brace Angle		Dihedral Angle		Brace Wall			Chord Wall			Weld Parameters						
	θ	φ	t	r	r ₁	r/t	r ₁ /t	T	r	r/T	t/T	τ	h/t	a/t	H/T	α _b	α _c
1	135°		4.00	0.20	0.20	0.05	0.05	8.00	0.20	0.025	0.50		1.41	0.62	0.65	48°	86°
2a	135°		"	to	to	to	"	"	to	to	"		1.41	0.35	min	19°	26°
2b	90°		"	0.80	0.40	0.20	0.10	"	0.80	0.10	"		1.00	0.60	0.75 max	37°	53°
3	90°		"	"	"	"	"	"	"	"	"		1.00	0.60	"	37°	53°
4	150°		"	"	"	"	"	"	"	"	"		2.00	1.46	"	47°	103°
5a	150°		"	"	"	"	"	"	"	"	"		2.00	0.40	"	13°	17°
5b	60°		"	"	"	"	"	"	"	"	"		1.15	0.48	"	25°	35°
6	60°		"	"	"	"	"	"	"	"	"		"	0.79	"	46°	74°
7	90°		"	"	"	"	"	"	"	"	"		"	0.48	"	25°	35°
8a	90°		"	"	"	"	"	"	"	"	"		"	"	"	"	"
8b	60°		"	"	"	"	"	"	"	"	"		"	"	"	"	"
9	60°		"	"	"	"	"	"	"	"	"		"	"	"	"	"
10	135°		"	"	"	"	"	"	"	"	"		"	"	"	"	"
11a	135°		"	"	"	"	"	"	"	"	"		"	"	"	"	"
11b	150°		"	"	"	"	"	"	"	"	"		"	"	"	"	"
12	150°		"	"	"	"	"	"	"	"	"		"	"	"	"	"

Table 3.2
Three-Dimensional X-Model Design Geometry

Position in Model	Model and Weld Profile Ref	Dihedral Angle		Brace Wall				Chord Wall			Weld Parameters						
		φ deg	r _b mm	r ₁ mm	r _b /t	r ₁ /t	T mm	r _c mm	r _c /T	t/T	h/t	F/T	H/T	a _b deg	a _c deg		
																t mm	r _b /t
Crown	X90 U 0.5	90°	4.00	0.20	0.05	0.20	0.05	0.05	8.00	0.20	0.025	0.5	1.00	-	0.187	18°	72°
	C 0.5	90°	"	to	to	to	to	to	"	to	to	"	"	0.25	0.375	"	45°
Saddle	U 0.5	120°	"	0.80	0.40	0.20	0.10	0.10	"	0.50	0.062	"	"	-	0.187	15°	45°
	C 0.5	120°	"	"	"	"	"	"	"	"	"	"	"	0.28	0.375	"	23°
Crown	X90 U 0.3	90°	2.40	"	"	0.08	0.08	0.08	"	"	"	0.3	1.67	-	0.187	18°	72°
	C 0.3	90°	"	"	"	to	to	to	"	"	"	"	"	0.25	0.375	"	45°
Saddle	U 0.3	120°	"	"	"	0.33	0.16	0.16	"	"	"	"	"	-	0.187	15°	45°
	C 0.3	120°	"	"	"	"	"	"	"	"	"	"	"	0.28	0.375	"	23°
Crown and Saddle	X60 U 0.5	120°	4.00	"	"	0.05	0.05	0.05	"	"	"	0.5	1.00	-	0.187	15°	45°
	C 0.5	120°	"	"	"	to	to	to	"	"	"	"	"	0.28	0.375	"	23°
Crown only	U 0.5	60°	"	"	"	0.20	0.10	0.10	"	"	"	"	"	-	0.187	"	105°
	C 0.5	60°	"	"	"	"	"	"	"	"	"	"	"	0.25	0.375	"	45°

Table 3.4

Position and Direction of Equivalent Loads for 2-d Models

Parent 3-d Model	3-d Model Details				Position ¹			Direction ¹		
	Position	θ	ψ	τ	a_1/t	a_2/T	a_3/T	λ_1	λ_2	λ_3
X90	Saddle	90°	120°	0.5	3.80	2.40	1.62	10°	22°	49°
"	"	"	"	0.35	3.92	2.51	1.36	9°	20°	52°
K	Saddle	90°	120°	0.5	3.70	2.40	1.75	14°	32°	66°
K	Crown	90°	120°	0.5	3.60	1.70	1.77	10°	65°	76°
K	"	135°	135°	0.5	3.42	1.30	3.72	8°	45°	160°

Note 1: Refer to Fig. 3.6c.

Table 3.5a

Two-Dimensional Photoelastic ModelsShape Parameters and Stress Concentration Factors at Chord and Brace Weld Fillets

Joint and Weld Parameters ²					Stress Concentration Factors ³							
ψ	α_c	H/T	h/t	r/T	Chord Fillet				Brace Fillet			
					Value			Posn. θ_{oc}	Value			Posn. θ_{ob}
					K_{soc}	K_{noc}	K_{oc}		K_{sob}	K_{nob}	K_{ob}	
90° 120° 135°	N.A. ⁴ " "	N.A. ⁴ " "	N.A. " "	0.25 " "	2.05 2.68 2.10	2.12 1.68 1.81	4.35 4.50 3.80	50° 34° 20°	2.60 2.50 1.85	1.67 1.80 2.05	4.35 4.50 3.80	40° 26° 25°
90° " " " "	60° " " " "	0.375 " " " "	1.25 " " " "	0.025 0.05 0.10 0.185 0.25	1.85 1.70 1.70 1.60 1.65	2.86 2.56 2.44 2.34 2.30	5.30 4.35 4.15 3.75 3.80	23° 26° 26° 24° 26°	2.25 2.15 2.10 2.15 2.20	2.04 1.95 1.83 1.46 1.43	4.60 4.20 3.85 3.15 3.15	12° 14° 11° 12° 12°
90° " " " " " "	45° " " " " " "	0.375 " " " " " "	0.75 " " " " " "	0.025 0.05 0.10 0.135 0.185 0.25 0.335	1.88 1.85 2.00 2.05 1.90 1.84 1.90	2.76 2.37 2.05 1.81 1.92 1.87 1.68	5.20 4.39 4.10 3.71 3.65 3.45 3.20	31° 26° 23° 37° 26° 16° 18°	2.63 2.60 2.76 2.72 2.48 2.35 2.37	1.93 2.03 1.53 1.55 1.77 1.52 1.38	5.07 5.27 4.21 4.22 4.40 3.57 3.28	24° 23° 21° 18° 19° 14° 16°
90° " " " " "	45° " " " " "	0.485 0.395 0.315 0.200 0.125 0.100	0.97 0.79 0.63 0.40 0.25 0.20	0.05 " " " " "	1.67 1.90 2.15 2.40 2.50 2.52	2.43 2.42 2.38 2.26 1.80 2.10	4.05 4.60 5.03 5.44 4.50 5.30	23° 23° 26° 22° 0° 27°	2.40 2.57 2.80 3.05 2.50 3.20	2.03 2.03 1.90 1.90 1.84 1.75	4.88 5.21 5.31 5.10 4.60 5.62	30° 20° 23° 29° 20° 17°
90° " " " " "	65° 55° 45° 35° 25°	0.375 " " " "	1.49 1.30 0.75 0.56 0.40	0.05 " " " "	1.60 1.70 1.74 1.75 1.90	3.46 3.22 2.88 2.34 2.02	5.55 5.48 5.05 4.10 3.84	27° 30° 28° 25° 19°	No result ⁵		3.71 4.53 5.18 5.16 5.50	14° 13° 26° 30° 31°
120°	30°	0.175	0.35	0.05	2.65	1.58	4.20	15°	2.25	1.67	3.75	24°
120° " " " " "	37° " " " " "	0.375 " " " " "	1.25 " " " " "	0.025 0.05 0.10 0.185 0.25 0.335	2.13 2.17 2.15 2.45 2.25 2.07	2.12 1.98 2.07 1.82 1.61 1.58	4.52 4.30 4.45 4.47 3.63 3.27	30° 24° 24° 33° 31° 23°	2.00 2.05 2.08 2.10 2.10 2.15	1.67 1.55 1.56 1.60 1.62 1.37	3.34 3.18 3.25 3.36 3.40 2.96	12° 15° 17° 12° 17° 12°
135°	22½°	0.230	0.46	0.05	2.00	1.70	3.40	0°	2.05	1.66	3.40	22°

Notes:- 1) Model dimensions $t = 15\text{mm}$ 2) Joint parameters $D/T = d/t = g/t =$
 $t/T = 0.5$
 $r_1/t = 0.1$
 $\alpha_b = 180^\circ - \psi - \alpha_c$

3) All stress concentration factors are positive

4) N.A. = not applicable; because fully blended profile

5) Linear extrapolation not possible

Table 3.5b Two-Dimensional Photoelastic Models

Shape Parameters and Stress Concentration Factors at Chord Weld Fillet

a) Crown Position of Single Plane K90/45 Joint: $\varphi = \theta = 90^\circ$

Joint Parameters		Weld Profile Parameters					SCFS Value			Pos ⁴
T	τ^1	Quality	H/T	h/t	r/T^2	α_c^3	K_s	K_n	K	φ
mm						deg				deg
80	0.5	Uncontrolled	0.1875	1.00	0.01	70°	2.50	5.30	13.30	37°
"	0.4		"	1.25	"	"	2.00	4.80	9.62	35°
71.1	0.45		0.211	"	0.011	"	2.15	4.65	10.04	28°
64	0.5		0.234	"	0.0125	"	2.20	5.30	11.55	30°
"	0.45		"	1.39	"	"	2.10	5.10	10.70	32°
"	0.39		"	1.60	"	"	1.85	4.40	8.08	32°
50	0.5		0.300	"	0.016	"	2.10	4.65	9.78	35°
"	0.4		"	2.00	"	"	1.70	4.40	7.45	33°
80	0.5	Uncontrolled	0.25	1.00	0.10	70°	2.30	2.94	6.77	34°
"	"		0.232	"	0.075	"	2.35	3.06	7.21	34°
"	"		0.215	"	0.05	"	2.30	3.60	8.36 ₅	32°
"	"		0.197	"	0.025	"	2.30	3.96	9.12 ₅	33°
"	"		0.1875	"	0.01	"	2.50	5.30	13.30	37°
50	0.5	Uncontrolled	0.25	1.20	0.05	70°	2.22	3.87	8.60	32°
"	"		"	0.80	"	60°	2.25	3.45	7.75	29°
"	"		"	0.50	"	45°	2.20	2.95	6.50	21°
"	"		"	0.33	"	30°	2.30	2.15	4.95	13°
80	0.5	Controlled	0.343	1.00	0.01	44°	2.03	4.00	8.15	24°
"	0.4		"	1.25	"	"	1.65	3.30	5.40	24°
71.1	0.45		0.386	"	0.011	"	1.80	3.90	7.00	20°
64	0.5		0.429	"	0.0125	"	1.90	4.60	8.68	22°
"	0.39		"	1.60	"	"	1.60	4.20	6.72	25°
55.5	0.45		0.494	"	0.014	"	1.65	4.35	7.18	22°
50	0.5		0.55	"	0.016	"	1.55	4.60	7.15	22°
"	0.4		"	2.00	"	"	1.35	4.45	6.02	20°

Notes

- 1) $\tau = t/T$ 2) $r_1 = 1.5\text{mm}$ and $r_b = 0.8\text{mm}$ 3) $\alpha_b = 90^\circ - \alpha_c$, except for controlled weld $\alpha_b = 20^\circ$ 4) Measurement of $\varphi = \pm 3^\circ$ 5) Subsurface measurement at 0.1mm from edge of fillet.

Table 3.5c Two-Dimensional Photoelastic Models

Shape Parameters and Stress Concentration Factors at Chord Weld Fillet

b) Saddle Position of Single Plane K90/45 Joint: $\theta = 90^\circ$; $\varphi = 120^\circ$

Joint Parameters		Weld Profile Parameters					SCFS Value			Pos ⁴
T	τ^1	Quality	H/T	h/t	r/t^2	α_c^3	K_s	K_n	K	φ
mm						deg				deg
80	0.5	Uncontrolled	0.1875	1.00	0.01	45°	2.90	3.88	11.25	21°
"	0.4		"	1.25	"	"	2.25	3.50	7.86	23°
71.1	0.45		0.211	"	0.011	"	2.50	3.81	9.52	20°
64	0.5		0.234	"	0.0125	"	2.65	3.74	9.90	24°
"	0.39		"	1.60	"	"	2.15	3.50	7.55	22°
50	0.5		0.300	"	0.016	"	2.70	3.15	8.48	19°
"	0.4	"	2.00	"	"	2.15	2.93	6.30	20°	
80	0.5	Uncontrolled	0.225	1.00	0.10	45°	2.58	2.34	6.05	24°
"	"		0.215	"	0.075	"	2.65	2.62	6.96	24°
"	"		0.20	"	0.05	"	2.70	2.77	7.48	21°
"	"		0.19	"	0.025	"	2.70	2.99	8.07	22°
"	"		0.1875	"	0.01	"	2.90	3.88	11.25	21°
80	0.5	Controlled	0.36	1.00	0.01	22°	2.70	2.21	5.97	12°
"	0.4		"	1.25	"	"	2.20	2.00	4.42	11°
71.1	0.45		0.40	"	0.011	"	2.35	2.35	5.17	10°
64	0.5		0.45	"	0.0125	"	2.40	2.40	5.77	10°
"	0.39		"	1.60	"	"	2.10	2.20	4.62	13°
50	0.5		0.576	"	0.016	"	2.35	2.35	4.60	10°
"	0.4	"	2.00	"	"	2.10	1.87	3.92	10°	

Notes1) $\tau = t/T$ 2) $r_i = 1.5\text{mm}$ and $r_b = 0.8\text{mm}$ 3) $\alpha_b = 15^\circ$ 4) Measurement of $\varphi = \pm 3^\circ$

Table 3.5d Two-Dimensional Photoelastic Models

Shape Parameters and Stress Concentration Factors at Chord Weld Fillet

c) Saddle Position of X90 Joint; $\theta = 90^\circ$; $\varphi = 120^\circ$

Joint Parameters		Weld Profile Parameters					SCFS Value			Pos ⁴
T	τ ¹	Quality	H/T	h/t	r/l ²	α_c ³	K_s	K_n	K	φ
mm					deg					deg
80	0.5	Uncontrolled	0.1875	1.00	0.01	45°	8.35	3.58	29.9	24°
"	0.4		"	"	1.25	"	6.80	3.05	20.8	25°
71.1	0.45		0.211	"	0.011	"	7.25	3.15	22.9	27°
64	0.5		0.234	"	0.0125	"	8.15	3.20	26.1	23°
"	0.39		"	"	1.60	"	6.40	3.19	20.4	25°
50	0.5		0.300	"	0.016	"	7.90	2.70	21.3	22°
"	0.4	"	"	2.00	"	6.30	2.62	16.5	22°	
80	0.5	Uncontrolled	0.225	1.00	0.10	45°	8.30	1.93	16.0	24°
"	"		0.215	"	0.075	"	8.33	2.13	17.8	24°
"	"		0.20	"	0.05	"	8.40	2.22	18.6	27°
"	"		0.19	"	0.025	"	8.43	2.78	23.4	24°
"	"		0.1875	"	0.01	"	8.35	3.60	29.9	24°
50	0.5	Uncontrolled to Controlled ⁵	0.30	1.00	0.016	45°	7.90	2.70	21.3	22°
"	"		"	"	"	$37\frac{1}{2}^\circ$	7.83	2.38	18.6	22°
"	"		"	"	"	30°	7.85	1.84	14.4	17°
"	"		"	"	"	$22\frac{1}{2}^\circ$	7.90	1.65	13.0	9°
50	0.5	Controlled	0.576	1.00	0.016	22°	7.00	1.75	12.2	12°
"	"		"	"	"	10°	7.00	1.33	9.4	4°
80	0.5	Controlled	0.36	1.00	0.01	22°	7.75	2.35	18.30	12°
"	0.4		"	"	1.25	"	6.20	2.15	13.48	12°
71.1	0.45		0.40	"	0.011	"	6.90	2.10	14.35	11°
64	0.5		0.45	"	0.0125	"	7.20	2.20	15.85	13°
"	0.39		"	"	1.60	"	5.70	2.15	12.25	10°
50	0.5		0.576	"	0.016	"	7.00	1.75	12.15	12°
"	0.4		"	"	2.00	"	5.65	1.69	9.58	12°

Notes

- 1) $\tau = t/T$ 2) $r_a = 1.5\text{mm}$ and $r_b = 0.8\text{mm}$ 3) $\alpha_b = 15^\circ$ 4) Measurement of $\varphi = \pm 3^\circ$
5) Gradual profile improvement.

Table 3.6 Two-Dimensional Photoelastic Models with Weld Toe Grinding Shape Parameters¹ and Stress Concentration Factors at Chord Weld Fillet

a) Saddle Position of X90 Joint $\theta = 90^\circ$, $\varphi = 120^\circ$

Quality	Weld Profile Parameters ²			SCF			
	H/T	r/T	p/T	K_s	K_n	Value	Pos'n ³
Uncontrolled	0.225	0.10	0	8.2	1.96	16.12	22°
"	"	"	0.0625	"	2.01	16.47	"
Unc. ground toe	"	"	0.0125	"	2.07	16.95	"
	"	"	0.025	"	2.13	17.50	23°
"	"	"	0.05	"	2.27	18.62	26°

b) Saddle Position of Single-plane K90/45 Joint: $\theta = 90^\circ$, $\varphi = 120^\circ$

Uncontrolled	0.225	0.10	0	2.6	2.35	6.12	18°
"	"	"	0.00625	"	2.47	6.42	20°
Unc. ground toe	"	"	0.0125	"	2.54	6.60	"
	"	"	0.025	"	2.59	6.75	23°
"	"	"	0.05	"	2.82	7.33	24°

Notes

1. All $T = 80\text{mm}$ and $\tau = 0.5$
2. $\alpha_c = 45^\circ$, $\alpha_b = 15^\circ$, $r_i = 1.5\text{mm}$ and $r_b = 0.8\text{mm}$
3. Measurement of $\varphi \pm 3^\circ$

Table 3.7 Two-Dimensional Finite Element ModelsShape Parameters and Stress Concentration Factors at Chord Weld FilletCrown Position¹ of Single Plane K90/45 Joint: $\psi = \theta = 90^\circ$

Weld Profile Parameters					SCFs				Notch Zone	
Quality	H/T	h/t	r/T ²	α_c^3	Value			Pos'n ⁴		
					K_s	K_n	K	ψ	Z	
Uncontrolled (r/T constant)	0.183	0.47	0.05	54°	2.18	3.72	8.12	24°	0.24T	
	"	0.56	"	60°	2.15	4.01	8.63	27°	0.25T	
	"	0.92	"	72°	2.20	4.30	9.45	29°	0.30T	
	"	1.33	"	78°	2.15	4.59	9.86	36°	0.34T	
	0.250	0.28	0.05	24°	2.10	2.26	4.75	12°	0.22T	
	"	0.39	"	36°	2.10	2.86	6.06	20°	0.26T	
	"	0.46	"	42°	2.05	3.10	6.36	21°	0.24T	
	"	0.54	"	48°	2.05	3.25	6.67	24°	0.25T	
	"	0.65	"	54°	2.10	3.66	7.70	23°	0.25T	
	"	0.80	"	60°	2.07	3.90	8.10	26°	0.25T	
	"	1.00	"	66°	2.05	4.08	8.36	28°	0.27T	
	"	1.33	"	72°	2.05	4.30	8.80	30°	0.30T	
	0.383	0.40	0.05	24°	1.95	2.20	4.27	14°	0.23T	
	"	0.58	"	36°	1.94	2.80	5.42	18°	0.25T	
	"	1.00	"	54°	1.95	3.59	7.00	23°	0.23T	
	"	1.33	"	60°	1.95	3.80	7.40	25°	0.28T	
	0.500	0.75	0.05	36°	1.85	2.74	4.80	18°	0.22T	
	"	1.33	"	54°	1.85	3.49	6.45	23°	0.25T	
	Uncontrolled (r/T varied)	0.250	1.33	0.02	69°	2.10	6.00	12.60	30°	0.35T
		"	"	0.033	72°	2.10	5.28	11.09	30°	0.35T
"		"	0.05	72°	2.05	4.30	8.82	30°	0.30T	
"		"	0.10	74°	2.07	3.38	7.00	33°	0.29T	
"		"	0.20	83°	2.05	2.65	5.43	40°	0.27T	
0.25		0.54	0.02	48°	2.10	4.33	9.10	20°	0.34T	
"		"	0.033	"	2.10	3.70	7.77	21°	0.32T	
"		"	0.05	"	2.07	3.20	6.63	24°	0.25T	
"		"	0.10	50°	2.07	2.68	5.55	28°	0.23T	
Fully blended (r/T varied)		0.05	0.025	0.05	90°	2.30	4.35	10.00	52°	0.31T
	0.10	0.05	0.10	"	2.23	3.13	6.98	45°	0.28T	
	0.20	0.10	0.20	"	2.13	2.25	4.80	39°	0.25T	
	0.25	0.125	0.25	"	2.07	2.05	4.25	39°	0.25T	

Notes1. $\tau = t/T = 0.5$. 2. $r_1/T = 0.05$ and $r_b/t = 0.10$.3. $\alpha_b = 90^\circ - \alpha_c$, except fully blended $\alpha_b = 90^\circ$. 4. Range of $\psi \pm 5^\circ$

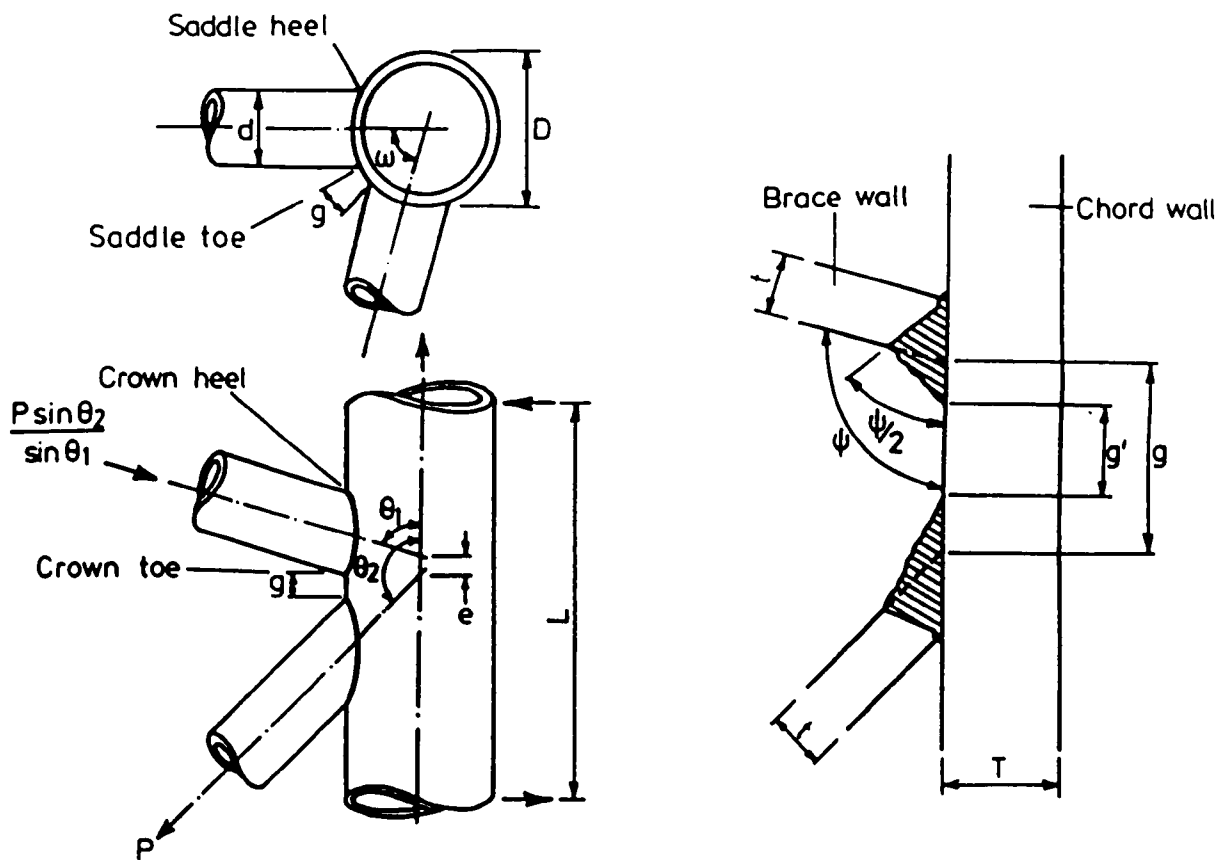


Fig. 3.1 Shapes, Dimensions and Loadings of 3-d Corner K Models

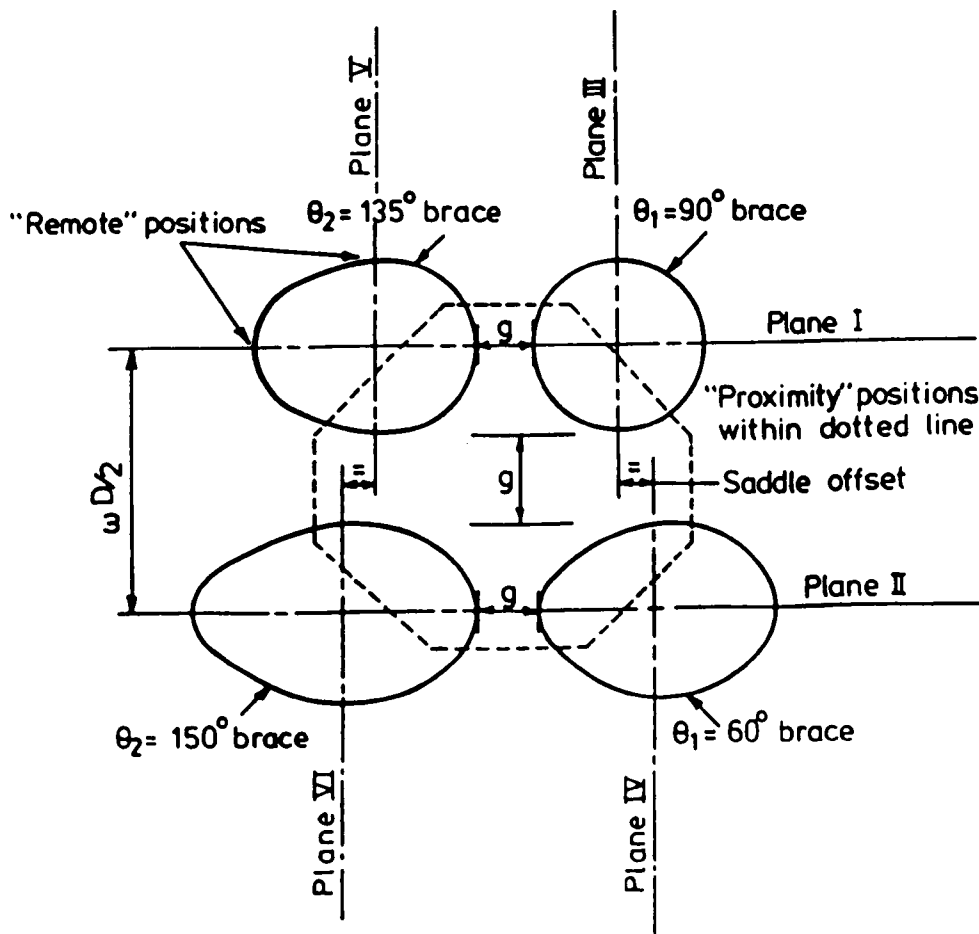
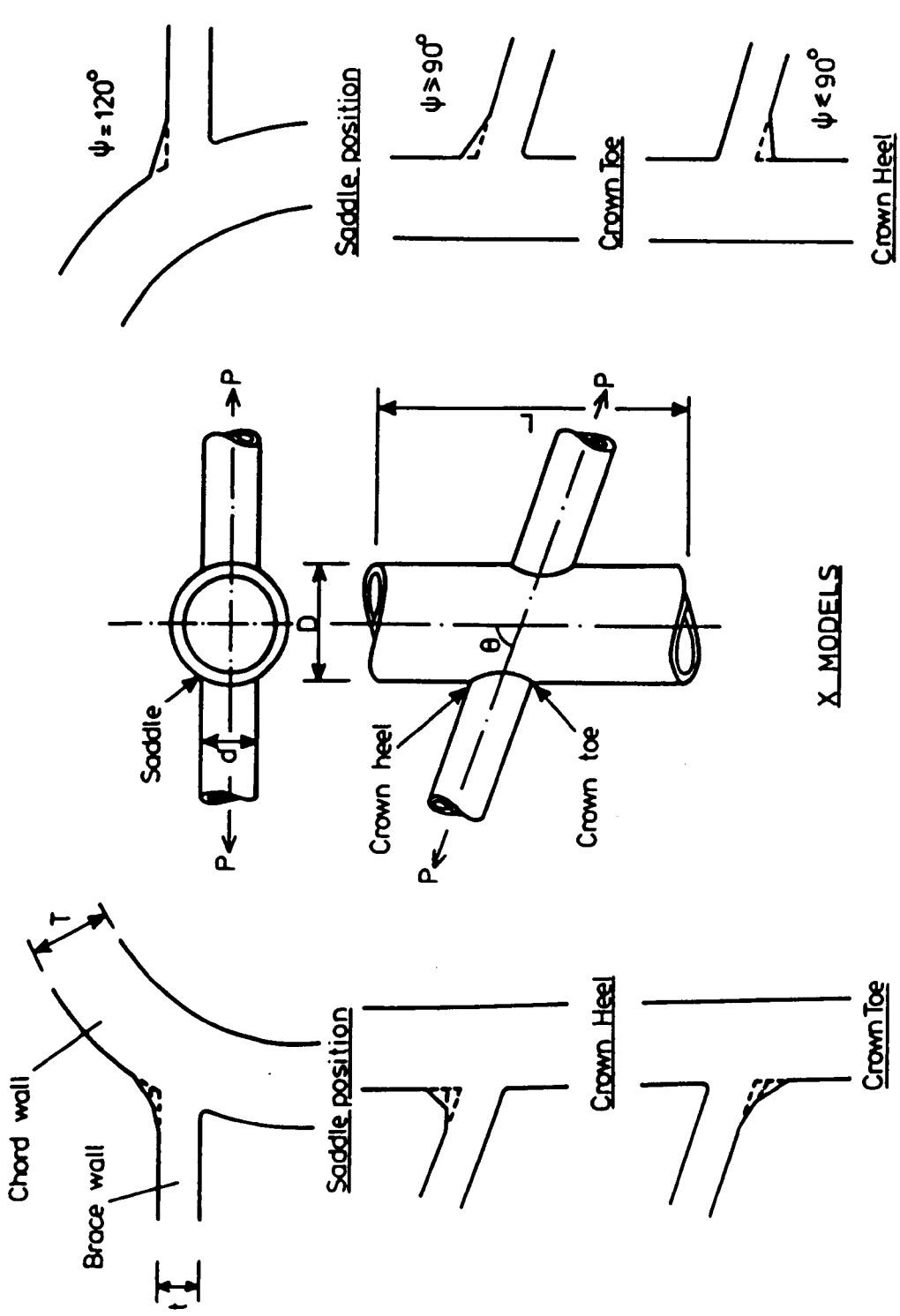


Fig. 3.2 Development of Chord in 3-d Corner K Models



Controlled Weld Profiles
(see also Fig. 3.7 d&e)

Uncontrolled Weld Profiles
(see also Fig. 3.7 c)

Fig. 3.3 Shapes, Dimensions and Loadings of 3-d X models

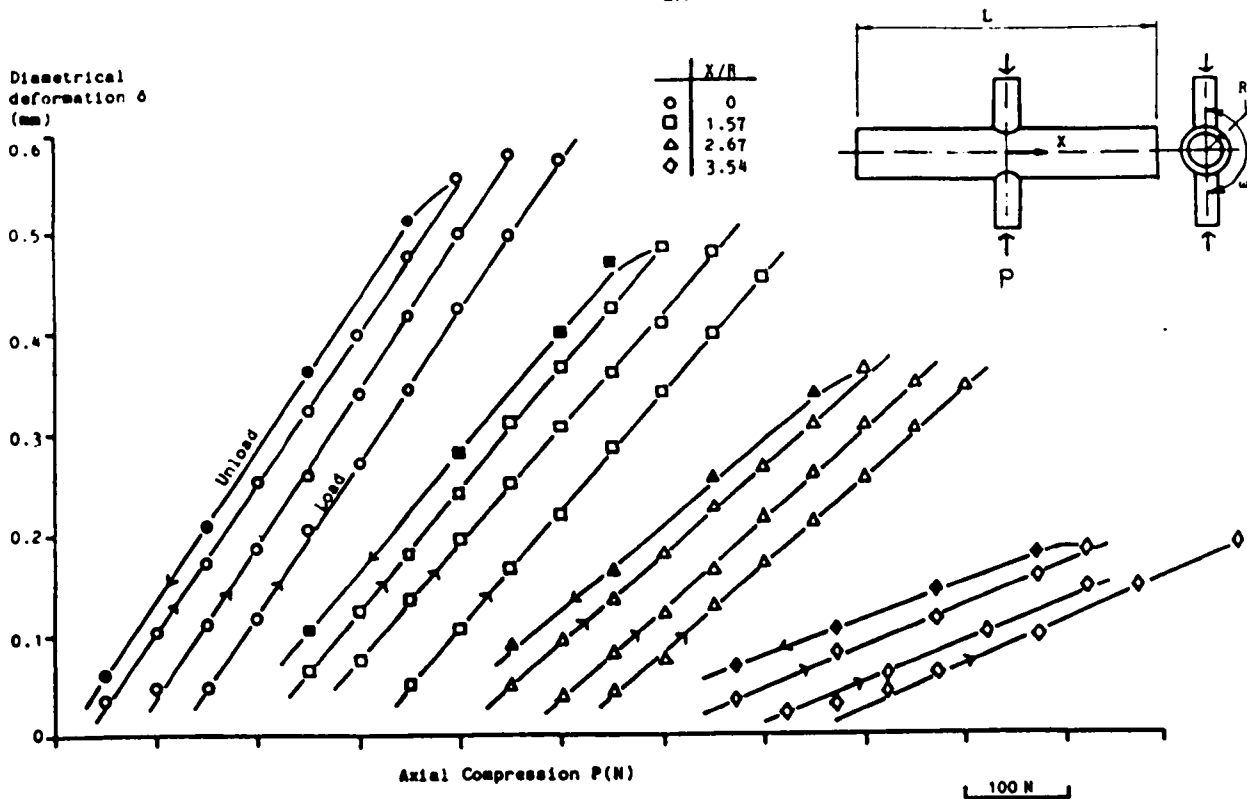


Fig. 3.4 Load/Deformation Curves for Different Positions in Chord Wall of X90 Model

Model Parameters D/T = 24.7
R/T = 11.84
d/D = 0.53

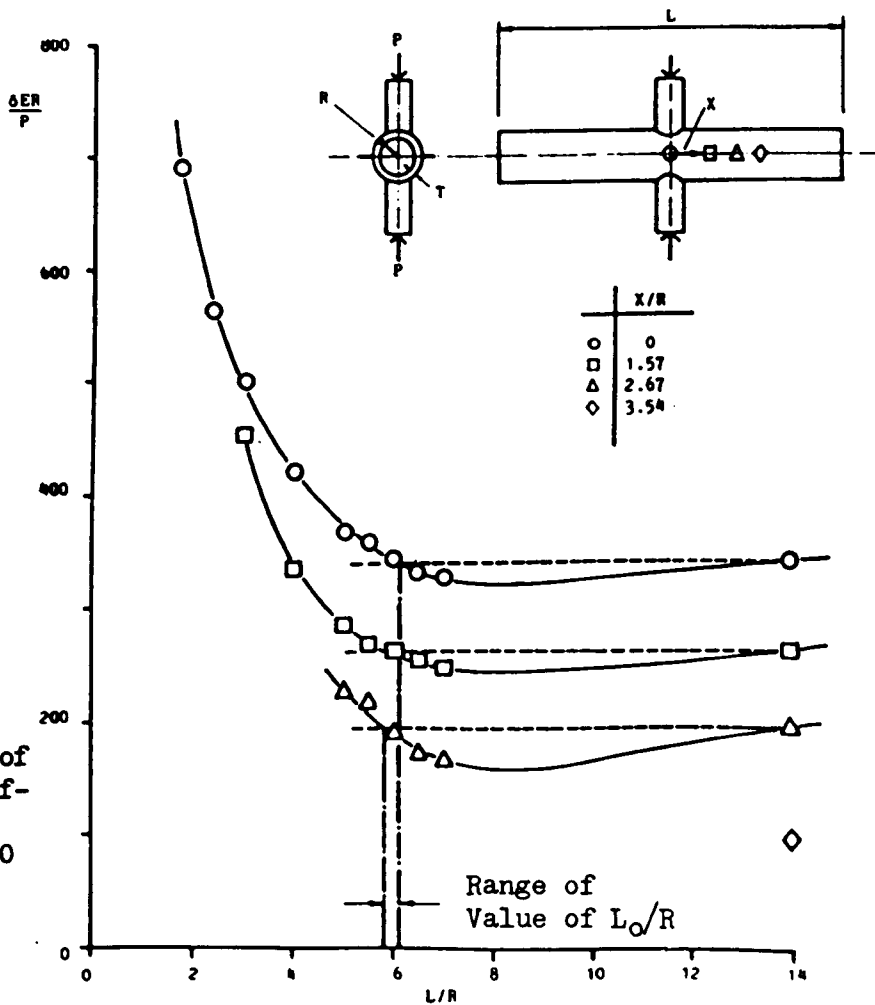


Fig. 3.5 Flexibility of Chord for Different L/R Values in X90 Model

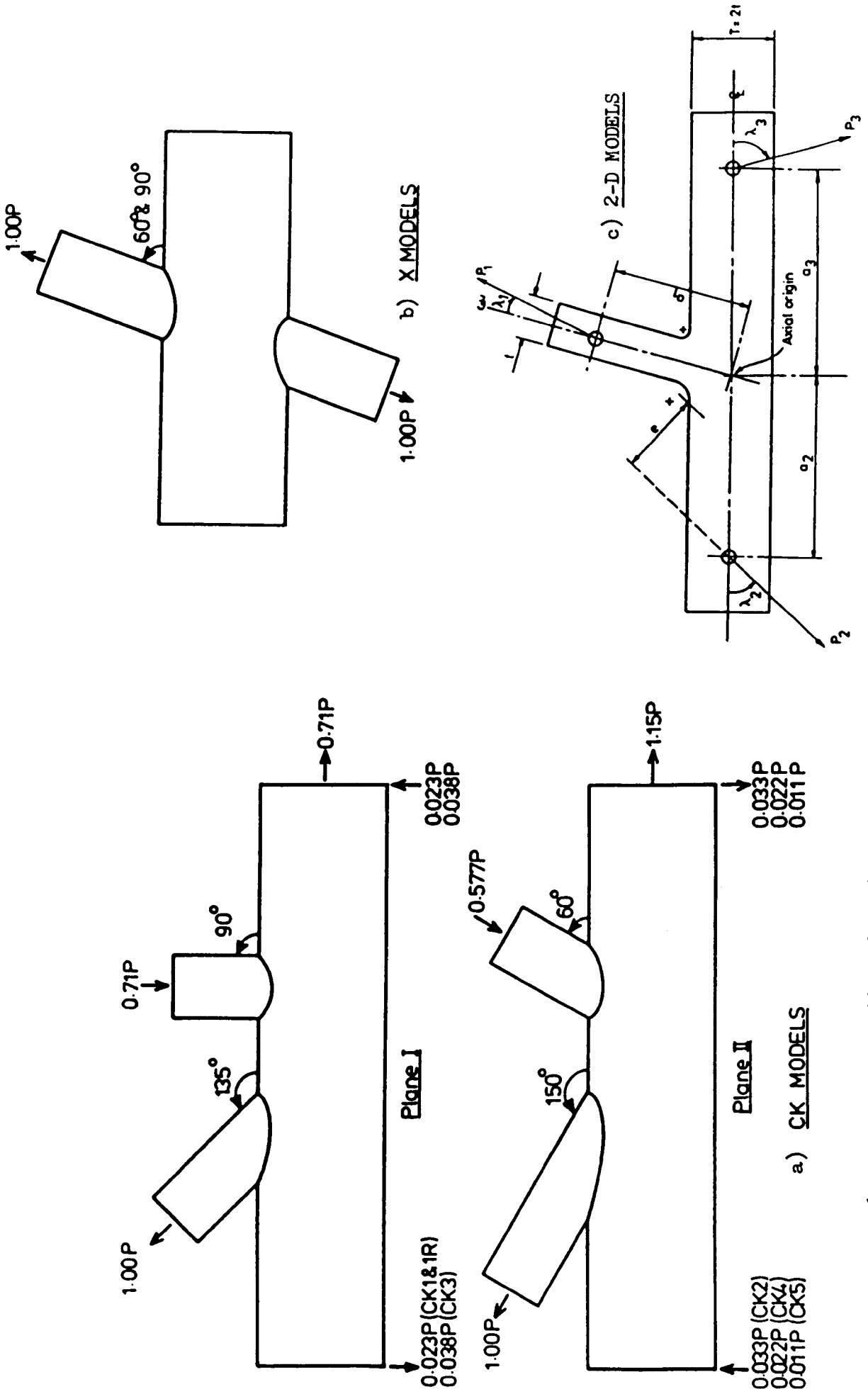


Fig. 3.6 Loads and Reactions in Models

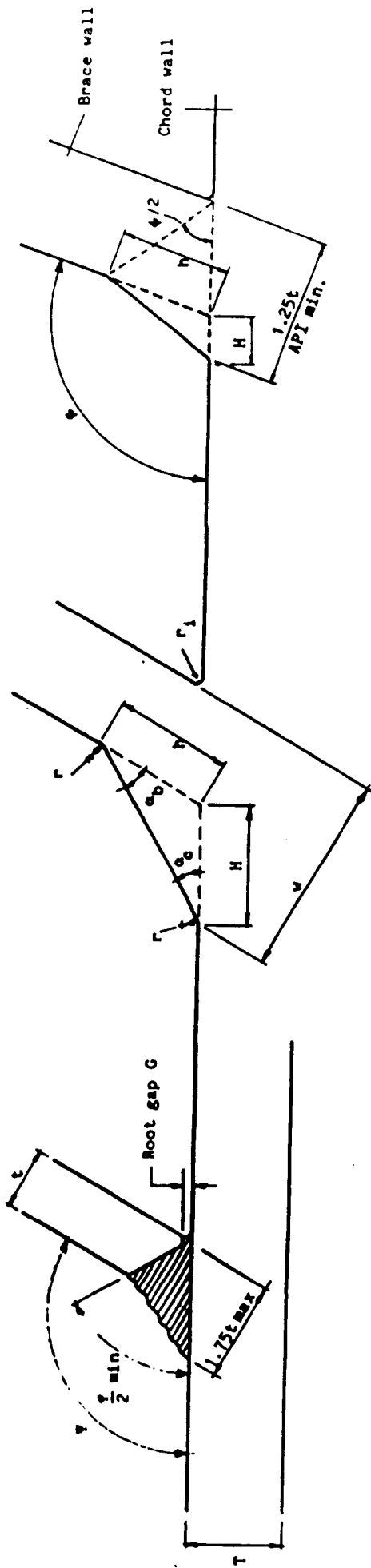


Fig. 3.7a API Specification Profile

Fig. 3.7b Idealised API Specification Profile

Fig. 3.7c Uncontrolled Profile

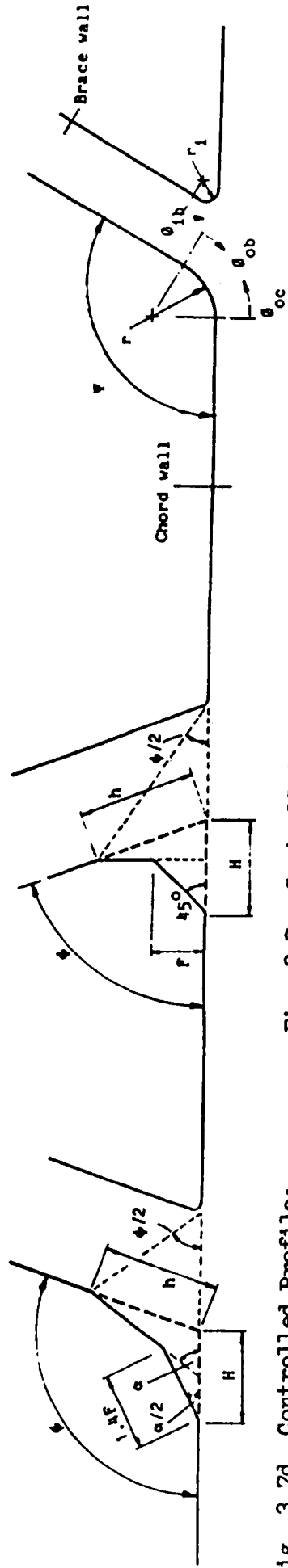


Fig. 3.7d Controlled Profile;
 $90^\circ < \psi < 150^\circ$;
 $0.5t < F < 16 \text{ mm}$

Fig. 3.7e Controlled Profile;
 $45^\circ < \psi < 90^\circ$

Fig. 3.7f Fully Radiused Profile

Fig. 3.7 Shapes of Weld Cross Sections

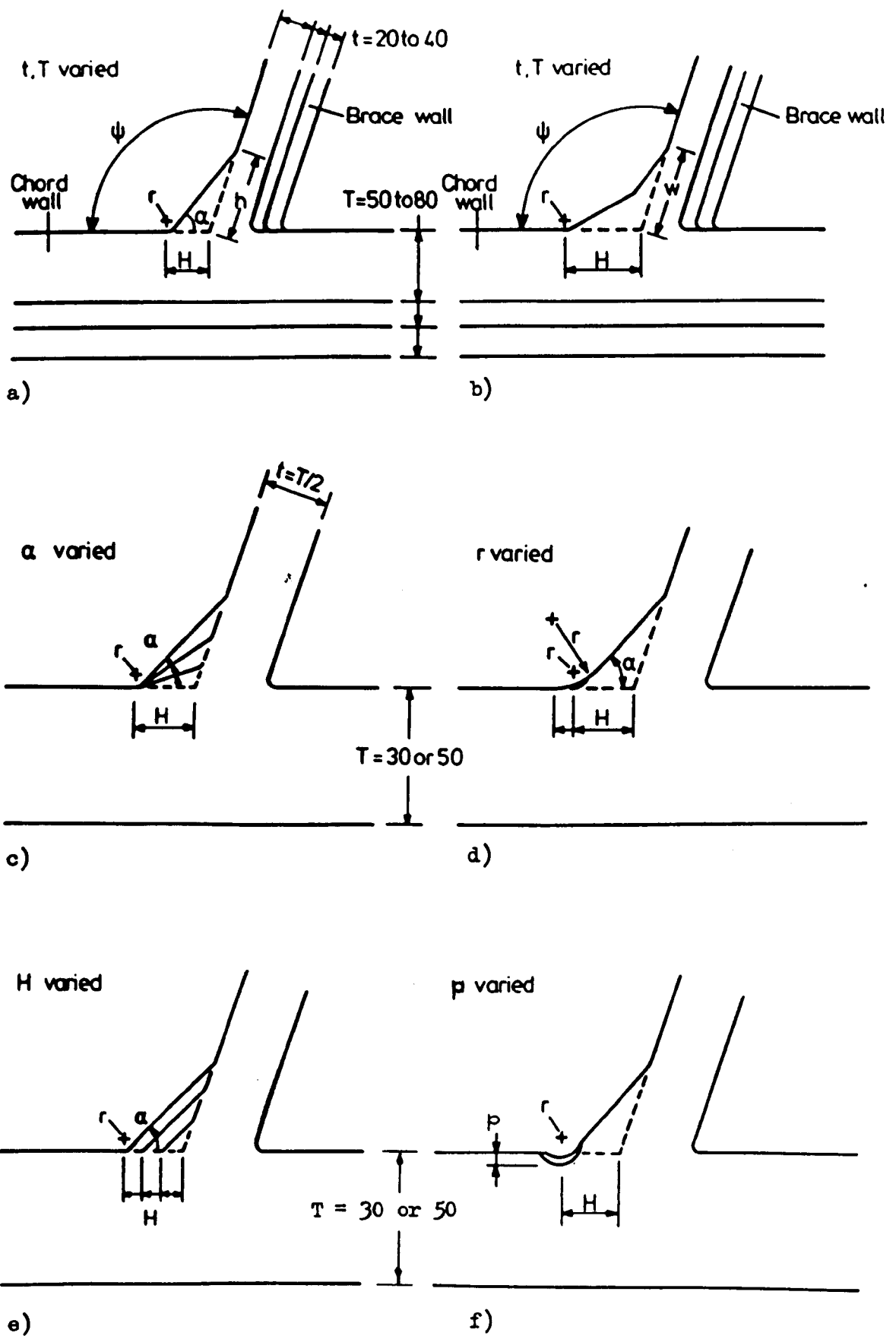


Fig. 3.8 Weld Profiles Studied using 2-d Models

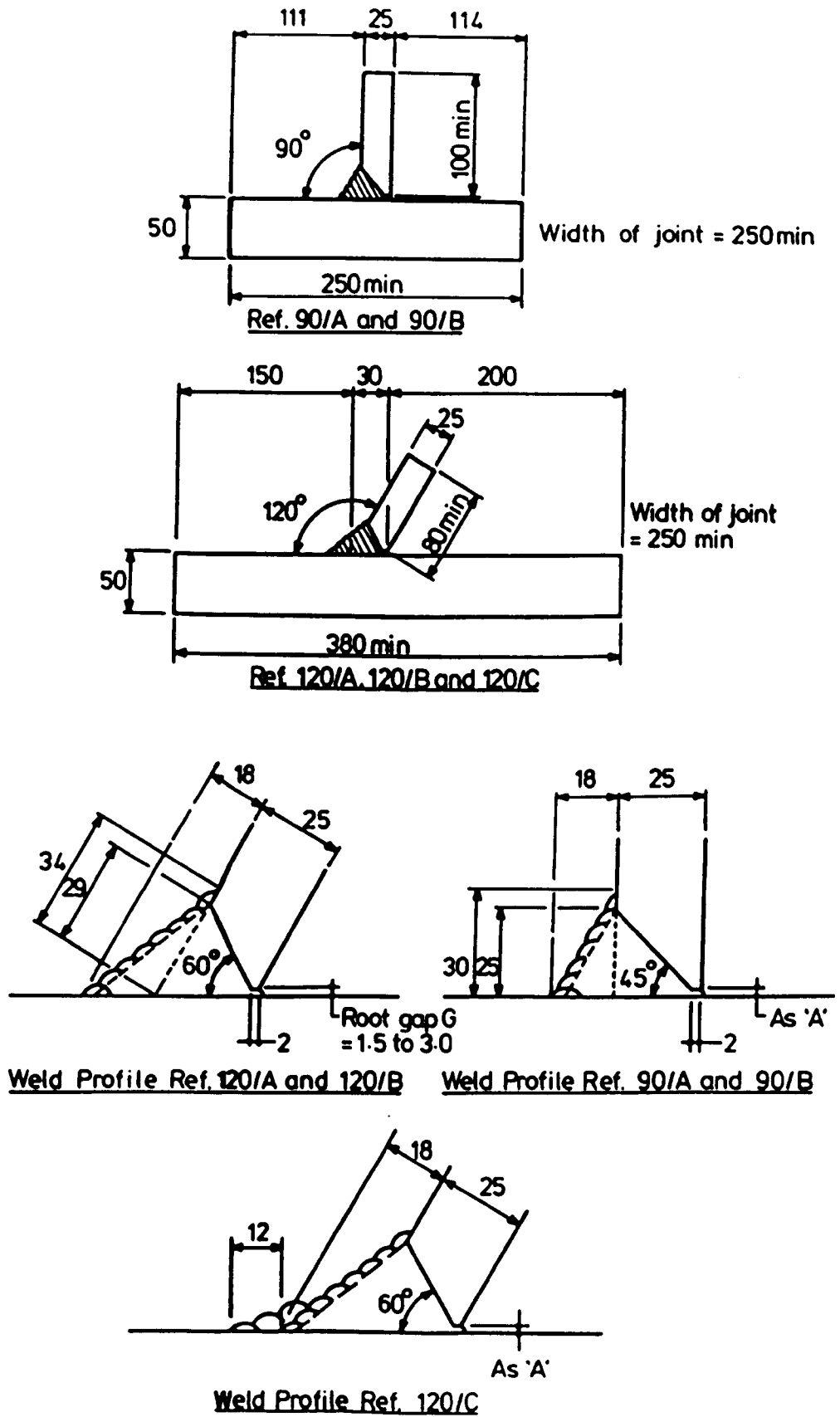


Fig. 3.9 Manufacturing Details for Steel Models



Plate 3.1 3-d CK Type Photoelastic Model (Pre-load condition)



Plate 3.2
3-d X Type Photoelastic
Model (Post-load con-
dition)

CHAPTER 4EXPERIMENTAL TECHNIQUES4.1 Introduction4.1.1 Choice of Stress Analysis Techniques

In three-dimensional (3-d) frozen stress photoelasticity, continuous stress distributions at the intersections of complicated tubular joints are readily analysable. Stress concentrations at the toes of realistic fillet weld shapes can be determined using homogenous, stress-free castings. In this work, as exact weld profiles were required, precision castings of 3-d photoelastic models were produced using re-usable patterns, moulds and cores. The models were made in a single casting operation.

The technique of precision casting epoxy resin models of multibraced tubular joints for photoelastic analysis was developed by Fessler and Perla (23), Whitehead (53), Little (18, 53) and Edwards (54).

The detailed analysis of the stresses in tube walls very near to welds that are in a plane of symmetry, may be considered as a two-dimensional problem. In a simple, single plane joint in which the brace inclination is 90° , strains parallel to the run of the weld are known to be small (10). Providing the stress distributions and constraints in a 3-d stress field are satisfied, 2-d models may be used to represent 3-d intersections in these planes. Hence, full size, flat models were accurately machined from precast sheets of an epoxy resin. The stresses in the tiny weld toe fillets were analysed in considerable detail. Room temperature photoelastic techniques were chosen because of the conventional nature of the work.

A finite element representation of some of the 2-d geometries was modelled using standard elements of the PAFEC 75 package.

The experimental techniques used to study plastic-elastic behaviour near weld toes were selected to satisfy the individual requirements of the models to be analysed. The models were full-size steel weldments cut into 2-d specimens.

Due to its recent application in the determination of plastic strains in keyed connections by Eissa (55), reflection photoelasticity was adopted. The technique had limited success because of the impracticalities involved in profiling random weld shapes and the very large strain gradients near weld toes.

To overcome these problems and also to determine residual plastic strain concentrations immediately after yielding, moire interferometry was introduced. This optical method of whole field strain analysis was developed by Post (56) and was shown to be particularly suitable in the resolution of large strain gradients and slip planes in inhomogenous materials.

4.1.2 Choice of Materials

All photoelastic models were manufactured using Araldite. This material has a successful history for the frozen-stress photoelastic analysis of complex 3-d models. The material has a very low Young's modulus and limited optical sensitivity at the stress-freezing temperature. Although the strains need to be greater than in a steel model only small loads and lightweight loading frames are required. The material is chemically and physically stable under load. Standard product literature is available (57).

Araldite was also used for room temperature transmission and reflection photoelasticity. In the former accurate profiles can be formed with negligible machining stresses. Precast sheets of Araldite are relatively inexpensive to make and several (usually up to 8)

different models were produced from the same piece of material.

Steel models were manufactured using offshore node quality plate and welding electrodes. Flat mild steel plates to BS 4360 grade 50D were joined using mild steel electrodes to BS 639, grades E43 and E51. These materials, which are in common use in the fabrication of offshore structures, were selected because their fatigue strength properties are documented elsewhere (eg 2, 32).

4.2 Experimental and Numerical Methods

4.2.1 3-d Frozen Stress Photoelasticity

Frozen-stress photoelastic models were used to study the behaviour of, and obtain 3-d stress fields near to the intersection of complex tubular joints. The frozen-stress technique enables post-loaded deformations and elastic stresses to be determined in accurate, realistic, small scale models. In this method, models manufactured from certain epoxy resins (such as Araldite) are loaded at a high temperature at which changes in material properties take place. When the model is cooled to room temperature, the displacements experienced at the high temperature are 'frozen' in the material. The model is said to be 'stress-frozen'.

This brief description of the process outlines the essential features of the technique which is well documented by Stanley (58), Durelli (59) and Heywood (60) etc.

A model in the stress-frozen condition can be sliced without relieving the stresses or deformations. When analysed in polarised light, the material exhibits birefringence in which dark band or 'fringes' are seen. The fringes represent the loci of points of equal maximum shear stress in the plane of the slice. This aspect of the theory of photoelasticity is described in greater detail in Section 5.1.1.

Frozen stress models are most conveniently calibrated for their material properties by a separate, simple test strip cast from the same mixture as the model.

4.2.2 2-d Photoelasticity

Two-dimensional photelastic models were used to examine stresses near to very small fillets in the conventional photoelastic manner. In this method, models were machined from materials (such as Araldite) which exhibit temporary birefringence when stressed. They were loaded in the plane of the model and analysed in a polariscope at room temperature. Fringe patterns represent contours of equal maximum shear stress in the plane of the model. A basic concept of 2-d photoelasticity is that the stresses in the plane of the model are not affected by the strains, perpendicular to the plane of the model, caused by the Poisson effect (60). The model is effectively in a plane stress condition.

Models are usually loaded by linkage mechanisms and/or freely hanging weights which introduce initial stresses due to self weight. These need not be measured because stresses can be obtained from differences in fringe orders due to two or more different loads.

4.2.3 Finite Element Methods

4.2.3.1 Finite Element Package

The PAFEC 75 package (61) was used also for the analysis of some two-dimensional models. The program defines nodal positions, element types and topology of the elements, material properties, displacement constraints and loads. The work was limited to using 2-d eight-noded isoparametric quadrilateral and six-noded isoparametric triangular elements for plane stress conditions to represent the crown plane of a 90° brace in a single plane K-type tubular joint.

The PAFEC output gives displacements, cartesian stresses and the directions and magnitudes of principal stresses at each node. At nodes common to two or more adjacent elements the average stress, computed from the stresses at the said node in each element, is given. The sensitivity of the mesh can be estimated by comparing the stresses at nodes common to adjacent elements. These should be equal. The sensitivity of the mesh, which was taken as the average stress divided by the maximum semi-difference between the (two or more) individual stresses, was also used to assess the errors in the output data in Chapter 7.

4.2.3.2 Finite Element Mesh Generation

The basis for the design of the finite element model to be used for weld shape variation was that the mesh gave acceptable element geometries for all chord and brace weld leg lengths, toe radii and toe angles studied. As shown in Fig. 4.1, a very fine mesh was used in the following regions of interest: (a) outside chord wall surface, within one wall thickness from the weld toe, (b) outside chord weld toe fillet, (c) weld toe (hypotenuse) near to (b), and (d) chord wall through thickness, radial to (b).

The model was first divided into four basic regions A, B, C and D, as shown in Fig. 4.1. The weld was contained exclusively in region D. The dividing lines for the regions were drawn perpendicular to the edges of the walls at the weld toes; outside fillet chord and brace weld toes for A and B, and inside fillet chord weld toe for C. Hence, changes in weld profile affected only the size, not the arrangement of the elements in these regions.

In the important areas of region D, ie around the weld toe fillets, a fine mesh was constructed radial to the circular arc of the fillets

for one-third of the wall thickness. Transition blocks were used to reduce the density of the elements in a manner appropriate to the gradients of surface and through thickness stresses obtained from other work (16, 20).

The mesh shown in Fig. 4.1 was Mark 3. Modifications to Mark 1 were to increase the number of elements along the outer chord wall (region A) within $0.25T$ of the weld toe. This was because the gradients of surface stress in this region were greater than predicted from photoelastic results. Modifications to Mark 2 were to rationalise the mesh in mid-region D for the large changes in weld size.

4.2.4 Reflection Techniques

4.2.4.1 Introduction

It was initially intended to study plastic-elastic surface strains in the steel models by reflection photoelasticity, a method commonly referred to as the 'photoelastic-coating technique' (62). The alternative names each describe, in part, the essential features of this technique.

The surfaces of the specimen, or model, that are the subject of the plastic strain analysis are polished to optical flatness. A thin layer (less than 1 mm thick) of a photoelastic material is bonded to the surface of the model. The edges of the layer, or photoelastic coating, are profiled identical to the edges of the model. When the model is loaded the strains in the model surface are equal to those in the layer. The strains in the layer are measured photoelastically. They remain elastic up to about 8% strain. Polarised light, emitted and collected by a special type of polariscope, passes twice through the photoelastic coating having been reflected from the model's polished surface. The polariscope is called a Vee-type reflection polariscope because of the 'vee' formed by the incident and reflected beams of light.

This brief description of the experimental technique outlines the essential features and explains why it was thought a suitable method of measuring plastic strains at weld toes in flat 2-d welded models. The technique is described in detail by Fessler and Eissa (63).

4.2.4.2 Photoelastic Coating

The positions of the photoelastic coatings are shown in Fig. 4.2. The material used was Araldite CT200 with 30 per cent by weight of hardener HT901. Pieces 25 x 25mm in size were ground to the finished thickness of 0.5mm. This thickness was calculated for the large plastic strains anticipated in weld toe regions to restrict the number of fringes to about 3 or 4. The procedures adopted by Eissa (63) for preparing the models for their photoelastic coatings and bonding of the layer were used in this work. The method of machining the layer to the exact model profile used in (63) could not be adopted here because of the irregular edge produced by the random deposition of weld metal as illustrated in Fig. 4.3. It was not possible to align an end milling cutter with the true edge of the model.

As a result of the concave and convex weld beads (with surface irregularities upto 1.5mm in the thickness of the model) profiling was carried out by hand using small flat, half round and triangular files. It was not possible to accurately profile the layer in the weld region. The weld toe radii in the layers were governed by the diameter of the circular file which was nearest to the true model radius. It was for these, and other reasons given in Chapter 8, that the measurement of strains at weld toes using the photoelastic-coatings methods was abandoned after only two models had been prepared and studied.

4.2.4.3 The Polariscopes and Mounting

The reflection polariscopes used in this work was designed and built

by Fessler and Eissa (55, 63). The details of the optical and polarising elements are given in reference (63). The polariscope, together with a new compact 120w sodium light source, was located inside a new air-cooled housing, as shown in Fig. 4.4. A bearing block was used to secure the polariscope with its optical axis horizontal to the housing unit. (The polarising elements would thus be parallel with the surface of the model.) The assembly was mounted on two travelling 'Myford' slides; one vertical allowing 100mm movement, and one horizontal allowing 140mm movement. A swivel bearing between the Myford slides allowed the apparatus to be moved out of position when installing a model in the loading rig.

The apparatus was small enough to be supported on the structural framework of a Denison testing machine. When in position, the quarter wave plate at the front of the polariscope was 20 to 25mm away from the photoelastic coating and parallel to the plane of the model. The centre of the field of view was located in the region of greatest interest for the two different model geometries shown in Fig. 3.9.

4.2.5 Moire Interferometry

4.2.5.1 Introduction

In the analysis of the elastic and plastic-elastic behaviour of welded 2-d steel joints, strains were determined from displacement fields by moire interferometry. This optical method of whole field strain analysis was developed by Post (56, 64). The experimental arrangement used in this work provides only in-plane displacements. These relate directly to normal and shear strains in a 2-d field. Because a detailed description of this method is given by Post (56), the following outlines the important features of the technique with quotations from this reference.

'Moire interferometry combines the concepts and techniques of geometrical moire and optical interferometry.' Patterns of interference, known as moire fringes, are produced by the relative movement of a real grating, attached to a specimen, and a virtual reference grating that is established by two coherent beams of light. The fringes are contour maps of points of equal in-plane displacement components in the surface of the specimen or model.

The sensitivity of displacements using this method is commonly in the order of tenths of a micron ($0.416\mu\text{m}$ is typical) per fringe. With high resolution photographic equipment and materials, strains from $20\mu\text{e}$ to 3% are resolvable and repeatable (65).

4.2.5.2 The Optical System

The essential elements of a moire interferometer are shown in Fig. 4.5a. A highly reflective, phase-type diffraction grating is firmly attached to, and in the plane of, a 2-d steel model. (This process will be described later.) The frequency of the grating is large, eg 1200 lines per mm. When the model is loaded, the grating deforms and moves with the surface of the model.

'Two beams of coherent light illuminate the specimen grating obliquely from angles $+\alpha$ and $-\alpha$. Various optical arrangements can be used to produce incident beams, but in each case the two beams are divided from common beam, they travel different paths, and they meet again at the specimen. Two coherent beams emerge from the specimen grating with warped wavefronts; they coexist in space and generate optical interference.' The directions of the emerging beams are prescribed by the diffraction equations given in Section 5.3.1.

'Numerous different optical schemes can be contrived to form the virtual reference grating. Any means that brings coherent beams equivalent to A and B in Fig. 4.5a onto the specimen grating would

suffice.' The optical arrangement used in this work is illustrated in Fig. 4.5b and Plate 4.1. This is a two-beam system in which two beams of light are incident on the model grating. In Fig. 4.5a, the plane of the virtual grating produced by the two beams is parallel to the lines on the model grating that are parallel to the y axis. Only the components of u displacements perpendicular to those lines are measured, ie parallel to the x axis. To obtain v displacements parallel to the y axis, the axes are effectively transposed by rotating the model through 90° . The model grating is a cross grating with two mutually perpendicular sets of lines.

In a two beam system, 'half the incident beam impinges directly on the specimen surface while the other half impinges indirectly in a symmetrical direction after reflection from a plane mirror. The entire optical system is shown schematically in Fig 4.5b including a lens that performs dual functions as a decollimating lens and an objective lens: it collects all the light that emerges essentially normal to the specimen surface and it focuses the specimen surface onto the film plane of the camera. A parabolic mirror is shown as a means to form the collimated beam, but a collimating lens is a feasible alternative. For static analyses, the required laser power depends primarily on the diffraction efficiency of the specimen grating, the magnification of the image, and the sensitivity of the film used to photograph the fringe pattern. Laser powers from 0.5 to 200 mW have been used successfully.'

The light source used was a 25mW Helium-Neon laser, of 632.8nm wavelength, manufactured by 'NEC' (type GLG 5700). Nominal beam diameter is 1.2 mm. The laser was powered by a 160 VA supply, also manufactured by 'NEC' (type GLS 5702). The spatial filter comprised a X20 objective lens and a 25 μ m diameter pin hole. The 100 mm diameter parabolic mirror had a focal length of 864 mm. The 80 mm diameter

decollimating lens, manufactured by 'Leitz', had a focal length of 300 mm. All mirrors were 'laboratory' quality, ie the surface is accurate to $\lambda/4$. The camera was a 'MPP' micro-technical camera with a remotely operated mechanical shutter (1 to 1/400 sec.), variable aperture ($f = 22$ to 4) and ground glass viewing screen for focussing purposes. A 'Calumet' roll film holder was inserted in the plane of the viewing screen. The film used was 'Kodak' Technical Pan black and white negative film 6415, size TP120. This gave a maximum size of negative 70 x 60 mm. The film was developed and printed onto 'Ilford' Ilfospeed 3 paper using 'Ilford' HQ Universal developer.

The apparatus was mounted on a 2 x 1 m optical table which comprised an ordinary timber table supported on four air springs for acoustic isolation, and a 10 mm thick steel plate. The latter was used as the optical surface and was levelled by adjusting the pressure in the air springs. Two soft mattresses were sandwiched between the plate and table for additional acoustic isolation.

4.2.5.3 Optical Adjustments

All optical components were fully adjustable for out-of-plane rotations ϕ and ω (see Fig. 4.5a for nomenclature) by means of finely threaded adjustment screws. The most important parameters to control are the angles of incidence, $\pm\alpha$, at the surface of the model. Post explains how this angle was precisely adjusted with the model in an undeformed condition. Referring to Fig. 4.5b, 'adjust the plane mirror while observing an aperture plate in plane A. Two bright dots will appear in plane A and they should be merged into one by adjusting the plane mirror; this adjusts the mirror perpendicular to the specimen. Attach a white card to aperture plate B and observe two bright dots on the card. They are from the two beams that form the interference

pattern. These dots should be merged by adjusting the angle of incidence α and the parallelism of lines in the specimen grating and virtual reference grating. Angle α can be adjusted by rotation or translation of the parabolic mirror. Parallelism can be adjusted by in-plane rotation of the specimen or by rotation of the plane mirror about an axis perpendicular to the specimen.'

After removing the white card at B, moire fringes were observed in the camera screen. Fine adjustment of the plane mirror adjacent to the model was necessary to obtain the 'null' field required for the exact optical configuration.

The fringe pattern emerging from the specimen is not unique - the pattern changes with the position at which it is observed. Thus, the fringe pattern must be recorded in a plane, parallel to the plane of the model, where the fringes are first reunited. In two beam interferometry, the beams reunite as they emerge from the model grating and should be recorded at the surface of the model grating. This is obviously impossible. Instead it is recorded by means of a camera.

'A camera reproduces in the image (or film) plane the phase relationships of the light that crosses the object (i.e. model) plane'. Light is collected by the decollimating lens and brought into focus by fine adjustment of the lens to position the camera's screen in the conjugate plane. This was achieved by bringing into focus small crosses that were scribed on the surface of the model grating using a razor edge. The size of the image can be varied by adjusting the object and image distances providing the lens law is upheld. A magnification factor of about 1.2 was used to obtain an image size 60 x 48 mm. The object and image distances used were approximately 550 mm and 660 mm, respectively. Fine focussing was achieved optically by observing the fringe pattern in the ground glass screen. When the image is recording

large model deformations, the wavefronts emitted from the specimen are extremely warped i.e. the object distance is finite and the limits on focussing distances are small. If the image is out of focus, fringes appear to merge with each other and dark bands are seen. These were eliminated by fine adjustment of the camera screen - distances of less than 5 mm were required to achieve this.

4.2.5.4 Auxiliary Specimen Grating

Moire fringes represent contours of displacements. These displacements are the sum of local deformations, that are to be measured, and rigid body rotations and translations, that must be eliminated. It was impossible to avoid in-plane and out-of-plane rigid body movement when applying external loads to the model. It was necessary to establish a secondary, or auxiliary specimen grating which would remain unstressed, undeformed and coincident with the model throughout the loading cycle. This was achieved by attaching a small reflective cross-grating (20 x 10 mm) to a bracket which was fixed to the rear of the model by a small bolt and wing nut. The arrangement is shown in Fig. 4.6 and Plate 4.2.

Mutual alignment with the model grating was established by in-plane rotation of the bracket by two adjustment screws tightened against the underside of the model. Out-of-plane alignment was achieved by machining the contact faces of the model and bracket. With the wing nut tightened and the adjustment screws released, the auxiliary grating experiences identical rigid body rotations and translations as the model. It can be used for alignment purposes for both the u and v displacement fields because the x and y lines on the model and auxiliary gratings are mutually perpendicular. 'This identity of angles is the true requirement, rather than making the angles (between the x and y lines) exactly 90° .' The position of the auxiliary grating,

relative to the model grating, is shown in Fig. 4.7.

'In practice, the specimen would be loaded and its orientation adjusted to null the fringes in the auxiliary specimen grating. This can be done either by fine adjustment of the angular orientation of the specimen grating or by adjustment of the virtual reference grating. After recording the fringe pattern, the specimen is rotated 90° and fine adjustments are made again to null the fringes in the auxiliary specimen grating.'

4.2.5.5 Carrier Patterns

The main purpose in using an auxiliary grating was to establish the unloaded orientation of the model and to eliminate in-plane and out-of-plane rigid body rotations. Providing the fringe pattern in the auxiliary grating remained unchanged during loading, these conditions would be satisfied. However, it was difficult to establish a consistent null field in the auxiliary grating during loading because of the sensitivity of the optical apparatus. The corresponding null field in the model was also difficult to analyse because fringe spacings were large. Thus a fringe pattern of small, uniform fringe spacing was introduced in the auxiliary and model gratings. This is called a carrier pattern. 'The number of fringes in the no-load or initial pattern can be made as large as desired by adjusting the apparatus'. If the plane mirror adjacent to the specimen is rotated about the vertical axis (y in Fig, 4.5a), a carrier pattern of extension is introduced. Uniformly spaced fringes parallel to the model grating lines are added to the initial field. Similarly, if the mirror is rotated about the horizontal axis perpendicular to the plane of the model (z in Fig 4.5a) a carrier pattern of rotation, characterised by uniformly spaced fringes perpendicular to the model grating lines, is introduced and added to the

initial field.

In this work, carrier patterns of extension were used. The frequency of the fringes in the carrier pattern was approximately 1 fringe per mm in the u field (N_x fringes) and 1.5 f/mm in the v field (N_y fringes). These values were established by counting the number of fringes in the auxiliary grating (of known size) at each load increment. The true values could be measured from enlargements of the negatives.

The procedure for establishing the correct carrier patterns in the auxiliary grating was as follows. Out-of-plane rotation (ω in Fig 4.5a) was corrected by rotation of the mirror about the z axis. In-plane rotation (θ in Fig. 4.5a) was corrected by adjusting the appropriate micrometer barrel until an arbitrary carrier pattern of extension was observed. The correct carrier pattern was established by rotating the mirror about the y axis.

4.2.5.6 Grating Mould Preparation

The moulds that were used for producing model and auxiliary gratings were manufactured and supplied by Post. These were crossed-line phase type gratings, generated optically on a high resolution photographic plate. 'Phase type gratings have furrowed or corrugated surfaces with either symmetrical or unsymmetrical furrow profiles.' The technique to produce an undulating surface profile was recently established (64). 'It is the undulation that transforms the surface of the photographic plate into a phase-type diffraction grating.' The frequency of the grating used in this work was 1200 lines per mm. 'The final step in producing the mold is to apply an ultrathin reflective coating of aluminium, or gold overcoated with aluminium, by evaporation (high-vacuum deposition).'

Vacuum deposition was carried out at a pressure of 10^{-5} atmospheres (atm) using pure 99.999% aluminium wire. A piece of wire, 0.5 mm

diameter x 150 mm long, was cut and rolled into a small bundle using tweezers (to avoid transferring grease to the wire from the fingers). The wire was placed in a tungsten basket (manufactured by Nordiko Ltd., type NB901) located in a vacuum chamber. The basket was connected across a 50 amp, 240 volt DC electrical supply.

The virgin mould was cut into 50 x 33 mm pieces and prepared for evaporation by washing in Kodak Photoflow 1:200 solution and allowed to drip dry. This was to reduce the adhesion between the mould and its coating during transfer to the model. The mould was secured in a (clean) aluminium bracket and the assembly was placed in the vacuum chamber about 200 mm away and directly above the basket. A thickness monitoring crystal was placed on a level with, and 50 mm away from the centre of the mould. A shield was inserted between the bracket and the mould and monitoring crystal. The arrangement is shown diagrammatically in Fig. 4.8.

When the pressure in the chamber reached about 2×10^{-6} atm, a current of between 30 and 33 amps heated the basket to the required boiling point of aluminium at this pressure. During this period, impurities such as grease etc. would evaporate and reduce the pressure to about 10^{-5} atm. When the aluminium began to evaporate, a deposition could be seen on the glass chamber. The current was immediately reduced to 28 to 30 amps to control the rate of evaporation. The shield was removed; exposing the mould and film thickness monitoring crystal to the vapour. The rate of deposition during coating was monitored by the film thickness display unit and controlled by regulating the electrical current. A deposition rate of 15 to 20 Å per second was used. The thickness of the layer was 700 ± 25 Å (7×10^{-5} mm). (In a private communication, Post recommended a thickness of $\lambda/10 = 680$ Å.) This exercise was timed to avoid using the thickness monitor for which a new,

expensive and disposable crystal is required with every 20,000 Å deposited. Thus, an evaporation period of 40 seconds and an electrical current of about 30 amps were used for future work. Using these empirical parameters, film thicknesses of 650 Å to 750 Å were obtained as measured by Talysurf.

The thickness and rate of deposition of the layer were controlled by an 'Edwards' FTM4 Thickness Monitor Unit. Its design and uses are documented (66). For this work, input parameters for aluminium and vacuum chamber geometry were:

Density = 2.70

Acoustic Impedence = 8.17

Tooling Factor = 135%

4.2.5.7 Specimen Grating Replication

Fig. 4.9 illustrates how the reflective grating was replicated on the surface of the model. (Auxiliary gratings were not replicated.) 'A pool of liquid adhesive is poured on the specimen and squeezed into a thin film by pressing against the mold. Epoxy adhesives are suitable. After polymerization, the photographic plate is pried off - only a small prying force is required - leaving a reflective diffraction grating bonded to the surface of the specimen. The weakest interface in the system occurs between the gelatin of the photographic plate and the evaporated aluminium or gold, which accounts for the transfer of the reflective film to the specimen. The result is a reflective, high-frequency phase-type diffraction grating formed on the specimen. Its thickness is about 0.025mm.' The resin used in this work was 'Stycast 1266' (manufactured by Emerson and Cummings). This is a low viscosity two-part adhesive. The mould was clamped to the model using a single spring clamp. The force was distributed over the area of the mould by

Araldite spreaders. Liquid resin flashing was wiped from all external edges of the mould and model using a piece of clean cartridge paper. After a minimum curing time of 24 hours, the mould was easily pried off with finger and thumb. The resulting grating is shown in Plate 4.3. The positions of the grating on the models are shown in Fig. 4.7.

The thickness of the resin layers were measured by Talysurf. They were all in the range 32 to 43 μm (0.032 to 0.043 mm). The surface profile shown in Fig. 4.10 was obtained by Talysurf. The depth of undulations varied from 250 to 1400 \AA ; the mean depth was approximately 610 \AA .

4.3 Model Manufacture

4.3.1 Three-Dimensional Photoelastic Model Manufacture

The manufacturing technique developed by Fessler and Perla (23) and Little (18) of precision casting Araldite models using re-usable moulds and cores was adopted for this experimental work. The technique is well documented in (18). Only the points particular to these models will be mentioned. The models were manufactured of Araldite CT200 with 30 per cent by weight of hardener HT901. The model consisted of a cast node (of one chord tube and four or two brace stubs for corner K and X nodes respectively) spigoted and glued to two chord and two brace extension tubes. The node casting was manufactured from re-usable patterns, dams, moulds and cores; each designed to permit the intended range of dimensions.

The pattern was used to form the inside surface of the mould. The pattern was assembled using Araldite cylinders; one thick walled cylinder for the chord and several solid cylinders for the braces. One pattern was made for each different geometrical configuration of model. Pattern No.1 was used for the mould for the corner K nodes ref. CK1, CK1R and CK2, pattern No.2 for CK3 and CK4, pattern No.3 for CK5,

pattern No.4 for X node ref. X90 and pattern No.5 for X60.

One mould was manufactured from each pattern. The moulds and brace cores were made of slate-resin. The moulds for the corner K nodes were cast in four separate segments; split along the chord axis in the (two) crown planes of the braces, and mid-way between them. The moulds for the X nodes were cast in two halves; split along the chord axis in the (single) crown plane of the braces. The chord core was a thick walled aluminium cylinder.

The "weld" fillets were formed on the pattern using plaster of Paris. Initially the intended design parameter for the outer fillet toe radius was a single value of $r/t = 0.20$. In practice, a single value at every fillet proved impossible to achieve. For the first corner K model, reference CK1, toe radii were scraped from the mould using a range of ad-hoc forming tools of various dihedral angles. The resulting radii were larger than desired and it was difficult to extract useful weld toe data. This model was remade as reference CK1R. The fillets for this model and the following one, reference CK2, were successfully formed on the model itself using a 2mm diameter file. However the small amount of undercut present (at three joints only) prevented this tedious operation from becoming a standard method. Subsequent profiles (for corner K models CK3, CK4 and CK5, and X models X90 and X60) were produced by allowing the surface tension of the liquid mould material to form toe radii at the sharp corners of the pattern. When the liquid resin of the model solidified against the inner surfaces of the mould, final toe radii were produced. It was found that although toe radius increases with the included angle forming the fillet, the results achieved are the smallest practical values. Fig. 4.11 shows the achieved weld toe radii at chord and brace ends of the weld fillet. These values are plotted against the dihedral weld angle, $180^\circ - \alpha$ (see

Fig. 3.7) as this appears to be the most influential variable, assuming the plaster of Paris fillets are consistently sharp. The post-loaded dimensions and geometric parameters of the models are given in Tables 4.1 to 4.8.

4.3.2 Two-Dimensional Photoelastic Model Manufacture

The models were manufactured from 3 mm thick, precast sheets of Araldite CT200 with 30 per cent by weight of hardener HT901. A calibration strip equal in size to the brace wall was cut from the same pre-cast sheet as each model. The models were profiled using side-milling cutters. The models were rough milled to approximate dimensions using a coolant (such as mineral oil) to prevent thermal edge stress. A final surface cut, between 0.05 and 0.1 mm deep, was made using a cutter of the exact diameter to form weld toe radii. The final cut was made without the coolant. Dowel holes were accurately positioned, drilled and reamed.

The size of the models was chosen as the smallest likely to model the fillets sufficiently accurately. Different models had brace width t = between 15 and 40 mm and chord width T = between 30 and 80 mm, which allowed the whole region of interest to be viewed in the polariscope at the same time. The thickness (ie 3 mm) was the smallest to ensure lateral stability of the models.

4.3.3 Two-Dimensional Steel Models Fabrication

4.3.3.1 As-welded Models

The test specimens, shown in Fig. 3.9, were fabricated by British Steel Corporation (BSC). Swinden Laboratories, Rotherham using offshore node quality flat steel plate in accordance with BS 4360-grade 50D. The chemical composition and mechanical properties of samples taken from the 50 mm thick chord wall plate were supplied by BSC, Scottish Shelton and

East Moors Group, Glasgow, and from the 25 mm thick brace wall plate by BSC, Scunthorpe Division. These are given in Table 4.9. The brace walls were chamfered to provide a minimum included angle equal to half the external dihedral angle of the joint. A root gap of between 1.5 and 3.0 mm was permitted during setting up. The plates were joined by a single sided, full penetration weld made by the manual metal arc process using electrodes to BS639 - Parts 1 and 4. These were designated 'uncontrolled' profiles as shown in Fig. 3.7c. Specimens described in Section 3.4.3. as type A were welded using 4 mm diameter, grade E51 electrodes and as type B using 4 mm diameter, grade E43 electrodes for butter passes and 2.5 mm diameter, grade E43 electrodes for capping passes. A preheat temperature of 100°C was used. The build-up sequence of these welds is shown in Fig. 4.12.

The 250 mm long specimens were individually welded using run-off/on tabs and were not post weld heat treated. No grinding or dressing of the weld profile was carried out. The profile at the toe of the welds were intended to conform to the requirements of profile tests such as the AWS "dime" or disc test. The weld toe profile parameters given in Table 4.14 show where this was achieved. Typical weld toe profiles (traced from X32 magnification shadow graphs) are shown in Fig. 4.13.

These models were used to represent real steel joints, welded in a manner representative of offshore practice, with "uncontrolled" weld profiles, ie no post weld treatment or improvements were made.

One of the Type A steel joints with the higher strength weld, i.e. grade E51, was later selected for study with an improved or "controlled" weld profile, as shown in Figs. 3.7d and 3.9. A 75 mm long piece was cut from the original weldment. The additional welding required to produce the controlled profile at the chord weld toe was carried out at The Welding Institute, Cambridge. Specimens described in Section 3.4.3.

as type C were completed using 4 mm diameter grade E51 electrodes (identical specification as type A). The build-up sequence and typical weld toe profiles are shown in Figs. 4.12 and 4.13, respectively. A preheat temperature of 100°C and an interpass temperature of 120°C were used. The profile at the toe of the weld satisfied the requirements of the disc test without post-weld dressing.

The weldments were cut by mechanical means into slices, fly cut on both sides and ground on one face. Reamed holes were formed at the correct positions of loading in preparation for the intended photoelastic coating and moire interferometry strain analysis techniques. The final thickness of the models were 10 mm for photoelastic coating methods and 4 mm for moire methods.

The following schedule summarises the models manufactured.

Dihedral angle	Weld Profile	Weld Grade
90°	Uncontrolled	E51
"	"	E43
120°	"	E51
"	"	E43
"	Controlled	E51

4.3.3.2 Post-Weld Heat Treated Models

To assess the effect of residual welding stresses in the weldments and determine the changes in mechanical properties, one of each of the 4 mm thick models in the above schedule were stress relieved. The models were placed in an electrically heated furnace and subjected to the following thermal cycle:

- (i) heated to 620°C at approximately 100°C per hour

- (ii) held at 620°C for 12 minutes
- (iii) controlled cooling from 620° to 400° at 80°C per hour
- (iv) air cooled to room temperature

Reamed holes were formed at the correct loading positions after the models were heat treated.

4.4 Dimensional Accuracy and Material Properties

4.4.1 3-d Photoelastic Models

The dimensional accuracy of the models were checked before loading. Only the diameters, out-of-roundness, straightness and inclinations of the tubes were measured at this stage. Other dimensions, e.g. wall thicknesses and weld sizes, were obtained from slices cut from the models after loading.

The model was set up on a surface table with the chord horizontal. A dial test indicator was traversed along the chord at eight equal circumferential positions. Measurements were made at five locations along the length of the chord. The diameter of the chord was also measured at these positions. The shape of the chord tube was calculated from these measurements. Fig. 4.14 shows a cross section of the chord in the plane of the loaded braces for one of the models. The angular inclinations of the braces to the chord tube were measured by vernier protractor. The deviation from the intended values were negligible.

The above measurements were taken to enable load induced deformations to be calculated from the post-loaded models.

The weld toe profile parameters, toe radii and local weld angle, were obtained by measuring the outline of slices, cut from the models after loading, on a shadow graph of 32 times magnification.

The important design dimensions and angles of the models, the applicable tolerances and the post loaded dimensions are listed in Table 4.10. The tolerances were those specified for previous work for the U.K. Offshore Steels Research Project (UKOSRP I), except that weld fillet tolerances were based on the API recommendations for complete joint penetration.

To determine the material properties, Young's modulus and material fringe value of the stress-frozen model, test strips were cut from a small block cast from the same mixture as the model. The strips were 5 mm

wide, 2.5 mm thick, 150 mm long and were loaded in uniaxial tension with a load of 0.6 lb. The strips were subject to the same thermal cycles as the model.

The frozen stress material properties of each model are given in Table 4.11.

4.4.2 2-d Photoelastic Models

The dimensional and angular accuracy of the 2-d photoelastic models were determined using micrometer and vernier protractor respectively. Dimensional checks were made on brace and chord wall widths, weld or fillet size, ie. distance to weld toe from intersection of outer wall surfaces, and loading positions. The thickness of the model was not checked because for a given load, variation in thickness is compensated by a change in stress, and in a 2-d photoelastic analysis, fringe order is proportional to the product of the stress and material thickness. Weld toe radii were measured using radius gauges on an enlarged (X32) shadow graph of the model. The values are presented in Table 4.12.

In general the models were very accurate; dimensional deviations less than 1.5% of design values. The largest deviations were due to removing material from the outside chord and brace walls to avoid undercut at weld toes.

The material fringe values of the three different sheets of Araldite used to make the models were determined using tensile test strips loaded in uniaxial tension. The results of this exercise, which show that the material is perfectly linearly elastic in the test range, are given in Fig. 4.15.

4.4.3 2-d Steel Models

The models were measured prior to loading for the following physical characteristics and mechanical properties;

- i) Dimensional accuracy, weld profile, HAZ regions
- ii) Yield strength, ultimate tensile strength, hardness
- iii) Surface roughness

4.4.3.1 Physical Characteristics

Model wall thicknesses were measured by micrometer and the brace-to-chord wall inclination was measured by vernier protractor. The values are given in Table 4.13. The weld toe profile parameters, ie radius and angle, were obtained from enlarged (32 times) shadow view-graphs of the weld toe region. The profiles were replicated using Plaster-of-Paris moulding compound and were machined to a thickness of 1 ± 0.1 mm for measurement. Using this technique, the profile at three different positions through the thickness of the model, ie each face and mid-thickness, could be viewed. Three models from each type of weldment were selected for measurement. The results are given in Table 4.14.

The extent of the heat affected zones were determined to assist in the interpretation of strain measurements in these regions. To reveal the HAZ boundaries the models were polished and etched in the areas of interest. Mechanical polishing was carried out by hand using 6 μ m (for 15 minutes) and 3 μ m (for 10 minutes) "Metadi" diamond compound. The surfaces were cleaned using a proprietary trichloroethane solvent eg. "Inhibisol" and etched using 'Nitral'; 5% nitric acid in ethyl alcohol.

The boundaries between the HAZ and weld material (WM), the HAZ and base metal (BM) were measured by travelling micrometer. They are shown in Fig. 4.16 at a position selected at random from each type of weldment.

4.4.3.2. Mechanical Properties

The yield strength, ultimate tensile strength and reduction in area of the constituent materials of the weldments were obtained using a Houndsfield tensile testing machine. The results are for as-welded models only. Small cylindrical test pieces were accurately machined from weldments type A and B only (Type C are the same as type A). Test pieces were taken from the following places;

- i) brace and chord wall base metal
- ii) weld material
- iii) heat affected zones adjacent to brace and chord walls
- iv) chord wall base metal very near to heat affected zones.

Two test pieces were cut from each of six locations from each of two weldments making a total of 24. The positions, size and shape of the test pieces are shown in Fig. 4.17. Load-extension curves were plotted manually as the test progressed. The end of the test was at fracture. Fig. 4.18 shows the load-extension curves for all positions from weldment type A. Note that total elongation values include the load-extension characteristics of the machine, shown as line OA on Fig. 4.18. Percentage reduction in area was measured on a reduction gauge.

The yield and ultimate tensile strengths and percentage reduction in area are given in Table 4.15. The results are compared to BSC Certificate and other published values. Fig 4.19 shows the variation in yield and tensile strengths across the weldments.

Hardness traverses were carried out across the BM-HAZ-WM boundaries, of weldments type A and B, in the as-welded and post-weld heat treated conditions. The Vickers Pyramid Hardness test was used. The width across the corners of the indentation was measured optically and its value converted to the hardness number, HV. The results are shown in Figs. 4.20 and 4.21 for weldments type B and A. respectively.

4.4.3.3. Surface Roughness

Surface roughness was measured using "Talysurf 4" mechanical surface measurement equipment. Roughness traverses (max. 10 mm in length) were carried out along the outer wall and weld edges, and across the ground faces of the models. The models were levelled on the plinth of the apparatus and the profiling stylus allowed to travel freely on the surfaces. The results are shown in Fig. 4.22.

Results for the ground faces of the models are presented for later comparison with post-yield conditions.

4.5 Loading

4.5.1 3-d Model Loading

The loading rig used for loading the corner K models is shown in Fig. 4.23a and Plate 4.4. Many of its features are determined by the physical characteristics of the stress-freezing process.

1. Very low Young's Modulus. The loads required are small enough to be applied by freely hanging weights but deflections of the model due to its own weight may be significant. Two-thirds of the self-weight of the model is eliminated by immersion in a dense oil, the remainder by air pockets in the tubes. The latter are the reason for the chord axis being horizontal. Imposed loads due to the self weight of the loading mechanism are nullified by adjustable counterweights. Correct loading is achieved by accurate measurement of the mechanism about the fulcrum point, i.e. rose bearing.

2. Large coefficient of expansion. The model must be allowed to expand freely as its position relative to the loading frame changes. This is made easier by the ball-pivoted bellcrank levers, whose use

leads to the axes of the loaded braces being horizontal. It is also the reason for the apparently complex chord supports. Overall expansion of the chord is accommodated by hanging the model off two pairs of steel links. One pair is braced, the other free to rotate and thus move horizontally in the direction of the chord axis.

3. Limited optical sensitivity of Araldite, the best available material. The model strains usually have to be greater than the elastic strains in the metal prototype. The chord distortions may therefore cause significant changes of θ , the inclination of the braces. To minimise parasitic bending moments, the points of application of the brace forces are arranged as near to the chord wall as possible. This was achieved using Araldite loading cups glued to the ends of the loaded braces.

The stress-freezing technique employed for the photoelastic analysis of any plane within a model is well documented (see section 4.2.1). The models CK1, CK1R and CK3 were loaded in a balanced axial tension (135° brace) and compression (90° brace). Models CK2, CK4 and CK5 were loaded in balanced axial tension (150° brace) and compression (60° brace). The equilibrium of forces for all corner K models is illustrated in Fig. 3.6a. In each model there are small transverse chord end reactions resulting from the different offset of brace axes in the plane of the loaded braces. The components of forces parallel to the chord axis are reacted by the single axial chord end reaction. This tensile reaction, situated at the end of the chord nearest to the brace loaded in compression minimises longitudinal adjustment of the loading rig during the thermal cycle. The ends of the chord extension tubes were free to ovalise.

The loading rig used for loading the X models is shown in Fig. 4.23b. The apparatus was designed and built by Buchan et al (52) to satisfy the features appropriate to photoelastic models of this type.

These are :-

1. Only one load is required. This is small enough to be applied by freely hanging weights to one of the braces. Other considerations are as given for the corner K model loading rig.
2. The ends of the chord are not supported and free to ovalise.

The magnitudes of the loads used in the braces loaded in tension in all 3-d models is given in Table 4.11. The intended mean axial strain in these braces was 0.50%. The differences in actual measured strains were due to inevitable variations in material properties and tube dimensions. These differences do not affect SCF results because all stresses in the model were normalised with respect to the actual mean axial stress in the brace; not the calculated value based on 0.5% strain. The equilibrium of forces in the X models is shown in Fig. 3.6.

4.5.2. 2-d Photoelastic Model Loading

The empirical determination of the equivalent 2-d loading system obtained from previous (18) and present 3-d photoelastic results was given in Section 3.3.1. In these models single point loads, which are equivalent to the membrane and shear forces in the tube walls sectioned at the first point of contraflexure, are applied to the chord and brace walls. The magnitudes, positions and directions of the point loads are given in Table 3.4 for the three different 2-d model geometries studied.

The correct loading of the models shown in Fig. 3.6 is produced by a measured force P_1 if the hinged links, which carry the reactions P_2 and P_3 , are in the intended positions. The nominal stress in the brace wall is defined as $\sigma_{nom} = P_1 / \text{cross sectional area of calibration strip}$.

The models in which the chord wall thickness $T = 30$ mm were loaded as shown in Fig. 4.24a. The models were mounted in the rig together with

a calibration strip located in the direction of the inclined tensile force applied to the brace wall. A simple turnbuckle was used to apply incremental loads to the system; load was transferred to models through pairs of matched mild steel links and 6 mm diameter dowels.

The models in which the chord wall thickness $T = 50$ to 80 mm were too large to be loaded in the above manner. These models were calibrated separately by freely hanging weights as shown in Fig. 4.24b. The models were mounted in the loading frame and incremental loads were applied, through matched links and dowels, to the brace wall. Because the calibration strips were subjected to the same incremental load magnitudes, fringe order readings in the models corresponded to nominal fringe orders in the calibration strip.

Loads were applied to the models in increments of 3 kg in the range 3 to 12 kg. This corresponds to a typical increase in fringe order in the brace wall of 0.072 fringes, for $t = 40$ mm and $MFV = 10.15$ (mean value) N/mm fringe, per 3 kg load.

4.5.3 Finite Element Model Loading

The forces acting on the finite element model were determined in the same manner as 2-d photoelastic models; axial forces causing membrane stresses, and shear forces causing bending and shear stresses. Axial loads were applied to the model uniformly across each wall at structural nodes. Shear forces were applied at the correct distances along each wall, also at structural nodes. Restraints were specific at two nodes to prohibit spatial movement in the plane of the model. All loads and restraints are shown in Fig. 4.1. The magnitudes of the loads produced a mean axial stress in the brace wall of unity. All stresses in the model were therefore stress indices.

4.5.4 Steel Model Loading

The steel models were loaded using the equivalent 2-d system

developed for the 2-d Araldite work, as described in section 4.5.2.

A loading rig was designed and built for each different experimental technique used. These were reflection photoelasticity and moire interferometry. Each rig was designed to accommodate the different loading geometries of the three models to be studied.

The loading rig used for reflection photoelasticity was designed to be used within the confines of a 50 ton Denison testing machine. The models were 10 mm thick.

The loading rig for use with the moire interferometer was mounted on the optical table and was therefore a relatively light and economical apparatus. Because the models were thin (4 mm), its capacity was small (3 ton).

Because the design concepts for the two loading rigs were obviously different, they are described separately.

4.5.4.1 Loading Rig for Reflection Photoelasticity Methods

A loading rig was designed and built to be used between the jaws of a hydraulically controlled 50 ton Denison tensile testing machine. The rig is illustrated in Fig. 4.25.

The rig was designed to enable the region of interest to be viewed through a vee-type reflection polariscope which was mounted, independently from the rig, on the outside of the testing machine.

Forces were applied to the model through a mechanism comprising pairs of matched links, $\frac{1}{2}$ inch diameter hardened steel dowels, a spreader beam and solid cylindrical blocks clamped in the jaws of the machine. The rig was designed to accommodate two different models and three different loading geometries for loads of up to (approximately) 30 tons.

The resulting framework was manufactured from grade 43 mild steel flat bar, round bar and rolled universal channel. Hardened steel drill bushes were used to locate dowel holes and reinforce the lugs near the

ends of the links, and in the webs of the channels.

With the model removed from the assembly, the loading rig was effectively in two parts; each part permanently attached to the machine through the solid cylinders clamped in its jaws. To re-assemble the model in the rig, the distance between the top and bottom jaws was reduced to allow the dowels to be located through the model with ample tolerance.

4.5.4.2 Loading Rig for Moire Interferometry Methods

The essential features of the loading rig are shown in Fig. 4.26 and Plate 4.5. The frame was sufficiently light to be man-handled into two mutually perpendicular positions whilst the model was loaded. The frame was rigid in bending and torsion for loads of up to 3 tonnes acting at one of several different locations. The rig was mounted off an eccentrically located rose bearing and suspended from a remote support frame by a stiff spring. For optical alignment, the rig was supported by three fine adjustment screws; micrometer barrels were used. The rig was also designed to accommodate two different models and three different loading geometries.

The resulting rectangular frame was manufactured from grade En24 steel plate and En3 rolled 'Tee', bolted at its corners and aligned for out-of-plane deviations using steel horseshoe shims. The holes to receive loading pins were accurately located and reamed. Attachments to react against the adjustment screws were bolted to the frame.

The models were loaded through pairs of matched links made from $\frac{1}{4}$ inch thick ground rectangular steel bar. Loading pins were $\frac{3}{8}$ inch diameter hardened steel dowels. Tensile load was applied to the links (attached to the brace wall) by a turnbuckle, located on the outside of the frame, through a $\frac{1}{2}$ inch diameter threaded bar. A 3 tonne capacity load cell, connected to a digital readout balancing box, measured the

load. A thrust bearing was introduced between the coupling and load cell to reduce frictional forces. Direction of loading was accomplished by passing the threaded bar through a hole in a machined block at the correct inclination.

Initial loads of between 0.2 and 0.5 kN were used to establish an artificial datum. Loads were then applied in increments of approximately 5 kN prior to yielding in the chord weld toe fillet. The corresponding incremental increase in strain in the brace wall was 0.02% strain. After yielding, load increases were governed by the spread of plasticity in the model.

4.6 Measurement

4.6.1 3-d Photoelastic Models

The important measurements were post-load deformations, actual weld profiles and fringe order readings.

4.6.1.1 Post Load Deformations

The model was set up on the surface table and measurements taken in the same manner and at the same positions as in Section 4.4.1. Load induced deformations of the chord were calculated. They are shown in Fig. 4.14 in the plane of loaded braces of some of the models. The results are compared to the deformations measured by Little (18), normalised with respect to chord diameter and Young's modulus which were both different. The displacements predicted from Mockford's parametric flexibility equations (67) are also shown in Fig. 4.14.

The post-load measurements were also used to detect evidence of unbalanced, inadequate or spurious brace loading before the model was destroyed by slicing.

4.6.1.2. Slicing, Sub-slicing and Photoelastic Measurement

Slices were cut from the model in the chain-dotted planes defined in Fig 4.27 for the 3-d CK and X models. The slices were 2.50 ± 0.15 mm thick. The procedure is previously documented (18). Each slice was measured by micrometer; variations in thickness being allowed for in the calculation of unit fringe order. Variation in the thickness of an individual slice was usually within ± 0.03 mm; occasionally this would exceed ± 0.05 mm near the ends of the slices remote from the important weld regions.

The slices were placed in a drying oven at 70° C for a minimum of 72 hours and stored in a dessicator containing silica-gel prior to being analysed.

For photoelastic measurement, the slices were mounted in a diffused light transmission polariscope and examined in normal-incidence polarised light. Fringe readings were made in monochromatic, circularly polarised light, using Tardy compensation to determine fractional fringe orders. A travelling microscope was used to enlarge the image and define the positions of measurements. Small scratches were made, perpendicular to the edge, on the slices (generally) about 5 mm from the weld toe. The centre of the scratch was used as datum and the positions of measurements were made relative to this. The position of the weld toe was established relative to the datum by viewing an enlarged (x32) shadow of the weld toe region.

The procedures for determining the magnitudes of stresses in the plane of the slice, and the magnitudes and directions of principal stresses which were not necessarily in the plane of the slice, were as follows.

Where a principal plane is known to be in the plane of the slice there exists at each point along the free boundary surface principal stresses σ_1 , parallel to the plane of the slice and σ_2 , perpendicular

to σ_1 . The edges of the model are free from external shear and normal stress. To determine σ_1 , the measured fringe order at each edge point was divided by the thickness of the slice to obtain unit fringe order $N = \sigma_1 / \text{material fringe value}$ (MFV is previously defined). The nominal fringe order N_{nom} in the brace loaded in axial tension was determined from brace walls fringe order readings (Section 5.1.4). The nominal stress

$$\sigma_{\text{nom}} = N_{\text{nom}} \cdot \text{MFV}$$

Further subslicing of the main slice was necessary to obtain surface principal stresses where their directions were not known from symmetry as shown in Fig. 4.28. The "through-thickness" subslices were cut 1.00 ± 0.05 mm thick perpendicular to the chord wall. The "surface" subslice was cut along the outer edge of the weld having a minimum thickness of 0.05 ± 0.03 mm. The main slice was sandwiched between fillets of 'quick-set' Araldite so that the subslices would not be lost whilst cutting. All subslices were orientated, labelled and dried prior to photoelastic measurement.

In the general case where a slice is cut out of a stress-frozen photoelastic model which does not contain a plane of symmetry, the principal stresses in the free surface of the model cannot be determined by the usual (normal incidence of light) photoelastic examination alone. This single measurement at any point in the edge of the slice (i.e. the surface of the model) only gives the secondary principal stress in the plane of the slice. The magnitudes of the true principal stresses σ_1 and σ_2 in the surface and the inclination Φ of σ_1 to the plane of the slice can only be determined from three measurements. Because oblique incidence is not suitable for the large stress gradients $\partial\sigma_1/\partial x$ and $\partial\sigma_1/\partial z$ (see Fig. 4.28) subslices have to be cut from the main slice and further measurements obtained from them. The surface slice (see Fig. 4.28) taken along the outer edge of the model when viewed in normal incidence (view on 'A') provides the direction Φ of the greater

principal stress relative to the plane of the slice. This is called the isoclinic angle at the surface. The through-thickness subslice gives $(\sigma_y - \sigma_x)$ and $(\sigma_z - \sigma_x)$ when viewed along lines of sight Y and Z respectively. As the stress perpendicular to the surface $\sigma_x = \sigma_3 = 0$, with value of ϕ from the surface subslice, σ_1 and σ_2 are defined by equations (5.3) and (5.4) in Section 5.1.3.

Where chord wall principal stress distributions were required, surface subslices were cut at the saddle positions of inclined braces. The thickness of the surface subslice is important. In consideration of the through-thickness stress gradients $\partial\sigma_z/\partial x$ and $\partial\sigma_y/\partial x$, a subslice-to-chord wall thickness ratio of 0.05 was accepted. Chord wall surface subslices were 0.40 ± 0.02 mm thick cut parallel to the outer chord wall where it meets with the weld toe. The surface slice when viewed on line of sight x (Fig. 4.28b) provides ϕ and $(\sigma_1 - \sigma_2)$. With the value of the hoop stress σ_y obtained from the slice in the circumferential plane, σ_1 and σ_2 are defined by equations (5.5) and (5.6) in Section 5.1.3.

4.6.2 Photoelastic Measurement of 2-d Models

The models were loaded, positioned in a diffused light transmission polariscope and examined in normal incidence polarised light. The edges of the models are boundaries free from external shear and normal stress. This is a plane stress analysis. There exists at each point along the free boundary a principal stress parallel to the edge of the model. The fringe order at each edge point $N = \sigma \times \text{model thickness} / \text{MFV}$. Similarly the fringe order in the calibration strip $N_{\text{nom}} = \sigma_{\text{nom}} \times \text{calibration strip thickness} / \text{MFV}$. The material fringe value is a constant for each precast sheet. Model and calibration strip were measured by micrometer for use in calculating stress indices. After linearity had been established, zero errors were eliminated by using differences of stresses due to two loads only.

4.6.3 Finite Element Output

The PAFEC output gives the following data of use in the analysis of the models;

- i) global cartesian co-ordinates
- ii) components of displacements
- iii) magnitudes of principal stresses
- iv) directions of principal stresses relative to global model axes and local element orientation
- v) maximum shear stress and
- vi) cartesian direct and shear stresses.

This data is given for every node belonging to every element. A further refinement of items iii), iv) and v) is made by the stress averaging routine. The principal stresses and directions at nodes, which are common to two or more adjacent elements, are presented as the average of the individual values at that node.

In this work, principal stresses were extracted from the PAFEC output in the following regions.

- i) along the edges of the outside chord and brace walls and weld fillet
- ii) through the thickness of the chord wall on a line perpendicular to the position of the maximum surface stress, and
- iii) as ii) but perpendicular to the chord weld toe.

4.6.4 Measurement of Strains in Steel Models using Reflection Techniques

In the measurement of strains using reflection techniques, calibration of the photoelastic layer material is necessary to convert the elastic strains recorded in the layer to the true elastic or plastic model strains. The values obtained by Eissa (63) for the material properties of the layer, i.e. Young's modulus, Poisson's ratio and MFV, were used in the early stages of this work. This was because the photoelastic materials were similar. However, it was intended that once the experimental method was established, the true properties of the material used in this work would be obtained.

It was shown (63) that if the profiles of the layer and model were identical, then maximum shear strains in the layer γ_L and model γ_m were equal. They were also proportional to fringe order n per unit thickness of the layer t_L . Using Araldite CT200 with hardener HT901 for the photoelastic coating:

$$\gamma_M = \gamma_L = 0.0021 n/t_L$$

The thickness of the layer was 0.5 ± 0.02 mm, but in any one model this did not vary by more than 0.01 mm. A layer thickness correction coefficient (determined by Eissa (63)) of 1.10, which was appropriate

to this thickness, was used.

Fringe orders were measured at the edges of the models at different load magnitudes. Maximum shear strains computed from the fringe orders are expressed in terms of the nominal shear strain in the brace wall which was calculated from the loading. These are shear strain indices.

4.6.5 Strains in Steel Models using Moire Methods

Fringe orders N_x are enumerated in Fig. 4.29. In this example, fringes are of u displacements in the x plane of the model. Where moire methods are used in the determination of strains and relative displacements between two points in the model, the location of the zero-order fringe is arbitrary. This is because rigid body translations and rotations are unimportant if relative displacements are required. In Fig. 4.29, a location in the weld region was chosen as the zero-displacement datum. Fringe count was made positive along the surface of the chord wall moving away from the weld toe. The centre of the dark fringe through the datum point was assigned zero order.

In assigning fringe order, Post (56) explains that the rules of topography of continuous surfaces govern the order of fringes. Adjacent fringes differ by plus or minus one fringe order, except in zones of local maxima or minima where adjacent fringes may have equal fringe orders. Local maxima and minima are usually distinguished by closed loops or saddle-shaped contours. Fringes of unequal orders cannot intersect. To be correct, the fringe order at any point must be unique, independent of the path of the fringe count used to reach the point.

In moire strain analysis, fringe order gradients are measured because derivations of displacements are required to calculate strains. Because each moire fringe, of order N , represents the loci of points of equal in-plane displacement u , it is shown (56) that

$$u = \frac{1}{f} N$$

where f is the frequency of the reference grating.

If the incremental displacement Δu between two points Δx apart is depicted in the fringe pattern by a small change in fringe order ΔN , then

$$\Delta u = \frac{1}{f} \Delta N$$

The strain ϵ_x is the derivative of displacement $\Delta u / \Delta x$. Hence, in the limit, fringe gradient $\partial N / \partial x$ is obtained.

$$\partial N / \partial x = f \epsilon_x$$

The fringe gradient, measured in a prescribed direction, is equal to the frequency of the reference grating and the strain in that direction. It is usual for orthogonal axes, x and y , parallel and perpendicular to the lines of the master grating to be used for analysis; u and v displacement fields are the components of in-plane displacements in the x and y planes, respectively. Normal and shear strains are obtained from the N_x and N_y fringe patterns as follows:

$$\epsilon_x = \frac{\Delta u}{\Delta x} = \frac{1}{f} \frac{\partial N_x}{\partial x}, \quad \epsilon_y = \frac{\Delta v}{\Delta y} = \frac{1}{f} \frac{\partial N_y}{\partial y}$$

$$\gamma_{xy} = \frac{\Delta u}{\Delta y} + \frac{\Delta v}{\Delta x} = \frac{1}{f} \left(\frac{\partial N_x}{\partial y} + \frac{\partial N_y}{\partial x} \right)$$

These strains may be determined from point-by-point measurement of the fringe gradients $\partial N_x / \partial x$, $\partial N_x / \partial y$, $\partial N_y / \partial y$ and $\partial N_y / \partial x$ obtained from N_x and N_y fringe patterns of u and v displacement fields.

4.6.6. Accuracy of Measurements

The accuracy of the photoelastic fringe order measurements, finite element output and moire fringe gradients is assessed in the analysis of errors given in Section 7.

Table 4.1

Three-Dimensional Model Geometry - Model Ref. CK1

Joint No.	Brace Angle		Dihedral Angle		Brace Wall					Chord Wall			t	Weld Parameters						
	θ	φ	Design	Actual	t	r	r ₁	r/t	r ₁ /t	T	r	r/T		t/T	h/t	a/t	$\frac{h-t}{t}$	N/T	α _b	α _c
	deg			deg	mm	mm	mm			mm	mm	mm							deg	deg
1	135°	45°	46.0°	3.91	1.80	2.50	0.46	0.64	8.05	0.70	0.09	0.49	1.36	0.97	0.73	0.58	39°	73°		
2a	135°	135°	136.6°	4.07	2.90	0.60	0.70	0.15	8.04	2.80	0.35	0.51	1.41	0.32	0.51	0.54	14°	24°		
2b	90°	90°	90.5°	3.90	1.35	0.30	0.35	0.07	8.04	1.45	0.18	0.48	1.11	0.66	0.91	0.56	45°	47°		
3	90°	90°	88.4°	3.90	2.70	0.70	0.70	0.18	7.86	1.40	0.18	0.49	1.31	0.67	0.97	0.52	36°	42°		
4	150°	30°	30.5°	3.96	0.40	2.50	0.10	0.63	7.85	0.70	0.09	0.50	1.20	1.11	0.60	0.66	74°	69°		
5a	150°	150°	150.5°	3.69	2.40	0.45	0.65	0.12	8.00	4.00	0.50	0.46	1.70	0.28	0.50	0.60	11°	16°		
5b	60°	120°	119.3°	3.67	2.55	0.30	0.70	0.08	8.00	1.30	0.16	0.46	1.48	0.52	0.79	0.48	24°	34°		
6	60°	60°	60.5°	3.95	1.00	0.80	0.25	0.20	8.10	1.10	0.14	0.49	1.20	0.79	0.87	0.57	37°	45°		
7	90°	120°	119.5°	4.22	3.20	0.35	0.76	0.08	8.02	1.40	0.17	0.52	0.98	0.39	0.71	0.46	25°	32°		
8a	90°	120°	118.2°	3.95	2.70	0.40	0.68	0.10	7.80	1.70	0.22	0.51	1.26	0.37	0.64	0.44	26°	32°		
8b	60°	120°	120.7°	3.80	1.80	0.55	0.47	0.15	7.80	2.90	0.37	0.49	1.15	0.35	0.64	0.41	17°	26°		
9	60°	120°	119.5°	3.80	1.80	0.50	0.47	0.13	8.07	1.60	0.20	0.47	0.91	0.36	0.62	0.41	24°	30°		
10	135°	120°	120.0°	4.13	2.90	0.30	0.70	0.07	8.10	1.40	0.17	0.51	0.89	0.23	0.33	0.27	17°	38°		
11a	135°	120°	122.0°	4.15	1.50	0.30	0.36	0.07	7.55	1.80	0.24	0.55	0.91	0.27	0.59	0.45	26°	23°		
11b	150°	120°	120.0°	3.80	2.55	0.30	0.67	0.08	7.55	1.45	0.19	0.50	0.86	0.30	0.57	0.39	25°	25°		
12	150°	120°	120.7°	4.07	2.40	0.35	0.59	0.08	7.97	2.50	0.31	0.51	0.70	0.24	0.51	0.36	23°	23°		

Table 4.2

Three-Dimensional Model Geometry - Model Ref. CK1R

Joint No.	Brace Angle		Dihedral Angle		Brace Wall					Chord Wall			t	Weld Parameters						
	θ	φ	Design	Actual	t	r	r ₁	r/t	r ₁ /t	T	r	r/T		t/T	h/t	a/t	$\frac{h-t}{t}$	N/T	α _b	α _c
	deg			deg	mm	mm	mm			mm	mm	mm							deg	deg
1	135°	45°	47.7°	3.83	0.60	1.75	0.15	0.46	8.13	0.40	0.05	0.47	1.09	0.84	0.66	0.46	63°	74°		
2a	135°	135°	137.0°	4.46	0.45	0.40	0.11	0.09	7.87	1.40	0.17	0.53	1.11	0.30	0.50	0.46	16°	24°		
2b	90°	90°	91.0°	3.87	1.20	0.40	0.31	0.10	7.87	1.15	0.14	0.49	1.15	0.63	0.86	0.49	39°	47°		
3	90°	90°	92.5°	3.89	1.20	0.40	0.31	0.10	7.92	1.00	0.12	0.49	1.17	0.61	0.85	0.48	37°	45°		
4	150°	30°	29.8°	4.08	0.60	3.00	0.15	0.75	7.84	0.70	0.09	0.51	1.51	1.34	0.64	0.84	74°	76°		
5a	150°	150°	149.6°	3.77	0.85	0.25	0.22	0.07	8.02	2.50	0.31	0.47	1.46	0.27	0.46	0.50	11°	17°		
5b	60°	120°	120.3°	3.65	1.15	0.50	0.31	0.13	8.02	0.80	0.10	0.46	1.31	0.43	0.68	0.39	20°	33°		
6	60°	60°	60.5°	4.28	1.05	0.80	0.25	0.19	7.98	0.90	0.11	0.52	1.08	0.74	0.70	0.50	69°	65°		
7	90°	120°	121.0°	4.16	2.30	0.35	0.55	0.08	7.93	0.95	0.12	0.52	1.10	0.38	0.62	0.47	22°	31°		
8a	90°	120°	119.2°	4.09	0.90	0.30	0.22	0.07	7.75	0.90	0.11	0.53	1.04	0.37	0.62	0.44	21°	32°		
8b	60°	120°	122.3°	3.96	0.95	0.90	0.24	0.23	7.75	1.00	0.13	0.51	0.97	0.33	0.51	0.34	24°	33°		
9	60°	120°	121.8°	3.84	1.60	0.60	0.42	0.15	8.09	2.00	0.24	0.47	1.00	0.37	0.65	0.43	23°	28°		
10	135°	120°	120.0°	4.40	0.75	0.30	0.18	0.07	7.95	1.50	0.19	0.51	0.90	0.24	0.30	0.26	15°	39°		
11a	135°	120°	121.7°	4.07	1.10	0.20	0.27	0.05	7.71	1.25	0.16	0.52	0.83	0.33	0.67	0.44	26°	25°		
11b	150°	120°	120.0°	3.69	1.75	0.30	0.47	0.08	7.71	0.90	0.11	0.48	0.76	0.27	0.63	0.38	26°	19°		
12	150°	120°	121.0°	4.07	1.15	0.40	0.28	0.10	7.93	1.20	0.15	0.51	0.82	0.25	0.45	0.33	27°	27°		

Table 4.3

Three-Dimensional Model Geometry - Model Ref. CK2

Joint No.	Brace Angle		Dihedral Angle		Brace Wall					Chord Wall			t	Weld Parameters						
	θ	φ	Design	Actual	t	r	r ₁	r/t	r ₁ /t	T	r	r/T		t/T	h/t	a/t	$\frac{h-t}{t}$	H/T	α _b	α _c
	deg			deg	mm	mm	mm			mm	mm	mm							deg	deg
1	135°	45°	44.5°	3.88	1.00	1.50	0.26	0.38	8.01	0.90	0.11	0.48	1.31	1.02	0.75	0.60	63°	73°		
2a	135°	135°	136.0°	4.12	0.80	0.45	0.19	0.11	7.74	0.90	0.12	0.53	1.28	0.35	0.56	0.43	14°	26°		
2b	90°	90°	90.0°	3.91	0.70	0.40	0.18	0.10	7.74	0.80	0.10	0.50	1.14	0.67	0.82	0.46	35°	52°		
3	90°	90°	90.0°	3.86	0.60	0.40	0.15	0.10	7.85	1.25	0.16	0.49	1.18	0.69	0.90	0.57	37°	52°		
4	150°	30°	33.5°	3.85	0.90	3.10	0.23	0.80	7.85	0.60	0.15	0.49	1.75	1.50	0.73	0.86	62°	84°		
5a	150°	150°	149.0°	3.70	1.00	0.20	0.27	0.05	7.73	1.10	0.14	0.48	1.51	0.25	0.46	0.48	12°	19°		
5b	60°	120°	121.7°	3.63	0.80	0.50	0.22	0.14	7.73	0.40	0.05	0.47	1.24	0.46	0.75	0.46	26°	34°		
6	60°	60°	58.0°	4.07	1.00	1.00	0.24	0.24	7.91	1.00	0.13	0.51	1.29	0.90	0.81	0.56	44°	73°		
7	90°	120°	120.0°	4.18	1.10	0.32	0.26	0.08	7.90	0.50	0.12	0.53	0.95	0.37	0.69	0.45	26°	28°		
8a	90°	120°	121.5°	3.96	0.90	0.60	0.23	0.15	7.70	1.20	0.16	0.51	1.01	0.31	0.53	0.36	20°	34°		
8b	60°	120°	119.7°	3.91	1.00	0.75	0.25	0.19	7.70	0.90	0.12	0.51	0.99	0.35	0.58	0.40	23°	32°		
9	60°	120°	120.0°	3.58	1.50	0.55	0.42	0.15	8.00	1.00	0.12	0.45	0.13	0.42	0.80	0.46	22°	26°		
10	135°	120°	120.5°	4.12	2.50	0.28	0.61	0.07	7.92	1.10	0.14	0.52	0.89	0.21	0.31	0.25	13°	35°		
11a	135°	120°	119.7°	4.11	1.00	0.30	0.24	0.07	7.57	1.20	0.16	0.54	0.83	0.32	0.63	0.45	23°	28°		
11b	150°	120°	122.0°	3.66	1.10	0.40	0.30	0.11	7.57	0.90	0.12	0.48	0.80	0.28	0.59	0.37	29°	23°		
12	150°	120°	122.5°	4.00	1.30	0.40	0.32	0.10	7.91	0.80	0.10	0.50	0.72	0.25	0.50	0.31	22°	26°		

Table 4.4

Three-Dimensional Model Geometry - Model Ref. CK3

Joint No.	Brace Angle		Dihedral Angle		Brace Wall					Chord Wall			t	Weld Parameters						
	θ	φ	Design	Actual	t	r	r ₁	r/t	r ₁ /t	T	r	r/T		t/T	h/t	a/t	$\frac{h-t}{t}$	H/T	α _b	α _c
	deg			deg	mm	mm	mm			mm	mm	mm							deg	deg
1	135°	45°	47.2°	3.82	0.70	1.80	0.18	0.47	7.97	0.30	0.04	0.48	1.28	0.78	0.56	0.41	41°	91°		
2a	135°	135°	135.0°	4.11	0.55	0.40	0.13	0.10	7.64	2.90	0.38	0.53	1.40	0.31	0.56	0.44	14°	23°		
2b	90°	90°	90.3°	3.83	1.10	0.35	0.28	0.09	7.64	0.60	0.08	0.50	1.30	0.70	0.97	0.53	33°	43°		
3	90°	90°	88.0°	3.98	0.75	0.35	0.19	0.09	7.82	0.60	0.08	0.51	1.13	0.71	0.92	0.51	44°	50°		
4	150°	30°	30.9°	3.93	0.40	2.40	0.10	0.61	7.96	0.50	0.06	0.49	1.48	1.08	0.56	0.67	67°	101°		
5a	150°	150°	150.0°	3.83	3.00	0.30	0.78	0.08	7.86	2.50	0.32	0.49	1.63	0.28	0.43	0.48	11°	19°		
5b	60°	120°	122.5°	3.68	2.80	0.50	0.78	0.14	7.86	1.20	0.15	0.46	1.62	0.42	0.57	0.40	18°	36°		
6	60°	60°	61.0°	3.85	1.30	1.05	0.33	0.27	8.00	0.85	0.11	0.48	1.04	0.70	0.73	0.45	39°	53°		
7	90°	120°	119.5°	4.28	1.00	0.25	0.23	0.06	7.84	1.00	0.13	0.54	1.05	0.33	0.51	0.38	18°	32°		
8a	90°	120°	118.0°	3.88	1.35	0.30	0.35	0.08	7.69	0.50	0.06	0.49	1.00	0.40	0.68	0.42	23°	29°		
8b	60°	120°	123.2°	4.14	1.50	0.60	0.36	0.14	7.75	1.00	0.13	0.53	0.97	0.34	0.58	0.42	21°	28°		
9	60°	120°	120.0°	3.87	1.10	0.90	0.28	0.23	8.29	1.20	0.14	0.47	1.02	0.41	0.68	0.42	26°	29°		
10	135°	120°	121.0°	3.96	0.80	0.30	0.20	0.07	7.86	0.50	0.06	0.50	1.02	0.27	0.35	0.25	15°	36°		
11a	135°	120°	120.5°	4.80	1.90	0.30	0.47	0.08	7.43	1.30	0.17	0.53	0.89	0.33	0.60	0.44	23°	27°		
11b	150°	120°	118.7°	3.91	0.60	0.35	0.15	0.09	7.30	1.75	0.24	0.53	0.64	0.29	0.58	0.41	30°	25°		
12	150°	120°	121.0°	4.42	0.70	0.30	0.15	0.07	8.35	2.00	0.23	0.52	0.41	0.21	0.40	0.32	23°	25°		

Table 4.5

Three-Dimensional Model Geometry - Model Ref. CK4

Joint No.	Brace Angle	Dihedral Angle		Brace Wall					Chord Wall			τ	Weld Parameters						
	ψ	Design	Actual	t	r	r_1	r/t	r_1/t	T	r	r/T		t/T	h/t	a/t	$\frac{b-t}{t}$	N/T	α_b	α_c
	deg	deg	deg	mm	mm	mm			mm	mm	mm							deg	deg
1	135°	45°	45.0°	3.88	1.40	1.90	0.36	0.49	7.90	0.37	0.05	0.49	1.42	0.92	0.66	0.51	45°	90°	
2a	135°	135°	134.7°	3.78	3.00	0.40	0.79	0.10	7.65	1.05	0.14	0.49	1.40	0.42	0.55	0.40	14°	29°	
2b	90°	90°	90.5°	4.00	0.75	0.40	0.16	0.10	7.65	0.80	0.10	0.52	1.05	0.57	0.73	0.39	35°	52°	
3	90°	90°	92.0	4.00	0.80	0.40	0.20	0.10	7.63	0.60	0.07	0.52	1.04	0.59	0.82	0.47	34°	45°	
4	150°	30°	30.6°	4.02	0.50	4.00	0.12	1.00	8.12	0.30	0.04	0.49	1.28	1.04	0.53	0.55	60°	48°	
5a	150°	150°	152.0°	3.84	5.50	0.25	1.43	0.06	7.96	2.70	0.34	0.48	2.11	0.24	0.43	0.52	9°	15°	
5b	60°	120°	120.6°	3.61	3.00	0.50	0.83	0.14	7.97	0.40	0.05	0.45	1.51	0.46	0.66	0.36	19°	34°	
6	60°	60°	59.5°	3.68	0.40	1.00	0.11	0.27	8.11	1.30	0.16	0.45	1.10	0.83	0.76	0.52	54°	69°	
7	90°	120°	120.3°	4.13	1.65	0.45	0.40	0.11	7.80	1.15	0.14	0.53	0.94	0.34	0.50	0.32	24°	36°	
8a	90°	120°	121.5°	3.77	0.90	0.37	0.23	0.10	7.56	1.30	0.17	0.50	1.04	0.36	0.63	0.42	22°	32°	
8b	60°	120°	120.5°	4.23	0.40	0.75	0.10	0.18	7.80	0.85	0.11	0.54	0.92	0.35	0.63	0.43	22°	28°	
9	60°	120°	119.5°	3.85	0.82	0.55	0.21	0.14	8.12	0.70	0.09	0.47	1.00	0.40	0.71	0.42	25°	31°	
10	135°	120°	121.0°	3.85	1.00	0.30	0.26	0.04	7.83	0.85	0.11	0.49	1.04	0.30	0.45	0.29	16°	35°	
11a	135°	120°	119.0°	4.29	1.15	0.40	0.27	0.09	7.41	0.60	0.08	0.58	0.76	0.34	0.68	0.44	30°	26°	
11b	150°	120°	123.2°	3.82	1.00	0.35	0.26	0.09	7.38	0.60	0.08	0.52	0.77	0.24	0.59	0.38	20°	22°	
12	150°	120°	120.5°	4.18	1.70	0.40	0.41	0.10	8.27	0.65	0.08	0.50	0.64	0.22	0.39	0.25	24°	29°	

Table 4.6

Three-Dimensional Model Geometry - Model Ref. CK5

Joint No.	Brace Angle	Dihedral Angle		Brace Wall					Chord Wall			τ	Weld Parameters						
	ψ	Design	Actual	t	r	r_1	r/t	r_1/t	T	r	r/T		t/T	h/t	a/t	$\frac{b-t}{t}$	N/T	α_b	α_c
	deg	deg	deg	mm	mm	mm			mm	mm	mm							deg	deg
1	135°	45°	44.7°	3.87	0.90	1.00	0.23	0.46	7.66	0.30	0.04	0.50	1.26	0.65	0.46	0.38	33°	90°	
2a	135°	135°	135.5°	3.96	1.80	0.35	0.45	0.09	7.80	1.50	0.19	0.51	1.15	0.36	0.71	0.55	21°	22°	
2b	90°	90°	90.0°	3.82	0.85	0.40	0.22	0.10	7.82	0.60	0.07	0.49	1.26	0.71	0.89	0.44	37°	52°	
3	90°	90°	90.0°	3.84	0.50	0.40	0.13	0.10	7.80	0.40	0.05	0.49	1.17	0.64	0.85	0.44	33°	47°	
4	150°	30°	31.2°	3.98	0.75	3.00	0.19	0.77	8.13	0.20	0.02	0.48	1.63	1.16	0.64	0.61	39°	76°	
5a	150°	150°	151.6°	3.78	6.00	0.20	1.58	0.05	8.01	1.70	0.21	0.47	2.30	0.19	0.31	0.38	8°	17°	
5b	60°	120°	119.4°	3.74	1.05	0.60	0.28	0.16	8.03	0.60	0.07	0.47	1.15	0.46	0.75	0.45	28°	33°	
6	60°	60°	62.0°	3.76	2.30	1.80	0.61	0.47	8.07	1.30	0.16	0.47	1.31	0.79	0.81	0.54	54°	63°	
7	90°	120°	120.3°	4.02	1.25	0.13	0.31	0.03	7.80	1.15	0.15	0.51	1.09	0.41	0.70	0.47	24°	30°	
8a	90°	120°	119.5°	3.98	0.70	0.35	0.17	0.09	7.75	0.65	0.08	0.51	0.97	0.41	0.74	0.47	26°	29°	
8b	60°	120°	119.0°	3.75	1.50	0.55	0.40	0.15	7.70	2.00	0.26	0.49	1.17	0.39	0.63	0.44	19°	29°	
9	60°	120°	119.3°	3.94	1.05	0.60	0.27	0.15	8.25	0.45	0.05	0.48	1.10	0.41	0.71	0.42	24°	32°	
10	135°	120°	120.0°	4.11	0.80	0.35	0.19	0.08	7.77	0.90	0.11	0.53	0.85	0.33	0.55	0.37	25°	32°	
11a	135°	120°	120.0°	4.07	1.30	0.30	0.32	0.07	7.70	1.00	0.13	0.53	0.93	0.29	0.47	0.33	20°	32°	
11b	150°	120°	122.0°	3.85	0.70	0.40	0.18	0.10	7.65	1.20	0.15	0.50	0.70	0.23	0.38	0.28	21°	30°	
12	150°	120°	121.5°	4.80	1.75	0.45	0.43	0.11	8.25	0.45	0.05	0.48	1.04	0.28	0.43	0.27	16°	35°	

Table 4.7

Three-Dimensional Model Geometry - Model Ref 190

Position in Model	Weld Profile Ref 1	Dihedral Angle ϕ		Brace Wall				Chord Wall		Weld Parameters							
		Pre Load	Post Load	t	r _b	r _i	r _b /t	r _i /t	T	r _c	r _c /T	t/T	h/t	F/T	H/T	ϕ_b	ϕ_c
		deg	deg	mm	mm	mm			mm	mm						deg	deg
Crown	U 0.5	90.0°	92.4°	3.85	1.60	0.40	0.41	0.10	7.60	0.55	0.070	0.49	1.20	-	0.22	12°	68°
	C 0.5	90.0°	91.6°	3.93	1.70	0.35	0.43	0.08	7.82	0.50	0.064	0.50	1.27	0.23	0.35	11°	40°
Saddle	U 0.5	120.0°	122.7°	4.18	0.65	0.30	0.15	0.07	8.07	0.42	0.052	0.51	1.03	-	0.18	9°	43°
	C 0.5	120.0°	124.2°	4.07	1.95	0.40	0.48	0.10	7.88	1.60	0.203	0.51	1.11	0.28	0.41	10°	20°
Crown	U 0.3	90.1°	92.5°	2.38	1.55	0.55	0.65	0.23	8.20	0.26	0.032	0.29	2.18	-	0.18	20°	75°
	C 0.3	89.9°	93.0°	2.17	1.00	0.40	0.46	0.21	8.07	0.34	0.042	0.27	2.08	0.25	0.40	22°	40°
Saddle	U 0.3	120.0°	126.8°	2.02	1.60	0.70	0.79	0.34	8.20	0.50	0.061	0.25	2.31	-	0.15	9°	45°
	C 0.3	120.0°	126.5°	2.93	2.00	0.15	0.68	0.05	8.24	0.42	0.051	0.35	1.70	0.26	0.34	10°	23°

Table 4.8

Three-Dimensional Model Geometry - Model Ref 160

Position in Model	Weld Profile Ref	Dihedral Angle ϕ		Brace Wall				Chord Wall		Weld Parameters							
		Pre Load	Post Load	t	r _b	r _i	r _b /t	r _i /t	T	r _c	r _c /T	t/T	h/t	F/T	H/T	ϕ_b	ϕ_c
		deg	deg	mm	mm	mm			mm	mm						deg	deg
Crown	U	60°	60.5°	4.04	0.95	1.05	0.23	0.26	8.30	0.30	0.04	0.49	1.27	-----	0.33	27°	60°
	C	60°	61.5°	3.92	1.25	0.90	0.31	0.23	7.84	0.70	0.09	0.50	1.23	0.13	0.40	23°	41°
Crown	U	120°	122.0°	4.15	4.00	0.55	0.96	0.13	8.27	1.60	0.19	0.50	0.93	-----	0.18	8°	39°
	C	120°	122.0°	3.87	2.60	0.50	0.67	0.13	7.84	2.60	0.33	0.49	1.08	0.23	0.34	6°	23°
Saddle	U	120°	125.5°	4.17	3.00	0.60	0.72	0.14	8.17	0.65	0.08	0.51	1.16	-----	0.17	7°	44°
	C	120°	124.0°	4.30	0.65	0.22	0.15	0.05	8.04	1.40	0.17	0.53	1.12	0.25	0.44	12°	19°

Note: U = uncontrolled, C = controlled weld profile

Table 4.9

Chemical Composition of Plate Casts

Plate Thickness mm	Cast No.	Element, weight %										
		C	Si	Mn	P	S	Cr	Mo	Ni	Cu	Nb	V
50	B4899 ¹	0.155	0.36	1.24	0.019	0.025	0.045	0.025	0.040	0.060	0.03	-
25	74423 ²	0.150	0.41	1.45	0.014	0.005	0.025	0.005	0.038	0.023	0.03	0.005

Mechanical Properties of Plate

Plate Thickness mm	Cast No.	Yield Stress N/mm ²	Tensile Stress N/mm ²	Elongation %	Charpy V Notch Energy J
50	B4899 ¹	364	529	30	44, 43, 31 ³
25	74423 ²	381	515	33	120, 116, 116, 117 ⁴

1. Data supplied by BSC, Scottish Shelton and East Moors Group, Glasgow
2. Data supplied by BSC, Scunthorpe Division
3. 10mm x 10mm x 2mm samples at -50°C
4. Samples at -20°C

Table 4.10

Dimensional and Angular Accuracy of 3-d Models

	UNIT	NOMINAL	TOLERANCE	GREATEST DEVIATION	LEAST DEVIATION
<u>Chord</u> ¹					
Mean diameter, D	mm	200.0	± 0.80	+ 0.75 - 0.54	+ 0.02 - 0.04
Out of roundness	mm	-	1.25	1.45	0.15
Wall thickness T	mm	8.0	± 0.45	+ 0.35 - 0.70	0
D/T ratio	-	25	± 1.6	+ 1.96 - 1.18	+ 0.02 - 0
<u>Brace</u> ¹					
Mean Diameter, d	mm	100.0	± 0.40	+ 0.27 - 0.32	± 0.03
Out of roundness	mm	-	0.65	0.45	0.03
Wall thickness, t	mm	4.0	± 0.22	+ 0.29 - 0.40	0
d/t ratio	-	25	± 1.6	+ 2.80 - 1.62	0
Brace/chord angle θ^1	deg	-	0.25	0.25	0.10
<u>Weld Fillet</u> ²					
Chord wall leg length; $H \sin \phi$	mm	2.8	± 0.2	+ 0.78 - 1.35	+ 0 - 0.06
Brace wall leg length; $h \sin \phi$	mm	4.0	± 2.0	+ 1.08 - 1.68	± 0.04
Chord weld toe angle α_c	deg	-	+ 8 - 13	+12 -34	0
Brace weld toe angle α_b	deg	-	+13 - 8	+27 -15	0

1) UKOSRP tolerance

2) API recommended tolerance

Table 4.11

3-d Model Material Properties and Loads

	Units	Model Ref.						
		CK1	CK1R	CK2	CK2 ¹	CK3	CK4	CK5
<u>Frozen Stress Material</u>								
Material fringe value (MFV)	N/mm.fr	0.236	0.238	0.252	0.246	0.230	0.230	0.239
Young's modulus	N/mm ²	17.2	16.8	17.4	17.3	15.7	15.6	15.7
Load in brace in tension	N	101	100	101	101	102	99	98
Cross-sectional area of ditto ²	mm ²	1221	1215	1218	1218	1192	1198	1208
Mean axial stress in ditto σ_{nom}	N/mm ²	0.0828	0.0823	0.0829	0.0829	0.0856	0.0826	0.0811
" " strain " "	%	0.48	0.49	0.48	0.48	0.54	0.53	0.52
Nominal fringe order in ditto = σ_{nom}/MFV	fr/mm	0.351	0.346	0.329	0.337	0.372	0.359	0.340

Note 1: material properties obtained from calibration strip cut from chord wall.

2: measured at approximately 1.5d from brace weld toe.

Table 4.12

Dimensional and Angular Accuracy of 2-d Photoelastic Models

Description	Dimensions mm						Standard Deviation ÷ Wall Thickness
	Nominal	Tolerance	Greatest Error	Least Error	Mean	Standard Deviation mm.	
Calibration strip thickness & Brace wall thickness t	15.0	±0.15	+0.02 -0.33	0	14.86	0.110	0.74%
	25.0	±0.25	+0.07 -0.25	-0.04	24.90	0.106	0.43%
	40.0	±0.40	+0.02 -0.20	+0.02	39.95	0.087	0.22%
Chord wall thickness T	30.0	±0.30	+0.18 -0.45	±0.01	29.97	0.12	0.42%
	50.0	±0.50	+0.03 -0.40	+0.03	49.84	0.14	0.29%
	80.0	±0.80	-0.35	-0.03	79.87	0.09	0.11%
Wall thickness ratio, $\tau = t/T$	0.5	±0.11	-0.1	-0.001	0.497	0.0042	N/A
Outside fillet radius r	0.75 to 7.52	Note 2	±0.1	±0.05	Values vary	Values vary	0.25%
	1.52						
Brace to chord angular deviation ψ	N/A	±0.25°	+0.3° -0.2°	+0.1° -0°	Note 3	Note 3	N/A

Notes:- 1) quotient of t and T tolerances,

2) not UKOSRP tolerance

3) insufficient data available

4) N/A = not applicable

135

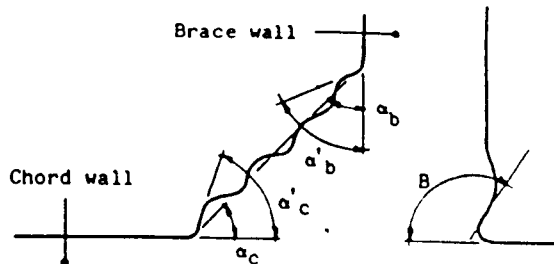
Table 4.13
Dimensional Accuracy of Steel Models

Description	Dimensions mm						Standard Deviation \div Wall Thickness
	Nominal	Tolerance	Greatest Error	Least Error	Mean	Standard Deviation mm.	
Brace wall thickness t	25.0	± 0.25	+0.20	+0.06	25.12	0.056	0.22%
Chord wall thickness T	50.0	± 0.50	-0.63	-0.10	49.70	0.172	0.34%
Wall thickness ratio $\tau = t/T$	0.5	$\pm 0.1^1$	+0.08	+0.03	0.505	0.0018	N/A
Brace to chord wall angular deviation ψ	90°	$\pm 0.25^\circ$	-0.42°	-0.10°	89.7°	Note 3	
	120°		-1.25°	-0.25°	119.2°		

See Table 4.12 for notes.

Table 4.14

2-d Steel Models: Actual Dimensions and Geometry



Notes

- 1. Average values, 2. Not measured.

Model Ref.	Slag	Brace Wall				Chord Wall			Weld Parameters					Pass Disc Test			
		t ¹ mm	r _b mm	r ₁ mm	r _b /t	r ₁ /t	r _c mm	r _c /t	h/t	H/T	α _b	α _c	α' _b		α' _c	β	
90/A-1	1	25.07	0.3	-	0.012	-	49.86	0.5	0.010	1.07	0.41	37°	42°	53°	49°	110°	Yes
	2	0.9	0.3	0.012	0.036	0.012	1.1	0.022	1.10	0.39	52°	41°	100°				
	3	1.3	0.5	0.020	0.052	0.020	0.6	0.012	1.09	0.42	-	58°	83°				No
90/A-2	1	25.09	1.1	0.3	0.044	0.012	49.37	0.9	0.018	1.096	0.43	38°	51°	52°	62°	96°	No
	2	0.9	0.3	0.012	0.036	0.012	0.7	0.014	-	-	-	43°	60°	102°			
	3	0.6	0.4	0.016	0.024	0.016	0.8	0.016	-	-	-	39°	56°	109°			No
90/A-3	1	25.10	0.5	0.25	0.020	0.010	49.40	0.9	0.018	1.08	0.43	38°	44°	52°	28°	75°	Yes
	2	0.75	-	0.030	-	-	0.4	0.008	-	-	-	50°	66°	-	-	-	
	3	0.3	0.6	0.024	0.012	0.024	0.75	0.015	-	-	-	55°	62°	-	-	-	No
120/A-1	1	25.08	0.7	0.15	0.028	0.006	49.72	0.5	0.010	1.35	0.42	23°	50°	37°	47°	-	Yes
	2	0.7	0.2	0.008	0.028	0.008	0.15	0.003	1.37	0.44	44°	40°	-	-	-		
	3	0.85	-	0.034	-	-	0.35	0.007	1.37	0.42	40°	38°	-	-	-	Yes	
120/A-2	1	25.14	1.0	0.3	0.040	0.012	49.75	0.8	0.016	1.35	0.41	24°	46°	36°	43°	-	Yes
	2	0.55	0.2	0.008	0.022	0.008	0.8	0.016	1.35	0.39	38°	48°	-	-	-		
	3	0.7	0.35	0.014	0.028	0.014	0.55	0.011	1.34	0.39	42°	44°	-	-	-	Yes	
120/A-3	1	25.20	0.8	0.3	0.032	0.012	49.65	0.7	0.014	1.36	0.42	23°	34°	37°	52°	-	Yes
	2	0.65	0.55	0.022	0.026	0.022	0.95	0.019	1.38	0.44	29°	43°	-	-	-		
	3	0.5	-	0.020	-	-	1.0	0.020	1.38	0.44	36°	50°	-	-	-	Yes	
120/C-1	1	25.15	0.6	0.4	0.024	0.016	49.80	1.15	0.023	1.48	0.76	23°	34°	18°	23°	72°	Yes
	2	1.15	-	0.046	-	-	1.0	0.020	1.47	0.76	34°	28°	80°	-	-		
	3	0.8	0.15	0.032	0.032	0.006	0.85	0.017	1.45	0.77	28°	28°	104°			Yes	
120/C-2	1	25.20	0.4	0.3	0.016	0.012	49.85	0.9	0.018	1.44	0.74	21°	25°	17°	35°	100°	Yes
	2	0.5	0.6	0.023	0.020	0.023	0.65	0.013	1.47	0.74	28°	40°	-	-	-		
	3	0.65	0.85	0.034	0.026	0.034	0.8	0.016	1.38	0.73	32°	35°	100°			Yes	
120/C-3	1	25.16	1.0	0.2	0.040	0.008	49.88	1.3	0.026	1.43	0.78	21°	35°	17°	28°	70°	Yes
	2	0.8	0.4	0.016	0.032	0.016	1.15	0.023	1.44	0.76	28°	26°	95°				
	3	0.4	0.25	0.010	0.016	0.010	1.1	0.022	1.47	0.76	26°	26°	80°			Yes	

Uncontrolled Weld Profiles

Controlled Weld Profiles

Table 4.15

Mechanical Properties of Steel Models obtained from
Houndsfield Test Specimens¹

Weld- ment Type	Material Designation and Location	Cross- sectional area ² mm ²	Yield Stress N/mm ²	Ultimate Tensile Stress	Reduction in Area %	
Type A	BM Chord wall	8.042	314	472	61	
		8.068	324	478	62	
	BM Chord wall near HAZ	8.068	343	506	60	
		8.042	314	484	63	
	BM Brace wall	8.143	352	501	64	
		8.093	344	500	62	
	HAZ Adjacent chord	8.093	392	531	67	
		8.093	404	527	58	
	HAZ Adjacent brace	8.068	475	567	7	
		8.118	502	565	35	
	WM Weld E51	8.194	479	581	25	
		8.245	457	577	45	
	Type B	BM Chord wall	8.143	296	478	59
			8.093	296	467	64
BM Chord wall near HAZ		8.143	302	478	62	
		8.143	325	482	62	
BM Brace wall		8.093	367	503	64	
		8.143	363	523	68	
HAZ Adjacent chord		8.100	385	519	60	
		8.140	390	522	60	
HAZ Adjacent brace		8.114	450	546	42	
		8.093	441	540	33	
WM Weld E43		8.093	435	508	75	
		8.118	435	522	72	
BSC Certificate and other published data ³						
		BM Chord wall	-	364	529	N/A
	BM Brace wall	-	381	515	"	
	WM Weld E51	-	430-460	520-550	"	
	WM Weld E43	-	390-430	480-510	"	

Notes

1. Mean gauge length = 11.45 mm
2. Calculated from mean specimen diameter, obtained from 4 measurements taken at 45° circumferential intervals.
3. ESAB Welding Consumables Product Literature.

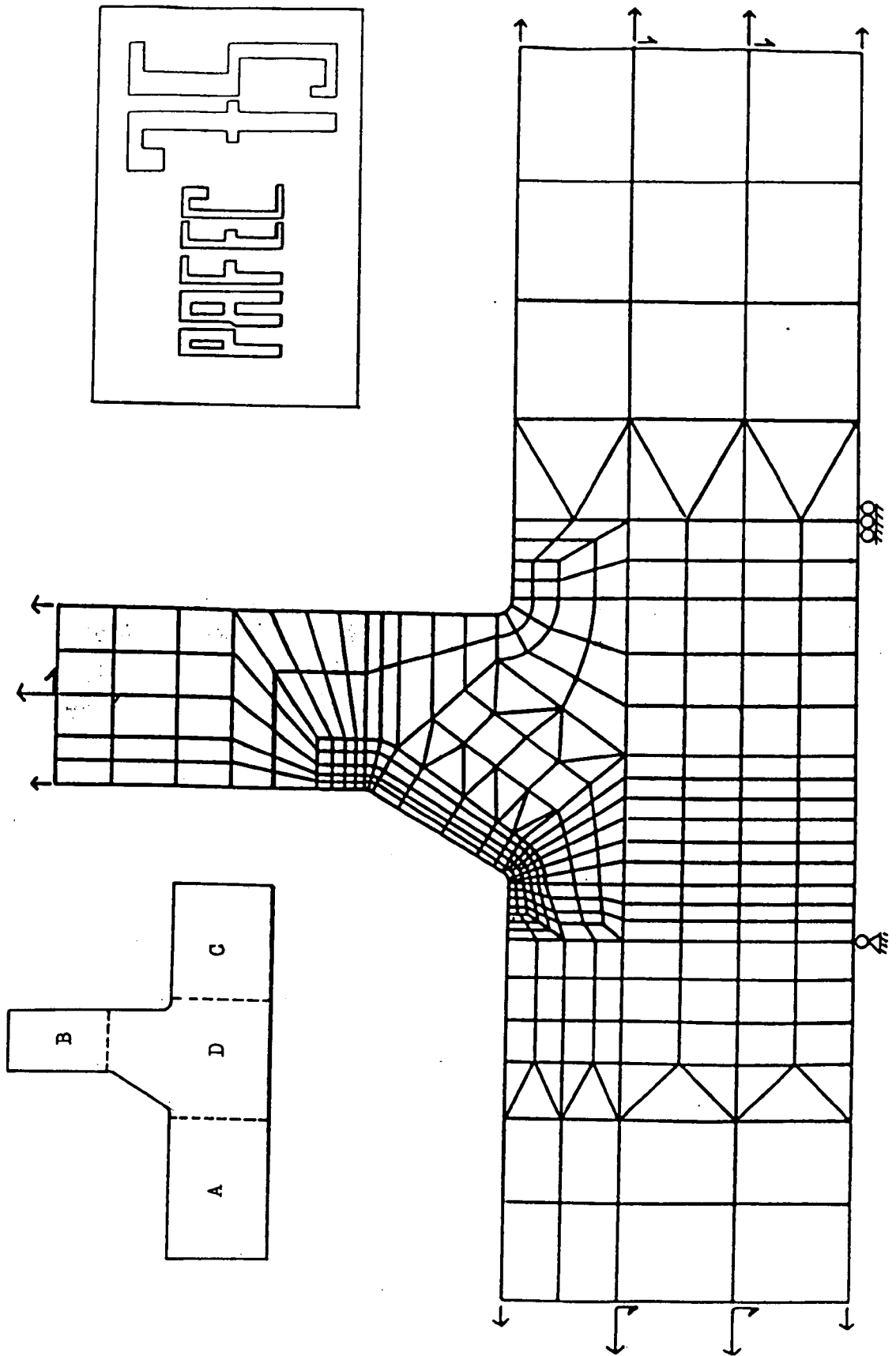


Fig. 4.1 Finite Element Mesh Used in 2-d Models

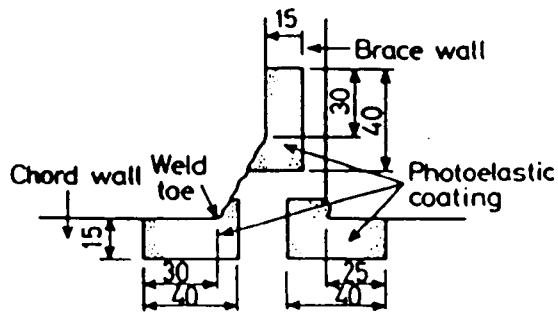


Fig. 4.2 Positions of Photoelastic Coatings

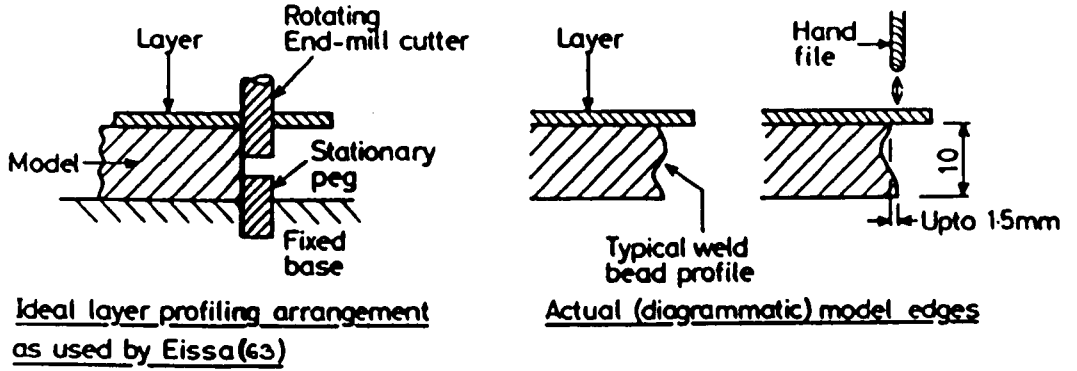


Fig. 4.3 Edge Profiling Photoelastic Coatings

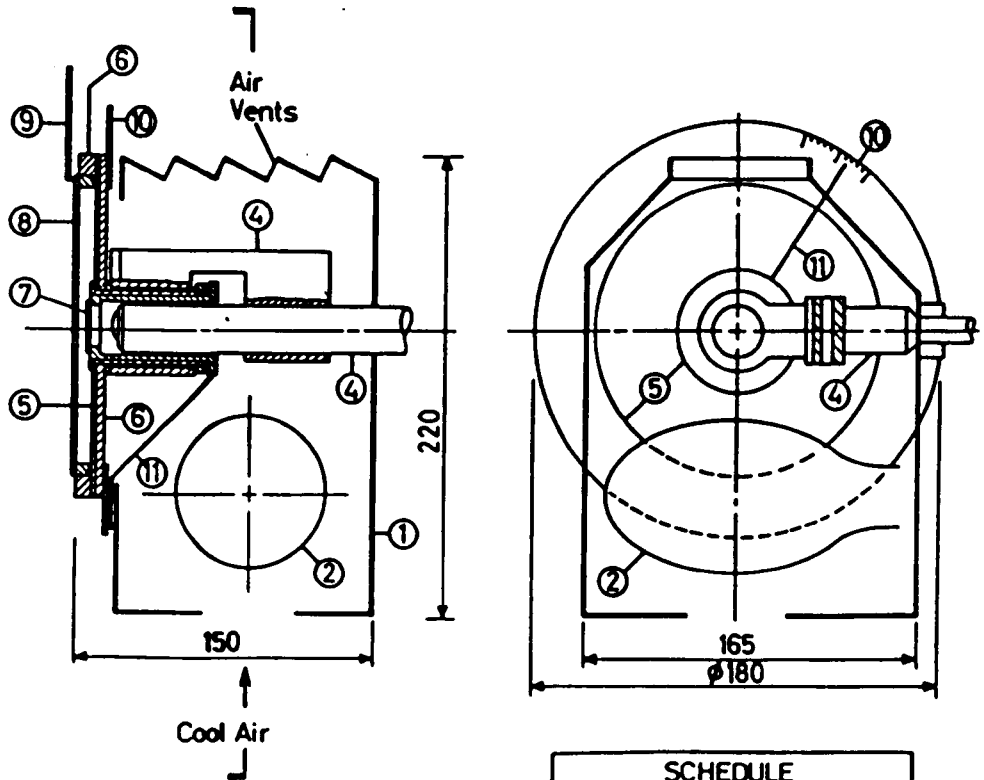


Fig. 4.4 Reflection Polariscope and Housing

SCHEDULE	
1	HOUSING
2	SODIUM LAMP
3	MICROSCOPE
4	MOUNTING BLOCK ETC.
5	POLARISER
6	CARRIERS
7	ANALYSER
8	QUARTER WAVE PLATE
9	Q.W.P. HANDLE
10	SCALE
11	POINTER TO ROTATE (7)

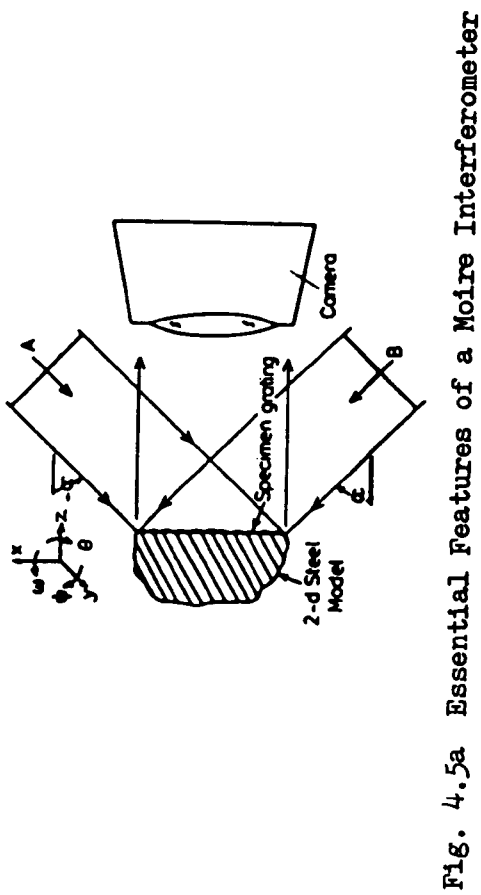


Fig. 4.5a Essential Features of a Moire Interferometer

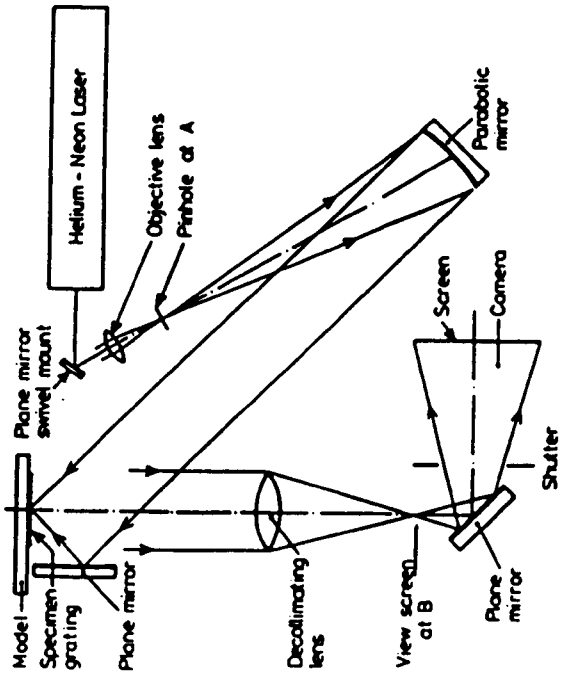


Fig. 4.5b Moire Interferometer

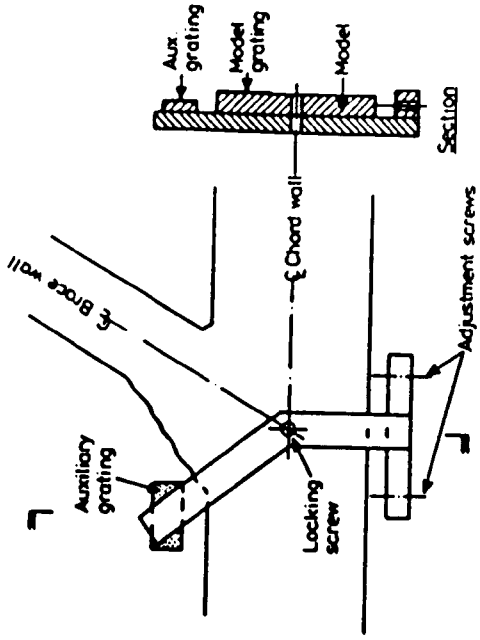


Fig. 4.6 Auxiliary Grating Bracket

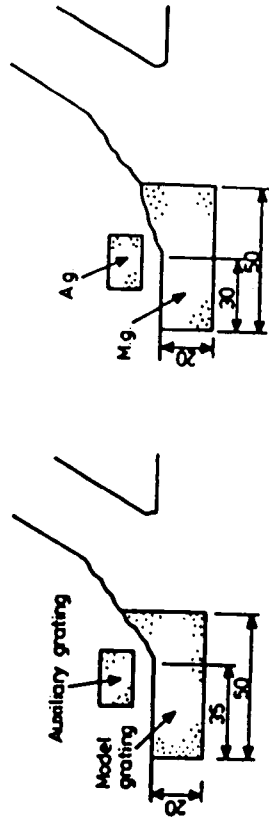
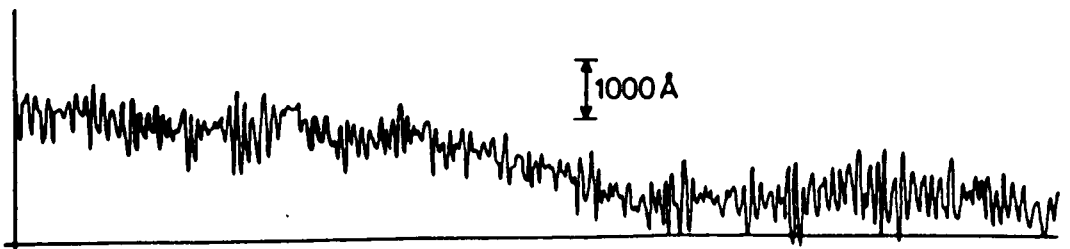
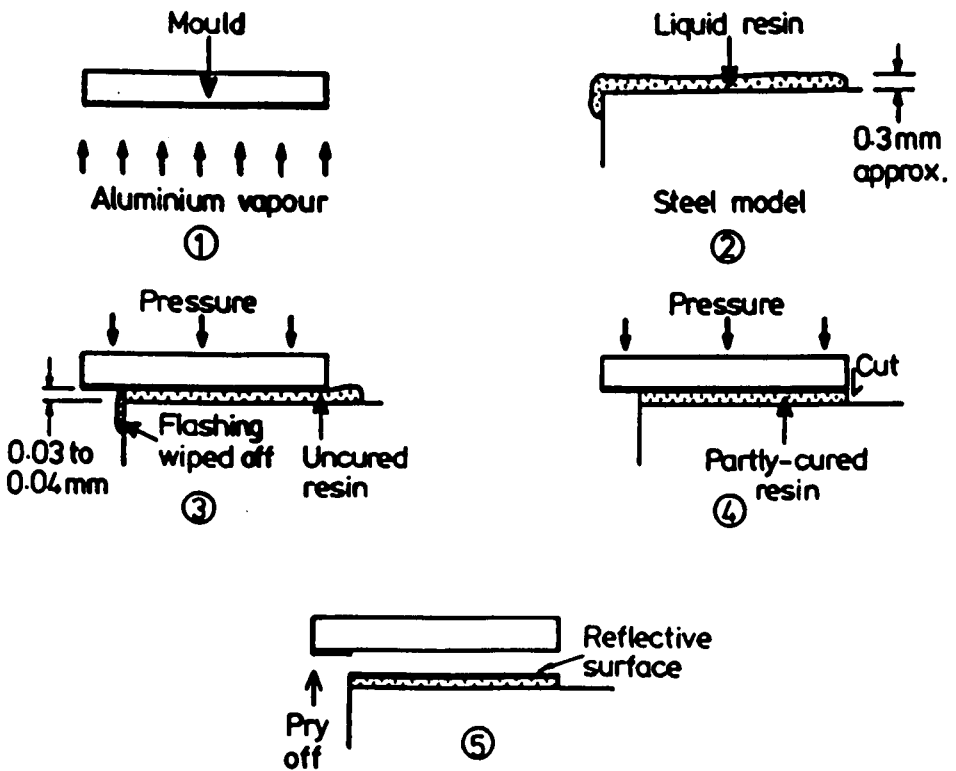
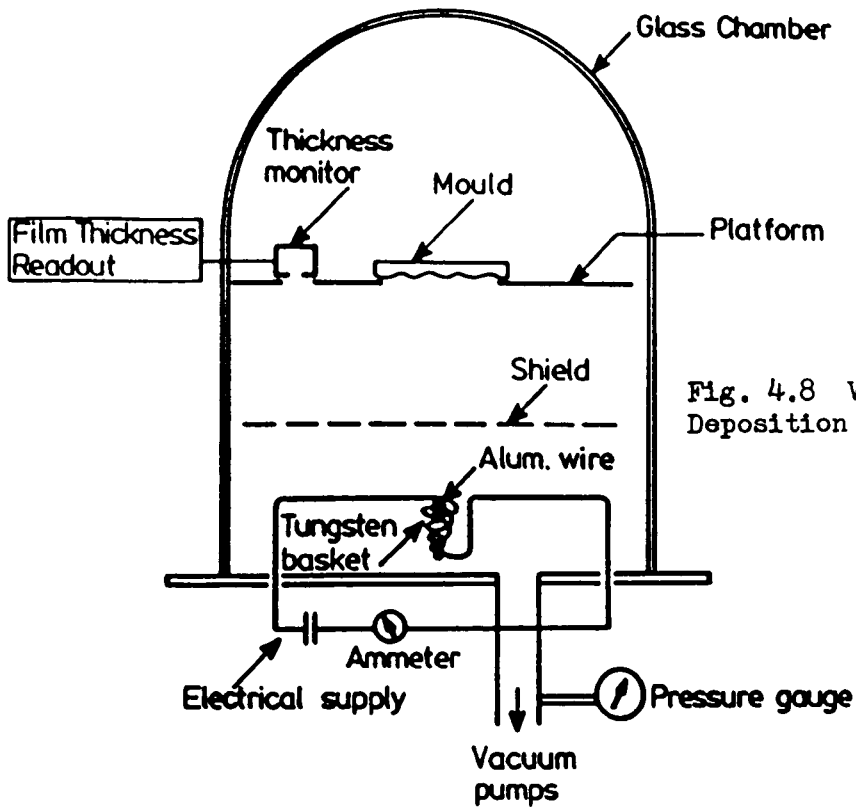
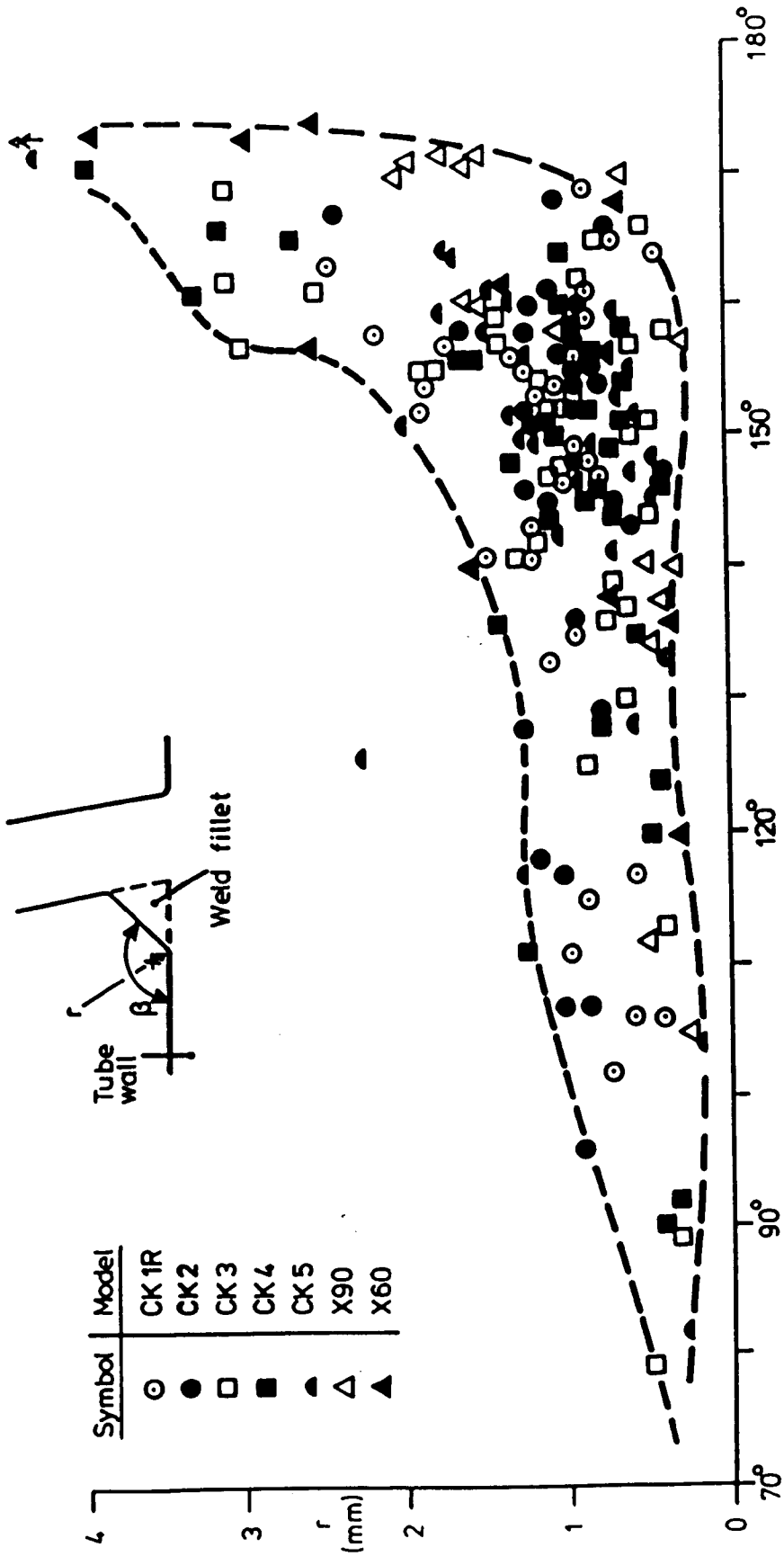


Fig. 4.7 Positions of Gratings in Moire Work





Weld Fillet Dihedral Angle $\beta = (180 - \alpha)$

Fig. 4.11 Weld Toe Radii Achieved in All 3-d Photoelastic Models

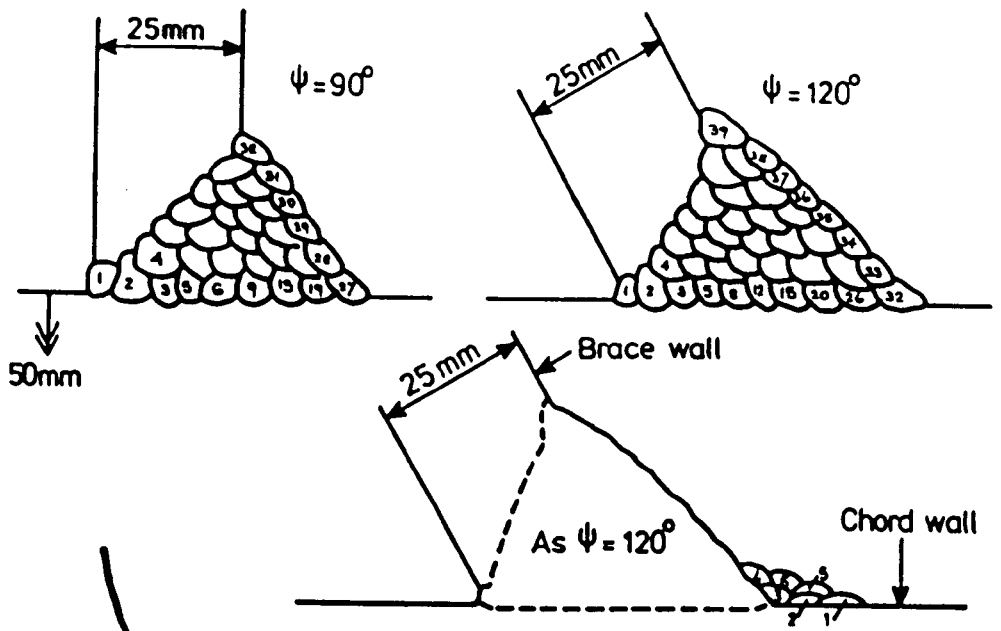


Fig. 4.12 Weld Build-Up Sequence

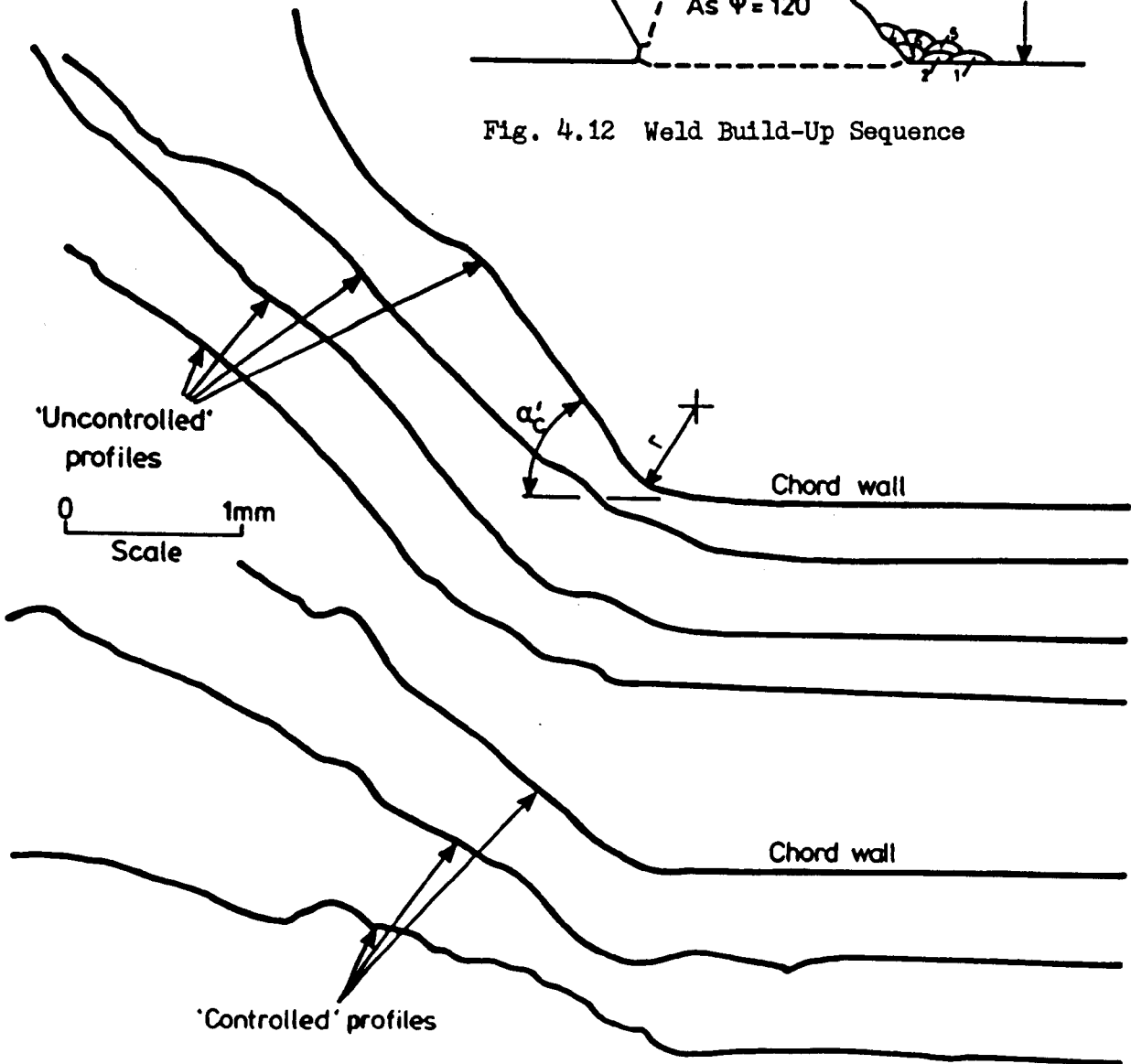


Fig. 4.13 Tracings of Weld Profiles in Steel Models

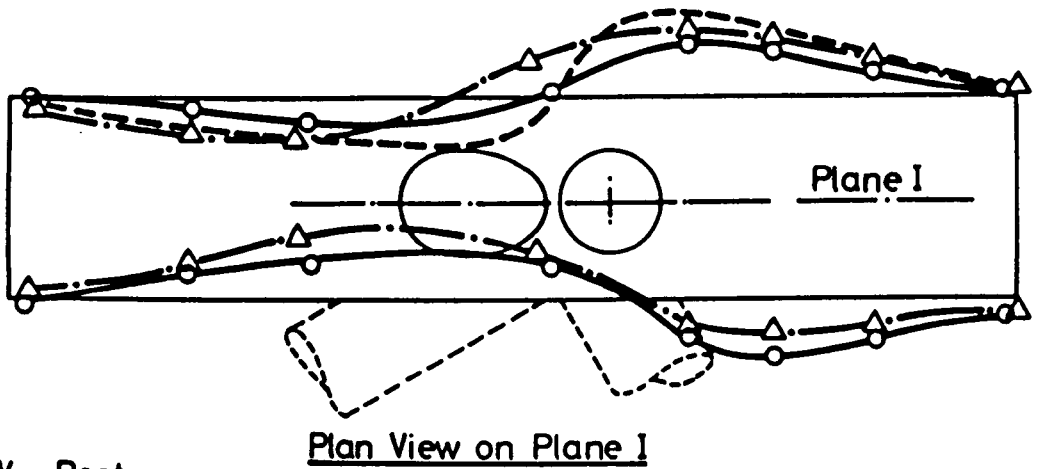
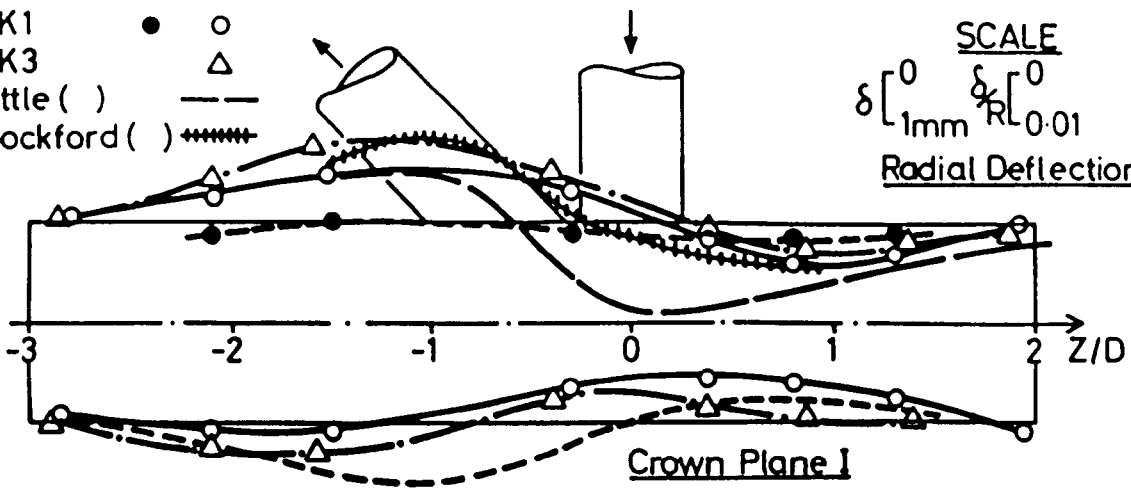
KEY

CK1
CK3
Little ()
Mockford ()

Load
Pre Post

● ○
△
—
+++++

SCALE
 $\delta [\begin{smallmatrix} 0 & 0 \\ 1\text{mm} & \text{RL} 0.01 \end{smallmatrix}]$
Radial Deflection



KEY

CK2
CK4

Post Load

□
◇

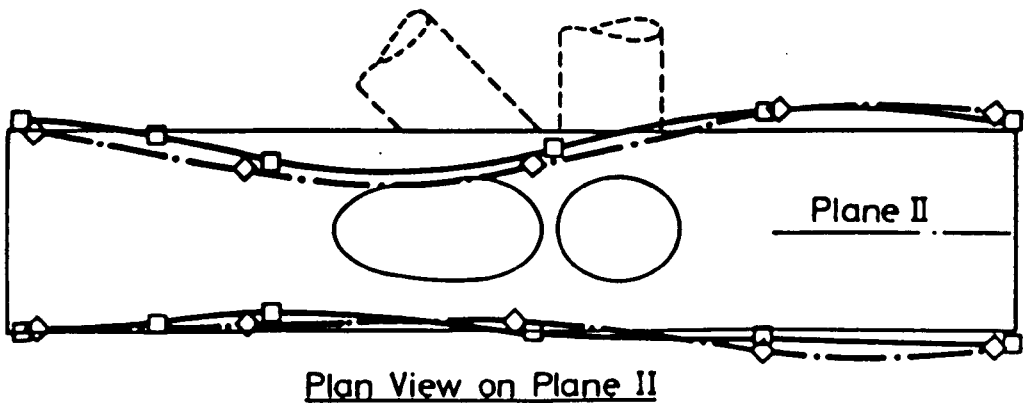
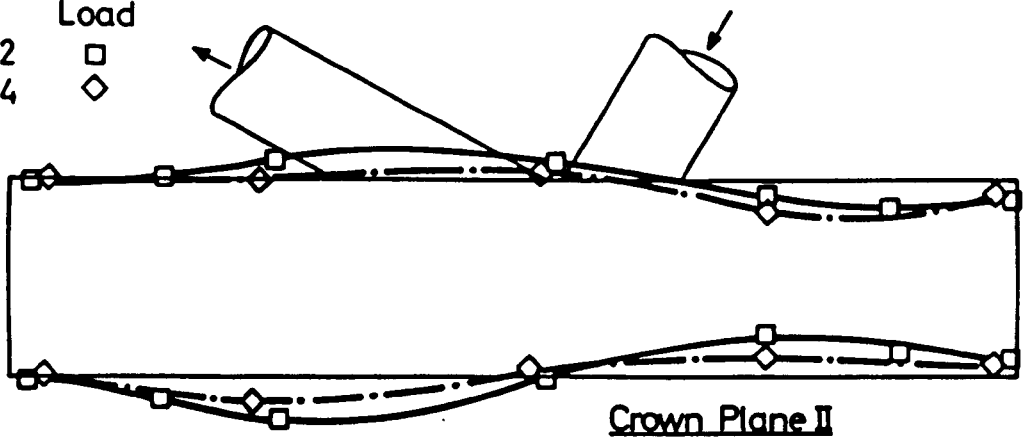


Fig. 4.14 Dimensional Accuracy and Load Induced Deformations in CK Model Chord Tube

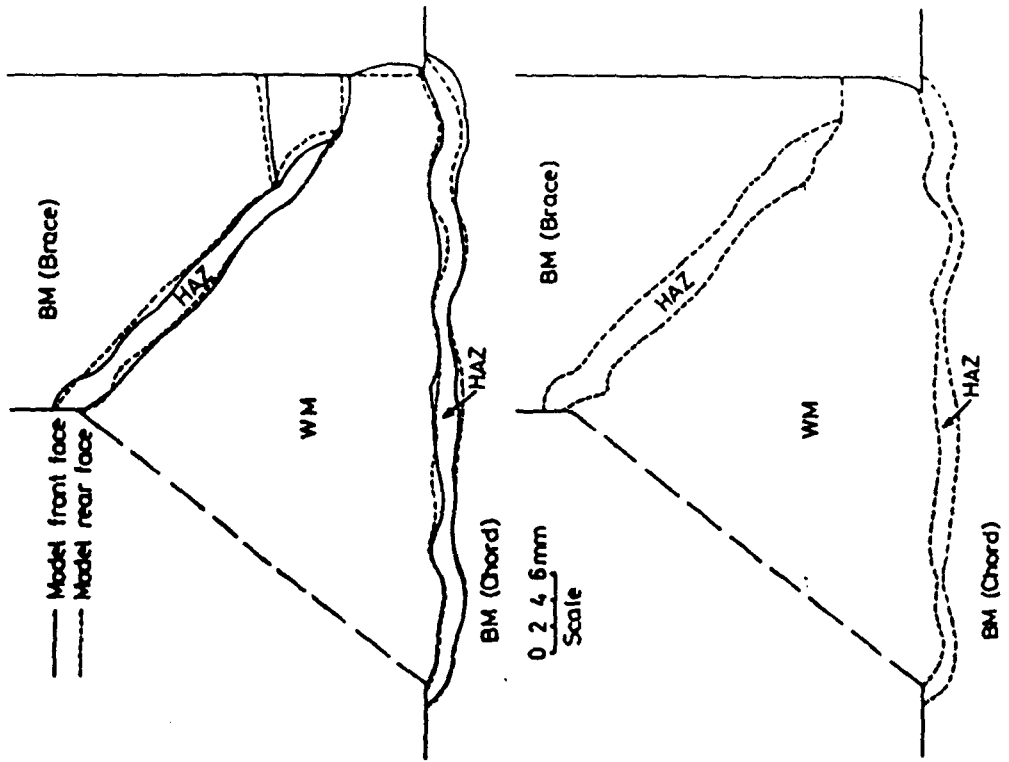


Fig. 4.16 Extent of Heat Affected Zones in Steel Models

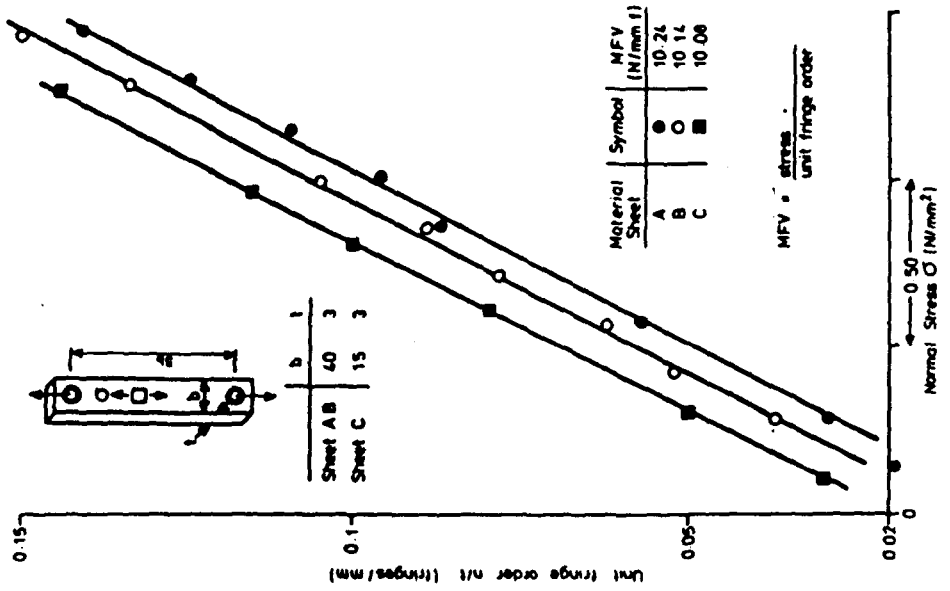
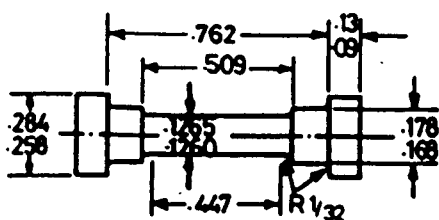
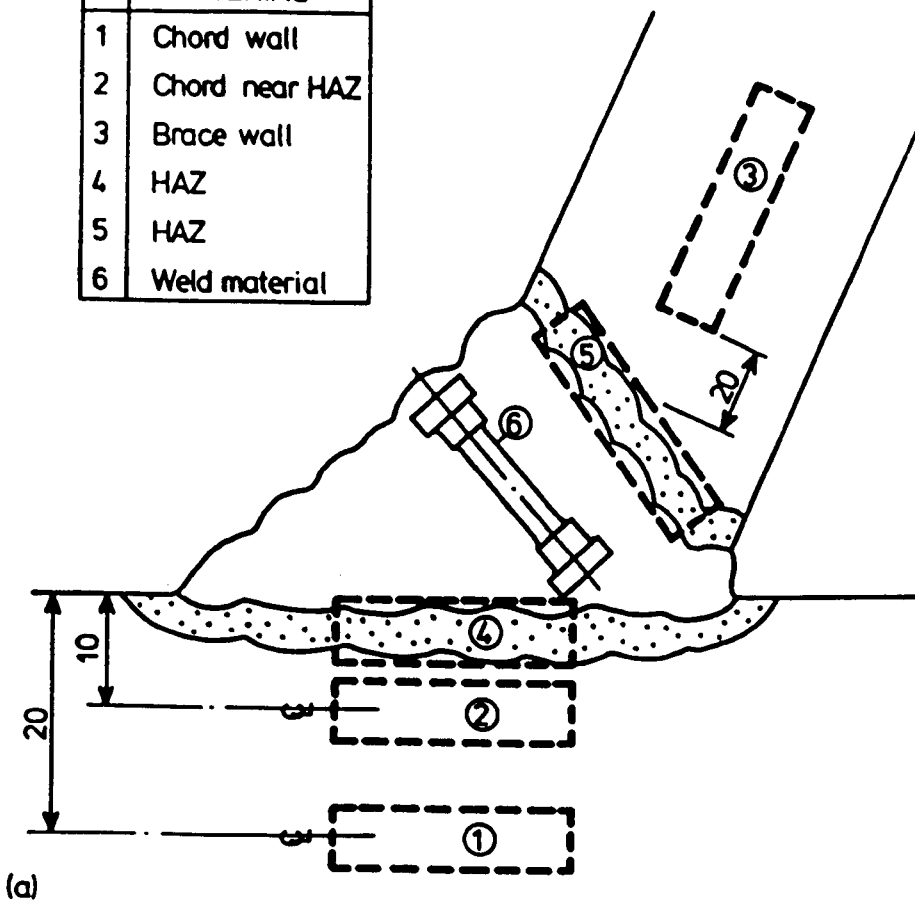


Fig. 4.15 2-d Photoelastic Model Calibration Test Results

No.	MATERIAL
1	Chord wall
2	Chord near HAZ
3	Brace wall
4	HAZ
5	HAZ
6	Weld material

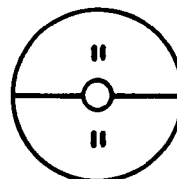


Specimen dims. inches

Area

Chuck No.

$\frac{1}{80}$
(in²)



(b)

Fig. 4.17 Locations, Size and Shape of Tensile Test Specimens

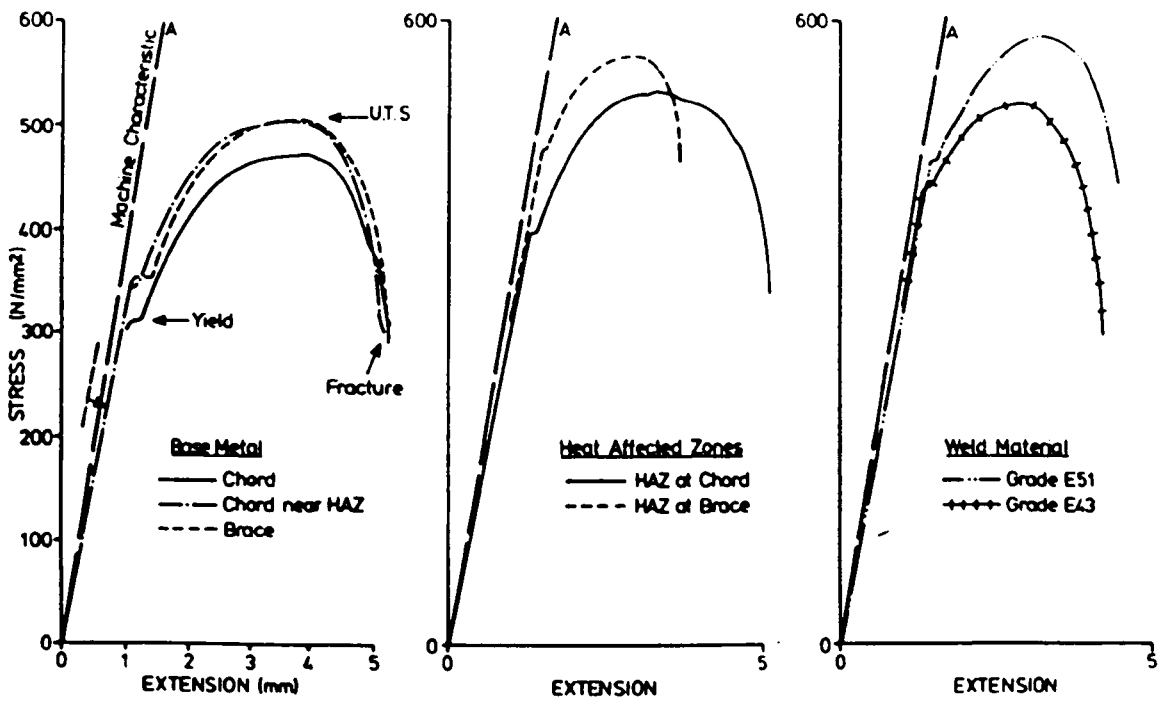


Fig. 4.18 'Houndsfield' Tensile Test Results

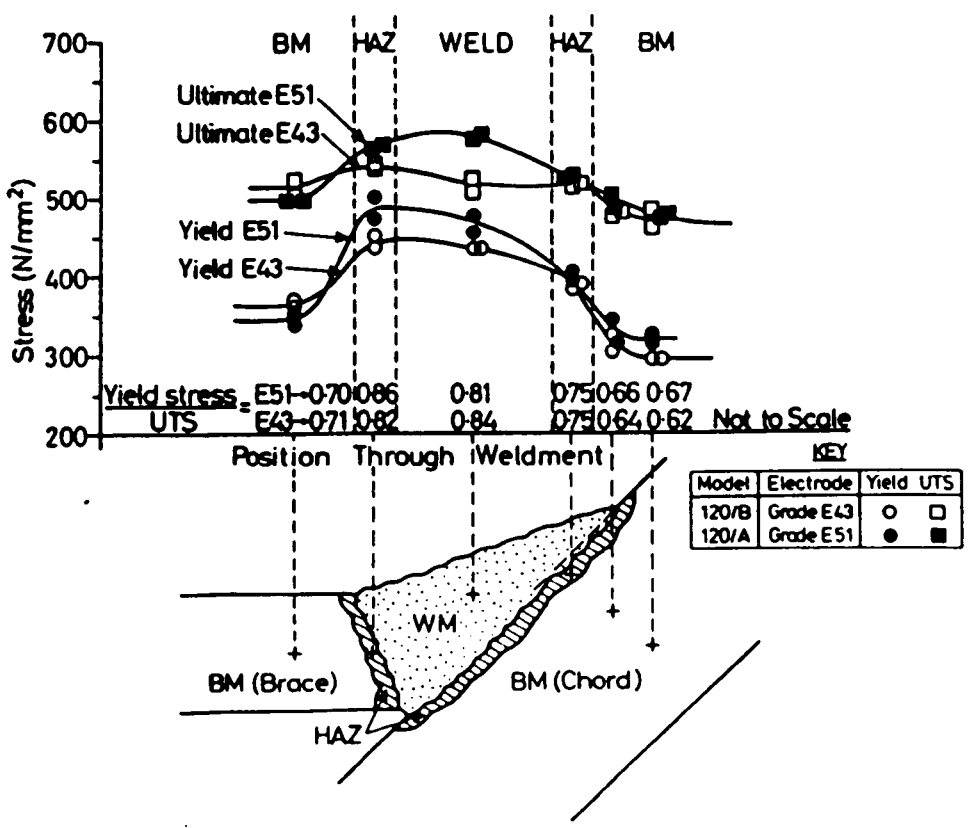


Fig. 4.19 Variation of Ultimate Tensile and Yield Stress in Steel Models

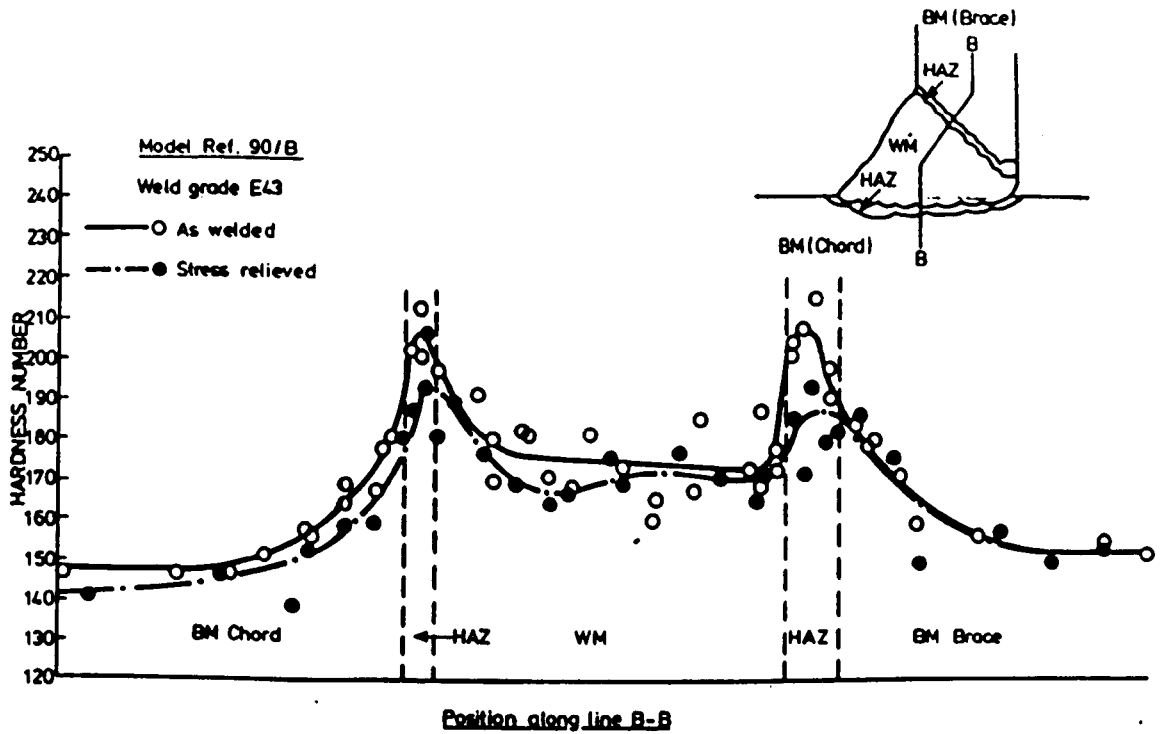


Fig. 4.20 Vickers Hardness Test Results - Ref. 90/B

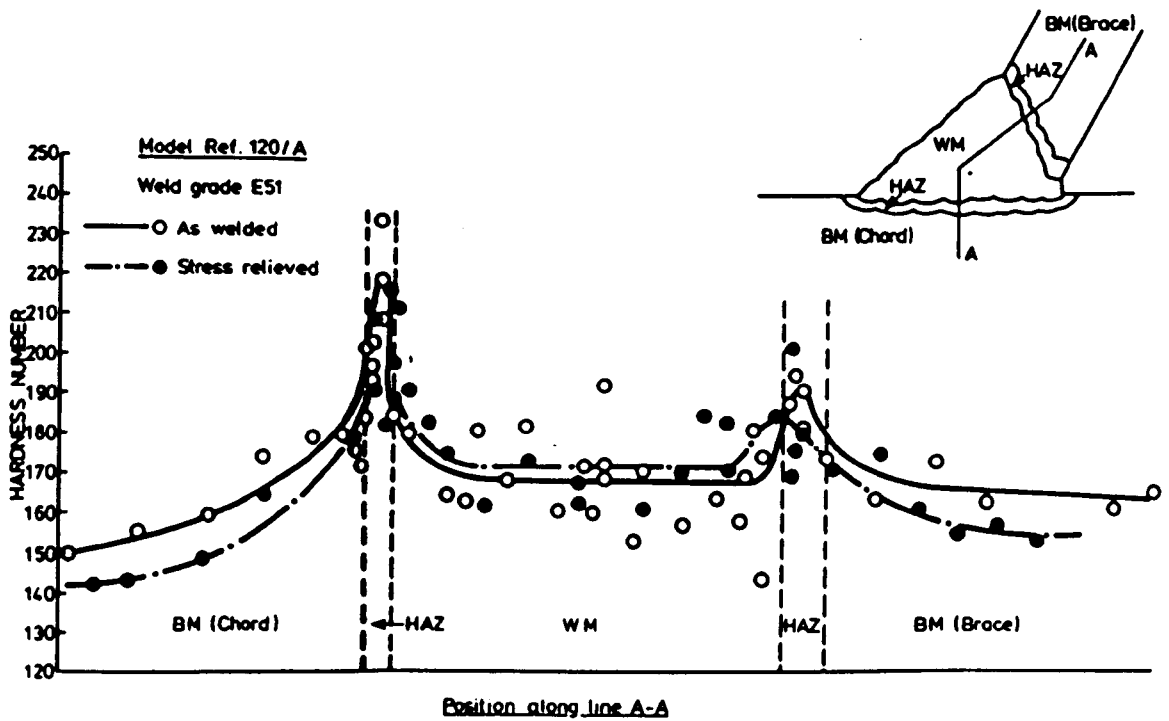


Fig. 4.21 Vickers Hardness Test Results - Ref. 120/A

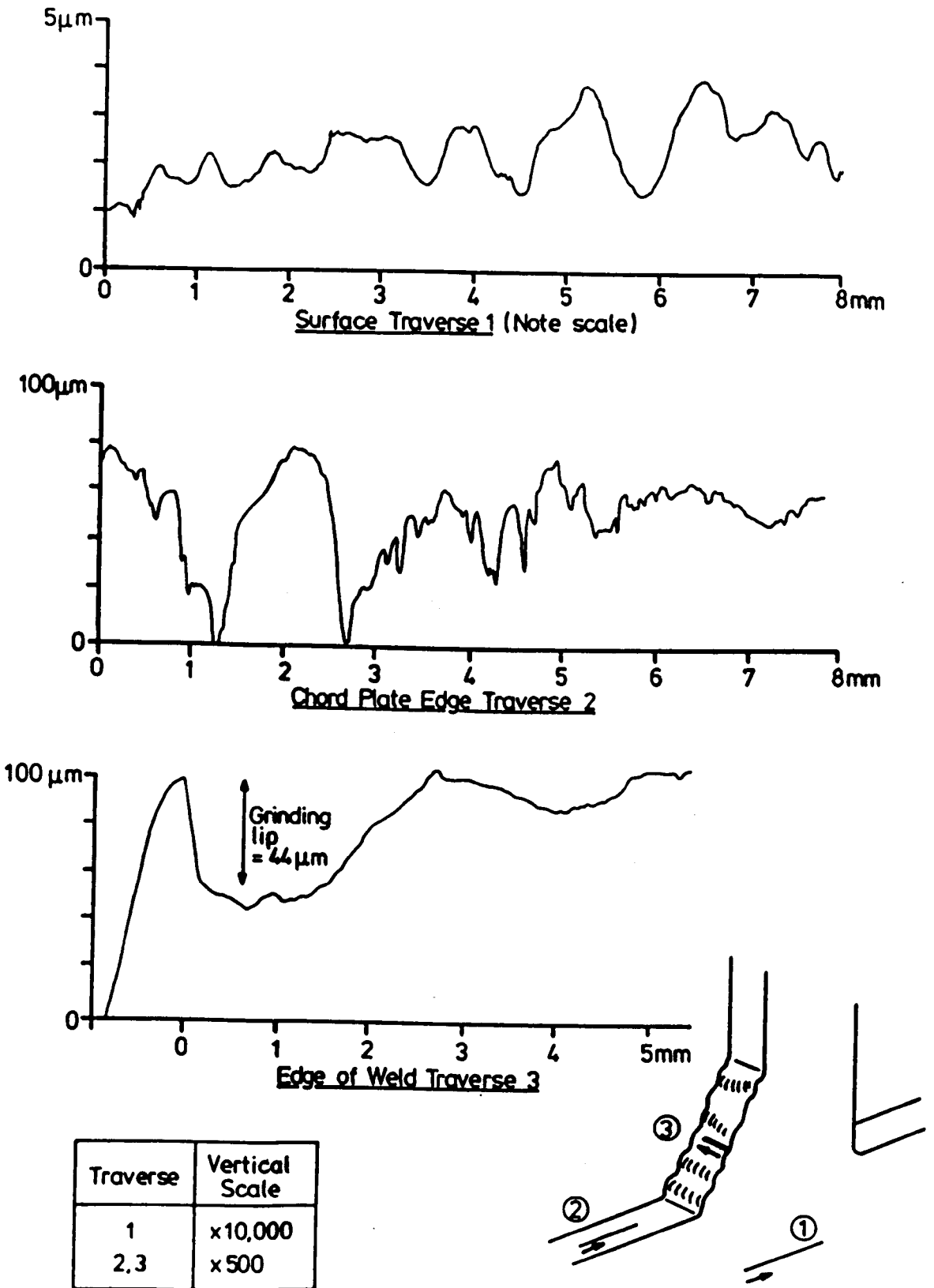
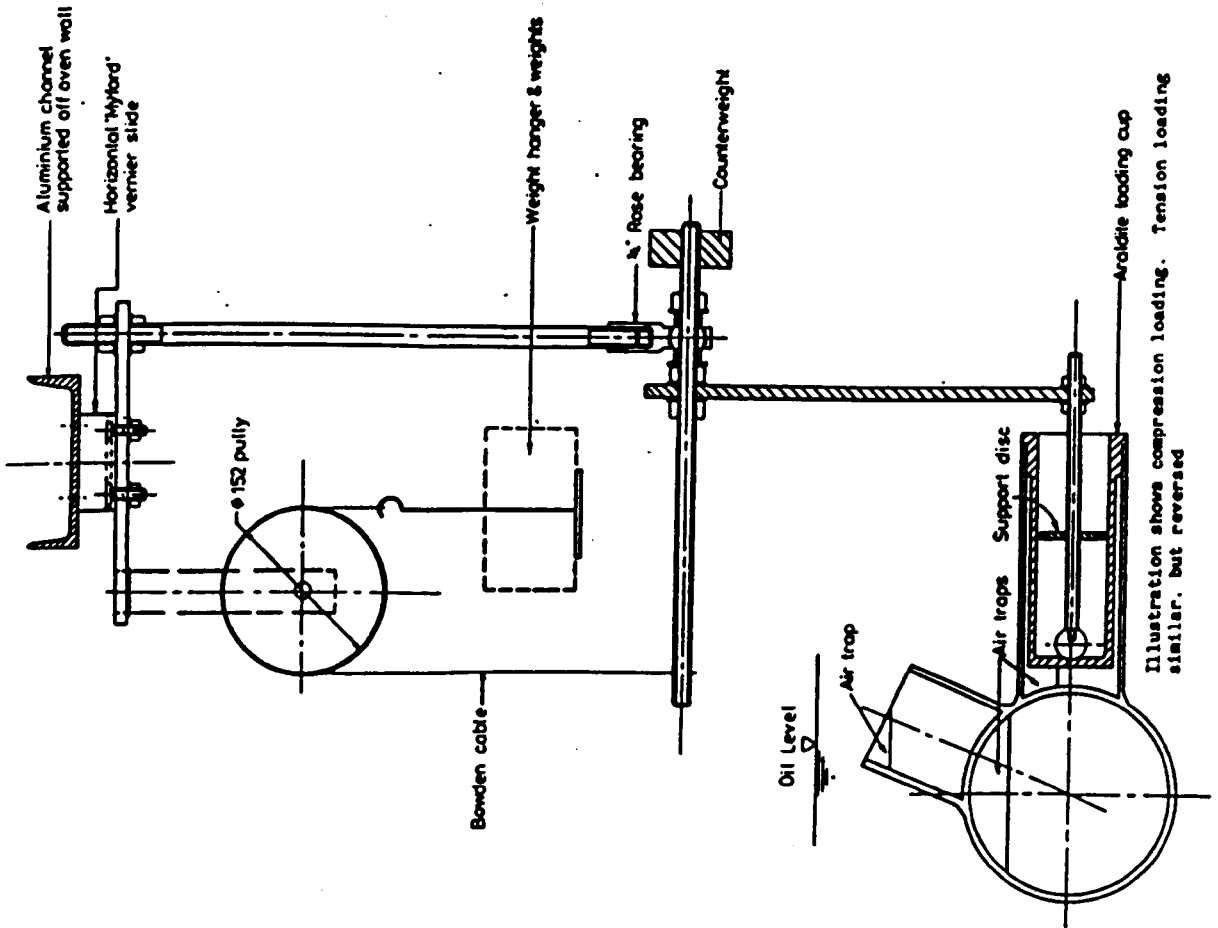
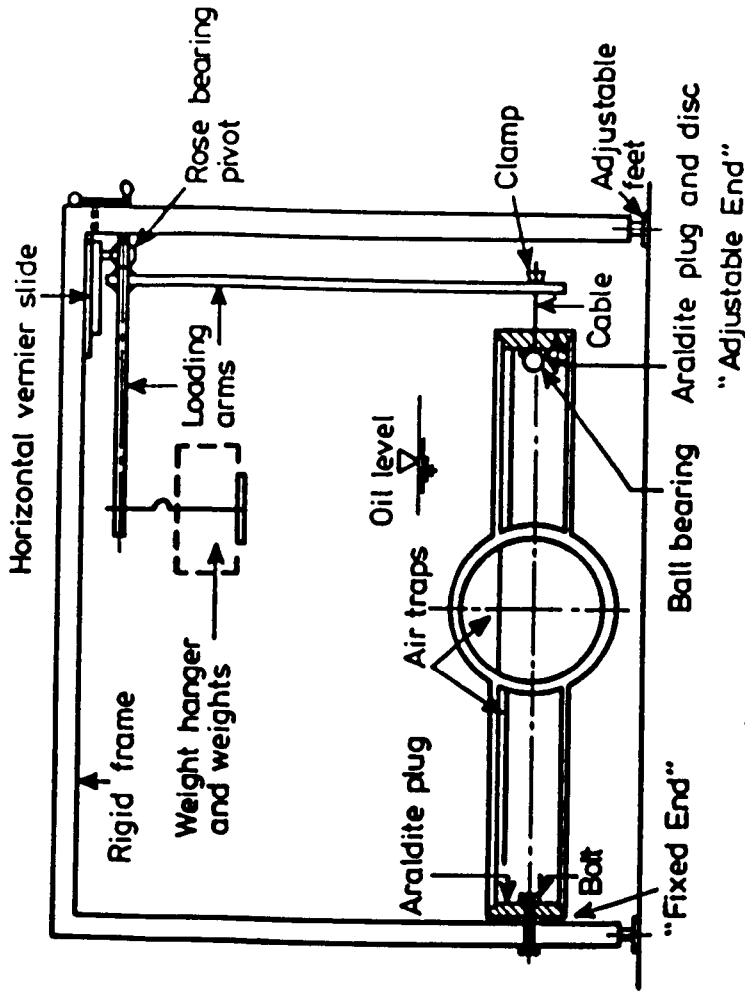


Fig. 4.22 Surface and Edge Roughness in Steel Models



a) CK Models



b) X-Models

Fig. 4.23 3-d Model Loading Rig

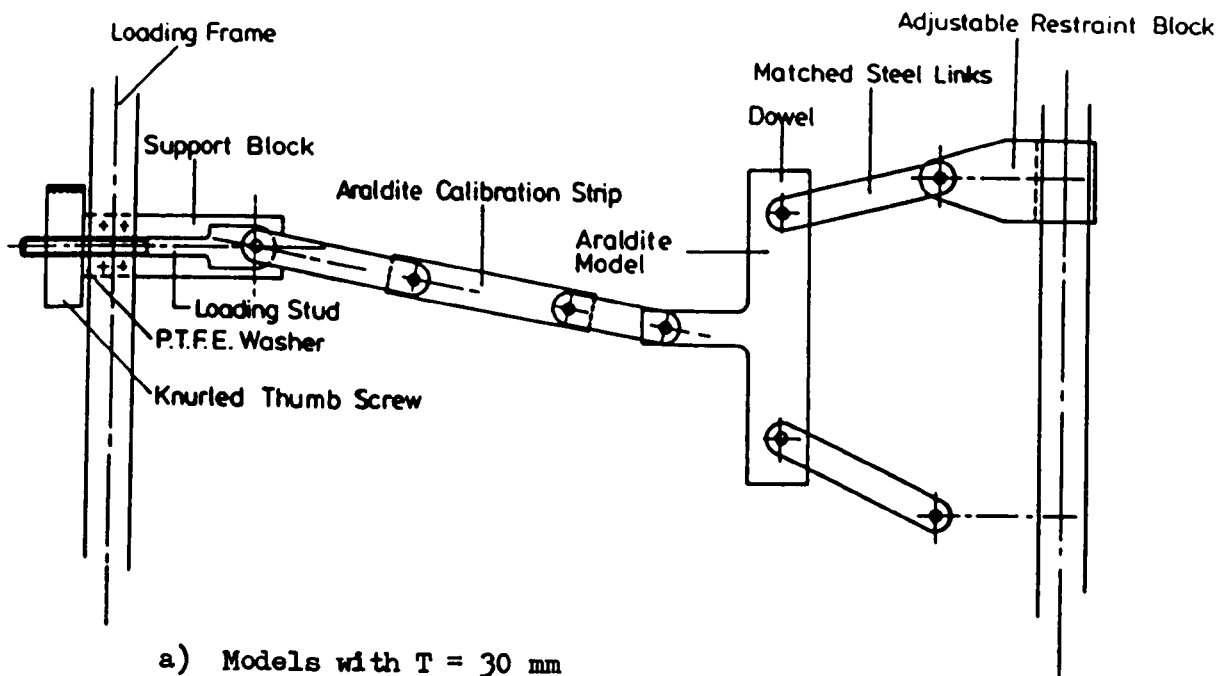
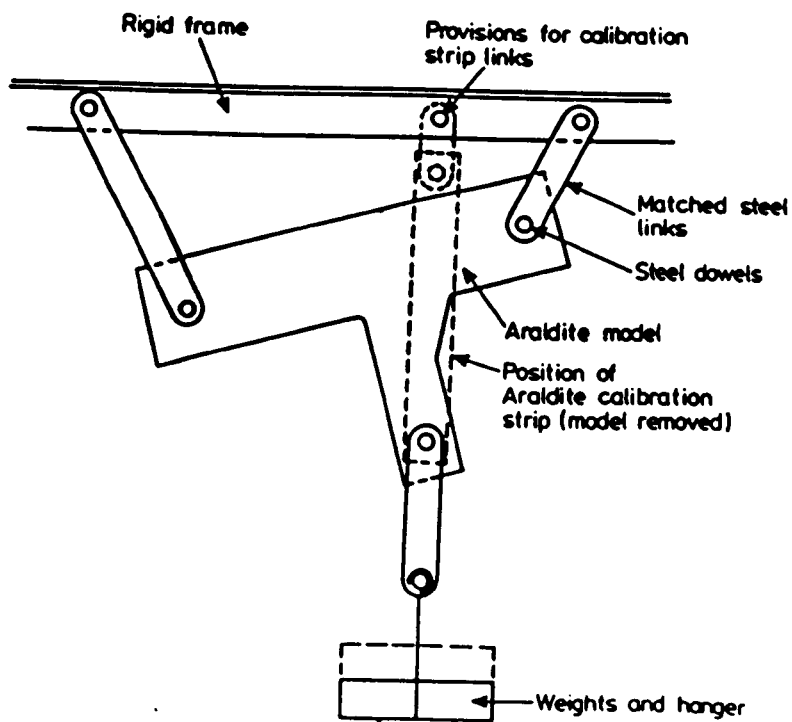


Fig. 4.24 Loading Arrangement for 2-d Photoelastic Models



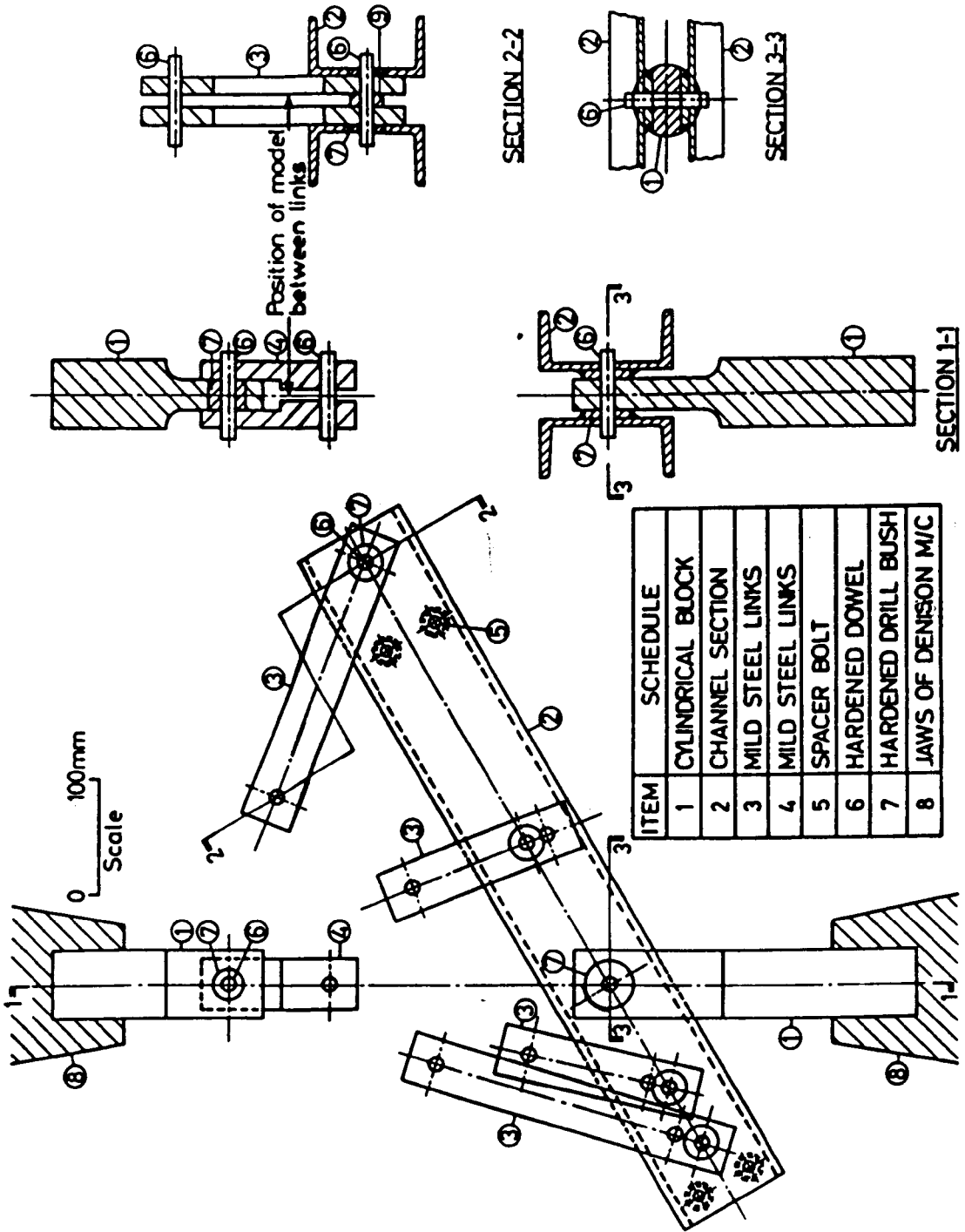


Fig. 4.25 Steel Model Loading Rig for Use in Reflection Techniques

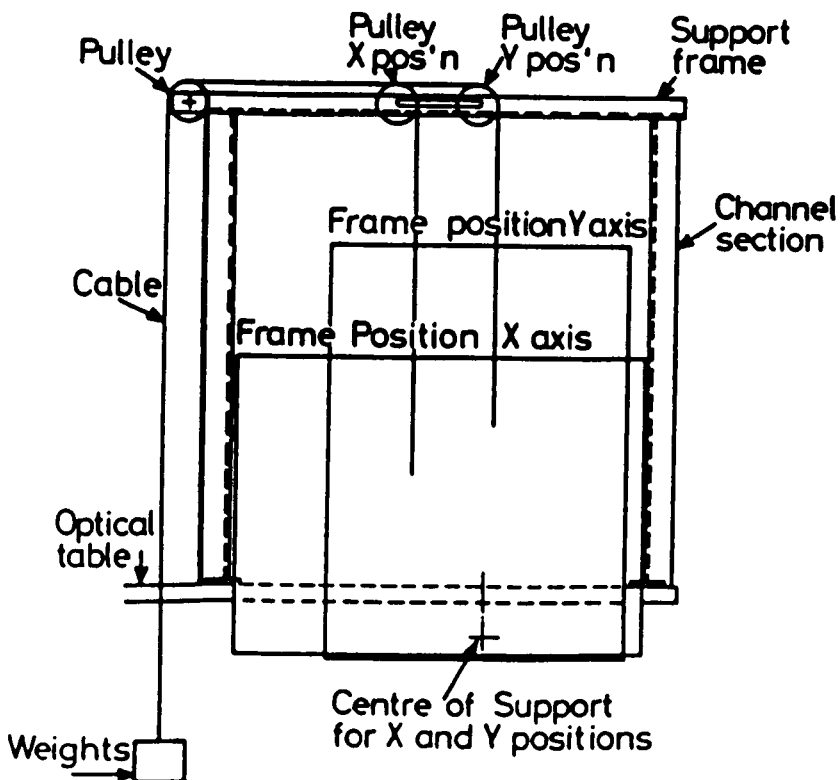
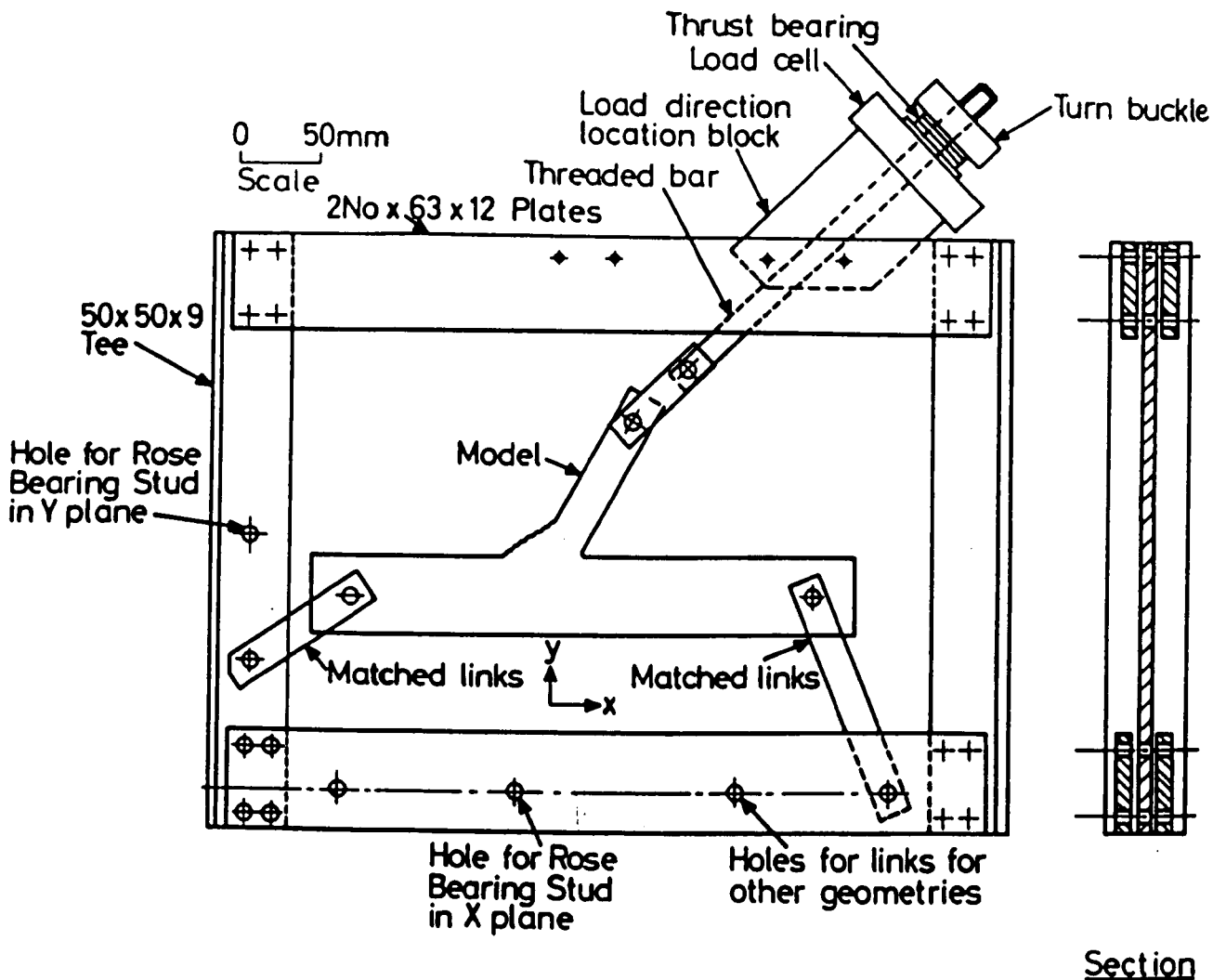


Fig. 4.26 Steel Model Loading Rig Used in Moire Work

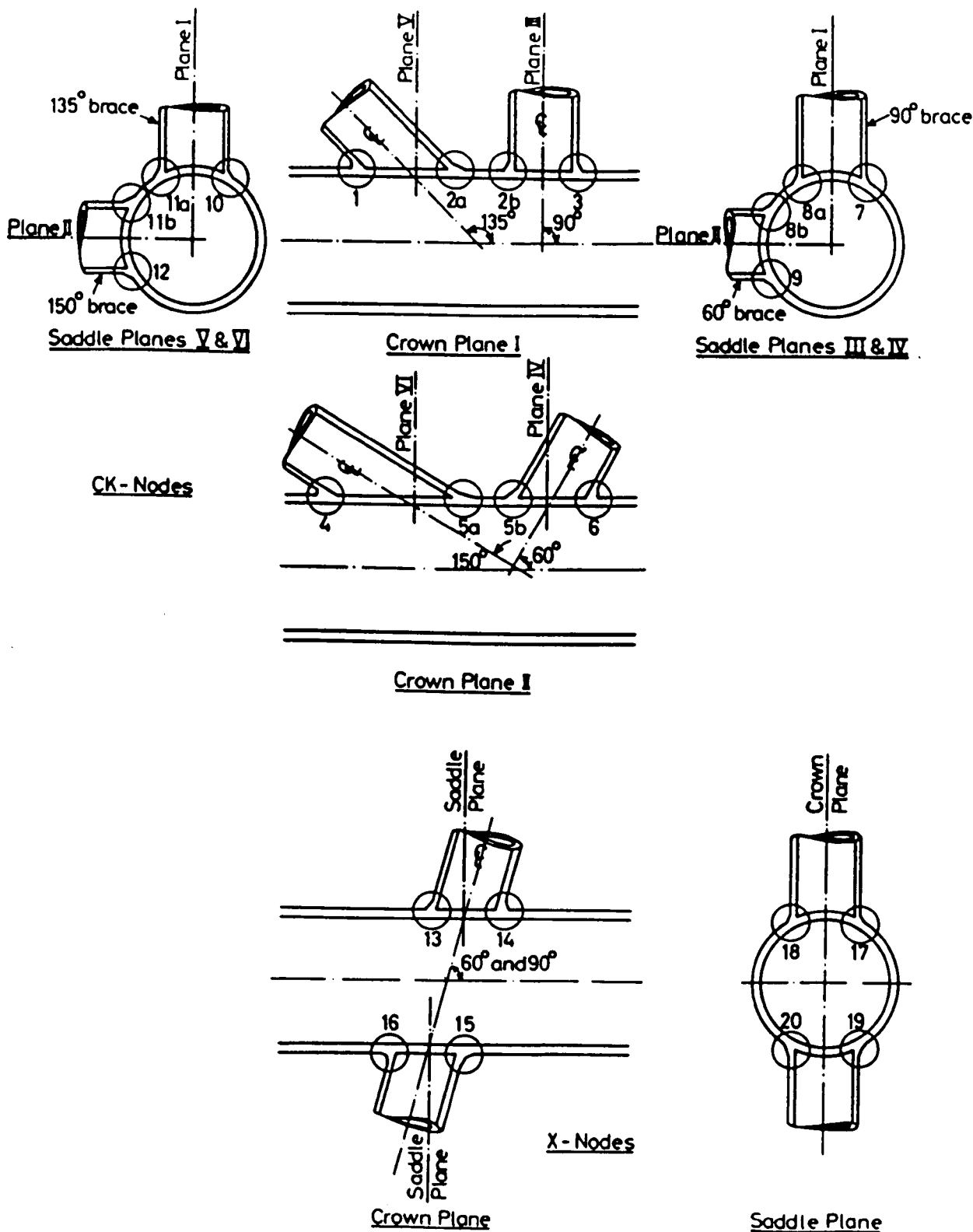


Fig. 4.27 Definitions of Planes and Junctions for Analysis in 3-d Photoelastic Models

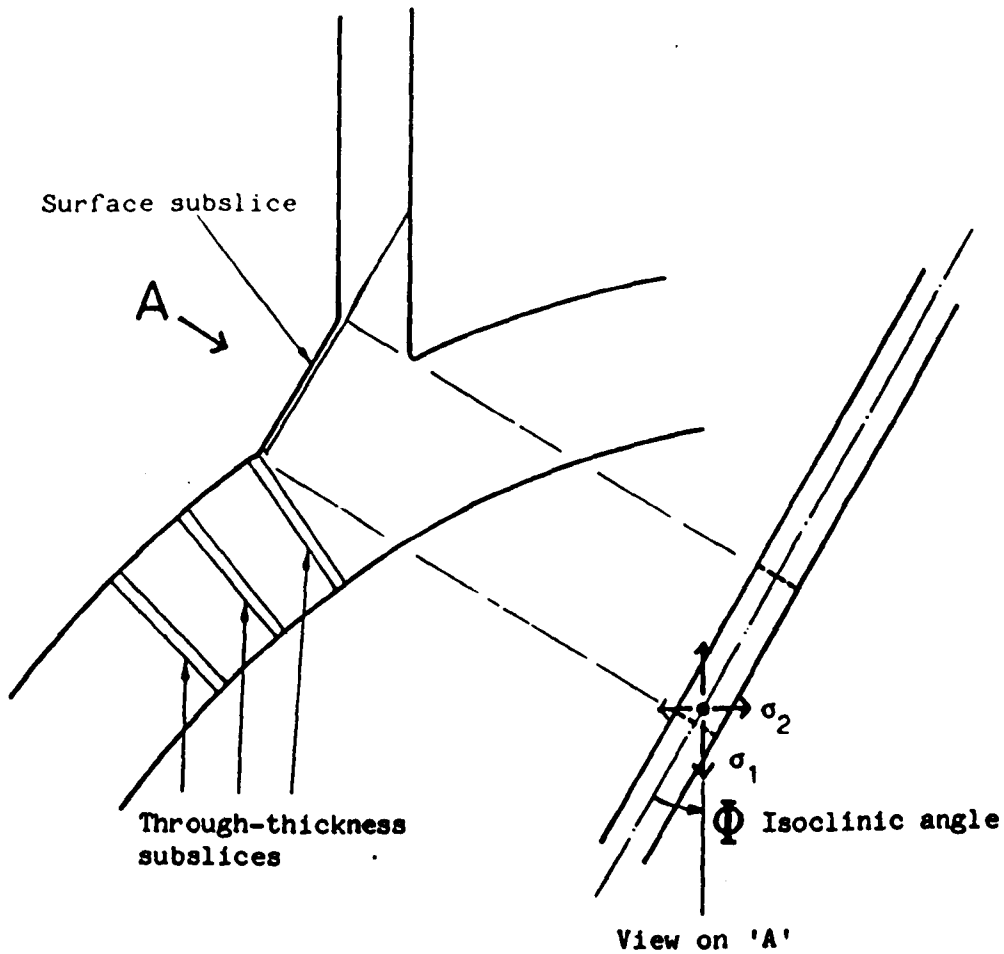


Fig. 4.28a 3-d Model Subslicing Diagram

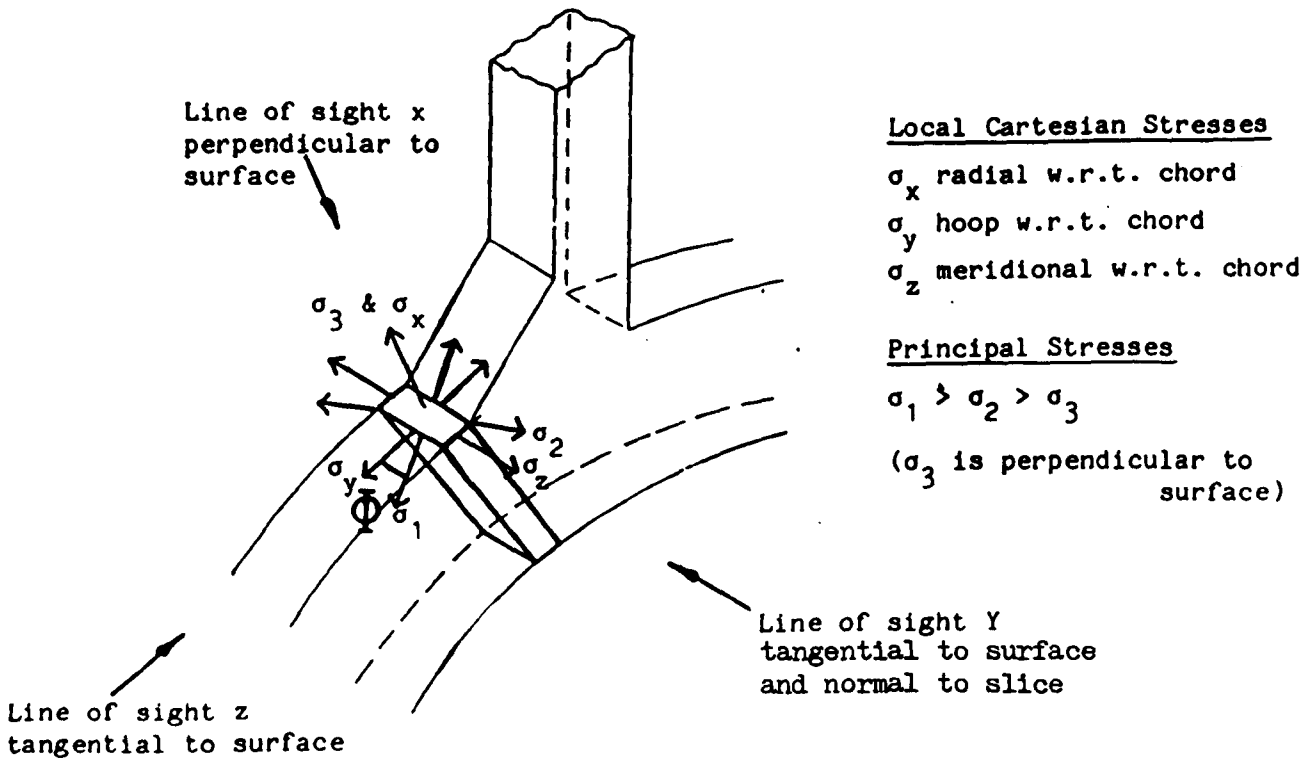


Fig. 4.28b Surface Stresses on a Loaded 3-d Model

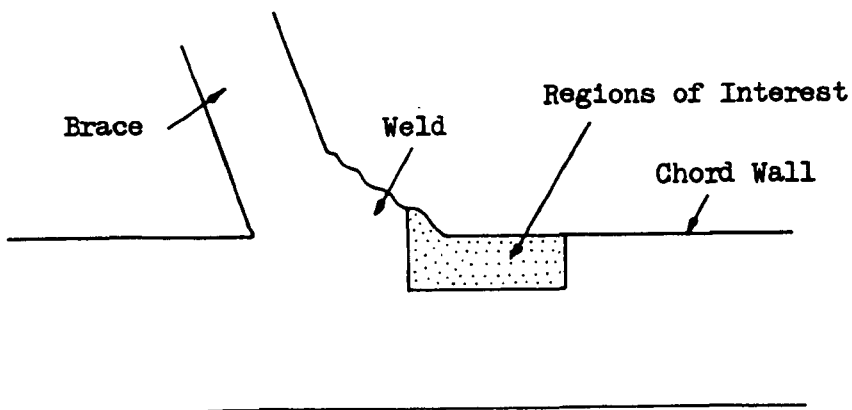
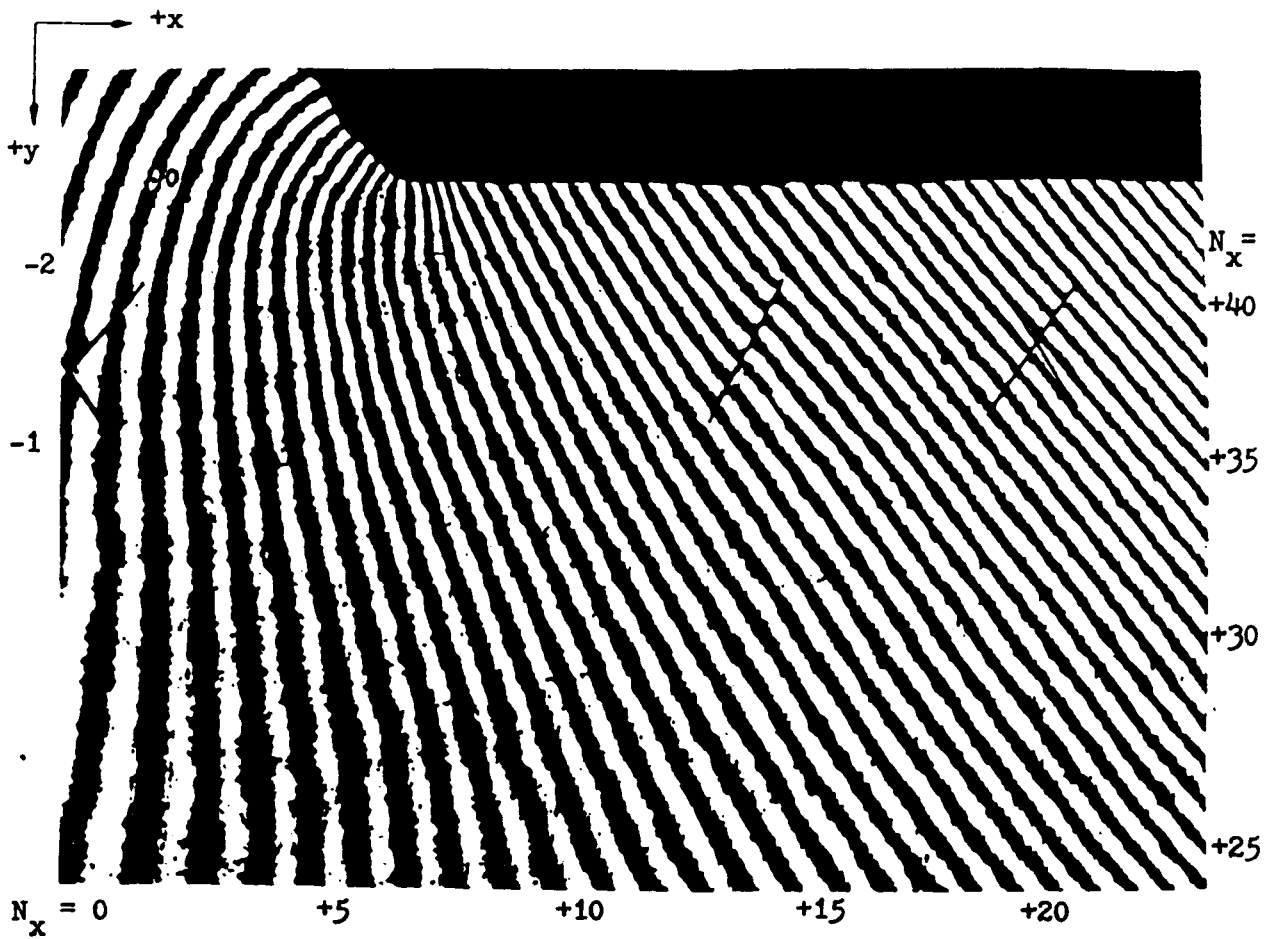


Fig. 4.29 Fringe Order Numbering in u Displacement Field

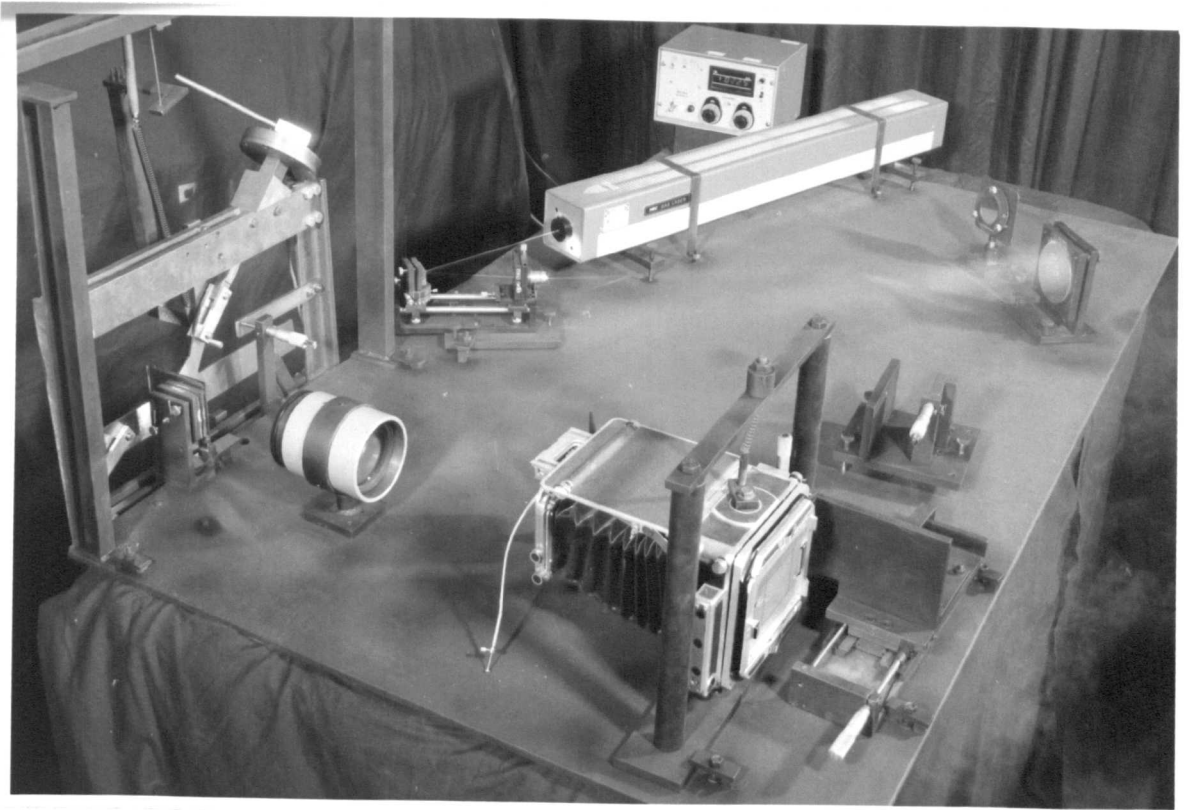


Plate 4.1 Optical Arrangement of Moire Interferometer (also showing a model in loading rig)

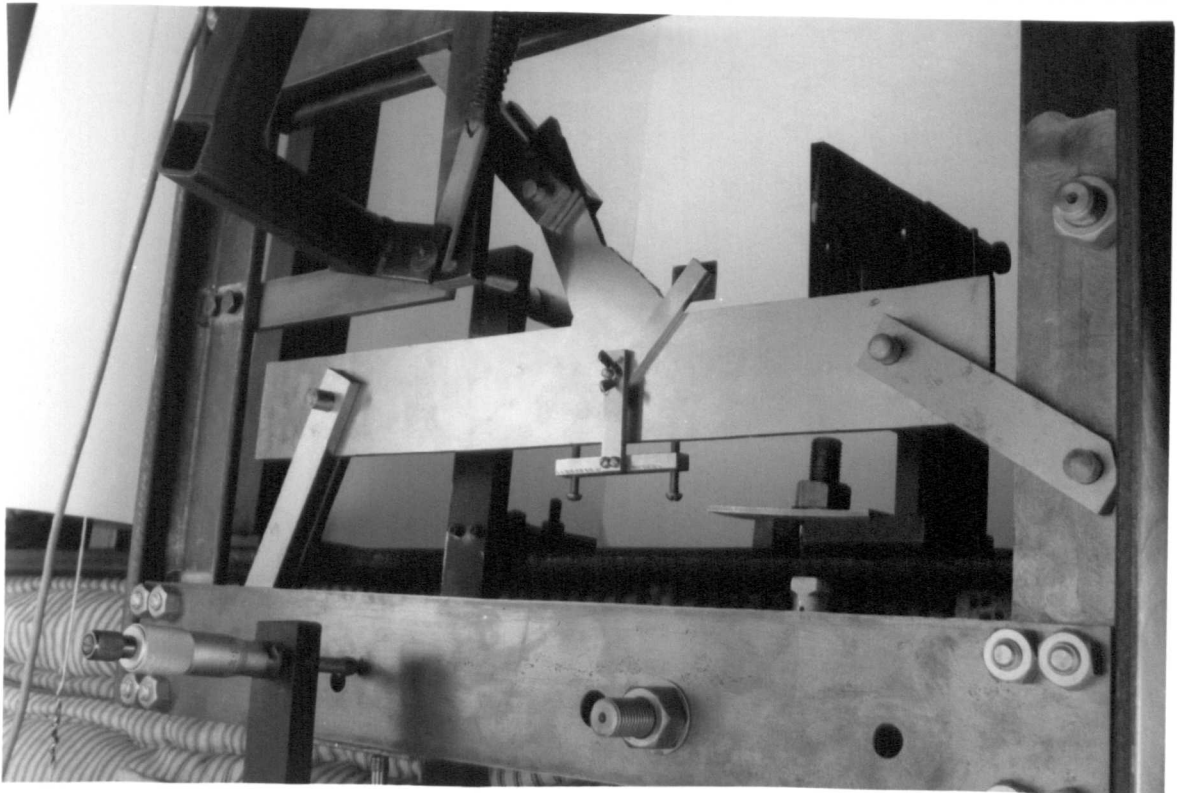


Plate 4.2 Rear View of Model Showing Auxiliary Specimen Grating Bracket

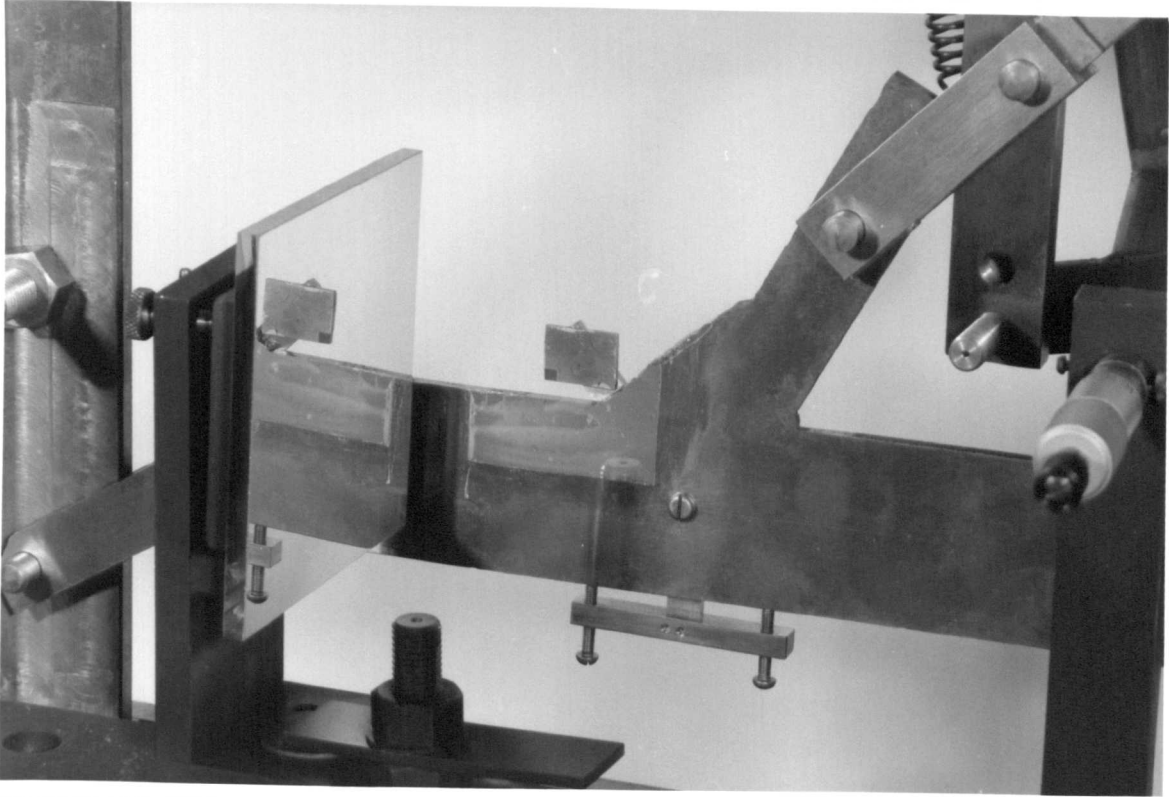


Plate 4.3 Reflective Moiré Grating Attached to Model in Region of Interest.
(Smears in surface of grating do not inhibit clarity of moiré fringes.)

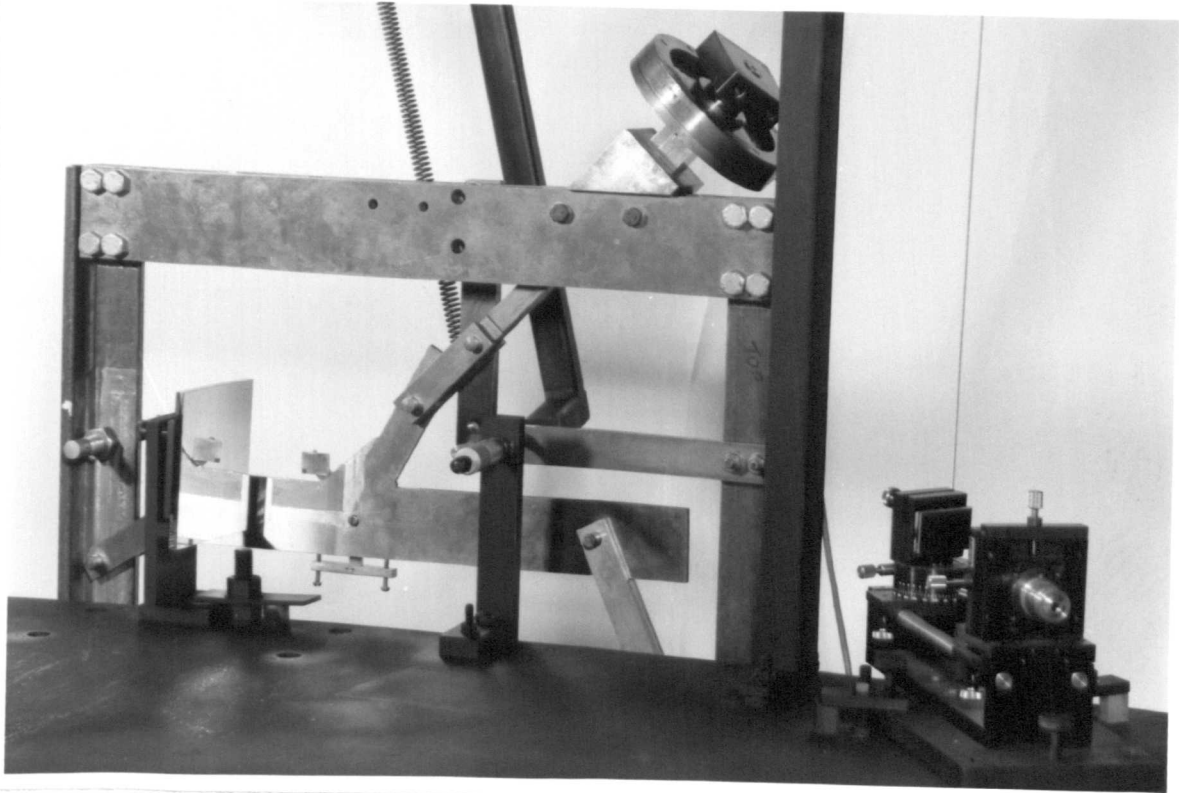


Plate 4.5 Detail of Steel Model Mounted in Loading Rig

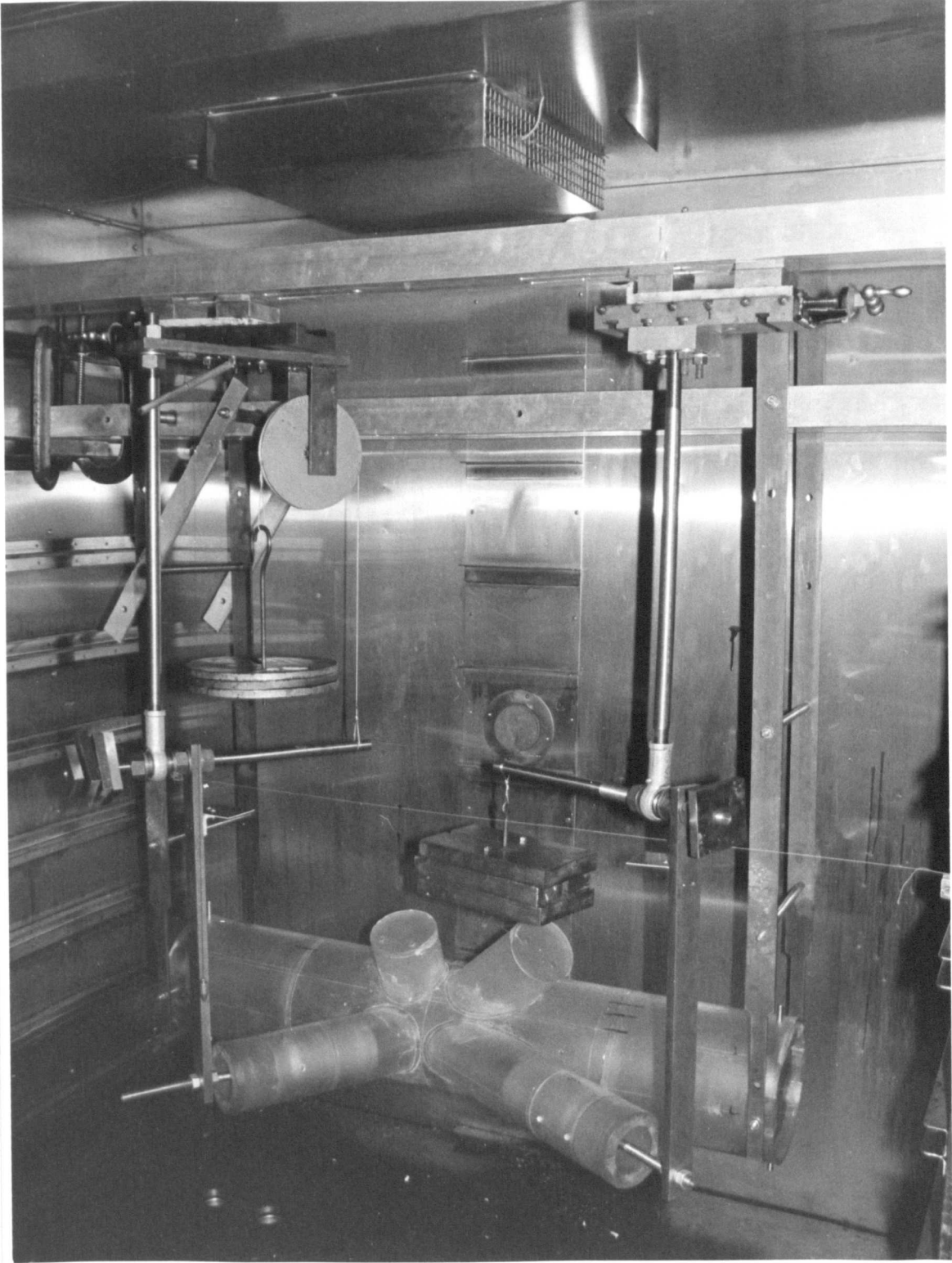


Plate 4.4 Loading Arrangement of 3-d CK Type Photoelastic Model

CHAPTER 5

ANALYSIS OF READINGS

5.1 Determination of Stresses by Photoelasticity

5.1.1 Theory of Photoelasticity

The physical principles and optical theory of photoelasticity are well established. Because the theory of photoelasticity is extensively documented in standard text books (e.g. 62, 68) only the main points relevant to this work will be mentioned.

Many transparent materials, such as Celluloid, Bakelite and certain Epoxy Resins, become optically anisotropic or "birefringent" when stressed. The refractive indices of birefringent materials are different in the planes of the principal stresses and are proportional to the magnitudes of these stresses. On entering the material plane-polarised light (of wavelength λ) is divided into two components in the planes of these stresses. Because of different refractive indices in these planes, the components of light travel at different velocities and emerge with a phase difference relative to each other. The phase difference is $n\lambda$, where n is an integral or fractional number, and is proportional to the difference in the magnitudes of the principal stresses ($\sigma_1 - \sigma_2$) and the thickness of the material t through which the light travels. The basic equation of photoelasticity, known as the "Stress-Optic Law" can be written as

$$n = Ct(\sigma_1 - \sigma_2) \quad \dots (5.1)$$

where C is the stress-optic coefficient.

When the material is viewed in a normal transmission polariscope, under certain conditions light emerging from the analyser is extinguished depending on the value of $n\lambda$ and the directions of the principal stresses. Dark bands, which are either isochromatic or isoclinic fringes are viewed. The isochromatic fringes represent the loci of points where n is an integer. The value of n , called the fringe order, is usually expressed in terms of the material fringe value (MFV) $F = \lambda/C$ as follows:

$$n = (\sigma_1 - \sigma_2)t/F \quad \dots (5.2)$$

The value of f can be determined is a uniaxial tensile calibration test in which $\sigma_2 = 0$. Thus $F = n\sigma/t$.

The isoclinic fringes represent the loci of points on the specimen where the directions of principal stresses are parallel and perpendicular to the plane of polarisation. With preferred orientation of the polariscope, the inclinations ϕ of principal stresses are given.

5.1.2 Positions of Photoelastic Fringe Order Readings in the Models

To obtain the magnitudes and positions of $\hat{\sigma}$ in the models and determine the gradients of stress near to and far from these maxima, continuous surface stress distributions are required. Stresses were measured on the outer and inner wall and fillet surfaces. Stress distributions were plotted from stress indices which were calculated from fringe order readings in the models. The directions of principal stresses acting in the surface of the models were measured directly from the models.

Fringe order readings were taken in the edges of all 3-d models in the planes defined by the chain-dotted lines in Fig. 4.27. Planes I and II are meridional planes (with respect to the chord) and stresses acting parallel to these planes are called "meridional stresses". Planes III to

VI are hoop planes and stresses in these planes are called "hoop stresses". Outside wall surface stresses in a hoop plane are shown in Fig. 4.28 with local co-ordinate nomenclature. Figure 4.28 represents a slice of material cut from a frozen-stress photoelastic model.

Fringe order readings were taken and stresses were calculated in the following positions in all 3-d and 2-d models:-

- 1) In the planes defined in Fig. 4.27, i.e. line of sight Y in Fig. 4.28b. These are meridional stresses at the "crown" positions (which are known by symmetry to be principal planes if the effect of the braces in the other plane is neglected) and cartesian hoop stresses at the "saddle" positions (which are not principal planes for inclined braces).

Readings were also taken in the following positions only in the 3-d corner K models:

- ii) In the direction perpendicular to (i), i.e. line of sight Z in Fig. 4.28b. These are cartesian hoop stresses at the "crown" positions and meridional stresses at the "saddle" positions. They were taken along the outside chord wall approach to the chord weld toes only.
- iii) In the line of sight X in Fig. 4.28b at the saddle positions in the chord wall only. These readings provide the inclinations ϕ of σ_1 to the hoop plane.

Photoelastic readings average through-thickness stresses. Gradients of stress in the direction of sight must therefore be considered. At the chord weld toe in Fig. 4.28b the value of σ_y is true because the variation of stress parallel to the run of the weld is negligible. However in the plane perpendicular to the run of the weld the gradient of σ_z is required to enable extrapolation to the weld toe. This is because the thickness of the subslice (approx. $0.13T$) cannot be neglected. The

selected points for extrapolation purposes in the chord were:

- at the chord weld toe
- commencement of linear σ_y distribution
- $0.2 \sqrt{rt}$ (location of strain gauge given by Irvine (6))
- between $0.2 \sqrt{rt}$ and the following position
- 5° arc at the saddle or $0.4 \sqrt[4]{RTrt}$ at the crown (as Irvine (6))

5.1.3 Determination of Principal Stresses and Strains

In the 3-d models, photoelastic readings in the meridional and hoop planes gave σ_z and σ_y directly. The radial stress σ_x is assumed to be zero. Readings taken normal to the edges in the plane of the slice gave ϕ . The magnitudes of the maximum and minimum principal surface stresses σ_1 and σ_2 are obtained from σ_y , σ_z and ϕ as follows:

$$\sigma_1 = \frac{1}{2} \left[\sigma_y + \sigma_z + \frac{\sigma_y + \sigma_z}{\cos 2\phi} \right] \quad \dots (5.3)$$

$$\sigma_2 = \frac{1}{2} \left[\sigma_y + \sigma_z - \frac{\sigma_y + \sigma_z}{\cos 2\phi} \right] \quad \dots (5.4)$$

Where principal stress distributions involving a number of photoelastic readings are required, it was more convenient to view the outside chord wall surface slice in the radial line of sight X in Fig. 4.28b. Principal stresses may be obtained from $(\sigma_1 - \sigma_2)$, ϕ (surface slice data) and σ_y (hoop slice data) as follows:-

$$\sigma_1 = \sigma_y + \frac{(\sigma_1 - \sigma_2)}{2} (1 - \cos 2\phi) \quad \dots (5.5)$$

$$\sigma_2 = \sigma_1 - (\sigma_1 - \sigma_2) \quad \dots (5.6)$$

The hoop and meridional surface strains ϵ_y and ϵ_z are obtained from the cartesian hoop and meridional stresses σ_y and σ_z by Hooke's Law as

$$\epsilon_y = \frac{1}{E} (\sigma_y - \nu\sigma_z) \quad \dots (5.7)$$

$$\epsilon_z = \frac{1}{E} (\sigma_z - \nu\sigma_y) \quad \dots (5.8)$$

Similarly the maximum and minimum principal surface strains ϵ_1 and ϵ_2 are obtained from σ_1 and σ_2 as

$$\epsilon_1 = \frac{1}{E} (\sigma_1 - \nu\sigma_2) \quad \dots (5.9)$$

$$\epsilon_2 = \frac{1}{E} (\sigma_2 - \nu\sigma_1) \quad \dots (5.10)$$

where E = Young's modulus (see Table 4.11)

ν = Poisson's ratio = 0.5 for stress-frozen Araldite.

In the 2-d models, all surface readings taken at the edges of the walls and fillets are principal stresses σ_1 and strains ϵ_1 because 2-d models represent principal planes in 3-d models.

5.1.4 Normalised Stress and Strain Indices

All stresses (and strains) are presented as stress (or strain) indices. A stress index I is defined as the ratio of the stress at any point in the model σ to the greatest mean axial stress in the braces σ_{nom} . A strain index J is similarly defined as ϵ/ϵ_{nom} .

In the 3-d CK models two co-planar braces were loaded in balanced axial tension and compression. To achieve a balanced loading condition, i.e. brace loads perpendicular to the chord are equal, the brace with the smallest inclination to the chord $(180 - \theta_2) < \theta_1$ (see Fig. 3.1) carries the greatest load. Because the cross-sectional area of the braces are equal, this brace is subject to the greatest mean axial stress. Hence, σ_{nom} is in the $\theta_2 = 135^\circ$ and $\theta_2 = 150^\circ$ braces for models loaded in planes I and II (see Fig. 3.6), respectively. These braces were loaded in tension for convenience. Positive indices represent tensile, and negative indices

compressive stresses (or strains). The mean axial stresses in the compression braces $\theta_1 = 90^\circ$ and $\theta_1 = 60^\circ$ are equal to $-\sigma_{nom} \times \sin \theta_2 / \sin \theta_1$.

The actual magnitudes of σ_{nom} in the braces are not important, the relative magnitudes between two co-planar loaded braces are. These were obtained by taking longitudinal fringe order readings, usually at 45° intervals, in the braces at a distance of at least $1.2d$ from the brace/chord intersection at the crown heel. The results are shown in Fig. 5.1 in which unit fringe order (fringe order/slice thickness) is plotted against circumferential position. The mean value of N_{nom} is proportional to σ_{nom} ($N_{nom} = \sigma_{nom} / MFV$) because MFV is assumed to be constant in each model casting. Stresses in the model were therefore always normalised with respect to the true nominal brace stress, irrespective of its intended magnitude. The relative magnitudes of the actual and intended nominal brace stresses are given in Table 5.1

In the 3-d X models, the braces were loaded in diametrically opposite axial tension. In the X90 model, brace wall thickness was varied giving $\tau = 0.5$ in one brace, and $\tau = 0.35, 0.30$ and 0.25 in the other brace. For the latter, σ_{nom} varied around the circumference of the brace; its magnitude (inversely proportional to τ) was calculated from the loading and the cross-sectional area at each position in the brace based on the local brace wall thickness. In the X60 model, τ and σ_{nom} were constant.

In the 2-d models representing a single plane $90^\circ/45^\circ$ K joint (analysed by Little (16)), stress indices were based on σ_{nom} in the 45° brace. This was taken as compressive so that outside wall surface stresses in the joints at the 90° brace (analysed in this work) were tensile. This enabled tensile loads to be applied to the models.

In the 2-d models representing the X90 saddle position, I was based on σ_{nom} in the 90° braces. Because the wall thickness ratio τ was varied, σ_{nom} was initially used for $\tau = 0.5$ and subsequently modified for other

values of τ , i.e. I (for $\tau \neq 0.5$) = $\sigma/\sigma_{\text{nom}}$ ($0.5/\tau$).

For all models (referring to Fig. 4.28b) hoop and meridional stress indices are $I_h = \sigma_y/\sigma_{\text{nom}}$ and $I_m = \sigma_z/\sigma_{\text{nom}}$, respectively. Principal stress indices are $I_{1,2} = \sigma_{1,2}/\sigma_{\text{nom}}$.

To determine strain indices $J = \epsilon/\epsilon_{\text{nom}}$, the nominal axial strain in a brace $\epsilon_{\text{nom}} = \sigma_{\text{nom}}/E$. However because E and ν are assumed to be constant in a model, hoop and meridional strain indices may be determined from I_h and I_m as follows

$$J_h = I_h - \nu I_m \quad \dots (5.11)$$

$$J_m = I_m - \nu I_h \quad \dots (5.12)$$

5.1.5 Graphical Presentation of Stress and Strain Distributions

Surface stress and strain indices obtained from 3-d models were plotted, along the outside and inside tube walls and weld fillets, in the planes defined in Fig. 4.27. Fig. 5.2 is an example of meridional outside surface stress distributions in the meridional, or crown plane in some of the CK models. The Figure is used to illustrate the features of this method of presentation.

Ordinates of stress indices were plotted perpendicular to the profile of each part of the intersection on scaled drawings of the junction. Surface stresses in tube walls were positioned as multiples of wall thickness S_c/T or S_v/t . Fillet stresses were positioned in terms of the angular position φ in the weld toe fillet arc. The origins of S and φ were at weld toes. Smooth curves were drawn through the ordinates and the resulting distributions were used to define surface stress or strain gradients, regions of linearity and non-linearity, and the magnitudes and positions of $\hat{\sigma}$.

The most convenient manner of presenting surface stress indices obtained from the 2-d models was to project the weld toe fillet profile

(including toe grinding) on a line continuous with the outside tube walls, and plot all values perpendicular to this line. This was to enable the effects of different weld sizes and shapes to be shown. Wall stresses were positioned in terms of S_c/T or S_v/t , and fillet stresses were positioned on the abscissa at $S_\phi = r_c \sin \phi_c/T$ or $r_b \sin \phi_b/t$. The resulting distributions defined linear and non-linear gradients at weld toes, commencement of linear stress regions, weld toe stresses, and the positions and magnitudes of $\hat{\sigma}$.

Through-thickness stress indices were obtained in the chord wall using 2-d finite element models. The variation of I_1 with distance on the inward path which a fatigue crack may take is shown schematically in Fig. 5.3a. The position of I_1 max in the outside weld toe fillet was chosen as the origin 0. Ordinates of I_1 were drawn perpendicular to a line OA which was drawn radial to the weld toe fillet arc. Stresses were always maximum along this radial line for a distance of approximately $0.1T$ in the interior of the model. Although the locus of I_1 max was slightly convex towards the weld toe (OB on Fig. 5.3a) it was convenient to continue the distribution along line OA due to the polar arrangement of the finite element mesh in this region. The distributions were used to identify the different regions, represented schematically on Fig. 5.3b, characterised by either an exponential or linear gradient of I_1 :

5.2 Determination of Elastic and Plastic-Elastic Strains using Reflection Photoelasticity

5.2.1 Theory of Reflection Photoelasticity

Reflection photoelasticity differs from normal transmission photoelasticity in that the strains in a birefringent coating are induced, by the action of in-plane, surface shear, from another specimen which is usually made from an opaque material. A photoelastic coating is bonded

to the model. The surface of the model is polished to reflect polarised light. Light passes (twice) through the coating, or layer, having been reflected on the mirrored surface of the model, and the usual optical principles of photoelasticity apply. Strains are measured as principal strain differences $\epsilon_1 - \epsilon_2$ and are proportional to the fringe order in the layer. The theory is documented by Dally (62). The relevant stress-strain and strain-optic relationships applicable to surface strains measured in this work are as follows.

In a uniaxial tensile test, principal strain difference in the photoelastic layer (subscript L) is

$$\epsilon_1 - \epsilon_2 = \frac{1}{E_L} \left\{ (\sigma_1 - \nu_L \sigma_2) - (\sigma_2 - \nu_L \sigma_1) \right\} = \frac{\sigma_1(1 + \nu_L)}{E_L} \text{ because } \sigma_2 = 0$$

where E_L and ν are Young's modulus and Poisson's ratio of the layer.

The strain-optic relationship is therefore

$$\epsilon_1 - \epsilon_2 = \frac{nf}{t_L} \cdot \frac{(1 + \nu_L)}{E_L} \quad \dots (5.13)$$

where n = fringe order, t_L = thickness of material, and f = MFV.

If the layer is correctly bonded to a model and the edge profiles are identical, maximum shear strains in the model γ_m are equal to those in the layer γ_L . At the interface

$$\gamma_m = \gamma_L = \frac{nf}{2t_L} \cdot \frac{(1 + \nu_L)}{E_L} \quad \dots (5.14)$$

because the light path is $2t_L$.

Thus, $\gamma_m = Cn/t_L$ (where C is a material constant) only if the layer is infinitely thin because only the strains in the surface of the layer, which is directly bonded to the model, are equal to the strains in the model. In regions where the stress-strain relationship is non-linear

and different at every position in the model, the (averaged) photoelastic measurements give strains in the layer that are less than those in the model. The effect is known as shear lag and was measured by Eissa (55) for different thickness of layers. Thus $\gamma_m = CC' n/t_L$ where C' is the shear lag correction factor for the actual value of t_L at each position in the model.

5.2.2 Determination of Maximum Surface Shear Strain Indices

Equation 5.14 was used to convert fringe order readings to maximum shear strains γ_m . These were divided by the mean shear strain in the brace γ_{nom} to give shear strain indices J . Because of the restrictions in the loading apparatus, it was not possible to measure γ_{nom} photoelastically. Thus, γ_{nom} was calculated from loading P , cross-sectional area A of the brace wall, E and ν as follows:

$$\gamma_{nom} = P(1 + \nu)/AE \quad \dots (5.15)$$

$$\text{Thus } J = \gamma_m/\gamma_{nom} \quad \dots (5.16)$$

5.2.3 Distributions of Elastic and Plastic-Elastic Shear Strains

Ordinates of elastic, plastic-elastic, and residual shear strains and strain indices were plotted perpendicularly to enlarged tracings of model profiles near weld toes. In the weld region, a straight base line was drawn tangentially to the weld toe fillet arc because of the irregular weld profile.

The resulting elastic distributions showed the usual features in the near weld toe region - surface strain gradients, and the magnitudes and positions of maximum values. Plastic-elastic distributions showed changes in surface gradients, maximum values and the spread of plasticity.

5.3 Displacements and Strains using Moire Interferometry

5.3.1 Theory of Moire Interferometry

Moire interferometry combines the optical properties of diffraction and interference of coherent, monochromatic light. See Fig. 5.4a. Diffraction is achieved when incident light is diffracted by a highly reflective, furrowed grating. Interference is achieved by the superposition of two such diffracted beams of light. Their wavefronts, being either plane or warped, coexist in space and combine to form bands (or fringes) of constructive and destructive interference. The orientation and spacing of the fringes depends on the directions of the beams emerging from the diffraction grating. The directions β of these beams are prescribed by diffraction equations in terms of the angle of incidence α , the wavelength λ of light, and the frequency of the grating F , i.e. the number of furrows per unit length. It is usual for α and λ to be constant and for F to be known prior to analysis.

If the grating is bonded to a model, deformations and rotations in the model cause changes in the frequency of the grating and the angle β of diffracted light. This causes changes in fringe spacing and inclination (relative to a predetermined set of cartesian axes) which are measured to determine the deformations and rotations.

The theory is documented by Post (56). The important relationships used in this work to measure in-plane displacements are as follows.

A diffraction grating splits a beam of light into several beams which emerged in preferred directions - β_{-1} , β_0 , β_{+1} . . . etc. as shown in Fig. 5.4b. In moire interferometry, reflective gratings are used in which the incident and diffracted beams of light are on the same side of the grating surface. The following 3-d diffraction equations define the components of the directions of diffracted beams;

$$\sin \beta_{mx} = \sin \alpha \cos \phi + m\lambda F \quad \dots (5.16)$$

$$\sin \beta_{my} = \sin \alpha \sin \phi \quad \dots (5.17)$$

where m is the diffraction order

and β_x , β_y , α and ϕ are defined in Fig. 5.4c.

If the angle of in-plane rotation ϕ in the grating is small, the two dimensional grating equations are

$$\sin \beta_{mx} = \sin \alpha + m\lambda F \quad \dots (5.18)$$

$$\beta_{my} = 0 \quad \dots (5.19)$$

In the two-dimensional arrangement illustrated in Fig. 5.4a, two beams of light A and B are incident on the model grating at symmetrical angles $\pm \alpha$. A special condition exists when light from the two beams emerging in the +1 and -1 order of the model grating are parallel to each other and perpendicular to the plane of the grating. Here $\beta_{+1} = 0$ and $\beta_{-1} = 0$ in emerging beams A' and B' respectively.

$$\text{Hence, for } m = +1 \text{ order, } \sin(-\alpha) = -\lambda F, \text{ and} \quad \dots (5.20a)$$

$$\text{for } m = -1 \text{ order, } \sin \alpha = \lambda F \quad \dots (5.20b)$$

This defines the angle of incidence α necessary to establish the condition where two diffracted beams are coincident and their angle of intersection is zero. If the model is subjected to a uniform tensile strain (say ϵ_x perpendicular to the direction of the furrows of the grating) the frequency of the model grating (see Fig. 5.4c) decreases to

$$F' = \frac{F}{1 + \epsilon_x}$$

Light from the first order of beam A emerges from the deformed grating at angle β_{+1} given by equations (5.18) and (5.20a) as follows

$$\sin \beta_{+1} = -\lambda F + \lambda F' = \frac{\lambda F \epsilon_x}{1 + \epsilon_x}$$

$$\beta_{+1} = -\lambda F \epsilon_x \quad \dots (5.21a)$$

Light from the -1 order of beam B emerges at

$$\beta_{-1} = \lambda F \epsilon_x \quad \dots (5.21b)$$

The two beams propagate in space with an angular separation $2\beta_1$ as shown in Fig. 5.4d. Walls of constructive and destructive interference are formed in space. A screen (or photographic plate) inserted in the plane B - B cuts these walls of interference and records light and dark bands appropriate to regions of constructive and destructive interference. The equation of interference defines the relationship between the distance, a , between the fringes (on section B - B), λ and β . From the outlined triangle in Fig. 5.4d

$$\sin \beta = \frac{\lambda/2}{a} \quad \dots (5.22)$$

The frequency of the fringes in the x direction, i.e. inverse of the spacing, is

$$A_x = \frac{2}{\lambda} \sin \beta \quad \dots (5.23)$$

Hence, from equation (5.21)

$$A_x = \frac{2}{\lambda} \cdot \lambda F \epsilon_x = 2F \epsilon_x \quad \dots (5.24)$$

Thus, moire fringe gradient A_x is equal to twice the model grating frequency F and the strain ϵ_x . A relationship also exists between the frequency f of the virtual grating and angle of incidence. Using the nomenclature in Fig. 5.4d with $\alpha = \beta$ and $f = A$, the equation of interference is

$$f = \frac{2}{\lambda} \sin \alpha = 2F \quad \dots (5.25)$$

because $\sin \alpha = \lambda F$ (equation 5.20)

Thus, the fundamental relationship between moire fringe gradient A and the strain ϵ in a prescribed direction is

$$A_{ij} = f\epsilon_{ij} \quad \dots (5.26)$$

where i is the orientation of the virtual and model gratings, and j is the component of strain parallel ($i = j$) and perpendicular ($i \neq j$) to the direction of i .

5.3.2 Positions of Fringe Gradient Measurements

Moire fringes represent contours of equal displacement and fringe gradients are proportional to strain. To deduce fringe gradients, a consistent sign convention was adopted in counting the fringes as shown in Fig. 4.29. A point in the weld region, 0 in Fig. 4.29, was arbitrarily chosen as datum. The dark fringe passing through this point was assigned zero order. This position, in the weld region, was chosen as datum because observations of fringe patterns at different load magnitudes showed minimal deformation in this region. Fringes were assigned increasing order, abiding by the rules given in Section 4.6.5, in the positive x direction.

Fringe gradients were measured, in two orthogonal directions parallel and perpendicular to the model gratings, on the lines defined in Fig. 5.5 as follows:-

- i) A-A'. The most important strains occur near to the weld toe in the outside surface of the chord wall. Principal strains measured in the edge of the model were used to determine surface strain gradients. Measurements were continued along the HAZ/weld metal boundary to determine the effects of the stronger HAZ.
- ii) B-B', C-C' and D-D'. Sub-surface lines were drawn parallel to the outside surface of the chord wall at various depths. Convenient values for $y/T = 0.04, 0.08$ and 0.16 . Measurements

made on these lines showed the positions of maximum plastic-elastic strains at different depths in the chord.

iii) E-E'. The positions of the maxima found in (ii) above gave the directions and positions of through-thickness lines of analysis in the chord wall.

5.3.3 Determination of Strains from Moire Fringe Patterns

Field fringe patterns N_x and N_y in the models represent the components of in-plane displacements in the x and y directions, respectively. Examples of these, obtained from one of the models, are given in Appendix 2. Derivatives of displacements are required to calculate strains. From equation 5.26

$$\epsilon_{ij} = \frac{1}{f} \frac{\Delta N_i}{\Delta_j}$$

However field fringe patterns, as used in this work, included carrier patterns of extension. These are patterns of uniformly spaced fringes that modify fringe gradients A_{xx} and A_{yy} (in separate x and y planes) by a constant amount. The artificial strains introduced in the models were measured in the auxiliary grating. These are given by

$$\epsilon_{xx}^{aux} = 1/f \cdot (\Delta N_x / \Delta x)^{aux}$$

$$\epsilon_{yy}^{aux} = 1/f \cdot (\Delta N_y / \Delta y)^{aux}$$

where subscript aux refers to measurements made in the auxiliary grating. Because these strains were subtracted from field strains to give true model strains, the value of ϵ^{aux} was arbitrary. The method of dealing with auxiliary fringe gradients is illustrated in Fig. 5.6. Two different carrier patterns of extension, i.e. pure rotation of the plane mirror parallel with the lines of the virtual reference grating, were added to

the same field fringe pattern. Fig. 5.6 shows the net result on model strains was independent of the magnitude of fringe gradients in the carrier pattern.

Using graphical methods, point by point measurement of fringe gradients were made by plotting fringe order against distance x or y , along the lines of interest. N_x fringe patterns gave the direct strains $\epsilon_{xx} = 1/f \cdot \Delta N_x / \Delta x$, and a component of the shear strain $\epsilon_{xy} = 1/f \cdot \Delta N_x / \Delta y$. N_y fringe patterns gave direct strain $\epsilon_{yy} = 1/f \cdot \Delta N_y / \Delta y$ and the other component of the shear strain $\epsilon_{yx} = 1/f \cdot \Delta N_y / \Delta x$. Total shear strain $\gamma_{xy} = \epsilon_{xy} + \epsilon_{yx}$. The procedure is illustrated in Fig. 5.7.

Strain Indices

Direct and shear strains are presented in terms of strain indices, i.e. multiples of the mean axial direct strain in the local brace wall, ϵ_{nom} . Because ϵ_{nom} could not be obtained using moire methods, it was determined from the load P , cross sectional area A , and E ; i.e.

$$\epsilon_{nom} = P/AE. \text{ Strains were measured at several values of } \epsilon_{nom}.$$

Elastic and plastic-elastic strain indices were obtained by dividing the incremental increase in strain $\Delta\epsilon$ by the increase in nominal brace strain $\Delta\epsilon_{nom}$; $J = \Delta\epsilon / \Delta\epsilon_{nom}$.

5.3.4 Sign Convention for Strains

A consistent sign convention was adopted for the strains ϵ_{xx} , ϵ_{xy} , ϵ_{yy} and ϵ_{yx} , and for the addition $\gamma_{xy} = \epsilon_{xy} + \epsilon_{yx}$. Referring to Fig. 4.29, N_x fringes were assigned increasing order in the $+x$ direction. The sign convention for the strains is as follows

$$+ve \ \epsilon_{xx} = \text{increase in } N_x \text{ fringe order in } +x \text{ direction} = \text{tension}$$

$$+ve \ \epsilon_{xy} = \text{ditto in } +y \text{ direction} = \text{clockwise rotation}$$

N_y fringes were also assigned increasing order in the $+x$ direction.

The strains appropriate to N_y fringe patterns are

+ve ϵ_{yy} = increase in N_y fringe order in +y direction = tension

+ve ϵ_{yx} = ditto in +x direction = anti-clockwise rotation.

ϵ_{yy} was shown to be consistent with the elastic strains in the surface of the chord wall where $\epsilon_{yy} =$ (approximately) $-\epsilon_{xx}$ because $\sigma_2 = 0$. ϵ_{yx} was shown to be consistent with the loading conditions. The change in the direction of rotation in ϵ_{yx} relative to ϵ_{xy} for the same fringe assignment is because of the change in the orientation of the model grating by 90° .

The sign convention for γ_{xy} is given by the addition of the component shear strains ϵ_{xy} and ϵ_{yx} . Positive values of γ_{xy} represents closing shear strain (negative values representing opening shear strain) in the corner of the element at the cartesian origin (see Fig. 5.7). In the calculation for γ_{xy} , rigid body rotations are eliminated because they introduce extraneous fringe gradients $\Delta N_x/\Delta y$ and $\Delta N_y/\Delta x$ of equal magnitude and opposite sign.

5.3.5 Distributions of Elastic and Plastic-Elastic Strains and Strain Indices

To show the variations in model and weld geometry, and the effects of post-weld heat treatment, distributions of surface, sub-surface and through-thickness strains were drawn. Surface values (line A-A' in Fig. 5.5) were presented in terms of

- i) elastic principal strain indices $J_1 = \epsilon_1/\epsilon_{nom}$, $J_2 = \epsilon_2/\epsilon_{nom}$
- ii) plastic-elastic ditto
- iii) inclinations ϕ of J_1 to axis of chord wall
- iv) plastic-elastic principal strains ϵ_1, ϵ_2
- v) residual principal strains $\epsilon_1^r, \epsilon_2^r$
- vi) principal strains during unloading $\epsilon_1 - \epsilon_1^r$, and
- vii) principal elastic response strains ϵ_1^e calculated for the same unloading cycle in vi)

The through-thickness results (line E-E') were presented in terms of i) ii) and iii) only.

Because of the large amount of computational time in obtaining principal strains, sub-surface results (lines B-B', C-C' and D-D') were restricted to maximum cartesian strain indices, i.e. $J_{xx} = \epsilon_{xx}/\epsilon_{nom}$.

All values were plotted against fractions of the chord wall thickness, i.e. x/T in the surface and sub-surface directions and y/T in the through-thickness direction. All origins were at chord weld toes.

Because the magnitudes of plastic-elastic strains are dependent on load (elastic values are not) the results are qualified in terms of the yield strain in the brace, ϵ_y , obtained in uniaxial tensile tests using $E = 205 \text{ kN/mm}^2$. The mean axial strain in the brace, ϵ_{nom} , was expressed as a fraction of ϵ_y .

Table 5.1

Nominal Fringe Order Magnitudes in Loaded Braces in 3-d CK Models

3-d Model Ref.	Average fringe order in tension brace		Average fringe order in compression brace		Ratio = $N_{nom(c)}/N_{nom(t)}$		
	$N_{nom(t)}$	s.d.	$N_{nom(c)}$	s.d.	Actual Values	Design Values	Difference
	f/mm	%	f/mm	%			%
CK1	0.252	4.0	0.351	3.5	0.718	0.707	+1.5
CK2	0.188	4.4	0.329	2.9	0.571	0.577	-1.0
CK3	0.262	4.3	0.372	2.8	0.704	0.707	-0.4
CK4	0.211	11.5	0.359	5.1	0.588	0.577	+1.9

s.d. = standard deviation as percentage of N_{nom} .

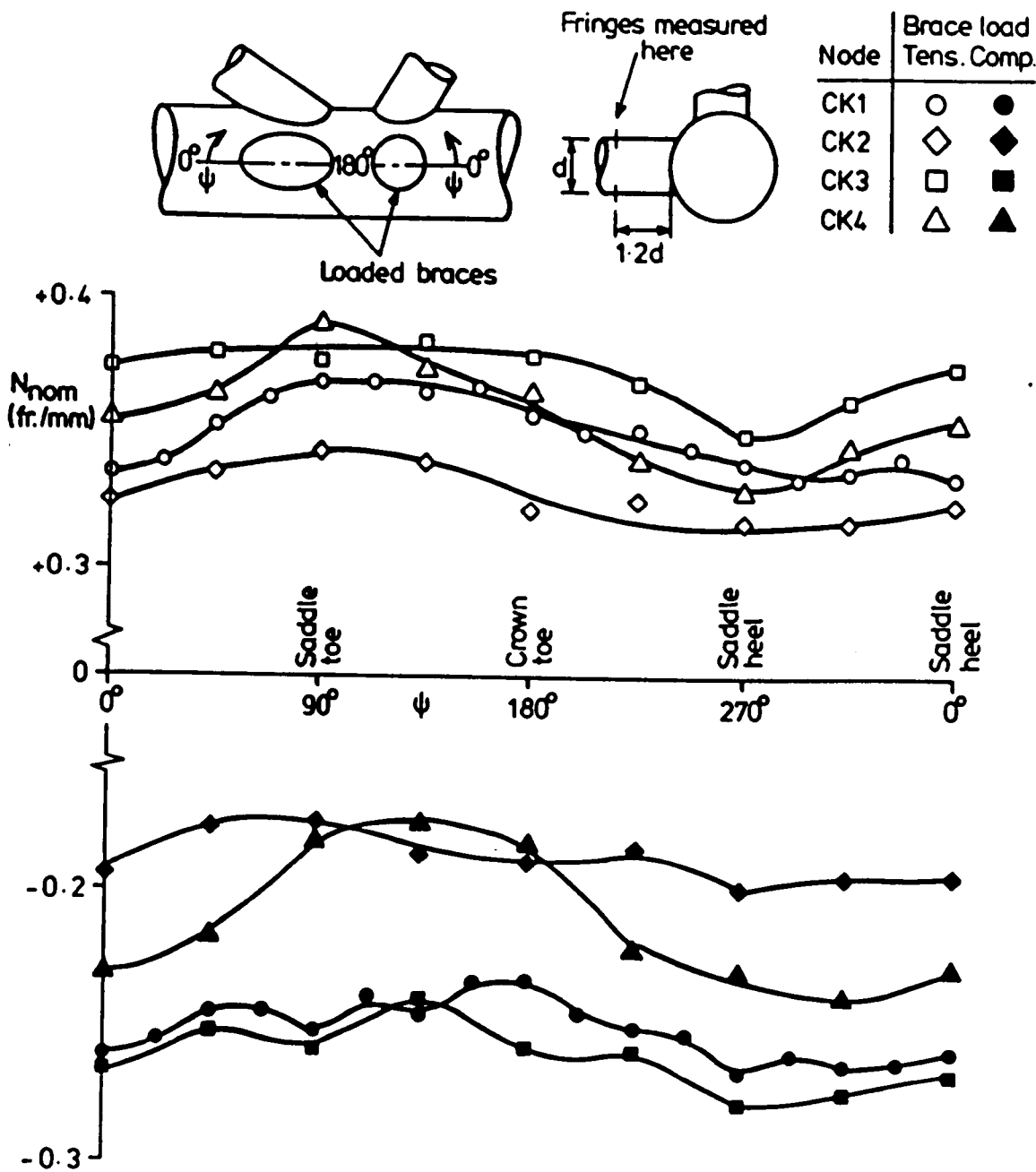


Fig. 5.1 Variation in Nominal Brace Fringe Order in Some CK Models

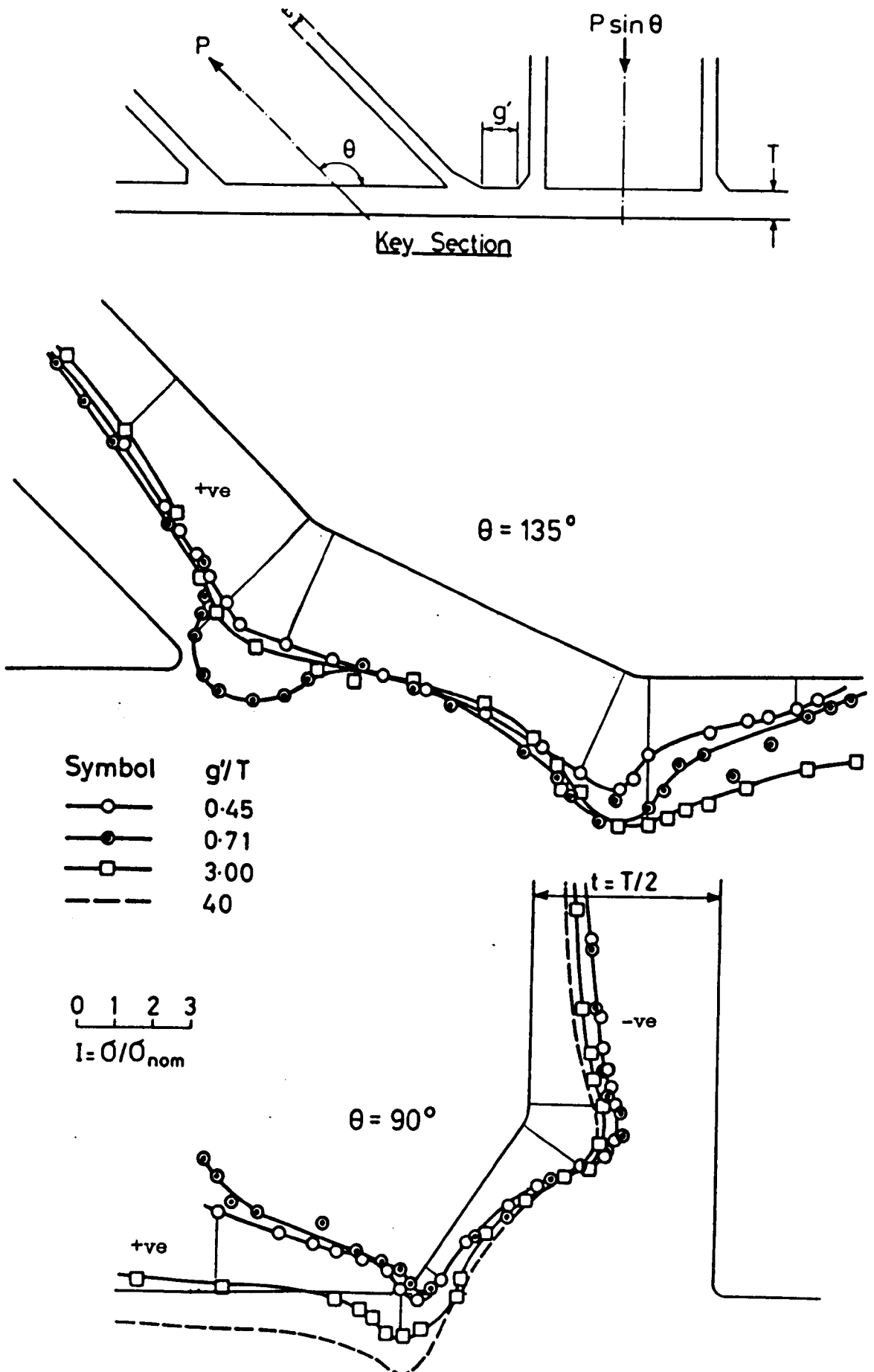
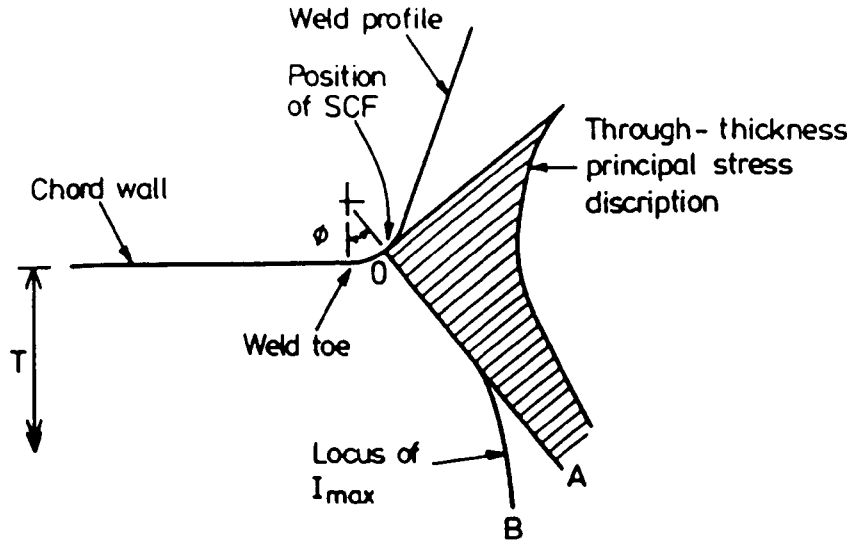
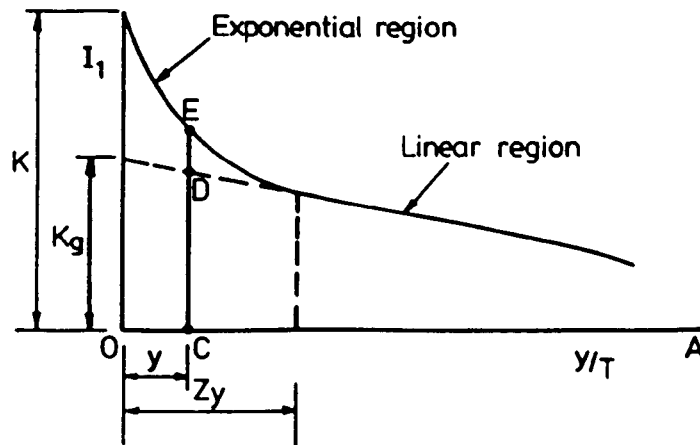


Fig. 5.2 Example of Meridional Surface Stress Index Distributions in Crown Plane I of CK Models



a)



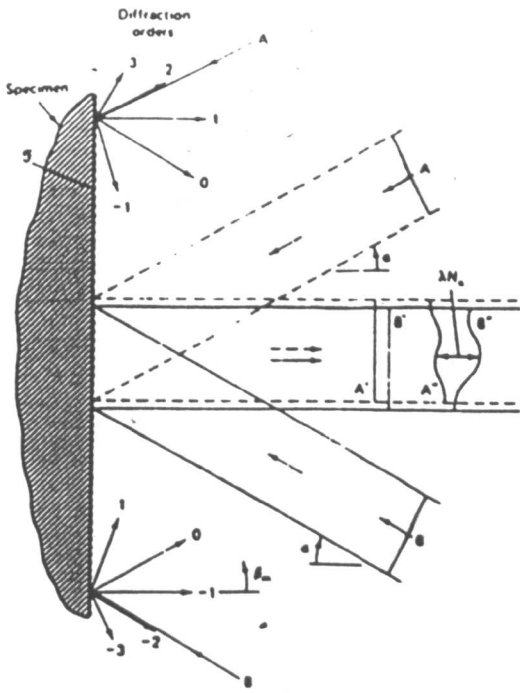
$$I_1 = CE$$

$$I_g = CD$$

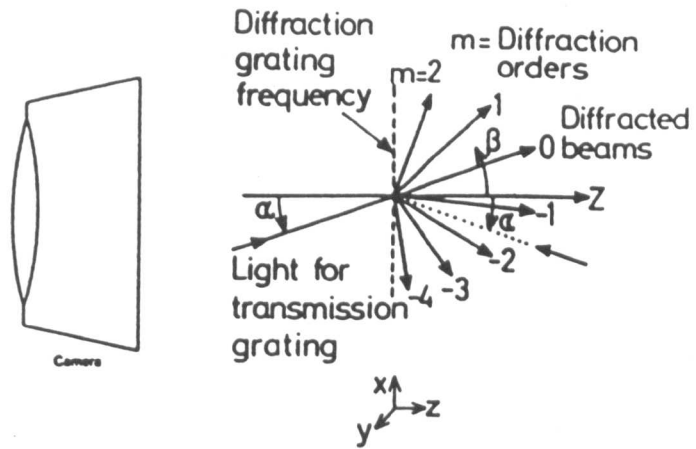
$$I_n = I_1 / I_g = CE / CD$$

b)

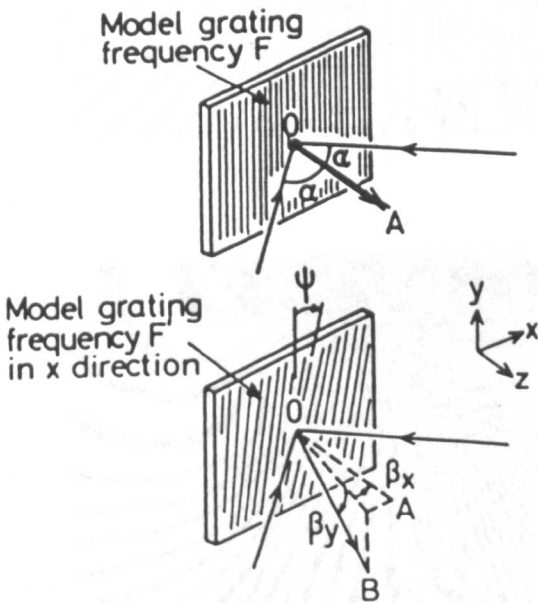
Fig. 5.3 Definitions of Through-thickness Principal Stress Distributions in Chord Walls



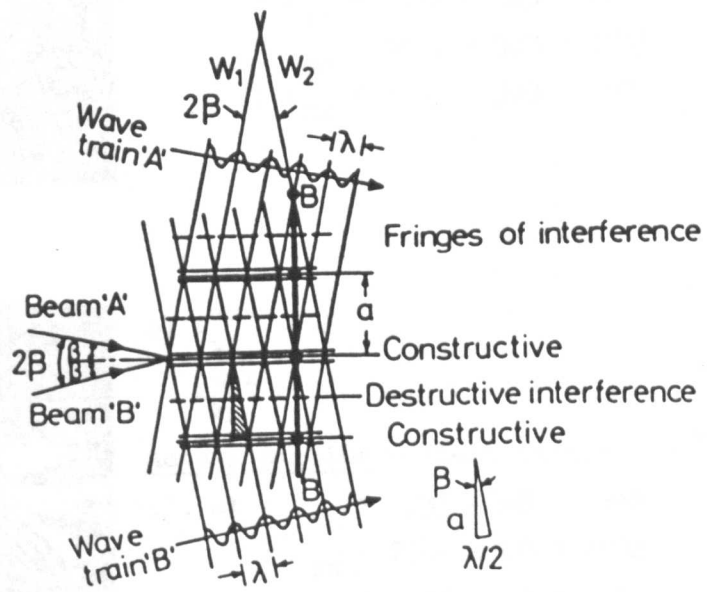
a)



b)

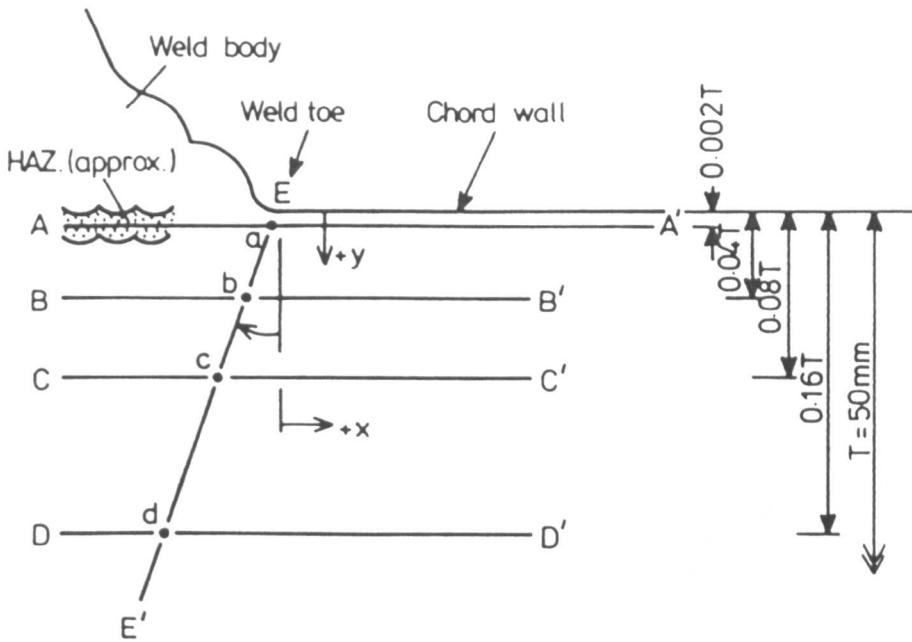


c)



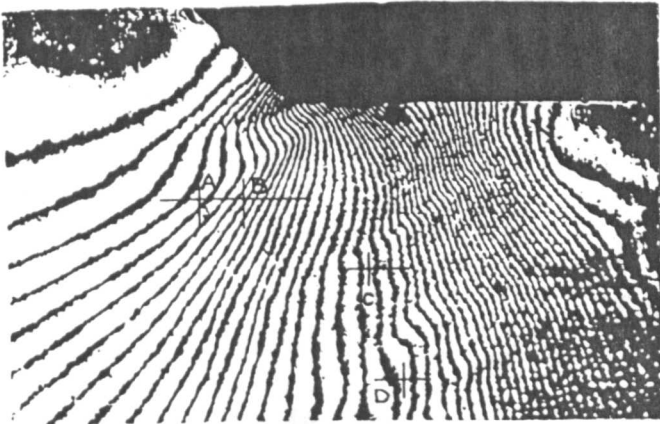
d)

Fig. 5.4 Optical Principles of Diffraction and Two Beam Interference of Light used in Moire Interferometry



Angle ϕ given by position of $\hat{\epsilon}_{xx}$ at a and d

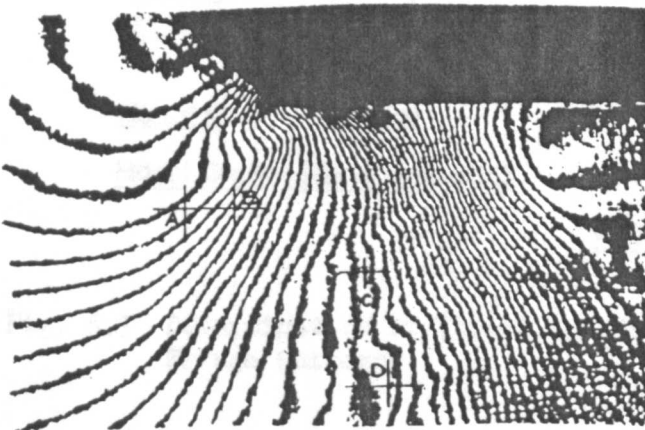
Fig. 5.5 Definitions of Lines of Analysis in Moire Work



a) $\epsilon_{xx}^{aux} = 303 \pm 4$
 $\epsilon_{xy}^{aux} \approx 0$

Actual Strains = field strains - ϵ^{aux}

\therefore at A $\epsilon_{xx} = 1208 - 303 = 905$
 B $\epsilon_{xx} = 3117 - 303 = 2814$
 C $\epsilon_{xx} = 1858 - 303 = 1555$
 D $\epsilon_{xx} = 1208 - 303 = 905$

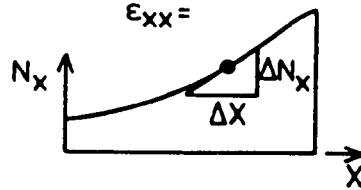
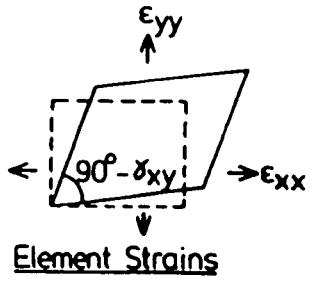


b) $\epsilon_{xx}^{aux} = 48 \pm 6$
 $\epsilon_{xy}^{aux} \approx 0$

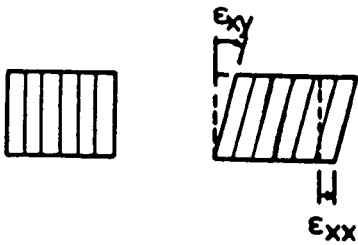
Actual Strains = field strains - ϵ^{aux}

\therefore at A $\epsilon_{xx} = 935 - 48 = 887$
 B $\epsilon_{xx} = 2900 - 48 = 2852$
 C $\epsilon_{xx} = 1611 - 48 = 1563$
 D $\epsilon_{xx} = 966 - 48 = 921$

Fig. 5.6 N_x Fringe Patterns in which the Frequency of the Carrier Pattern in the Auxiliary Grating was Varied. Apparent strain in auxiliary grating = ϵ_{xx}^{aux}



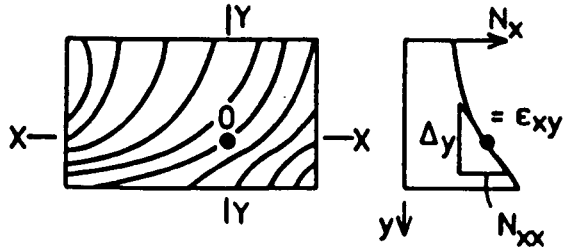
Fringe Gradients on X-X



No Load

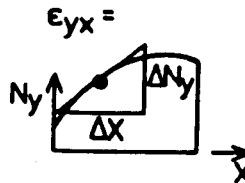
Loaded

Model Grating (Diagrammatic)

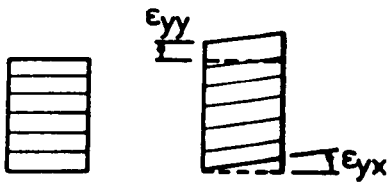


U Field N_x Fringes

Fringe Gradients on Y-Y



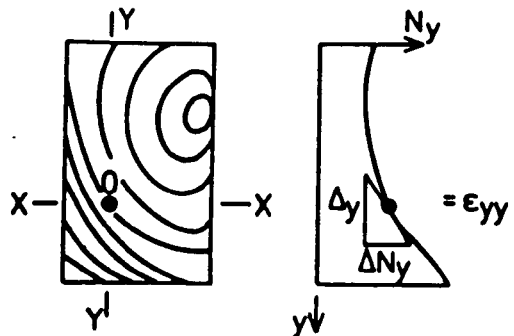
Fringe Gradients on X-X



No Load

Loaded

Model Grating (Diagrammatic)



V Field N_y Fringe

Fringe Gradients on Y-Y

Fig. 5.7 Determination of Direct and Shear Strains using Moire Fringe Patterns

CHAPTER 6RESULTS6.1 Presentation of Results

In this Chapter, elastic and plastic-elastic results are dealt with separately. Elastic values, obtained from 3-d and 2-d photoelastic and 2-d finite element models, are presented as distributions of meridional, hoop and principal stress indices. Some strains, calculated from these stresses are shown in the important positions. Only outside chord wall principal stresses are given because, for the tube geometries used in this work, they are more important in fatigue life calculations than brace wall principal stresses. The inclinations ϕ of maximum principal stress to hoop planes are also given. In general principal stresses have only been determined for positions which are not in planes of symmetry, e.g. saddle positions near to inclined braces. Elsewhere, principal stresses were assumed to be in local planes of symmetry, i.e. all crown positions and saddle positions near a 90° brace.

Plastic-elastic values, measured in 2-d steel models using photoelastic coatings fringe orders or moire fringe patterns, are presented as distributions of cartesian (relative to the chord wall) or principal strain indices, actual strains and residual strains. Photoelastic coatings were used to measure outside wall and weld surface strains near to brace and chord weld toes. Moire methods were used to determine surface and through-thickness strains near to the chord weld toes only.

In all distributions the following features are readily identified;

- i) repeatability of readings,
- ii) regions of stress (or strain) linearity near to weld toes,
- iii) lines of extrapolation in the determination of shell SCFs and SNCFs,
- iv) uncertainties associated with iii),
- v) positions of maximum values in weld toe fillets,
- vi) effects of changes in tube configuration and weld profile on maximum values.

Because stress distributions are important in the determination and interpretation of SCFs, the results are presented in the following:

- 6.2 Elastic stress and strain distributions
- 6.3 Elastic stress and strain concentration factors
- 6.4 Stress zones
- 6.5 Plastic-elastic strain distributions
- 6.6 Plastic-elastic strain concentration factors
- 6.7 Extent of plastic regions
- 6.8 Effect of out-of-plane strains on in-plane strains

6.2 Elastic Stress and Strain Distributions

6.2.1 Meridional and Hoop Surface Stresses

Meridional and hoop stresses, defined in Fig. 4.28b, are the stresses that would be calculated from strains measured by cross gauges bonded to the outside surfaces of the tube walls and weld fillet in the planes defined by the chain dotted lines in Fig. 4.27.

Fig. 5.2 shows examples of meridional surface stress distributions in 3-d corner-K models near loaded braces for three different brace spacings, g' . The figure is used to show the important features of stress distributions between two (oppositely loaded) brace walls, and compare the stresses in this region with those at remote positions (shown

dotted in Fig. 5.2). It gives an impression of the extent of the notch effects because the stress indices are plotted perpendicular to the profile on scale drawings of the junctions. Surface stress distributions for all the joints in the CK models in the planes defined in Fig. 4.27 are presented in Figs. 6.1 to 6.16.

Stresses in the braces and in the weld are independent of brace spacing g'/T but in the chord the stresses are strongly influenced by the proximity of the adjacent brace. In the crown planes (Figs. 6.1 to 6.8), the adjacent braces were loaded in balanced axial tension or compression. Stresses obtained at unloaded braces (e.g. in Fig. 6.1, junction 1 was unloaded in models CK2, 4 and 5) are also shown. Although these stresses are typically small ($I \leq 1.25$) and opposite in sense (except in Fig. 6.2), they must be considered in multi-planar loading. In the saddle planes (Figs. 6.9 to 6.16) the adjacent braces were unloaded. However, because of close proximity to loaded braces, stresses obtained at unloaded braces may be significant (see Figs. 6.10, 6.11 and 6.15) and must be considered in multi-planar loading.

Internal brace wall and fillet stresses are not significantly affected by brace proximity. At no positions on the models are these stresses maximum. The differences in stresses at the fillets are attributed to the differences in the weld toe radii given in Tables 4.1 to 4.8.

The chord wall surface stresses for the 3-d X-joints are given in Figs. 6.17 to 6.22. The important parameters in these models were weld size and shape, brace inclination θ and wall thickness ratio τ . The results provide the gradients and extent of the regions of stress linearity and show the effect on the chord weld toe SCF of uncontrolled and controlled weld profiles (see Fig. 3.7). Comparative results are by Wordsworth (5) and Dijkstra (69).

These Figures show that outside chord wall stresses are only significantly influenced by the shape of the weld for distances of between 1T and 2T from the toe of the (smaller) uncontrolled weld. It appears therefore that weld profile has little effect on linear stress gradients. However, because the stresses in the linear region are extrapolated to, and measured at the weld toe, the magnitude of the extrapolated stress is dependent on leg length. Inside chord wall stresses are presented to show the effects, if any, of weld profile on the maximum through thickness chord wall stresses.

Figs. 6.23 to 6.25 show detailed surface stress distributions in, and near the welds for uncontrolled and controlled profiles in the 3-d X60 model. Values obtained for the different weld profiles are plotted on the same diagram to show the true effects of the weld improvements. In the crown plane, (Figs. 6.23 and 6.24) where the linear stress gradients in the chord wall are small, the reductions in maximum stresses $\hat{\sigma}$ are small. The controlled profile moves the position of $\hat{\sigma}$ away from the intersection of the outside wall surfaces, a distance of approximately $2/3$ of the increase in weld leg length. Inside brace wall stresses are greater in the X60 model than in all CK models because of the larger brace wall bending moments caused by chord tube ovalising.

At the saddle position in Fig. 6.25 (note the change of scale of stress index) the benefits of the controlled weld profile are clearly seen. Because of the large linear stress gradients in the chord wall, the controlled weld profile transposes the hoop stress distribution a distance nearly equal to the increase in weld leg length, shifting the position of $\hat{\sigma}$ into a lower stress field. The reduction in $\hat{\sigma}$ in the chord fillet is about 40%. Brace wall and internal fillet stresses are not affected by weld profile.

Figs. 6.26 to 6.28 show distributions of brace and chord wall stress indices obtained from 2-d photoelastic models. These models represent the crown and saddle positions of a 3-d single-plane, tubular K-joint used by Fessler and Little (16). All stress indices are multiples of the mean axial brace stress in the parent 3-d model; not the mean axial stress in the brace of the 2-d representation. The 2-d results show good agreement with 3-d results in the crown ($\psi = 90^\circ$) and saddle ($\psi = 120^\circ$) positions of the $\theta = 90^\circ$ brace. They are within the range of experimental error quoted by Little (18) in the following regions:- (a) fully blended fillets and weld toes, and (b) in the chord and brace walls for distances of $0.75T$ and $1.2t$ from their respective weld toes. The 2-d results at the crown $\psi = 135^\circ$ position of the $\theta = 45^\circ$ were in good agreement in the fillets but in poor agreement elsewhere. The close agreement between 2-d and 3-d values enabled further 2-d photoelastic models to be analysed in which changes in weld size and profile were made. Examples of these are given in Figs. 6.29 to 6.31.

In Fig. 6.29 the results from a 2-d model, in which five changes in weld profile were made at the brace and chord weld toe fillets, are given. The results are for the crown ($\psi = 90^\circ$) position, i.e. same tube geometry as in Fig. 6.26. The distributions show the effect of weld toe radii on tube wall weld fillet stresses. Weld leg length and weld angle were constant. The single curves for inside wall and fillet stresses are the mean of five similar distributions.

Figs. 6.30 and 6.31 give examples of hoop stress distributions obtained at the saddle ($\psi = 120^\circ$) position in a X90 joint. Fig. 6.30 shows the stresses obtained for weld profiles similar to those used in 3-d work. Because chord wall stresses are in good agreement with 3-d values given in Fig. 6.17, Fig. 6.30 could be superimposed onto Fig. 6.17 to complete the distribution curves.

Fig. 6.31 gives examples of stress distributions obtained for the

saddle position in a X90 joint for models with two different depths of weld toe grinding; $p/T = 0.0125$ and 0.05 . The original weld profile with $p/T = 0$ (dotted line) is uncontrolled. The results show that weld toe grinding disturbs wall stresses for a distance of approximately $0.3T$ from the original weld toe, and $\hat{\sigma}$ increases with increasing depth of grinding.

Figs. 6.32 and 6.33 show examples of 2-d finite element meridional stress distributions obtained at the crown ($\psi = 90^\circ$) position of the $\theta = 90^\circ$ brace in a single-plane K joint for an uncontrolled weld profile. In each Figure, the (four different) weld leg lengths are the same; in Fig. 6.32 weld angle (α_c) is constant and hence brace weld leg length decreases with decreasing chord weld leg length; in Fig. 6.33 the brace leg length is constant and hence weld angle increases with decreasing chord weld leg length. Chord wall stresses are almost independent of weld size and shape, i.e. $\pm 3\%$ variation. Weld toe stresses are also within $\pm 4\%$ in similar models. Hence, differences in stresses occur only in the weld toe fillet where $\hat{\sigma}$ are greater for larger weld angles.

The verification of the 2-d F.E. model is given in the outside fillet surface stress distributions shown in Fig. 6.34. The model used to compare 3-d and 2-d photoelastic results with 2-d F.E. results was geometrically identical to the crown ($\psi = 90^\circ$) position in a K joint (16). The weld profile was fully blended with $r/T = 0.25$. The 2-d F.E. distribution curve shows agreement, i.e. to within $\pm 8\%$, with 3-d photoelastic values. Stress gradients very close, i.e. less than $0.15T$, to weld toes are greater in the finite element model than in photoelastic tests.

6.2.2 Magnitudes and Directions of Principal Surface Stresses

The magnitudes σ_1 and σ_2 and directions ϕ of the principal surface stresses are defined in Fig. 4.28a. They are the maximum and minimum stresses that would be calculated from strains measured by gauge rosettes bonded to the outside surfaces of the chord wall in the saddle planes defined in Fig. 4.27. The results are for 3-d CK models only.

The magnitudes of principal stress indices I_1 and I_2 in the chord at saddle positions are shown in Figs. 6.35 to 6.38 for $\theta = 90^\circ, 60^\circ, 135^\circ$ and 150° respectively, i.e. in descending acuteness. The inclination ϕ of I_1 to the hoop plane are shown in Fig. 6.39 and 6.40 for $\theta = 135^\circ$ and 150° braces. The values of ϕ for $\theta = 90^\circ$ and 60° are small, less than 9° and 18° respectively, and are not significant in the interpretation of principal stress distributions. Each figure shows curves for the results obtained at the saddle toe position, see Fig. 3.1, for the gap parameter in the range $0.57 < g'/T < 6.0$. At the saddle heel position (remote from other braces) the brace gap g' is the distance around the circumference of the chord to a weld toe. This varied in different models from $g'/T = 45$ to 51. The average value of $g'/T = 48$ used in Figs. 6.35 to 6.40 is used to denote the similar, averaged results obtained from different models.

Separate diagrams are used for I_1 and I_2 for clarity and to show the important variations;

- i) all maximum values of I_1 occur at the weld toes but some I_2 curves, particularly for $\theta = 135^\circ$ and 150° braces, show maxima between $0.1T$ and $0.25T$ from the weld toe.
- ii) the smaller principal stresses are significant.
- iii) for $\theta = 90^\circ$ and 60° braces, $I_2 \approx \frac{1}{2}I_1$ suggesting that
 - a) the smaller principal strains are small and b) even allowing for a possible reduction in I_2 in steel components due to

a lower value of Poisson's ratio ($\nu = 0.5$ in frozen-stress, photoelastic material), the smaller principal stresses should not be ignored.

An important feature of the distributions of ϕ given in Figs. 6.39 and 6.40 is the inclination of the brace nearest to the junction under consideration in the same saddle plane. This is particular to the chosen geometry in which the $\theta = 90^\circ$ and 60° braces and the $\theta = 135^\circ$ and $\theta = 150^\circ$ braces are in close proximity to each other. For $g'/T \ll 6$, σ_1 is orientated towards the axis of the nearest adjacent brace, i.e. $\phi \rightarrow |90^\circ - \theta|$. At the remote side for $g'/T = 48$ the σ_1 is in the hoop direction within 2 to 3 chord wall thicknesses from the chord weld toe.

6.2.3 Relationship Between Cartesian Surface Stresses and Strains

Figs. 6.41 to 6.43 show meridional and hoop, stress and strain index distributions in the outside, interbrace chord walls in the crown planes I and II and the saddle plane III (see Fig. 4.27) of the CK models. The stress curves are drawn through ordinates of photoelastic measurements obtained from slices and sub-slices. Because the positions of meridional and hoop stress photoelastic readings were not always coincident, strains were determined from stresses obtained from the stress curves. The generalised form of Hooke's Law was used with Poisson's ratio = 0.5.

These distributions uncover a number of interesting points which were not apparent in the individual meridional or hoop stress distributions. At the chord weld toe of the $\phi = 90^\circ$ brace (point B in Fig. 6.41), hoop and meridional stresses are similar in magnitude for $g'/T = 3$ because of the balanced axial loading configuration. Thus hoop strains are greater than meridional strains, a point that may be

overlooked in the instrumentation of this region using line gauges. Similar results are found near the $\phi = 120^\circ$ brace (Fig. 6.42) for $g'/T = 5.7$. Elsewhere, if hoop strains were ignored, predicted meridional stresses would be greater than those measured. In the saddle plane in (Fig. 6.43) the smaller strains are not significant.

6.2.4 Axial and Bending Stress Components

In the CK models, outside and inside wall surface stresses were resolved into membrane (or axial) and bending stresses. Figs. 6.44 to 6.46 show axial and bending stress distributions in crown planes I and II and saddle plane III. The positions and values of stress indices at the outer and inner, chord and brace wall surfaces were recorded. The means and semi-difference of opposite values gave axial and bending stress components. By isolating the wall bending stress which is induced by chord ovalisation, these diagrams show that $\hat{\sigma}$ is strongly influenced by wall bending.

In Section 6.2.1 it was noted that chord stresses are strongly influenced by the proximity g of adjacent braces. Figs. 6.44 to 6.46 show that, because axial stresses are independent of g , outside surface stress distributions are almost entirely dependent on wall bending in the real weld toe-to-toe gap. It is apparent that the ratio g'/T is an important parameter in the evaluation of stresses in the gap region of K type tubular joints.

6.2.5 Principal Through-Thickness Stresses

Principal stresses, measured in the chord wall of a 2-d model representing the crown ($\phi = 90^\circ$) position of a single plane K-joint, were obtained using F.E.M. The line chosen to study the effect of weld profile on the elastic stress fields near to the positions of $\hat{\sigma}$ is denoted by OA in Fig. 5.3a.

Figs. 6.47 and 6.48 show the through-thickness I_1 distributions for uncontrolled weld profiles on OA. In each Figure chord weld leg length was constant; in Fig. 6.47 chord weld angle was varied; in Fig. 6.48 weld toe radius was varied. The distributions show two distinct regions, represented schematically on Fig. 5.3b as:

i) Exponential region. The extent of this region is called the through-thickness notch zone, Z_y .

ii) Linear region. At depths in the approximate range $0.07 < y/T < 0.17$, principal stresses decay linearly with distance.

Fessler and Marston (20) used 3-d photoelastic models to show a linear decrease in both meridional and hoop through-thickness chord stresses in the crown plane of a $K90^\circ/45^\circ$ tubular joint. As shown in Table 2.2, the distances to the commencement of the linear region were in the range $0.07 \leq y/T \leq 0.28$ from the weld toe.

The stress curves in the linear regions were extended to the edge of the fillet, i.e. $y = 0$, and the value of the ordinate drawn to intersect this line is called the through-thickness geometric stress index I_g . The ratio of I_1/I_g is called the through-thickness notch index I_n . For the uncontrolled weld profile parameters studied, I_n was found to decay exponentially with through-thickness distance. Figs. 6.49 and 6.50 show distributions of I_n for the respective I_1 distributions given in Figs. 6.47 and 6.48. Values for I_n are plotted in the range $0.001 \leq y/T \leq Z_y$. The trends in the variations of I_n are more consistent in Fig. 6.49, in which the weld toe radius r was constant, than in Fig. 6.50 where r was varied.

The results approximate to the empirical expression

$$I_n = C + m \log_e(y/T) \quad \dots (6.1)$$

where m is the slopes of straight lines typically drawn in the range

$0.005T < y/T < 0.05T$. The lower limit of this range of exponential stress decay represents a depth of material (0.4 mm) of about the same size as sharp slag intrusion found in welds (70). Because of flaws, through-thickness stresses within 0.4 mm (0.005T) of the edge of the fillet are not useful in practice.

The geometric through-thickness stress index is given by:

$$I_g = K_g + q(y/T) \quad \dots (6.2)$$

The experimental values for C and m (eq. 6.1) and for K_g and q (eq. 6.2) are given in Table 6.1. When $\alpha_c = 0$, a linear through-thickness distribution is assumed in which the outer and inner chord wall stresses are obtained from surface shell stresses.

The inclinations ϕ of I_1 to OA are given in Figs. 6.46 and 6.47. The curves show that in the exponential region, i.e. $y/T < 0.07$, the direction of I_1 is tangential to the edge of the fillet to within $\pm 10^\circ$, i.e. OA approximates to the loci of $I_{1(\max)}$.

6.3 Elastic Stress Concentration Factors

6.3.1 Definitions of Stress Concentration Factors, SCFs

In the introduction to this work several different SCFs were identified in the nature of the surface stress distributions near to weld toes. The surface stress distribution given in Section 6.2 shows that stress concentrations in tubular connections arise near weld toes from two basic causes; the structural response between two (or more) tubes (shell stress) and the local severity of weld toe geometry (notch stress). The stresses in the fillet are the product of these two stresses. They are divided by the mean axial stress in their own loaded brace σ'_{nom} to determine i) maximum SCF and ii) weld toe SCF.

The maximum value of the surface stress index at every position in

a tubular joint is called the stress concentration factor, K . Because of the geometry of the welds used in this work more than one stress concentration is found in every joint; these are near to weld toes at each end of the external face of the fillet weld. The SCFs at the chord and brace wall ends of the weld are given by K_c and K_b respectively. The maximum stress usually occurs at a small angular distance in the weld toe fillet arc. This position is given by ϕ measured from the weld toe (see Fig. 1.3). The value of the stress index at $\phi = 0^\circ$ is called the weld toe SCF, K_t . The maximum stress in the internal fillet is given by K_i .

Notch stresses occur in tube walls for small distances from weld toes. The linear, or near-linear, stress distributions in the walls beyond the extent of notch stresses is extrapolated to the weld toe to give a shell SCF, K_s (see Fig. 1.3). Because shell stresses are traditionally measured at weld toes, notch SCFs, K_n , are given by K/K_s , where K is the local SCF in the same fillet at which K_s was measured. Principal SCFs are qualified by additional subscripts 1 or 2.

6.3.2 Determination of SCFs

In the 3-d corner K models different braces were subjected to different load magnitudes because of balanced axial loading. (Stress indices are based on the mean axial stress in the brace in tension.) To determine K and K_s for each brace in the CK models, the measured stresses were divided by the nominal stress in "their own" brace, σ'_{nom} . Referring to the loading in Fig. 3.6, stress indices have been multiplied by the following to obtain maximum and shell SCFs:-

Loaded Plane	Brace Angle	$\frac{\text{SCF}}{\text{Stress Index}}$
I	$\theta_1 = 90^\circ$	$-1.41 = -\sin 90^\circ / \sin 135^\circ$
	$\theta_2 = 135^\circ$	+1.00
II	$\theta_1 = 60^\circ$	$-1.73 = -\sin 60^\circ / \sin 150^\circ$
	$\theta_2 = 150^\circ$	+1.00

Notch concentration factors K_n are quotients of K and K_s and always positive.

It is also necessary to make all the chords free of beam stresses particular to the chosen loading configuration. Referring to Fig. 3.6, the chord adjacent to the 135° and 150° braces carries no load whereas the chord adjacent to the 90° and 60° braces carries the reactions to the load components parallel to the chord axis. The mean stress due to these components is

$$\sigma_{\text{beam}} = (d/D)(t/T)(\cos \theta_1 \sin \theta_2 - \cos \theta_2) \sigma_{\text{nom}} \quad \dots (6.3)$$

For loading in Plane I, $\sigma_{\text{beam}} / \sigma_{\text{nom}} = 0.18$. For loading in Plane II, $\sigma_{\text{beam}} / \sigma_{\text{nom}} = 0.28$. This value was subtracted from the surface stresses in appropriate parts of the chords before calculating meridional K_s values for the crown positions at the 90° and 60° braces. The (smaller) meridional stresses were also modified by this value at the saddle positions of the 90° and 60° braces.

In the 3-d X models, the braces were equally loaded and the chord end reactions were zero. In the 2-d models stress indices are presented in terms of the mean axial stress in the brace of the parent 3-d model. There were no chord end reactions in these models. SCFs are therefore equal to the value of the appropriate stress indices in 3-d X models and 2-d models.

Tables 6.2 and 6.3, 3.5 and 3.6 , and 3.7 give the magnitudes K and the positions ϕ of all SCFs obtained from 3-d photoelastic, 2-d photoelastic and 2-d F.E. models respectively. For all results saddle positions are separated from the crown because the loads differ. Although the braces are in tension and the chord is primarily in bending, brace and chord values are presented together because of their geometric proximity. In the 3-d CK models it is important to distinguish results for the 'toe' position, near to an adjacent brace, from 'heel' results, remote from other braces, as shown in Fig. 3.1.

6.3.3 Maximum SCFs, K

Maximum fillet stresses depend on weld toe and tubular joint geometry. In the 3-d models, weld toe radii were (unavoidably) accidentally variable, and weld angles and leg lengths were difficult to control. Results for K are tabulated because it is not useful to present figures showing the variation of K with any of the tubular or weld toe geometrical parameters.

In the 2-d work the tubular parameters g' , θ and ϕ and type of parent 3-d model (K or X) were common to each set of models in which weld toe parameters or weld profile were varied. Fig. 6.51 shows the combined effects of τ and weld profile where, for two welds of different but constant size and shape, chord and brace wall thicknesses were progressively reduced as given in Section 3.3.2 . The predominant variable parameter was leg length to thickness, H/T . The results are normalised in terms of the brace to chord wall thickness ratio τ . The justification for dividing by the brace/chord wall thickness ratio is that because chord wall deformations are related to brace load, rather than brace nominal stress, shell SCFs should be roughly proportional to τ . Wordsworth's (5) parametric equations appear to be based on this assumption.

For the saddle positions the results fall into two distinct scatter bands; the uncontrolled profile in which $\alpha_c = 45^\circ$, and the controlled profile in which $\alpha_c = 22^\circ$. Because the weld toe radius parameter was in the same, relatively small range, $0.01 < r_c/T < 0.016$ for both profiles, it is assumed that this has only a secondary effect on the SCF. At the crown position, the reduction in SCF is limited at larger values of H/T by smaller stress gradients (away from the weld) in this plane of a K joint.

The variation of peak SCF with weld toe radius is shown in Fig. 6.52 to be dependent on position on a node, i.e. crown or saddle, and in Fig. 6.53 to be dependent on weld angle for a specified position on a node. In both figures K , which decreases with increasing r_c/T and decreasing α_c , can be generalised to an empirical expression

$$K = A(r_c/T)^j \quad \dots (6.4)$$

Values for the constant A and exponent j are given in Table 6.4.

In Fig. 6.52 the results from models in which H/T was varied (open symbols) do not fit the family of curves for constant leg length (filled in symbols). The size effect of weld leg length is clearly demonstrated, although there are insufficient results to be quantitative.

6.3.4 Shell SCF K_s

These linear extrapolation results are presented in Figs. 6.54 to 6.61 to show the effect of variation of position (crown and saddle), dihedral angle ϕ , brace proximity g'/T and weld size H/T on K_s .

The crown toe shell SCFs at the chord weld toe, presented in Fig. 6.54a, all increase with brace spacing. If they were divided by $\sin^2\phi$, to use the perpendicular footprint stress as datum, the $\phi = 150^\circ$ values would be greater than the $\phi = 135^\circ$ ones, i.e. the curves would be in the

same sequence as the values. The low values for $\phi = 90^\circ$ and $\phi = 120^\circ$ in close proximity (small g'/T) are associated with the opposite directions of loading of adjacent braces and the magnitude of their mean stresses being smaller than in their neighbours (to achieve 'balanced' loading). At the remote crown heel of the $\theta = \phi = 90^\circ$ brace, brace proximity is at least the distance to the end of the model, approximately $40T$. The crown toe shell SCFs at the brace weld toe, shown in Fig. 6.54b, appear to vary little with brace spacing but are significantly higher than the heel values in Fig. 6.55 for the same braces.

In Fig. 6.55, K_s has been plotted against $\sin^2\phi$ to show that K_{sc} is independent of brace inclinations θ (θ is the supplement of the dihedral angle ϕ at the crown of these joints) if the nominal stress is changed from the mean stress in the brace to the component perpendicular to the chord axis stress in the 'foot print' of the brace on the chord. This change of nominal stress recognises that the chord is primarily in bending and has been found to satisfactorily co-relate flexibility measurements of a very wide range of tubular joints (67). The variation of K_{sb} with ϕ has been identified as the sum of two separate effects; chord wall bending carry over and maldistribution of brace wall loading. The latter is due to the increased stiffness of the brace wall at the heel for small angles of ϕ . The saddle values should be considered separately from the crown because the loadings differ. The results from two previous frozen-stress photoelastic tests (16, 21) are in good agreement with the chord results.

Chord shell stress concentration factors K_{sc} at the crown toe positions for different g'/T are compared with the heel values in Fig. 6.56; heel values are part of Fig. 6.55. The relationship between the toe values and θ is more complicated and also appears to be related to g'/T . In Fig. 6.56, the maldistribution of load between the heel and toe positions

is represented by A for $g'/T = 3$ and B for $g'/T = 0.5$.

Fig. 6.57 shows the variation of hoop shell SCFs with g'/T and θ . As shown in Fig. 6.57a, the saddle toe shell SCFs at the chord weld toe for $\theta = 90^\circ$ brace differ considerably from those for inclined braces. At the saddle of the $\theta = 90^\circ$ brace, close proximity (i.e. $g'/T = 0.45$ to 0.71) of an unloaded brace stub has considerable effect on interbrace wall bending and hence the value of K_{sc} . A maximum is observed in the region of $g'/T = 1.0$. The increased stiffness of inclined braces near to each other is seen in the low values of K_{sc} when $g'/T < 1$. Fig. 6.57b shows that the stresses at the brace weld toe are similar to those at the chord, suggesting that chord ovalisation induces comparable bending stress into the brace. This is not a feature of joint flexibility in the crown planes. Fig. 6.58 shows principal shell SCFs for the same positions and brace inclinations as in Fig. 6.57. The differences between K_s and K_{s1} are easily identified from these figures, but the reasons for the differences are complex. At the saddle toe position, between two braces in close proximity, the direction of the principal planes are influenced by the inclinations of i) the brace under consideration and ii) the unloaded brace stub. For values of ϕ (see Fig. 4.28a) exceeding about 25° , shear stresses in the hoop plane become significant as would be expected from the line of action of loads in an inclined brace. Hence, for $\theta = 150^\circ$ and $g'/T = 0.57$, $K_{s1} = +0.92$ and $K_s = 0$ because $\phi = (\text{approx.}) 49^\circ$.

Figs. 6.59 to 6.61 show the variations in K_s with weld leg length H/T for different tubular joints (K or X), loading, position (crown or saddle) and brace wall angle ψ . The results are expressed in terms of τ , for the same reason as given in Section 6.3.3 for maximum SCFs. K_s is therefore normalised with respect to the chord wall thickness T ; not the brace wall thickness t .

The variation of K_s with weld leg length can be deduced from the relevant surface stress distribution curves. For example, the gradients of linear stress in the 3-d X models (Figs. 6.17 to 6.22) are small in the crown planes and large in the saddle planes. Gradients also increase with increasing θ . Larger welds, i.e. increase H/T , transpose stress distributions away from the intersections of the joints and, because notch stresses appear to be almost insensitive to changes in weld size, the effect manifests itself entirely in the value of K_s , as shown in Fig. 6.59.

The 2-d photoelastic and F.E. results in Fig. 6.60 show an increase in K_s with decreasing leg length for the crown position in a single-plane K joint. For triangular fillet weld shapes (i.e. excluding fully blended profiles) F.E. and photoelastic results are in good agreement in the range $0.25 < H/T < 0.5$. The results from models with fully blended profiles (square symbols) suggest that the absence of the triangular fillet changes the cross-sectional properties of the chord wall at the weld toe, and hence the value of K_s . The chain dotted line in Fig. 6.60 is a plot of stress indices obtained from a model having a sharp intersection between chord and brace wall, i.e. no weld fillet. If K_s were independent of the size of weld, all values of K_s would lie on this line.

The values for K_s fit the following empirical relationships:-

$$K_s = \tau(5.7 - 4.6 H/T) \quad \dots (6.5a)$$

for photoelastic models in the range $0.187 < H/T < 0.55$, and

$$K_s = \tau(4.7 - 2.0 H/T) \quad \dots (6.5b)$$

for F.E. models (with fillet welds) in the range $0.183 < H/T < 0.50$.

Fig. 6.61 shows the results for K_s obtained in the same 2-d photo-

elastic models used to determine K values in Fig. 6.51. The single scatter bands across the range of results in Fig. 6.61 show the independence of K_s from α_c and τ . The results fit the following empirical relationships:-

$$K_s = \tau(18.2 - 7.8 H/T) \quad \text{at the saddle X node position} \quad (6.6a)$$

$$K_s = \tau(6.0 - 2.0 H/T) \quad \text{at the saddle K node position} \quad (6.6b)$$

for photoelastic models in the range $0.187 \ll H/T \ll 0.55$.

The components of K_s , in the 3-d CK models, due to axial and bending stresses are given in Table 6.5 where $K_{s(a)}$ and $K_{s(b)}$ refer to the extrapolated axial and bending stresses respectively. The values have been corrected for "beam" stresses (eq. 6.3) and normalised with respect to σ'_{nom} .

6.3.5 Notch SCFs, K_n

The maximum fillet surface stresses occur at an angular position ϕ' in the fillet measured from the weld toe. The variation of ϕ' with the weld angle α is shown in Fig. 6.62. In general $\phi' \approx \frac{1}{2}\alpha$.

The results from 2-d photoelastic and F.E. models suggest that the angular position ϕ of $\hat{\sigma}$ influences the value of K_n . 3-d photoelastic analysis shows that chord wall stresses increase with distance from the point of contraflexure (e.g. see Fig. 6.17). These stresses continue to increase to a position approximately halfway around the fillet. The 2-d results in Figs. 6.32 and 6.33 show weld angle influences notch stresses exclusively in the weld fillet, i.e. from $\phi = 0^\circ$ to $\phi = \frac{1}{2}\alpha_c$, a distance $r \sin \frac{1}{2}\alpha$.

Fig. 6.63 shows the relationship between K_n and $\sin \frac{1}{2}\alpha_c$ for the crown position in a single plane K joint only. The results are for a constant weld toe radius and fit the following empirical expression

$$K_n = 1 + v \sin(0.5 \alpha_c) \quad \dots (6.7)$$

where $v = 5.0$ for photoelastic models

and $v = 5.6$ to 5.8 for finite element models; the weld leg length being responsible for the small variation.

The weld leg length has practically no influence on K_n when r/T is constant. However, when r/T is varied and α is a particular value, weld leg length is surprisingly significant as shown on Fig. 6.64.

In Fig. 6.65 K_n is plotted against r/T for i) fillet welds with different α_c and ii) fully blended profiles. Because the leg length in a fully blended profile varies with radius ($H/T = r/T$), the results for K_n do not follow the same trends as for the fillet welds.

Fig. 6.66 shows the variations in K_n with position (saddle or crown) and weld angle α . The notch effect is thought to be influenced by stress gradients near to weld toes. Because stress gradients are generally greater at saddle than at crown positions, values for K_n are treated separately at these locations.

The results in Fig. 6.66a are for the saddle toe and heel positions (see Fig. 3.1) in the 3-d CK models. The scatter in the results is an indication that other geometric parameters, to those identified in the Figure, influence K_n . The curves are drawn for results in three different weld angle groups.

Fig. 6.66b shows the combined effects of r and α on K_n . The results were obtained from two 2-d photoelastic models at the crown ($\phi = \theta = 90^\circ$) position. Curves developed from empirical expressions by Pappalettere (40) and Lawrence (41) are shown with the crown values from this work because of geometric similarities. Although the results from the other work were not appropriate to tubular joints, variations in K_n with r/T show similar trends.

The results from Figs. 6.64 to 6.66 can be generalised by the empirical expression

$$K_n = 1 + B_c (r_c/T)^{k_c} \quad \text{at the chord fillet} \quad \dots (6.8a)$$

$$K_n = 1 + B_b (r_b/t)^{k_b} \quad \text{at the brace fillet} \quad \dots (6.8b)$$

Values for B_c and k_c are presented in Table 6.4.

6.3.6 Summary of Principal SCFs at Weld Toes in CK Models

Figs. 6.67 and 6.68 present, in tabular form the magnitudes σ_1 and σ_2 and directions ϕ of all chord weld toe principal stresses. The values include notch stresses. The crown positions are known by symmetry to be principal planes (if the effect of other non-planar brace stubs is neglected) and the isoclinic angle is assumed zero. The meridional stress is therefore the maximum principal stress σ_1 . The saddle positions of inclined braces are not principal planes. Here σ_1 tends towards the hoop rather than the meridional chord axis. The dotted lines, which represent the 'foot-prints' of unloaded brace stubs, distinguish saddle toe from saddle heel positions. The vectors are indicative only of typical magnitudes and directions of σ_1 and σ_2 . The direction of principal stresses obtained by Wylde (10) in a single plane K joint are given in Fig. 6.6.7.

6.3.7 Comparison of SCFs with Other Work

In Chapter 2 the development of experimental and numerical stress analysis techniques for 3-d tubular joints was described. This work led to the publication of parametric formulae used to predict the extrapolated shell, or hot-spot, SCF.

Kuang (4), Wordsworth (5) and Efthymiou (27) have published parametric equations for single-plane K joints in balanced axial loading for K_{sc} only. These equations have been evaluated for the shapes used in this work and are compared with K_g values obtained in this work for corner K joints in Fig. 6.69. Strain gauge results published

by Wylde (10) and Ohtake (19), F.E. results by Clayton (71) and photo-elastic results by Fessler and Little (16, 17) and Marston (21) for single-plane K joints of similar shapes are also shown. Fig. 6.69 shows the difference between corner K and single-plane K joints; the unloaded brace stub in the corner K configuration being responsible for the increased SCF at the saddle toe and decreased SCF at the saddle heel. Marston loaded each brace ($\theta = 90^\circ$ and 135°) separately. Comparative results for $g'/D = 0.09$ are obtained by superposition of stresses for the case of balanced axial loading. The method of analysis and shape parameters used for the authors' work given in Fig. 6.69 are as follows:

<u>Source</u>	<u>Method</u>	<u>Shape Parameters</u>		
		<u>D/T</u>	<u>d/D</u>	<u>t/T</u>
This work	Photoelasticity	25.0	0.50	0.50
Little (16, 17)	"	25.6	0.53	"
Marston (21)	"	25.3	"	0.48
Wylde (10)	Strain gauge	28.4	"	0.53
Ohtake (19)	"	23.3	0.41	0.59
Clayton (71)	F.E.M.	24.3	0.50	0.50

Lawrence (41) used finite element analysis of 2-d double V-welded joints to derive notch SCFs in the form $(K_n - 1) \propto (r/T)^{-0.5}$. The position of $\hat{\sigma}$ is confined to a very small region near the weld toe. The angular position φ of the stress concentration in the fillet is 15° (approx.) from the weld toe. This agrees with the authors' 3-d work where for geometries of similar weld angle $30^\circ < \alpha < 50^\circ$, values of φ are in the range 5° to 25° . Atzori and Pappalettere (40) also used F.E.M.s to arrive at the same type of expression for K_n . Applying these results (40, 41) to our shapes and loadings lead to the dotted and chain-dotted curves shown in Fig. 6.66b.

6.4 Stress Zones

6.4.1 Definitions of Stress Zones

The schematic surface stress distribution in the tube walls, shown in Fig. 1.3, are characterised by three regions. These are notch stress zone, linear stress zone and non-linear stress zone.

Notch zones Z_n are defined by the distance, measured from weld toes, to the commencement of the region in which the gradients of stress vary so slowly that they are considered to be linear. Further from the weld toe, at a distance Z_l , the curvature of the tube causes a non-linear decay in wall bending moments and hence, outside wall surface stresses. The linear stress zone exists between these two points.

6.4.2 Notch Zones

Some distances, from the brace and chord weld toes to the point where the surface stresses vary linearly with positions, were measured and called z_{nb} and z_{nc} respectively. They appear to vary little with fillet radius but their relationship to weld angle is shown in Fig. 6.70. Some of the chord values are seen to extend beyond $0.2\sqrt{rt}$ (which for this geometry is $0.7t$ and $0.35T$ - the position which has been proposed for one of two strain gauges to be used for linear extrapolation to determine K_g (6)). Notch zones for all 3-d models and some 2-d models are presented in Tables 6.2 and 6.3, and 3.7, respectively.

6.4.3 Linear Stress Zones

In the determination of shell SCFs tangents were drawn to the linear parts of the surface stress distribution curves and the end positions of the linear region, Z_n and Z_l , were noted. The values obtained from the I_1 curves in Figs. 6.35 to 6.38 (in the saddle planes of the 3-d CK model) are shown in Fig. 6.71. The large range of values for Z_n and Z_l indicates the uncertainties involved in measuring these distances.

Linear stress zones are small; typically $0.75T$. The distance to the end of this zone $Z_{\ell} < 0.5g'$. Notch zones are typically $0.25T$ to $0.3T$. Both values decrease with brace gap when $g'/T < (\text{about}) 2$.

6.5 Plastic-Elastic Strain Distributions

6.5.1 Surface Strains, Near Weld Toes, Obtained using Reflection

Photoelasticity

Reflection photoelasticity methods of measuring elastic and plastic-elastic maximum shear strains were used to analyse two models. Because of the difficulties associated with this method, results are available for only one of the models. They are presented to show that attempts were made to measure plasticity at, and near to weld toes. The steel model chosen for analysis is shown in Fig. 6.72 with the surface strains near to chord and brace weld toes.

Strains were measured at several increments of load - which is expressed in terms of γ_{nom} calculated from the load cell output and cross sectional area of the brace wall. The Figure shows maximum shear strain contours for one loading and one unloading cycle with the maximum value of $\gamma_{\text{nom}} = 0.11\%$. The residual plastic strains measured at (about) zero load are shown in dotted lines.

Maximum fillet and weld toe strains were recorded and plotted against γ_{nom} in Fig. 6.72 to show the changes in strain during the tests. Neglecting the initial strains due to self weight etc. which were not measured, strain indices, and hence, strain concentration factors were calculated.

Fig. 6.73 shows distributions of surface shear strain indices for the chord and brace weld toe regions. Elastic values were calculated between $\gamma_{\text{nom}} = 0.045\%$ and 0.087% , and plastic-elastic values were calculated at $\gamma_{\text{nom}} = 0.11\%$. The differences between the two curves represents plastic strain indices at $\gamma_{\text{nom}} = 0.11\%$. The curves shown in Fig. 6.73 are characterised by linear and notch strain distributions

with the position of maximum strain in the fillet at an angular position $\varphi = 20^\circ$ to 45° . In the weld body strains decreased rapidly to zero.

6.5.2 Chord Wall Strains Obtained Using Moire Interferometry

Results have been obtained in four different steel models in the positions referred to in the following schedule of Figure numbers.

		Steel Model No.	2	3	4	5
		Position	Saddle	Saddle	Saddle	Crown
		ψ	120°	120°	120°	90°
		Weld Profile ¹	U	U	C	U
		Weld Grade	E51	E51	E51	E51
		Heat Treatment	No	Yes	No	No
Positions of Measurement ²	Loading	Strain Values	Figure Nos.			
Chord wall outside surface line A-A'	Loaded values	$J_1 J_2$	6.75	6.76	6.77	6.78
	Residual and (one) loaded values	$\epsilon_1^R \epsilon_2^R$	6.79	6.80	6.81	6.82
	Change of strain during unloading	$\epsilon_1^e \epsilon_1^p$	6.83	6.84	6.85	6.86
Sub-surface chord wall lines B-B', C-C' and D-D'	Loaded values	J_{xx}	6.87	-	-	-
Through-thickness chord wall line E-E'	Loaded values	$J_1 J_2$	6.88	-	-	-
At strain concentration	Variation with load	$\epsilon_1^R \epsilon_1^e$ $J_1 J_2$	<div style="text-align: center;"> } 6.89 6.90 </div>			

1. U = uncontrolled H/T ≈ 0.40 C = controlled H/T = 0.75

2. See Fig. 5.5

Fig. 6.74 shows, schematically, the maximum strains $\hat{\epsilon}$ in the model measured at different loads. The loads are expressed in terms of $\epsilon_{nom}/\epsilon_{yield}$ in the brace wall. Initial values, measured at $\epsilon_{nom}/\epsilon_y = 0.02$, are given at A, and elastic values at B. The gradient of AB is the

elastic strain index J . Strains measured at first observed yield and at higher values are given at C and D, respectively. Residual strains are given at F. The reduction DF comprises elastic response DE and plastic reversal EF.

Cartesian strains were obtained from fringe order measurements $\epsilon_{xx} = \partial u / \partial x$, $\epsilon_{yy} = \partial v / \partial y$ and $\gamma_{xy} = \partial u / \partial y + \partial v / \partial x$. The magnitudes ϵ_1 , ϵ_2 and ϵ_1^R , ϵ_2^R and directions ϕ^R of principal loaded and residual strains were calculated from cartesian values. Strain indices $J_{ij} = \epsilon_{ij} / \epsilon_{nom}$, where ϵ_{nom} is the mean axial strain in the brace wall. Elastic response strains ϵ^e were calculated from J and $\Delta \epsilon_{nom}$ - the reduction in the load. Plastic reversal strains are given by $\epsilon^P = (\epsilon - \epsilon^R) - \epsilon^e$.

6.5.2.1 Surface Strain Indices

Elastic and plastic elastic values of J_1 , J_2 and ϕ are shown in Figs. 6.75 to 6.78 for measurements made in line A - A' in Fig. 5.5. The elastic values in Figs. 6.75 and 6.76 (open symbols) may be compared with the 2-d photoelastic chord wall surface distributions of I_1 (assume $I_2 = 0$) shown in Fig. 6.27. The agreement in surface values in linear regions is within $\pm 10\%$. Peak values cannot be compared because weld toe geometries are different. Notch zones in steel models are generally smaller, i.e. 0.05T to 0.15T, than in photoelastic models. Plastic-elastic distributions are given at the onset of first observed yielding and for larger strains, i.e. approaching 2%.

In steel model No. 2 (Fig. 6.75) first yield was observed in the parent (chord wall) plate near to the weld toe at a position approximating to the edge of the HAZ at $\epsilon_{nom} / \epsilon_{yield} = 0.28$. The strain in the model at the position and onset of first yield was 0.346%. Local yielding was identified in the moire fringe pattern as a small slip line (about 2 mm long in which the fringes were closely spaced) which followed the approximate arc of the HAZ/parent plate boundary.

Plastic-elastic strain indices are also given for $\epsilon_{\text{nom}}/\epsilon_{\text{yield}} = 0.53$. This corresponds to $\sigma_{\text{nom}} \approx 200 \text{ N/mm}^2$; a typical maximum value used in jacket design (43). At this loading, a SNCF = 17 occurred at the weld toe in a model in which the elastic SNCF = 4.6. Plastic strains in the chord wall were measured for a distance of 4.5 mm (0.09T) from the toe.

The inclinations ϕ of J_1 to A - A' are in the range $20^\circ < \phi < 30^\circ$ in the weld, and $0^\circ < \phi < 15^\circ$ in the chord wall.

In steel model No. 3 (Fig. 6.76) first yield was observed very close to the weld toe in the HAZ. Because of the difficulties in locating the exact position of the weld toe the position where yielding first occurred was between 0.2 and 0.7 mm from the toe. At this point in the test $\epsilon_{\text{nom}}/\epsilon_y = 0.36$; an increase in load at first yield over model No. 2 of 28%. The yield strain in the model was 0.402%; an increase of 0.056% strain or 115 N/mm^2 . This represents the additional yield stress in the models attributed to heat treatment. However this is not a reliable or accurate measure of residual welding stress because it was derived from 'observed' first yield values in models with slightly different weld toe geometry.

Plastic-elastic indices are given for $\epsilon_{\text{nom}}/\epsilon_y = 0.53$ for comparison with the results in model No. 2. The effects of heat-treatment are quite dramatic. Plastic-elastic strains were measured up to 3.7 mm (0.074T) from the weld toe. In this region, three peak values of large plastic strain were measured corresponding to SNCFs = 10.7, 8.9 and 13.0; the latter occurring at 0.06T from the toe. In between these peaks, strain indices were only 30% greater than elastic values in the same positions.

The effects of controlled weld profiles are given in the results for steel model No. 4 in Fig. 6.77. The onset of yielding was not observed in this model. It was not apparent that yielding had occurred until considerable plastic strains were present. Measurements were made

at loads corresponding to $\epsilon_{\text{nom}}/\epsilon_y = 0.53$ (for comparison with Figs. 6.75 and 6.76), 0.63 and 0.73. At $\epsilon_{\text{nom}}/\epsilon_y = 0.53$, maximum plastic-elastic strains measured in the weld material were approximately twice those measured in the chord wall and HAZ. A SNCF = 5.7 was considerably less than in the uncontrolled weld profiles. The increase in plastic strain and spread of plasticity at higher loads was fairly uniform, reflecting perhaps the improved weld toe profile.

The variation in ϕ with loading was less consistent than in previous models; elastic values were in the range $-4^\circ < \phi < +14^\circ$, plastic-elastic values $-8^\circ < \phi < 34^\circ$.

The results for the crown, $\phi = 90^\circ$, model No. 5 are shown in Fig. 6.78. The elastic values agree with 2-d photoelastic results to within 11%. First yield occurred near to the HAZ/parent plate boundary at $\epsilon_{\text{nom}}/\epsilon_y = 0.265$. The yield strain in the model was 0.214% - considerably lower than in $\phi = 120^\circ$ models with uncontrolled welds. Three further load stations were used to study the changes, in magnitude and position, of SNCFs. A unique feature in this model was that up to $\epsilon_{\text{nom}}/\epsilon_y = 0.35$, the SNCF at the weld toe increased by only 7%. The maximum strain indices in the HAZ/plate boundary region increased by more than 225%. Maximum strain indices of between 10 and 11.6 near the weld toe were lower than in $\phi = 120^\circ$ models with uncontrolled welds.

6.5.2.2 Plastic-elastic and Residual Plastic Strains

Distributions of principal plastic-elastic and residual plastic surface strains are shown in Figs. 6.79 to 6.82 for steel models Nos. 2 to 5, respectively. The plastic-elastic strains ϵ_1 were measured at $\epsilon_{\text{nom}} = 0.53 \epsilon_y$, and the residual plastic strains ϵ_1^R were measured at $\epsilon_{\text{nom}} = 0.02 \epsilon_y$, the smallest practical value. The reduction in ϵ_{nom} was therefore $950\mu\epsilon$. In these Figures, hatched areas represent reductions in strains $\epsilon_1 - \epsilon_1^R$ due to elastic memory ϵ^e and plastic reversal ϵ^P .

This data is useful in the prediction of maximum plastic strain range for a particular stress ratio $R = (\text{min/max load}) + 0.04$, i.e. a brace wall stress range of 7 to 200 N/mm². The Figures also define the true extent of plasticity.

6.5.2.3 Elastic and Plastic-Elastic Strain Reductions

The reductions in plastic-elastic strains, due to a reduction of 950 $\mu\epsilon$ in ϵ_{nom} , are shown in Figs. 6.83 to 6.86. The elastic strain response ϵ_1^e calculated from elastic strain indices J_1 and strain range ($\Delta\epsilon_{\text{nom}} = 950\mu\epsilon$) are also shown. The difference in these quantities, given by EF in Fig. 6.74, represents the magnitudes of plastic reversal strains ϵ^p in the model - shown hatched in Figs. 6.83 to 6.86.

Plastic reversal strains are greatest, up to 0.4%, in the heat treated model No. 3 at the positions corresponding to the large plastic strains in Fig. 6.76. Absolute values are uncertain because they are computed from 4 measurements, i.e. $\epsilon^p = (\epsilon_1 - \epsilon_1^r) - J_1 \Delta\epsilon_{\text{nom}}$. Thus, the true extent and magnitude of plastic reversal in models Nos. 4 and 5 may be disguised in the (inevitable) errors.

6.5.3 Sub-surface Chord Wall Strains

Sub-surface distributions of elastic and plastic-elastic strain indices J_{xx} are shown in Fig. 6.87 for depths of 0.04T (= 2 mm), 0.08T and 0.16T from the outside chord wall. These are, respectively, lines B - B', C - C' and D - D' in Fig. 5.5. The distributions show the positions of maximum J_{xx} at three different depths and illustrate the manner of plastic growth in the models - narrow bands of large plastic strain between essentially elastic regions.

Fig. 6.87 also gives the positions of the most useful through-thickness line of analysis - E - E' in Fig. 5.5. Line E - E' was defined by the positions of \hat{J}_{xx} at each depth.

6.5.4 Through-thickness Chord Wall Principal Strains

Fig. 6.88 shows the position of the line of analysis E - E' in which principal plastic-elastic strains were maximum. The angular position of this line was $\varphi = 32^\circ \approx \alpha/2$.

Distributions of elastic and plastic-elastic J_1 , J_2 and ϕ are shown. It is assumed that line E - E' approximates to the direction of early fatigue crack growth. The smaller strains are, in general, not significant. The direction ϕ of J_1 (\blacktriangledown symbols) is almost perpendicular to E - E', i.e. $32^\circ - \phi$ is small.

6.6 Plastic-Elastic Strain Concentration Factors, SNCF

6.6.1 Definitions of SNCFs

The plastic-elastic strain indices distributions, shown in Figs. 6.75 to 6.78, are characteristically similar to the elastic stress distribution curves. It is therefore convenient to define SNCFs in a manner similar to SCFs. The maximum value of J_1 is the SNCF. A shell strain concentration factor, SNCF_s is obtained by linear extrapolation of surface strain indices to the weld toe.

6.6.2 Maximum SNCF

Values for SNCF are given in Table 6.6 for each load station shown in Fig. 6.89. The variations in SNCF with loading are shown in Fig. 6.90. It is assumed that the models' behaviour is linearly elastic between a and b, and the onset of yielding is at b. The curves show the effects of heat treatment, weld profile, ψ and loading on SNCFs.

In the models with uncontrolled profiles, the rate of increase in SNCF (\hat{J}_1) with load, and the load at which yielding takes place - between $\epsilon_{\text{nom}}/\epsilon_y = 0.2$ to 0.3 - appear to be independent of heat treatment and ψ . The rate of change in plastic-elastic SNCFs is fairly uniform, as shown ($\Delta \bullet$ symbols) and assumed ($\circ \odot$ symbols), in different models.

6.6.3 Shell SNCFs

Shell SNCFs are obtained from the extrapolation of surface strains outside the plastic zone. The variation of $SNCF_s$ with load, given in Table 6.6, shows the effects of strain redistribution during yielding. The results show decreases in $SNCF_s$ of between 5% and 15% at the onset of yielding and further differences, from elastic values, at higher loads.

Because shell factors are extrapolations from elastic strains (albeit modified by plastic behaviour in the model) they were used to determine elastic shell SCFs K_{S1} (the value of $K_{S2} \approx 0$). They are compared, in Table 6.6, with values obtained in 2-d photoelastic models. The agreement with elastic calculated values is within 15%.

6.7 Extent of Plastic Regions

Regions of plastic deformation were traced from residual moire fringe patterns at loads corresponding to $\epsilon_{nom}/\epsilon_{yield} = 0.02$ after initial and gross yielding. It is assumed that the extents of residual plastic strains are equal in area to the extents of plastic-elastic strains. Contours of plastic deformation are shown in Figs. 6.91 to 6.94 for steel models Nos. 2 to 5, respectively. They show plasticity spreading more rapidly in the parent plate than in the weld. In all models plasticity was partially arrested in the HAZs. As a result, plastic deformation in the weld extended for less than 2.5 mm from the toe.

6.8 The Effect of Out-of-Plane Strains on In-Plane Strains

In moire interferometry, out-of-plane rotations ω or undulations in the surfaces of the models cause extraneous fringe gradients and apparent strains $\epsilon' = 1 - \cos \omega$. To determine the magnitude of ω ,

surface measurements were made, using Talysurf apparatus, on one of the models in an unloaded condition in which residual plasticity was present. The surface profiles given in Fig. 6.95 show lateral contractions, in the order of $20 \mu\text{m}$ ($10 \mu\text{m}$ per face), in the regions of plasticity relative to undeformed regions remote from these areas. In the chord wall plate (beyond the region of in-plane plastic deformation) relative lateral contractions, also about $20 \mu\text{m}$ were measured. The resulting undulations in the surface of the model were $\omega = \pm 0.15^\circ$. The extraneous strain ϵ' was thus $4 \mu\epsilon$. Although this is a negligible quantity, it is important to show that out-of-plane Poisson effects were considered.

Table 6.1 Empirical Constants and Exponents for Geometric and Notch
Through-thickness Stress Distributions

Crown Position of Single plane K90/45 Joint: $\phi = \theta = 90^\circ$

Weld Profile Parameters			Geometric Stress		Notch Stress	
H/T	r_c/T	α_c	K_g	q	C	m
0.183	0.05	78°	+3.60	-15.30	+0.17	-0.333
"	"	54°	+3.40	-11.20	+0.25	-0.290
"	"	0°	+2.18	-4.34	+1.00	0
0.25	0.05	72°	+3.45	-14.30	+0.26	-0.295
"	"	54°	+3.23	-10.75	+0.32	-0.267
"	"	36°	+2.85	-5.10	+0.41	-0.222
"	"	24°	+2.63	-6.80	+0.60	-0.150
"	"	0°	+2.07	-4.12	+1.00	0
0.50	0.05	54°	+2.83	-9.47	+0.29	-0.260
"	"	36°	+2.17	-6.30	+0.38	-0.240
"	"	0°	+1.85	-3.43	+1.00	0
0.25	0.02	69°	+4.73	-25.8	+0.02	-0.320
"	"	72°	+4.30	-23.3	+0.16	-0.300
"	0.10	74°	+3.45	-13.8	+0.35	-0.282
"	0.20	83°	+3.46	-13.5	+0.59	-0.187
0.25	0.02	48°	+4.06	-13.7	+0.22	-0.250
"	0.033	"	+3.07	-9.4	+0.40	-0.255
"	0.05	"	+3.05	-9.8	+0.38	-0.242
"	0.10	50°	+2.91	-9.6	+0.42	-0.250

Note

for $\alpha = 0^\circ$ $K_g = K_s$

Stress Concentration Factors - Magnitudes, Positions, and Shell and Notch Components

Joint No.	Brace Angle θ	Local Angle ϕ	OUTSIDE BRACE FILLET					OUTSIDE CHORD FILLET					INTERNAL FILLET		INSIDE CHORD
			Value			Position	Notch Zone	Value			Position	Notch Zone	Value	Position	Value
			K_{sob}	K_{ob}	K_{nob}	θ_b	Z_b	K_{soc}	K_{oc}	K_{noc}	θ_c	Z_c	K_i	θ_i	K_{ic}
1	135°	45°	+1.60	+2.44	1.52	10°	0.56t	+1.15	+1.52	1.33	0°	0.16T	+1.72	20°-30°	-0.36
2a	135°	135°	+3.15	+3.40	1.08	15°	0.20t	+1.85	-3.05	1.65	12°-25°	0.18T	-1.28 ¹	70°	-0.67
2b	90°	90°	+2.82	+3.32	1.18	10°-15°	0.32t	-1.13	-1	-1	-1	-1	+2.04	55°	-2.12
3	90°	90°	+1.91	+2.49	1.30	15°-20°	0.50t	+1.63	-2.26	1.39	5°	0.20T	+1.63 ¹	45°	-1.38
7	90°	120°	+1.76	+2.19	1.24	10°	0.30t	+2.05	-2.97	1.45	28°	0.15T	+2.05 ¹	85°	-1.07
8a	90°	120°	+3.18	+4.03	1.27	13°	0.38t	+3.40	-4.52	1.33	20°	0.15T	+2.49 ¹	80°	-2.05
10	135°	120°	+1.70	+1.52 ²	<1	-2	-2	+1.35	+2.35	1.74	25°	0.12T	-1.25 ¹	70°	-0.68
11a	135°	120°	+1.50	+1.96	1.31	5°-15°	0.65t	+1.50	+2.56	1.70	18°	0.35T	+0.90 ¹	120°	-0.76

Note 1: Point of surface contraflexure occurs within fillet

Note 2: Maximum stress index does not occur within fillet

Three-Dimensional Model Ref. CK1^R

Stress Concentration Factors - Magnitudes, Positions, and Shell and Notch Components

Joint No.	Brace Angle θ	Local Angle ϕ	OUTSIDE BRACE FILLET					OUTSIDE CHORD FILLET					INTERNAL FILLET		INSIDE CHORD
			Value			Position	Notch Zone	Value			Position	Notch Zone	Value	Position	Value
			K_{sob}	K_{ob}	K_{nob}	θ_b	Z_b	K_{soc}	K_{oc}	K_{noc}	θ_c	Z_c	K_i	θ_i	K_{ic}
1	135°	45°	+1.65	+2.80	1.70	18°	0.28t	+1.20	+2.50	2.08	8°	0.14T	+2.40	0°-10°	-0.45
2a	135°	135°	+3.20	+5.15	1.61	15°	0.34t	+2.60	+4.03	1.55	15°	0.17T	-1.60 ¹	75°	-1.04
2b	90°	90°	+2.90	+3.59	1.75	13°	0.20t	-1.07	-1	-1	-1	-1	+2.26	40°	-2.28
3	90°	90°	+2.19	+3.14	1.43	15°	0.22t	+1.70	+2.52	1.48	20°	0.15T	+2.05 ¹	55°	-1.35
7	90°	120°	+1.13	+1.67	1.48	10°	0.28t	+1.70	+2.83	1.67	30°	0.18T	+1.48	55°	-0.43
8a	90°	120°	+4.31	+4.95	1.15	5°-15°	0.40t	+4.60	+6.25	1.36	8°	0.20T	+3.11 ¹	120°	-3.20
10	135°	120°	+1.10	+1.75	1.59	6°	0.44t	+1.35	+2.50	1.85	15°-25°	0.23T	-1.47 ¹	40°	-0.71
11a	135°	120°	+1.58	+2.30	1.45	5°	0.37t	+1.65	+2.83	1.75	10°	0.27T	+1.20 ¹	120°	-0.73

Note 1: Point of surface contraflexure occurs within fillet

Loaded braces = 90° and 135°

Brace gap g = 1.25T

Three-Dimensional Model Ref. CK2

Stress Concentration Factors - Magnitudes, Positions, and Shell and Notch Components

Joint No.	Brace Angle θ	Local Angle ϕ	OUTSIDE BRACE FILLET					OUTSIDE CHORD FILLET					INTERNAL FILLET		INSIDE CHORD
			Value			Position	Notch Zone	Value			Position	Notch Zone	Value	Position	Value
			K_{sob}	K_{ob}	K_{nob}	θ_b	Z_b	K_{soc}	K_{oc}	K_{noc}	θ_c	Z_c	K_i	θ_i	K_{ic}
4	150°	30°	+2.35	+3.90	1.66	4°-10°	0.60t	+0.65	+1.35	2.07	53°	0.20T	+2.70	5°	-0.70
5a	150°	150°	+2.13	+2.90 ²	1.36	-	0.32t	+1.00	+1.30	1.30	15°	0.18T	-1.60	80°	-0.42
5b	60°	120°	+2.46	+3.38	1.37	5°	0.43t	-0.35	-1	-1	-1	-1	+2.00 ¹	55°	-1.63
6	60°	60°	+1.60	+2.25	1.40	20°-45°	0.30t	+0.73	+1.73	2.38	53°	0.14T	+1.74	23°	-1.35
8b	60°	120°	+1.39	+2.60	1.87	0°	0.21t	+1.30	+2.46	1.89	10°	0.18T	+2.08	75°	-1.13
9	60°	120°	+2.20	+2.98	1.35	7°	0.34t	+2.14	+4.07	1.89	13°	0.23T	+3.11	90°	-1.58
11b	150°	120°	+1.20	+1.82	1.52	3°	0.40t	0	+0.70	-	30°	-	-1.10 ¹	70°	-0.63
12	150°	120°	+1.80	+2.12	1.18	0°	0.32t	+1.48	+2.44	1.65	7°-10°	0.20T	-1.86 ¹	60°	-1.23

Note 1: Point of the surface contraflexure occurs within fillet

Note 2: Approximate value

Loaded braces = 60° and 150°

Brace gap g = 1.25T

Table 6.2

Stress Concentration Factors - Magnitudes, Positions, and Shell and Notch Components

Joint No.	Brace Angle ψ	Local Angle ϕ	OUTSIDE BRACE FILLET					OUTSIDE CHORD FILLET					INTERNAL FILLET		INSIDE CHORD
			Value			Position	Notch Zone	Value			Position	Notch Zone	Value	Position	Value
			K_{sob}	K_{ob}	K_{nob}	θ_b	Z_b	K_{soc}	K_{oc}	K_{noc}	θ_c	Z_c	K_i	θ_i	K_{ic}
1	135°	45°	+1.62	+2.75	1.70	8°	0.33t	+1.05	+1.85	1.76	4°-8°	0.33T	+2.29	35°	-0.40
2a	135°	135°	+2.50	+3.68	1.47	8°	0.80t	+3.77	+4.03	1.07	8°	0.09T	-1.07 ¹	90°	-0.95
2t	90°	90°	+2.19	+2.97	1.35	25°	0.52t	+0.14	+1.77	-	18°	0.26T	+1.87	50°	-2.34
3	90°	90°	+2.22	+3.25	1.46	15°	0.25t	+1.92	+3.13	1.63	10°	0.26T	+1.70 ¹	40°	-1.44
7	90°	120°	+1.27	+1.92	1.51	6°	0.30t	+1.70	+2.46	1.44	12°	0.08T	+1.77	85°-96°	-0.82
8a	90°	120°	+4.48	+5.40	1.21	8°	0.46t	+3.46	+5.83	1.68	7°-15°	0.36T	+3.11 ¹	60°	-2.36
10	135°	120°	+1.32	+2.00	1.52	10°	0.35t	+1.20	+2.54	2.12	20°	0.23T	-1.55	45°	-0.78
11a	135°	120°	+2.61	+2.96	1.14	0°-15°	0.20t	+2.40	+3.58	1.49	10°-15°	0.36T	-1.35 ¹	0°	-1.37

Note 1: Point of the surface contraflexure occurs within fillet

Loaded braces = 90° and 135°

Brace gap g = 3.875T

Three-Dimensional Model Ref. CK4

Stress Concentration Factors - Magnitudes, Positions, and Shell and Notch Components

Joint No.	Brace Angle ψ	Local Angle ϕ	OUTSIDE BRACE FILLET					OUTSIDE CHORD FILLET					INTERNAL FILLET		INSIDE CHORD
			Value			Position	Notch Zone	Value			Position	Notch Zone	Value	Position	Value
			K_{sob}	K_{ob}	K_{nob}	θ_b	Z_b	K_{soc}	K_{oc}	K_{noc}	θ_c	Z_c	K_i	θ_i	K_{ic}
4	150°	30°	+1.72	+3.06	1.78	22°	0.38t	+0.50	+1.19	2.38	56°	0.20T	+1.65	20°-30°	-0.54
5a	150°	150°	+2.63	+3.11	1.18	8°	0.30t	+2.40	+3.10	1.29	7°	0.18T	-1.50	80°	-0.77
5b	60°	120°	+2.24	+2.91	1.30	10°-15°	0.36t	+1.61	+2.63	1.63	10°-15°	0.16T	+1.55 ¹	60°	-2.16
6	60°	60°	+1.55	+3.03	1.96	15°	0.44t	+1.00	+2.00	2.00	10°-15°	0.23T	+1.38	22°	-1.48
8b	60°	120°	+1.68	+2.60	1.55	8°	0.40t	+2.35	+3.30	1.40	15°	0.14T	+1.71	90°	-1.42
9	60°	120°	+2.18	+3.04	1.40	12°	0.16t	+2.08	+3.46	1.66	17°	0.17T	+2.46	90°	-1.47
11b	150°	120°	+1.20	+1.64	1.37	10°	0.29t	+1.76	+2.62	1.49	13°	0.09T	-1.33 ¹	45°-55°	-0.73
12	150°	120°	+1.40	+1.48	1.06	5°	0.15t	+1.06	+1.76	1.66	22°	0.25T	-1.03	45°	-0.47

Note 1: Point of surface contraflexure occurs within fillet

Loaded braces = 60° and 150°

Brace gap g = 3.875T

Three-Dimensional Model Ref. CK5

Stress Concentration Factors - Magnitudes, Positions, and Shell and Notch Components

Joint No.	Brace Angle ψ	Local Angle ϕ	OUTSIDE BRACE FILLET					OUTSIDE CHORD FILLET					INTERNAL FILLET		INSIDE CHORD
			Value			Position	Notch Zone	Value			Position	Notch Zone	Value	Position	Value
			K_{sob}	K_{ob}	K_{nob}	θ_b	Z_b	K_{soc}	K_{oc}	K_{noc}	θ_c	Z_c	K_i	θ_i	K_{ic}
4	150°	30°	+2.20	+3.76	1.71	16°	0.63t	+0.67	+1.61	2.40	20°	0.06T	+2.15	15°	-0.43
5a	150°	150°	+2.90	+2.95	1.02	4°-8°	0	+2.95	+3.44	1.17	8°	0.10T	-1.75	110°	-0.42
5b	60°	120°	+2.32	+3.15	1.36	10°-15°	0.42t	+1.05	+2.20	2.09	18°	0.12T	+1.55 ¹	45°	-2.20
6	60°	60°	+1.80	+2.60	1.44	20°	0.35t	+1.05	See Note 2	-	-	-	+1.40	30°	-1.32
8b	60°	120°	+2.35	+3.55	1.51	15°	0.17t	+3.13	+3.73	1.20	10°	0.13T	+2.50 ¹	75°	-2.49
9	60°	120°	+1.20	+1.90	1.56	7°-12°	0.11t	+1.18	+2.25	1.91	12°	0.08T	+2.22	95°	-1.10
11b	150°	120°	+1.05	+1.72	1.64	15°	0.16t	+1.52	+2.02	1.33	15°-20°	0.05T	-1.30	65°	-0.73
12	150°	120°	+0.90	+0.95	1.06	5°-10°	0	+1.10	+1.92	1.74	10°	0.11T	-0.88	40°	-0.40

Note 1: Point of surface contraflexure occurs within fillet

Note 2: No result due to presence of photoelastic inclusion

Loaded braces = 60° and 150°

Brace gap g = 6.50T

Table 6.2 (cont.)

Table 6.2 Three-Dimensional Models Ref. X90 and X60.

Stress Concentration Factors - Magnitudes, Positions, and Shell and Notch Components

Model	Ref Position	Joint Parameters τ ϕ Weld ¹	OUTSIDE BRACE FILLET				OUTSIDE CHORD FILLET				INTERNAL FILLET		INSIDE CHORD						
			Value	K_{sob}	K_{ob}	K_{nob}	ϕ_c	Pos. Zone	Notch Zone	Value	K_{oc}	K_{nob}	ϕ_c	Pos. Zone	Value	K_i	ϕ_i	Value	K_{ic}
X90	Crown	90° U	+2.37	-2	-	-	0.45t	-	-	-	0.95T	-	-	-	-	-	-	+0.6	-
		" C	+2.25	-	-	-	0.40t	-	-	-	0.32T	-	-	-	-	-	-	+0.9	-
	Saddle	120° U	+8.15	-	-	-	0.30t	-	-	-	0.65T	-	-	-	-	-	-	-5.4	-
		" C	+8.00	-	-	-	0.28t	-	-	-	0.46T	-	-	-	-	-	-	-5.0	-
Crown	90° U	+1.75	-	-	-	0.40t	-	-	-	0.35T	-	-	-	-	-	-	+0.2	-	
	" C	+1.67	-	-	-	0.35t	-	-	-	0.28T	-	-	-	-	-	-	+0.2	-	
Saddle	120° U	+4.25	-	-	-	0.35t	-	-	-	0.33T	-	-	-	-	-	-	-2.3	-	
	" C	+6.13	-	-	-	0.17t	-	-	-	0.45T	-	-	-	-	-	-	-3.3	-	
X60	Crown	60° U	+1.35	+2.65	1.96	1.96	18°	0.40t	-	-	0.26T	+0.5	60°	+0.5	60°	+0.5	+0.5	-	-
		" C	+1.45	+2.52	1.74	1.74	15°	0.46t	-	-	0.21T	+0.6	60°	+0.6	60°	+0.6	+0.7	-	-
	Saddle	120° U	+3.25	+3.71	1.14	1.14	10°	0.50t	-	-	0.20T	-4.7	0°	-4.7	0°	-4.7	+0.9	-	-
		" C	+2.72	+3.65	1.34	1.34	10°	0.45t	-	-	0.30T	-5.2	0°	-5.2	0°	-5.2	+1.2	-	-
Saddle	0.5 U	+4.65	+5.90	1.27	1.27	12°	0.40t	-	-	0.22T	-3.6	5°	-3.6	5°	-3.6	-3.3	-	-	
	" C	+5.10	+6.75	1.32	1.32	12°	0.40t	-	-	0.23T	-4.0	18°	-4.0	18°	-4.0	-3.1	-	-	

Note 1: U = uncontrolled; C = controlled weld profile

Note 2: No values for K_{ob} , K_{oc} , K_i , ϕ_b , ϕ_c and ϕ_i available for X90 model.

Table 6.4 2-d Photoelastic and F.E. Results

Constants of Empirical Equations for K and K_n

Peak SCF $K = A(r/T)^j$

Notch SCF $K_n = 1 + B(r/T)^k$ All H/T = 0.25 except ¹ where H/T = r/T

Joint		Weld	Peak SCF Constants		Notch SCF Constants		
Position	Node	Quality	a_c	A	J	B_c	k_c
Saddle	X	Uncontrolled fillet	45°	+8.6	-0.27	+0.36	-0.42
	K		"	+3.4	-0.25	+0.70	-0.30
Crown	K	Uncontrolled fillet	70°	+3.3	-0.30	+0.82	-0.36
	"		72°	+3.1	-0.35	+0.74	-0.50
	"	"	48°	+2.75	-0.30	+0.63	-0.42
	"	Fully blended ¹	90°	+2.0	-0.54	+0.37	-0.75

Table 6.5

Axial and Bending Stress Component of Shell SCF.

Source	Brace angles		Proximity	Gap R'/T	At Chord Weld Toe			At Brace Weld Toe		
	θ	\downarrow			Axial $K_{s0c(a)}$	Bending $K_{s0c(b)}$	Total	Axial $K_{s0c(a)}$	Bending $K_{s0c(b)}$	Total
Fig. 6.44	135°	45°	Remote	0.71	+0.20	+1.00	+1.20	+0.65	+1.00	+1.65
				3.00	+0.25	+0.80	+1.05	+0.75	+0.85	+1.60
	90°	90°	Near	"	+0.85	+1.75	+2.60	+0.90	+2.30	+3.20
				"	+1.30	+2.45	+3.75	+1.05	+1.75	+2.80
Fig. 6.45	150°	30°	Remote	0.51	+0.10	+0.55	+0.65	+1.25	+1.15	+2.40
				3.00	-0.10	+0.30	+0.20	+0.90	+0.85	+1.75
	60°	150°	Near ¹	"	+0.10	+0.55	+0.65	+1.05	+1.15	+2.20
				"	+0.30	+0.70	+1.00	+0.45	+1.50	+1.95
Fig. 6.46	60°	120°	Remote	0.64	+0.10	+0.55	+0.65	+1.25	+1.15	+2.40
				3.00	-0.10	+0.30	+0.20	+0.90	+0.85	+1.75
	90°	120°	Near	"	+0.10	+0.55	+0.65	+1.05	+1.15	+2.20
				"	+0.30	+0.70	+1.00	+0.45	+1.50	+1.95
Fig. 6.46	60°	120°	Remote	0.64	+0.25	+0.95	+1.20	+0.60	+0.90	+1.50
				3.00	+0.25	+1.25	+1.50	+0.60	+1.00	+1.60
	90°	120°	Near	"	-0.10	+0.10	0	+1.35	+1.10	+2.45
				"	-0.45	+2.15	+1.70	+1.00	+1.25	+2.25
Fig. 6.46	60°	120°	Remote	0.64	+0.25	+0.95	+1.20	+0.60	+0.90	+1.50
				3.00	+0.25	+1.25	+1.50	+0.60	+1.00	+1.60
	90°	120°	Near	"	-0.15	+1.65	+1.50	+0.90	+1.40	+2.30
				"	+0.25	+0.95	+1.20	+0.60	+0.90	+1.50
Fig. 6.46	60°	120°	Remote	0.64	+0.25	+1.90	+2.15	+0.65	+1.60	+2.25
				3.00	+0.45	+1.65	+2.10	+0.65	+1.55	+2.20
	90°	120°	Near	"	+0.20	+1.00	+1.20	+0.45	+0.75	+1.20
				"	+0.25	+1.00	+1.25	+0.40	+1.10	+1.50
Fig. 6.46	60°	120°	Remote	0.64	+0.25	+1.90	+2.15	+0.65	+1.60	+2.25
				3.00	+0.45	+1.65	+2.10	+0.65	+1.55	+2.20
	90°	120°	Near	"	+0.20	+1.00	+1.20	+0.45	+0.75	+1.20
				"	+0.25	+1.00	+1.25	+0.40	+1.10	+1.50
Fig. 6.46	60°	120°	Remote	0.64	+0.25	+1.90	+2.15	+0.65	+1.60	+2.25
				3.00	+0.45	+1.65	+2.10	+0.65	+1.55	+2.20
	90°	120°	Near	"	+0.20	+1.00	+1.20	+0.45	+0.75	+1.20
				"	+0.25	+1.00	+1.25	+0.40	+1.10	+1.50
Fig. 6.46	60°	120°	Remote	0.64	+0.25	+1.90	+2.15	+0.65	+1.60	+2.25
				3.00	+0.45	+1.65	+2.10	+0.65	+1.55	+2.20
	90°	120°	Near	"	+0.20	+1.00	+1.20	+0.45	+0.75	+1.20
				"	+0.25	+1.00	+1.25	+0.40	+1.10	+1.50
Fig. 6.46	60°	120°	Remote	0.64	+0.25	+1.90	+2.15	+0.65	+1.60	+2.25
				3.00	+0.45	+1.65	+2.10	+0.65	+1.55	+2.20
	90°	120°	Near	"	+0.20	+1.00	+1.20	+0.45	+0.75	+1.20
				"	+0.25	+1.00	+1.25	+0.40	+1.10	+1.50
Fig. 6.46	60°	120°	Remote	0.64	+0.25	+1.90	+2.15	+0.65	+1.60	+2.25
				3.00	+0.45	+1.65	+2.10	+0.65	+1.55	+2.20
	90°	120°	Near	"	+0.20	+1.00	+1.20	+0.45	+0.75	+1.20
				"	+0.25	+1.00	+1.25	+0.40	+1.10	+1.50
Fig. 6.46	60°	120°	Remote	0.64	+0.25	+1.90	+2.15	+0.65	+1.60	+2.25
				3.00	+0.45	+1.65	+2.10	+0.65	+1.55	+2.20
	90°	120°	Near	"	+0.20	+1.00	+1.20	+0.45	+0.75	+1.20
				"	+0.25	+1.00	+1.25	+0.40	+1.10	+1.50
Fig. 6.46	60°	120°	Remote	0.64	+0.25	+1.90	+2.15	+0.65	+1.60	+2.25
				3.00	+0.45	+1.65	+2.10	+0.65	+1.55	+2.20
	90°	120°	Near	"	+0.20	+1.00	+1.20	+0.45	+0.75	+1.20
				"	+0.25	+1.00	+1.25	+0.40	+1.10	+1.50
Fig. 6.46	60°	120°	Remote	0.64	+0.25	+1.90	+2.15	+0.65	+1.60	+2.25
				3.00	+0.45	+1.65	+2.10	+0.65	+1.55	+2.20
	90°	120°	Near	"	+0.20	+1.00	+1.20	+0.45	+0.75	+1.20
				"	+0.25	+1.00	+1.25	+0.40	+1.10	+1.50
Fig. 6.46	60°	120°	Remote	0.64	+0.25	+1.90	+2.15	+0.65	+1.60	+2.25
				3.00	+0.45	+1.65	+2.10	+0.65	+1.55	+2.20
	90°	120°	Near	"	+0.20	+1.00	+1.20	+0.45	+0.75	+1.20
				"	+0.25	+1.00	+1.25	+0.40	+1.10	+1.50
Fig. 6.46	60°	120°	Remote	0.64	+0.25	+1.90	+2.15	+0.65	+1.60	+2.25
				3.00	+0.45	+1.65	+2.10	+0.65	+1.55	+2.20
	90°	120°	Near	"	+0.20	+1.00	+1.20	+0.45	+0.75	+1.20
				"	+0.25	+1.00	+1.25	+0.40	+1.10	+1.50
Fig. 6.46	60°	120°	Remote	0.64	+0.25	+1.90	+2.15	+0.65	+1.60	+2.25
				3.00	+0.45	+1.65	+2.10	+0.65	+1.55	+2.20
	90°	120°	Near	"	+0.20	+1.00	+1.20	+0.45	+0.75	+1.20
				"	+0.25	+1.00	+1.25	+0.40	+1.10	+1.50
Fig. 6.46	60°	120°	Remote	0.64	+0.25	+1.90	+2.15	+0.65	+1.60	+2.25
				3.00	+0.45	+1.65	+2.10	+0.65	+1.55	+2.20
	90°	120°	Near	"	+0.20	+1.00	+1.20	+0.45	+0.75	+1.20
				"	+0.25	+1.00	+1.25	+0.40	+1.10	+1.50
Fig. 6.46	60°	120°	Remote	0.64	+0.25	+1.90	+2.15	+0.65	+1.60	+2.25
				3.00	+0.45	+1.65	+2.10	+0.65	+1.55	+2.20
	90°	120°	Near	"	+0.20	+1.00	+1.20	+0.45	+0.75	+1.20
				"	+0.25	+1.00	+1.25	+0.40	+1.10	+1.50
Fig. 6.46	60°	120°	Remote	0.64	+0.25	+1.90	+2.15	+0.65	+1.60	+2.25
				3.00	+0.45	+1.65	+2.10	+0.65	+1.55	+2.20
	90°	120°	Near	"	+0.20	+1.00	+1.20	+0.45	+0.75	+1.20
				"	+0.25	+1.00	+1.25	+0.40	+1.10	+1.50
Fig. 6.46	60°	120°	Remote	0.64	+0.25	+1.90	+2.15	+0.65	+1.60	+2.25
				3.00	+0.45	+1.65	+2.10	+0.65	+1.55	+2.20
	90°	120°	Near	"	+0.20	+1.00	+1.20	+0.45	+0.75	+1.20
				"	+0.25	+1.00	+1.25	+0.40	+1.10	+1.50
Fig. 6.46	60°	120°	Remote	0.64	+0.25	+1.90	+2.15	+0.65	+1.60	+2.25
				3.00	+0.45	+1.65	+2.10	+0.65	+1.55	+2.20
	90°	120°	Near	"	+0.20	+1.00	+1.20	+0.45	+0.75	+1.20
				"	+0.25	+1.00	+1.25	+0.40	+1.10	+1.50
Fig. 6.46	60°	120°	Remote	0.64	+0.25	+1.90	+2.15	+0.65	+1.60	+2.25
				3.00	+0.45	+1.65	+2.10	+0.65	+1.55	+2.20
	90°	120°	Near	"	+0.20	+1.00	+1.20	+0.45	+0.75	+1.20
				"	+0.25	+1.00	+1.25	+0.40	+1.10	+1.50
Fig. 6.46	60°	120°	Remote	0.64	+0.25	+1.90	+2.15	+0.65	+1.60	+2.25
				3.00	+0.45	+1.65	+2.10	+0.65	+1.55	+2.20
	90°	120°	Near	"	+0.20	+1.00	+1.20	+0.45	+0.75	+1.20
				"	+0.25	+1.00	+1.25	+0.40	+1.10	+1.50
Fig. 6.46	60°	120°	Remote	0.64	+0.25	+1.90	+2.15	+0.65	+1.60	+2.25
				3.00	+0.45	+1.65	+2.10	+0.65	+1.55	+2.20
	90°	120°	Near	"	+0.20	+1.00	+1.20	+0.45	+0.75	+1.20
				"	+0.25	+1.00	+1.25	+0.40	+1.10	+1.50
Fig. 6.46	60°	120°	Remote	0.64	+0.25	+1.90	+2.15	+0.65	+1.60	+2.25
				3.00	+0.45	+1.65	+2.10	+0.65	+1.55	+2.20
	90°	120°	Near	"	+0.20	+1.00	+1.20	+0.45	+0.75	+1.20
				"	+0.25	+1.00	+1.25	+0.40	+1.10	+1.50
Fig. 6.46	60°	120°	Remote	0.64	+0.25	+1.90	+2.15	+0.65	+1.60	+2.25
				3.00	+0.45	+1.65	+2.10	+0.65	+1.55	+2.20
	90°	120°	Near	"	+0.20	+1.00	+1.20	+0.45	+0.75	+1.20
				"	+0.25	+1.00	+1.25	+0.40	+1.10	+1.50
Fig. 6.46	60°	120°	Remote	0.64	+0.25	+1.90	+2.15	+0.65	+1.60	+2.25
				3.00	+0.45	+1.65	+2.10	+0.65	+1.55	+2.20
	90°	120°	Near	"	+0.20	+1.00	+1.20	+0.45	+0.75	+1.20
				"	+0.25	+1.00	+1.25	+0.40	+1.10	+1.50
Fig. 6.46	60°	120°	Remote	0.64	+0.25	+1.90	+2.15	+0.65	+1.60	+2.25
				3.00	+0.45	+1.65	+2.10	+0.65	+1.55	+2.20
	90°	120°	Near	"	+0.20	+1.00	+1.20	+0.45	+0.75	+1.20
				"	+0.25	+1.00	+1.25	+0.40	+1.10	+1.50
Fig. 6.46										

Table 6.6

Magnitudes and Positions of Elastic SNCF and SCFs and Plastic-Elastic SNCFs

Steel Model No. 1	Brace Load ² $\epsilon_{nom}/\epsilon_y$	Strain Concentration Factors								SCFs		Note 4 K_s
		SNCF ₁	SNCF ₂	SNCF _{a1}	SNCF _{a2}	SNCF _{n1}	SNCF _{n2}	Pos'n ³ S/T	Calculated K_1	Calculated K_{s1}		
2	0.19	4.60	-1.95	2.20	-0.75	2.1	2.6	0	4.41	2.17	2.5	
	0.28	6.65	-1.00	2.15	-0.60	3.1	1.7	+0.03	-	2.16	-	
	0.53	17.0	-5.4	2.00	-0.50	8.5	10.8	0	-	2.03	-	
3	0.18	3.64	-1.05	2.27	-0.55	1.6	1.9	0	3.65	2.31	2.5	
	0.36	6.00	-0.80	1.95	-0.50	3.1	1.6	+0.01	-	1.98	-	
	0.53	13.0	-5.75	N/A	N/A	N/A	N/A	+0.07	-	N/A	-	
4	0.28	2.65	-0.75	1.55	-0.50	1.7	1.5	0	2.66	1.54	N/A	
	0.53	5.70	-3.10	1.55	-0.50	3.7	6.2	-0.01	-	1.54	-	
	0.63	7.15	-3.45	2.20	-1.20	3.3	2.9	0	-	2.02	-	
	0.73	7.50	-3.60	N/A	N/A	N/A	N/A	0	-	N/A	-	
5	0.21	3.25	-0.95	2.20	-0.65	1.5	1.5	0	3.26	2.20	2.0	
	0.265	4.35	-1.10	2.10	-0.60	2.1	1.8	+0.02	-	2.11	-	
	0.32	5.32	-1.85	2.25	-0.45	2.4	4.1	+0.03	-	2.32	-	
	0.35	7.45	-2.40	N/A	N/A	N/A	N/A	+0.035	-	N/A	-	
	0.52	11.50	-4.30	2.15	-0.40	5.3	10.7	-0.02	-	2.23	-	

- Notes
1. Defined in Section 6.5.2
 2. ϵ_y based on uniaxial $\sigma_y = 381 \text{ N/mm}^2$ in brace wall and $E = 205 \text{ kN/mm}^2$
 3. Measured from weld toe; +ve in chord wall, -ve in weld
 4. Elastic shell SCFs from 2-d photoelastic models.
N/A : not available
Notch strain concentration factor $SNCF_n = SNCF/SNCF_s$

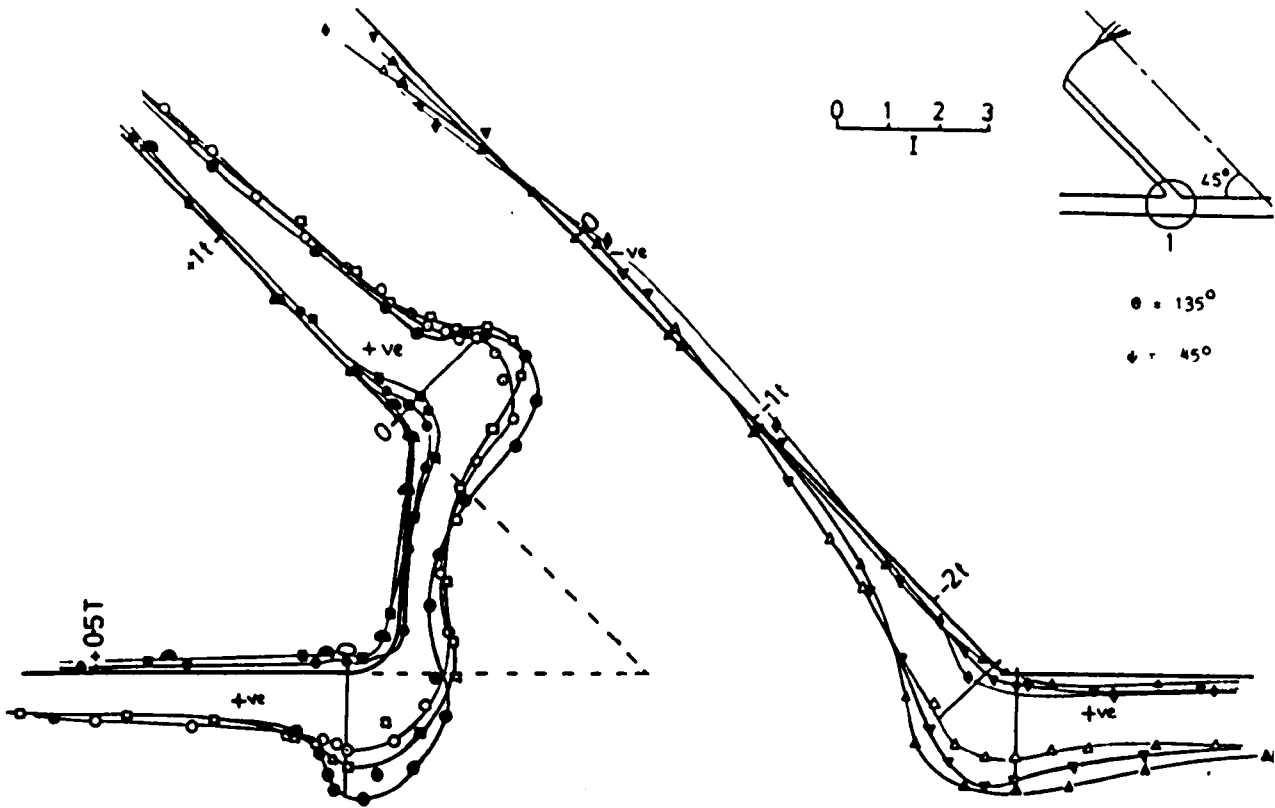


Fig. 6.1 Principal Stresses in CK Models, Junction 1

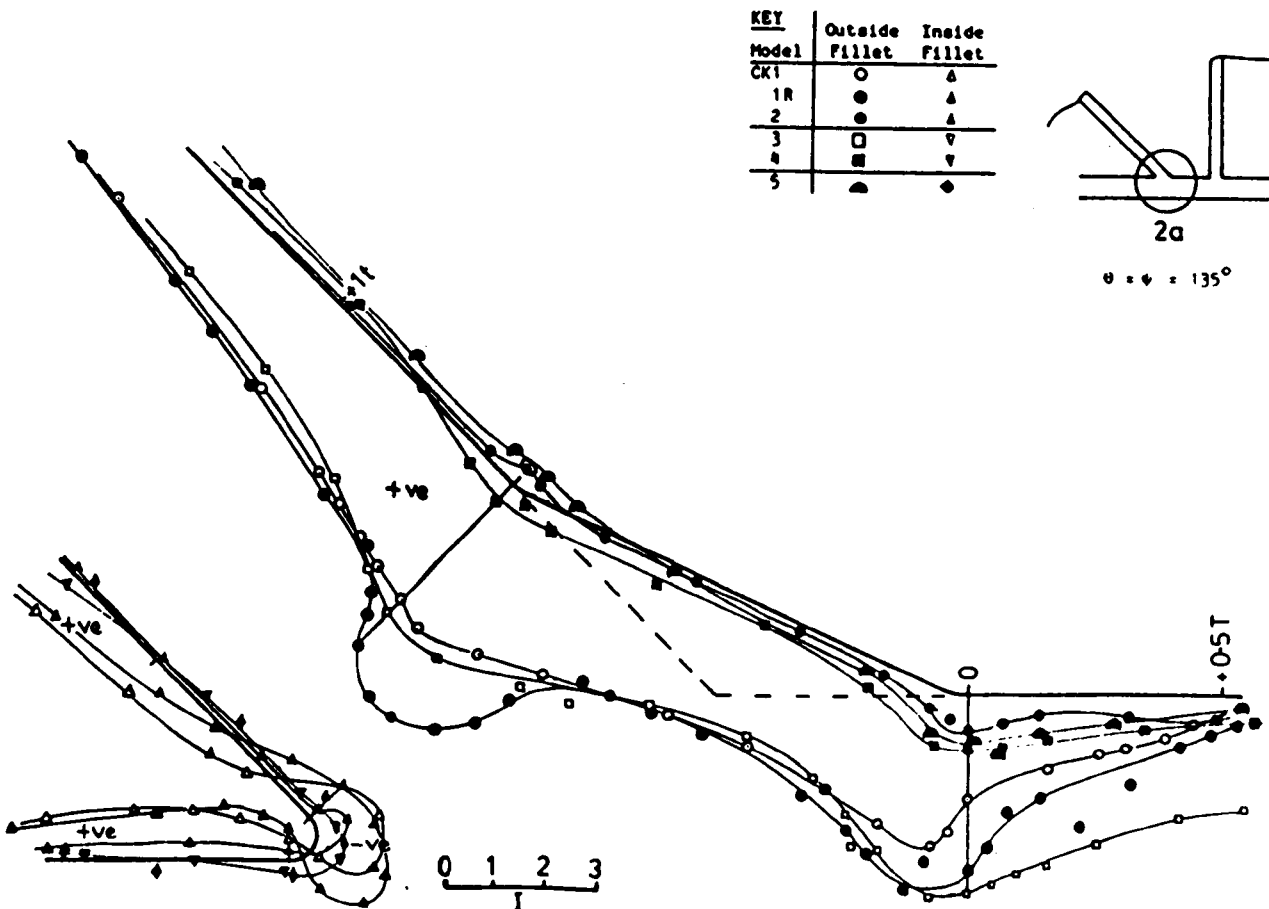


Fig. 6.2 Principal Stresses in CK Models, Junction 2a

KEY	Outside Fillet	Inside Fillet
Model		
CK1	○	△
1R	●	▲
2	●	▲
3	□	▽
4	■	▼
5	▲	◆

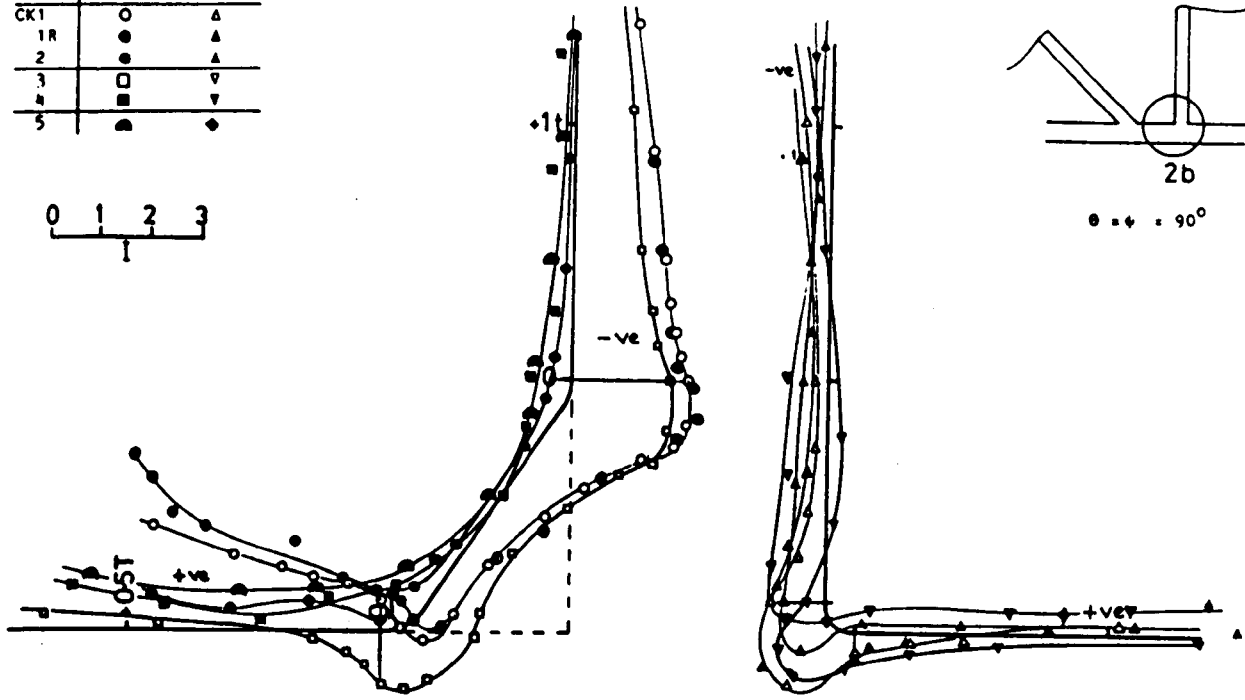
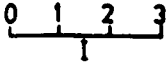


Fig. 6.3 Principal Stresses in CK Models, Junction 2b

KEY	Outside Fillet	Inside Fillet
Model		
CK1	○	△
1R	●	▲
2	●	▲
3	□	▽
4	■	▼
5	▲	◆

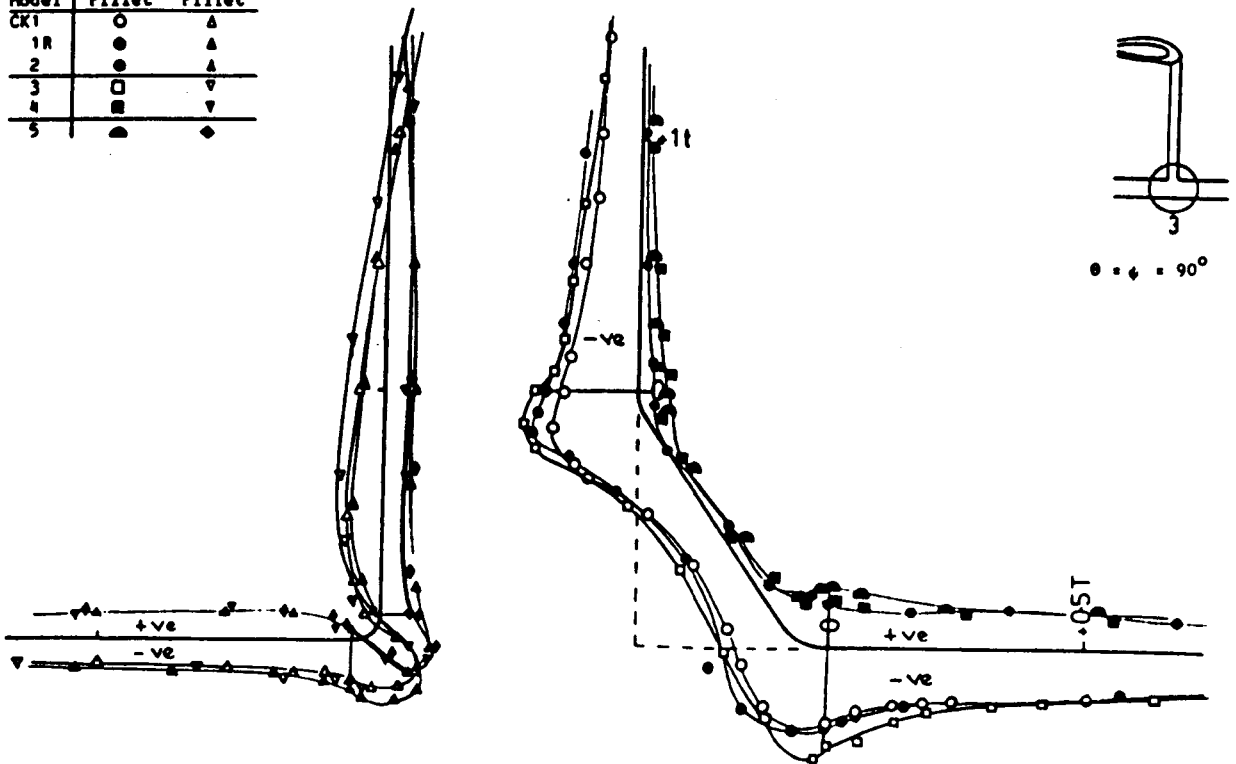


Fig. 6.4 Principal Stresses in CK Models, Junction 3

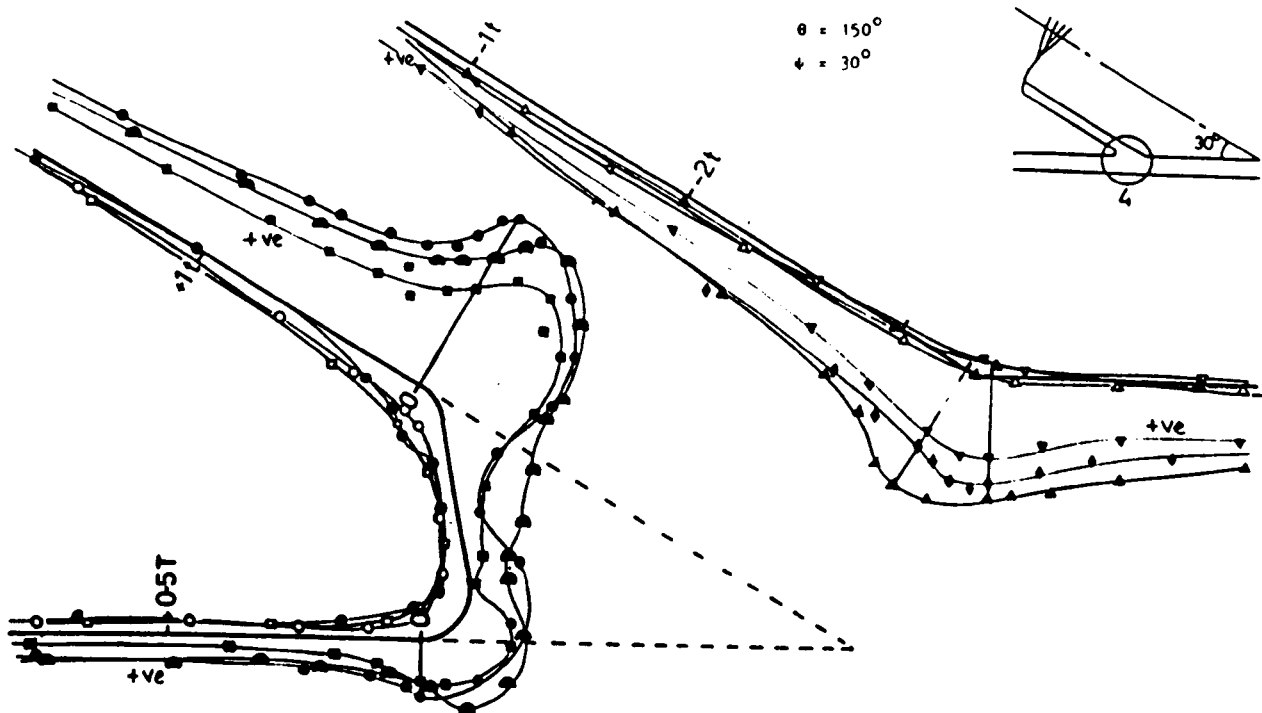


Fig. 6.5 Principal Stresses in CK Models, Junction 4

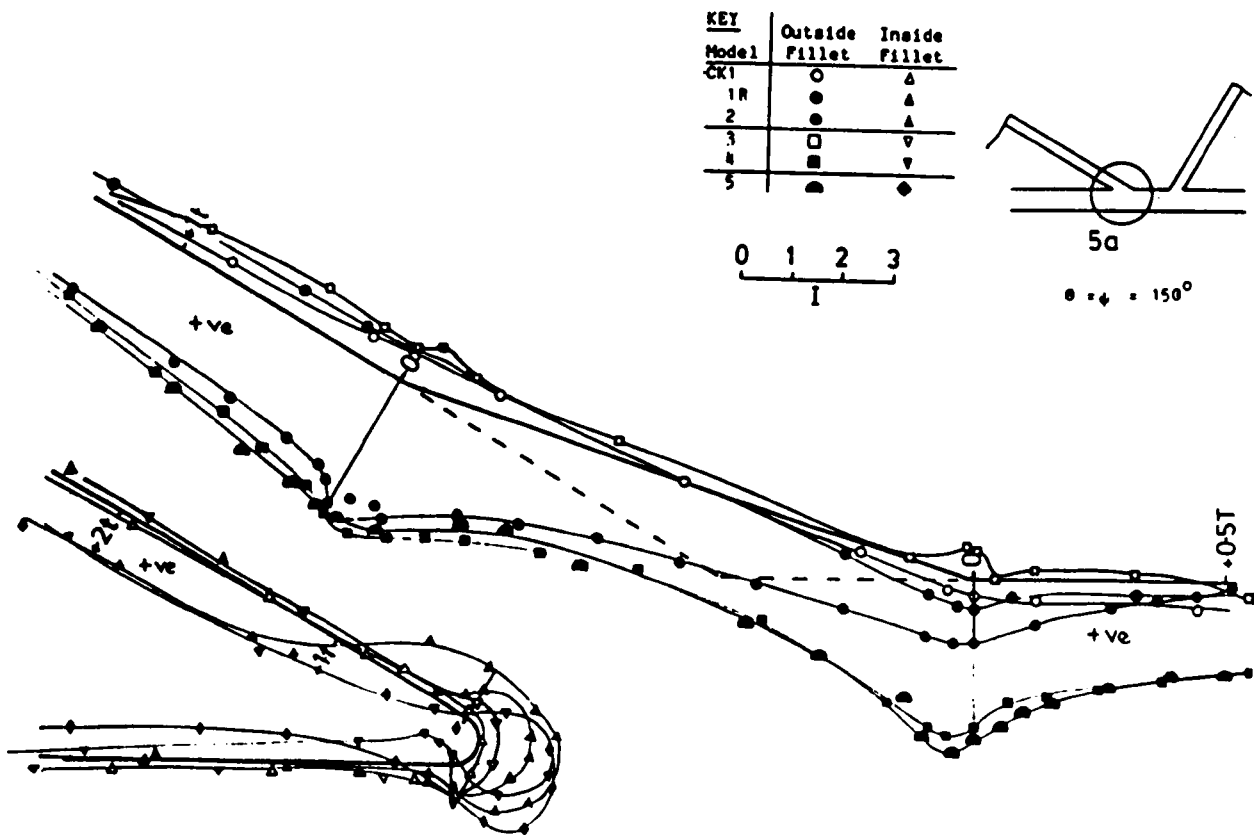


Fig. 6.6 Principal Stresses in CK Models, Junction 5a

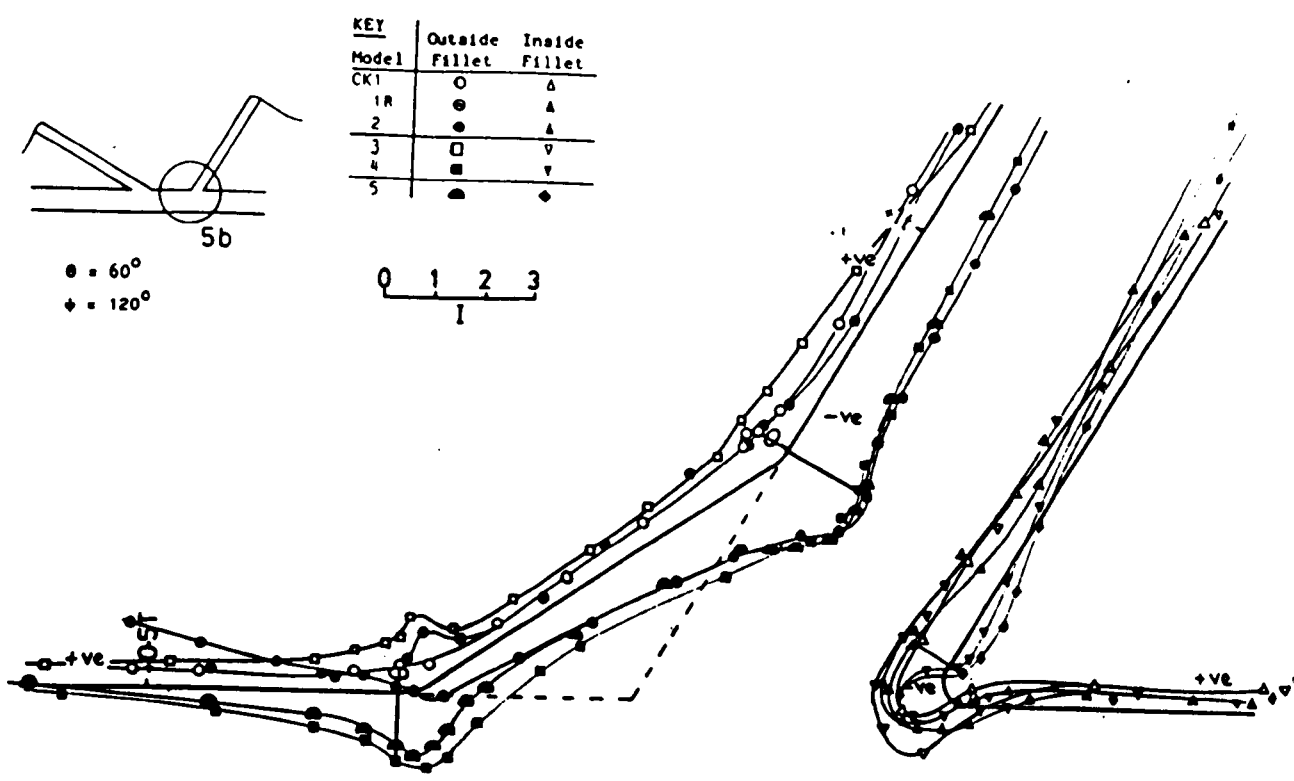


Fig. 6.7 Principal Stresses in CK Models, Junction 5b

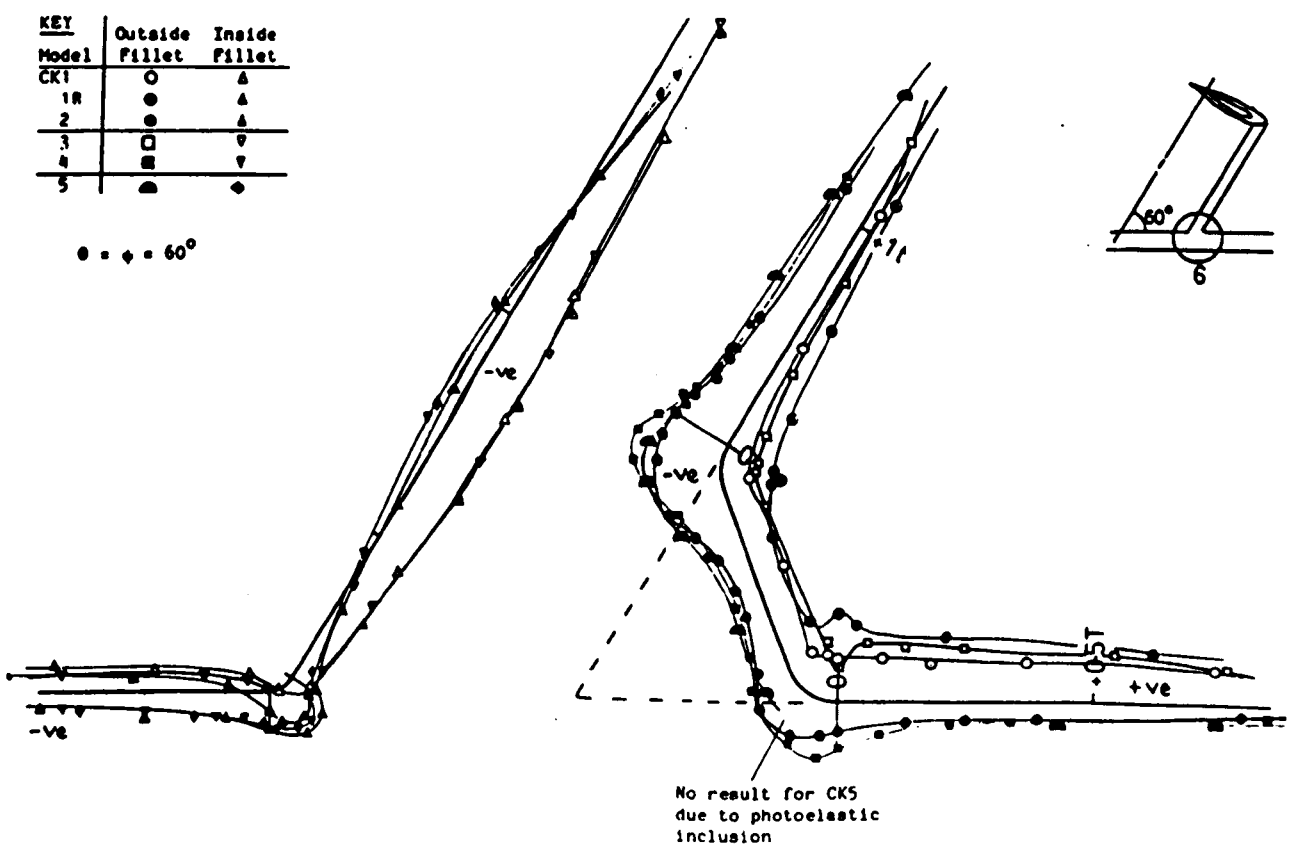


Fig. 6.8 Principal Stresses in CK Models, Junction 6

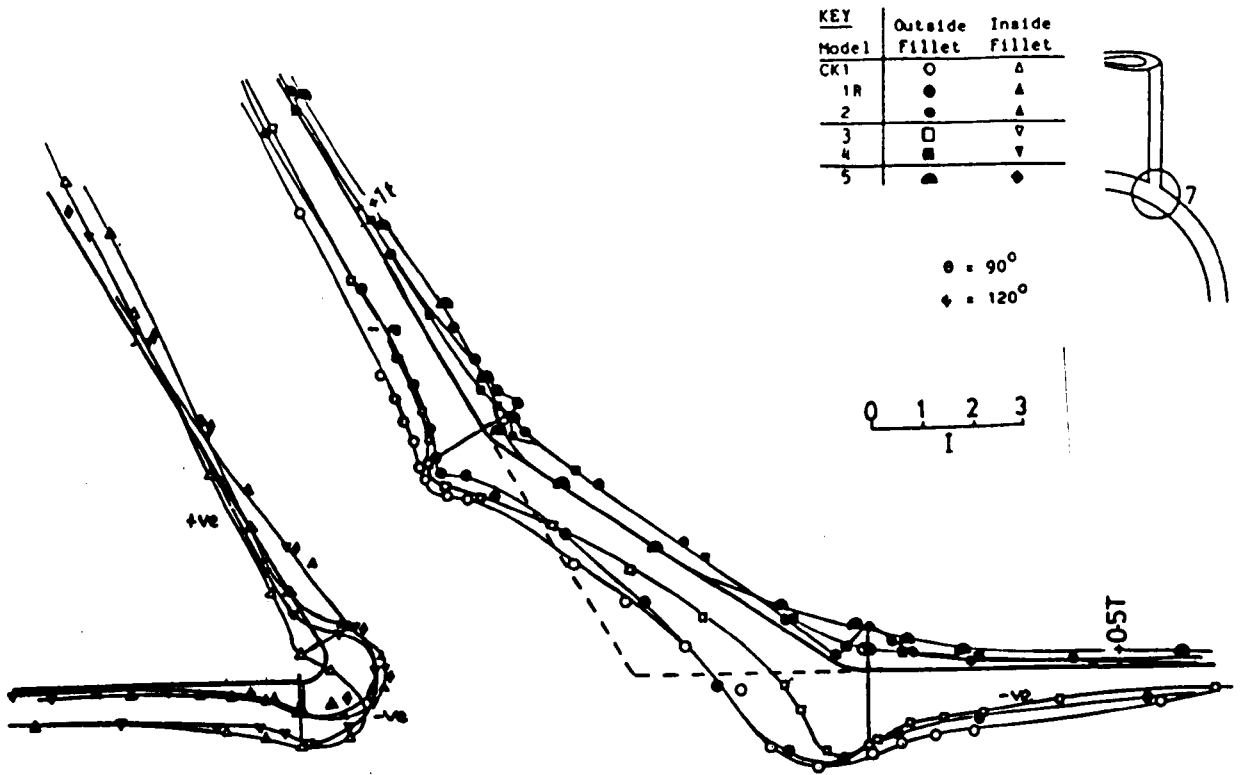


Fig. 6.9 Principal Stresses in CK Models, Junction 7

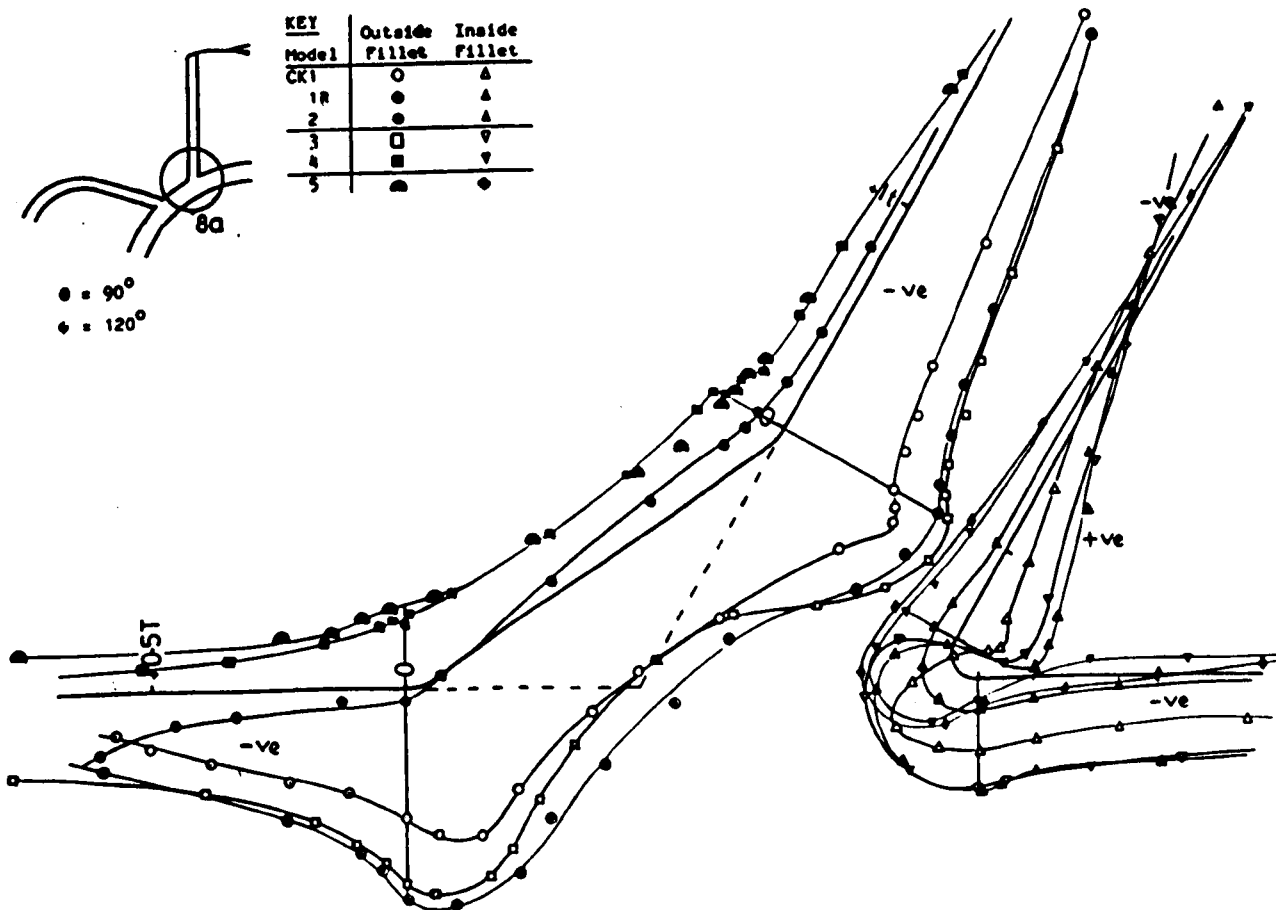


Fig. 6.10 Principal Stresses in CK Models, Junction 8a

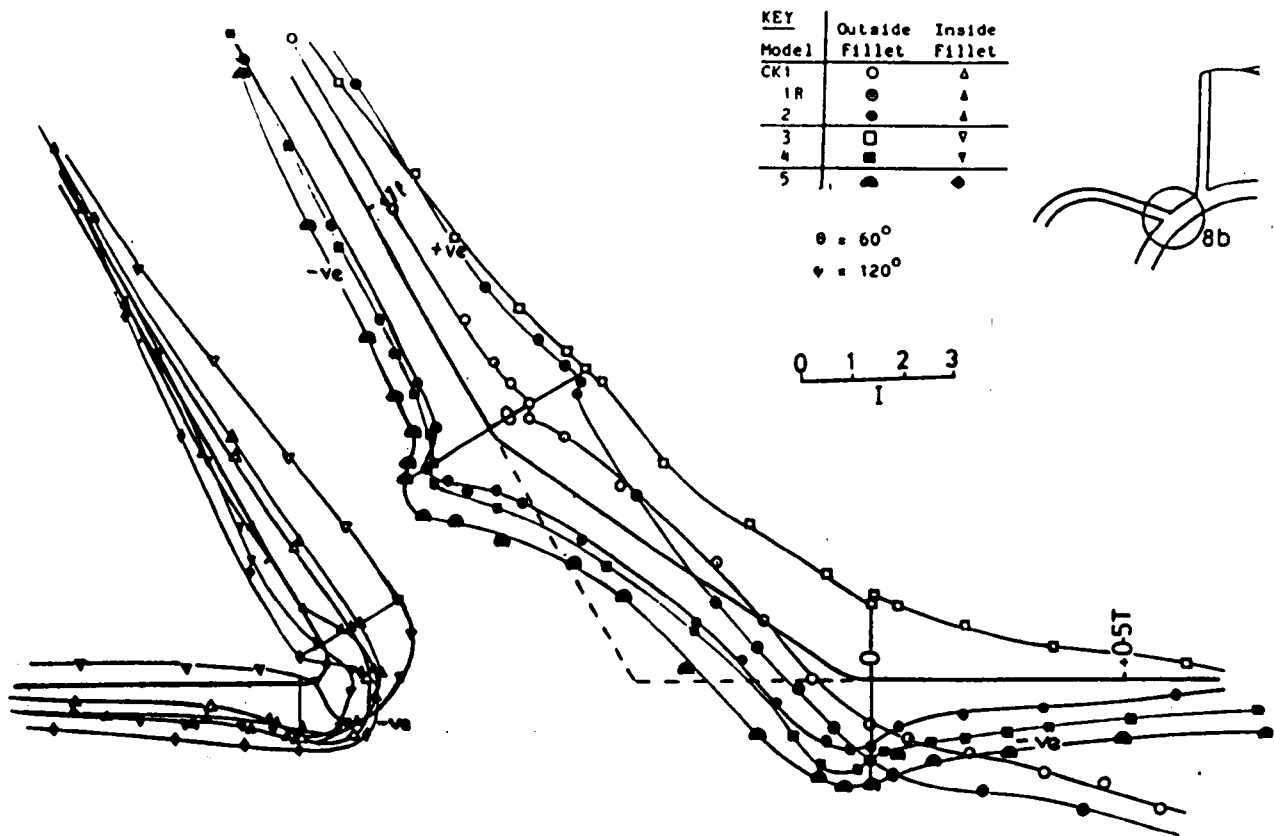


Fig. 6.11 Hoop Stresses in CK Models, Junction 8b

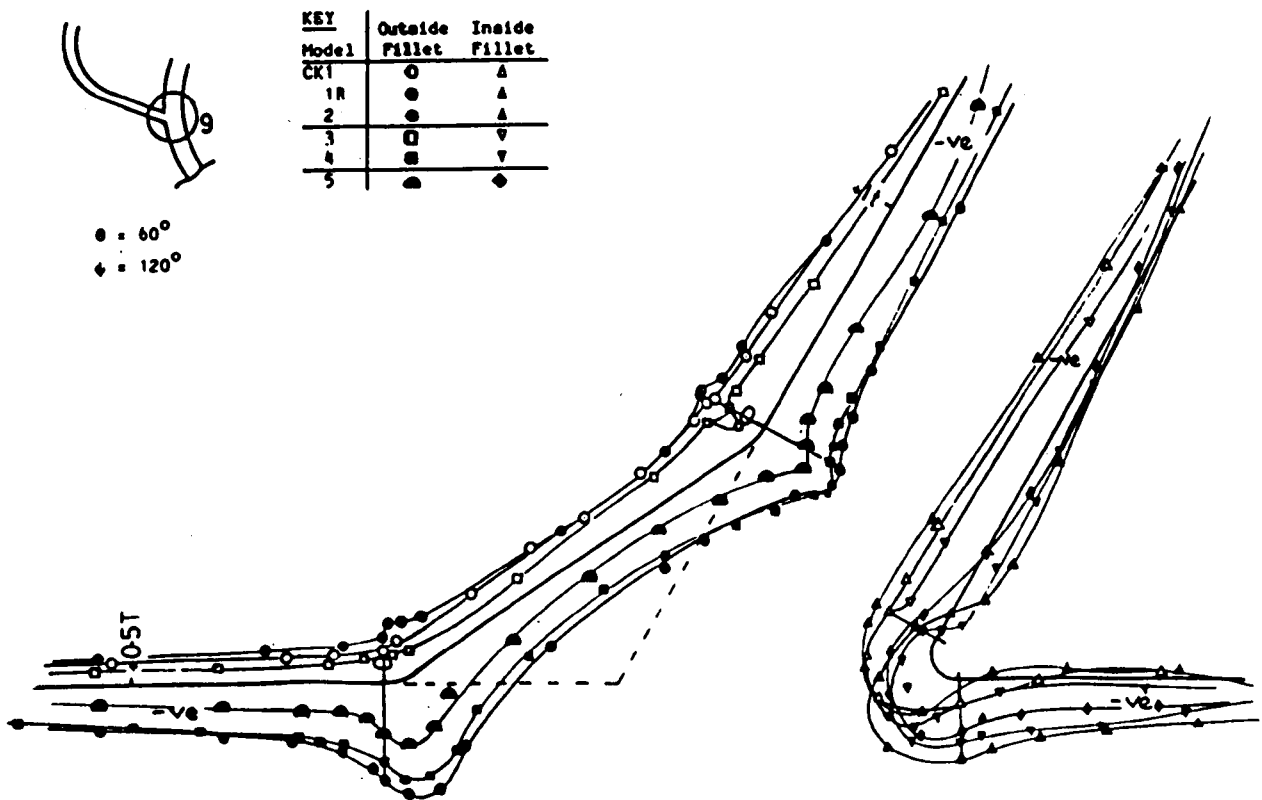


Fig. 6.12 Hoop Stresses in CK Models, Junction 9

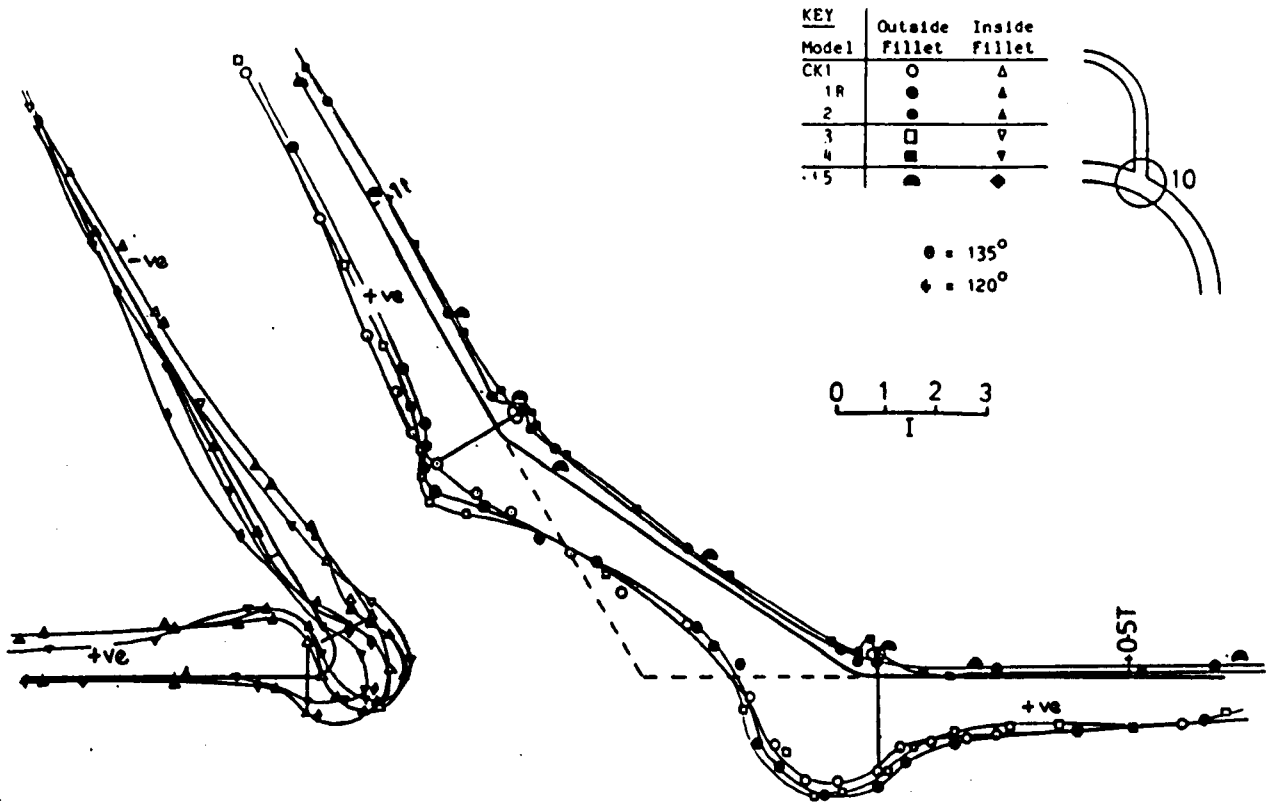


Fig. 6.13 Hoop Stresses in CK Models, Junction 10

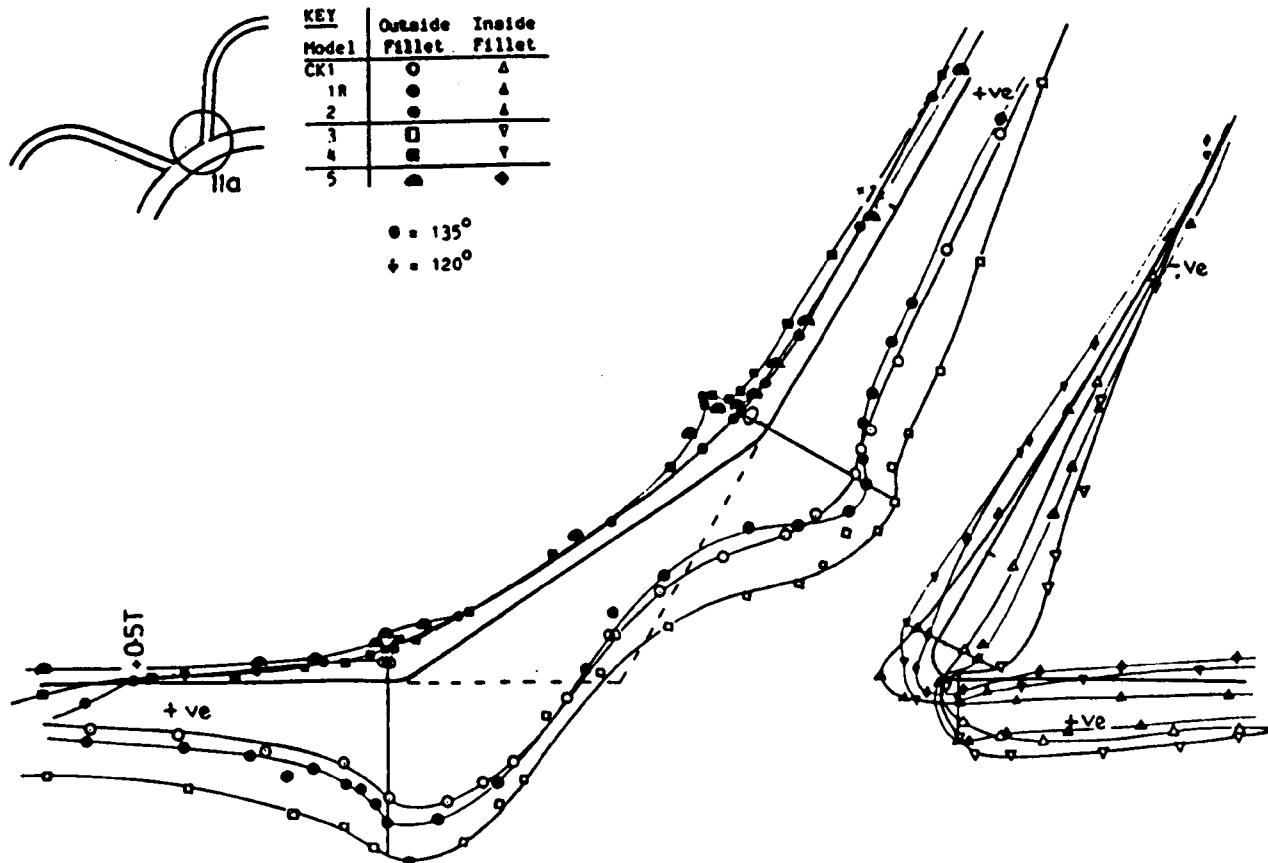


Fig. 6.14 Hoop Stresses in CK Models, Junction 11a

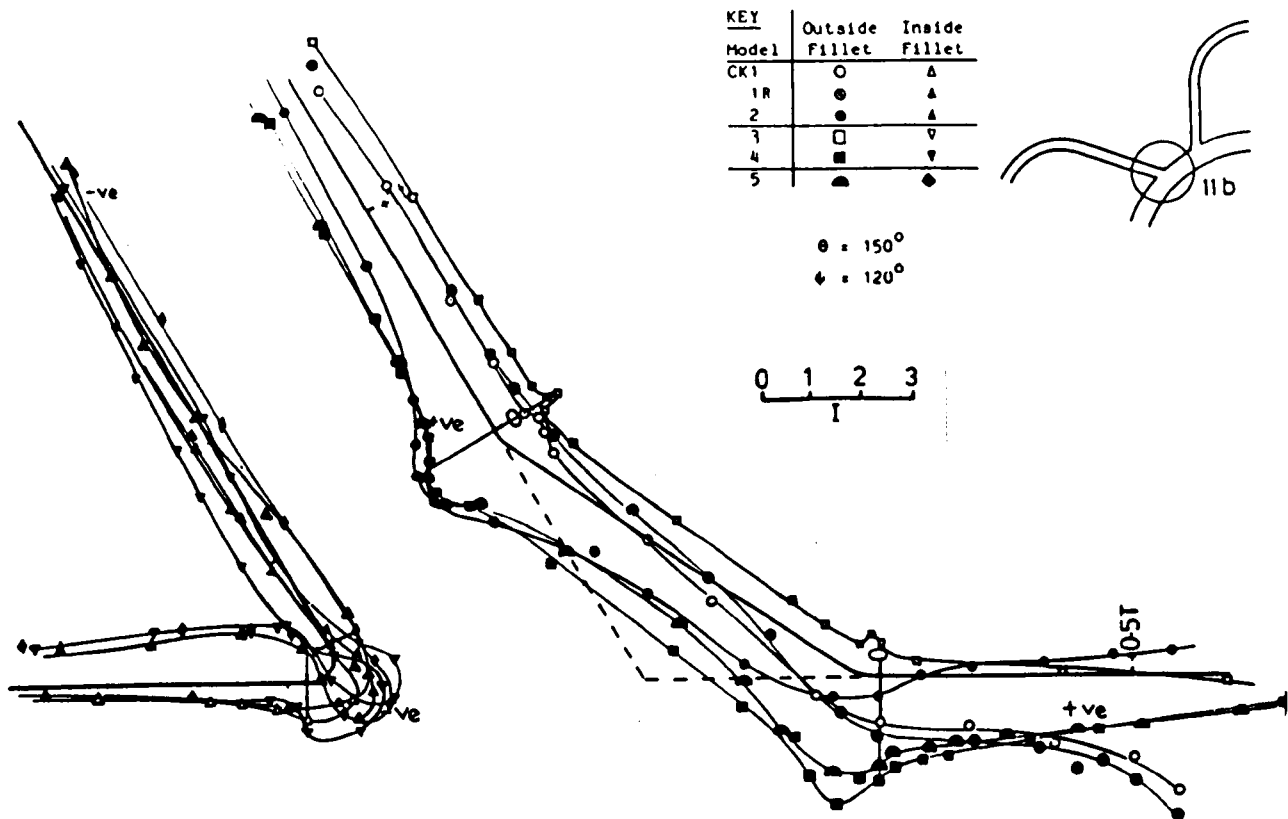


Fig. 6.15 Hoop Stresses in CK Models, Junction 11b

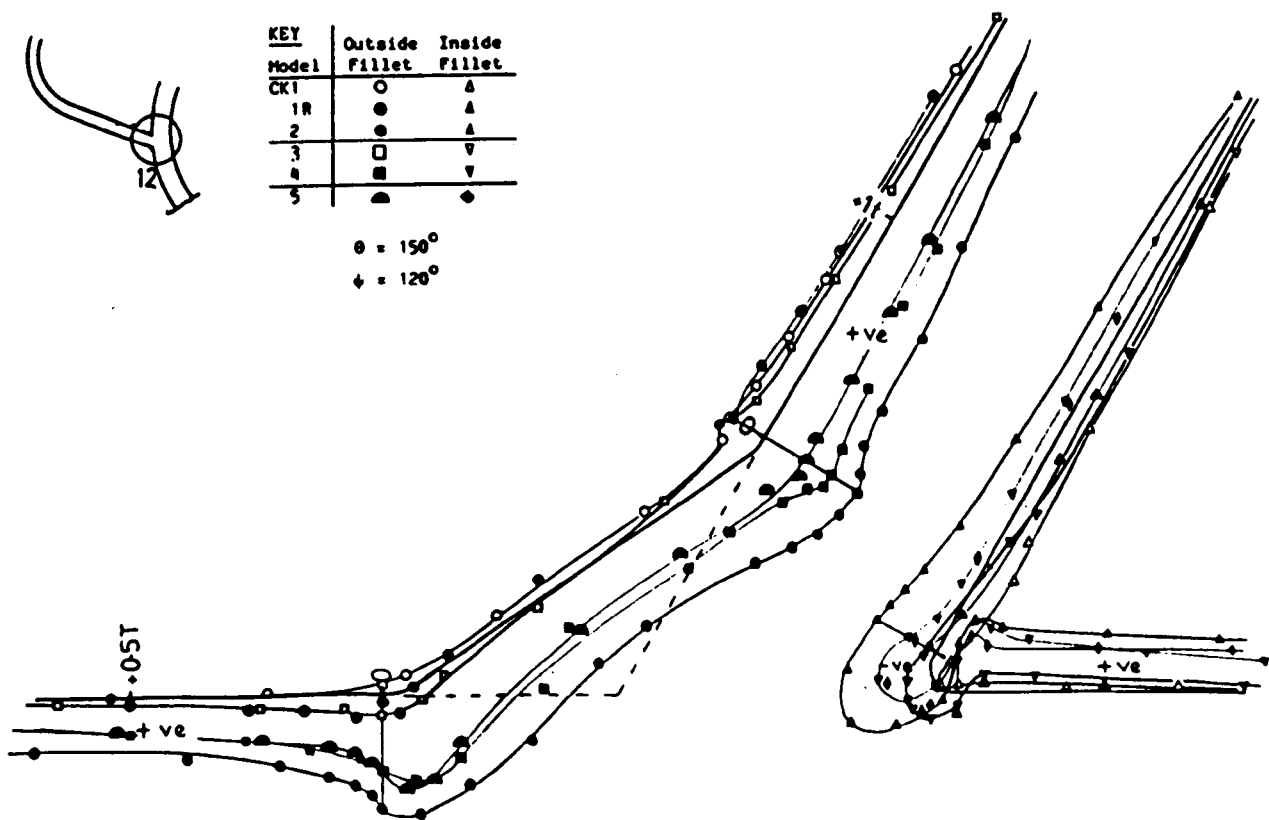


Fig. 6.16 Hoop Stresses in CK Models, Junction 12

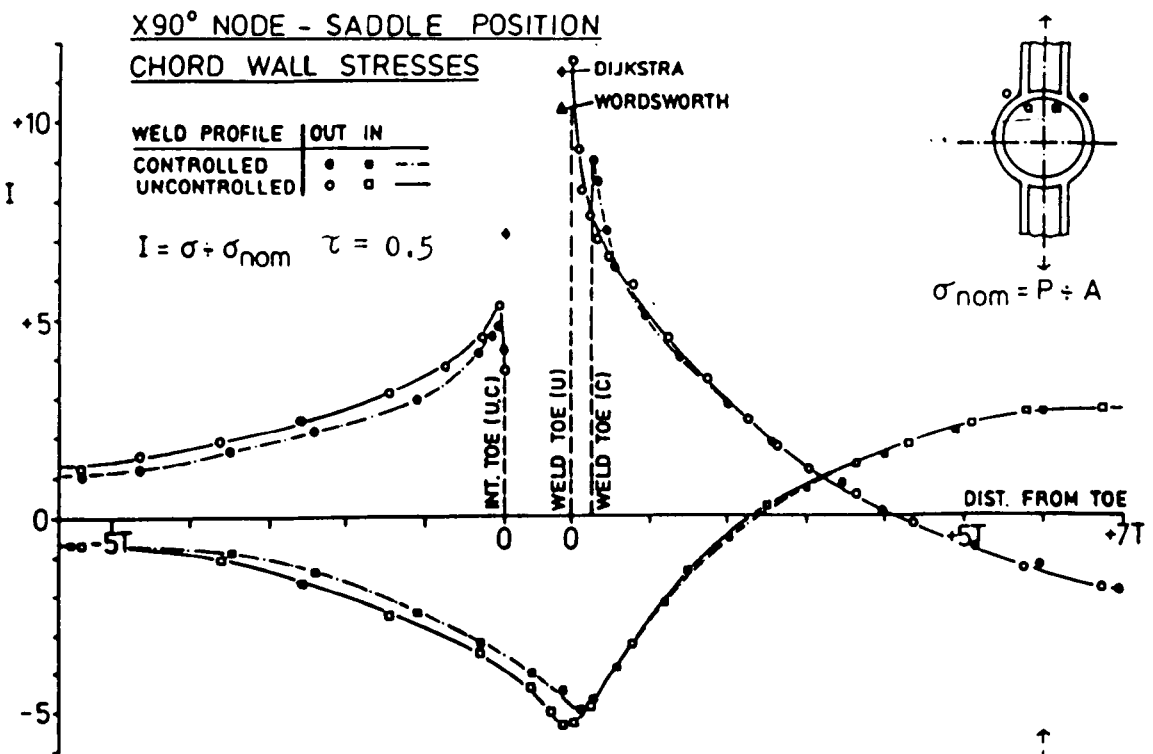


Fig. 6.17

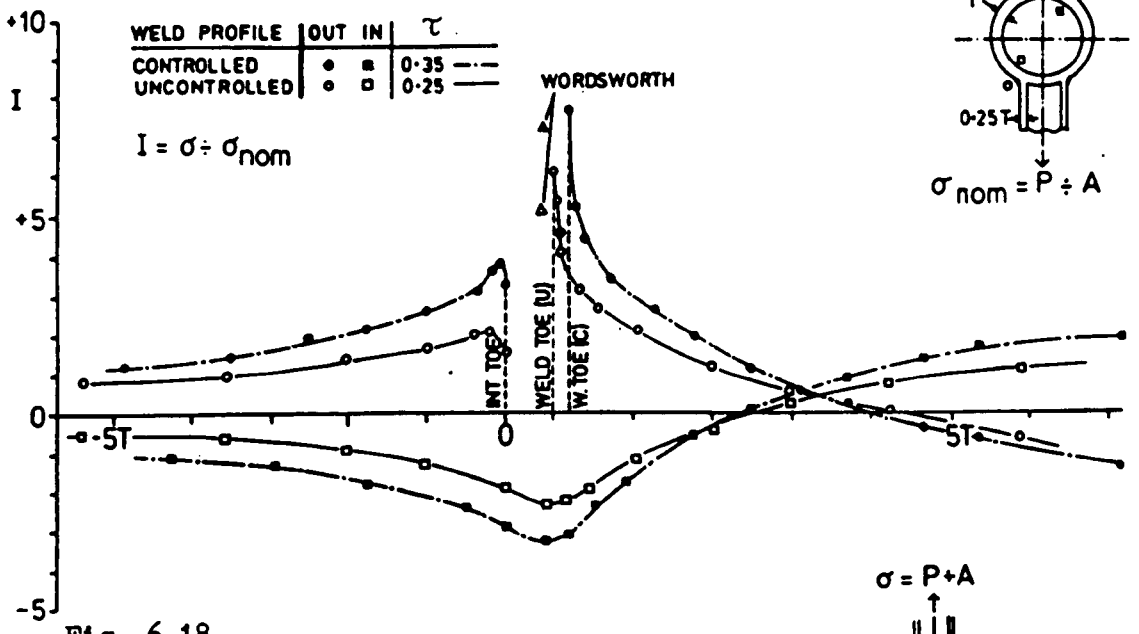


Fig. 6.18

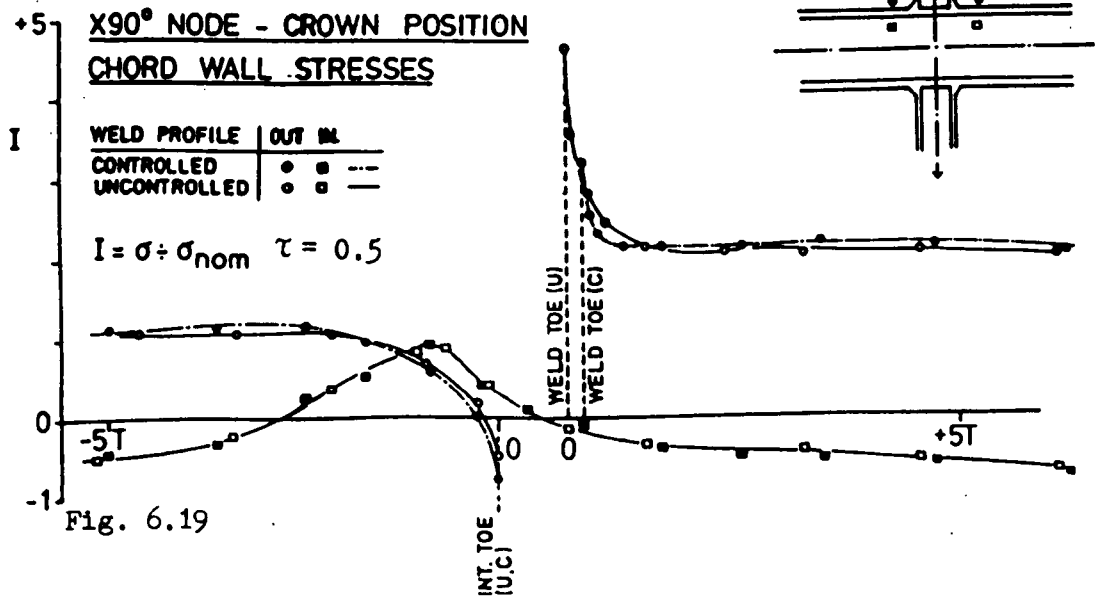
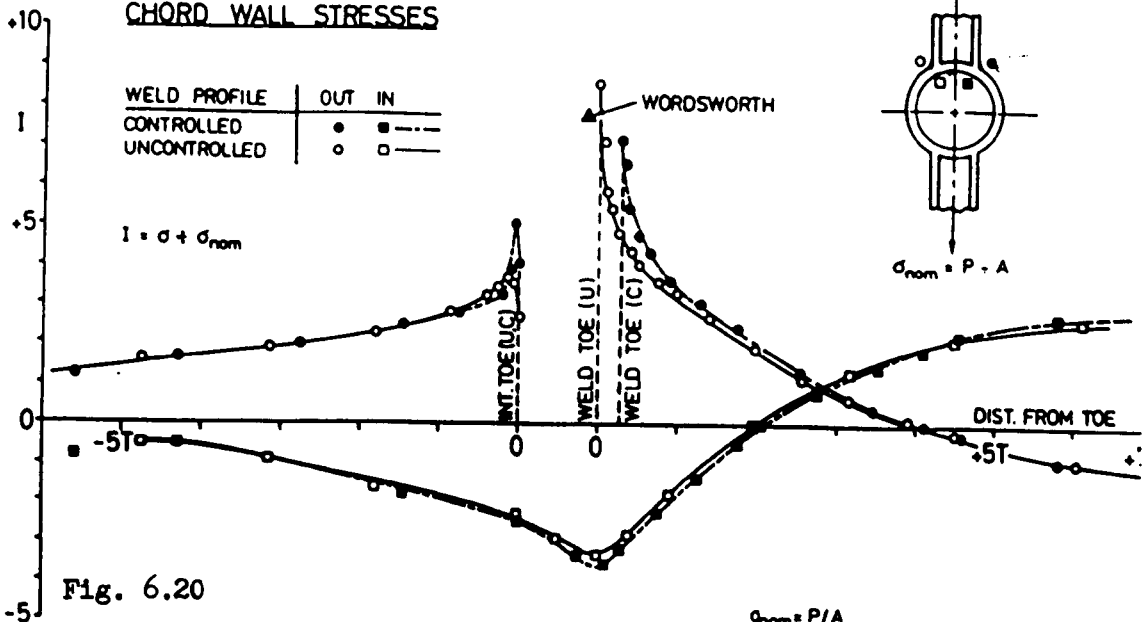
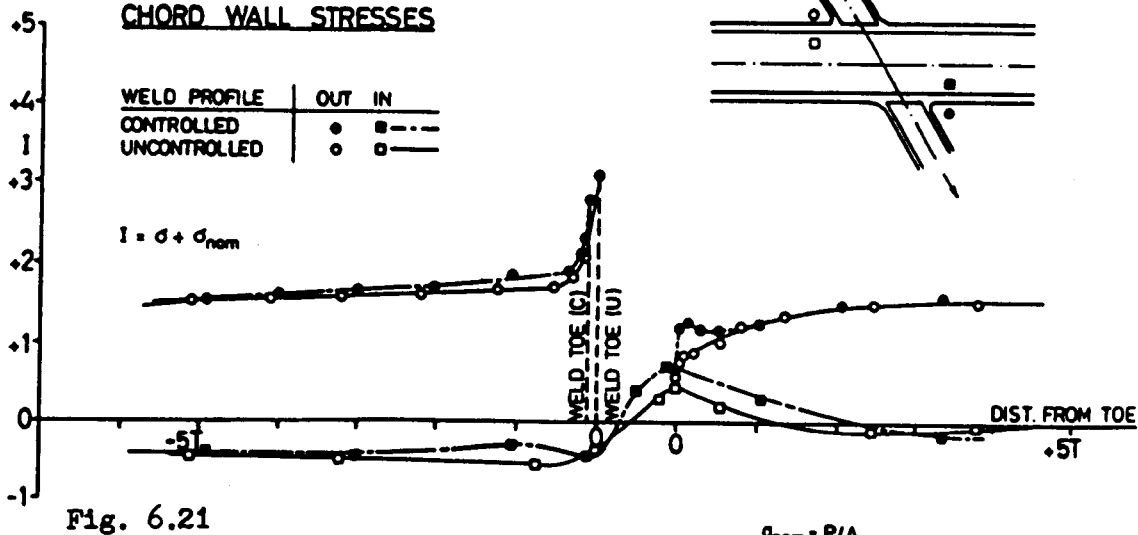


Fig. 6.19

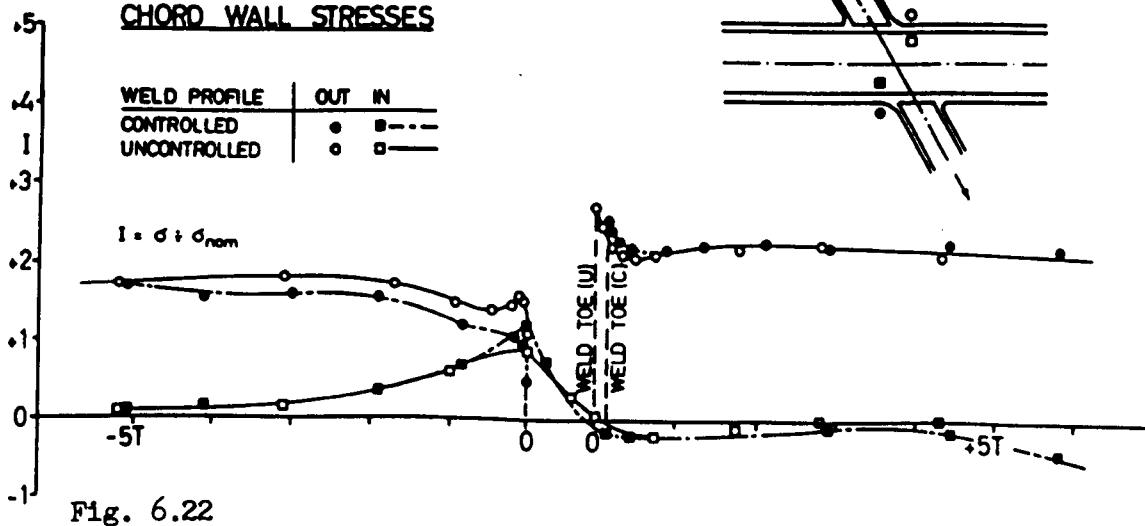
X60° NODE - SADDLE POSITION
CHORD WALL STRESSES



X60° NODE - CROWN HEEL POSITION
CHORD WALL STRESSES



X60° NODE - CROWN TOE POSITION
CHORD WALL STRESSES



KEY

Weld Profile	Outside Fillet	Inside Fillet
U	○	△
C	●	▲

$\theta = \psi = 60^\circ$

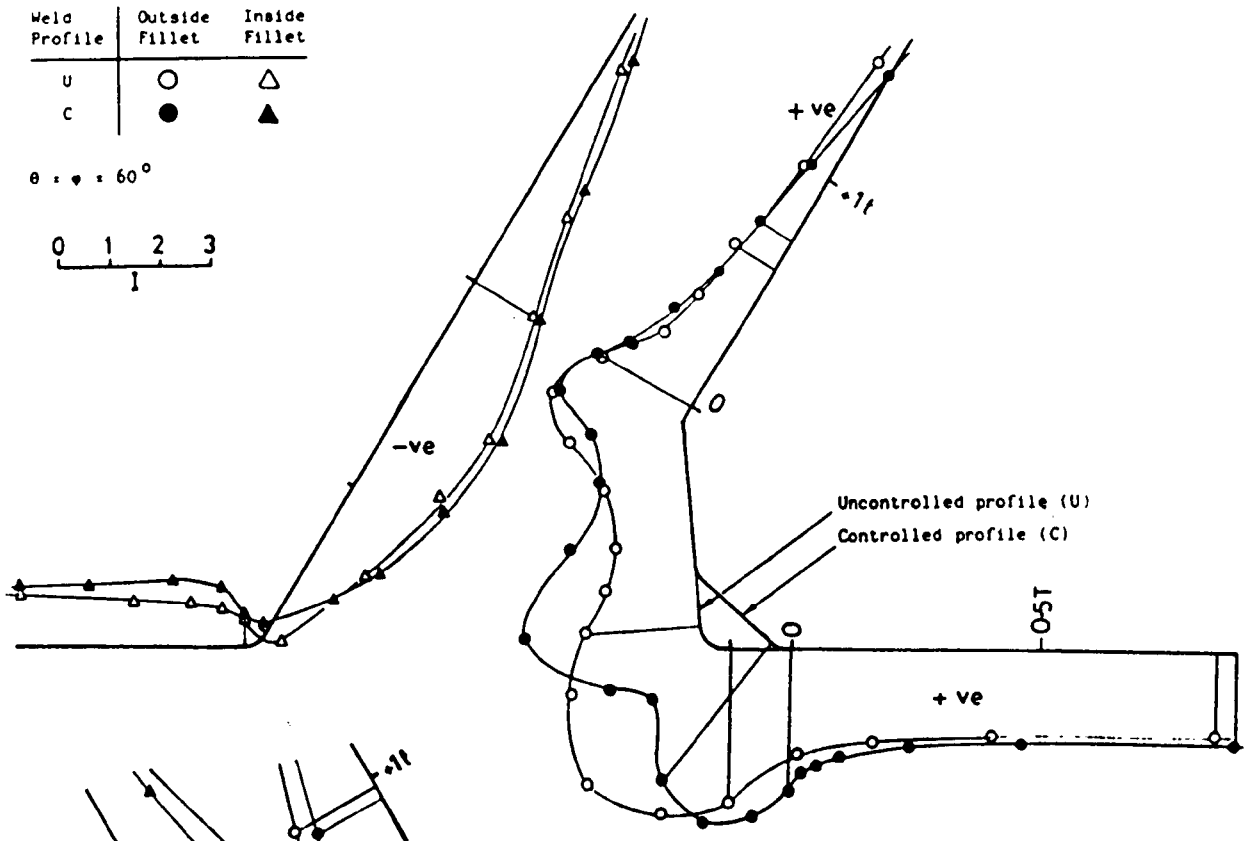
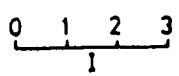


Fig. 6.23 Principal Stresses in X60 Model, Junctions 14 and 16

$\theta = 60^\circ; \psi = 120^\circ$

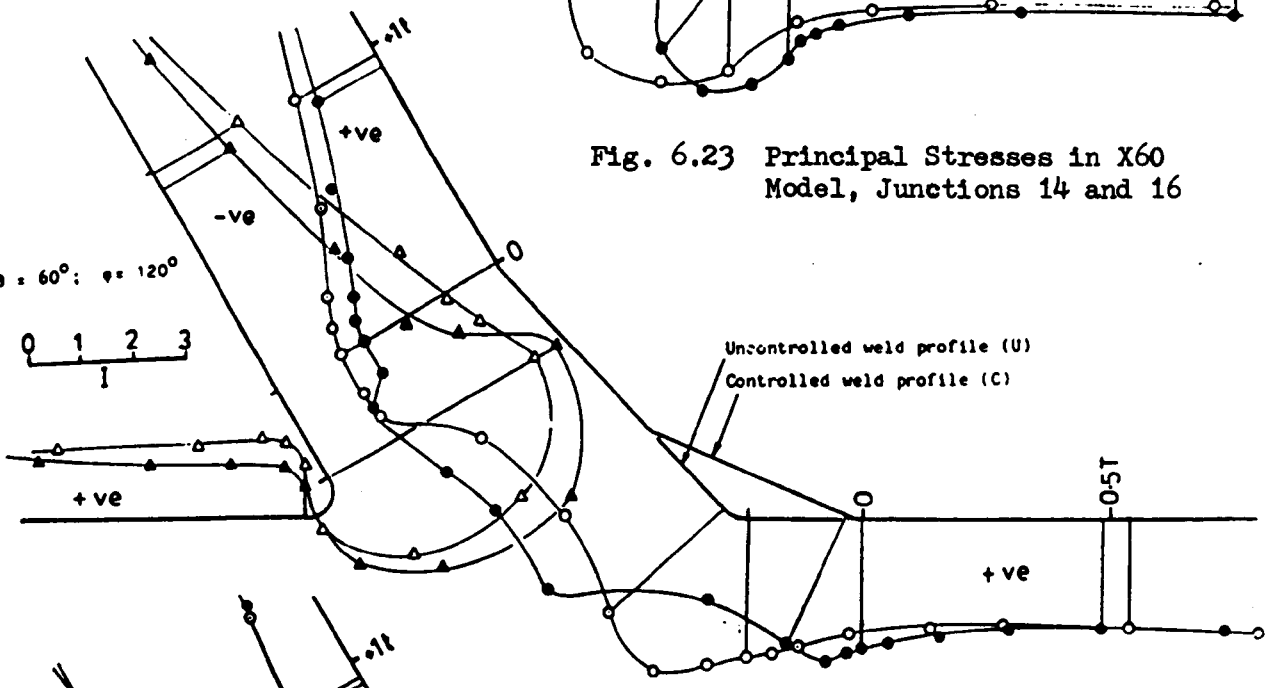
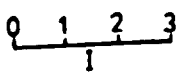


Fig. 6.24 Principal Stresses in X60 Model, Junctions 13 and 15

$\theta = 60^\circ; \psi = 120^\circ$

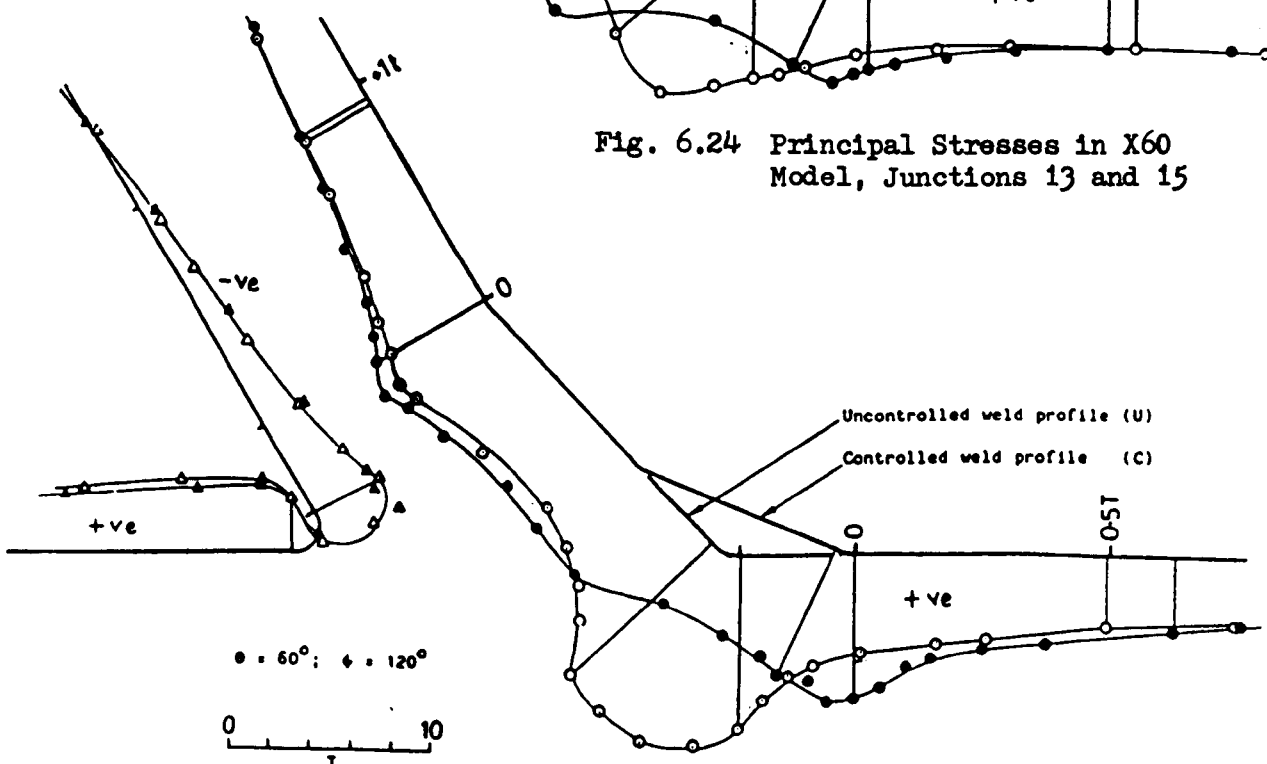


Fig. 6.25 Hoop Stresses in X60 Model, Junction 17 and 20

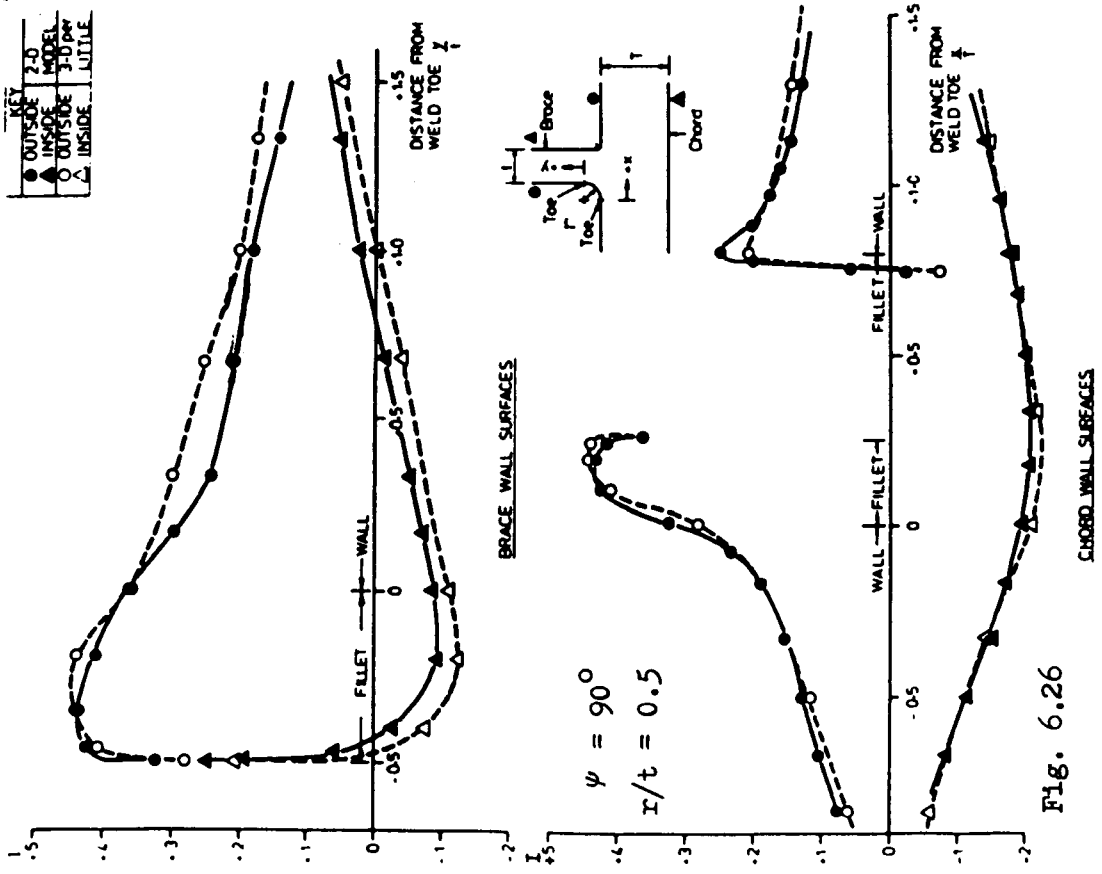


Fig. 6.26

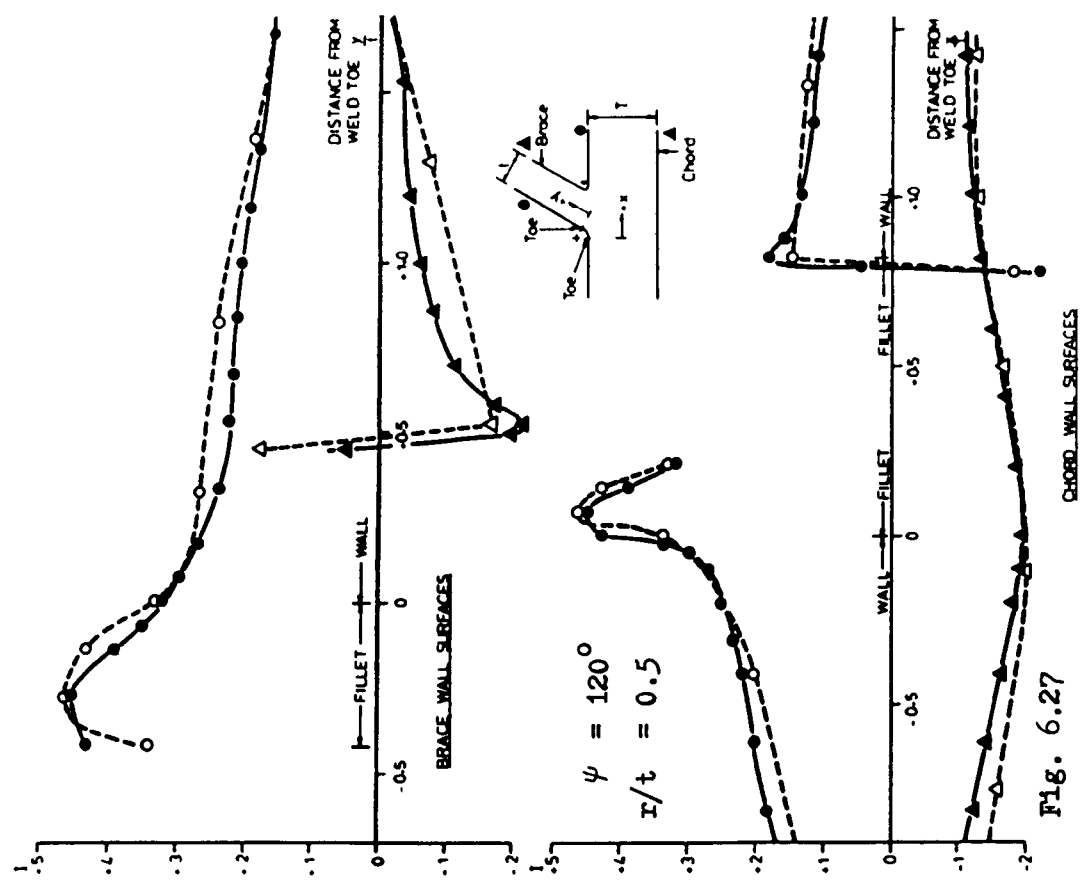


Fig. 6.27

Comparison of Surface Stresses in 2-d and 3-d Models

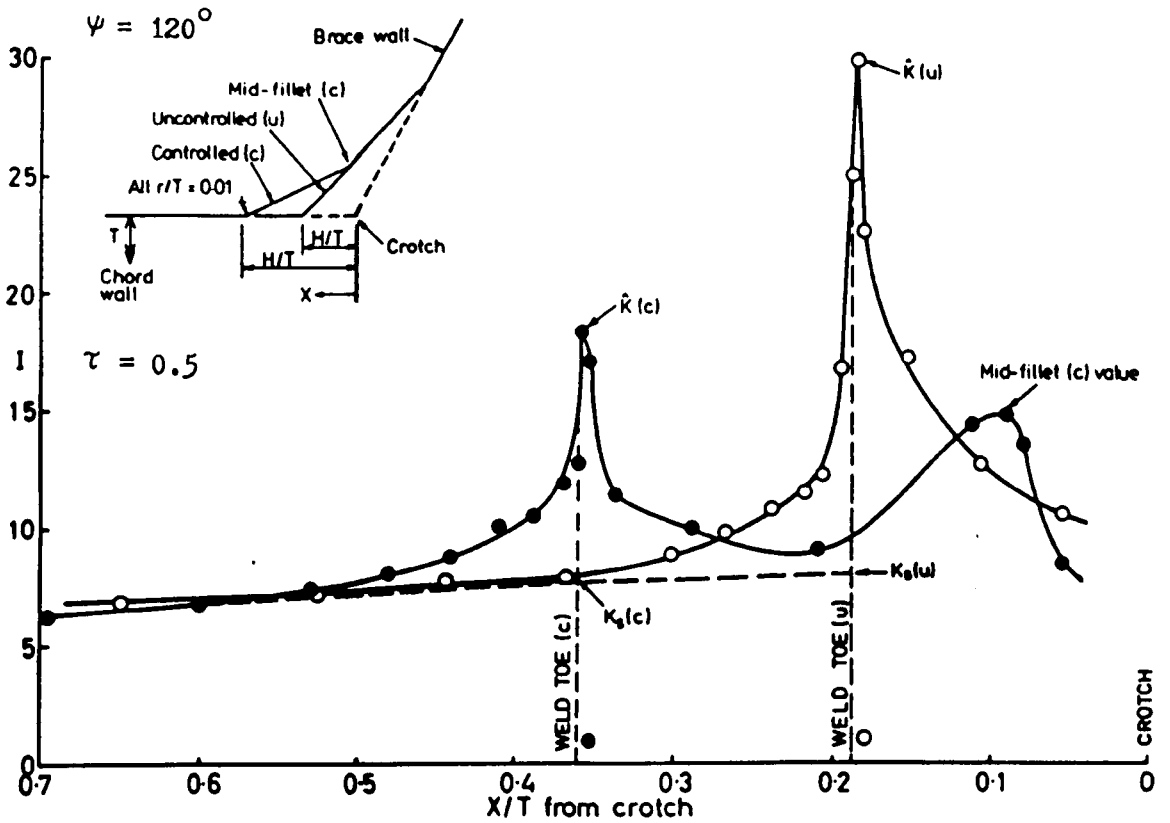


Fig. 6.30 Effect of Weld Profile on Stresses in Saddle Planes in X Nodes

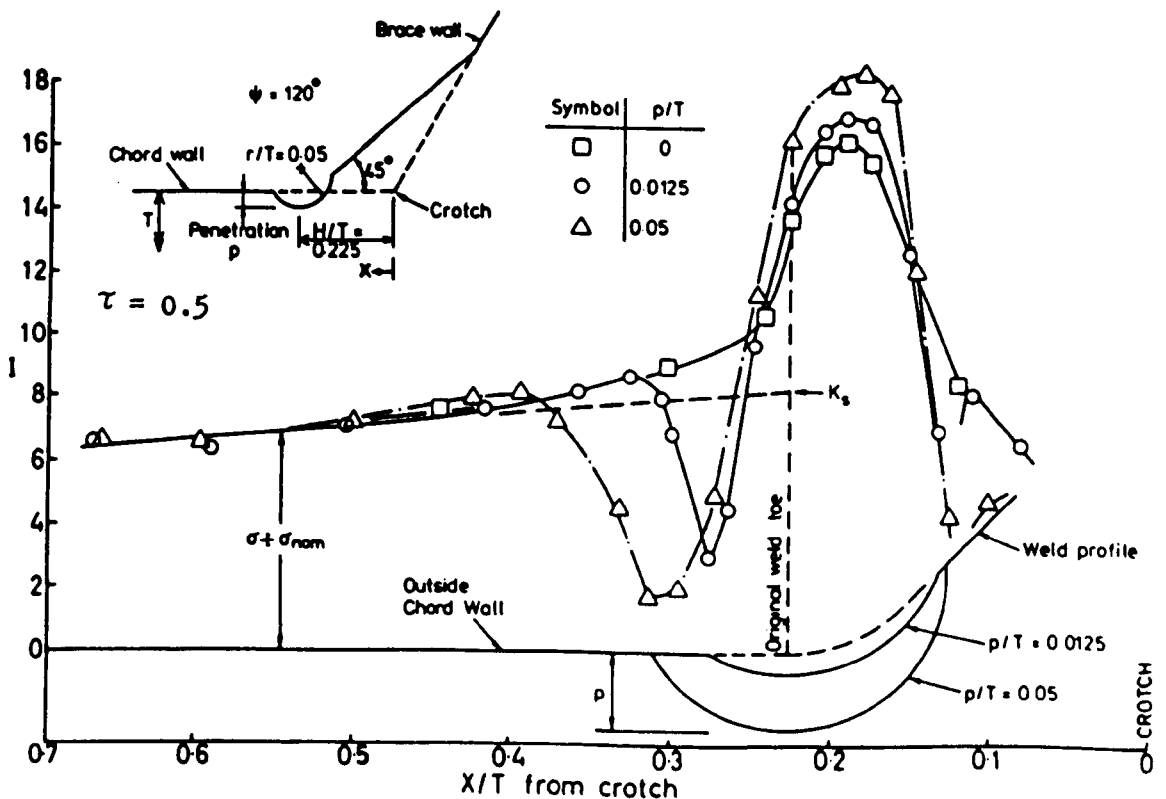


Fig. 6.31 Effect of Undercut on Stresses in Saddle Planes in X90 Nodes

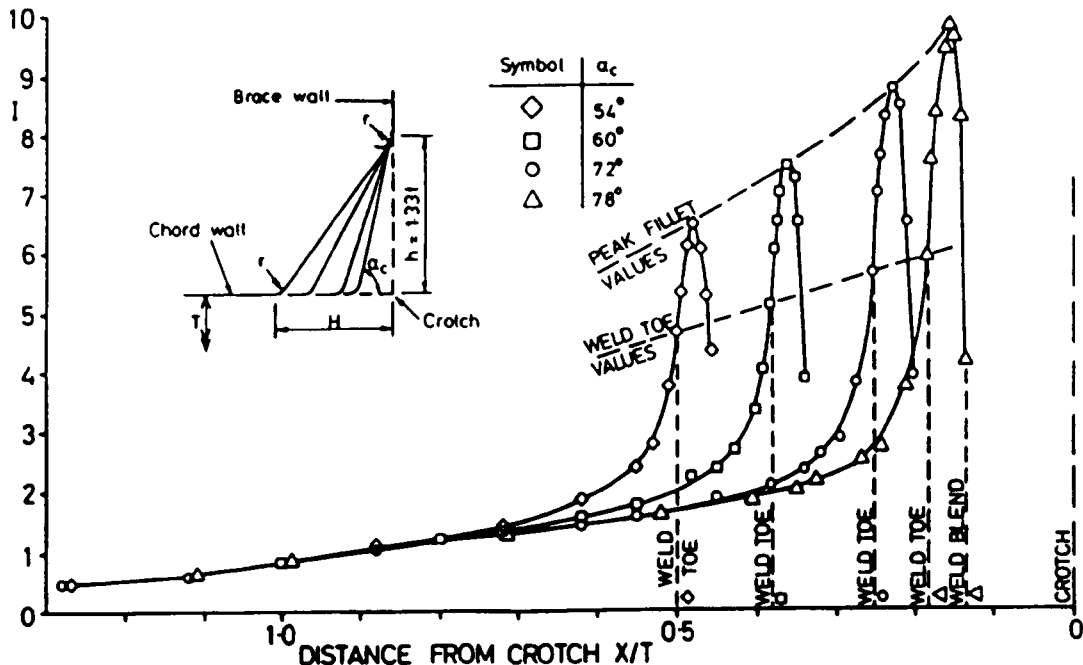


Fig. 6.32 Effect of Weld Size and Angle on Stresses in Crown Planes in K Nodes

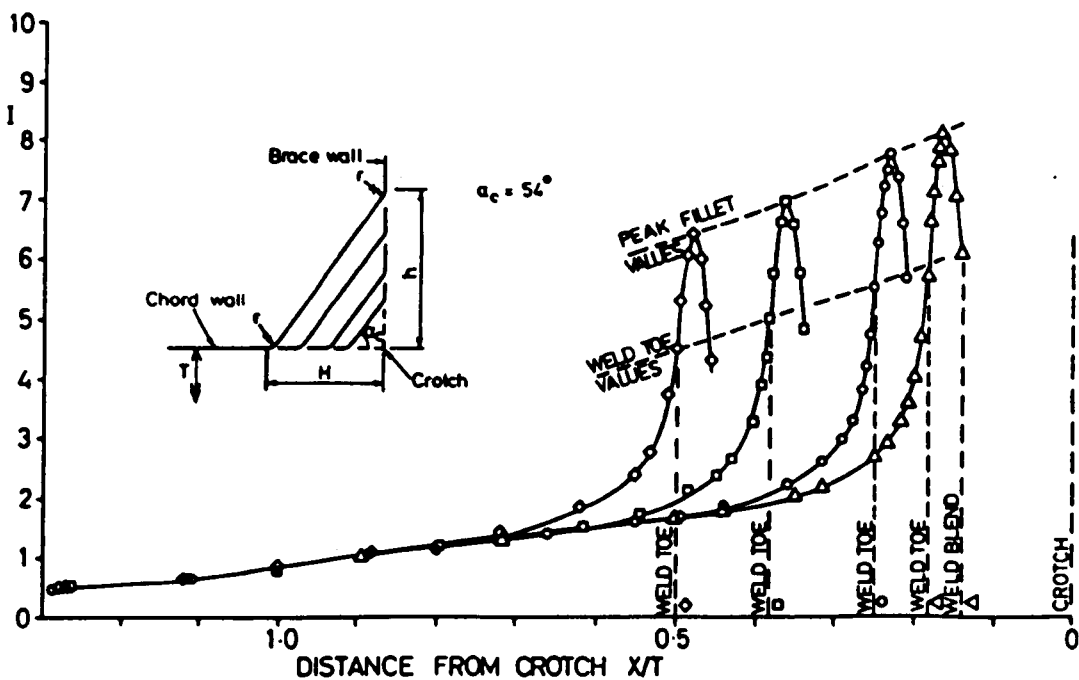


Fig. 6.33 Effect of Weld Size Only on Stresses in Crown Planes in K Node

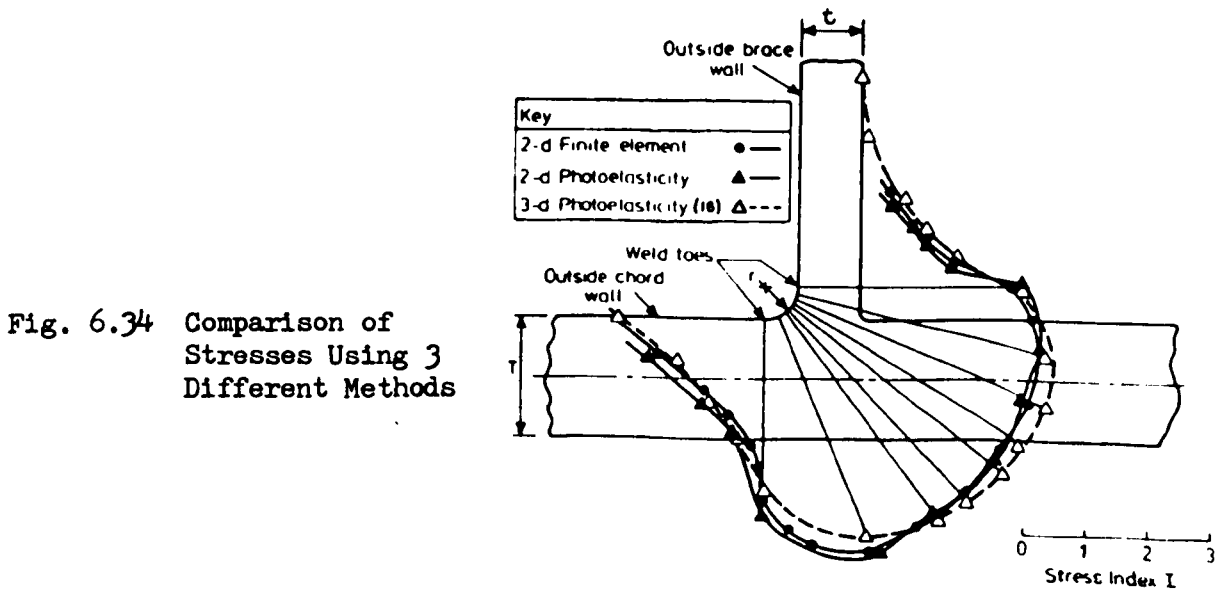
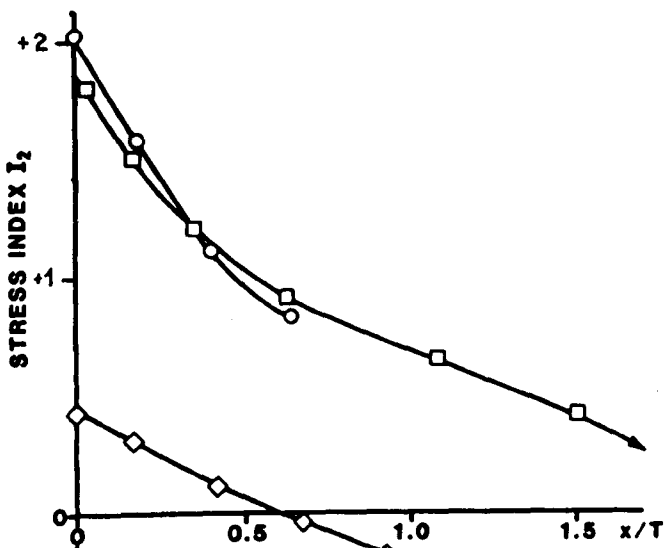
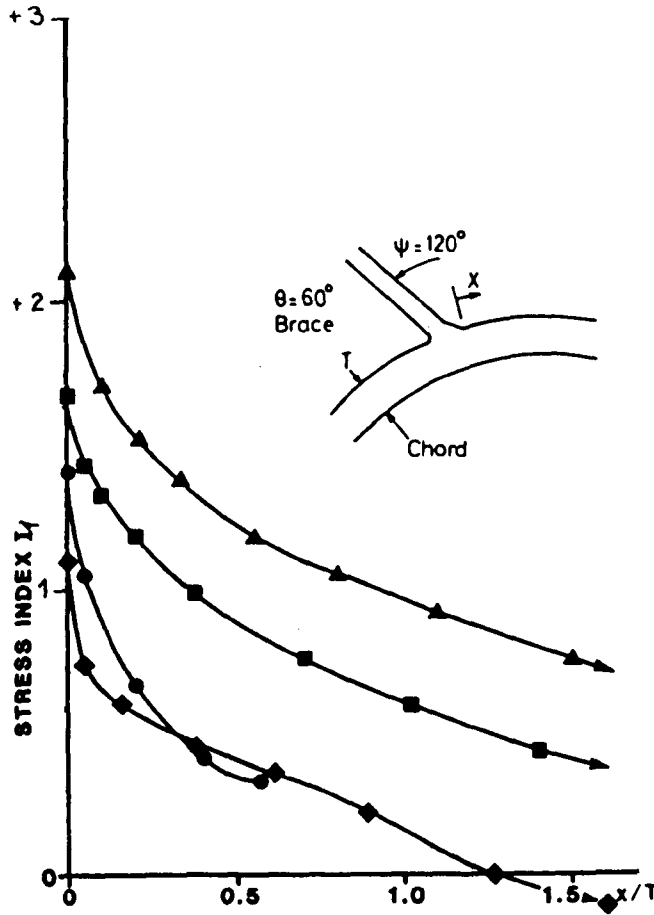
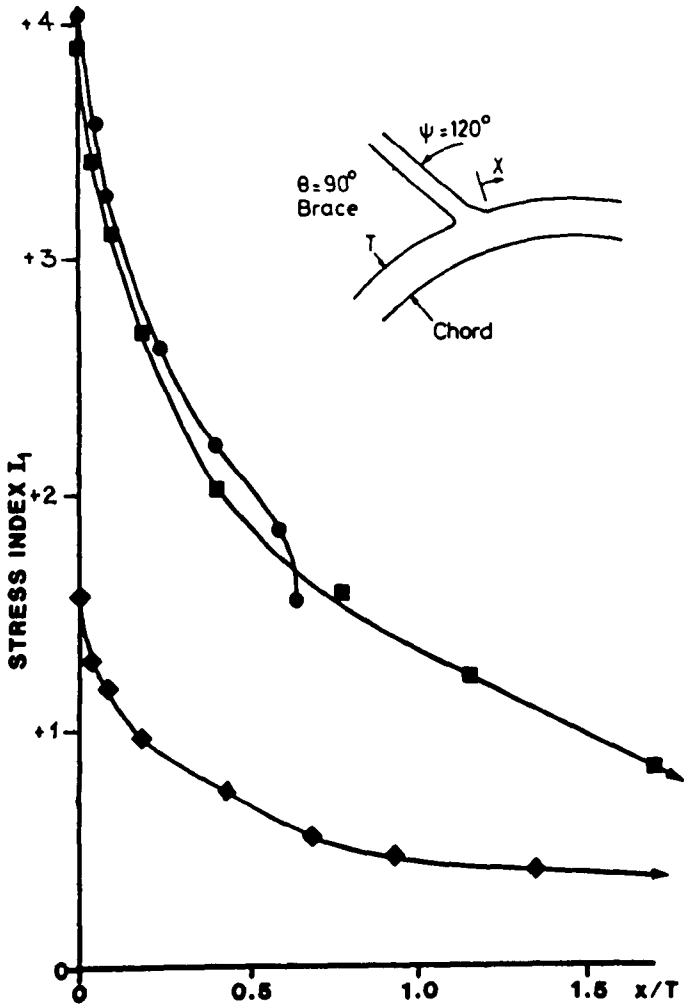
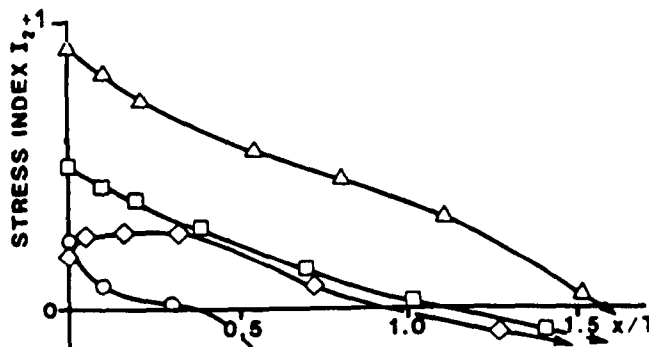


Fig. 6.34 Comparison of Stresses Using 3 Different Methods



g/T	0.64	3.44	48
I_1	●	■	◆
I_2	○	□	◇



g/T	0.57	3.0	6.0	48
I_1	●	■	▲	◆
I_2	○	□	△	◇

Fig. 6.35

Fig. 6.36

Principal Chord wall Surface Stress Distributions in Saddle Planes in CK Models

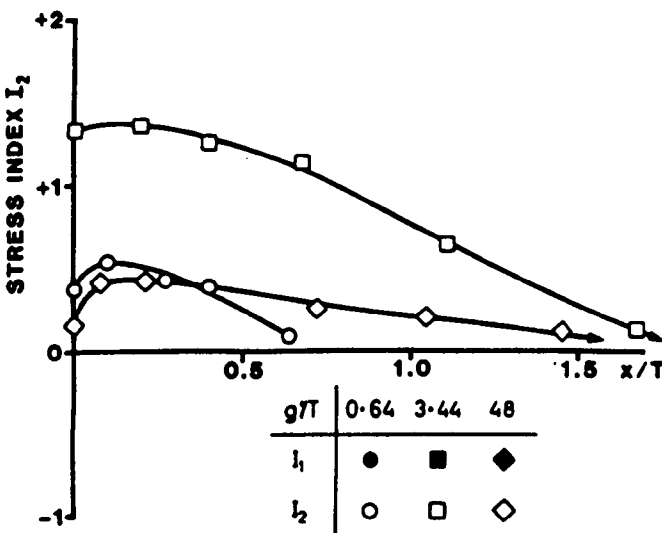
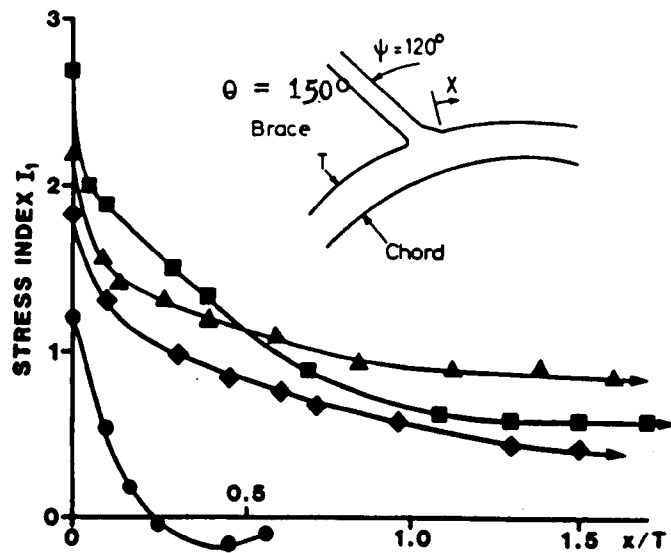
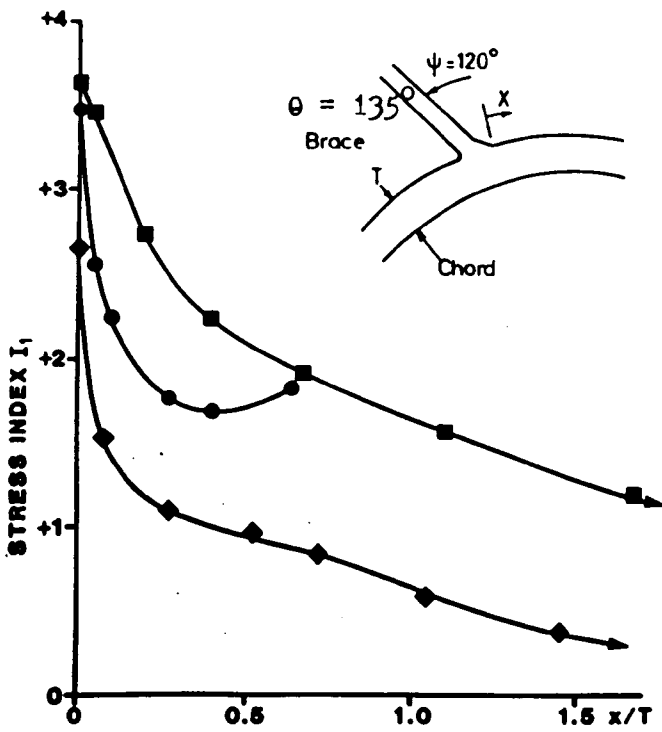


Fig. 6.37

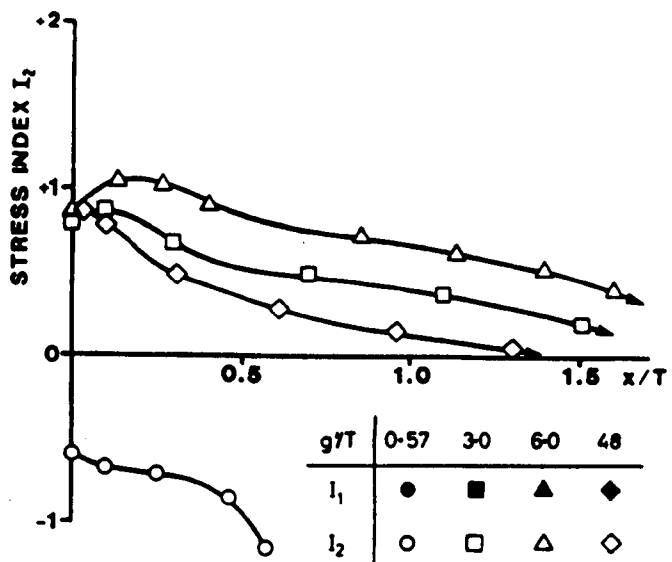


Fig. 6.38

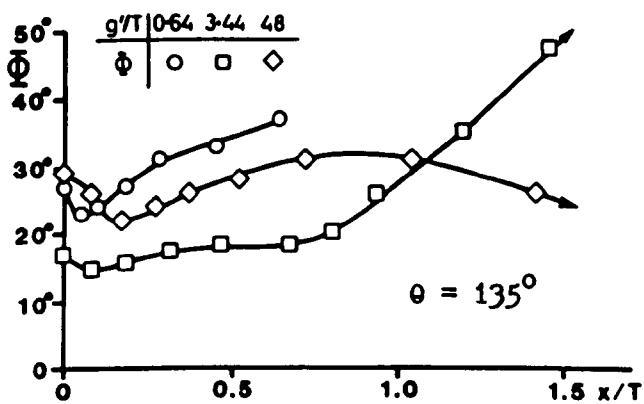


Fig. 6.39

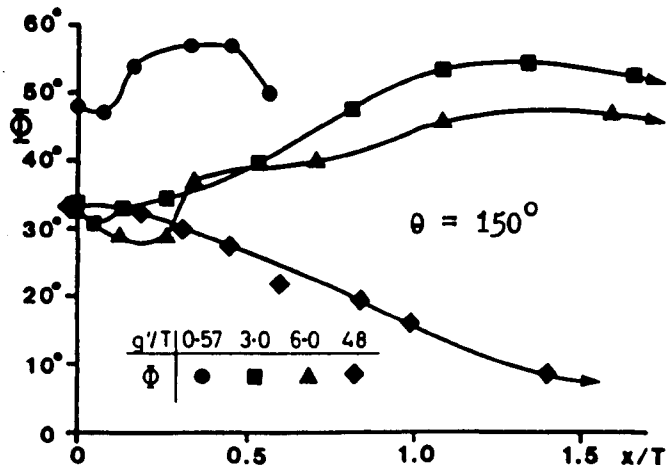
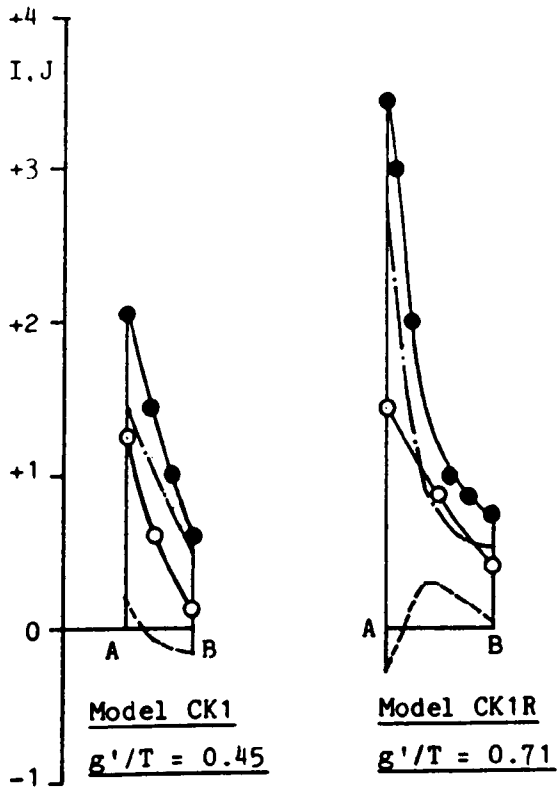


Fig. 6.40

Magnitudes and Directions of Principal Chord Wall Surface Stress Distributions in Saddle Planes in CK Models



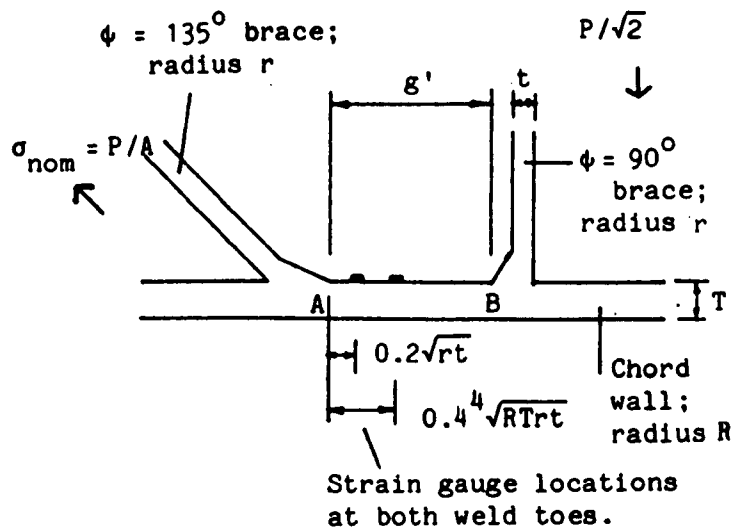
Key	Stress	Strain
Meridional	—●—	---●---
Hoop	—○—	---○---

ϵ_m, ϵ_h

Extrapolated meridional and hoop hot-spot strains resp.

$$I = \frac{\sigma}{\sigma_{nom}}$$

$$J = \frac{\epsilon}{\epsilon_{nom}}$$



Crown Plane I Between Braces

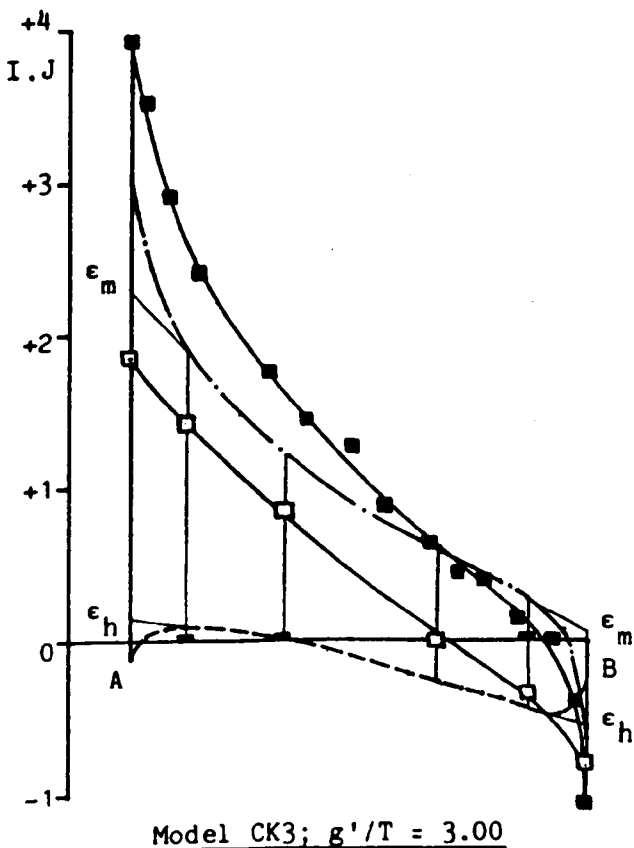


Fig. 6.41 Meridional and Hoop (Principal) Stress and Strain Distributions in Crown Plane I in 3-d CK Models

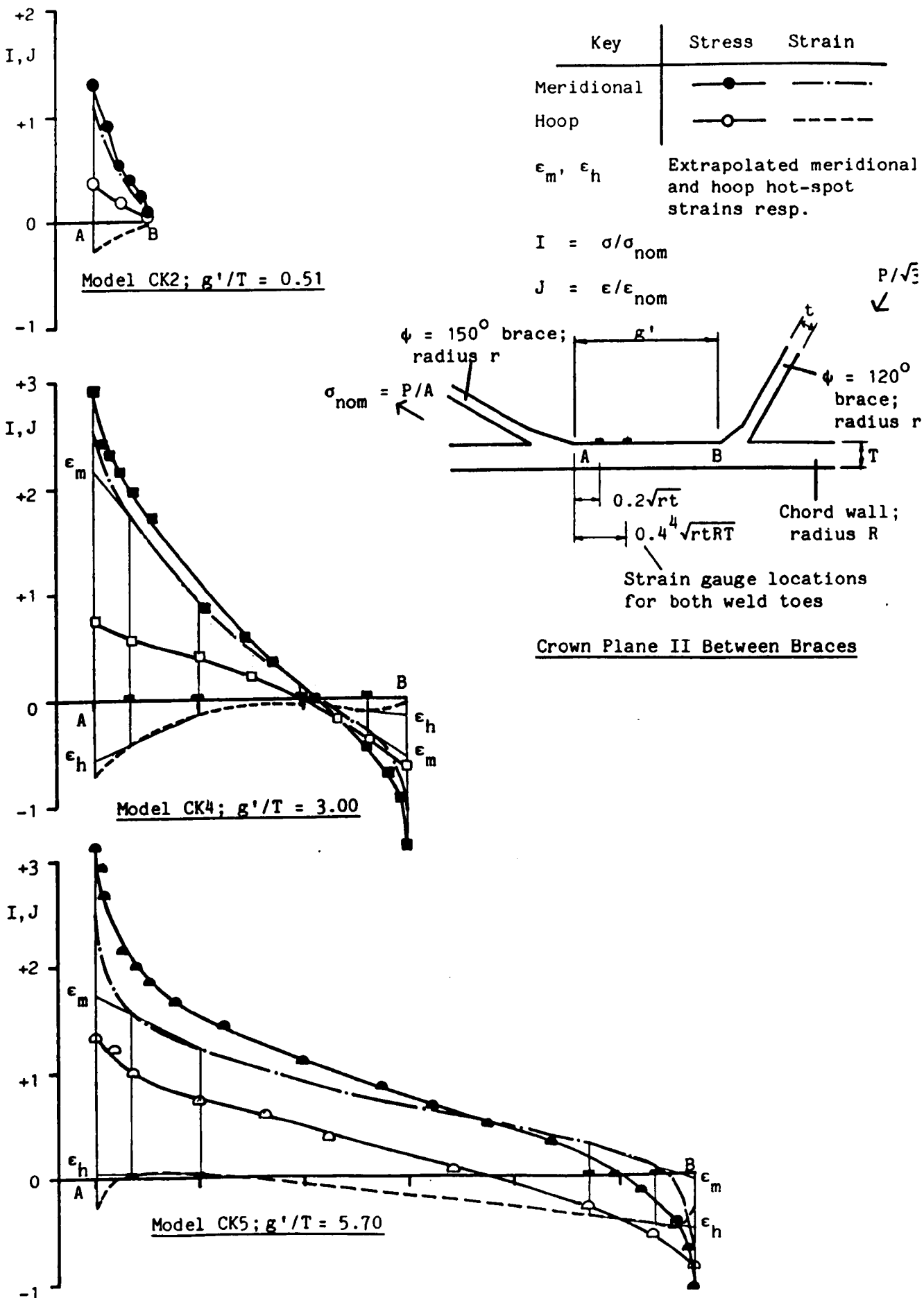


Fig. 6.42 Meridional and Hoop(Principal) Stress and Strain Distributions in Crown Plane II in 3-d CK Models

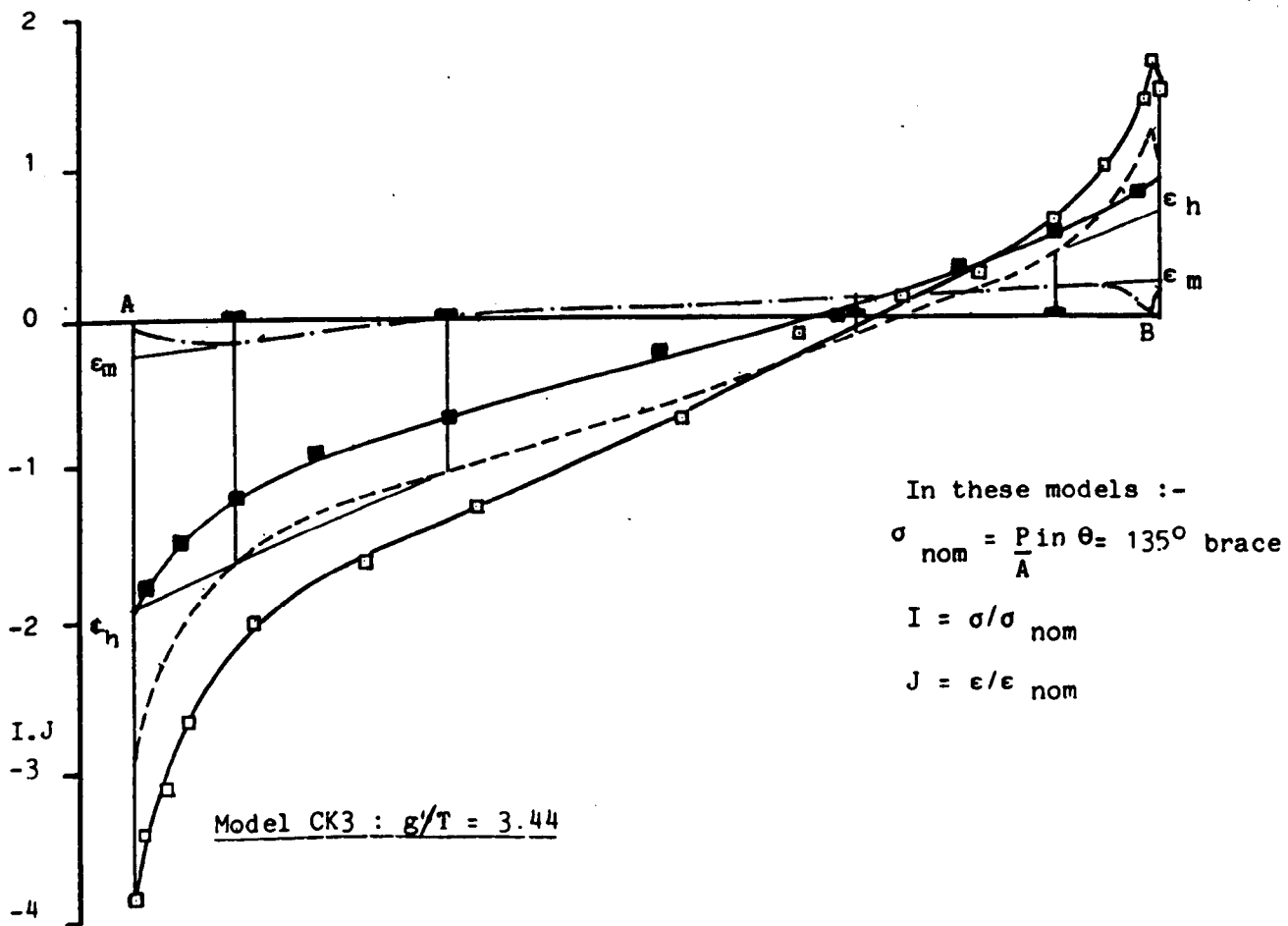
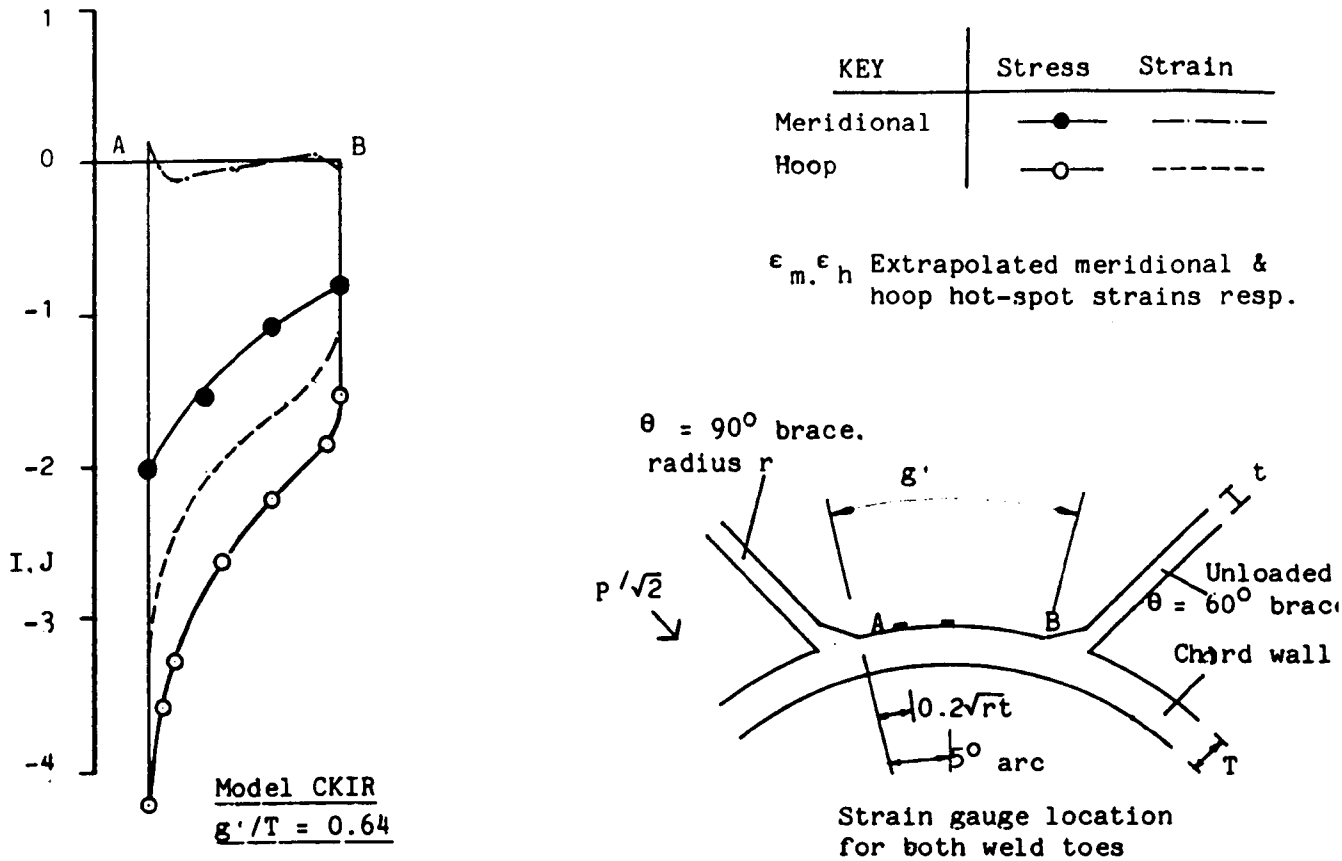


Fig. 6.43 Meridional and Hoop (Principal) Stress and Strain Distributions in Saddle Plane III in 3-d CK Models

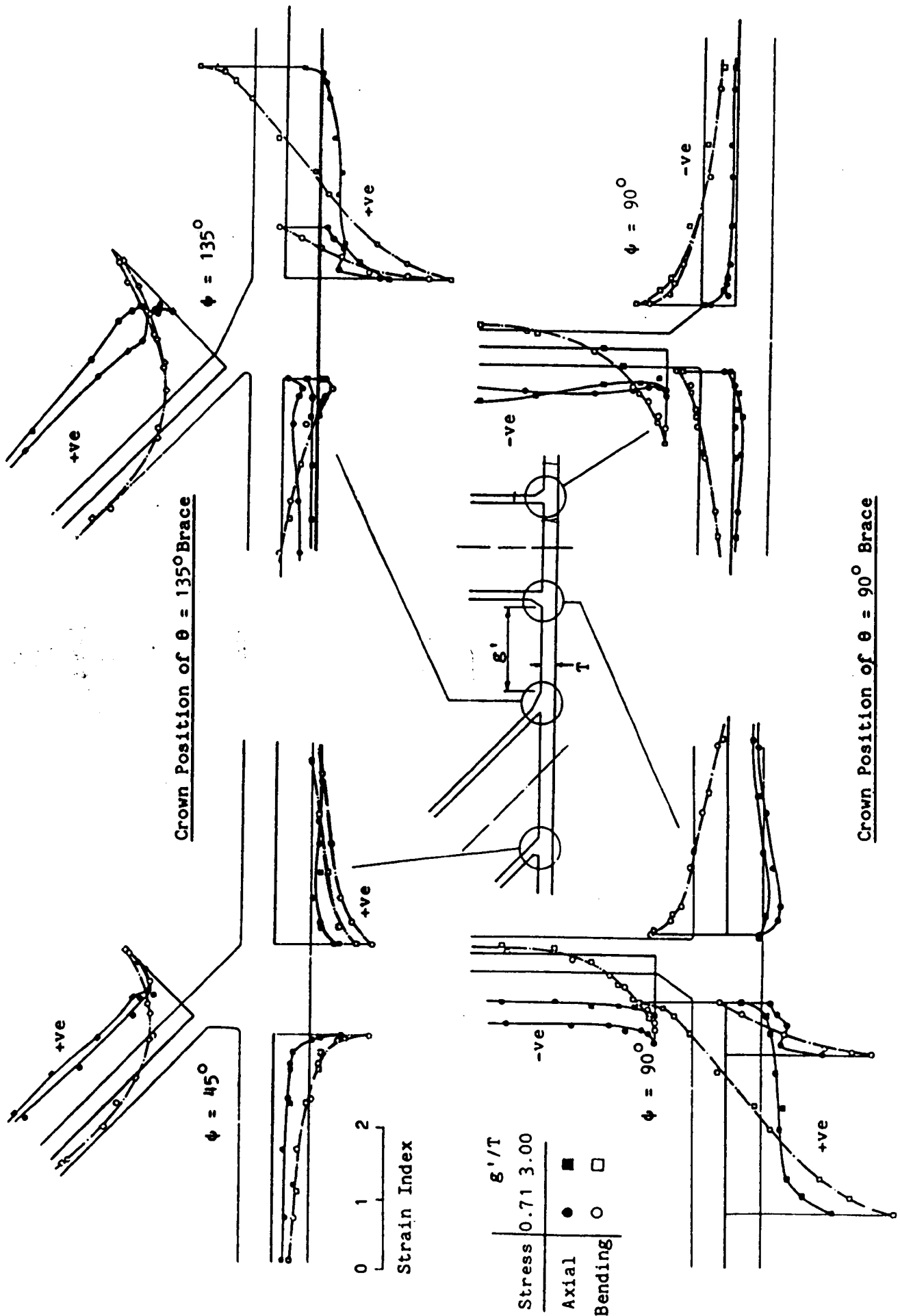


Fig. 6.44 Axial and Bending Stresses in Crown Plane I in CK Models

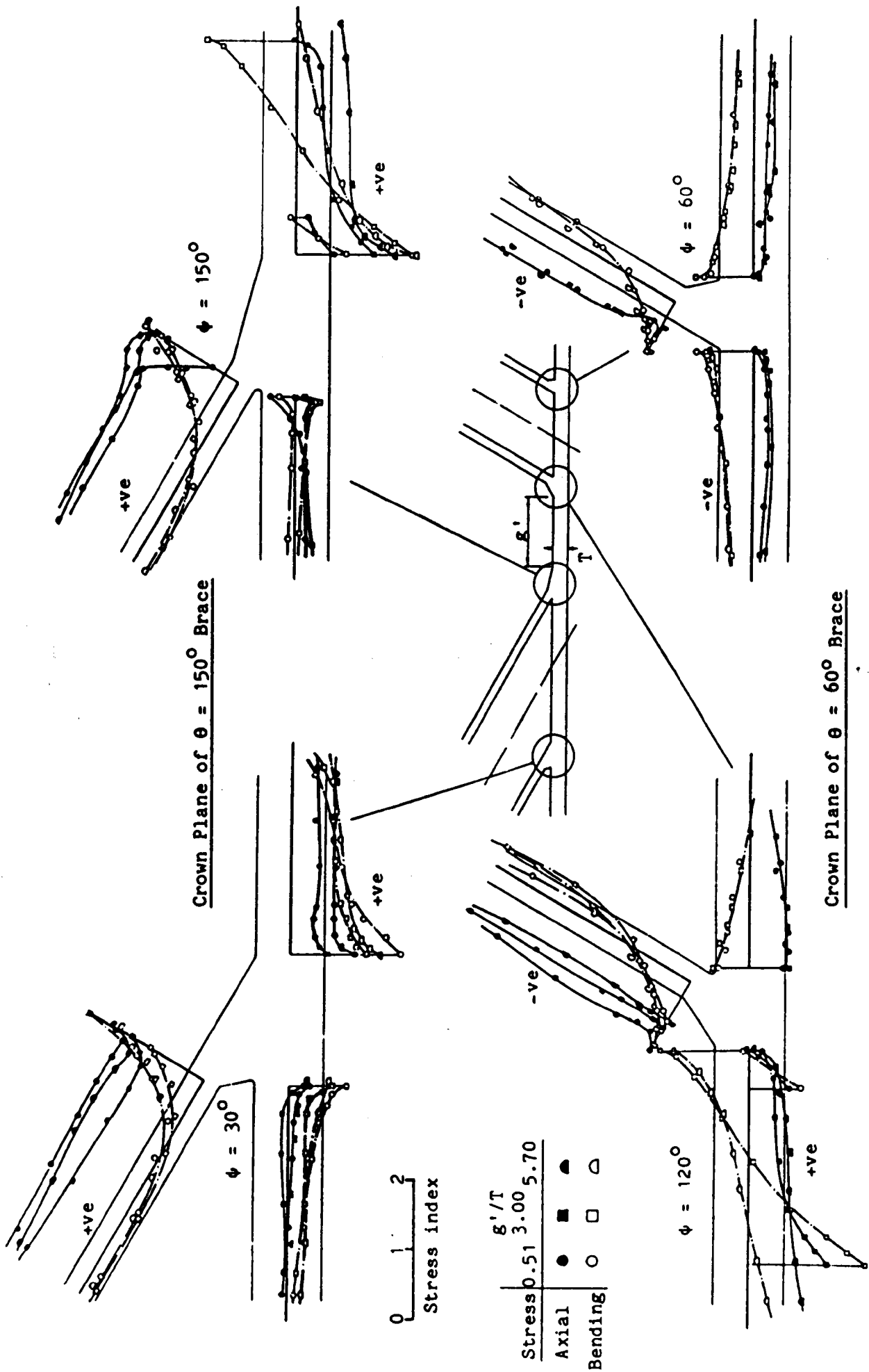


Fig. 6.45 Axial and Bending Stresses in Crown Plane II in CK Models

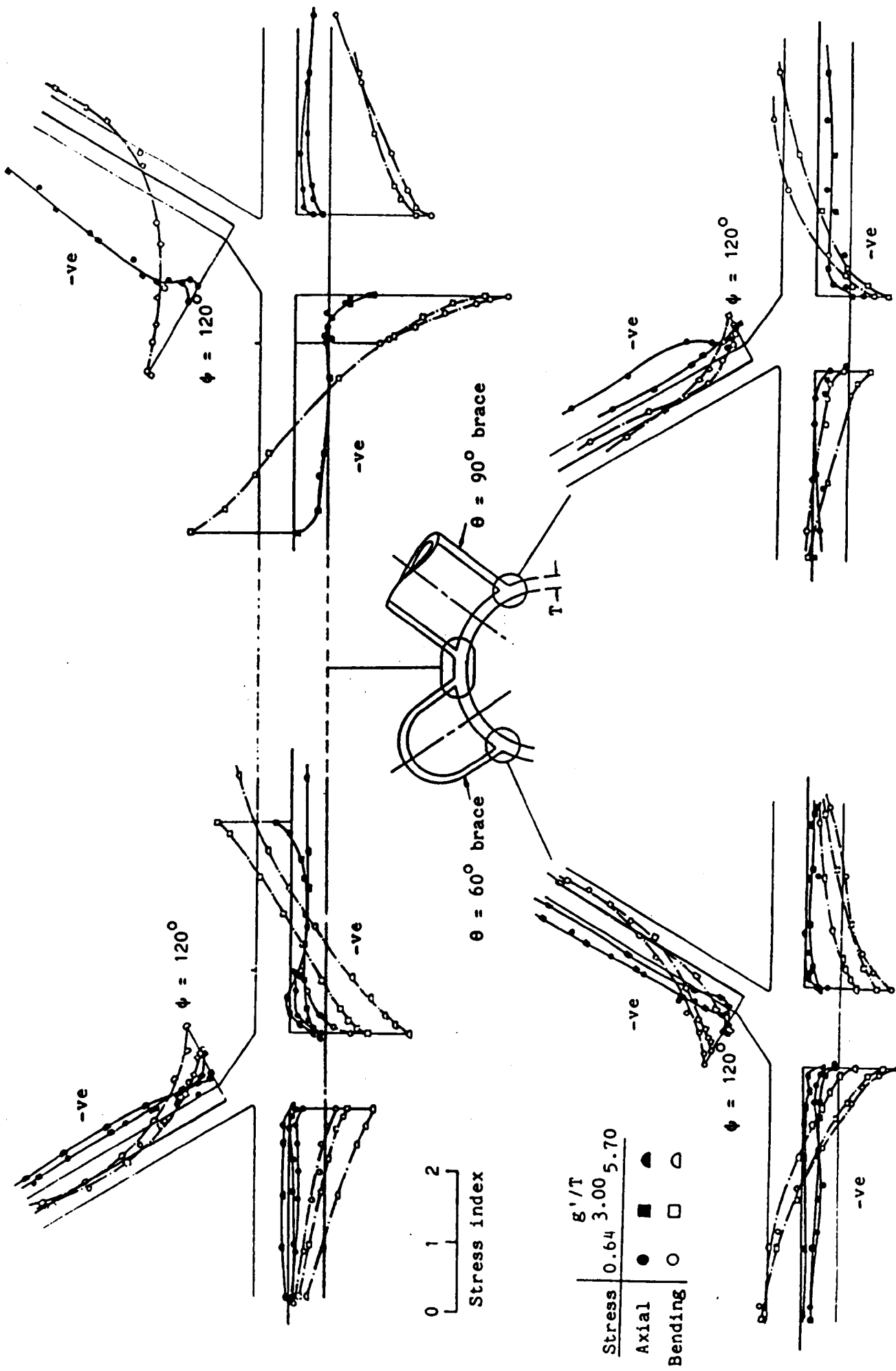


Fig. 6.46 Axial and Bending Stresses in Saddle Plane III in CK Models

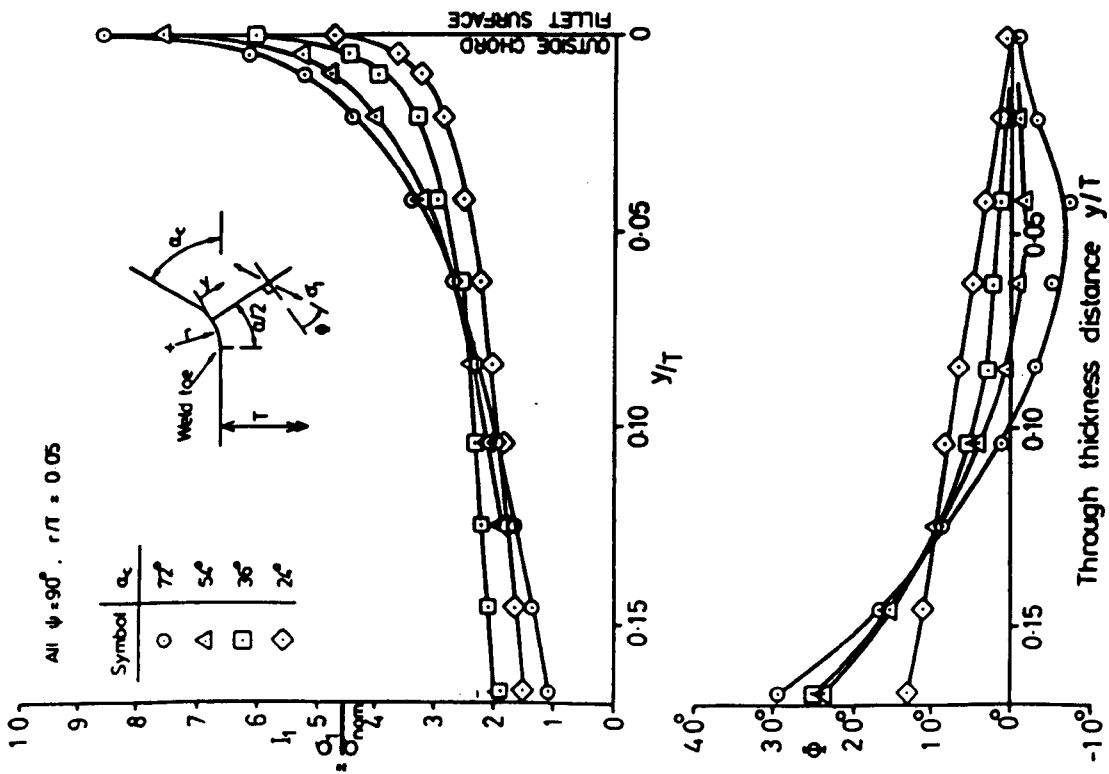
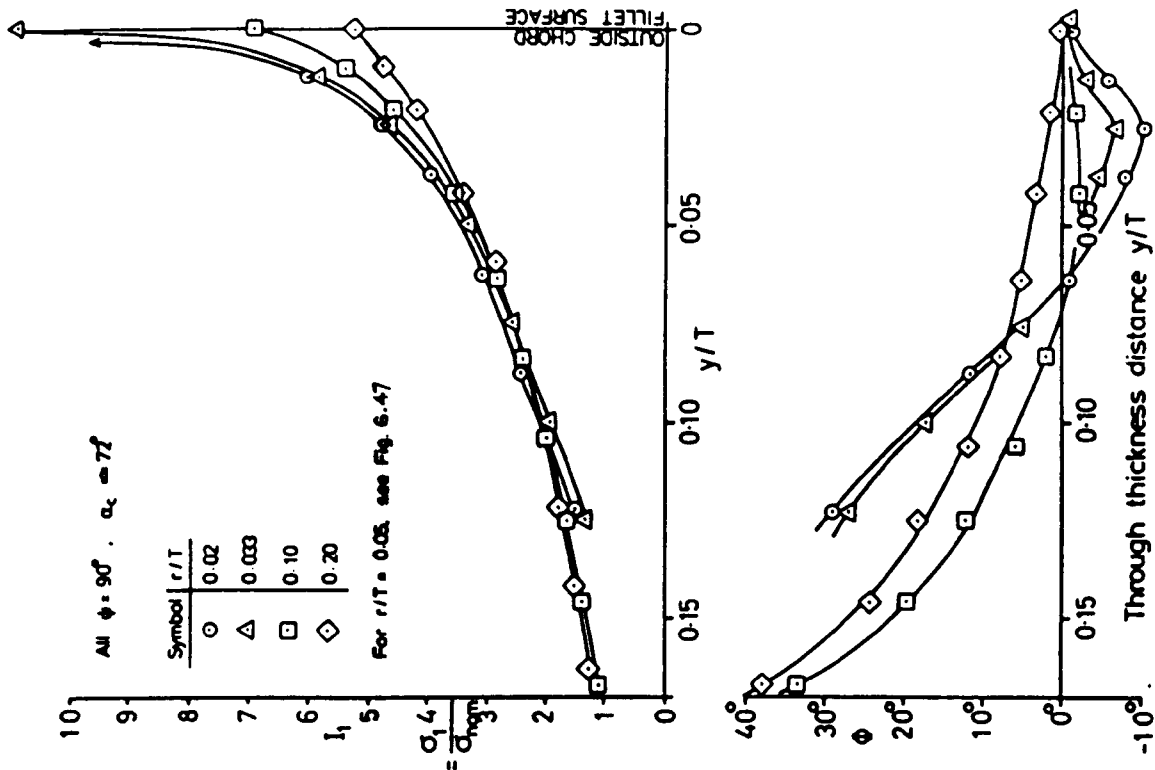


Fig. 6.48 Effect of Weld Toe Radius

Fig. 6.47 Effect of Weld Angle

Magnitudes and Directions of Through-Thickness Principal Stresses in Crown Plane in K No. 22

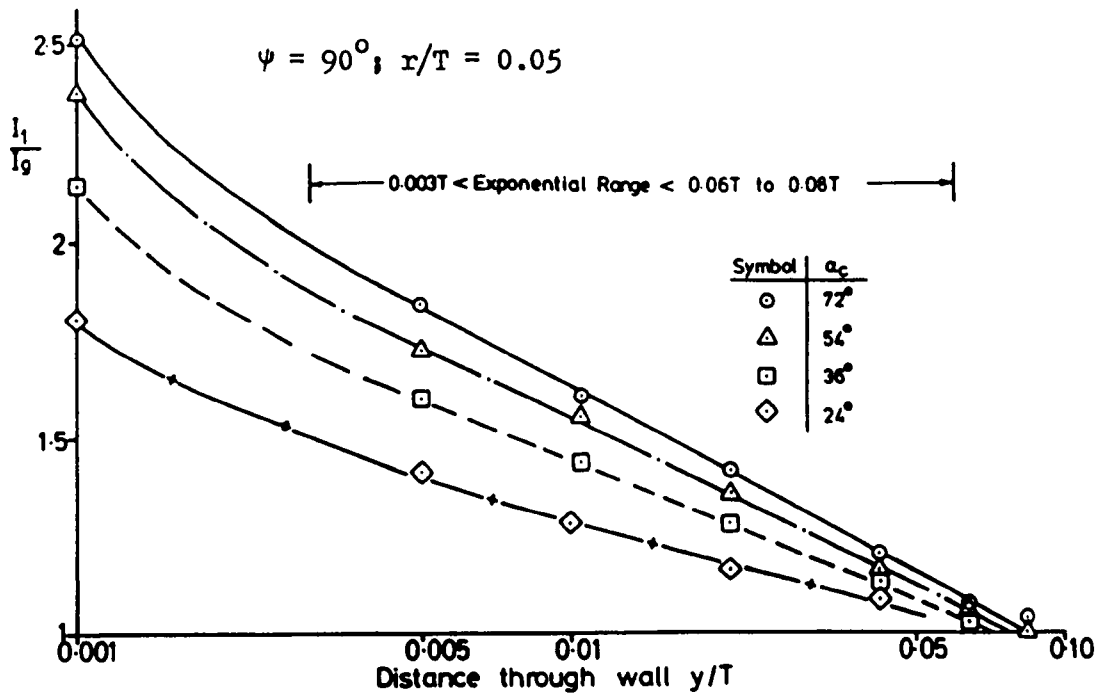


Fig. 6.49 Effect of Weld Angle

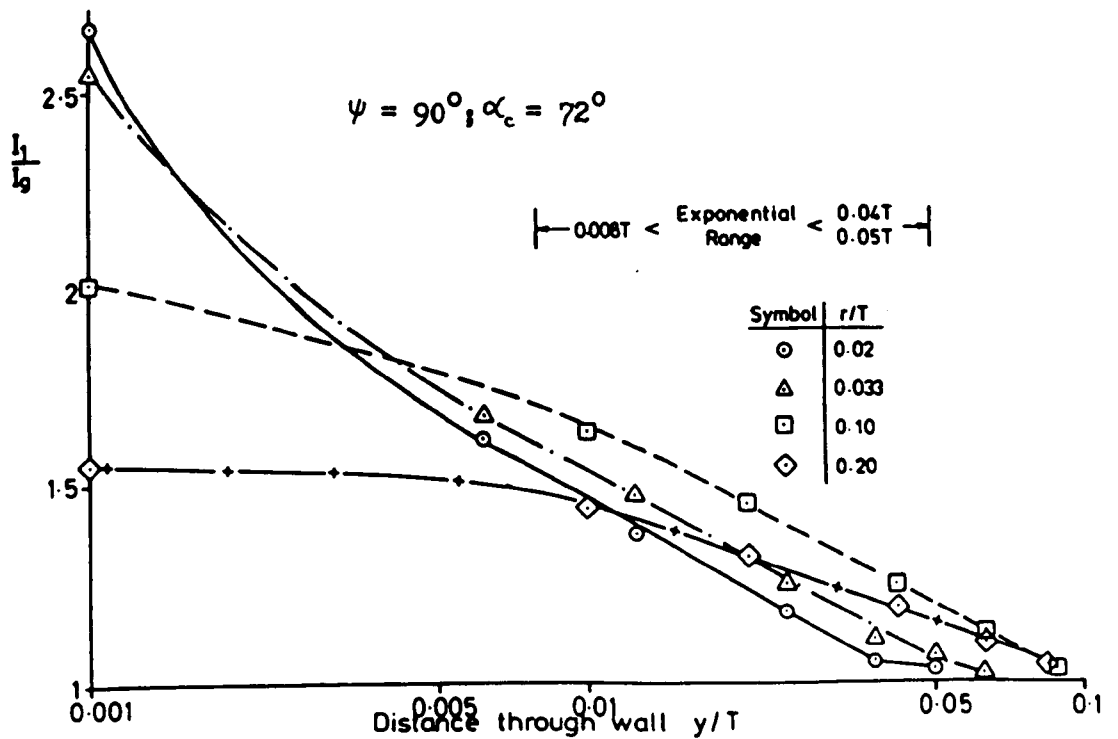


Fig. 6.50 Effect of Weld Toe Radius

Through-Thickness Notch Stress Indices in Crown Plane in K Nodes

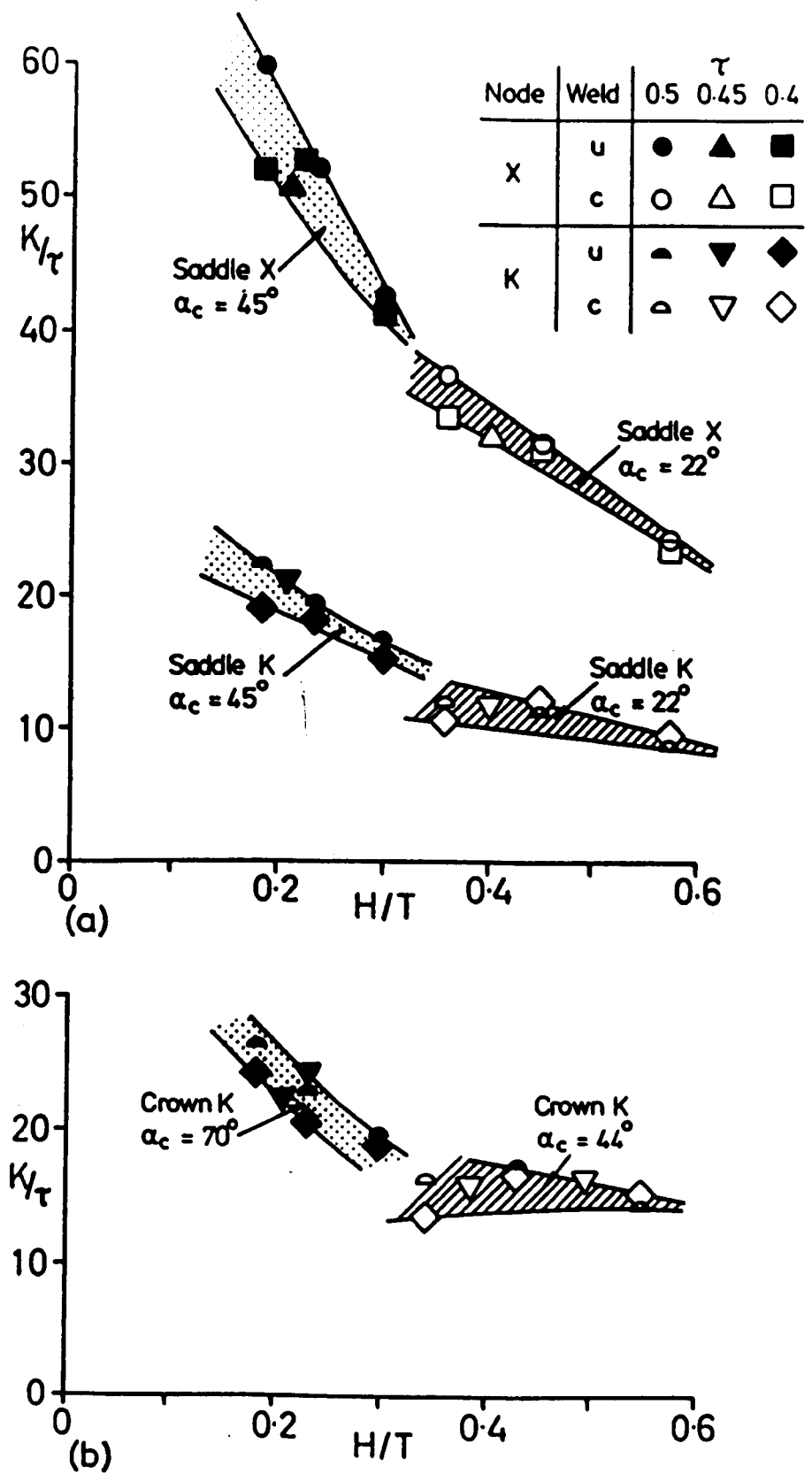


Fig. 6.51 Effect of Weld Profile and τ on SCFs in Different Positions

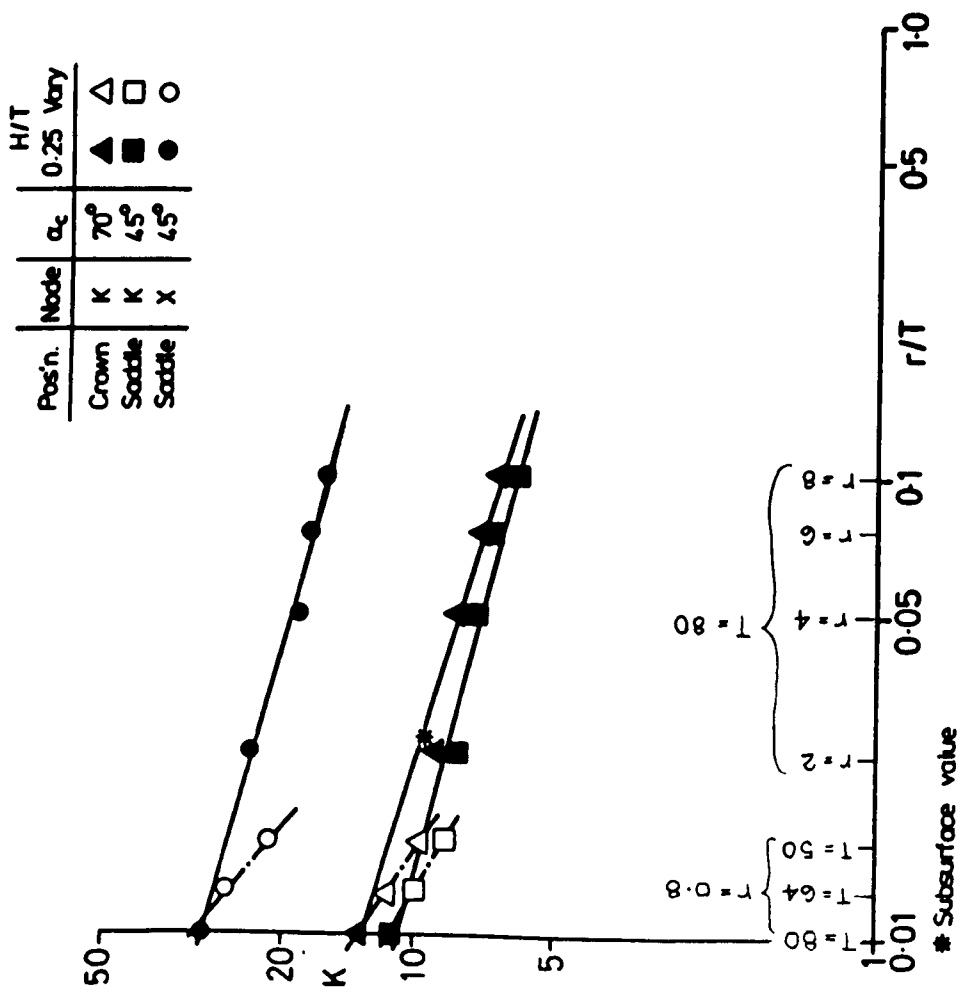


Fig. 6.52 Effect of Position, Weld Toe Radius and Leg Length on SCFs

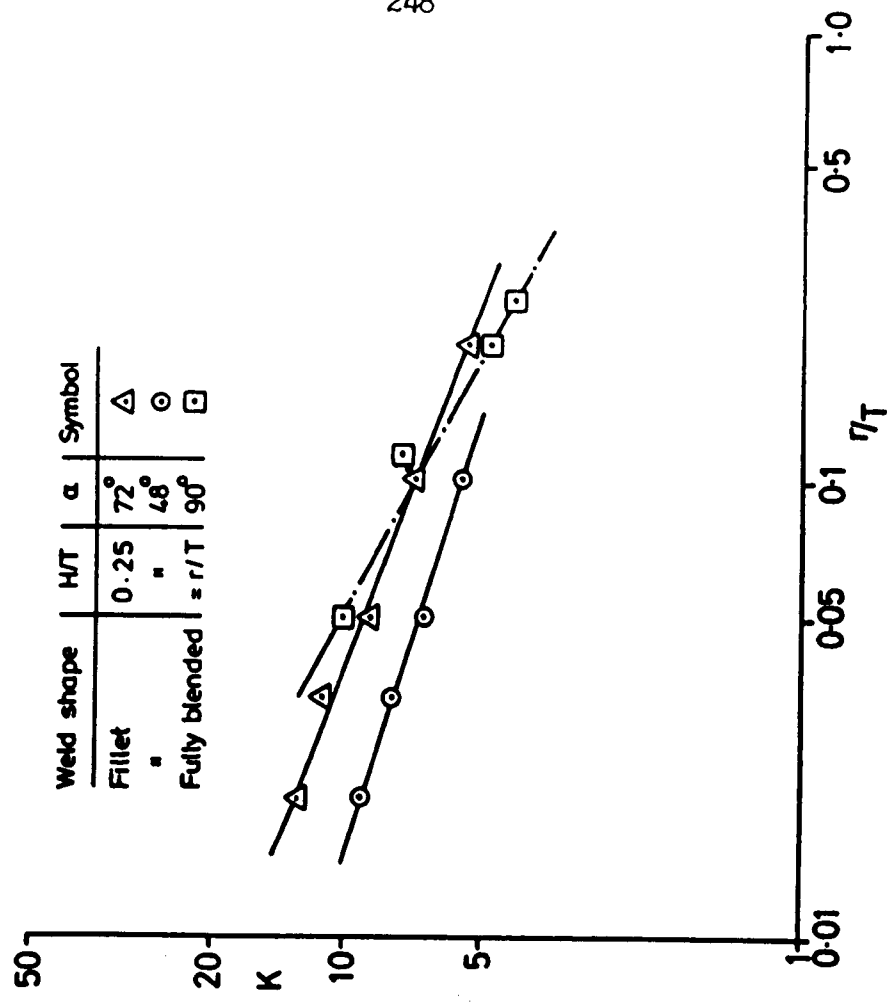


Fig. 6.53 Effect of Weld Shape and Weld Toe Radius on SCFs at Crown Positions in K Nodes

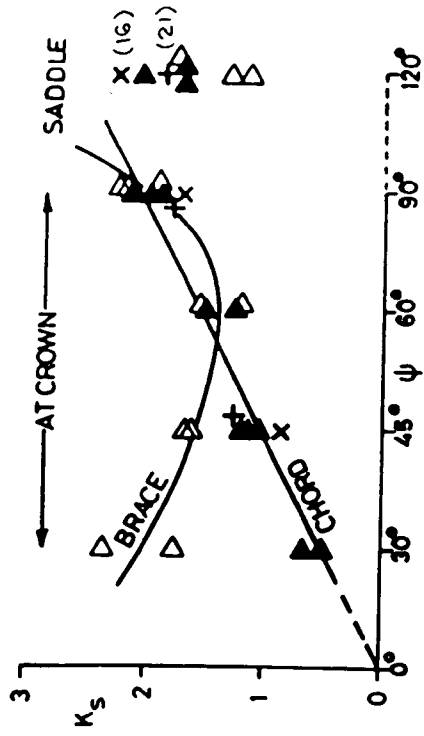


Fig. 6.55 Effect of ψ and Position on Shell SCFs in CK Models

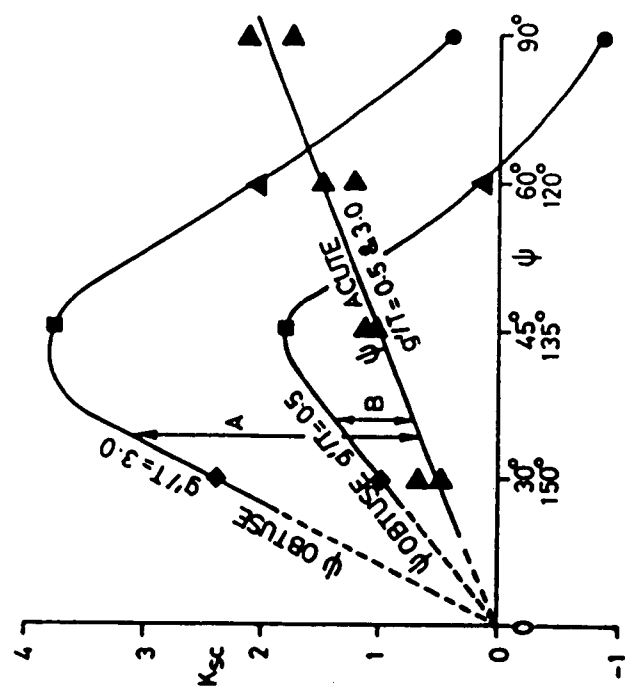
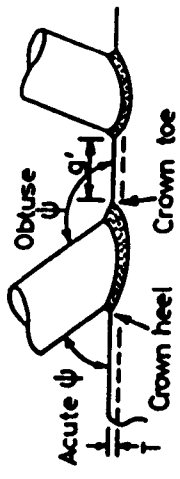
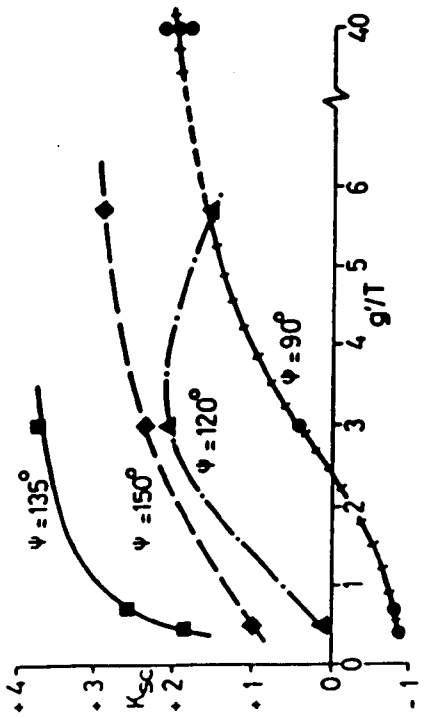
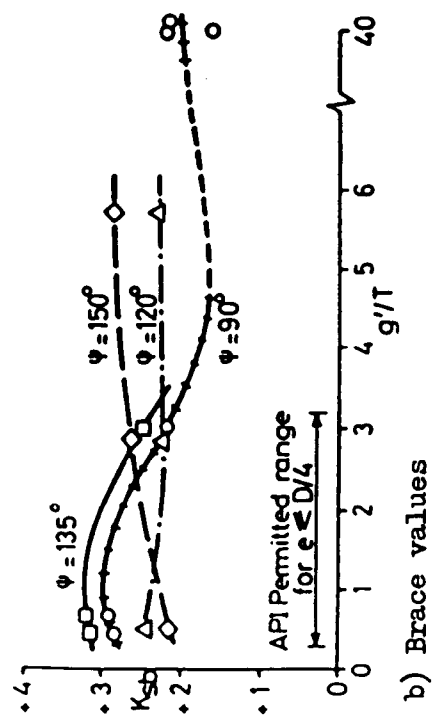


Fig. 6.56 Comparison of Crown Heel and Toe Shell SCFs in CK Models



a) Chord values



b) Brace values

Fig. 6.54 Effect of Brace Inclination and Proximity on Shell SCFs in Crown Planes in CK Models

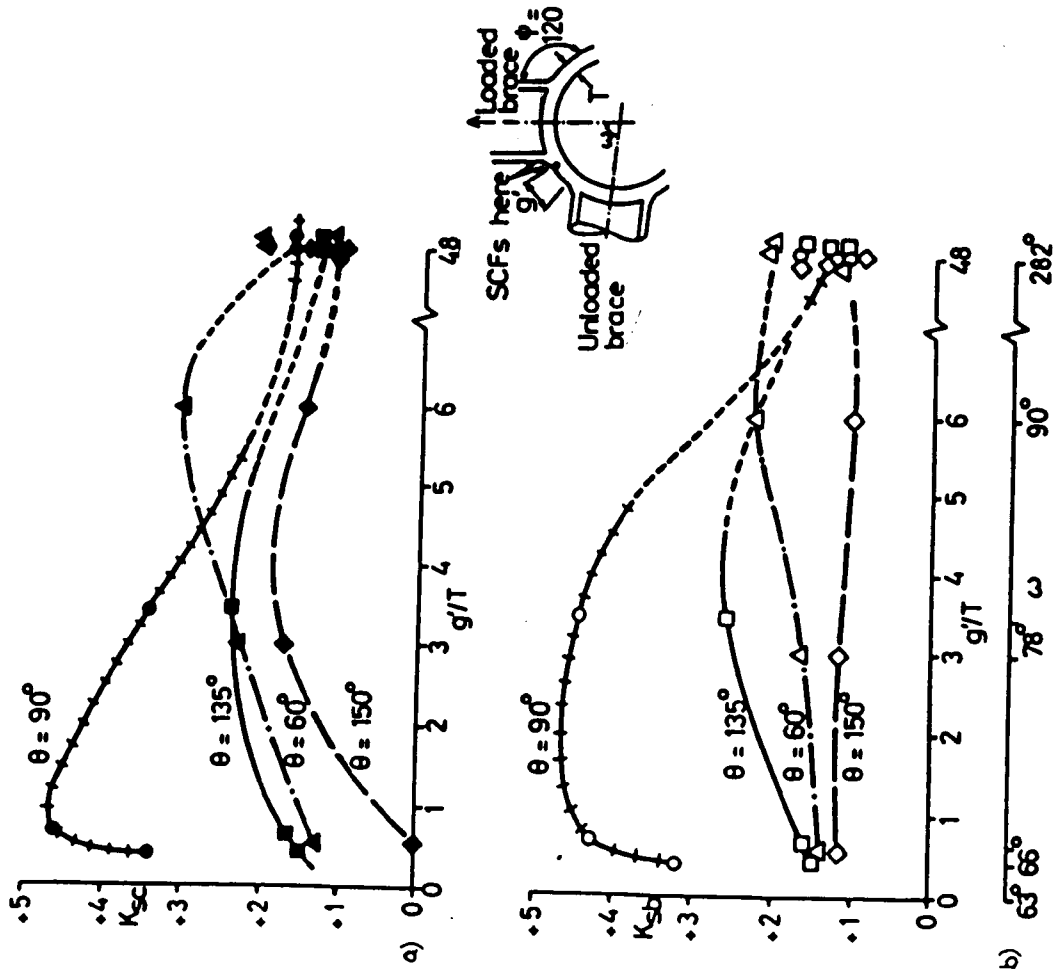


Fig. 6.57 Chord and Brace Hoop Values

Effect of Brace Inclination and Proximity on Shell SCFs at Saddle Positions in CK Models

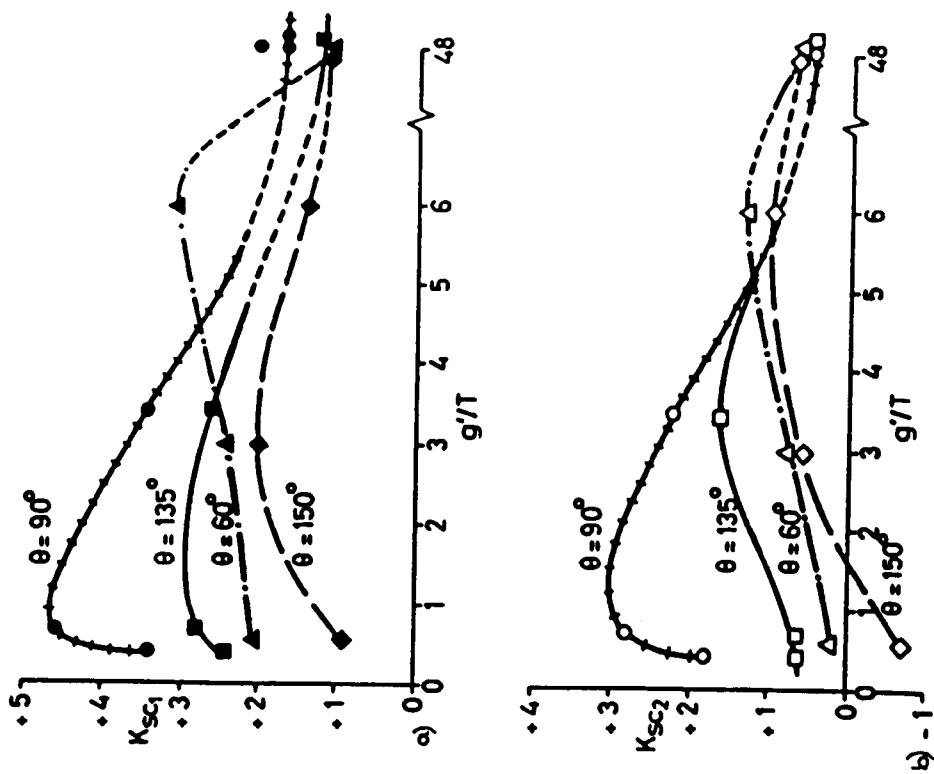


Fig. 6.58 Max. and Min. Principal Chord Values

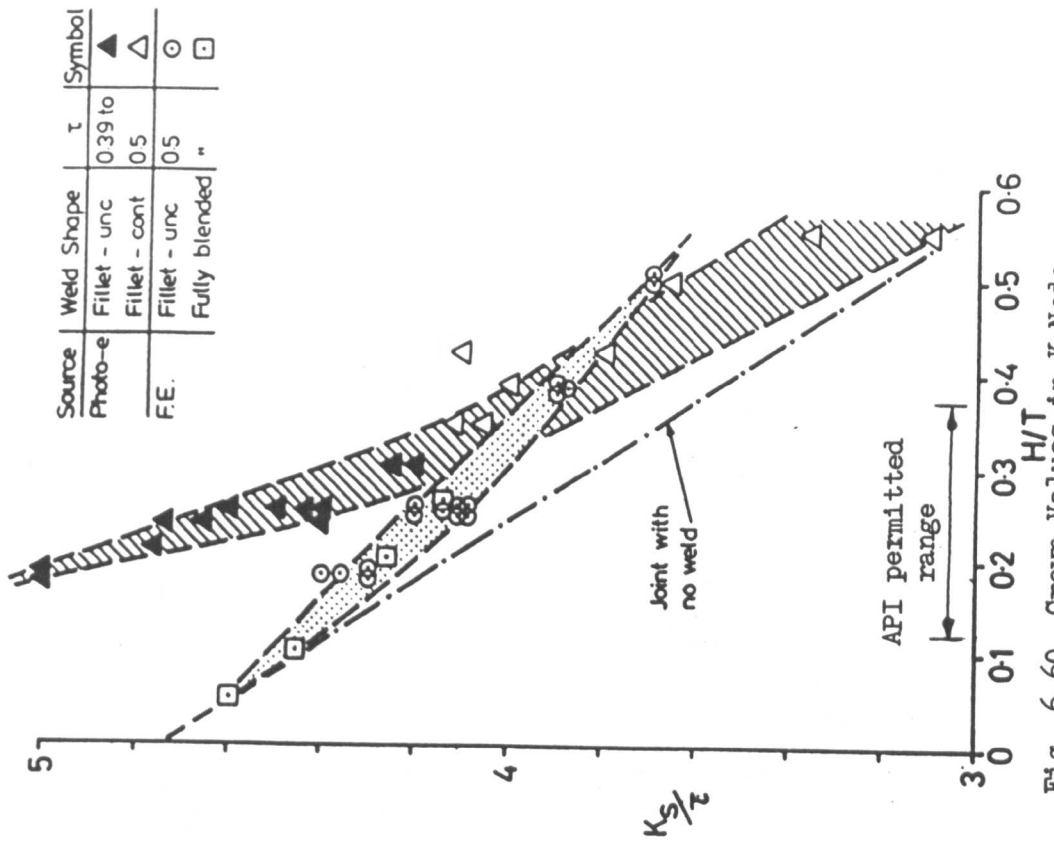


Fig. 6.60 Crown Values in K Node

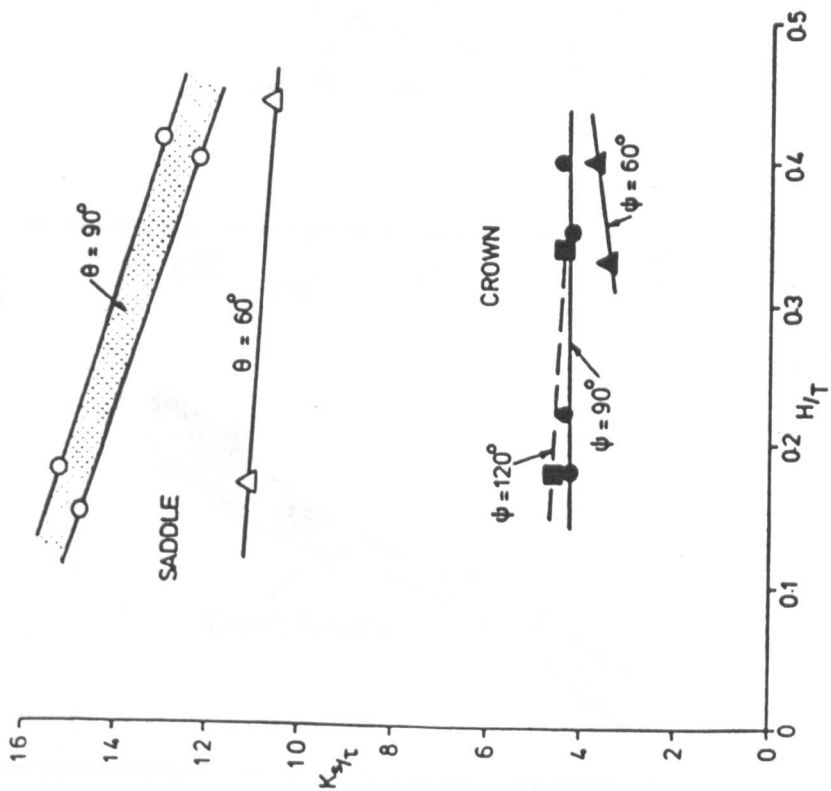


Fig. 6.59 3-d X Model Values

Effect of Position, Weld Profile and Leg Length on Shell SCFs

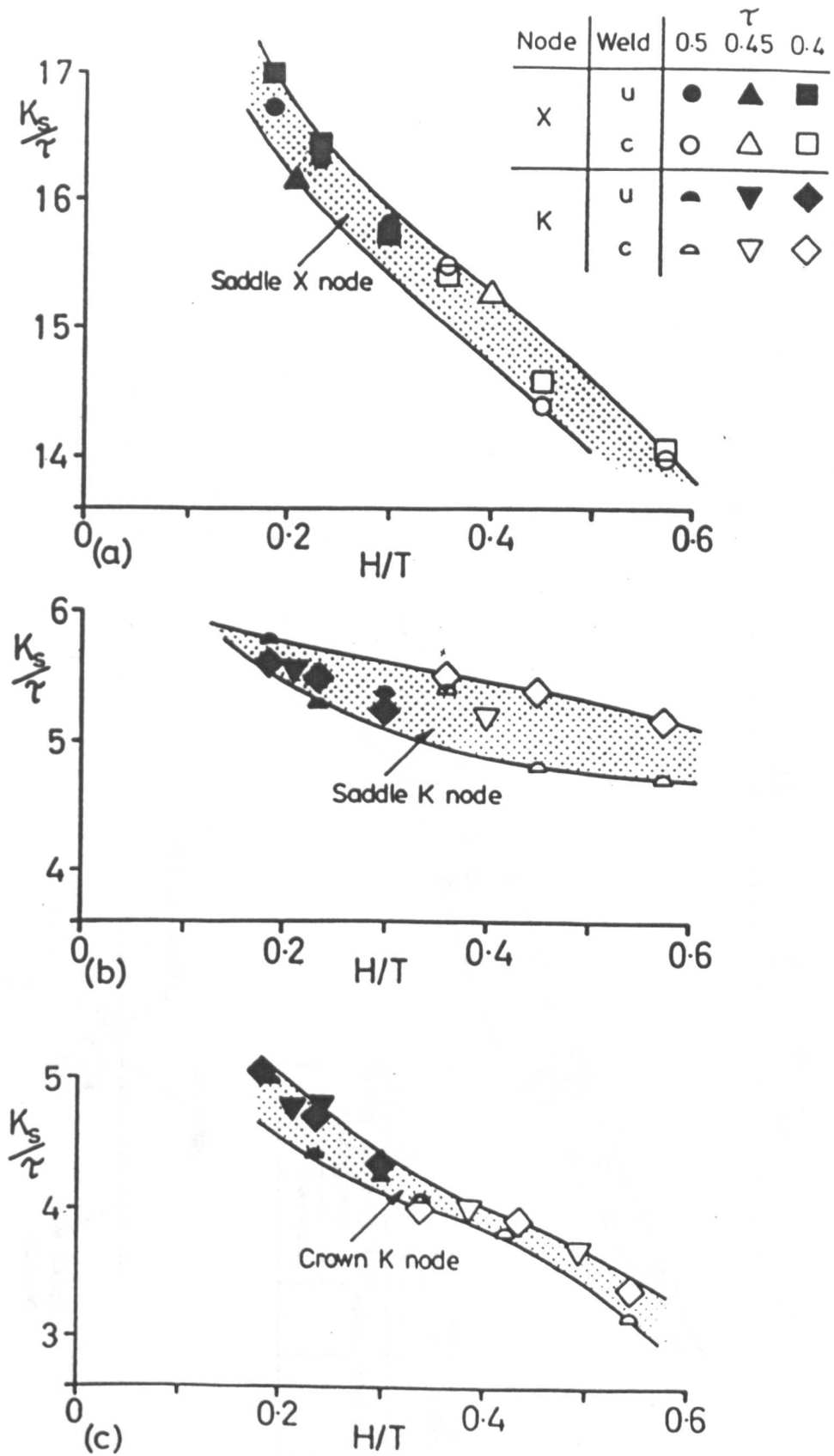


Fig. 6.61 Effect of Weld Profile and τ on Shell SCFs at Different Positions

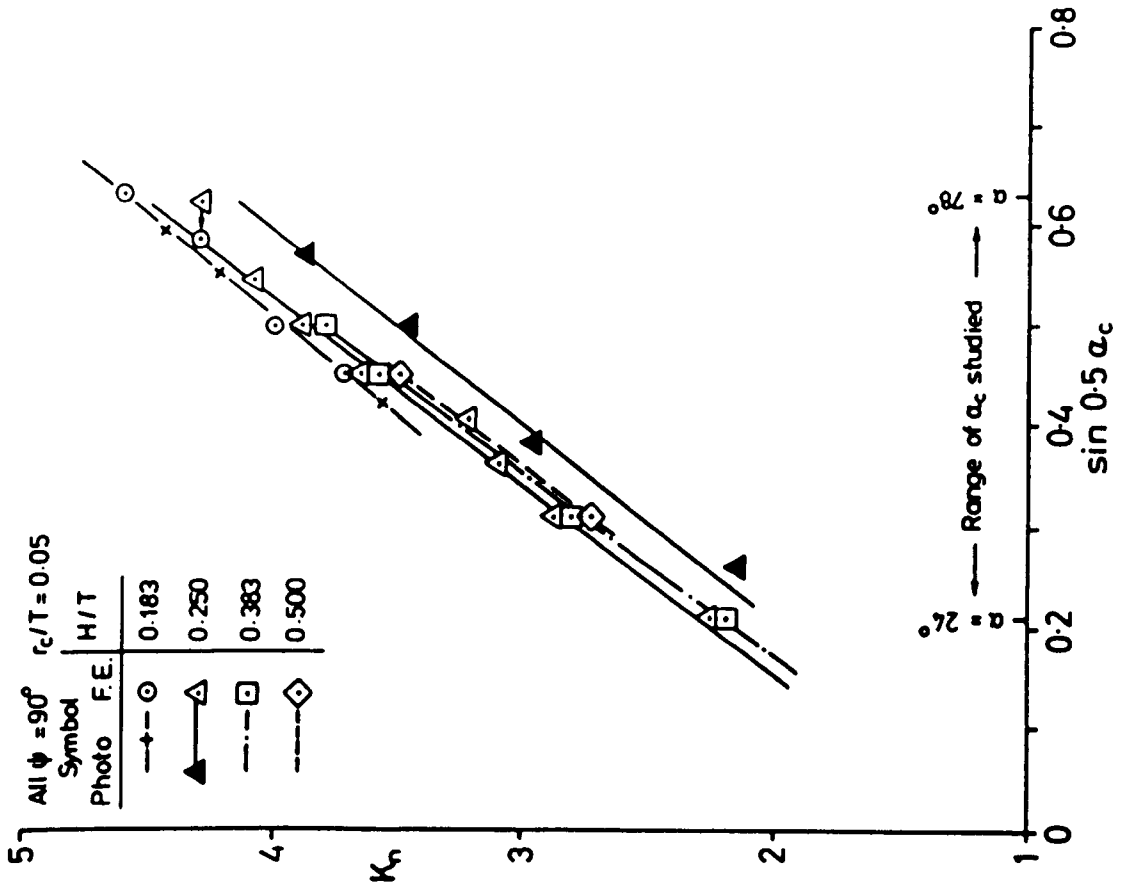


Fig. 6.63 Effect of Weld Angle and Leg Length on Notch SCF in Grown Position in K Node

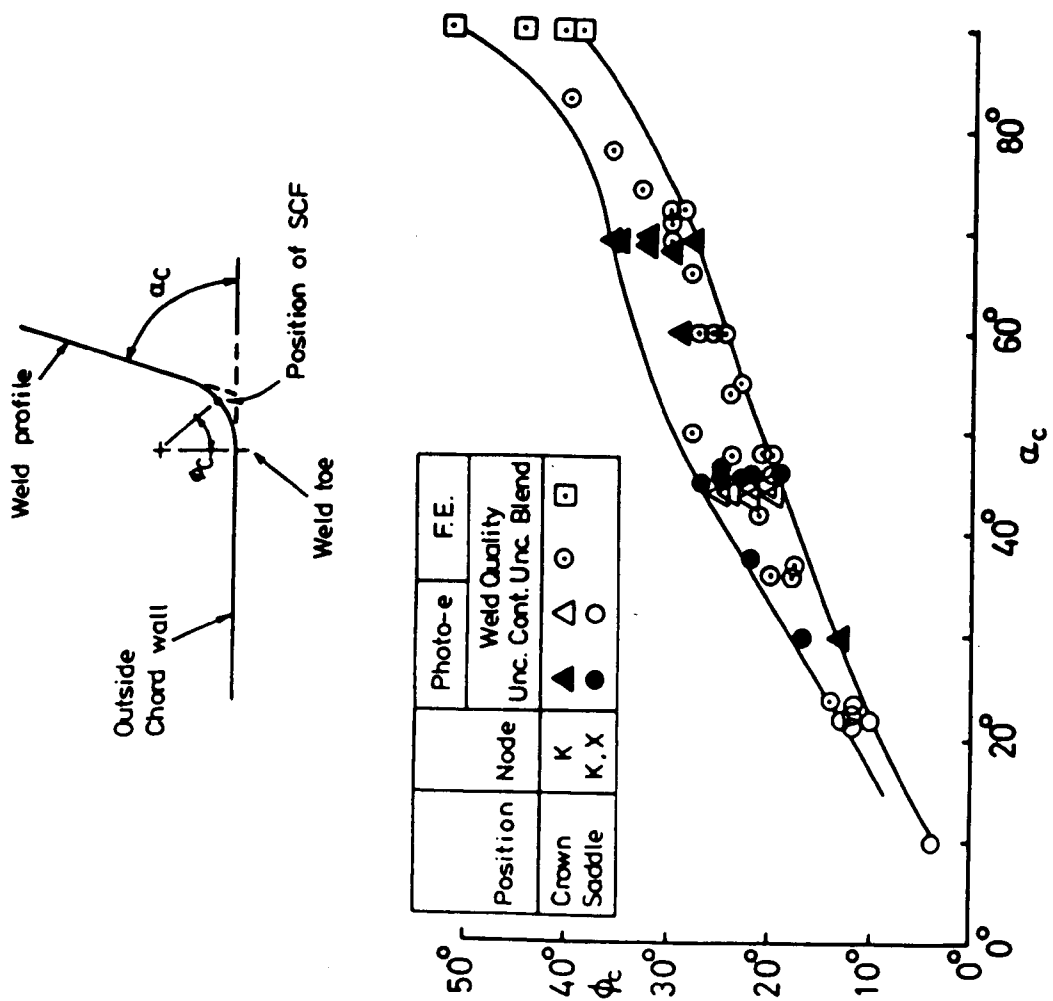


Fig. 6.62 Variation in Position of SCF with Weld Angle

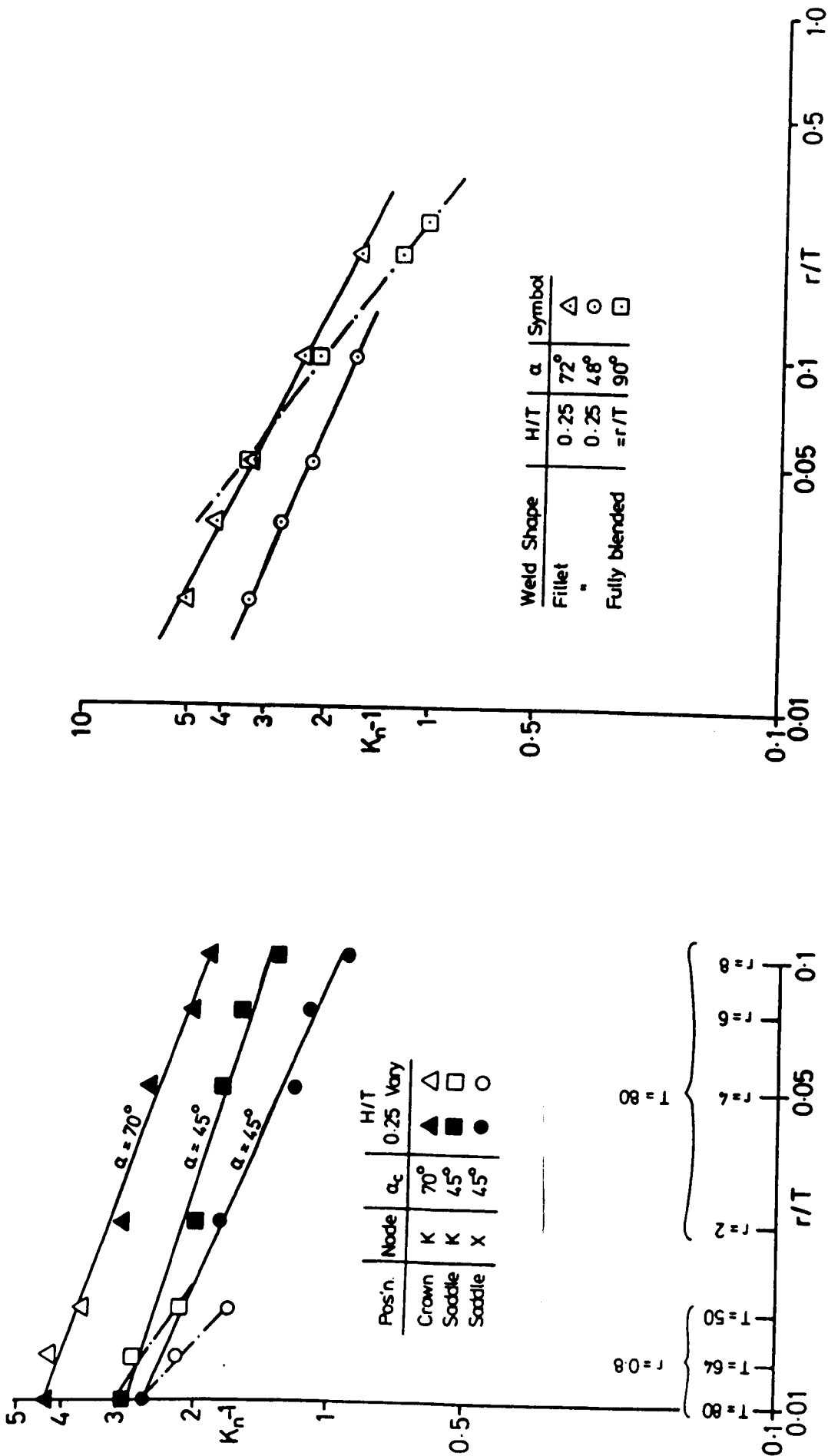


Fig. 6.64 Effect of Position, Weld Toe Radius and Leg Length on Notch SCFs

Fig. 6.65 Effect of Weld Shape and Weld Toe Radius on Notch SCFs at Crown Position in K Node

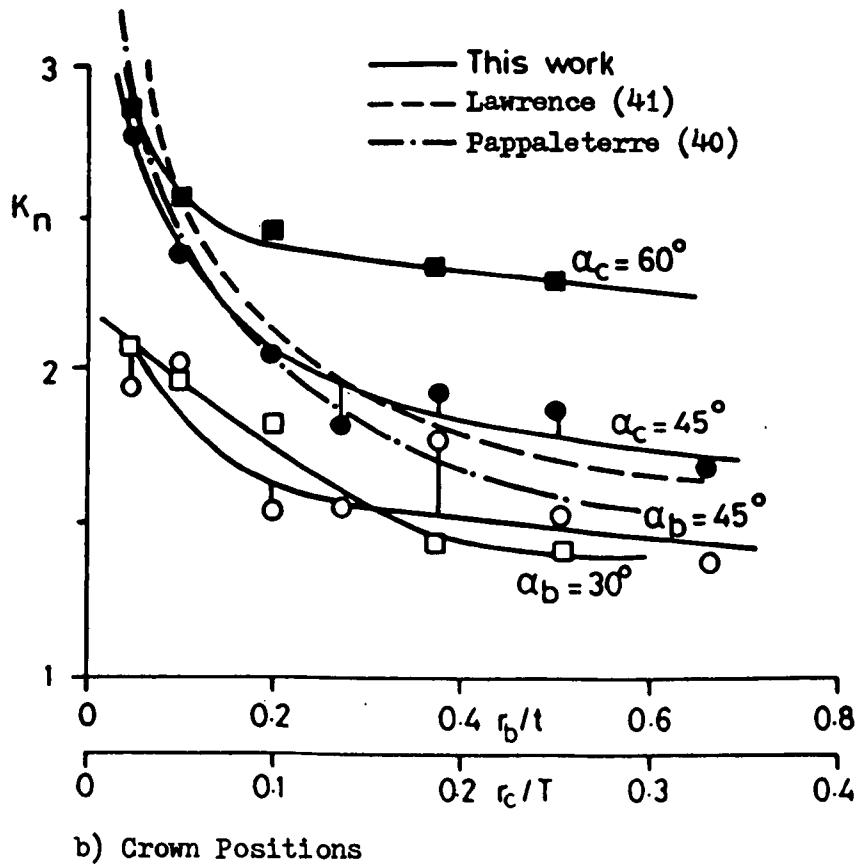
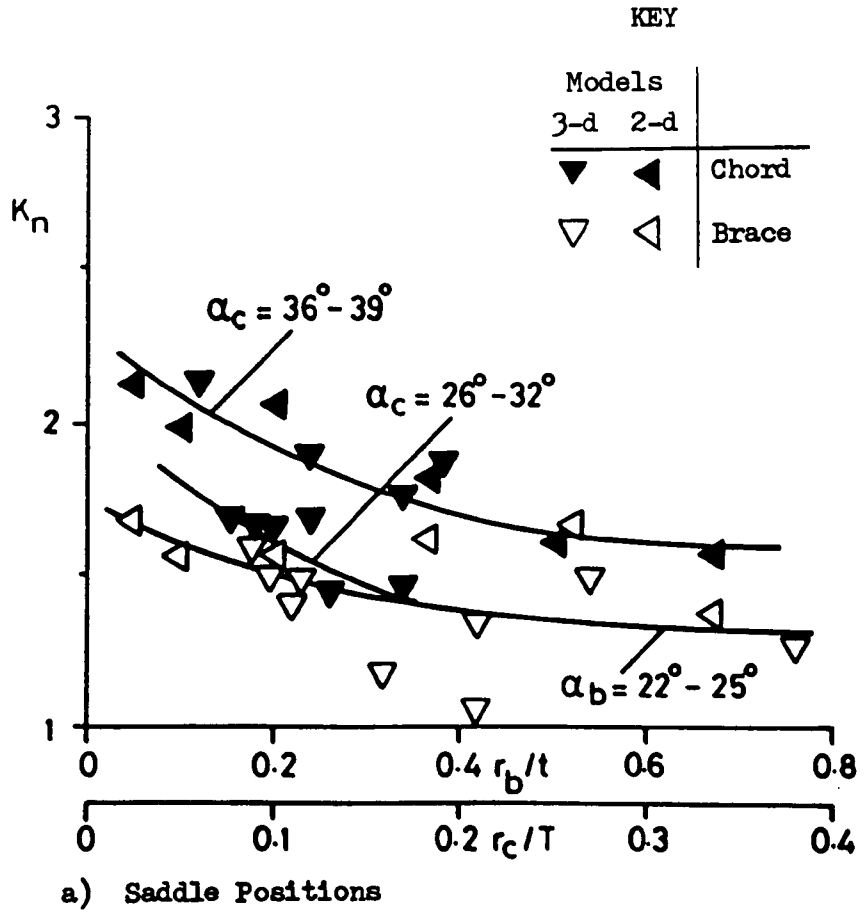


Fig. 6.66 Effect of Weld Angle and Toe Radius on Notch SCFs in 3-d and 2-d Models

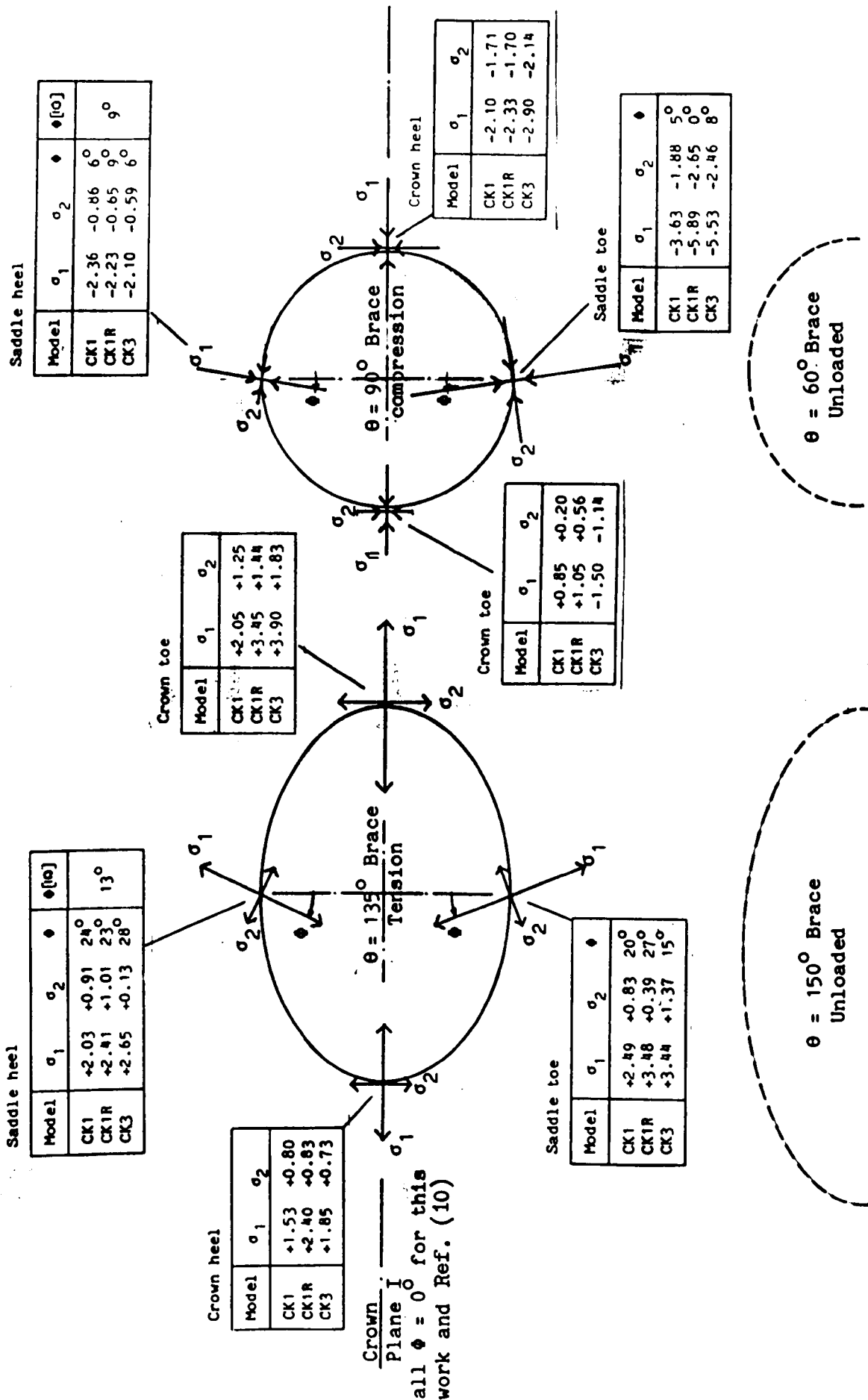


Fig. 6.67 Summary of Magnitudes and Directions of Principal Stresses at Chord Weld Toes at $\theta = 90^\circ$ and 135° Braces in CK Models

Notes

1. $SCF = \sigma$ (at weld toe) / $|\sigma'_{nom}|$ (in own loaded brace)
2. These values included notch effects

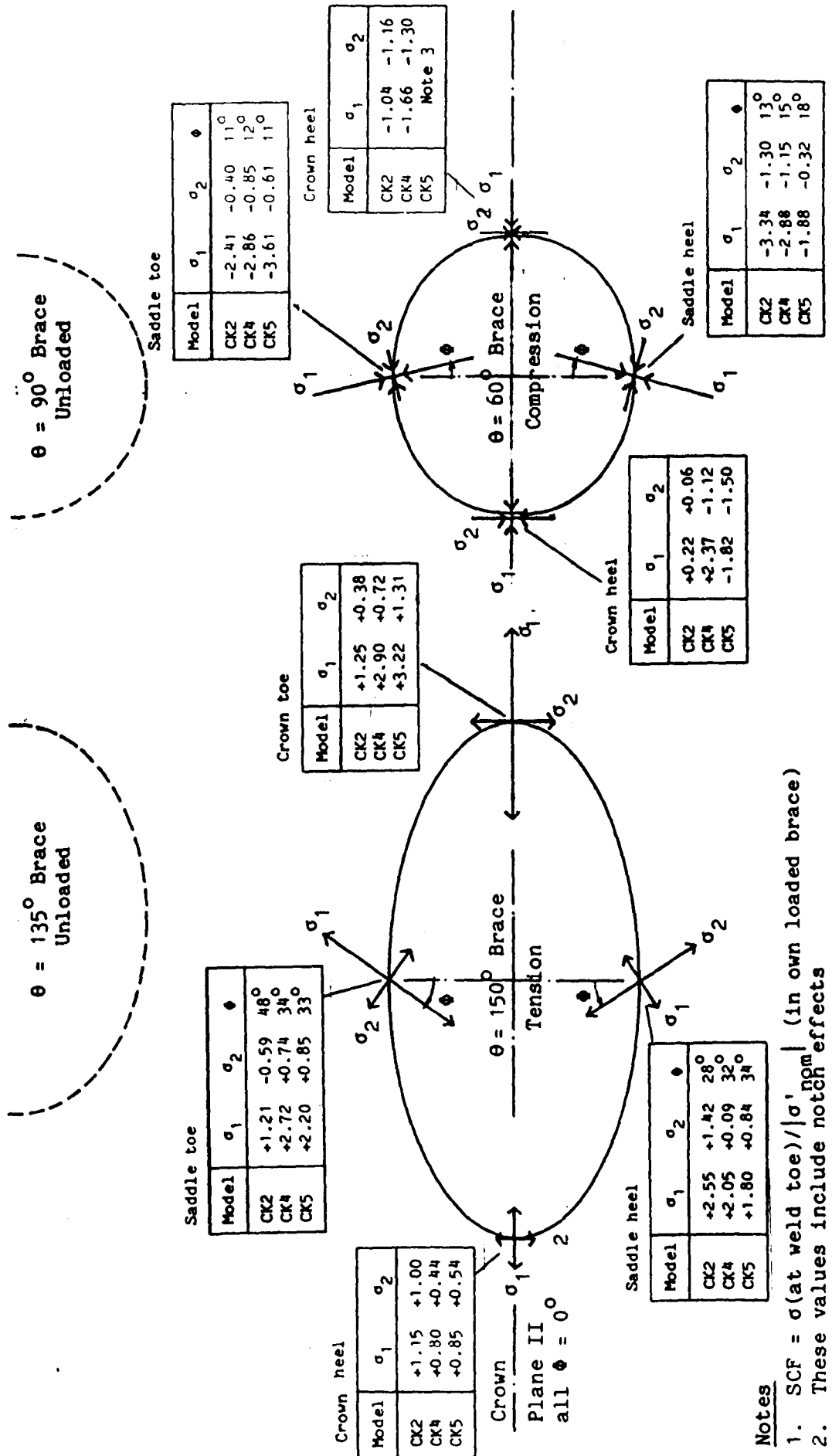


Fig. 6.68 Summary of Magnitudes and Directions of Principal Stresses at Chord Weld Toes at $\theta = 60^\circ$ and 150° Braces in CK Models

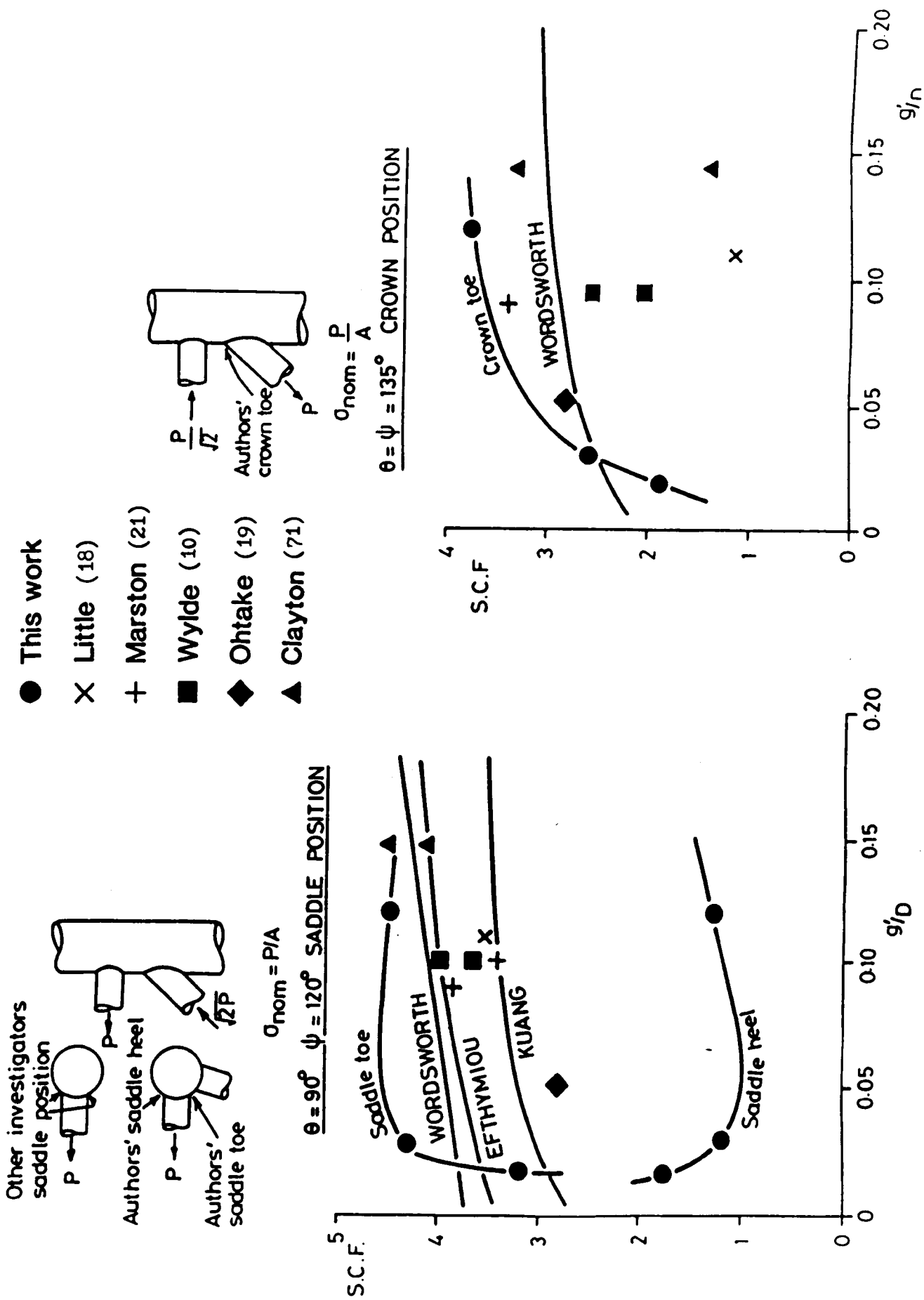


Fig. 6.69 Comparison of Shell SCFs Obtained in This Work with SCFs Predicted by Parametric Equations of, or Measured by, Other Investigators

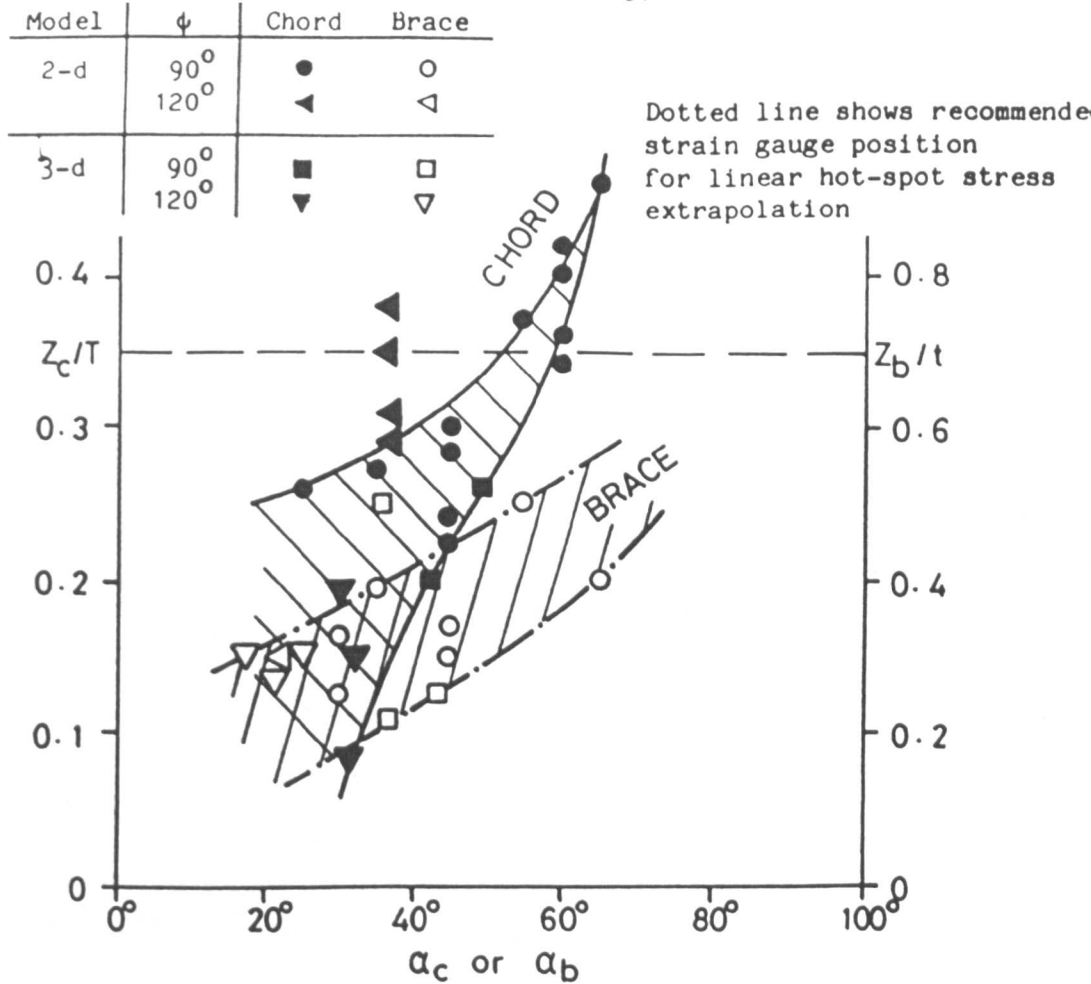


Fig. 6.70 Effect of Weld Angle and Position on Size of Notch Zones (all $\theta = 90^\circ$)

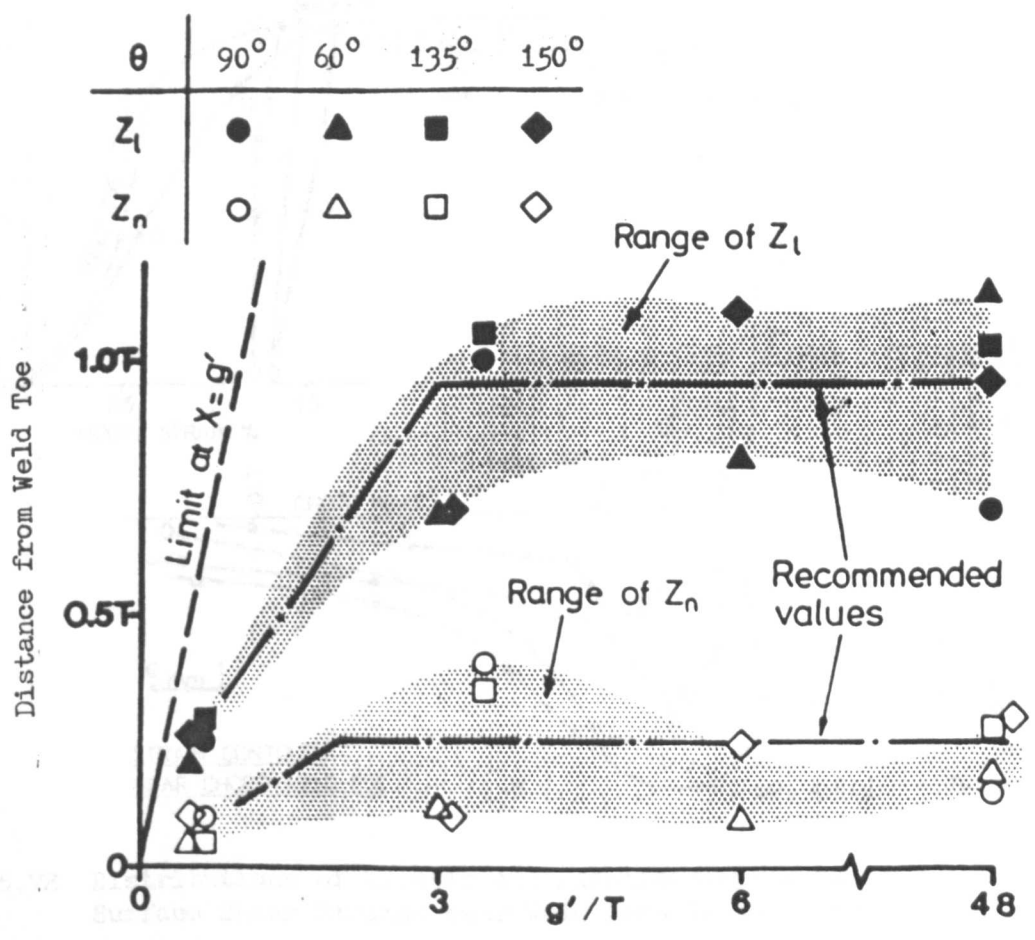


Fig. 6.71 Extent of Linear Stress Regions and Recommended Strain Gauge Positions for Use in Two-Point Extrapolation Methods

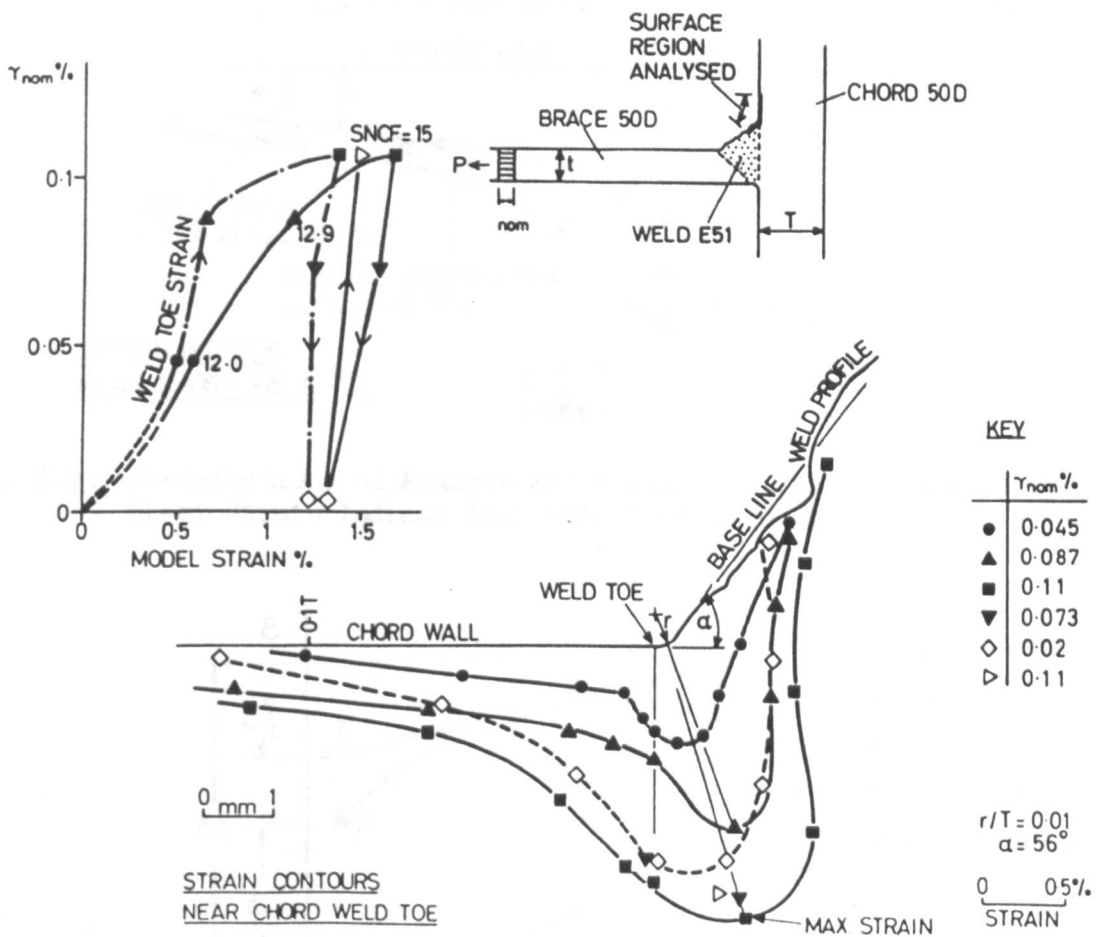
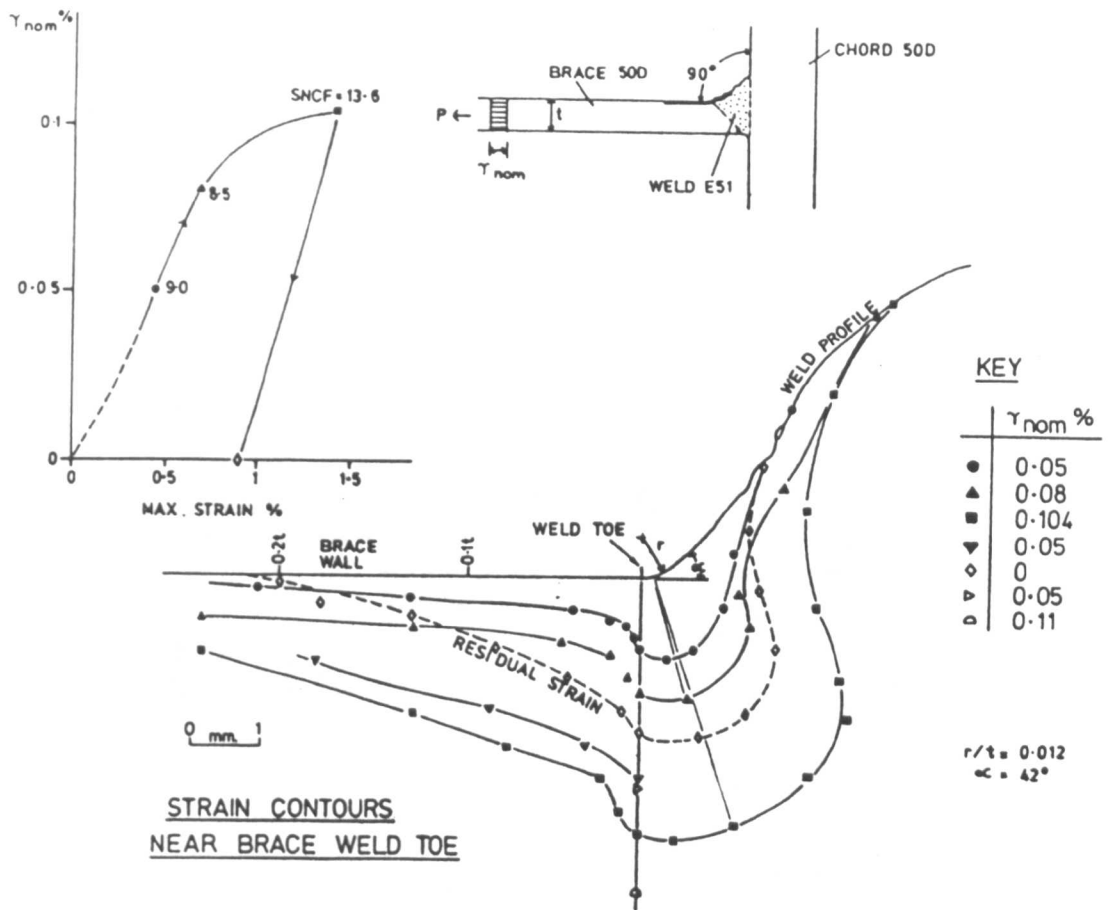


Fig. 6.72 Distributions of Elastic and Plastic-Elastic Maximum Surface Shear Strains Near Weld Toes in Steel Model No. 1

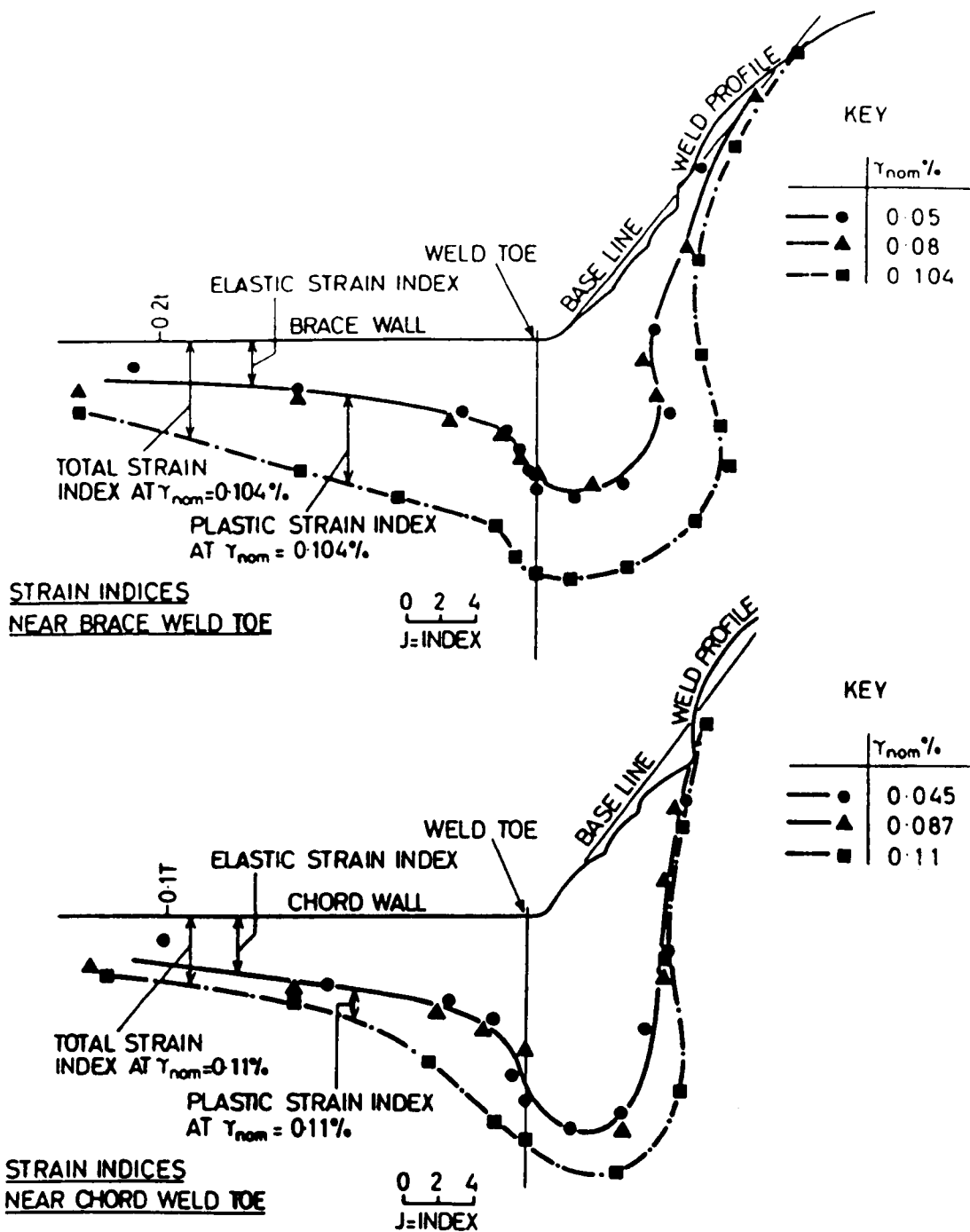


Fig. 6.73 Distributions of Elastic and Plastic-Elastic Maximum Surface Shear Strain Indices Near Weld Toes in Model No. 1

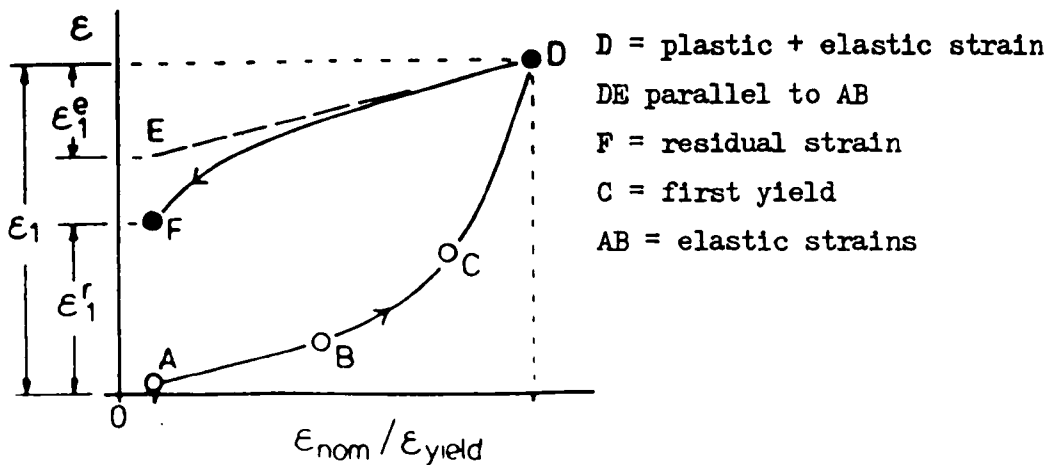


Fig. 6.74 Definitions of Strains at Different Load Magnitudes

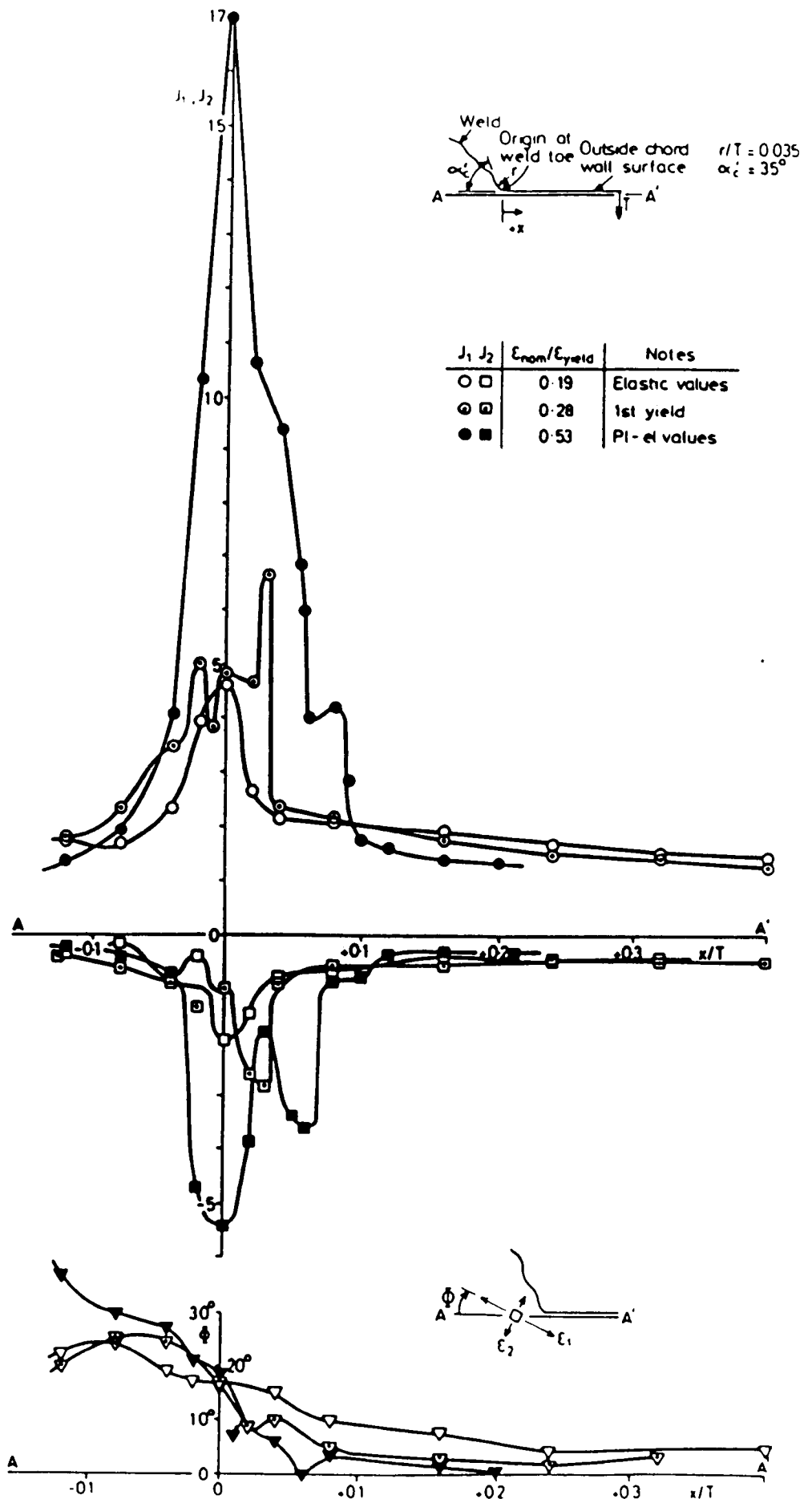


Fig. 6.75 Magnitudes and Directions of Elastic and Plastic-Elastic Principal Strain Indices in Steel Model No. 2

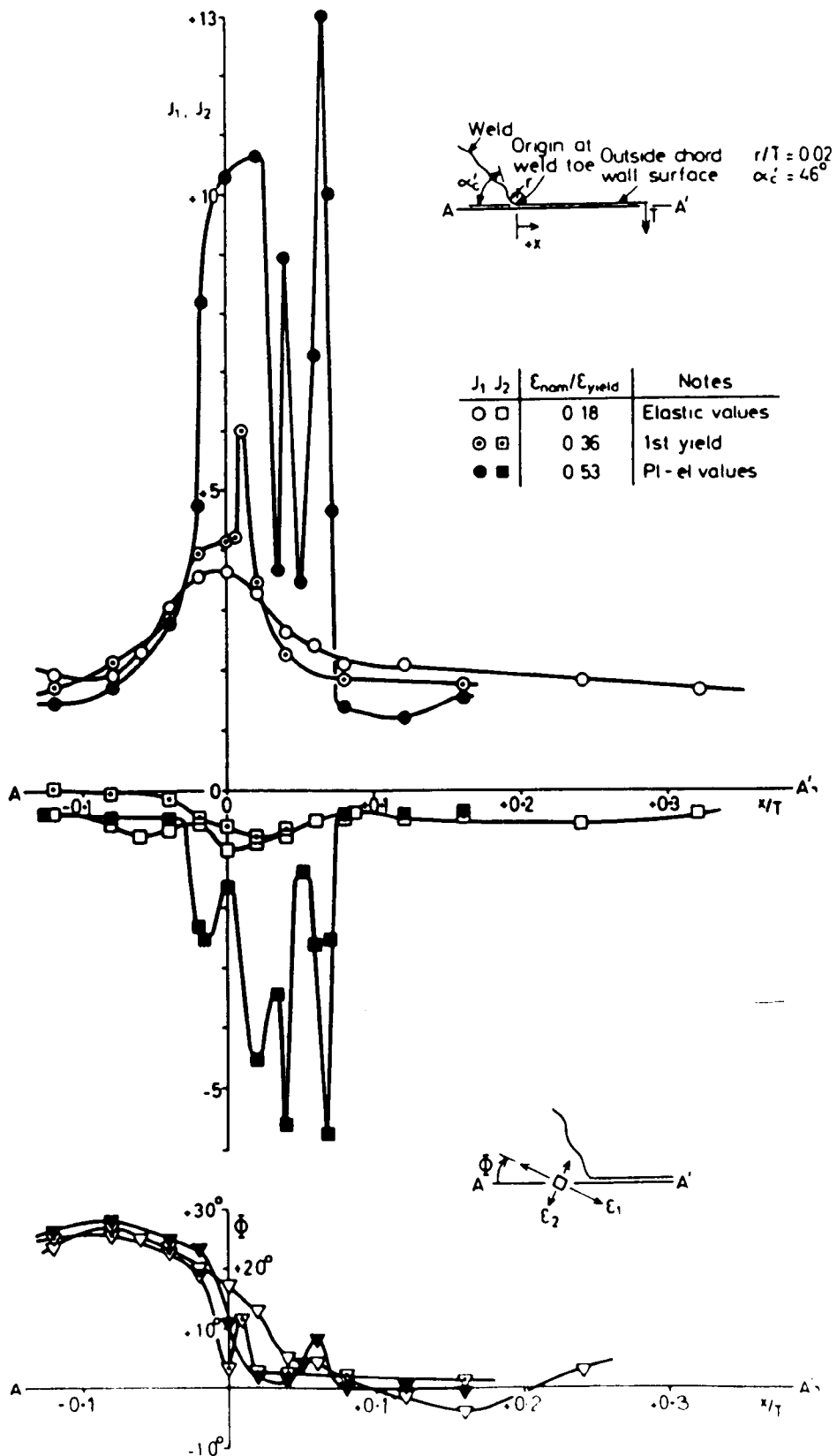


Fig. 6.76 Magnitudes and Directions of Elastic and Plastic-Elastic Principal Strain Indices in Steel Model No. 3

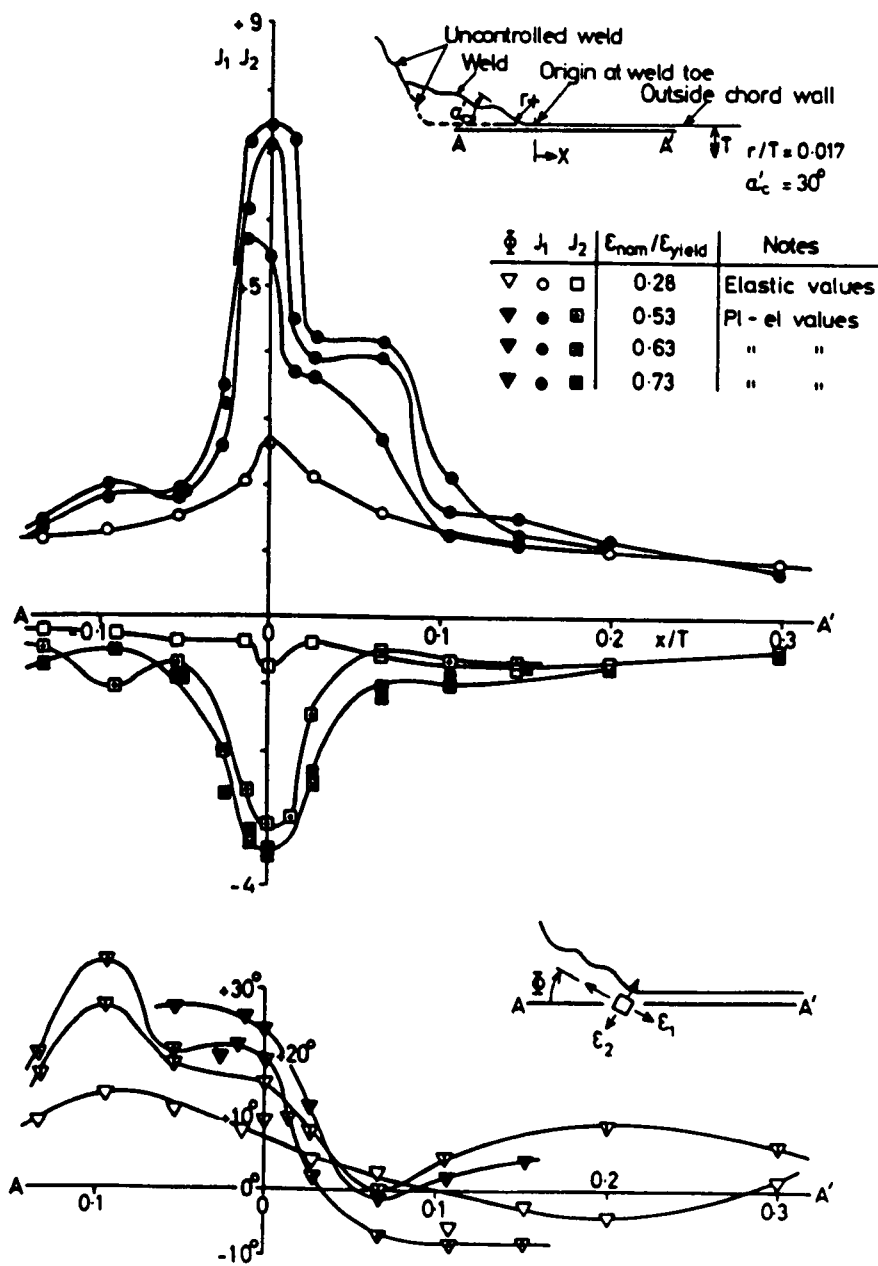


Fig. 6.77 Magnitudes and Directions of Elastic and Plastic-Elastic Principal Strain Indices in Steel Model No. 4

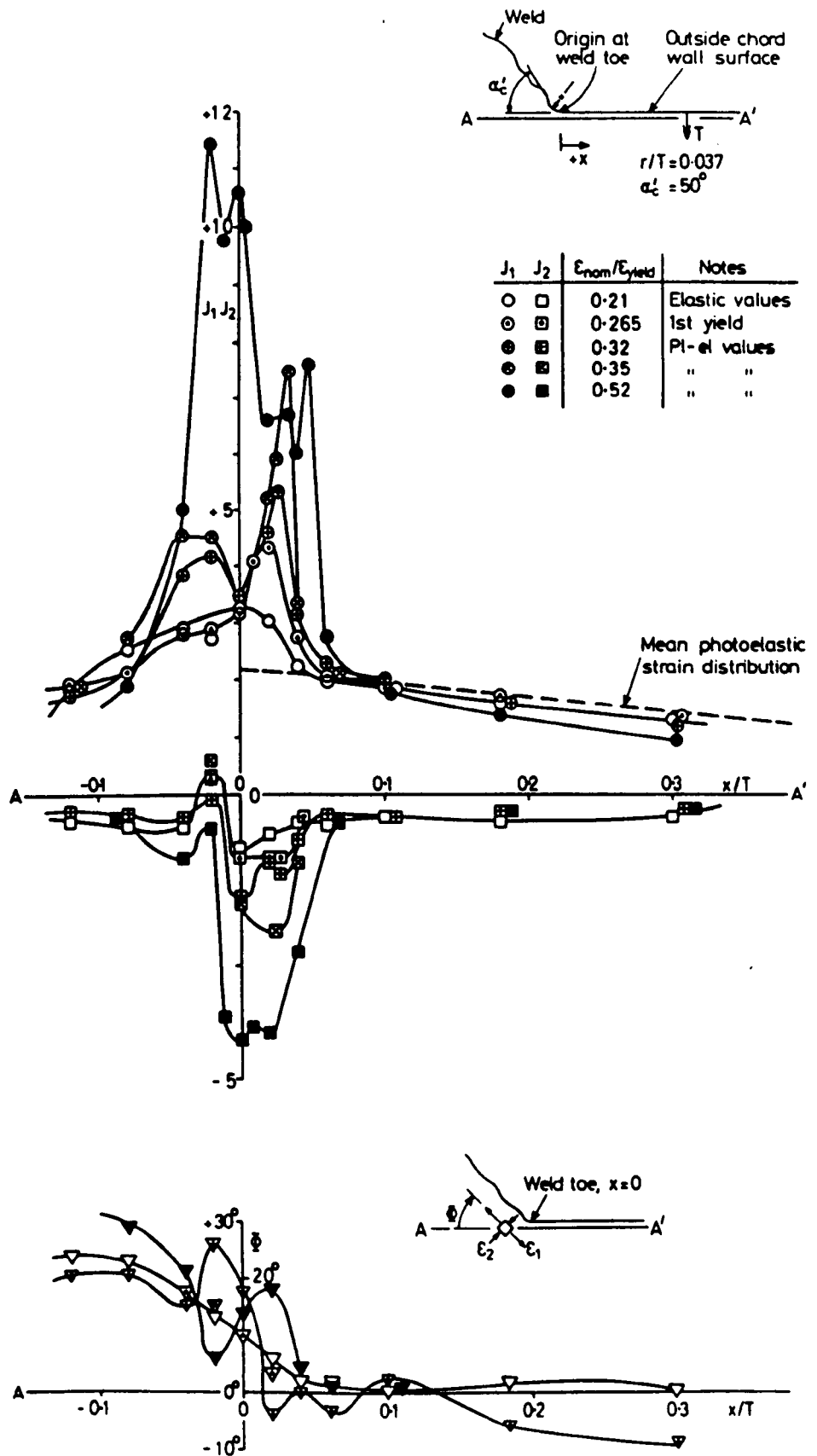
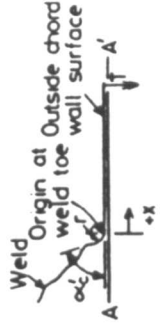


Fig. 6.78 Magnitudes and Directions of Elastic and Plastic-Elastic Principal Strain Indices in Steel Model No. 5

$\psi = 120^\circ$
Heat treated condition

$\epsilon_{nom} / \epsilon_{yield}$	Strain
0.02	ϵ_1
0.53	ϵ_2



$\psi = 120^\circ$
As welded condition

$\epsilon_{nom} / \epsilon_{yield}$	Strain
0.02	ϵ_1
0.53	ϵ_2

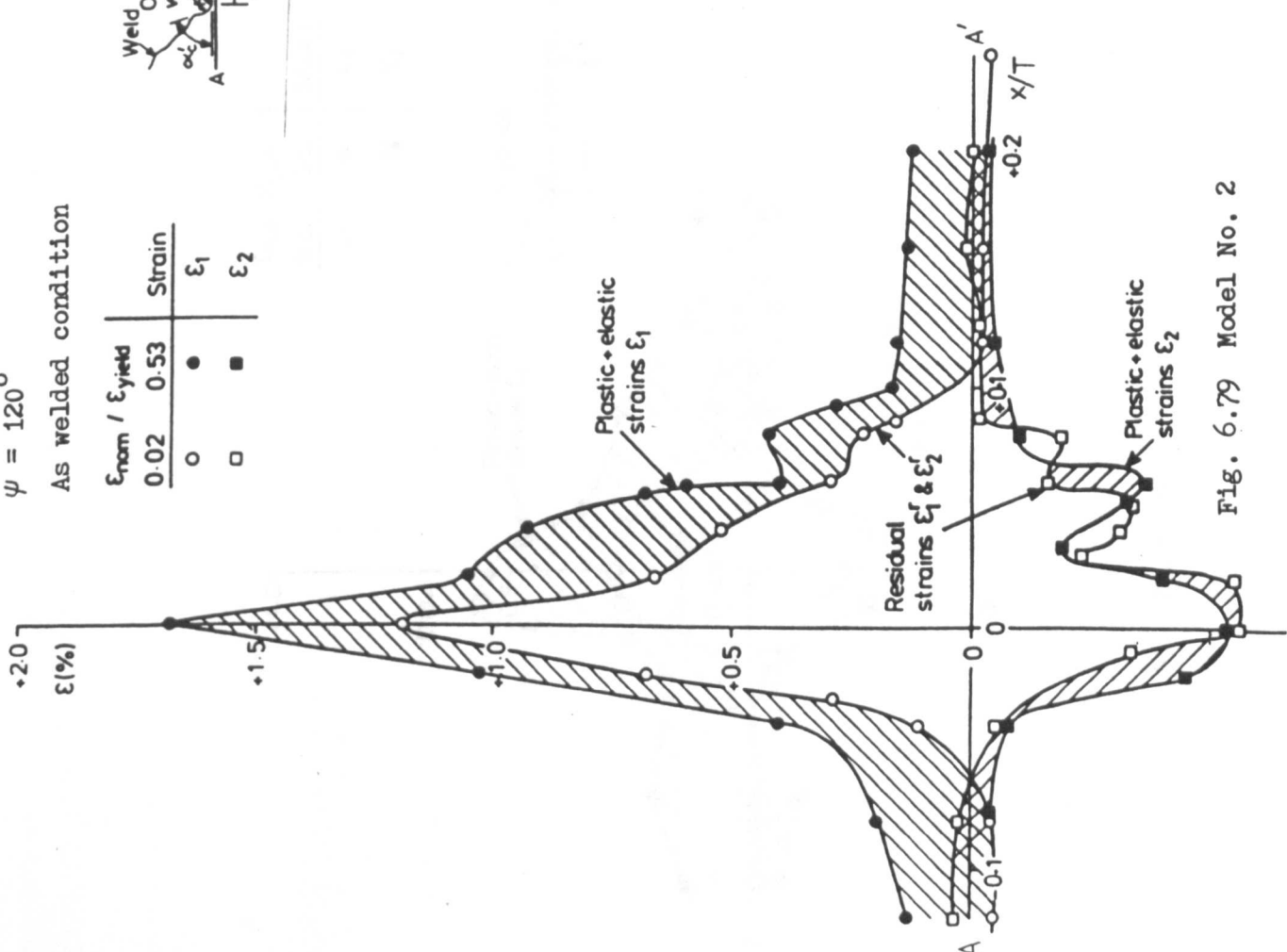


Fig. 6.79 Model No. 2

Fig. 6.80 Model No. 3

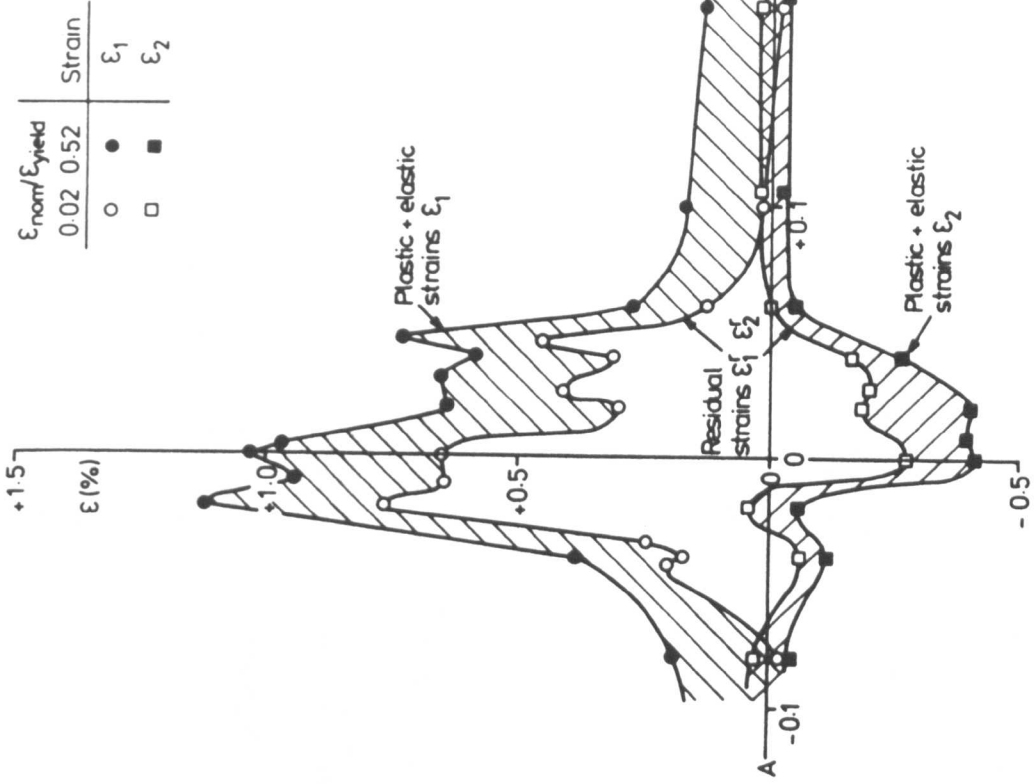


Fig 6.82 Model No 5

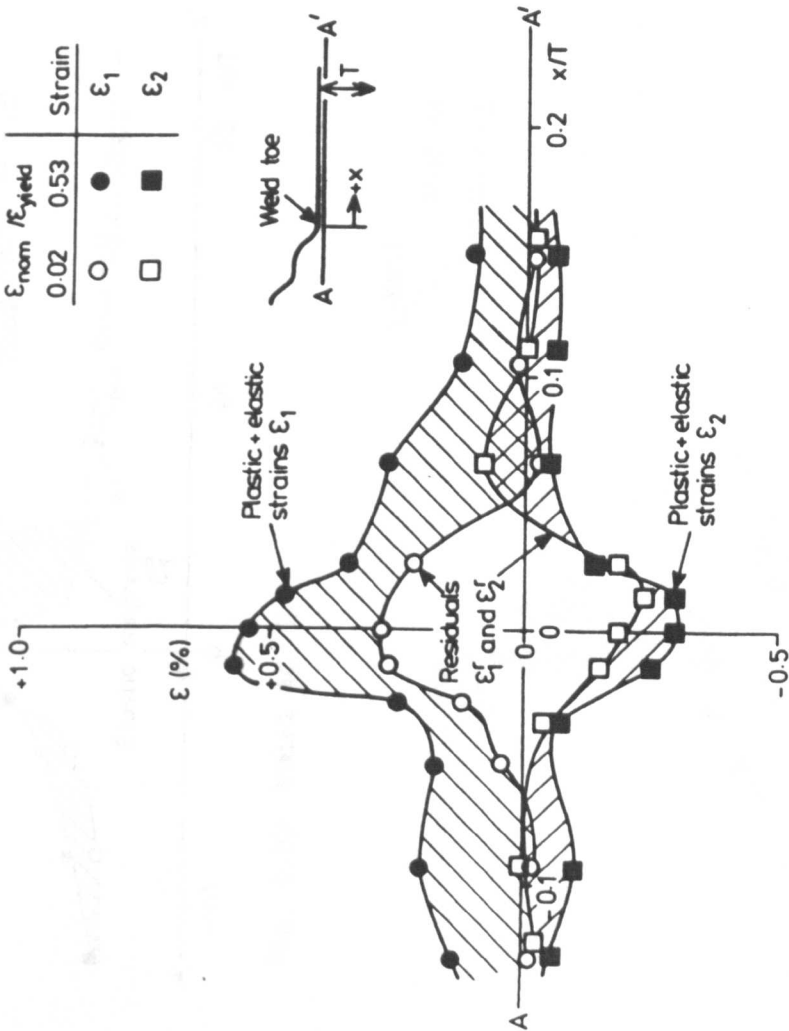


Fig 6.81 Model No 4

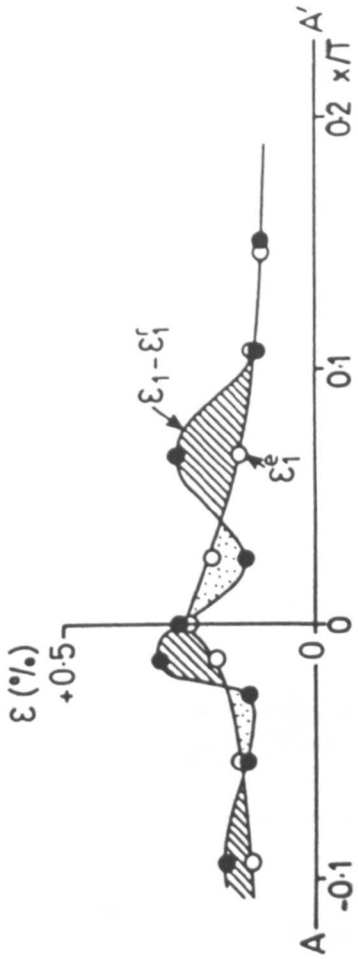


Fig. 6.85 Model No. 4

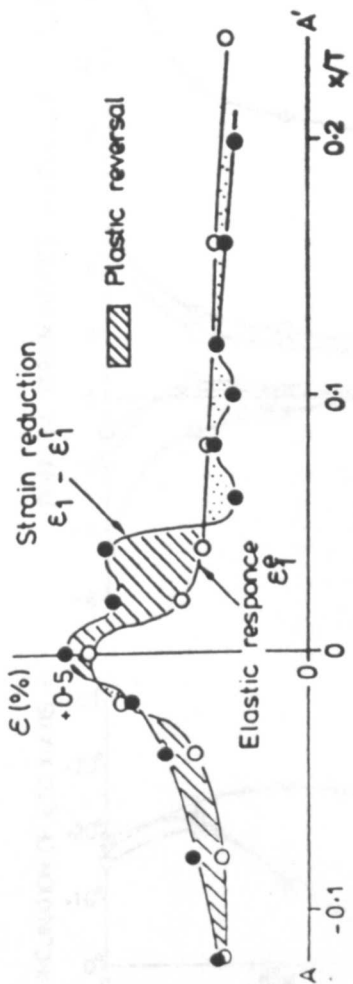


Fig. 6.83 Model No. 2

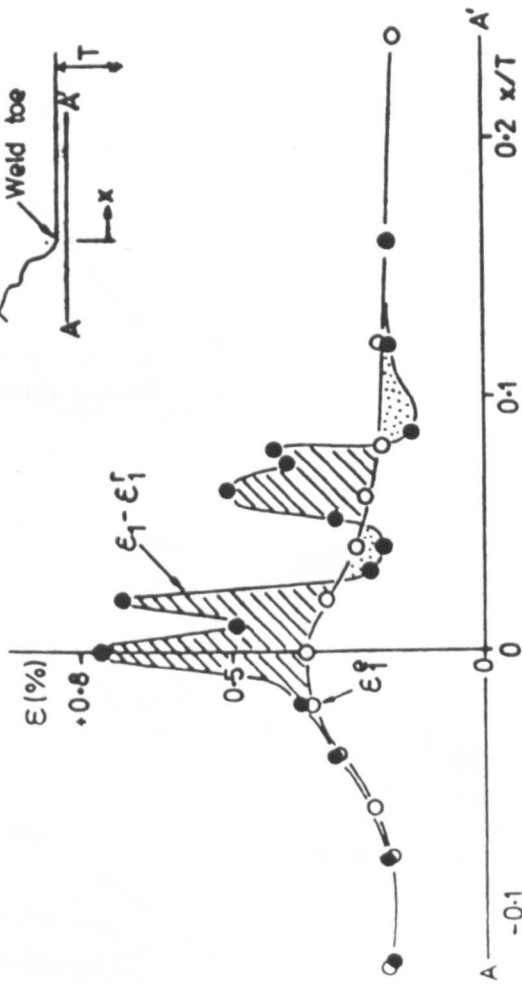
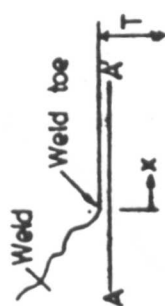


Fig. 6.84 Model No. 3

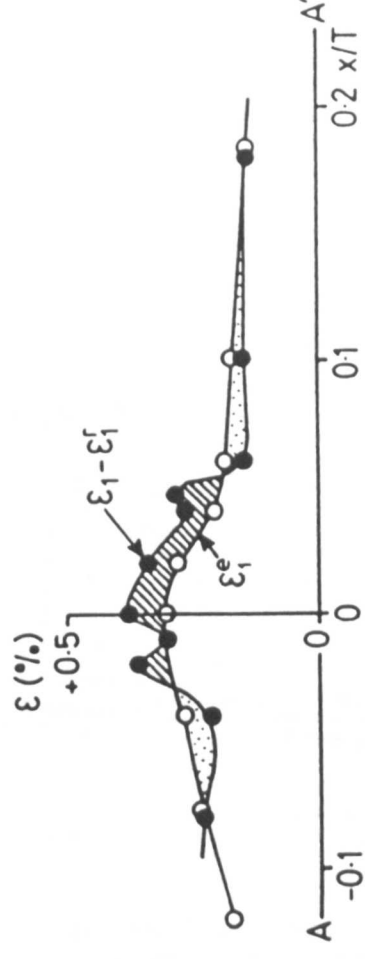


Fig. 6.86 Model No. 5

Comparison of Plastic-Elastic and Elastic Strain Reductions for a Decrease in Brace Wall Loading from $\epsilon_{nom} \approx 985\mu\epsilon$ to $\epsilon_{nom} \approx 35\mu\epsilon$

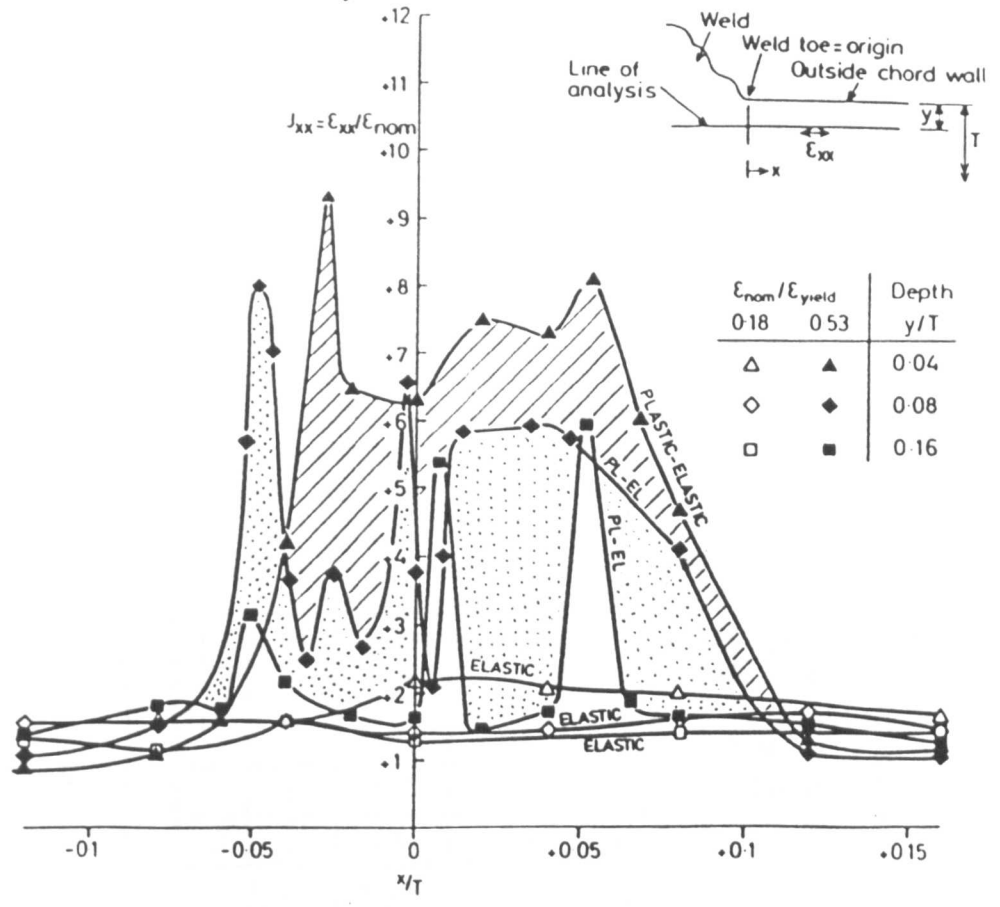


Fig. 6.87 Maximum Cartesian Sub-surface Strain Indices (J_{xx}) in Chord Wall in Steel Model No. 2

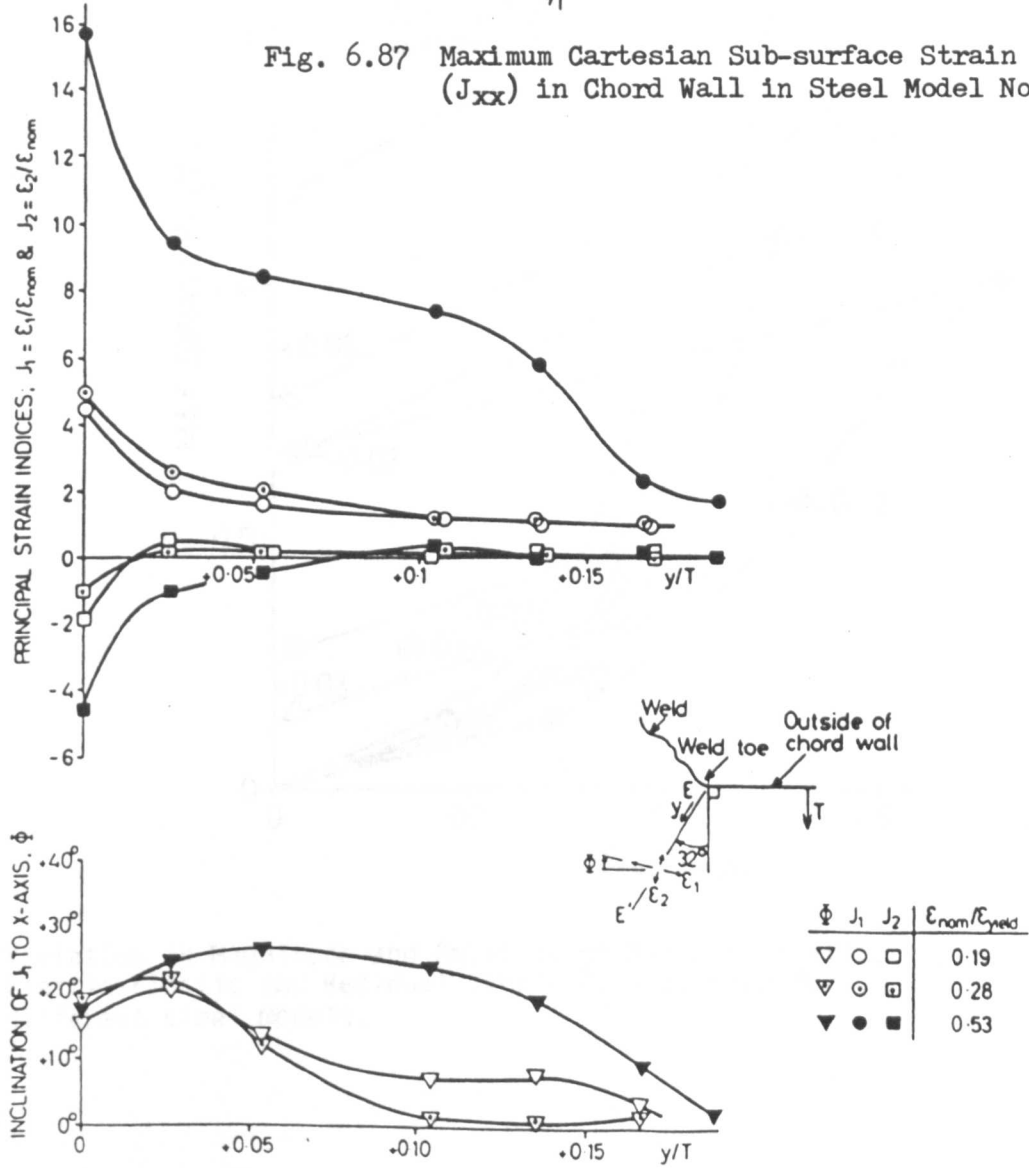


Fig. 6.88 Magnitudes and Directions of Principal Through-Thickness Strain Indices in Steel Model No. 2

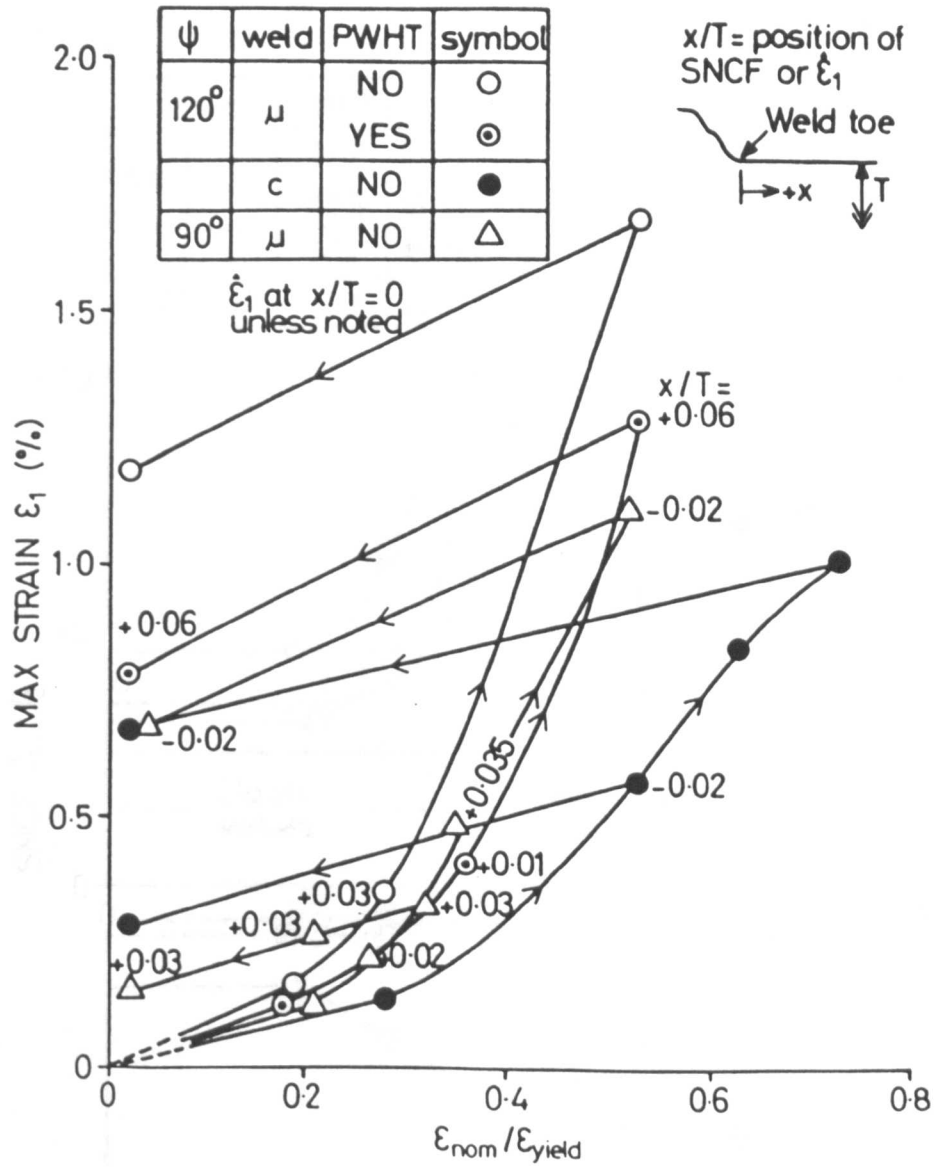


Fig 6.89 Variation in Magnitude and Position of Maximum Elastic, Plastic-Elastic and Residual Strain $\hat{\epsilon}_1$ with Load for different steel models.

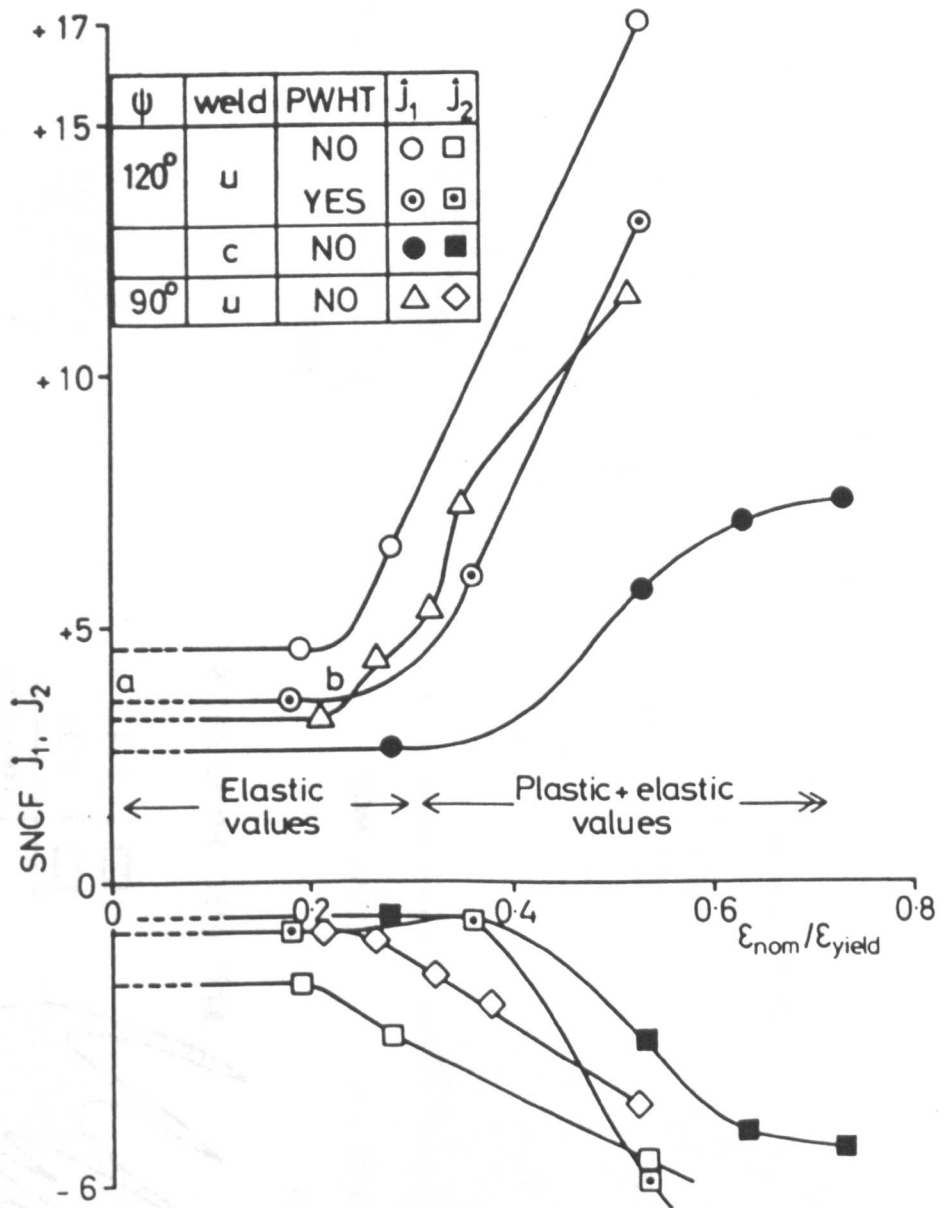


Fig 6.90 Variation in Maximum and Minimum SNCFs \hat{J}_1 and \hat{J}_2 with Load for different Steel Models

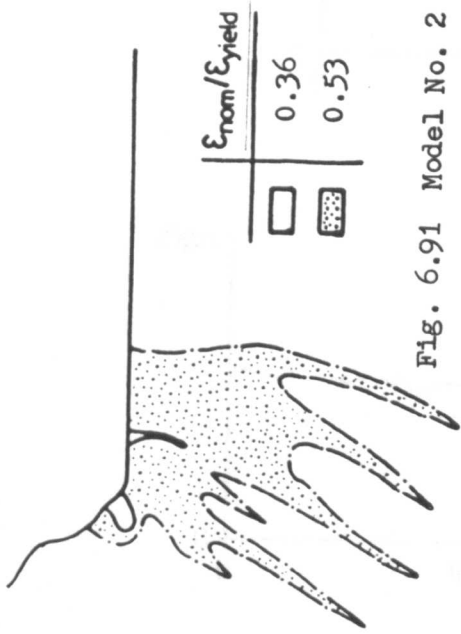


Fig. 6.91 Model No. 2

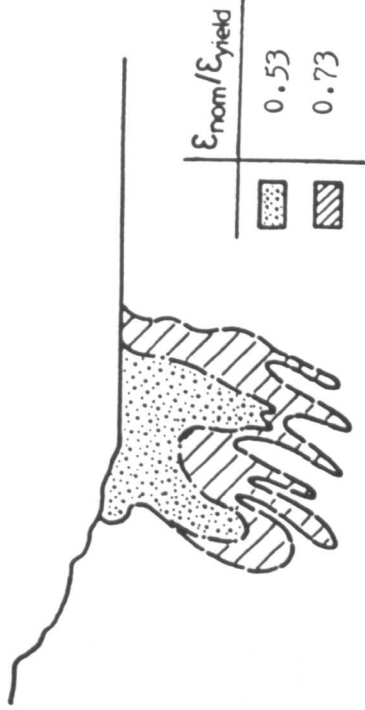


Fig. 6.93 Model No. 4

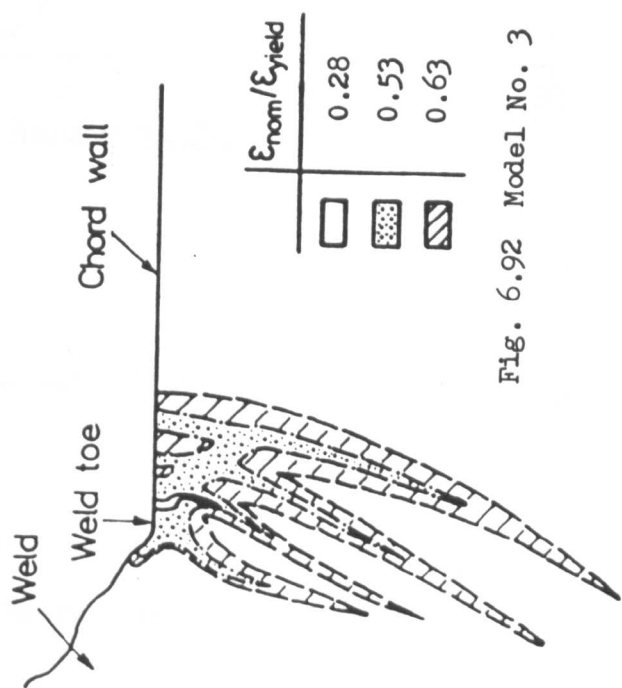


Fig. 6.92 Model No. 3

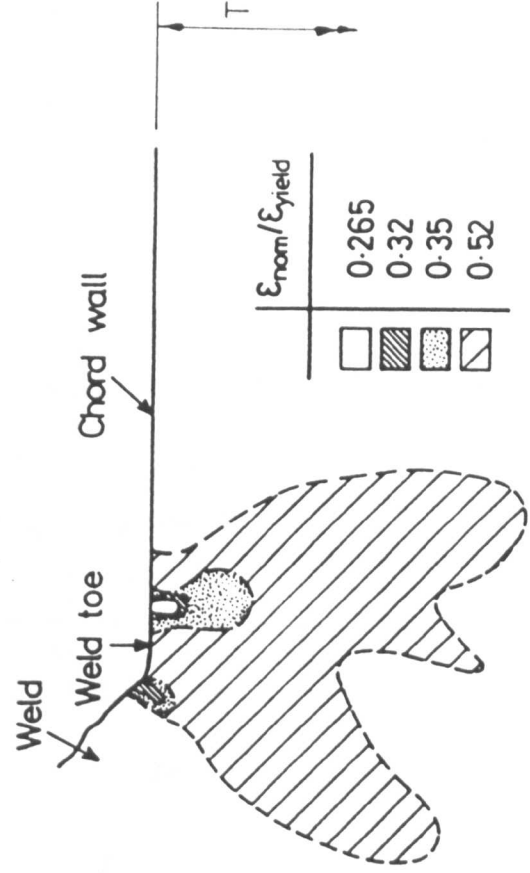


Fig. 6.94 Model No. 5

0 5mm
0 0.1T

Extent of Plastic Zones in Chord Wall and Weld in Steel Models at Different Loads

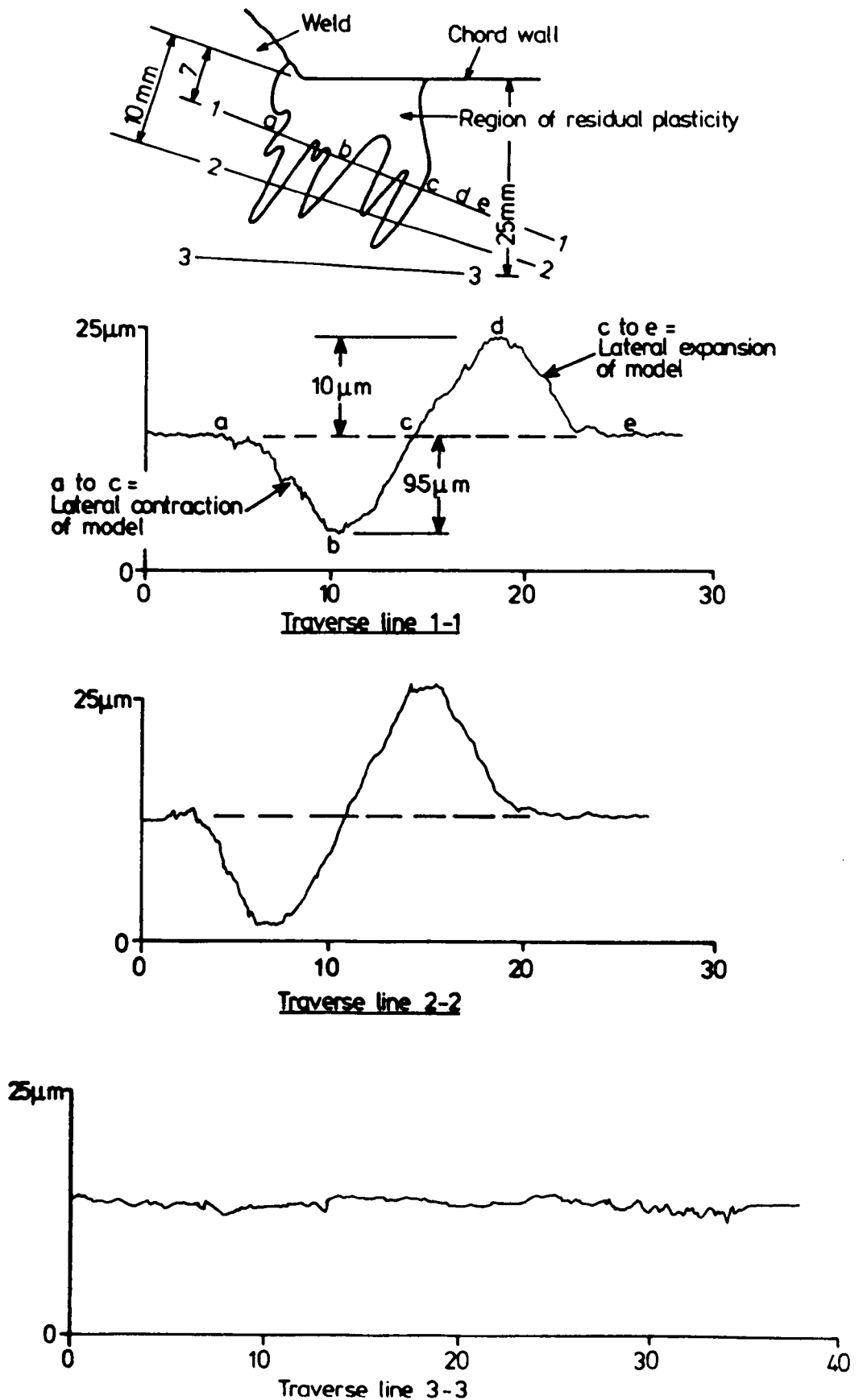


Fig. 6.95 Surface Measurements in Unloaded Steel Model in which Plastic Deformations were Present

CHAPTER 7

ANALYSIS OF ERRORS

The standard deviation for each part of each experimental method has been obtained and used to determine standard error values.

7.1 3-d Photoelastic Methods

The main sources of error in 3-d photoelastic work have been considered in the following sections.

7.1.1 Model dimensions

7.1.2 Model loading

7.1.3 Photoelastic readings

7.1.4 Interpretation of stress distributions.

7.1.1 Errors due to Deviations in 3-d Model Dimensions from

Design Values

The dimensional accuracy and standard deviation of model dimensions from the design values, for which SCFs are quoted, are presented in Table 4.10. In 3-d work, the effects of divergence of the non-dimensional ratios t/T , D/T , d/D and g'/T , and the angle θ on chord shell SCFs (K_{sc}) were assessed by using the parametric equations developed by Wordsworth (5) for single plane K joints in balanced axial loading. To assess the effects of the weld leg length parameter H/T , surface stress gradients were used. Crown and saddle planes were considered separately because of the different significance of the geometric ratios at these positions. Where sufficient data existed, standard deviations were obtained from population histograms in Fig. 7.1.

The standard error of a function obtained from a number of individual quantities is given by

$$e_{sd} = \left\{ \sum_{i=1}^n \left(\frac{\partial K_{sc}}{\partial x_i} \right)^2 \cdot e_i^2 \right\}^{0.5}$$

where e_{sd} = standard error in the value of K_{sc}

K_{sc} = $f(x)$

x = individual dimensional components

e_i = standard error in component x

n = number of components of error

a) At the crown positions

i) t/T

$$(t/T)_{design} = 0.5, (t/T)_{mean} = 0.489, s_{mean} = 0.022$$

Hence the standard deviation based on the design value of $t/T = 0.5$ was $s = +0.011$ and -0.033 .

Standard error in the value of K_{sc} using parametric equations (5) was

$$e_i = +2.2\% \text{ and } -6.6\%$$

ii) D/T

$$(D/T)_{design} = 25, (D/T)_{mean} = 25.22, s_{mean} = 0.45$$

$$\therefore s_{design} = +0.67 \text{ and } -0.23$$

$$e_i = 1.7\% \text{ and } -0.5\%$$

iii) d/D

$$(d/D)_{design} = 0.5, (d/D)_{mean} = 0.4993, s_{mean} = 0.001$$

$$\therefore s_{design} = +0.0003 \text{ and } -0.0017$$

$$e_i < 0.1\%$$

iv) g'/T

Because actual weld toe-to-toe gap values of g'/T were used in the results for K_{sc} , errors were in the measurement of g' . The maximum error was ± 0.04 mm, or $\pm 0.005T$.

The mean value of surface stress index gradient in the gap regions was $\partial I/\partial T = -2.5$ (approx).

$$\therefore e_{1 \max} = \pm 0.0125 \text{ (expressed as a stress index)}$$

v) θ

$$\theta_{\text{design}} = 60^\circ, 90^\circ, 135^\circ \text{ and } 150^\circ.$$

Insufficient data exists to determine s for each value of θ . However, maximum divergence from θ_{design} was 0.25°

$$\therefore e_{1 \max} = 0.65\%.$$

vi) H/T

Because weld leg length varied for each joint, differences in design values and those achieved were considered.

$$\{(H/T)_{\text{design}} - (H/T)_{\text{actual}}\}_{\text{mean}} = -0.04, \quad s_{\text{mean}} = 0.07$$

$$\therefore s_{\text{design}} = +0.03 \text{ and } -0.11.$$

The mean surface stress gradients for all joints was $\partial I/\partial T = -0.95$ (approx)

$$\therefore e_1 = +0.10 \text{ and } -0.03 \text{ (expressed as stress indices)}$$

Summation of standard error at crown positions gives $e_{sd} = \begin{array}{l} +4.3\% \\ \hline -2.0\% \end{array}$

b) At the saddle position1) t/T

$$(t/T)_{\text{design}} = 0.5, \quad (t/T)_{\text{mean}} = 0.508, \quad s_{\text{mean}} = 0.024$$

$$\therefore s_{\text{design}} = 0.032 \text{ and } -0.016$$

$$e_1 = +6.4\% \text{ and } -3.2\%$$

ii) $\underline{D/T}$

$$(D/T)_{\text{design}} = 25, (D/T)_{\text{mean}} = 25.34, s_{\text{mean}} = 0.75$$

$$\therefore s_{\text{design}} = +1.09 \text{ and } -0.41$$

$$e_1 = +3.1\% \text{ and } -0.8\%$$

iii) $\underline{d/D}$

$$(d/D)_{\text{design}} = 0.5, (d/D)_{\text{mean}} = 0.5002, s_{\text{mean}} = 0.001$$

$$\therefore s_{\text{design}} = +0.0012 \text{ and } -0.0008$$

$$e_1 < 0.1\%$$

iv) $\underline{g'/T}$

Maximum error in measurement of g' = ± 0.07 mm or $0.009T$ (approx)

due to curvature of tube. Mean value in gap of $\partial I/\partial T = -1.65$

$$\therefore e_{1 \text{ max}} = \pm 0.014$$

v) $\underline{\theta}$

Maximum divergence $\pm 0.25^\circ$

$$\therefore e_1 = 0.45\%$$

vi) $\underline{H/T}$

$$\left\{ (H/T)_{\text{design}} - (H/T)_{\text{actual}} \right\}_{\text{mean}} = -0.06 ; s_{\text{mean}} = 0.045$$

$$\therefore s_{\text{design}} = -0.015 \text{ and } -0.105$$

Mean value of all $\partial I/\partial T = -1.05$

$$\therefore e_1 = +0.11 \text{ (max) and } +0.016 \text{ (min).}$$

Summation of standard error at saddle positions gives $e_{sd} = \underline{\underline{+4.8\%}}$
 $\underline{\underline{-1.4\%}}$

7.1.2 Errors due to Model Loading

7.1.2.1 Direction and Magnitude of Applied Loads

The directions of the applied axial brace loads in the CK models were visually checked for angular alignment, in the horizontal plane of loading, at the maximum stress freezing temperature of 135°C . This was carried out by observing the shadow of a thin wire, which was established parallel to the axis of the chord prior to filling the tank with the oil, on an etched cross grating of 1 mm pitch and 40 mm long. The grating was attached to the rear face of the vertical leg of the rig (see Plate 4.4) which was known to be normal to the direction of the loading rod. The maximum observed deviation was 0.5 mm; hence maximum angular deviation was 0.72° .

The point of load application was made deliberately close to the chord tube to minimise errors due to spurious shear forces. The average bending stress index was about 0.005. The loading rods were placed concentric to the brace tube to within ± 0.25 mm, i.e. in 0.5 mm clearance holes. The maximum deviation of stress at any point around the brace was $\pm 1.35\%$.

The accuracy of the magnitudes of the loads was estimated by measurement of the horizontal and vertical arms of the loading rig. These were measured by tape measure to within ± 0.5 mm of the specified dimensions. The correct loads (i.e. hanging weights) were within ± 10 gms. The magnitude of the loads was therefore correct to $\pm 0.6\%$ although the forces due to the self-weight of the loading assembly were negated by counter-weights, residual forces due to friction were not known or measured.

Because of all the uncertainties associated in the above, the magnitudes of the mean axial stresses in all braces were calculated photoelastically. Fringe measurements of longitudinal brace stress were

made at approximately $1.2d$ from the crown heel. 8 (16 for CK1) slices were cut at 45° ($22\frac{1}{2}^\circ$ for CK1) intervals from each loaded brace of some models. Fringe order per unit thickness N_{nom} obtained from each slice are plotted in Fig. 5.1. The ratio of the mean value of N_{nom} in the compression and tension braces are given in Table 5.1.

Fig. 5.1 shows that stresses are usually greatest in line with the saddle toe ($\varphi = 90^\circ$) for braces in tension, and saddle heel ($\varphi = 270^\circ$) for braces in compression. The stresses at the intersection of the tubes would be over-predicted by an average of 6.5% at these positions. The minima occurred (roughly) diametrically opposite to the maxima, resulting in a corresponding under-prediction of between 5% and 6%. Stresses in line with crown positions ($\varphi = 0^\circ$ and 180°) were within $\pm 2\%$ of the mean.

These values represent the summation of all load misalignment and load magnitude errors.

7.1.2.2 Unbalanced Self-Weight of Models

During loading the models were simply supported at both ends of the chord. To eliminate stresses in the tubes caused by beam bending the models were 'floated' in oil with air pockets in the tubes adding to the buoyancy. The size of the air pockets were calculated separately for each tube. Because the size of the air pocket depended on the submerged density of the model, the specific gravity of the oil at 135°C was measured. It was 0.805. The density of Araldite was taken as 1.23 kg/m^3 (57).

The effectiveness of the pockets relied on the correct amount of air being trapped. The small differences in thermal expansion of oil and air would keep the air in the pockets near to the intended volume. However, when draining the oil after loading, an oil meniscus was visible inside the tubes 2 to 3 mm higher than the air trap level.

It was possible, therefore, that the air pocket in the chord had contracted in volume by up to 16%.

The maximum meridional stress index in the chord tube due to residual self weight of the model was calculated to be ± 0.03 . Because the braces were loaded in the neutral plane of the chord, these stresses were negligible in the crown plane, and half the maximum value at the saddle positions.

7.1.3 Errors due to Photoelastic Fringe Order Readings

7.1.3.1 Fringe order magnitudes

The repeatability of fringe order readings was assessed by making several readings at selected points on one of the models (CK1R). In general, repeatability was found to be independent of fringe order, but sensitive in regions of large fringe gradient or where fringes ran nearly parallel to the edges of the model. The latter conditions occurred near weld toes where greatest accuracy was required.

Fringe order readings, their means and standard deviations were as follows. (Maximum and minimum values underlined.)

Location	Fringe order, n		Mean \bar{n}	Standard Deviation sd	sd/ \bar{n}
Brace wall, approx 1.2d from joint	<u>0.68</u> 0.68 <u>0.66</u>	<u>0.70</u> <u>0.68</u> 0.67	0.678	0.012	1.8%
Chord wall, approx 0.25T from $\theta = 90^\circ$ saddle weld toe.	<u>1.68</u> <u>1.72</u> 1.70 <u>1.68</u>	1.72 <u>1.75</u> <u>1.72</u> 1.69	1.708	0.023	1.3%
Chord weld fillet at ditto	2.90 2.87 2.87 2.91 2.93 <u>2.90</u>	2.90 <u>2.85</u> <u>2.85</u> 2.91 <u>2.96</u> <u>2.91</u>	2.897	0.030	1.0%

7.1.3.2 Positions of Fringe Measurement

A travelling microscope was used to enlarge the image of a slice and define the positions of measurement. Providing all readings were taken in the same direction of travel, thus avoiding backlash, these were repeatable to ± 0.04 mm, i.e. $\pm 0.005T$. The maximum error in stress index, based on the largest stress gradient (used in extrapolation methods) was ± 0.02 , or $\pm 0.7\%$ near to weld toes.

7.1.3.3 Fringe Orders at Edges

In some models, shallow surface layers which were photoelastically opaque made it impossible to read fringe orders at true edges. In these instances, measurements were made at distances up to 0.03 mm from the edges.

Marston (21) showed that, away from notches, through-thickness fringe orders were proportional to stress and varied linearly with distance up to $0.2T$ from the edge. It was therefore possible to make an estimation of the error in subsurface measurement of fringes by linear extrapolation to the edges. In the chord wall, where through thickness stress gradients were largest, typical errors in $N = 2$ fringe orders were -0.01 to -0.013 , i.e. an under-prediction of between 0.5% and 0.65% .

7.1.3.4 Errors due to Variations in Stress Through a Slice

Gradients of stress in the direction of sight cause errors because photoelastic readings average through-the-slice stresses. In the planes of symmetry these were always parallel to the run of weld. An estimation of the errors in hoop stresses near to chord weld toes in saddle planes was made by photoelastic measurement of a slice having first been 2 mm thick, and later fly cut 1 mm thick. Results are as follows:-

Fringe order n	slice thickness t	n/t	Difference
2.93	1.96	1.49	0.02
1.55	1.03	1.51	
2.22	1.96	1.13	0
1.17	1.03	1.13	
1.72	1.97	0.87	0.01
0.91	1.03	0.88	

The maximum difference was 0.02 fringes/mm. This equated to a stress index of 0.05, or $\pm 0.6\%$ of the fillet SCF.

7.1.4 Errors due to Interpretation of Stress Distributions

The uncertainties in the determination of shell SCFs from extrapolation of stresses in the linear regions are a major source of error in this work. An assessment of the range of values for K_g , resulting from the arbitrary choice of the 'best' tangent drawn to the stress plots, revealed maximum deviations of about $\pm 3\%$ at the crown and remote saddle positions, and $\pm 5\%$ at the near saddle positions. The greatest errors in the value of K_g were in the saddle planes between inclined braces where linearity is not always well defined.

7.1.5 Summation of Errors in 3-d Photoelastic Work

Standard, or mean, percentage errors have been assessed for each source of error in the determination of stress indices near to chord weld toes. The errors resulting from positional (Section 7.1.3.2) and extrapolation (Section 7.1.4) procedures are omitted in the summation of peak SCF values.

The standard error of equally weighted functions is given by

$$e_{sd} = \left\{ \sum_{i=1}^n e_i^2 \right\}^{0.5}$$

where e_{sd} = total standard error
 e_i = standard error of each source of error
 n = number of sources of error.

The standard error values e_{sd} for 3-d photoelastic models are:

SCF	Position		
	Crown	Saddle toe	Saddle heel
Peak, K	+5.0%	+8.2%	
	-3.2%	-5.8%	
Shell, K_s	+5.8%	+9.6%	+8.8%
	-4.3%	-7.7%	-6.6%

7.2 2-d Photoelastic Methods

Similar procedures to those used in the analysis of errors in 3-d photoelastic models have been adopted for 2-d work. The main sources of error have been considered in the following sections.

7.2.1 Model dimensions

7.2.2 Model loading

7.2.3 Photoelastic readings

7.2.4 Extrapolation Methods

7.2.1 Errors due to Deviations in 2-d Model Dimensions from Design Values

The dimensional deviations are presented in Table 4.12. In 2-d work, the effects of divergence of the non-dimensional ratios t/T , H/T and r/T and weld angle α on chord shell (K_{sc}) and peak (K_c) SCFs were assessed by using empirical expressions derived in this work. Crown and saddle positions were considered together because dimensional deviations were similar. Standard deviations were obtained where sufficient data existed.

1) t/T

$$(t/T)_{\text{design}} = 0.5, (t/T)_{\text{mean}} = 0.497, s_{\text{mean}} = 0.0042$$

$$\therefore s_{\text{design}} = +0.001 \text{ and } -0.007$$

$$\therefore e_1 = +0.2\% \text{ and } -1.4\%$$

ii) H/T

$$\{(H/T)_{\text{design}} - (H/T)_{\text{actual}}\}_{\text{mean}} = +0.005, s_{\text{mean}} = 0.003$$

$$\therefore s_{\text{design}} = +0.008 \text{ and } -0$$

The chord wall surface stress gradient was $\partial I/\partial T = -2.46$

$$\therefore e_1 = 0 \text{ and } -0.7\%, \text{ based on the weld toe shell SCF.}$$

The following data was obtained from a limited sample.

iii) r/T

$$\{(r/T)_{\text{design}} - (r/T)_{\text{achieved}}\}_{\text{mean}} = +0.001 \quad s_{\text{mean}} = 0.0025$$

$$\therefore s_{\text{design}} = +0.0035 \text{ and } -0.0015.$$

Deviations in weld toe radii affect only peak SCF values. The empirical expression approximated to a power law in which the exponent (at crown positions) was approximately $-\frac{1}{3}$.

$$\therefore e_1 = +1.0\% \text{ and } -2.2\%$$

iv) α

$$\{\alpha_{\text{design}} - \alpha_{\text{actual}}\}_{\text{mean}} = +0.15^\circ \quad s_{\text{mean}} = 0.46^\circ$$

$$\therefore s_{\text{design}} = +0.61^\circ \text{ and } -0.31^\circ$$

Deviations in weld angle affect only peak SCF values in the relationship $K = f(\sin 0.5 \alpha)$. For $\alpha = 45^\circ$

$$\therefore e_1 = +1.3\% \text{ and } -0.7\%$$

Summation of standard error at crown positions for shell SCF values gives

$$e_{sd} = \begin{array}{l} +0.2\% \\ -1.6\% \end{array}$$

and for peak SCF values gives

$$e_{sd} = \begin{array}{l} +1.6\% \\ -2.8\% \end{array}$$

7.2.2 Errors due to Model Loading

The positions of the loads in the 2-d loading system were measured using a travelling microscope from the intersection of two scribed lines representing the axes of the chord and brace walls. Deviations up to ± 0.4 mm were measured. Errors in distance modified the ratio of bending to total stress at weld toes. The maximum error in chord wall stresses, based on $T = 30$ mm models, was $\pm 1.05\%$.

The directions of loading were measured using a travelling microscope. Maximum angular deviation of chord wall loading was typically $\pm 1.5^\circ$. Corresponding errors in stresses at weld toes were $\pm 0.8\%$. Angular deviations of brace wall loadings were less than 0.5° and errors in stresses were less than 0.3% .

Load magnitude was controlled in a calibration strip positioned in the direction of brace wall loading. Errors in load magnitude were therefore proportional to the relative thicknesses of the calibration strip and model walls. These were in the range $-0.04 \text{ mm} < t_{cal} - t_{model} < 0.12 \text{ mm}$. The corresponding maximum error, based on $t = 15$ mm, was 0.8% .

The summation of errors due to model loading yields $e_1 = \pm 1.6\%$.

7.2.3 Errors due to Photoelastic Fringe Order Readings

7.2.3.1 Fringe Order Magnitude

The repeatability of fringe measurement was assessed by making several (e.g. 10) readings at 3 different load magnitudes at selected points in the surfaces of models. Errors in stress indices were obtained by considering the sum of the standard deviations computed for the fringe

orders measured at each load magnitude. The measurements taken at the chord wall of a crown plane model are given in Table 7.1. The average error was 1.15%.

7.2.3.2 Positions of Fringe Measurement

Positional accuracy was ± 0.04 mm. Errors in stress indices were negligible - less than 0.1%.

Because the edges of these models were carefully machined, edge effects found in 3-d castings were not present in 2-d models. Fringe order measurements were therefore made at true edges.

7.2.4 Errors due to Extrapolation Methods

The errors in the value of shell SCFs were small because of the inherent linearity of stresses outside the notch zone produced by the 3-point loading system. An assessment of this error was made by replotting stress ordinates and graphically evaluating K_s . Differences in the magnitude of K_s were typically $\pm 1.5\%$ to $\pm 2.0\%$.

7.2.5 Summation of Errors in 2-d Photoelastic Work

The determination of standard error e_{sd} is given in Section 7.1.5. The values are

$$\text{Peak SCF, } K; e_{sd} = \begin{array}{l} +2.5\% \\ -3.4\% \end{array}$$

$$\text{Shell SCF, } K_s; e_{sd} = \begin{array}{l} +4.5\% \text{ (max)} \\ -5.4\% \text{ (max)} \end{array}$$

7.3 Finite Element Methods

A typical F.E. mesh comprised 250 elements and 800 to 850 nodes. In the fillets, elements were specified at 8° to 12° intervals (depending on the weld angle). In the important regions in the outside chord wall, elements were specified such that the increase in stress over one element

was less than 50%. This is indicative of a reasonably fine mesh.

Surface stresses at a node sharing (two) adjacent elements were compared in the important positions. The semi differences, expressed in terms of the mean value, were

- i) 0.11 @ weld toes
- ii) 0.02 in the chord wall @ $x/T = 0.25$, i.e. near end of notch zone
- iii) 0.01 @ stress concentrations, and $x/T > 0.3$

This mismatch is given (61) as the approximate error in the results.

Surface stresses normal to free surfaces σ_2 were checked and compared to σ_1 . The values of σ_2/σ_1 , which varied with weld toe radii, were

- i) 0.02 to 0.05 at weld toes, for $r/T = 0.25$ to 0.02 respectively
- ii) 0.02 in the chord wall
- iii) 0.03 to 0.1 at stress concentrations, for r/T as in (i).

The mismatch is the value of σ_2/σ_1 with zero is also given (61) as the approximate error in the results.

The repeatability of stresses in the linear regions, $x/T > 0.25$, was less than 2%. The errors identified above were 2%. The effect on the magnitudes of extrapolated shell SCFs was a mean variation of $\pm 2.5\%$.

In summary, errors in weld toe stresses were in the region of 11% because of large surface stress gradients. At the positions of stress concentrations in the weld toe fillets, errors in SCFs were between 3% and 10% for corresponding values of $r/T = 0.25$ to 0.02. Errors in shell SCFs were 2.5%

7.4 Reflection Photoelasticity

The errors in reflection techniques in which 2-d photoelastic coatings are profiled with the edges of steel models, are given by Fessler and Eissa (63). The sources of error identified by Eissa are summarised below. Variations in the material properties E and ν for Araldite CT200/MY 901 at room temperature determined by Edwards (54) have been used.

7.4.1 Sources of Error

- i) Variation in E and ν (54) were $\pm 2.5\%$
- ii) Variation in material fringe value F was $\pm 0.95\%$ (See Fig. 4.15)
- iii) Variations in layer thickness t_L were $\pm 2\%$, i.e. ± 0.01 mm in a mean value of 0.5 mm,
- iv) A correction factor C' , used to compensate for shear lag through the thickness of the photoelastic layer, given in (63), of 1.10 (corresponding to $t_L = 0.5$ mm) was used in this work. A 2% variation in t_L gives a 0.4% variation in C' for $t_L = 0.5$ mm.
- v) The reinforcing effect of the layer was less than 0.1% (63).
- vi) Time edge effects were measured by Marston (21). All photoelastic readings were taken within $2\frac{1}{2}$ hours of completing edge profiling. The change in fringe order in the edge of a slice after 162 minutes out of a drying cabinet was given in (21) as -0.068 fringes/mm. For $t_L = 0.5$ mm and a typical elastic fringe order in a weld fillet of +1.5 fringes/mm the percentage error was -1%. For smaller strains measured in the weld and chord wall surfaces, maximum time edge errors were typically -5%.

- vii) Incorrect layer profiling was the most significant source of error because measurements were made in the edges. In this work, edges were profiled using hand files - the best practical method. An estimation of the possible error in the strains measured in the weld toe fillet in the layer, compared to the actual strains in the model, was not attempted.
- viii) Errors due to the misalignment of loading linkages are assumed to be comparable to those in the 2-d photoelastic work in Section 7.2.2. These are $\pm 1.85\%$ at chord weld toes.
- ix) Errors in the magnitude of loading were assessed by the repeatability of an elastic fringe order at a prescribed position in the chord wall surface. For $\gamma_{nom} = 0.045\%$, the variation in load magnitude (recorded in the Denison testing machine) was in the region of ± 0.5 kN to ± 0.7 kN, i.e. a mean deviation of 6.6% . This error may be interpreted as the repeatability of photoelastic fringe order measurement.

7.4.2 Summation of Error in Reflection Photoelasticity

The expression for maximum shear strain in a photoelastic coating material is

$$\gamma_L = \frac{C'(1 + \nu_L)}{E_L} \cdot \frac{fn}{2t_L}$$

The percentage error in C' , ν_L , E_L , f , n and t_L has been applied to each of the component sources in the above expression. The quantity n is the direct summation of errors due to load magnitude, load position and time edge effects. The standard error e_{sd} in γ_L is as follows:

- $\pm 10.2\%$ at the position of the maxima, excluding edge profile effects
- $\pm 15.5\%$ in the chord wall beyond the extent of the notch zone.

It is assumed that edge profile effects are negligible in this region.

The greater errors in the smaller strain values were due to the sensitivity of small fringe orders to time edge effects and positions of measurement.

7.5 Moire interferometry Methods

Moire interferometry is a new development at Nottingham University. Because only four models (of different geometry and post-welded condition) were tested, there was not the opportunity to accumulate a library of standard data with which to assess the accuracy and repeatability of the technique. However, the potential sources of error have been considered in the following sections.

7.5.1 Optical alignment

7.5.2 Directions and magnitudes of loads

7.5.3 True alignment of auxiliary grating throughout a test

7.5.4 Location of points of measurement on different fringe pattern photographs

7.5.5 Measurements of strains from fringe patterns

7.5.6 Identical model and model grating edge profiles.

7.5.1 Errors due to Optical Alignments

Perfect optical alignment is achieved when a) the plane mirror adjacent to the model is perpendicular to the model, b) the incident beam is parallel and impinges on the model grating at angle $\pm \alpha = \sin^{-1} (\lambda F/2)$. These criteria were satisfied by observing the reflected images of the model grating as two bright dots which were brought together in the plane of the objective lens (A in Fig. 4.5b) and adjusting the orientation of the model until a null field was observed in the camera screen. Any deviations from this arrangement were seen as carrier patterns in the auxiliary grating. Extraneous fringe gradients were eliminated by

deducting carrier pattern values from field values to give true model fringe gradients.

Thus, optical alignment errors were virtually eliminated in the analysis of moire fringe patterns.

7.5.2 Errors due to Model Loading

7.5.2.1 Accuracy of Load Cell

The load cell was calibrated using an Instron testing machine. It was loaded in compression through ball bearings centred on the cell. The test was carried out three times and the mean relationship between load cell output v (volts) and the testing machine P (kN) was

$$v = 0.302 \pm 0.005 P$$

i.e. a maximum deviation of $\pm 1.65\%$.

7.5.2.2 Self Weight of Model and Linkages

In the determination of strain indices, errors due to self weight were eliminated by computing J from the difference in strains at two (or more) load magnitudes. In the determination of actual strains, the magnitude of ϵ_{nom} in the brace wall, due to self weight, was calculated to be about $1.5 \mu\epsilon$. Assuming typical SNCFs of between 3 and 5 at weld toes the error in elastic strains at these positions would be in the region of $6 \mu\epsilon$, i.e. 0.5% of elastic strains in weld toes.

7.5.2.3 Out-of-plane Displacements of Linkages

This affects the distribution of load in the (4 mm) width of the model. Although this source of error was not investigated, the reasonable agreement in surface strains measured in the linear regions using moire, photoelastic and F.E. methods suggest that the loads were applied centrally in the model.

7.5.2.4 Direction of Loads (i.e. Linkages) at Large Model Deformations

The directions of the linkages were measured by vernier protractor in one of the tests at load magnitudes $\epsilon_{\text{nom}}/\epsilon_{\text{yield}} = 0.02$ and 0.52 . Maximum angular deviation of brace and chord wall linkages were $0^{\circ}20'$ and $0^{\circ}30'$ relative to the outside edge of the chord wall. These values include model wall deformations. They are real effects which are difficult to separate from the extraneous effects introduced in the loading. However, errors in weld toe stresses in 2-d photoelastic models due to 1.5° misalignment were estimated at 0.8% . The errors in steel model (elastic) strains would be, pro-rata, about 0.3%

7.5.3 True Alignment of Auxiliary and Model Grating During a Test

This is an important relationship because rigid body rotations are eliminated using auxiliary gratings. The true identity of axes in the auxiliary and model gratings must be maintained throughout a test. If relative movement occurs the effects on strains are as follows.

In-plane rotation introduces a carrier pattern of rotation. This has no effect on direct strains ϵ_{xx} and ϵ_{yy} and a compensating (equal and opposite) effect on the shear strain components ϵ_{xy} and ϵ_{yx} . Out-of-plane rotation would be disastrous; all strains would be modified by unknown quantities. Rotations can only be detected with the model in an elastic condition. In the tests, model and auxiliary fringe patterns were repeatable at load and no-load magnitudes. No rotation of the auxiliary grating was therefore observed.

7.5.4 Location of Points of Measurement on Different Fringe

Pattern Photographs

This was facilitated by scribing two small crosses on the model grating and measuring the position of the weld toe relative to the crosses using a travelling microscope. The position of the weld toe

was located on the photograph from these measurements. Photographs were in general, 6 times magnification for measuring elastic and small plastic strains (i.e. less than 0.06%) and 12 times magnification for larger plastic strains.

The position of the weld toe could not be identified to better than ± 0.2 mm ($0.004T$) and ± 0.5 mm ($0.01T$) in the uncontrolled and controlled weld profiles, respectively. The accuracy in the measurement of the distance between the centre of the crosses was ± 0.05 mm in the model and ± 0.5 mm in the photographs. This equates to an additional error in the position of the weld toe of $\pm 0.001T$. Although strains were measured at the same position throughout the test, the positions of strains relative to the actual weld toe are equal to the above. Errors in extrapolated shell SNCFs were $\pm 3\%$ and $\pm 5\%$ in models with uncontrolled and controlled weld profiles, respectively.

7.5.5 Measurement of Strains from Fringe Patterns

These errors are due to repeatability in the measurement of fringe gradients (or fringe spacing) in the same, or different, photographs at the same load magnitude. The deviations (which were assessed in steel model No. 5) are given in Table 7.2. Two photographs of different scale, at two different load magnitudes were considered; plastic-elastic strains ϵ_{xx} and residual plastic strains ϵ_{xx}^r were measured. Four measurements of fringe spacing were made at two different positions using a travelling microscope. Standard deviations in each fringe pattern were 1.3% to 8.3% depending on scale and position. Deviations in auxiliary values ϵ_{xx}^{aux} were less than 1.4%.

The resulting standard deviations in $\epsilon_{xx} - \epsilon_{xx}^{aux}$ obtained from 8 measurements in two fringe patterns were 4% to 6.3%

7.5.6 Identical Model and Model-Grating Edge Profile

The edges of moire gratings were not exactly identical to model edge profiles because of difficulties in replication (see Section 4.5.2) Observations showed resin flashing and resin migration in some of the edges. This resulted in overhanging and/or withdrawn gratings up to 0.1 mm (0.002T) from the edges. The error in maximum strain can be assessed using the through-thickness J_1 distributions in Fig. 6.88. Gradients of J_1 near the edges were 80/T (elastic) and 320/T (pl-el). The corresponding error in strains measured at 0.002T from the (assumed) real edge is $\pm 1.4\%$.

In the linear wall regions, through-thickness gradients were in the order of 20/T. The corresponding error is therefore $\pm 1.3\%$.

7.5.7 Summation of Errors in Moire Work

In the measurement of weld toe strains, the significant errors were accuracy of loading, fringe gradient measurement and edge profile effects. These accumulate to 12.5%.

In the extrapolation of linear chord wall strains, i.e. shell SNCFs, the above errors plus positional errors were significant. These accumulate to 13.3%.

7.6 Summary of Errors in All Methods

The following maximum errors have been assessed for each of the different experimental or numerical methods used in this work.

Method	Peak Values	Extrapolated Shell Values
3-d photoelasticity	+8.2% -5.8%	+9.6% -7.7%
2-d photoelasticity	+2.5% -3.4%	+4.5% -5.4%
2-3 finite elements	10%	2.5%
Reflection techniques	10.2% ¹	15.5%
Moire interferometry	12.5%	13.3%

1. Excluding edge profile effects

Table 7.1

Repeatability of Fringe Order Measurements in 2-d Photoelastic Models

Load cycle	N_{nom}	Fringe Order readings n	Mean \bar{n}	s.d. s
A	1.01	2.58, 2.56, 2.54, 2.56	2.554	0.032
	1.02	2.61, 2.50, 2.59, 2.56		
	1.01	2.52, 2.55		
	2.01	5.20, 5.16, 5.20, 5.18	5.139	0.037
	1.98	5.09, 5.11, 5.10, 5.11		
	2.01	5.15, 5.15, 5.11, 5.11		
	3.00	7.69, 7.71, 7.74, 7.73	7.734	0.031
	2.98	7.73, 7.76, 7.73, 7.68		
	2.98	7.76, 7.80, 7.74, 7.74		
B	1.01	2.62, 2.62, 2.67, 2.66	2.634	0.019
	1.01	2.61, 2.63, 2.63, 2.63		
	2.00	5.20, 5.18, 5.20, 5.25	5.222	0.026
	2.04	5.19, 5.26, 5.23, 5.23		
	2.01	5.25, 5.23		
	3.00	7.84, 7.84, 7.90, 7.86	7.820	0.040
	3.02	7.81, 7.77, 7.81, 7.80		
	3.02	7.79 7.76		

For load cycle A, stress indices ($I = \Delta n / \Delta N_{nom}$) were

$$\text{mean} = 2.590, \text{ max} = 2.621, \text{ min} = 2.559$$

$$\text{i.e. } \underline{e_1} = \pm 1.2\%$$

For load cycle B, stress indices were

$$\text{mean} = 2.593, \text{ max} = 2.622, \text{ min} = 2.563$$

$$\text{i.e. } \underline{e_1} = \pm 1.1\%$$

Table 7.2

Assessment of Deviations in Strains Measured at a Point in Different Moire Fringe Pattern Photographs

Brace load $\epsilon_{nom}/\epsilon_y$	Position in Surface	Photo No.	N_x Field Fringe Spacing a_{xx} (mm)	ϵ_{xx} ($\mu\epsilon$) ² Mean s.d.	N_x Auxiliary Fringe Spacing a_{aux} (mm)	ϵ_{aux}		Model Strains $\epsilon_{xx} - \epsilon_{aux}$ Mean s.d.
						Mean	s.d.	
0.52	Weld toe i.e. $x = 0$	1	0.533 0.508 0.520 0.520	9304 1.9%	0.980 0.992 0.981 0.973	424 0.7%	8870 4.2%	
		2	0.254 0.291 0.279 0.267	9257 5.8%	0.990 1.025 0.995 1.012	414 1.4%		
	$x = +9$ mm from toe	1	3.02 3.10 3.20 3.17	1550 2.6%	As above			1175 6.9%
		2	1.49 1.47 1.65 1.57	1634 5.0%				
0.02 after 0.52	weld toe	3	0.737 0.698 0.711 0.711	6594 2.3%	1.127 1.123 1.115 1.125	371 0.5%	6124 6.1%	
		4	0.355 0.393 0.406 0.432	6400 8.3%	1.115 1.115 1.112 1.105	374 0.4%		
	$x = +9$ mm	3	18.5 19.0 18.5 18.5	253 1.3%	As above			-116 4%
		4	10.0 9.7 9.7 9.5	260 2.1%				

Notes 1. N_x fringe patterns in Model No. 5 used in analysis2. ϵ_{xx} = Scale of photo $\times 10^6/2400 \times a_{xx}$ 3. a_{aux} obtained from enlargements of negatives

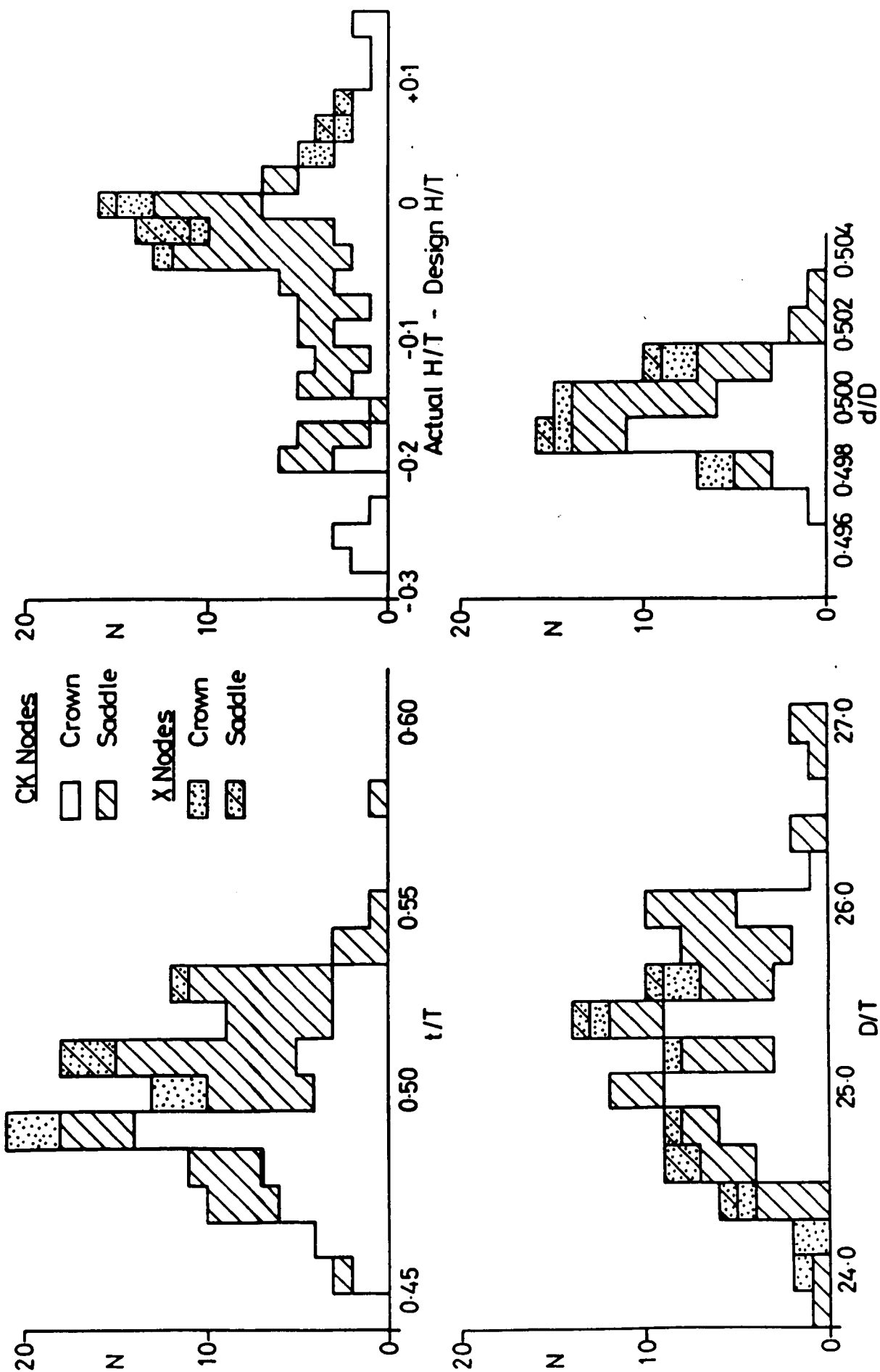


Fig. 7.1 Population Histograms for Geometric Ratios in All 3-d Photoelastic Models

CHAPTER 8DISCUSSION8.1 Application of Stress Analysis Techniques to the Determination of Stresses in Tubular and Welded Joints

The suitability of the different experimental and numerical methods used in the determination of elastic and plastic elastic, surface and through-thickness, stress and strain distributions is discussed. The fundamental principles of each technique are well established and are not dealt with here.

8.1.1 Frozen Stress Photoelasticity

3-d frozen stress photoelasticity made the largest contribution in the elastic work. Eight models (6 CK-type and 2 X-type tubular joints) were analysed. To enable realistic size weld profiles to be formed in the models a chord wall thickness of 8 mm (nominal) was used. The expertise currently available at Nottingham University allowed almost total freedom in the design of 3-d tubular joints; four different inclinations of braces in different positions were attached to a chord tube. Slices were cut in all crown and saddle planes, and stresses in the surfaces of walls and welds were measured. Subslices gave stresses parallel to the run of the weld, and some surface subslices gave inclinations of principal stresses. With these data, the entire 3-d surface stress field was fully described in the important planes.

The tubes were made long enough to avoid end conditions restraining the natural ovality of each tube. Considerations were also given to ensuring that accurate balanced axial load magnitudes were applied to each brace, and parasitic shears and bending moments were eliminated.

The models yielded far more information than originally intended. These were axial and bending stresses, recommendations for the positions of strain gauges used in the hot-spot method and types of strain gauges required to predict maximum SCFs, and the errors involved in ignoring these recommendations. These were in addition to peak, shell and notch SCFs.

8.1.2 2-d Room Temperature Photoelasticity

Full to half scale Araldite models were used to study, in detail, stresses at weld toes. They were used for two main reasons:

- i) economy; relatively inexpensive to manufacture and up to 8 different weld profile changes were made to one piece of material
- ii) accuracy; weld profiles were produced using end mill cutters in the range of toe radii $0.01 < r/T < 0.25$ and weld angle $10^\circ \leq \alpha_c \leq 70^\circ$.

The models were designed on the following basis;

If a very thin slice was cut from a plane of symmetry in a frozen-stress 3-d model, annealed and reloaded at room temperature by loads of the correct magnitude and direction, the principal stresses in the 2-d model would be equal to those in the original plane of the stress-frozen slice. Due to the curvature of the tubes this is impossible to achieve in all positions. To satisfy the equilibrium of loads, chord wall stresses inside the brace tube were greater than in the parent 3-d model. Having established equality in the important positions, near outside weld toes, large variations in weld shape and size were analysed. Care was taken **NOT** to overstep the boundaries afforded by 2-d analysis, particularly in the case of weld size where large welds may change structural compatibility in the joint. This was controlled by studying the effects of weld size in 3-d X models prior to using large welds in 2-d models.

8.1.3 Finite Element Methods

2-d, plane stress, finite element models were used in collaboration with some of the 2-d photoelastic models to obtain the positions and magnitudes of SCFs in weld fillets of different size and shape. The mesh was designed to facilitate changes in weld geometry with a minimum number of nodal co-ordinates to be altered. Although the technique was not used extensively and restricted to one shape of joint, sufficient data was extracted to make the effort of producing the mesh worthwhile. The stress distributions in weld toe fillets obtained using 2-d F.E. and photoelastic methods are fairly compatible in terms of time, expenditure and reliability of results.

8.1.4 Reflection Techniques

It was anticipated that reflection photoelasticity was a sufficiently sensitive technique to study plastic-elastic strains near to weld toes of real steel weldments. The methods used by Fessler and Eissa (55) to measure plastic contact strains in keyways was adopted for this work. The essential differences between Eissa's work and this work were that the former used machined specimens manufactured from isotropic and homogeneous materials. Welded joints with irregular microscopic weld toe profiles do not offer these desirable features.

The results failed to show the localised effects of the different material properties near to weld toes. True strain gradients were not measured because of a shear lag effects and inaccuracies in layer profiling in the weld toe regions. Small fringe order measurements were severely affected by time-edge effects. An additional problem was that of the photoelastic layer debonding at strains in the model in the order of 1%.

It was for these main reasons that reflection techniques were abandoned for moire interferometry methods.

8.1.5 Moire Interferometry

It is thought that the use of moire interferometry to study plastic-elastic strains in welded joints which represent principal planes in tubular joints is the first in the U.K. The optical apparatus and portable, light weight loading rig was designed and built to measure whole field elastic and plastic-elastic strains in 2-d steel models manufactured using offshore quality steels and procedures.

The elastic results compared favourably with photoelastic values; this data being used only to verify the experimental procedures. The surface and through-thickness plastic-elastic SNCFs and distributions of plastic-elastic strain indices and residual strains were unique. Strains were measured from 20 $\mu\epsilon$ to 2%.

The application of this experimental technique to offshore structures is obviously in its infancy. Its potential, in furthering an understanding of plastic-elastic behaviour near welds, is considerable.

8.2 Evaluation of Results to Design Requirements

8.2.1 Separation of Stresses Near to Welds

In the 1984 Houdremont Lecture, Marshall (43) dealt with the relationship between fatigue failure and maximum stresses near crack initiation sites at weld toes in terms of notch stresses and the assumptions implicit in the use of the hot-spot stress method. The different geometric scales at which stresses in complex tubular joints should be evaluated were as follows:-

- i) global, i.e. space frame design,
- ii) geometric, i.e. behaviour of tubular connections, and
- iii) local microscopic, i.e. effect of weld toe profile.

In this work it is shown that an important assumption in the application of stress analyses, parametric equations, fracture mechanics and

fatigue testing results to the assessment of the safety of offshore structures is the separability of a shell SCF and a notch SCF. This may be stated as follows:-

1) The elastic stress concentration due to structural incompatibility of the deformation of tubes forming tubular joints depends only on:

D/T and d/t	the diameter to thickness ratio of each tube
d/D	the diameter ratio of adjacent tubes
t/T	the thickness ratio of adjacent tubes
g	the distance between them (expressed as a ratio, g/T or g/D)
θ	the angle between their centre lines
ϕ	the local inclination of tube walls; it is a function of θ and the position of the point around the line of brace-to-chord intersection.

It is called K_s ; shell stress concentration factor. In the interpretation of fatigue test results, in which gross plasticity occurs and through-thickness cracking is the failure criterion, K_s is also referred to as the geometric, or hot-spot SCF. It is measured in such a way that the presence of the weld is ignored. Hence,

2) K_s is assumed to be independent of shape and size of the fillet weld, and weld toe profile.

3) The 'local' elastic stress concentration caused by the discontinuities of curvature of the joint surfaces, called K_n ; notch stress concentration factor is assumed to depend only on:

r/T or r/t	the weld toe radius to wall thickness ratio
H/T and h/t	the length of chord and tube surface 'covered' by the weld, i.e. its size
α_c or α_b	the weld toe angles which are functions of ϕ , H and h .

Local weld toe notch effects are incorporated in the S-N fatigue design curves. The assumption in the design rules (e.g. (7, 8)) is that the weld merges smoothly with the tube wall so that values for K_n are similar to those in butt welds. The position in the tubular joint is therefore assumed to be unimportant in the determination of notch stresses. Hence,

4) K_n is assumed to be independent of the 'global' parameters which affect K_s , i.e. it is independent of K_s .

The results from this work can be used to determine how realistic these (almost inevitable) assumptions are. The elastic results for the 3-d CK models were used to qualify assumptions 1) and 4) in considering θ , ψ and g . The 3-d X models were used to qualify assumptions 2) and 4) (in the chord wall only) in considering θ , ψ , τ and H . The 2-d models (excluding steel models) were used to qualify assumptions 2), 3) and 4) in considering τ , weld profile and weld toe parameters r , H and α with constant global parameters θ and ψ for different types of tubular joints.

The effect on stresses of the large number of geometric configurations in an offshore structure were assessed using a substructuring technique. Certain planes of symmetry were chosen for detailed analysis. The results from 3-d photoelastic models analysed in this and previous work (18) were used to find these positions and determine the lengths of chord and brace walls that could be realistically modelled in a 2-d plane stress environment. These planes were at the crown and saddle positions of single-plane non-overlapped K joints, and the saddle positions of X joints. In all cases $\theta = 90^\circ$ and the braces were loaded in axial tension.

8.2.2 Surface Stress Distributions

The surface stress distributions in the outer surfaces of braces and chords were found to contain ^{regions} positions which are sufficiently linear to allow linear extrapolation to the weld toe. Although the uncertainties of this linearisation are a large source of error the concept of a shell stress concentration factor K_s is so useful that this uncertainty has to be accepted to generalise the results.

The surface stress distributions given in Figs. 6.17 to 6.22 for the 3-d X models show that points of surface contraflexure and zero wall bending are independent of τ and weld size; up to leg length $H = 0.44 T$. This is important in the design of 2-d. models because different size welds were studied in the same Y shape model loaded in the same positions and directions.

8.2.3 Surface Strain Distributions

The surface strain distributions in Figs. 6.41 to 6.43 are presented to assist in the interpretation of strain gauge readings in CK type tubular joints. Where the brace gap parameter $g'/T \geq 3$, sufficient linearity exists between the recommended strain gauge positions to permit confident extrapolation. For values of $g'/T < 0.71$ the practical application of measurement is further complicated by the large strain gradients in which the size of the smallest gauge would be significant. Comprehensive instrumentation with rosette or biaxial strip gauges may not be necessary at the saddle toe of the $\theta = 90^\circ$ brace, where minor strain indices are small. This is not the case at the crown toe of the $\theta = 90^\circ$ and 60° braces where hoop strains are predominant. Here biaxial strip gauges are essential, but rosettes are not. These effects are attributed to the bending and ovalisation of the chord and have been shown to apply for this brace diameter ratio ($\beta = 0.5$) only.

8.2.4 Axial and Bending Stress Distributions

These stress distributions (Figs. 6.44 to 6.46) help to explain the large variation in K_s at chord weld toes and the smaller variation in K_s at brace weld toes in CK type joints.

The interbrace chord walls in the crown planes I and II (Figs. 6.44 and 6.45) have SCFs dominated by wall bending. The bending stress gradient which varies inversely with the gap parameter g'/T is a measure of the shear force between the opposing braces. Tensile axial stresses in the chord wall are a result of the horizontal component of axial load in the inclined brace walls. Chord wall bending between the $\phi = 150^\circ$ and 120° junctions for $g'T = 3.0$ and 5.7 is given in Fig. 6.45. Although the stresses near to both weld toes are similar, the distributions between these points differ. The bending stress plots diverge at about $1T$ from both weld toes; coincidentally a recommended strain gauge position (6). It is therefore recommended that where interbrace activity is anticipated, stresses further than one wall thickness from chord weld toes should not be used in hot-spot extrapolation procedures.

Axial and bending stress distributions at saddle positions in Plane III are shown in Fig. 6.46. These diagrams represent two separate model loadings in which the $\theta = 90^\circ$ brace was loaded separately from the $\theta = 60^\circ$ brace. Chord wall bending is the primary stress concentrating effect, but only at $\theta = 90^\circ$ brace does axial stress (due to the circumferential component of brace load) contribute significantly to chord weld toe SCF. Both axial and bending stress gradients are steep and sensitive to small changes in brace proximity.

At $\theta = 60^\circ$, because of the zero load in the adjacent brace, bending stress gradients are fairly constant and insensitive to the gap parameter g'/T ; only the absolute values change. Consequently, because axial stresses are small, K_s increases linearly with the gap parameter for the range of values studied.

Figs. 6.44 to 6.46 also show the effects of brace wall bending on brace wall SCFs. Because the chord is a thin-walled tube, axial brace loads ovalise the chord and consequently bend the braces. These bending stresses decay rapidly. A point of contraflexure is created by the Poisson effect where radial deformation of the tube is restrained by the 'footprint' of the weld on the chord. If a brace is in tension, hoop restraint produces compressive stresses on the outer brace wall. It is surprising that the magnitude of this hoop restrained bending stress is the same for all braces, despite the inclined braces having less flexibility than the $\theta = 90^\circ$ brace.

8.2.5 The Effect of Hoop Stresses in Crown Planes

An important consideration in the determination of hot-spot stresses from strain gauge readings in the crown plane is the effect of the frequently neglected hoop stresses. These are presented for the interbrace chord walls in planes I and II (see Fig. 3.2) of the 3-d CK models in Figs. 6.41 and 6.42. The relative magnitude of hoop stresses at weld toes are roughly proportional to the axial load in the nearest brace, suggesting that hoop stresses are less sensitive than meridional stresses to the different joint geometries g' and θ . In such complex configurations of loading and geometry as exists at the toes of the $\theta = 90^\circ$ and 60° braces ($\phi = 90^\circ$ and 120° respectively), hoop and meridional stresses are almost of equal magnitude. This would not be the case at the heel where hoop stress is approximately the product of Poisson's ratio and the meridional stress.

The hoop strains measured by gauges would not be negligible at these positions. If the hoop strains were ignored the errors in the value of i) weld toe SCF and ii) extrapolated shell SCF at the different positions are given in Table 8.1.

8.2.6 Comparison Between Hoop and Maximum Principal Stresses in Saddle Planes

A further complication to the determination of extrapolated hot-spot stresses occurs in the saddle planes III to VI (Fig. 3.2) near inclined braces in multibraced CK type joints. Irvine (6) suggests that hot-spot stresses are evaluated from maximum principal stresses in these planes. If $\theta \neq 90^\circ$, principal stresses in the outside surfaces of the chord wall near to weld toes do not lie in the saddle planes. This is due to changes in direction of the principal stress trajectories from the hoop direction in the chord to an axial direction in the brace; an angular difference of $|90-\theta|^\circ$. The situation is further complicated at saddle toe positions by the close proximity of other inclined braces. Here σ_1 is orientated towards the axis of the nearest brace. The result is that extrapolated values of hoop stress K_s are smaller than corresponding values of σ_1 , K_{s1} .

At these positions it is usual for hot-spot stresses at chord weld toes to be determined from hoop stresses because these act normal to the run of a weld. The hoop values, obtained by cross gauges, are less than maximum principal values, obtained by gauge rosettes, for distances up to $1.5T$ from weld toes. The differences were measured and are expressed in terms of $\eta = K_s/K_{s1}$ given in Table 8.2.

Table 8.2 shows that values of K_s/K_{s1} for the smallest brace spacing ($g'/T < 1$) are strongly influenced by the proximity of other braces. For $g'/T > 1$ the hoop stress values are not much smaller than K_{s1} values for $60^\circ \leq \theta \leq 135^\circ$, i.e. $\eta > 0.91$. The values of η for $\theta = 150^\circ$ are lower. If hoop strains, obtained from line gauges only, had been used to calculate K_s the under-prediction would have been worse, e.g. $K_s(\text{hoop values only})/K_{s1} = 0.73$ for $\theta = 150^\circ$ and $g'/T = 3.00$.

8.3 Discussion on Stress Concentration Factors

In the assessment of results in this work the separation of peak, shell and notch SCFs is essential. The different effects on SCFs of global tube geometry (θ , ψ , ω and g) and weld profile (r , α , H and h) are discussed separately.

8.3.1 The Effects of Tube Geometry on Shell SCFs

Shell bending stresses arise because of the need to maintain compatibility of chord bending displacement between crown and saddle positions and between adjacent braces in close or remote proximity for a particular brace inclination. In the 3-d CK models, the presence of unloaded braces in close proximity to loaded braces significantly affected the stress distributions and hot-spot stresses in the loaded fillets. Structural behaviour may therefore be the result of a complex maldistribution of load due, not only to the relative stiffness of the saddle and crown positions but also due to the restraint on the freely deforming chord of the (relatively) rigid unloaded brace stub. This is shown by considering the differences in the values of K_{sc} between toe (near to other braces) and heel (remote from other braces) positions of 3-d models. See Figs. 6.54 and 6.57. At the toe position, crown and saddle chord SCFs K_{sc} depend on brace spacing g' . At the crown toe, the opposite brace stresses due to balanced loading of adjacent braces increase the stress gradients in the chord and this increases K_{sc} there.

These results affect the definition of an 'isolated' brace. API (7) states that in a simple, non-overlapped K node, if offset $e > D/4$ the joint should be considered as several independent braces. For the tube and weld parameters used in this work, this corresponds to $g'/T = 2.67$ in the crown plane of the 90° and 135° braces. It can be seen from Fig. 6.54a that the value of K_{sc} for $\psi = 90^\circ$ at $g'/T = 2.67$ is not equal to

K_{sc} at the remote position where $g'/T = 40$. Brace interaction is therefore significant in some cases when $e > D/4$.

Also at the toe, the crown brace values (Fig. 6.54b) appear to be independent of brace spacing and brace inclination, but the saddle brace values (Fig. 6.57b) are not. At the saddle positions, values of K_{sb} are typically in the same order as K_{sc} (except for $\theta = 150^\circ$ at $g'/T < 2$) because chord wall bending moments are consistently distributed in the brace wall. At the crown positions there is no obvious relationship between K_{sb} and K_{sc} .

At the remote heel position, the crown chord SCF K_{sc} (Fig. 6.55) is approximately proportional to $\sin^2\theta$, the brace inclination. The variation of the crown brace SCF K_{sb} with θ is more complicated. It appears to be the result of two separate effects peculiar to tubular joints. The first is the result of moment distribution between chord and brace walls. It is shown that chord walls are predominantly in bending and the stresses are proportional to $\sin^2\theta$. Because carry-over stresses are a function of τ , brace wall stresses are also proportional to $\sin^2\theta$. The second effect is maldistribution of brace load caused by the increased stiffness of the tube at the heel. As brace angle decreases the brace wall opposite the heel is more flexible and attracts less load. Heel stresses in the brace are therefore greater at small angles of θ . The effect is null at $\theta = 90^\circ$.

8.3.2 The Effect of Weld Profile on Maximum and Shell SCFs

8.3.2.1 Maximum SCFs

The reductions in maximum SCF that may be achieved by weld profiling by design or by weld toe parameter control are shown in Figs. 6.51 to 6.53. The benefits of controlled weld profiles are summarised in Fig. 8.1 for the three different positions studied using 2-d photoelastic models.

For each joint, in which T and τ only were varied, $\eta' = K_{(c)}/K_{(u)}$ i.e. controlled weld SCF divided by uncontrolled weld SCF. Reductions in SCF are shown to be greater at saddle (where surface stress gradients are steeper) than at crown positions. A dramatic thickness effect, however, is seen at the crown where η' reduces rapidly for $T > 64$ mm. This may be explained by the severe weld profile ($\alpha_c = 70^\circ$) and small toe radii ($r = 0.01T$) often encountered at this position. This is not found at the saddle where $\alpha_c < 45^\circ$, as recommended by Marshall (43) for the controlled profile.

The reductions in maximum SCF with respect to weld toe radii for uncontrolled and fully blended profiles are shown in Fig. 6.53. In the expression $K = A(r/T)^j$, the exponent j for fillet welds is approximately $-\frac{1}{4}$ at the saddles, and $-\frac{1}{3}$ at the crown; the values apparently independent of weld angle α_c . Values for the constant A obviously include shell stresses. The large differences in the values of A and j between fillet and fully blended profiles show that the two types of weld shapes must be treated separately even though individual parameters (e.g. r and H) may be similar.

The effect of weld toe grinding on SCF and stresses near the ground zone are given in Table 3.6 and shown in Fig. 6.31. The increase in SCF with depth p is roughly proportional to the square of the residual chord wall section modulus, i.e.

$$K \text{ (with grinding)} = f \left[\frac{(T-p)^2}{T} \right]^2$$

The stress distributions show a rapid decrease in stress near the end of the ground profile. The results verify that, in the determination of a hot-spot stress, strains (or stresses) measured at the recommended ECSC position (6) of $0.2\sqrt{rt}$ ($= 0.35T$ in this work) would not be affected by the extent of weld toe grinding used in this work.

8.3.2.2 Shell SCFs

The shell SCFs obtained from 3-d CK models were for nominally similar weld size at each position on the model, i.e. brace leg $h = t/\sin \phi$ and chord leg $H = 0.375T/\sin \phi$. There was no quantifiable effect on K_s of weld leg length. The 2-d model results given in Fig. 6.60 and 6.61 show it is important to state where K_s was measured because reductions in weld size increases the value of K_{sc} . This would be expected from the surface stress distribution. Uncontrolled weld profile design leads to variations in the magnitude of K_{sc} (at chord toe) of 10% to 25% in the permitted range of H/T . The effect is exaggerated by the changing cross-sectional properties of the chord wall caused by a shift of the neutral axis as the size of the weld fillet reduces.

It should be noted that the usual assumptions regarding shell factors in assumption 1 in Section 8.3.1 do not define the position of K_s ; if it refers to the weld toe, it must depend on the size of the weld (H or h). Fig. 6.61 shows that the range of weld sizes permitted by API rules leads to significant variations of K_s , qualifying assumption 2 in Section 8.3.1.

8.3.3 The Effect of Weld Profile and Position on Notch SCFs

Notch stresses are associated with the highly localised surface deformations in the vicinity of the weld toe. They are primarily a measure of the severity of toe geometry and are therefore presented in terms of toe radii and local weld angle. The results suggest that notch effect is not only a function of toe geometry but is also dependent on the location on the joint at which it is measured. The magnitude of K_n for similar values of r/t (or r/T) in joints of different wall angle is significantly affected by the local stress distribution. Fig. 6.29 shows that progressively "dressing" a weld changes the stress distributions near a weld toe and the value of K_n in the fillet. The reductions in

K_n with respect to weld toe radii for the uncontrolled and fully blended profiles are shown in Figs. 6.64 and 6.65. In the empirical expression $K_n = 1 + B(r/T)^k$, the exponent k varies with α_c and position. At the saddles, there are insufficient data to explain the values of B and k . At the crown, results from the finite element models in which $\alpha_c = 48^\circ$ and 72° suggest both B and k increase in proportion to a function of $\sin \alpha$. However there are insufficient data to quantify these trends.

Using F.E. methods to study fillet welded T and X joints (not tubulars) with $\alpha = 45^\circ$, Lawrence et al (41) expressed the notch-root stress in terms of toe radii to wall thickness as follows:-

$$K = B(r/t)^k + 1$$

where $B = +0.35$ (axial load) and $+0.19$ (bending)

$$k = -0.5$$

These results are in broad agreement with this work where the above load cases are combined.

In the variation of K_n with weld toe radii and position, saddle results (Fig. 6.66a) are separated from crown values (Fig. 6.66b) because of the different stress gradients at these positions. The saddle K_n values are lower than corresponding crown values, but both show K_n proportional to r/t or r/T .

In conclusion, notch SCFs increase with decreasing fillet radius to wall thickness ratio r/T (see Fig. 6.64 and 6.65), and increasing weld angle α (see Figs. 6.63 and 6.66). Weld leg length has almost no influence on K_n when r/T is constant. This qualifies assumption 3 in Section 8.3.1. Assumption 4 is qualified by the significant differences in K_n between the crown and saddle position of the same brace in which the predominant variable was fillet radius (Fig. 6.66).

8.4 Relationship between Surface Stress Distributions and Strain Gauge Positions and Types

Continuous surface stress distributions provide:

- i) the gradients of linear stresses required in the extrapolation of true shell SCFs,
- ii) the positions of the ends of the linear regions at which points stresses used in two-point linear extrapolations would yield the same hot-spot SCF as obtained in (i), and
- iii) show which stresses, i.e. hoop and/or meridional are important in the determination of shell SCFs.

These items are the basis for the following discussion and recommendations for the instrumentation of 3-d CK type tubular joints.

8.4.1 Notch Zones

These are important in the determination of consistent extrapolated hot-spot SCFs because gauges should not measure notch affected strains. Notch zones increase with increasing α and decreasing r/T . They are not affected by weld leg length - the notch zone is shifted along the tube surface equal to the increase in H . Notch zones also decrease with brace gap when $g'/T < 1$ to 2. Most values for notch zone measured in this work did not exceed the ECSC recommended distance $0.2 \sqrt{rt}$ for the position of the strain gauge nearest to weld toes.

8.4.2 Recommendations for Strain Gauge Positions in CK Type Tubular Joints

8.4.2.1 Crown toe positions

Instrumentation of the outside chord surface between co-planar braces would be difficult where $g'/T < 0.71$ if a useful stress distribution was required to determine K_S . Line gauges may be used because hoop strains

are small and the crown plane is a principal plane. Little (18) showed that gauges may be placed up to one chord wall thickness either side of the crown plane with negligible error in peak fillet stress.

For brace gap values in the range $3 < g'/T < 6$, stresses are affected by proximity even when the axial offset (e in Fig. 3.1) exceeds $D/4$. In these positions, the ECSC recommended gauge distances $0.2 \sqrt{rt}$ and $0.4^4 \sqrt{rtRT}$ from a weld toe are acceptable, for any wall angle ψ , in the determination of K_s .

It is also suggested that the parameter g'/T is used to characterise interbrace chord wall SCFs; the effect of e/D is global and less significant for the tube geometries ($\gamma = 12.5$, $\beta = \tau = 0.5$) used in this work.

8.4.2.2 Crown heel positions

Chord wall stress distributions show well defined notch zones, which do not exceed $0.33T$, and small stress gradients. The regions of stress linearity were between $0.33T$ and $1.8T$ for $30^\circ < \psi < 90^\circ$. Weld-toe hoop stresses were found to be significant mostly at $\psi = 60^\circ$ and 90° where cross (T or X) gauges should be used.

8.4.2.3 Saddle toe positions

The presence of a non-planar brace significantly affects chord wall hoop stresses at the saddle between two non-planar braces. The most important position is at $\theta = 90^\circ$ for $g'/T \approx 1$. For $g'/T = 0.64$, stress linearity is difficult to define, but is taken to exist between $0.05T$ and $0.3T$. In ^{long?}reality, both braces ($\theta = 90^\circ$ and 60°) would probably be loaded, limiting the linear stress region to approximately $0.2T$. At this spacing, single gauges (2 mm length) would be required to obtain a reliable value of K_s .

For greater gap separation, e.g. $g'/T = 3.44$, chord hoop stresses are affected by the curvature of the tube. Near to the $\theta = 90^\circ$ brace stress gradients vary slowly between $0.36T$ and $1.1T$ from the weld toe.

Two-point extrapolation of stresses from gauges placed in this region would give differences in the value of K_S of about 5%.

8.4.2.4 Saddle heel positions

Chord hoop stresses decay more slowly at the saddle heel of each brace than at the saddle toe because the heel is isolated from other braces. Regions of stress linearity extend near to the points of contraflexure; for $\theta = 90^\circ$, this is $0.8T$ to $1.25T$, and for $\theta = 60^\circ$, it is $1.2T$ to $1.6T$. Cross gauges should be used because meridional strains cannot be ignored. Notch zones do not exceed $0.25T$. For $\theta < 60^\circ$, gauge rosettes are required to establish the directions and magnitudes of principal hot-spot stresses because the inclination ϕ of σ_1 (see Figs. 6.39 and 6.40) are significant up to $1T$ from weld toes.

8.4.3 Errors in Shell SCFs from Arbitrary Strain Gauge Positions

The determination of hot-spot SCFs K_{HS} by two-point linear extrapolation methods is important at saddle positions where stress gradients vary slowly from the end of the notch zone ($0.25T$ to $0.36T$) to between $1.1T$ to $1.6T$ from weld toes. (In the crown positions, regions of stress linearity are mostly well defined and these errors are small.) In Fig. 8.2a, two strain gauges are positioned at distances X_a and X_b from the weld toe. In Fig. 8.2b ordinates are drawn at the centres of the gauges to intersect a principal stress distribution curve obtained from a photoelastic model at the remote $\theta = 90^\circ$ saddle position. These ordinates provide the points required for K_{HS} . The best tangent drawn to the linear region of the photoelastic stress distribution provides K_{S1} , the true shell SCF.

In Fig. 8.2c, K_{HS} is compared to K_{S1} for a possible range of strain gauge positions. The broken lines limit the positions where gauges can be located; the smallest distance between the centres of 3 mm cross gauges

is 8 mm. For a typical 2 in thick chord wall $X_b - X_a > 0.16T$. The nearest gauge to the weld should not be located in the region of notch stress; $x_a > Z_c = 0.25T$ in this example.

The curves show the possible under-prediction of maximum principal hot-spot stress when X_a exceeds the notch zone and X_b exceeds the region of stress linearity.

8.5 Quantitative Analysis of Plastic-Elastic Strains using Moire

Fringe Patterns

Informative data on the behaviour of models or materials can be obtained from the moire fringe patterns alone. Fringes are very sensitive to changes in strains in inhomogenous materials; Fig. A2.5 shows smaller strains in HAZs than in the weld or parent plate. Sudden changes in fringe direction are a feature of deformations in anisotropic or different materials. Fringe patterns show slip planes associated with plasticity. Rapid changes in fringe gradient of up to $10^4 \mu\epsilon/\text{mm}$ were detected over distances in the order of 0.3 mm.

One of the main difficulties in the interpretation of fringe patterns is coping with the directions and magnitudes of shear strains and rigid body rotations, which are not separable in one pattern alone. Anticlockwise rotation of N_x fringes, and clockwise rotation of N_y fringes indicate clockwise rotations in the model. Only when the two fringe patterns are considered can shear strains be distinguished from total rotations.

8.6 The Effect of Plastic-Elastic and Residual Plastic Strains on Design

8.6.1 Use of Plastic-Elastic Surface Strain Distributions

In the discussion on the prediction of SCFs from stresses obtained by strain gauges, the possibility of the nearest gauge to the weld toe

measuring plastic strains was not considered. The surface strain distributions given in Figs. 6.75 to 6.82 show plasticity was confined to about $0.14T$ from the toe, i.e. less than half of $0.2\sqrt{rt}$, and should, therefore, never be measured. However, yielding influences strains beyond the plastic regions. The effect on shell SNCFs, given in Table 6.6, is a 30% increase in controlled welds and, up to 16% decrease in uncontrolled welds. The implications are that large plastic strains at weld toes could reduce surface strains at gauge positions remote from the weld and cause an under-prediction of the extrapolated hot-spot strain concentration factor.

The plastic-elastic strain distributions show that behaviour cannot be predicted using elastic values alone. Despite the greater elastic SNCF at weld toes, first yield was usually observed near the HAZ/plate boundary where tensile test results gave about 30% lower yield strengths (see Fig. 4.19) than in the HAZ or weld metal.

At greater loads, the positions of maximum strains in the uncontrolled welds reverted back to weld toes. A localised plastic hinge resulted. Plastic zones progressed more rapidly through the thickness than in the surfaces of the model. The controlled profile reduced localised plastic hinge effects and greater regions of plastic-elastic strains (of smaller magnitude) resulted.

§.6.2 Residual Plastic Strains and Plastic Reversal

The residual and plastic-elastic strain distributions gave principal strain ranges $\Delta\epsilon_1$ in the model for a mean axial load in the brace wall of $\sigma_{nom} = 7$ to 200 N/mm^2 . The strains were plotted on the same axes to show the reductions - hatched in Figs. 6.79 to 6.82.

In Figs. 6.83 to 6.86, these reductions of $\Delta\epsilon_1$ are compared with principal elastic response strains ϵ_1^e . The results show that the strain range $\Delta\epsilon_1$ near weld toes is not equal to the product of the elastic SNCF

and load range; the difference is ϵ^P . This could be overlooked in fatigue design if strain range is computed from elastic SNCFs and load range.

Table 8.1

Error in Meridional Weld Toe and Shell SCF if Chord Wall Hoop Strains are Ignored in Crown Plane of CK Models for $g'/T \approx 3$

Crown Plane Fig. 3.2	Brace		Position Fig. 3.1	SCFs		$\frac{K_t^m}{K_t}$	$\frac{K_s^m}{K_s}$
	θ	ϕ		K_t	K_s		
I	135°	45°	Heel	+1.85	+1.05	1.07	0.96
		135°	Toe	+3.90	+3.77	1.02	0.82
	90°	90°	"	+1.50	+0.14	0.82	-0.67
		90°	Heel	+2.90	+1.92	0.84	0.97
II	150°	30°	Heel	+0.80	+0.50	0.97	1.05
		150°	Toe	+2.90	+2.40	1.16	1.19
	60°	120°	"	+2.37	+1.61	1.02	0.80
		60°	Heel	+1.66	+1.00	0.81	0.95

K_t = weld toe SCF obtained from meridional and hoop strains

K_s = shell SCF ditto

K_t^m = K_t obtained from meridional strains only

K_s^m = K_s ditto

Table 8.2

Comparison between Principal and Hoop Shell SCFs

g'/T	$\theta = 90^\circ$		$\theta = 60^\circ$		$\theta = 135^\circ$		$\theta = 150^\circ$	
	K_{s1}	η	K_{s1}	η	K_{s1}	η	K_{s1}	η
0.57	-	-	2.05	0.63	-	-	0.92	0.00
0.64	4.60	1.00	-	-	2.80	0.59	-	-
3.00	-	-	2.45	0.95	-	-	2.00	0.81
3.44	3.45	1.00	-	-	2.65	0.91	-	-
6.00	No result		3.15	0.99	No result		1.47	1.03
48.0	1.78	0.95	1.15	0.98	1.25	0.96	1.15	0.75

$$\eta = K_{sh}/K_{s1}$$

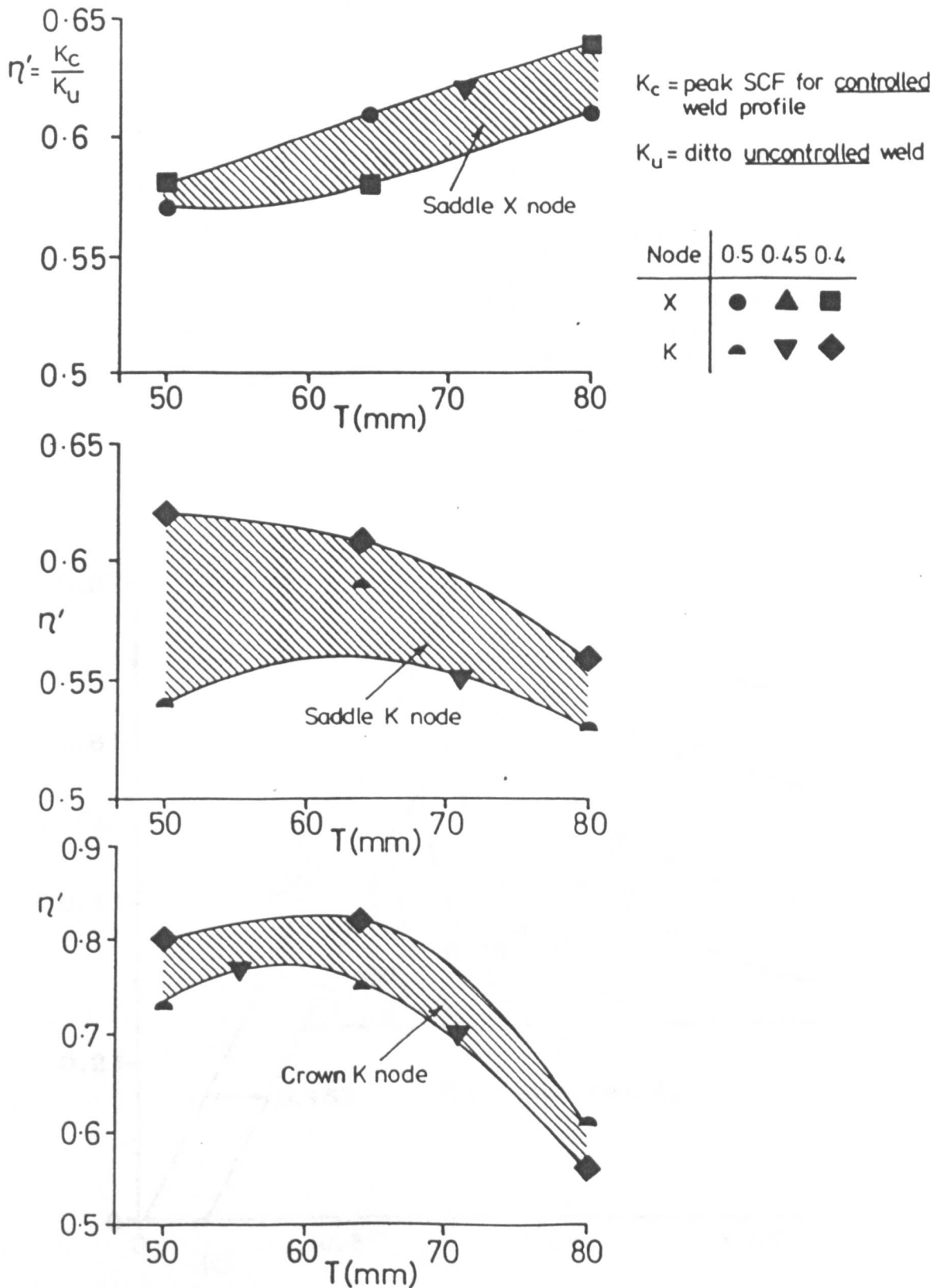


Fig. 8.1 Effect of Wall Thickness on Ratio of SCFs in Controlled and Uncontrolled Weld Profiles

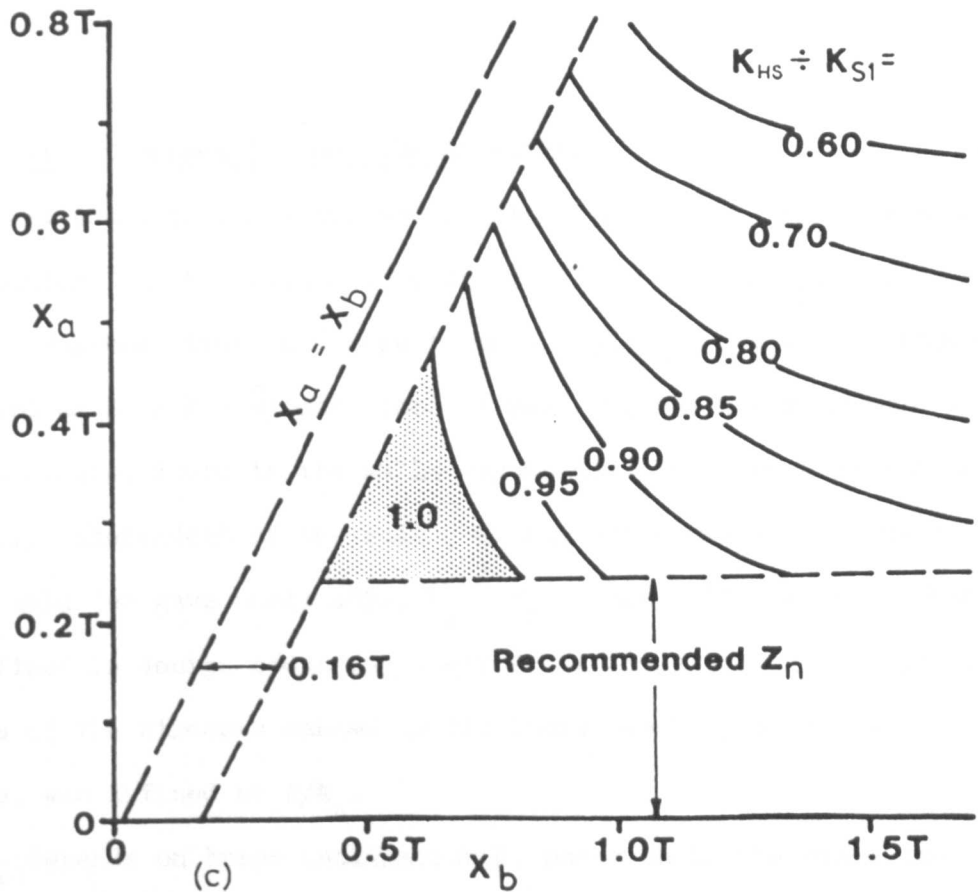
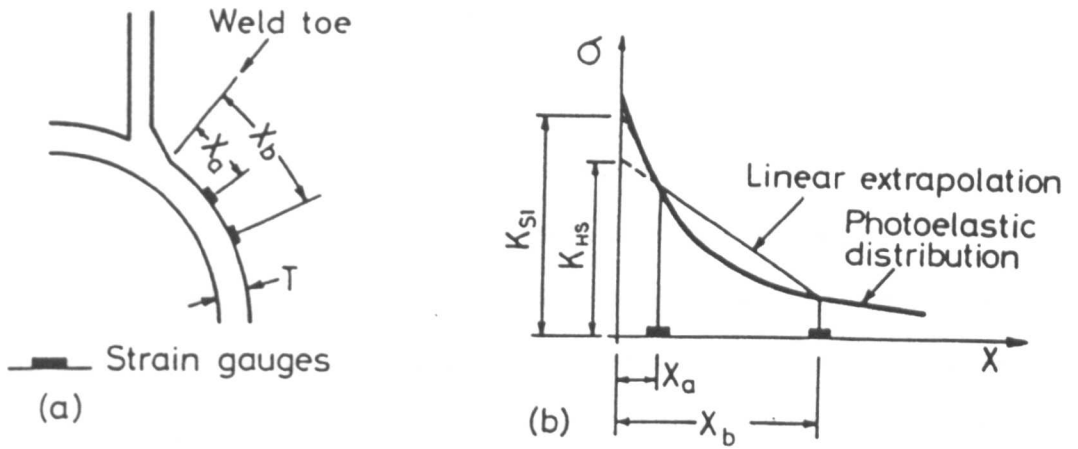


Fig. 8.2 Under-Prediction of Hot-Spot SCFs due to using Two Strain Gauges Outside the Linear Range at Saddle Heel for $\theta = 90^\circ$ in CK Models

CHAPTER 9CONCLUSIONS9.1 Synopsis of This Work

An experimental study determined elastic stresses and plastic-elastic strains near to weld toes in certain types of welded tubular joints used in offshore structures. Photoelastic and finite element methods gave elastic values. A moire interferometer was designed and built to study plastic-elastic and residual plastic strains in real weldments. Reflection photoelasticity was also used to determine plastic-elastic strains but was not found to be a suitable technique for this work.

9.2 Elastic Stresses in 3-d Tubular Joints

Small scale photoelastic models gave continuous surface stress distributions in the walls and welds of corner K and X type tubular joints. Maximum stresses $\hat{\sigma}$ were found in the weld toe fillet arcs and expressed as SCFs $K = \hat{\sigma}/\text{mean brace stress}$. Linear distributions of surface stress, found in the walls remote from weld toes, were shown to be nearly independent of the weld. Linear extrapolation of these stresses to the weld toe gave shell SCFs, K_s . K_s is compatible with the hot-spot SCF defined in design codes of practice. A notch SCF, K_n , which is a measure of the stresses caused by the local severity of the weld toe profile, was defined as K/K_s .

K_s depends on brace inclination θ , position in the brace-to-chord intersection, i.e. dihedral wall angle ϕ , brace gap g , wall thickness ratio τ , and weld size, H .

In the CK joints - with τ and H nominally constant - $K_{s(\max)} \approx 4.6$ was found at the chord weld toe in the saddle plane for $\theta = 90^\circ$ and $g/T \approx 1$. At the remote positions (where g is unimportant) crown values at chord weld toes were proportional to $\sin^2\theta$ and saddle values were nearly independent of θ because all ϕ were equal. In the X joints, $K_{s(\max)} = 8.15$ (brace toe) and 7.65 (chord toe) occurred in the saddle plane for $\theta = 90^\circ$, $\tau = 0.5$ uncontrolled weld profiles ($H \approx 0.18T$). A 15% reduction in chord values was measured using controlled weld profiles ($H \approx 0.4T$). In the crown planes where shell stress gradients were small, weld profile had little effect on K_s . Thus, K_s also depends on surface stress gradients.

The distances to the commencement of linear stress regions were measured from weld toes and called notch zones Z_n . In the chord walls Z_n depend on g and weld angle α .

K_n depends on weld toe radius r , α and H . There was considerable scatter in K_n in CK joints because the values were obtained in different positions and were affected by local surface stress gradients. Other models were used to study notch stresses.

9.3 Elastic Stresses in 2-d Joints in the Planes of Symmetry in Tubular Joints

2-d photoelastic and finite element models gave surface stresses in weld toe fillets. Empirical expressions for K_s and K_n with respect to r , α , and H were determined. SCFs in models with identical weld shapes were affected by position (crown or saddle) and type of joint (K or X).

For particular tube geometry, the variation in K and K_n with weld toe radii approximated to

$$K = A(r/T)^j \quad \text{and} \quad K_n = 1 + B(r/T)^k$$

The value of A and B decreased with α in uncontrolled fillets, and was smallest in fully blended welds. The exponents j and k , which

represent the rate of change of a SCF with r/T , were greatest in fully blended welds. This was attributed to the greater shift in the position of $\hat{\sigma}$ in these welds.

Notch factors were also found to be related to weld angle by

$$K_n = 1 + v \sin 0.5 \alpha_c ; \text{ with } r/T \text{ constant.}$$

It was found that the angular position of $\hat{\sigma}$ occurred at $\varphi \approx 0.5\alpha$ in the weld toe fillet. The relationship for K_n implies that, where r/T is constant, SCFs depend on the position φ of $\hat{\sigma}$, rather than α .

Through thickness distributions of σ_1 in the chord wall radial to the weld toe fillet showed an exponential notch stress decay for depths of up to $0.08T$ from the position of $\hat{\sigma}$ in the surface. Linear distributions, called geometric stresses were measured up to $0.15T$ from the surface. Notch and geometric stresses were affected by weld shape and size; the rates of decrease in stresses i) increased with larger α and smaller r/T , and ii) were greater for smaller H/T .

The depth of the through-thickness notch zone Z_y was consistently in the range $0.06 < Z_y/T < 0.08$ (for constant r). These are smaller than surface notch zones.

9.4 Plastic-Elastic and Plastic Residual Strains

Elastic, plastic-elastic and plastic residual strain distributions were obtained in the surfaces and through the thickness of steel Y joints manufactured to offshore specifications. They were tested using reflection photoelasticity and moire interferometry methods. The latter was used to detect the onset of yielding and measure strains in the range 0.002% to 2.0%.

First yield usually occurred in the surface of the chord wall at the interface between the parent plate and HAZ. At typical values of brace stress (used in jacket design, i.e. 180 to 200 N/mm^2) plastic-elastic

SNCFs of between 13 and 17 were measured in models in which the corresponding elastic values were 3.6 and 4.6, respectively. Residual strain distributions showed plastic reversal was present in the HAZ and weld metal, but was not always present in the parent plate.

In the interior of the model, i.e. depths in the chord of between 0.05T (2.5 mm) and 0.20T (10 mm) plastic slip (or Luder's) bands were identified in the moire fringe patterns. Because moire interferometry is a high-sensitivity experimental technique, strain gradients could be measured at the interfaces of the bands. Gradients of $10^4 \mu\epsilon/\text{mm}$ were typical.

It is thought that the results from this work are the first (in the U.K.) measurements of plastic-elastic and residual plastic strains at weld toes in steel joints that have been manufactured and tested in a manner which simulates the behaviour of a brace-to-chord connection. Moire interferometry has a wide, potential application in the study of plastic-elastic, residual welding and residual plastic strain determination, defect assessment and crack initiation periods. However, the author does not claim that the 3-d plastic-elastic behaviour of a tubular joint can be deduced from these results.

9.5 The Contribution of this Work to Offshore Structures Research Programmes

This work has formed part of the Cohesive Research Programme into the Fatigue of Offshore Structures. The programme was funded by the Department of Energy, Trade and Industry and the Science and Engineering Research Council. The studies, which have been carried out at five U.K. universities, have dealt with residual welding stresses, geometry and weld profile effects, stiffened joints and crack growth in air, biologically active environments and sea water.

The relevance of this work in the Cohesive Fatigue Programme (and other co-operative ventures) is that the effects of multibrace tubular geometry, and weld shape and size which are largely unknown and overlooked in fatigue design, can be considered in the interpretation of hot-spot methods, residual stress fields and (possibly) crack initiation data. The continuous surface stress distributions in the tube walls and the weld are an important illustration of the relative magnitudes of shell and notch stresses - those which are considered in fatigue analysis and those ignored.

9.6 Recommendations for Future Work

One of the main deficiencies in the design rules against fatigue failure concerns the methods of extrapolation of hot-spot SCFs when more than one brace influences the stress distributions. 3-d photoelasticity is ideally suited to study this phenomenon but the present work has only started this study. The extents of linear stress distributions should be further investigated in multibrace tubular joints in which the important (varied) geometric parameters are i) inclinations of adjacent braces ii) brace gap separations in meridional and circumferential planes, and iii) tube diameter ratio β . Typical shapes envisaged are corner KT joints in which brace inclinations are different and the circumferential brace gap is varied by changes in β , or by changes in the circumferential angle between the braces.

There is now a wide scope for work, using moire interferometry methods, in studying plastic-elastic behaviour in models of steel or other materials. A current topic for discussion is the effect of weld quality, i.e. profile, material properties, flaws, undercut, etc. on fatigue crack initiation life. This work has established the procedures to measure plastic strains. It is therefore suggested that further

plastic-elastic investigations are made on specimens with various profile qualities subjected to fatigue loading. The effectiveness of improvement techniques, such as toe grinding, TIG dressing and hammer or shot peening should be studied to assist in the interpretation of recent UKOSRP II data as assessed by Godfrey and Hicks (72).

APPENDIX 1A1 Photoelastic Measurement of 3-d X90 Model

A problem was encountered in the photoelastic measurement of the X90 model. A stress-frozen edge effect, approximately 0.3 mm deep, was observed in the slices cut from the model. The effect was a permanent increase in (tensile) fringe order of between +0.5 and +0.7 fringes/mm; too large to be ignored. A region of photoelastically dead material 0.06 to 0.08 mm deep, called rind, was also observed in the edges. The problem was diagnosed as secondary curing during the stress freezing cycle caused by a faulty thermostat on the temperature control unit under reading the temperature by about 5°C. The maximum stress freezing temperature would therefore have been 140°C. The result of this was that true stresses in the edges of the model could not be measured directly in the surfaces. Thus, maximum principal surface stresses were obtained in the walls by linear extrapolation, to the edges of the model, of through-thickness values. Marston (21) showed that within 0.2T of the edges of tube walls, fringe orders were proportional to $(\sigma_y - \sigma_x) \approx \sigma_y$ (because σ_x and τ_{xy} were small when $y < 0.2T$) and stress gradients $\partial\sigma_y/\partial x$ were linear (see Fig. 4.28b)

The positions, values and linear extrapolations of chord wall fringe order measurements in the saddle planes are shown in Fig. A1.1. Similar exercises were carried out in all other planes.

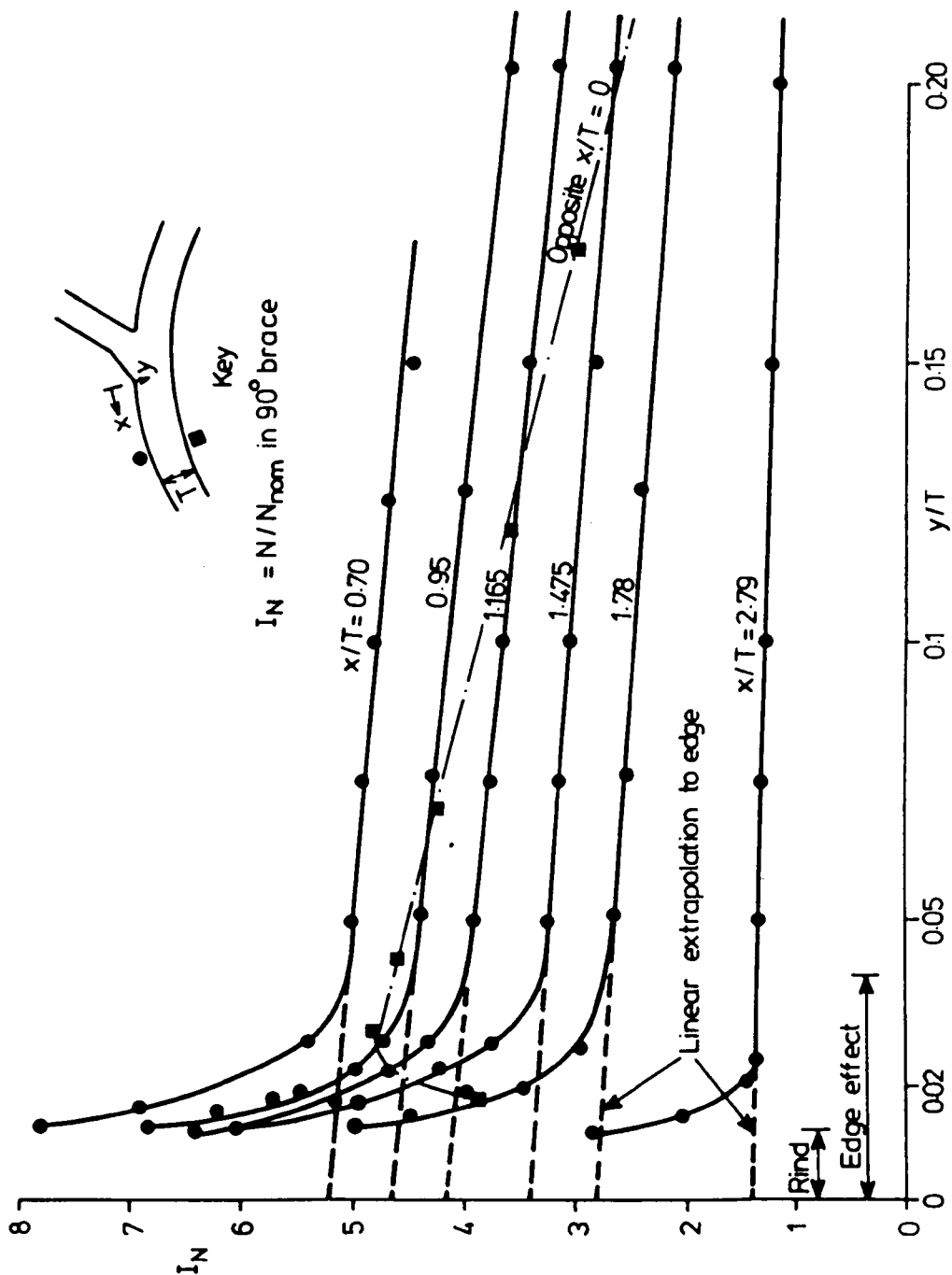


Fig. A1.1 Measurement of Fringe Order Index, I_N in Edges of 3-d Model X90 from Through-Thickness Readings

APPENDIX 2

A2 Illustrative Example of Determination of Strains from Moire

Fringe Patterns

Moire fringe patterns shown in Figs. A2.1 to A2.12 were obtained in the testing of steel model No. 2, on as-welded, $\psi = 120^\circ$ joint with an uncontrolled weld profile. Fringe patterns N_x and N_y are presented in the sequence of loading to show the development of elastic, plastic-elastic and residual plastic strains. These were deduced from differences in the measurement of moire fringe gradients in the loaded and unloaded (or initial) model fringe patterns.

Initial fringe patterns (Fig. A2.1) are the result of out-of-plane imperfections in the surface of the model grating and the carrier patterns of extension added to the 'best' null fields obtainable in each plane. (Refer to Section 4.2.5). In all fringe patterns, carrier gradients were subtracted from field fringe gradients (shown in the Figures) to give true model fringe gradients.

Elastic strains were obtained from differences in model fringe gradients determined in the elastic (Fig. A2.2) and initial (Fig. A2.1) fringe patterns. Similarly, strains at first yield (Fig. A2.3), plastic-elastic strains (Fig. A2.5) and residual plastic strains (Figs. A2.4 and A2.6) were obtained.

Increases in direct strains were identified by increases in fringe gradients perpendicular to the lines of the grating, i.e. no rotation of fringes. Shear strains and rigid body rotations were identified by changes in fringe gradients parallel to the lines of the grating. In the N_x fields, anti clockwise fringe rotation indicates clockwise deformations in the model; it is vice versa in the N_y fields. Because of this, rigid body rotations manifest themselves in the fringe patterns as fringe rotations - equal and opposite in magnitude. They were therefore eliminated in the addition of fringe rotations when obtaining shear strains.

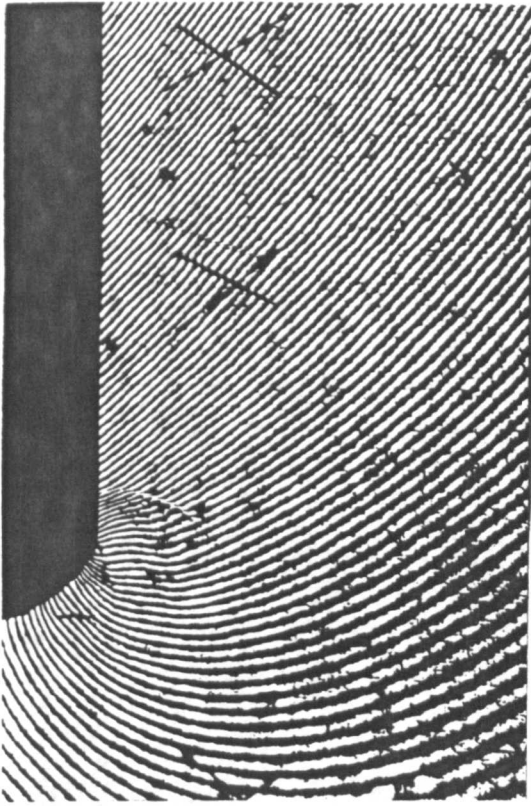


Fig. A2.3a First Yield Field $\epsilon_{nom}/\epsilon_y = 0.28$

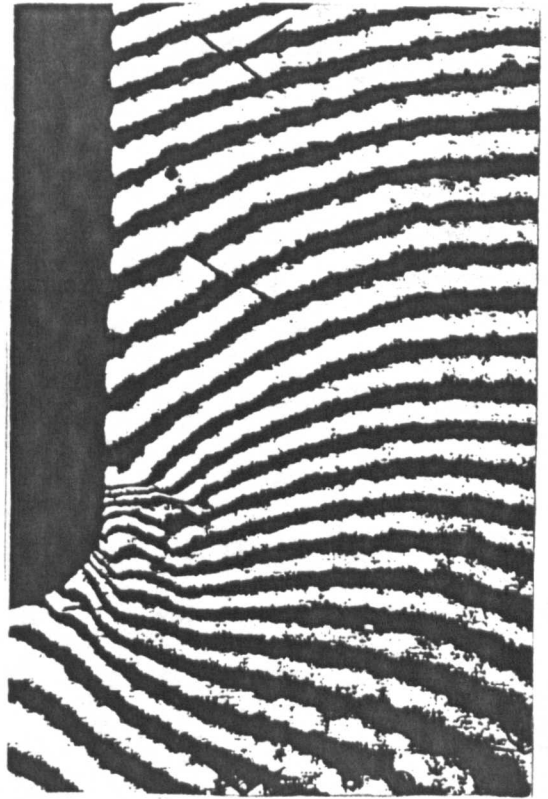


Fig. A2.4a Residual Field $\epsilon_{nom}/\epsilon_y = 0.2$ after 0.28

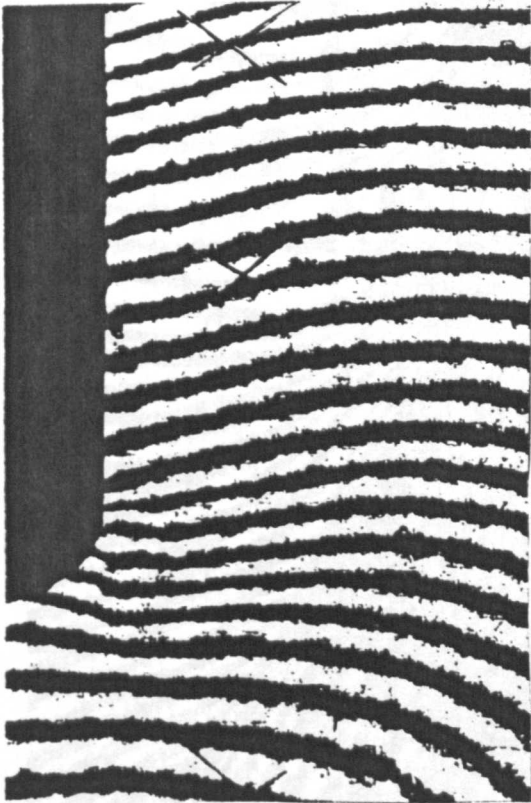


Fig. A2.1a Initial Field $\epsilon_{nom}/\epsilon_y = 0.02$

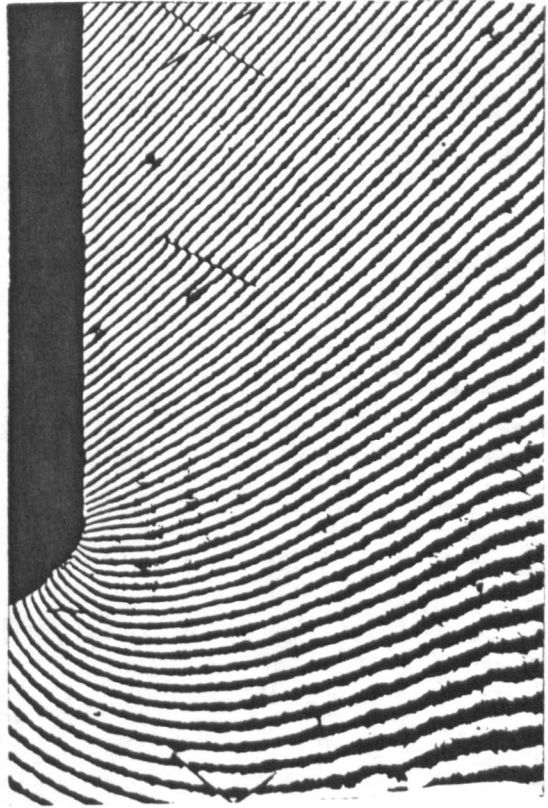


Fig. A2.2a Elastic Field $\epsilon_{nom}/\epsilon_y = 0.19$

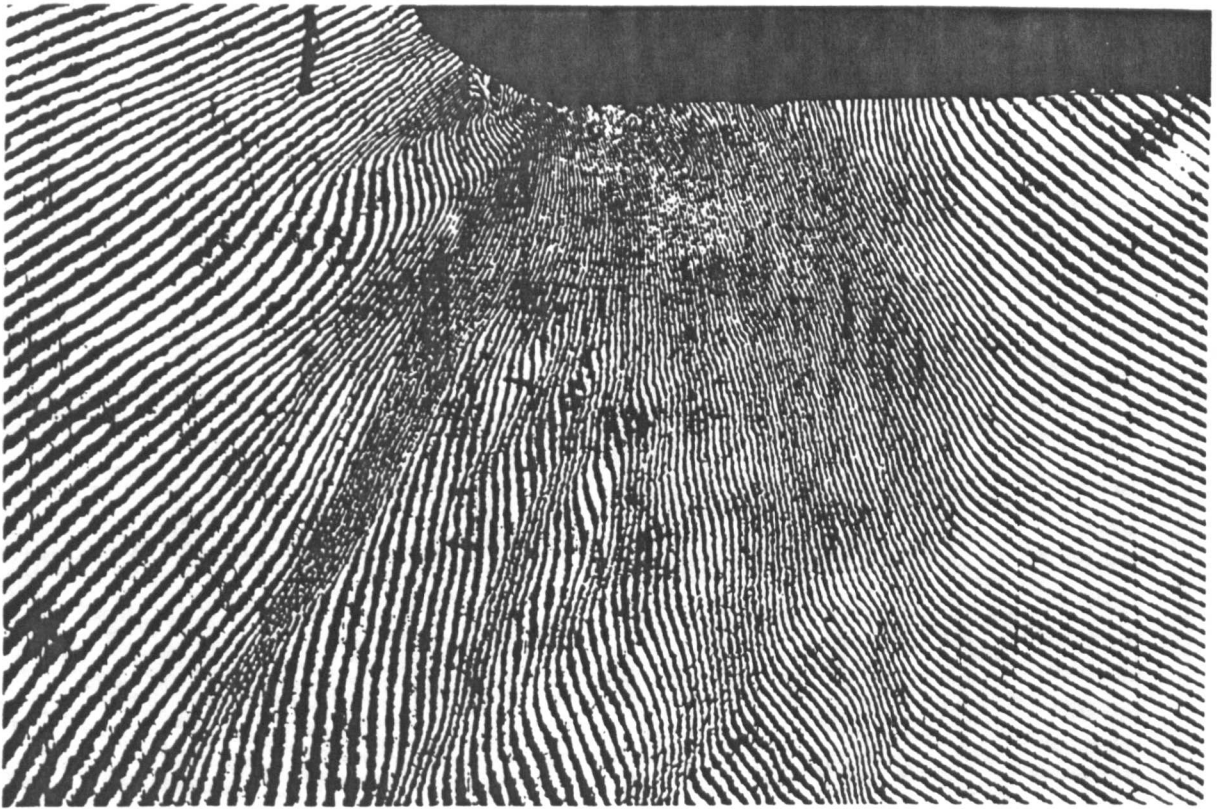


Fig. A2.5a Plastic-Elastic Field, $\epsilon_{\text{nom}}/\epsilon_y = 0.53$

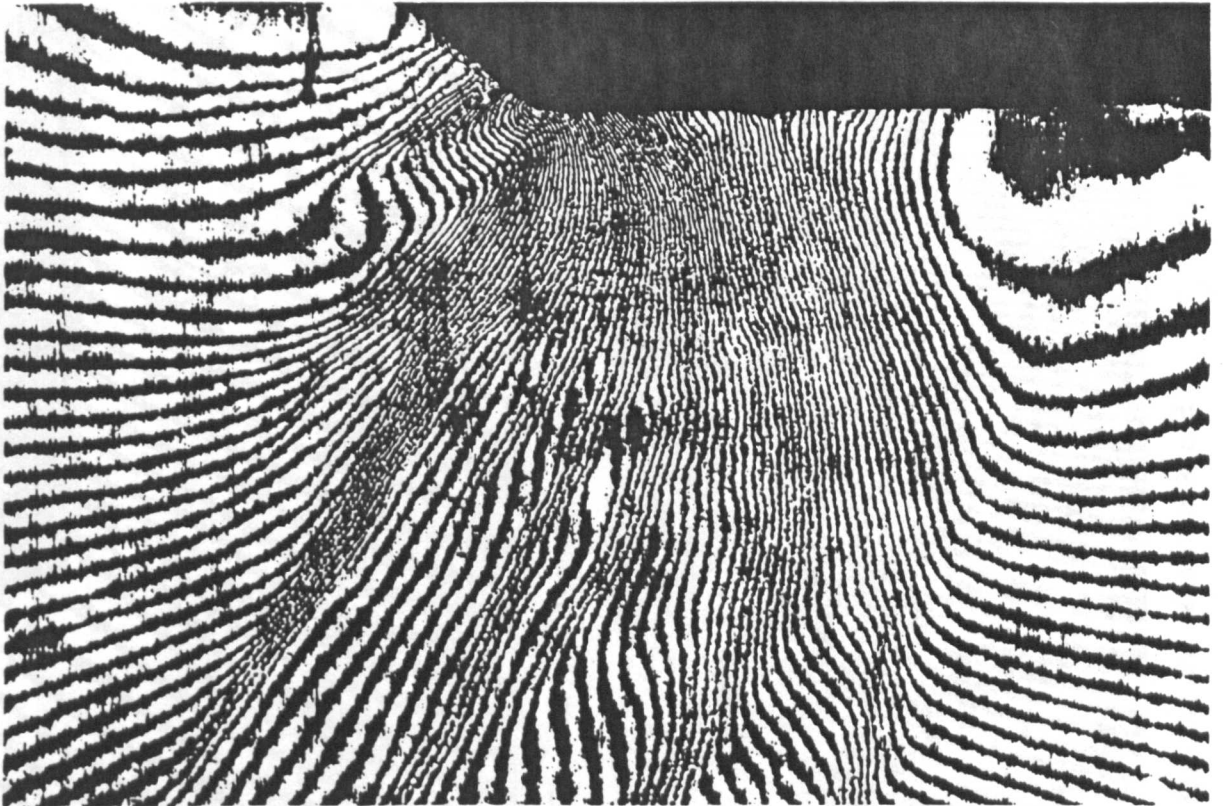


Fig. A2.6a Residual Plastic Field, $\epsilon_{\text{nom}}/\epsilon_y = 0.02$ after 0.53

Moiré N_x Fringe Patterns Near Chord Weld Toe in Steel Model No. 2

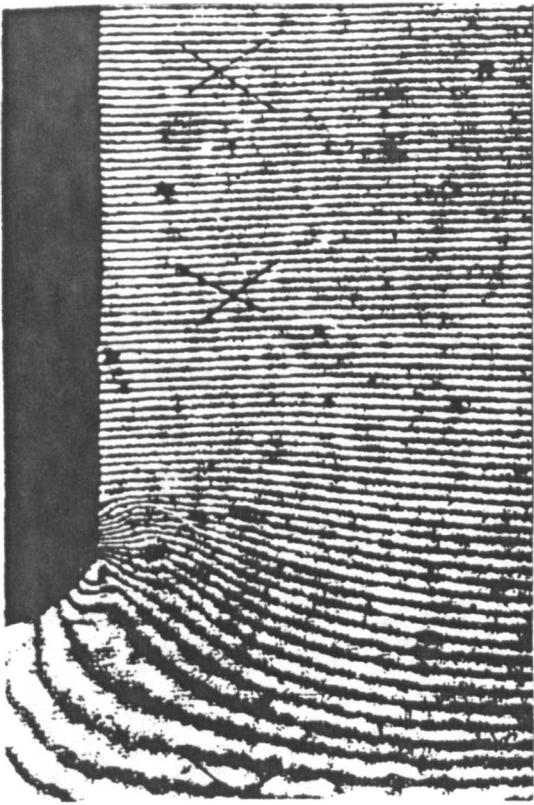
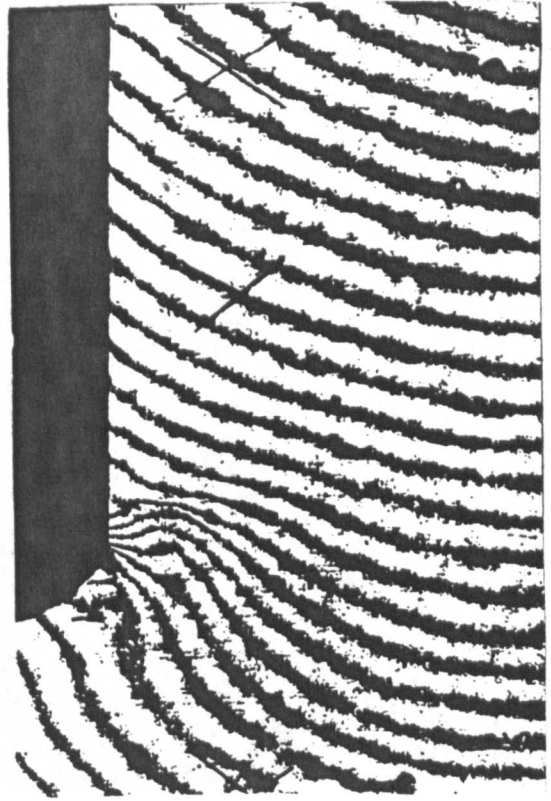


Fig. A2.3b First Yield Field $\epsilon_{nom}/\epsilon_y = 0.28$



A2.4b Residual Field $\epsilon_{nom}/\epsilon_y = 0.02$ after 0.28

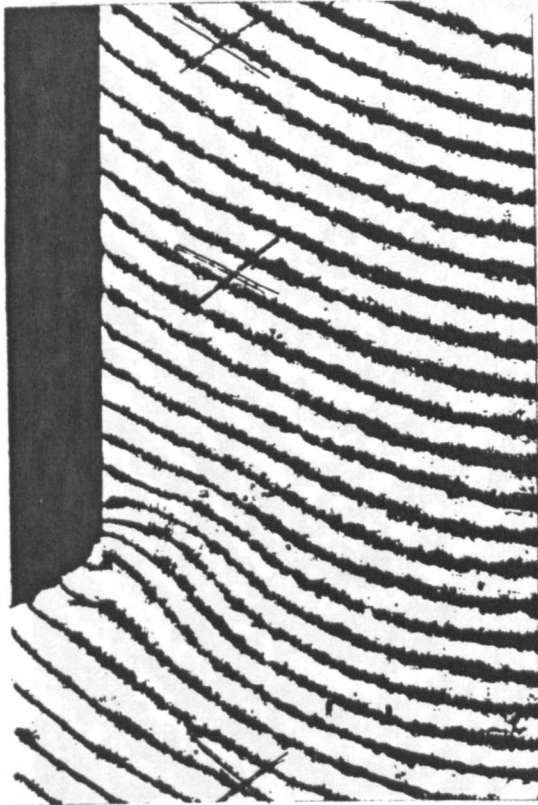


Fig. A2.1b Initial Field $\epsilon_{nom}/\epsilon_y = 0.02$

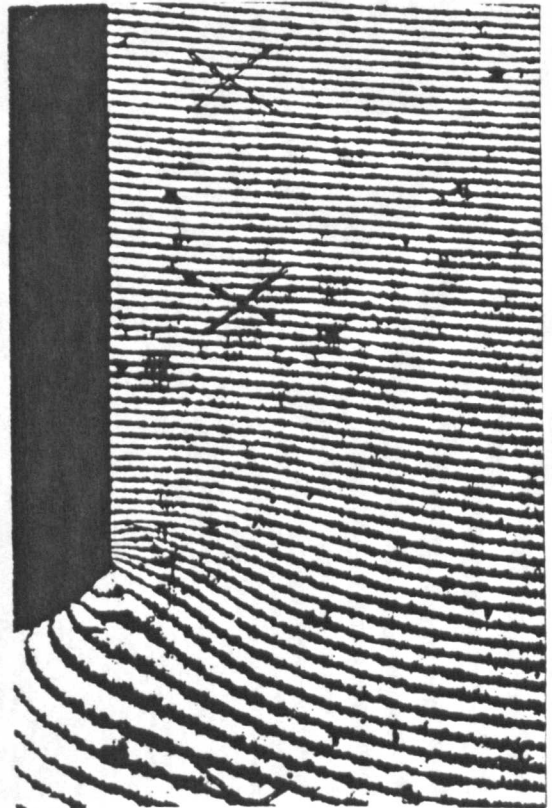


Fig. A2.2b Elastic Field $\epsilon_{nom}/\epsilon_y = 0.19$

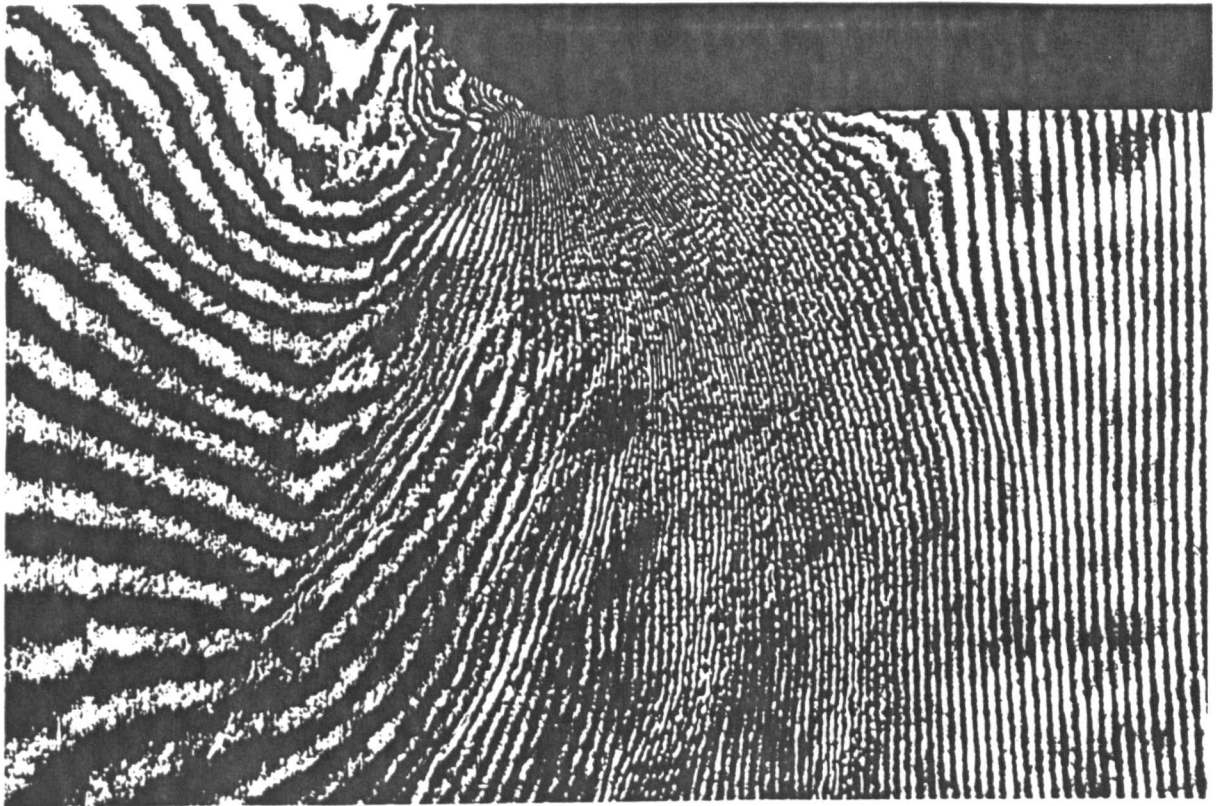


Fig. A2.5b Plastic-Elastic Field, $\epsilon_{\text{nom}}/\epsilon_y = 0.53$

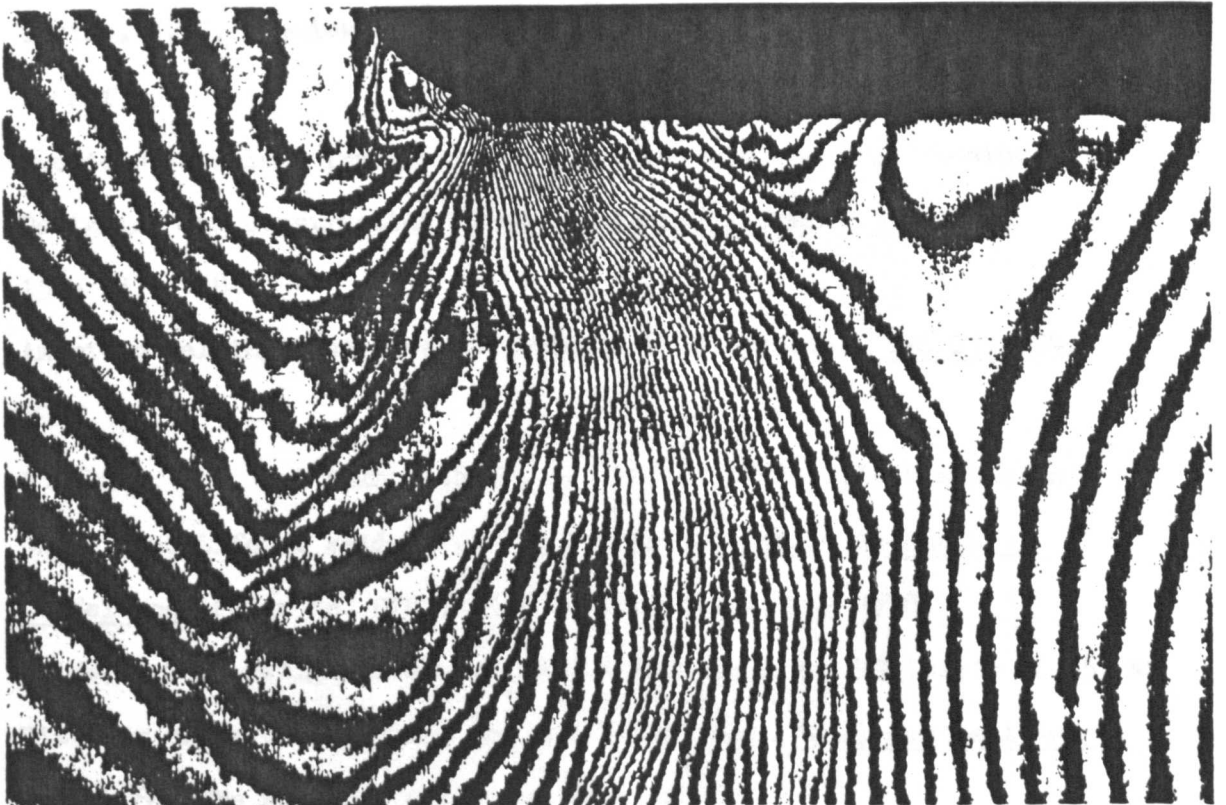


Fig. A2.6b Residual Plastic Field, $\epsilon_{\text{nom}}/\epsilon_y = 0.02$ after 0.53

Moire N_y Fringe Patterns near Chord Weld Toe in Steel Model No. 2

REFERENCES

1. McDonald, A., Brown, G. and Kerr, J., The Influence of Geometrical and Loading Parameters on the Fatigue Life of Tubular Joints. Paper 10.2. Int. Conf. Steel In Marine Structures, Paris, 1981.
2. Cotton, H.C. Welded Steel for Offshore Construction. 15th John Player Lecture, Proc. I.Mech.E., Vol. 193, 1979.
3. Wylde, J.G. and Iwasaki, T., Corrosion Fatigue Tests on Welded Tubular Joints. QMAE, New Orleans, U.S.A., Feb. 1984.
4. Potvin, A.B., Kuang, J.G., Leick, R.D. and Kahlich, J.L., Stress Concentrations in Tubular Joints, SPE Journal August 1977.
5. Wordsworth, A.C., Stress Concentration Factors at K and KT Tubular Joints. Conf. on Fatigue In Offshore Structural Steel, I.C.E., London, Feb. 1981.
6. Irvine, N.M., Review of Stress Analysis Techniques used in UKOSRP. As Ref. 5.
7. American Petroleum Institute, Recommended Practice for Planning, Designing and Constructing Fixed Offshore Platforms, API RP2A, 15th Ed., 1984.
8. American Welding Institute, Structural Welding Code. AWS D1.1-84; 1984.
9. Bouwkamp, J.G. and Mukhopadhyay, A. Effect of Tensile Overstrain on Fatigue Life of Welded Tubular Joints. Offshore Technology Conference, Paper No. OTC 3255, Houston, Texas, May 1978.
10. Wylde, J.G., Fatigue Tests on Welded Tubular K and KT Joints of 457 mm Diameter under Out-of-Plane and Axial Loading. Final Contract Report 3612/4/84, The Welding Institute, July 1984.

11. British Standards Institution, Code of Practice for Fixed Offshore Structures, BS6235, 1982.
12. U.K. Department of Energy, Offshore Installations: Guidance on Design and Construction, HMSO, 1984.
13. Bouwkamp, J.G., Recent Trends in Research on Tubular Connections. Journal of Petroleum Technology, Nov. 1966.
14. Bouwkamp, J.G., Cyclic Loading of Full Size, Tubular K Joints. SPE Journal, April 1978.
15. Gulati, K.C., Wang, W.J. and Kan, D.K.Y., Analytical Study of Stress Concentration Effects in Multibrace Joints Under Combined Loading. Offshore Technology Conference, Paper No. OTC 4407, Houston, May 1982.
16. Little, W.J.G., Fessler, H. and Shellard, I.J., Elastic Stresses due to Axial Loading of Tubular Joints with Overlap. 2nd Int. Conference on Behaviour of Offshore Structures, BOSS'79, London 1979.
17. Fessler, H. and Little, W.J.G. Fillet Stresses in Tubular Joints Obtained by Photoelastic Techniques, Proc. Int. Symposium on Integrity of Offshore Structures, Glasgow, April 1978.
18. Little, W.J.G., The Effect of Overlap on the Stress Distributions in K and KT Type Tubular Joints. Ph.D. Thesis, University of Nottingham, 1982.
19. Ohtake, F. et al. Static and Fatigue Strength of High Tensile Strength Steel Tubular Joints for Offshore Structures, Paper No. OTC 3254, as Ref. 9.
20. Fessler, H. and Marston, E. A Micropolariscope For Automatic Stress Analysis, Journal of Strain Analysis, Vol. 22, No. 1, 1987.

21. Marston, E., An Automatic Micropolariscope; Its Design, Development and Use for Tubular Joint Stress Analysis, Ph.D. Thesis, University of Nottingham, 1985.
22. Frocht, M.M. Photoelasticity Vol. 2, Chapter 8, John Wiley, 1960.
23. Fessler, H. and Perla, M., Precision Casting of Epoxy Resin Photoelastic Models. Journal of Strain Analysis, Vol. 8, No. 1, 1973.
24. Wordsworth, A.C. and Smedley, G.F., Stress Concentrations at Unstiffened Tubular Joints. European Offshore Steels Research Seminar, Cambridge 1978.
25. Kuang, J.G., Potvin, A.B. and Leick, R.D., Stress Concentration in Tubular Joints. Offshore Technology Conference, Paper No. OTC 2205, Houston, Texas, 1975.
26. Gibstein, M.B., Parametric Stress Analysis of T Joints, Paper 26, European Offshore Steels Research Seminar, Cambridge, U.K. Nov. 1978.
27. Efthmiou, M. and Durkin, S., Stress Concentrations in T/Y and Gap/Overlap K-Joints, Proc. 4th Int. Conf. on Behaviour of Offshore Structures (BOSS '85), Delft, July 1978.
28. Liaw, C.Y., Litton, R.W. and Reimer, R.B., Improved Finite Elements for Analysis of Welded Tubular Joints, Offshore Technology Conference, Paper No. OTC 2642, Houston, Texas, May 1976.
29. Pan, R.B., Plummer, F.B. and Kuang, J.G., Ultimate Strength of Tubular Joints, Paper No. OTC 2644, as Ref. 28.
30. Marshall, P.W. and Graff, W.J., Limit State Design of Tubular Connections, Int. Conf. on Behaviour of Offshore Structures (BOSS '76) Norwegian Institute of Technology, Trondheim, 1976.
31. Buitrago, J., Zettlomoyer, N. and Kohlich, J.L., Combined Hot-Spot Stress Procedures for Tubular Joints. Proc. 16th Offshore Technology Conf., Paper No. OTC 4775, Houston, Texas, May 1984.

32. Back, J. de, Wardenier, J. and Kurobane, Y., The Fatigue Behaviour of Hollow Section Joints, Proc. 2nd Int. Conf. on Welding of Tubular Structures. Boston, Mass., July 1984.
33. Gurney, T.R., Fatigue of Welded Structures. Cambridge Univ. Press, 2nd ed., 1979.
34. Irvine, N., Comparison of Tubular Joint Stress Analysis Methods in the Near Weld Region. as Ref. 1.
35. Gibstein, M., Stress Concentrations in Tubular Joints; Its Definition, Determination and Applications. as Ref. 1.
36. Dover, W.D. and Connolly, M.P. Fatigue Fracture Mechanics Assessment of Tubular Welded Y and K Joints. Proc. Int. Conf. on Fatigue and Crack Growth in Offshore Structures. I.Mech.E., London, April 1986.
37. Atzori, B. and Pappalettere, C., SCFs for Welded T-Joints, 8th A.I.A.S. Conference, Cagliari, Italy, Sept. 1979.
38. Atzori, B., Blasi, G. and Pappalettere, C., Evaluation of Fatigue Strengths of Welded Structures by Local Strain Measurements, Experimental Mechanics, Vol. 25, No. 2, 1985.
39. Pappalettere, C., Stress Concentration Factors for Cruciform Welded Joints. Proc. SEM Spring Conference on Experimental Mechanics, Las Vegas, June 1985.
40. Atzori, B. and Pappalettere, C., Stress Concentration Factors for Cruciform Welded Joints with Lack of Penetration, 5th ASME Failure Prevention and Reliability Conference, Dearborn, Mi., Sept. 1983.
41. Lawrence, F.V., Ho., N.-J. and Mazumdar, F.K., Predicting the Fatigue Resistance of Welds. Annual Review Material Science, No. 11, 1981.
42. Burdekin, F.M., Chu, W.H., Chan, W.T.W. and Manteghi, S., Fracture Mechanics Analysis of Fatigue Crack Propagation in Tubular Joints. as Ref. 36.

43. Marshall, P., The Houdremont Lecture; Connections for Welded Tubular Structures, as Ref. 32.
44. Back, J. de and Vaessen, G.H.G., Effect of Plate Thickness, Temperature and Weld Toe Profile on the Fatigue and Corrosion Fatigue Behaviour of Welded Offshore Structures; Part II, ECSC Convention 7210-KG/601, Delft, May 1984.
45. Yoshida, K., Inui, T. and Iida, K., Behaviour Analysis and Crack Initiation Prediction of Tubular T-Connections, Offshore Technology Conference, Paper No. OTC 2854, Houston, Texas, May 1977.
46. Tiejun Chen and Shuiyun Wu, The Elastic-Plastic Finite Element Analysis of Tubular Joints of Offshore Drilling Platforms, Proc. 4th Int. Conf. on Behaviour of Offshore Structures (BOSS '85), Delft, July 1978.
47. UEG, Design of Tubular Joints for Offshore Structures, UR33, 1985.
48. Den Hartog, J.P. Strength of Materials, New York, McGraw-Hill, 1949.
49. Roark, R.J. and Young, W.C. Formulas for Stress and Strain. New York, McGraw-Hill, 1976.
50. Mockford, P.B. The Experimental Determination of the Flexibility of Tubular Joints in Offshore Structures. Ph.D. Thesis, University of Nottingham, 1985.
51. Fessler, H. and Edwards, D.E., Design and Stress Analysis of a light, cast 90° - 45° K Joint. Paper TS4.4, as Ref. 1.
52. Buchan, A., Fessler, H., Ollerton, E. and Wong, J., Stress Analysis of Cast Nodes, 1st Progress Report to DoEn, January 1986.
53. Fessler, H., Little, W. and Whitehead, P., Precision casting of Epoxy Resin Models using Expendable or Re-usable Moulds. 8th All-Union Conference of Photoelasticity, Tallinn, USSR, 1979.

54. Edwards, D.E. Design and Stress Analysis of Cast Tubular Joints. Ph.D. Thesis, University of Nottingham, 1983.
55. Eissa, M.H.M., Stress Analysis of Keyed Connections. Ph.D. Thesis, University of Nottingham, 1982.
56. Post, D., Moire Interferometry. SESA Handbook on Experimental Mechanics, Prentice-Hall Inc., 1986.
57. Ciba-Geigy Data Sheet; 'Araldite Epoxy Resins'.
58. Stanley, P., Basic Photoelastic Theory and Polariscopes Techniques, Methods and Practice for Stress and Strain Measurement, BSSM Monograph, 1979.
59. Durelli, A.J. and Riley, W.F., Introduction to Photomechanics. Prentice-Hall, 1965.
60. Heywood, R.B. Designing by Photoelasticity. Chapman and Hall, 1952.
61. PAFEC 75; Data Preparation Manual, PAFEC Ltd., 1978.
62. Dally, J.W. and Riley, W.F., Experimental Stress Analysis, McGraw-Hill Inc., 1965.
63. Fessler, H. and Eissa, M.H.M. The Photoelastic-coating Technique for Plastic-Elastic Contact. Experimental Mechanics. Sept. 1983.
64. Post, D. and Basehore, M.L., High-frequency, High reflectance, Transferable Moire Gratings. Experimental Techniques, 8, No. 5, May 1984.
65. Post, D., Private Communication, March 1987.
66. Edwards High Vacuum, Film Thickness Monitor Model, FTM⁴ Operation Manual.
67. Fessler, H., Mockford, P.B. and Webster, J.J., Parametric Equations for the Flexibility Matrices of Single Brace Tubular Joints in Offshore Structures. Proc. Inst. Civ. Eng., Part 2, 81, 1986.

68. Frocht, M.M. Photoelasticity Vol. I, John Wiley and Sons.
69. Dijkstra, O.D., Hartog, J., The Dutch Large Scale Tests, as Ref. 24.
70. Watkinson, F. et al., Fatigue Strength of Welded Joints in High Strength Steels and Methods for its Improvement. Fatigue of Welded Structures, The Welding Institute, Brighton 1970.
71. Clayton, A.M. Private Communications to Department of Mechanical Engineering, University of Nottingham, Aug. 1976 and March 1978.
72. Godfrey, P.S. and Hicks, J.G. Control of Fatigue Performance of Welded Joints by Attention to Profile and by Various Post-Weld Treatments. Proc. 3rd Int. ECSC Conference, Steel In Marine Structures, Delft, June 1987.

ACKNOWLEDGMENTS

I would like to acknowledge the people who have guided and assisted me in this work. Thanks are due to Professor H. Fessler for his guidance and timely comments in getting the best possible achievements out of me, and to Professor G. Warburton for extending to me the use of the department's facilities. I would thank also the department's technicians for their skilled and enthusiastic assistance; Messrs. B. Mynett, R. Pickard, P. Elson and, in particular, Mr. A. Higgins who manufactured several excellent 3-d photoelastic models. I am grateful to Dr. D. DeCogan and Mr. E. Inameti, in the Electrical Engineering Department, for their assistance in the use of the evaporation equipment, and to Mrs. Janis Henshaw who typed this thesis with barely an error.

This work has been jointly supported by the Marine Technology Directorate of SERC and the Department of Energy to whom I offer my thanks.